Acoustic propagation near porous and elastic boundaries

Thesis

Acoustic Propagation near Porous and Elastic Boundaries

Thesis submitted by

Stephen Tooms M.Sc.

for the degree of

Doctor of Philosophy

July 1990

Department of Engineering Mechanics
Faculty of Technology
Open University
Milton Keynes
England

Abstract

A model for predicting the response of a system composed of a fluid halfspace, overlying a porous ground layer, resting on an elastic halfspace, to incident plane waves, is developed to include further porous elastic layers within the ground. The dynamic properties of the porous elastic layers are modelled using a modified Biot formulation.

Using the same boundary conditions a Fast Field algorithm for Layered Air Ground Systems (FFLAGS) is formulated to predict acoustic propagation and acoustic-seismic coupling in the model layered system due to a point source in a horizontally stratified atmosphere. This is a full wave solution. Results are compared to those of existing propagation prediction methods. FFLAGS has been used to predict (i) the effects of temperature gradients on short range propagation over an asphalt like surface, (ii) sensitivity of received sound pressure levels to ground parameters for various atmospheric conditions, and (iii) the influence of ground parameters on acoustic-seismic coupling. Predictions of acoustic surface waves in the presence of an upward refracting atmosphere using Creeping wave theory and the FFP method have been shown to agree.

Dispersion equation based predictions of surface wave types have been assessed. It has been shown that the high velocity surface waves predicted by dispersion equation solutions on porous and elastic ground surfaces are not predicted to be excited by a point source. However several other surface wave modes have been predicted in layered systems, similar to those predicted in visco-elastic media.

The influence of ground elasticity on received sound pressure levels is examined. Measurable effects of elasticity of the surface are predicted for low density materials, and measured over a low density polyester foam.

Controlled experiments have been performed to study the effect of soil wetting on acoustic to seismic coupling. It is found that the observed effects can be modelled using FFLAGS.

"The ground flew up
and hit me in the hed."
Artemus Ward.

Acknowledgement

Firstly I would like to thank Dr Keith Attenborough for his encouragement and advice, his willingness to find me more time when I needed it, and his ability to find the means to send me to conferences and borrow equipment (even when I didnt use it). I would like to thank Dr Richard Raspet, Dr Jim Sabatier, Hendrick Schmidt and Dr Ken Gilbert for enlightening conversations, and Dr Charles Don and Dr Thomas Pritz for help and advice with experimental work. I would like to thank Craig Howorth for helping with experiments, David Berry, Dr Kai Ming Li, Yu Chen and Dr Jeanette Brooks for advice and providing a stimulating working environment, and Dr Nick Heap for reading this manuscript. Lastly I would like to thank Dr Heather Moore without whose support, advice, practical help and encouragement I could not have completed this thesis.

Contents

List of Figures

List of Tables

Chapter 1

Introduction

A well known phenomenon in outdoor sound propagation is ground effect, whereby there is interference between direct and reflected paths leading to a broad peak in the excess attenuation spectrum. The frequency location of this peak in the excess attenuation spectrum has been found to be very sensitive to the parameters describing the ground. The softer the ground, the lower the frequency of the peak. The frequency and height of this excess attenuation peak is also sensitive to the geometry used. In studies of outdoor sound propagation it has been conventional to employ as simple a model of the ground as possible. Hence in considering sound propagation over the ground surface it has been common to model the ground as a locally reacting impedance surface or as a rigid-porous structure. In studies of low frequency propagation [3] the ground is sometimes modelled as a perfectly reflecting surface.

It is well known that a buried microphone will give a response to a signal from an acoustic source. In studies of acoustic-seismic coupling it has been suggested that it is unnecessary to include the porosity of the ground surface [4]. On the other hand several studies of acoustic-seismic coupling [5] have considered it necessary to include both the porosity and the elasticity of the ground. Predictions have been made of the acoustic impedance of the ground using porous and elastic models which show marked effects due to the elasticity of the ground. However it has not been shown that these predicted elastic effects appear in measured normal surface impedances of

ground surfaces.

The main purpose of this thesis is to investigate the importance of different aspects of the ground model for predictions of acoustic propagation over the ground and of the coupling of acoustic energy into the ground, at short ranges (up to a few hundred metres). These aspects of the ground model are; the porous structure of the ground, and the elastic structure of the ground.

In order to carry out this task a Fast Fourier propagation model (FFLAGS) is developed in chapters 3 and 4 which incorporates a layered porous and elastic ground and a layered atmosphere. This model is formulated to include nearfield effects around a point source.

The excess attenuation predicted using this model is compared to predictions based on simpler propagation models in chapter 5.

In chapter 6 the influence of the porous structure of the ground on predicted acoustic to seismic coupling is examined by making comparisons of FFLAGS predictions to those of a propagation model including a visco-elastic ground, and those of an asymptotic approximation.

In chapter 7 the influence of both the porous and elastic nature of the ground on sound propagation is examined in the presence of atmospheric sound velocity gradients. Recent predictions of an acoustic surface wave at the interface with a linear sound velocity gradient [6] are investigated using comparisons between FFLAGS, another numerical (FFP) propagation model using a locally reacting ground model, and a residue series solution. Finally in this chapter predictions of a ray tracing model and FFLAGS are compared for a downward refracting sound velocity gradient.

In chapter 8 the influence of the elasticity of a surface on propagation over it is examined theoretically and compared to experimental results. This is done in the following way. The porous and elastic parameters of a polyester foam are measured directly using non-acoustic techniques. The excess attenuation over a rigidly backed layer of the foam is measured and compared to that predicted using rigid-porous and poro-elastic models of the foam. Also the effects of soil wetting on acoustic-seismic coupling are examined.

In chapter 9 two applications of the FFLAGS program are demonstrated. These are the prediction of surface particle velocity due to acoustic seismic coupling from a heavy vehicle (including both acoustic and seismic sources), and an examination of the importance of near surface sound velocity gradients in predictions of excess attenuation at short range over a highly reflective surface.

Chapter 2

Literature Review

2.1 Rigid porous models

Rigid porous models of the ground surface model the ground as a rigid solid structure containing pores saturated with a fluid (air). Acoustic propagation via the air in the pores is allowed, and the structure of the pores as it affects this propagation is then modelled to predict the effect on the received signal both above and within the porous structure. The air in the pores can be regarded as an effective fluid having a complex density and a complex propagation constant for acoustic propagation through the fluid.

If the propagation constant in the effective fluid is much larger than that in the fluid above it then the ground surface can be viewed as locally reacting [7]. In this case the ground surface may be modelled as an impedance surface with normal surface impedance given by an impedance model which assumes propagation in the porous solid is only normal to the surface. If the surface cannot be characterised as locally reacting then the propagation within the ground must be modelled . Morse and Ingard [7] showed that the fluid density and propagation constant in the pore fluid will both be complex because of the frictional loss, and gave equations for the complex fluid density ρ_c and acoustic wave velocity c_c in terms of the angular frequency ω, flow resistivity σ, and density ρ_f and velocity c_f in the unrestricted fluid,

$$\rho_c = \rho_p \left(1 + \frac{i\sigma}{\rho_p \omega}\right), \tag{2.1}$$

$$c_c = c_p \left(1 + \frac{i\sigma}{\rho_p\,\omega}\right)^{-1/2}. \tag{2.2}$$

One pore structure dependent parameter is used; flow resistivity σ. It is suggested that the value of ρ_p should be slightly greater than ρ_f, and that of c_p should be slightly less than c_f, but these relationships are not defined.

Zwikker and Kosten [8] developed a model for the effective density and effective compressional modulus of a fluid in a porous medium. This was done by making the assumption that the effective density could be calculated considering only viscous effects, and that compressional modulus could be calculated using only thermal effects. Zwikker and Kosten considered a straight circular tubular pore of radius a_o with its axis in the x direction. The tube is filled with a fluid of density ρ_o and has a pressure gradient along it's length. The viscosity of the fluid is η. The effective density was calculated as follows. The driving force on an annulus of the fluid due to the pressure gradient was equated to the viscous and inertial forces on the annulus;

$$-2\pi r\,dr\,dx\,\frac{dp}{dx} = \frac{\partial}{\partial r}(-2\pi r\eta\,dx\,\frac{dv}{dr})\,dr + 2\pi r\rho_o\,dr\,dx\,\frac{dv}{dt}. \tag{2.3}$$

This leads to a differential equation in the fluid velocity v in the x direction.

$$\frac{1}{\eta}\frac{dp}{dx} = \frac{d^2v}{dr^2} + \frac{1}{r}\frac{dv}{dr} + \frac{i\omega\rho_o}{\eta}v. \tag{2.4}$$

The solution for v is

$$v = \frac{1}{i\omega\rho_o}\frac{dp}{dx} + AJ_0((i\omega\rho_o/\eta)^{1/2}r). \tag{2.5}$$

The value of A is found by solution of the equation at the wall of the pore where $v = 0$. v is averaged over a cross section of the tube. The average value of v is

$$\bar{v} = \frac{dp}{dx}\frac{1}{i\omega\rho_o}\left[1 - \frac{2J_1(\mu\sqrt{j})}{\mu\sqrt{j}J_0(\mu\sqrt{j}}\right] \tag{2.6}$$

where $\mu^2 = \omega\rho_o o^2/\eta$. The effective fluid density ρ_c can be defined by

$$\frac{-dp}{dx} = \rho_c\frac{\partial\bar{v}}{\partial t} = -i\omega\rho_c\bar{v}. \tag{2.7}$$

Substituting in the equation for $\bar{v}$ gives

$$\rho_c = \rho_o \left[1 - \frac{J_1(\mu\sqrt{i})}{\mu\sqrt{i}J_0(\mu\sqrt{i})} \right]^{-1} . \tag{2.8}$$

The effective bulk modulus of the fluid in the same tube is now considered including only thermal effects. Taking the Boyle-Gay-Lussac Law for small variations;

$$p = p_0(s + (\gamma - 1)\theta') \tag{2.9}$$

(where s is the condensation $\delta\rho/\rho_o$, and $\theta' = \delta T/[(\gamma-1)T_o]$), and the thermal equation;

$$\frac{\partial\theta'}{\partial t} = \frac{\partial s}{\partial t} + \nu\nabla^2\theta' \tag{2.10}$$

where $\nu = \lambda/(\rho_o C_v)$, λ is the thermal conductivity of the fluid, and C_v is the specific heat capacity of the fluid at constant volume. The condensation can be eliminated from the two equations, leading to the differential equation;

$$\frac{\partial^2\theta'}{\partial r^2} + \frac{1}{r}\frac{\partial\theta'}{\partial r} + \frac{i\omega\gamma}{\nu}\theta' = \frac{i\omega p}{p_o\nu} \tag{2.11}$$

Applying the boundary condition that $\theta' = 0$ at the pore wall the solution is found

$$\theta' = \frac{1}{\gamma}\frac{p}{p_o}\left[1 - \frac{J_0(\sqrt{i\omega\gamma/\nu}r)}{J_0(\sqrt{i\omega\gamma/\nu}a_o)} \right] . \tag{2.12}$$

The condensation is then calculated by substitution of this result into equation 2.9. As for the velocity the condensation is averaged over the cross sectional area of the tube. The effective bulk modulus of the fluid k_c is defined by

$$k_c = \rho\frac{dp}{d\rho} = \frac{p}{s} = \gamma p_o \left[1 + \frac{2(\gamma-1)J_1(\mu\zeta\sqrt{i})}{\mu\zeta\sqrt{i}J_0(\mu\zeta\sqrt{i})} \right]^{-1} , \tag{2.13}$$

where $\zeta = \sqrt{\eta\gamma C_p/\lambda}$. These results have been simplified for low and high frequencies

Delaney and Bazley [9] developed a power law relationship between the ratio of frequency to flow resistivity, and normal surface impedance and propagation constant, using data measured over fibrous absorbants. These

empirical power law relationships were shown to agree well with the theory for propagation through tubular pores given by Zwikker and Kosten [8]. There is only one parameter (flow resistivity) describing the pore structure. These power law relationships have been widely used in characterising ground from acoustical measurements [10]. However the values of flow resistivity inferred from these measurements do not generally agree with the actual flow resistivity of the ground [11].

Attenborough [12] took a microstructural approach to the problem. He used as a basis for his model an examination of the fluid flow through a cylindrical pore due to Rayleigh, and a parallel sided slit as extremes of the pore cross sectional shapes. From Zwikker and Kosten [8] it is assumed that viscous and thermal effects can be treated separately.Examining only thermal effects, for a non-viscous conducting fluid a complex effective fluid density in the pores is derived for each of the extreme pore shapes, along with an effective complex compressibility. This is basically the work of Zwikker and Kosten [8], and Janse [13]. Examining only viscous effects a dynamic viscosity coefficient may be derived by assuming a non-conducting viscous fluid(as an alternative to complex density). This work is reported in Biot's paper on the subject [14]. All of these calculated complex variables are functions of the dimensionless parameters λ_c for circular pores, and λ_s for slit pores. λ_i (i being c or s) is related to the thickness of the viscous boundary layer.

$$\lambda_i = l\left(\frac{\omega}{\nu}\right)^{1/2} = \frac{m}{A}\left(\frac{\omega}{\nu}\right)^{1/2} \tag{2.14}$$

Where l is a characteristic pore dimension, m is the hydraulic radius, ν is the kinematic viscosity of air and A is m/l, being unity for slits and 0.5 for circular pores [12]. Attenborough then showed that after defining $\lambda_p = \lambda_i/n$ where n is a pore shape factor being 1.0 for circular pores, and 0.5 for slits, approximate equations for complex density and compressibility valid for both circular pores and slit like pores, could be derived.

$$/labelexa1\rho_p = \rho_0\left[1 - 2\left(\lambda_p\sqrt{i}\right)^{-1} T\left(\lambda_p\sqrt{i}\right)\right]^{-1} \tag{2.15}$$

$$C_p(\omega) = (\gamma p_o)^{-1} \left[1 + 2 \left\{ (\gamma - 1) \frac{T\left(N_{pr}^{1/2} \lambda_p \sqrt{i}\right)}{\left(N_{pr}^{1/2} \lambda_p \sqrt{i}\right)} \right\} \right] \tag{2.16}$$

where

$$T(x) = \frac{J_1(x)}{J_0(x)} \tag{2.17}$$

and $J_i(x)$ are Bessel functions of order i. Extending these results to a bulk medium introduces extra constraints. Real pores will not be straight and their tortuosity must be considered, pores are not all identical and will have differing tortuosities, cross sections and sizes. The pore parameters should be related to measurable bulk parameters. By using the relationship

$$\sigma = (8\mu q^2)/(l^2\Omega) = (8\mu q^2 A^2)/(m^2\Omega), \tag{2.18}$$

where q^2 is the tortuosity defined in the same way as Carman [15]. Attenborough then substituted for the hydraulic radius m in the equation for λ_p to produce:

$$\lambda_p^2 = \frac{2q^2 s\omega\rho_0}{n^2 A^2 \Omega\sigma} \tag{2.19}$$

From this it is possible to combine the dynamic pore shape factor n , the ratio A and the static pore shape factor s into a single pore shape factor ratio s_p. The tortuosity q^2 has been related to the porosity by the Bruggeman relation [16]

$$q^2 = \Omega^{-n'}. \tag{2.20}$$

The pore size distribution can be related to the pore shape factor ratio s_p [17]. For a log-normal pore size distribution,

$$e(r) = \frac{1}{\delta} \left(\frac{1}{2\pi} \right)^{1/2} exp \left[\frac{-(\Phi - \bar{\Phi})^2}{2\delta^2} \right] \tag{2.21}$$

,where $\Phi = -log_2(r)$ and $\bar{\Phi}$ is its mean value, the relationship between s_p and the standard deviation in the pore sizes δ is given by

$$s_p = 0.5 \quad exp[1.5(\delta . ln2)^2]. \tag{2.22}$$

Hence if the pores are all circular and of equal size $s_p = 0.5$. The propagation constant can be obtained from $\sqrt{\rho_c C_c}$ and the characteristic impedance of the material from $\sqrt{\rho_c / C_c}$.

2.2 Porous elastic models

Propagation in fluid filled porous elastic media has been examined since the late 1940s with regard to its applicability to geological problems. Biot introduced his theory of elastic wave propagation in two parts in 1956 [14]. This began by examining stress strain relations in an isotropic elastic porous solid containing a fluid. This showed that in the absence of dissipation the material could be described by four distinct elastic constants; two corresponding to solid Lame constants, one corresponding to the modified bulk modulus of the fluid and a fourth corresponding to a coefficient of coupling between the volume change in the solid, and that in the liquid.

The kinetic energy in the medium was described in terms of three mass coefficients; and via Lagrange's equations , equations of motion for dilatational, and rotational(shear) waves in the medium in the absence of dissipation were derived. It was shown that one rotational and two dilatational waves exist, and equations for their velocities were derived.

The derivation of the equations of propagation was then repeated including a dissipative term in the Lagrange equations, as a function of the velocity difference between the fluid and solid, and hence as a function of the frictional forces on the walls of the pores due to the viscosity of the fluid. Poiseuille flow in the pores was assumed, giving a simple form to the dissipative term. An approximate limiting frequency was then derived as a function of pore diameter and fluid viscosity above which Poiseuille flow breaks down.

In the second part of Biot's paper [14] the viscous forces on the pore walls were examined for two pore shapes (circular capilllary and parallel sided slit) at frequencies above that at which Poiseuille flow breaks down. It was shown that for flow at these frequencies a modified viscosity coefficient could be calculated which corrected for the non-Poiseuille flow.

Biot later [18] published a detailed derivation of the stress strain relations for porous elastic media. In the same paper the problem of the attenuation of waves due to movement of fluid into and out of cracks in the solid frame and the areas of intergranular contact were also considered.

In his next paper on the subject [19] the derivation of the equations of propagation was changed, and a 'viscodynamic operator' introduced, which included the effects of both the viscous forces and the inertial forces between solid and fluid, including the modified viscosity on the breakdown of Poiseuille flow. This altered the form of the equations of motion. Biot then went on to examine propagation through anisotropic porous elastic media and the problems involved in scale model tests to determine the viscodynamic operator experimentally.

Stoll [20] developed a theory of elastic wave propagation in porous media based on the work of Biot. Stoll attempted to include in the calculation of attenuation the effect not only of viscous forces due to the relative movement of solid and fluid, but also the effect of the movement of fluid into and out of the contact area between grains as the frame expands and contracts; in a similar way to that of Biot. Stoll also attempted to relate the fast longitudinal and shear velocities of a porous solid to the static stress on the solid. This could be related to depth of burial and hence theoretical velocity-depth relations were derived. Attenborough [12] examined the difference between his own model of propagation in rigid porous media and the rigid frame limit of the Biot model. He found that the viscodynamic operator only agreed with his equivalent function for cylindrical pores, and hence a modification of the Biot operator involving a pore shape factor ratio s_p as described in section 2.1 was necessary in order for agreement to be made for both cylindrical and slit like pores.

There have been several experimental tests of Biot's model. Plona [21] measured two compressional wave speeds and a shear wave speed in a water saturated porous structure of glass beads , for each of four samples of differing porosities. The faster compressional wave was comparable to the compressional speed of waves in the glass of the beads. The second compressional speed was less than that of sound in water. Berryman [22], using the self consistent theory [23,24] to calculate the elastic constants, showed that Plona's experimental results agreed to within ten percent with Biot model predictions of the three wave speeds for each of the four structures.

Ogushwitz [25] found reasonable agreement with Biot predictions for wave speeds and attenuations in fluid saturated materials ranging from sandstone to kaolinite suspensions.

Measurement of 'slow wave' propagation constants in soils and snow using probe microphones [26] have shown agreement with the predictions of the Rayleigh Attenborough rigid porous model which agrees precisely with the rigid frame limit of Attenborough et al's modified Biot Stoll model. Allard et al [27] showed that Biot's model for elastic wave propagation in porous materials was more self consistent than those of Rosin [28], Beranek [29] or Zwikker and Kosten [8]. Burridge and Keller [30] rederived the equations which govern the mechanical behaviour of a porous elastic solid due to doubt cast on the validity of the Biot equations by Cleary [31]. They found that their equations agreed precisely with Biot's when the dimensionless viscosity was small, and tended to the equations governing a visco-elastic solid when the dimensionless viscosity was of order one.

2.3 Acoustic-Seismic coupling

Acoustic-seismic coupling is the transfer of acoustic vibration in the air into vibration of the solid structure of the ground.

Acoustic-seismic coupling has been studied since the late 1940s [32] with regard to the effect on seismic reflection surveys of using airborne explosive sources. It had been found experimentally that for certain grounds the use of an airborne explosive source lead to reduced unwanted "ground roll" (mainly pseudo-Rayleigh wave) relative to that produced by underground explosive sources, and the ground roll that existed was of nearly single frequency. This made signal processing to remove the ground roll from the signals far simpler. By modelling the ground as a fluid layer overlying an elastic half-space it was found that coupling of acoustic energy into the ground roll occurred most efficiently at a frequency where the dispersive pseudo-Rayleigh wave had the same phase velocity as the airborne phase velocity, and this would explain the domination of the ground roll signal by

one frequency. Mooney and Kaasa [33] found that an appreciable amount of energy was transferred into the ground even when the above resonance condition could not be achieved.

Since then a military interest in acoustic-seismic coupling has developed, due to interest in the use of acoustic and seismic sensors in detection and security systems. Thus McCarty and Dalius [34] found (not surprisingly) that the air coupled seismic signal was much larger in amplitude than that produced directly from the vibration of the launch pad during the launch of a rocket. The air coupled seismic signal was also used in an attempt to detect distant rocket firings [35] Several experimental investigations have used arrays of geophones and microphones at various distances from sources emitting acoustic waves and mechanically isolated from the ground, and from vehicles constituting combined acoustic and seismic sources, over various ground surfaces in order to characterise acoustic coupling as a function of ground type. [36], [37], [38]

In the work by Bass et al [38] seismic coupling was investigated in the frequency band 20 to 300Hz. A loudspeaker was suspended a measured distance above the ground. The ground seismic structure was measured using standard seismic refraction techniques and hence a surface layer 5.3 to 6.9 metres deep was detected, with a lower seismic velocity than the substrate. The source signal was a swept frequency signal between 20 and 700 Hz. The receivers were microphones at heights between 0.0 and 2.0 metres, and geophones (with a linear response only up to 100Hz) buried at a depth of approximately 0.05m. The ratios of seismic particle velocity (vertical, radial, and transverse from a line through a point under the source) in the ground to acoustic pressure above the ground was recorded. It was found that these ratios exhibited peaks at certain low frequencies (less than 100Hz). Normal surface impedance of the ground was also measured,over a frequency range from 100Hz to 1kHz, and was fitted (very poorly) to a semi-empirical one parameter impedance model [9]. The frequency range over which the impedance was measured did not cover the valid range for the seismic coupling experiment (up to 100Hz). It was found that the peaks

in the seismic coupling coefficient altered in frequency when the height of the source was altered. It was also found that some of these peaks were near the frequencies predicted by a simple waveguide model [39], although for other peaks the alteration in frequency with height of source could not be explained by this simple model.

Bass and Bolen's [40] further experimental work on the subject included the measurement of the seismic structure of two ground surfaces, together with measurement of soil samples for bulk density and flow resistivity , and the use of probe microphones to measure the acoustic propagation in the soil. The acoustic-seismic transfer function was then measured and compared to the transfer function predicted by a single layer Biot type ground model. Agreement was reasonable, though much of the measured fine structure in the coupling could not be predicted, probably due to a combination of errors in the measurements and the simple model involved. Recently Sabatier [4] has suggested that in making predictions of acoustic-seismic coupling it is unnecessary to model the ground as poro-elastic. Instead the ground can be modelled as a visco-elastic layered medium incorporating a very low seismic velocity near surface layer. By altering the predicted near surface seismic velocities nearly identical results can be produced using both visco-elastic, and porous-elastic ground models.

2.4 Propagation models

To model acoustic propagation over and into a layered porous elastic ground under a (possibly layered) fluid half-space there are a few possible routes. Firstly it may be possible to derive an analytical solution. The alternative is numerical propagation models, of which there are several types available.

2.4.1 Analytic propagation models

Several workers have produced analytical models of propagation from a point source in air above a ground surface to a receiver in the air [41,42,43,44,45,46]. The method employed by Chien and Soroka [42], Donato [43], and Attenbor-

ough, Hayek and Lawther [44], for propagation over a rigid-porous halfspace, is the representation of the reflected field by a Hankel transform in horizontal wavenumber. This is changed into a contour integration where the integration path is deformed into one of steepest descent. The pole traversed by the deformation of the integration path is considered to give rise to a surface wave [47] and the integrand is approximated in various ways. Attenborough, Hayek and Lawther give two results, one less approximate than the other. Mechel [47] stated that higher order approximations such Attenborough et al [44] were prone to serious errors, and could be less accurate than the simpler approximations, giving Attenborough et al [44] as an example. It will be shown here that when compared to a numerical integration Attenborough et al's higher order approximation is the more accurate of the two presented.

Nobile and Hayek [46] derive an asymptotic series solution for propagation above a locally reacting halfspace and show good agreement between it and a direct numerical integration. Thomasson [41] models propagation above a rigid, non-porous backed porous layer and replaces the Bessel function in the Hankel transform by a second integration and transforms the variable of integration. The derivation makes a local reaction approximation, although a correction to give an extended reaction solution is given, but not in an easily calculable form. Attenborough [48] has shown that Thomasson's formulation is identical to Rudnick's [49] with Chien and Soroka's correction [42]. Nicholas, Berry and Daigle [50] use the more approximate of the two extended reaction solutions given by Attenborough, Hayek, and Lawther [44], but replace the surface impedance and reflection coefficient at the surface of the lower halfspace by their non-porous backed thin layer equivalents.

Acoustic pressure within a rigid porous medium under a fluid halfspace containing a point source has been modelled by Brekhovskikh [51], Paul [52,53], and Richards, Attenborough et al [54]. Paul [52,53] considers the field in both media, but the solutions he produces in the lower medium are very complex in the first paper [52] and in the second he fails to take account

of the pole in the complex wavenumber plane. Brekhovskikh [55] does not go into detail in his explanation, he models the ground as a fluid and hence does not explicitly consider the inclusion of the complex refractive index at the surface in detail. Richards, Attenborough et al [54] use a steepest descent method to obtain the velocity potential of the pore fluid in the porous medium. The method includes the effect of the pole, which leads to a surface wave.

Attenborough and Richards [48] model solid particle motion in a porous elastic solid halfspace under a fluid halfspace containing a point source. Starting from a Hankel transform representation , the Bessel function is replaced by a Hankel function, the variable of integration transformed, and the integration limits modified . Only the contributions from branch points, saddle points, and poles in the complex horizontal wavenumber plane are calculated, ignoring contributions from the remainder of the integration path.

These analytical propagation models have usually been shown to produce consistent results where they can be compared. One of the main problems with the analytical approach to modelling propagation in layered porous elastic media is the difficulty of modelling complicated ground and air structures.

Residue series solution

Pierce [56] and Berry and Daigle [57] both derived a residue series solution to the problem of propagation in an upward refracting sound velocity gradient over an impedance surface. This method has two basic limitations. These are that the ground is modelled as an impedance plane, and that the sound velocity gradient can only be a linear upward refracting one.

2.4.2 Numerical Propagation Models

Most numerical propagation modelling techniques have only recently been applied to aeroacoustical problems, and most of the literature regarding them in acoustics is in application to ocean acoustics problems [58]. Ocean acoustics is usually restricted to the study of long range effects, and there-

fore these numerical propagation models were used at a range of many wavelengths. This study is mostly interested in medium range propagation (up to a few hundred metres) and is interested in using a 'full wave' model of propagation.

There are four numerical models which could be considered. These models are:

1 Fast Fourier method (FFP).

2 Normal Mode.

3 Parabolic Equation (PE).

4 Rasmussen's method.

A direct numerical integration method of the type used by Mechel [47] could be used. However this method is very limited in that atmospheric effects cannot be included.

The Fast Fourier Method

The basis of the FFP method of predicting pressure and wave amplitudes in a range independent environment from a point source is the solution of the depth separated wave equation [59]. From a linear wave equation in terms of wave field potentials:

$$\left[\nabla^2 + \frac{1}{c^2}\frac{\partial^2}{\partial t^2}\right]\Psi(r,z,t) = H(r,z,t) \tag{2.23}$$

where $H(r,z,t)$ is the forcing term. By applying a Fourier transform in time one obtains a frequency domain wave equation, the Helmholtz equation:

$$\left(\nabla^2 - k_m^2\right)F(r,z,\omega) = h(r,z,\omega) \tag{2.24}$$

where k_m is the propagation constant in the medium. Applying a forward Hankel transform in terms of range to this differential equation [60],

$$\Gamma_{(k,z)} = \int_{r=0}^{\infty} J_i(k_h.r).F(r,z).r.dr, \tag{2.25}$$

one then obtains the depth separated wave equation:

$$\left(\frac{d^2}{dz^2} + \left(k^2 - k_m^2(z)\right)\right)\Gamma(k,z) = \bar{h}(k,z), \tag{2.26}$$

where, for a point source,

$$\bar{h}(k,z) = \frac{1}{2\pi}\delta(z - z_0). \tag{2.27}$$

Solutions to this equation are depth dependent only and are equivalent to solutions to the wave equation for continuous plane wave incidence. In order to obtain a range dependent solution one must obtain depth dependent solutions to the depth separated wave equation, and then perform the inverse Hankel Transform on the solution to equation 2.26 , which is in terms of horizontal wavenumber. The transform (integration) over horizontal wavenumber is equivalent to an integration over all angles of incidence, where the horizontal wavenumber is the horizontal component of the wavenumber in the medium.

The exact range dependent solution is in the form;

$$F_{(x,d)} = \int_{k_h=0}^{\infty} J_\nu(k_h.x).\Gamma(k_h,d).dk_h, \tag{2.28}$$

where Γ is the depth dependent Greens function. For a receiver in the upper half space the depth dependent Greens function (Γ) for pressure is [59],

$$\Gamma = k_h\left[\frac{1}{\beta}e^{i.|h_s - h_r|.\beta} + R.e^{i.|h_s + h_r|.\beta}\right], \tag{2.29}$$

where,

$$\beta = \left(l_j^2 - k_h^2\right)^{\frac{1}{2}}$$

and l_i is the propagation constant in the medium. Note that here the horizontal wavenumber is included in the Green's function, whereas it is often written explicitly in equation 2.28. The exact solution (equation 2.28)is the inverse Hankel Transform pair to equation 2.25. At least several hundred calculations of the Bessel function would be required for an accurate calculation of the result, so to achieve numerical efficiency the equation 2.28 can be approximated to the sum of two Fourier Transforms which are approximated by Fourier series. The Fourier series approximation also has the

advantage over direct calculation of the Bessel functions that much work [54] [59]has been done on modifications to improve the numerical stability of the transform.

A large argument approximation to the Bessel function [61] is:

$$J_\nu(z) \simeq \frac{1}{\sqrt{2\pi z}} \left[e^{i(z-\pi\nu/2-\pi/4)} + e^{-i(z-\pi\nu/2-\pi/4)} \right] \tag{2.30}$$

This approximation together with the replacement of the integration by a finite sum gives the approximate equation for $F_{(x,d)}$:

$$F_{(x_m,d)} \simeq \frac{\delta k N^{1/2}}{2\pi m^{1/2}} \left[e^{-i\pi/4} \sum_{n=0}^{N-1} \Gamma_{(k_n,d)} n^{\frac{-1}{2}} e^{\frac{2i\pi mn}{N}} + e^{i\pi/4} \sum_{n=0}^{N-1} \Gamma_{(k_n,d)} n^{\frac{-1}{2}} e^{\frac{-2i\pi mn}{N}} \right]. \tag{2.31}$$

Because most calculations for underwater acoustics are done at ranges very much larger than a wavelength the second of these sums (which is equivalent to an in-going wave) is typically assumed to be very small and is generally ignored [59], [62]. For calculations very close to the source (where there is a "nearfield") this second sum can make an important contribution to the accuracy (see figure 2.1) and can be calculated with very little extra computational effort [54].

So Γ is calculated for a set of values of horizontal wavenumber $k_h = k_n$ corresponding to values of n from 0 to $N-1$ where:

$$k_n = k_{h(min)} + n.\delta k \tag{2.32}$$

The value of $k_{h(min)}$ is normally set to be very close to zero. However when $k_{h(min)}$ is zero the singularity at the origin will cause errors in the result. This problem is accounted for by the offset of the path of integration (see below). Two Fast Fourier transforms are then performed on this set of values of Γ for positive and negative exponents in equation 2.31 to calculate $F_{(x_m,d)}$.

This Fourier series approximation can then be improved by corrections to allow for the truncation of the integral to infinity to a finite wavenumber, $k_{h(max)}$, and the avoidance of pole(s) on the real axis, which together lead to inaccuracies and oscillations in the result.

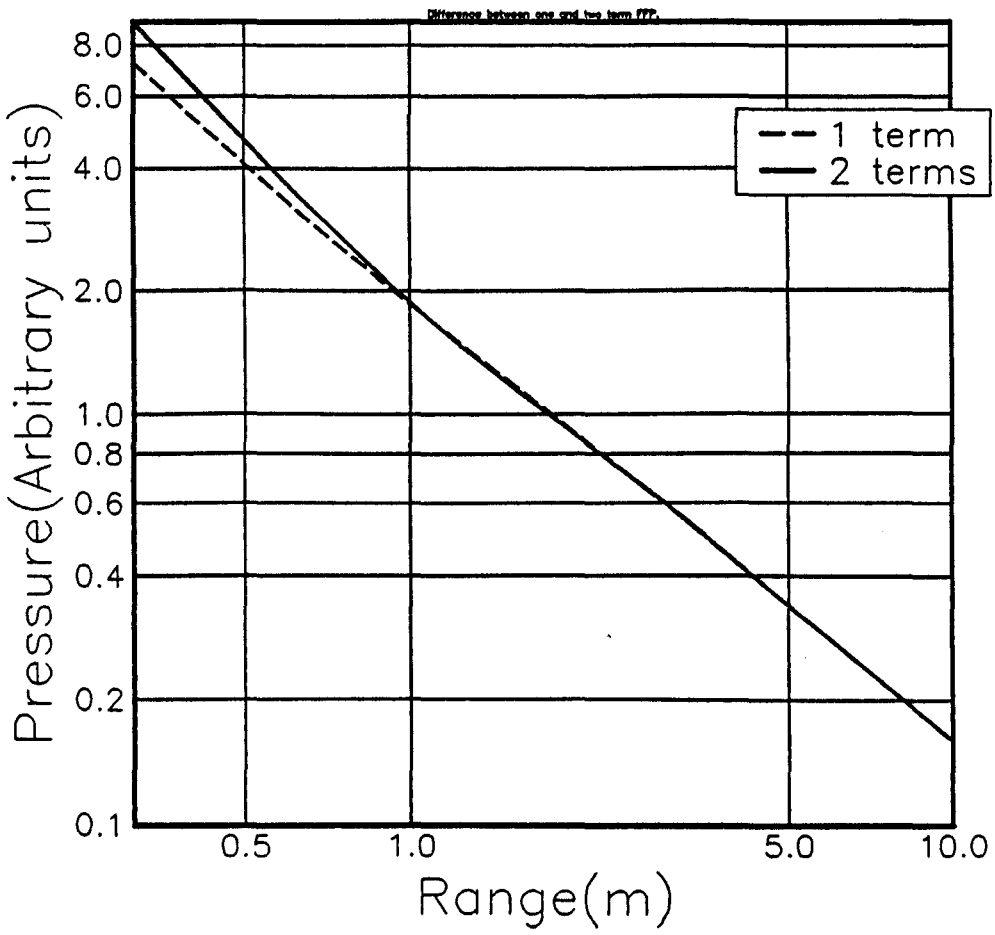

Figure 2.1 Predicted excess attenuation over a rigid boundary using one and two exponential functions in the FFP, at a frequency of 100Hz.

When the continuous function Γ is discretized, the sum, Equation 2.31 is only close to the exact solution, Equation 2.28 if,

$$\int_{k_0}^{k_0+\delta k} \Gamma(k)e^{ikr}dk \simeq \delta k\Gamma(k_0)e^{ik_0r}. \tag{2.33}$$

This will be a good approximation if δk is small enough so that

$$e^{ik_0r} \simeq e^{i(k_0+\delta k)r} \tag{2.34}$$

and

$$\Gamma(k_0) \simeq \Gamma(k) \tag{2.35}$$

for all k between k_0 and $k_0 + \delta k$.

The former condition will be true everywhere except at the origin on the complex k-plane for reasonable values of δk. The latter condition will also be true everywhere for reasonably small δk except where the path of integration passes close to or through poles or other singularities. There are two methods used to avoid poles in the case of lossless media, where integration along the real axis of horizontal wavenumber space would go through singularities (and so the integrand would be poorly represented by the discretization). The first and less satisfactory is the introduction of artificial attenuation in the lossless medium, and then multiplication of the result by a factor $e^{\alpha r}$, where α is the attenuation in nepers per metre and r is the range in metres. The second method is to choose an integration path avoiding the poles. The simplest way to approach this is to integrate along a line of constant negative imaginary horizontal wavenumber in wavenumber space (see figure 2.2). This is theoretically very similar to the artificial addition of attenuation, but allows more scope for corrections. This method is more difficult to apply than the first as it then requires corrections for the extra path from the point on the negative imaginary axis to the origin, but it is more theoretically correct [59], [54]. This second method is used by Richards and Attenborough[54]. k_n in Equation 2.31 is modified so that,

$$k_n = (n - i\alpha)\delta k \tag{2.36}$$

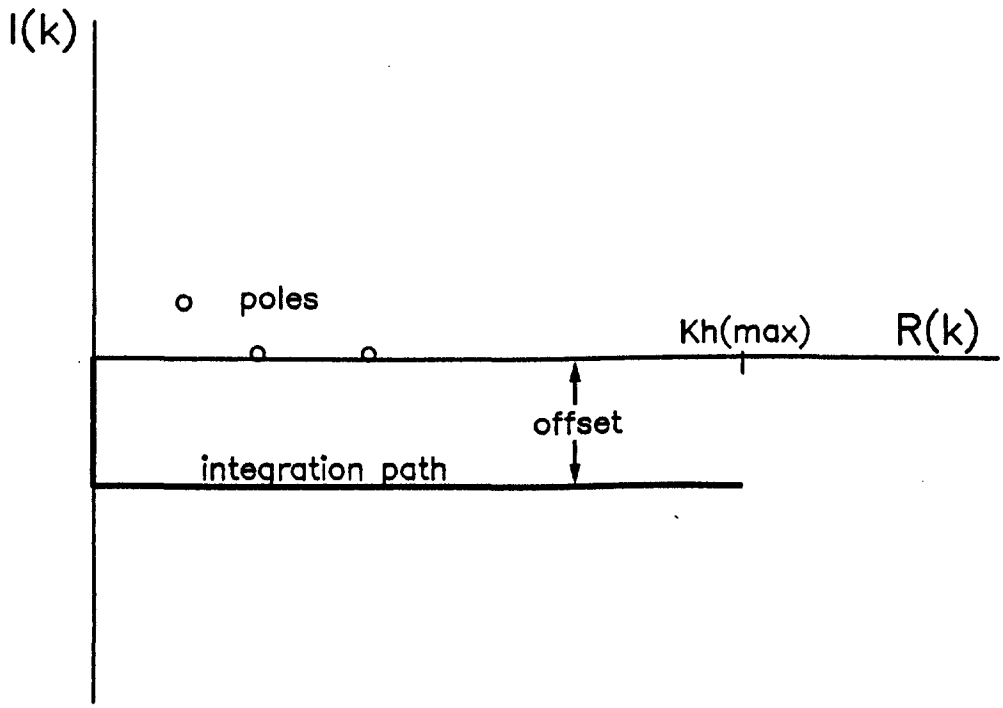

Figure 2.2 Path of integration in k-space with negative imaginary offset to avoid poles.

, and Equation 2.31 is replaced by,

$$F_{(x_m,d)} \simeq \frac{\delta k N^{1/2}}{2\pi m^{1/2}} e^{2\pi m\alpha/N} \quad \left[e^{-i\pi/4} \sum_{n=0}^{N-1} \Gamma_{(k_n,d)} (n - i\alpha)^{\frac{-1}{2}} e^{\frac{2i\pi mn}{N}} \right. \\ \left. + \quad e^{i\pi/4} \sum_{n=0}^{N-1} \Gamma_{(k_n,d)} (n - i\alpha)^{\frac{-1}{2}} e^{\frac{-2i\pi mn}{N}} \right] . \quad (2.37)$$

To represent the integration from the wavenumber offset $-i\alpha\delta k$ to the origin along the negative imaginary wavenumber axis, a function $\bar{g}(k)$ is chosen where,

$$\bar{g}(k) = A(1 - e^{-k\Delta}). \quad (2.38)$$

A and Δ are chosen such that $\bar{g}'(0) \simeq \Gamma'(0)$. Hence, with k_n as specified in Equation 2.36,

$$\begin{aligned} A &= N\Gamma(k_1)/(\Delta.k_{N-1}, \quad \alpha = 0 \\ A &= iN\Gamma(k_0)/(\alpha\Delta.k_{N-1}), \quad \alpha > 0 \end{aligned} . \quad (2.39)$$

For non-zero values of α this gives,

$$G_{(k_n,d)} = \Gamma_{(k_n,d)} + \frac{iN\Gamma_{(k_0,d)}}{\alpha\Delta} \left[1 - e^{(\Delta(i\alpha - n)k_{N-1}/N)} \right] . \quad (2.40)$$

The choice of α is critical to the accuracy of the result; too large a value introduces an error because the function $\bar{g}(k_0)$, which is an approximation to $\Gamma(k_0)$, will become more approximate as α becomes larger. Too small a value will lead to poor representation of the integrand near to singularities and the condition in equation 2.35 will not be fulfilled.

To represent the sums from the upper limit of the chosen wavenumber range in Equation 2.37 to infinity,

$$\sum_{n=N}^{\infty} G_{(k_n,d)} (n - i\alpha)^{\frac{-1}{2}} e^{\frac{2i\pi mn}{N}}, \quad (2.41)$$

and its inward going analogue, an assumption must be made about the form of the integrand for $n > N - 1$. If one considers propagation in the air, and the source and receiver heights are equal then it can be assumed that $G(k_n) \simeq G(k_{N-1})$ for $n > N - 1$. This is demonstrated in figure 2.3.

If the source and receiver heights differ in air then the integrand decays exponentially with increasing horizontal wavenumber (k_h). Taking first the

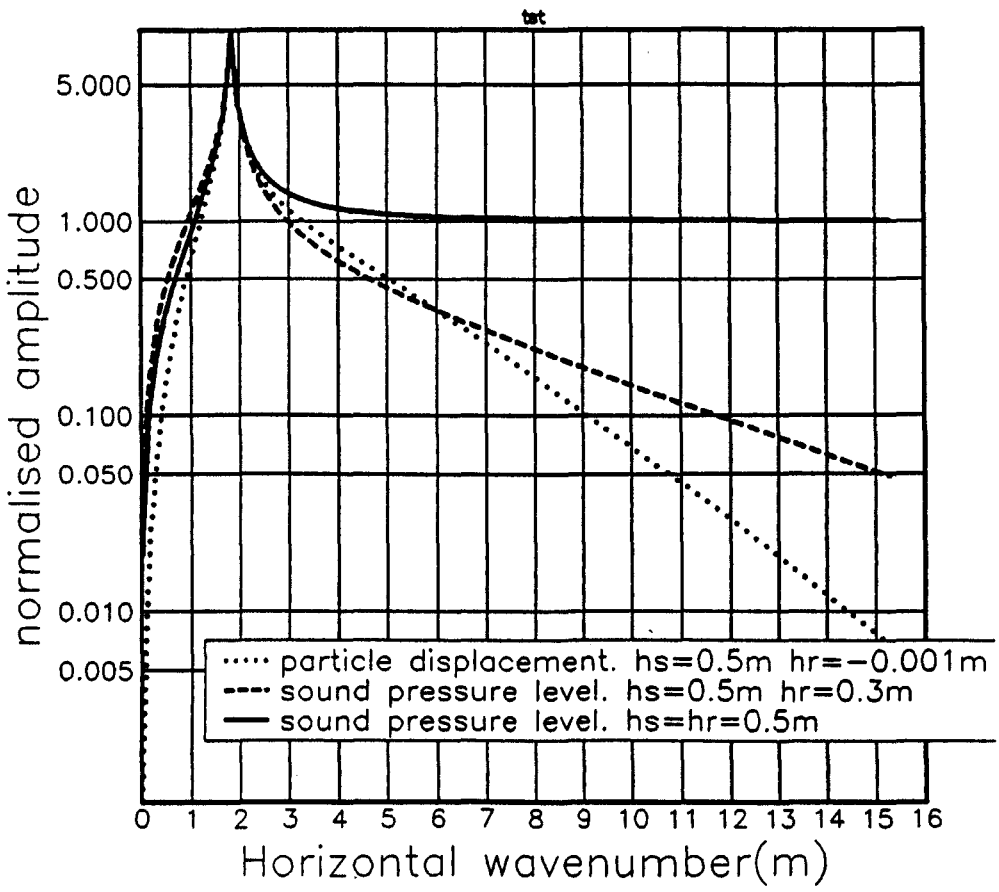

Figure 2.3 Normalised FFP integrands for equal source(hs) and receiver(hr) heights in an air halfspace, for hs-hr=0.2metres, and for surface vertical particle velocity.

case of equal source and receiver heights; With some rearrangement, equation 2.37 can be altered to add a small correction to each $G(k_n)$ in the FFT

$$C_{(k_n,d)} = G_{(k_n,d)}.(n - i\alpha)^{-1/2} + G_{(k_{N-1},d)}N^{-1/2}S^*, \qquad (2.42)$$

where S^* is an approximation to the sum,

$$S = \sum_{j=1}^{\infty}(j + [(n - i\alpha)/N])^{-1/2}. \qquad (2.43)$$

If source and receiver heights are not equal, then for large horizontal wavenumber (k_h) the depth dependent Greens Function (Γ) is given by

$$\Gamma \simeq Ke^{-(|hs-hr|.k_h)}. \qquad (2.44)$$

K is a constant. In the following argument K is unity. If $|hs - hr|$ is large enough the value of Γ becomes insignificantly small at the upper limit of the range of integration. Hence for large vertical separation of source and receiver no correction is necessary for the integrand above the limit of integration. If $|hs - hr|$ is non-zero but not large then the Greens function decays, but not rapidly enough to become insignificant at the upper end of the integration range. The definition of $|hs - hr|$ being large depends on the range of integration chosen. If the maximum horizontal wavenumber is four times the propagation constant (l_0) in the air and $|hs - hr| = \lambda/\pi$, the exponentially decaying part of the integrand at the maximum horizontal wavenumber is 0.0025 of the exponentially decaying part at $k_h = l_0$. Hence for $0 \lessapprox |hs - hr| \lessapprox \lambda/\pi$ a different correction is needed. A form for this correction function is suggested by Richards and Attenborough [54] [63]. The function $\bar{g}(k)$ in (Equation 2.38), is replaced by

$$\bar{g}(k) = (A + e^{-k_h|hs-hr|})(1 - e^{-k_h\Delta}). \qquad (2.45)$$

For k_h large $\bar{g}(k) \rightarrow A + e^{-k_h|hs-hr|}$. By subtracting $\bar{g}$ from Γ one therefore obtains a constant value for the modified Γ at large k_h. This can be dealt with in the same way as for the case of equal source and receiver heights. For k_h small (if $\Delta > |hs - hr|$) $\bar{g}(k) \rightarrow (A + 1)(1 - e^{-k_h\Delta})$, and suitable

values of A and Δ are chosen so that $(g'(0) = \Gamma'(0))$. For a non-zero value of α;

$$A + 1 = iN\Gamma(k_0)/(\alpha\Delta.k_{N-1}). \tag{2.46}$$

Δ must be chosen to be larger than $|hs - hr|$. Equation 2.40 can then be replaced by,

$$G_{(k_n,d)} = \Gamma_{(k_n,d)} - \left(A + e^{(-k_h|hs-hr|)}\right)\left[1 - e^{(\Delta(i\alpha-n)k_{N-1}/N)}\right]. \tag{2.47}$$

The Hankel transform of $\bar{g}(k)$ must finally be added to the Hankel transformed result. However this is generally small.

The two fast Fourier transforms can be calculated from one (hence speeding up the calculation), using the identity that the inverse Fourier transform of a function is the reverse of the forward transform of that function(The nth term of the transformed series of N terms is equal to the (N-n)th term of the inverse transformed series). Inclusion of both terms gives a final form for the Hankel transform of,

$$F_{(x_m,d)} \simeq \frac{\delta k N^{\frac{1}{2}}}{2\pi m^{\frac{1}{2}}}\left[e^{-i\pi/4}\sum_{n=0}^{N-1} C_{(k_n,d)} e^{\frac{2i\pi mn}{N}} e^{\frac{2\pi m\alpha}{N}} + e^{i\pi/4}\sum_{n=0}^{N-1} C_{(k_{N-n},d)} e^{\frac{2i\pi(N-m)n}{N}} e^{\frac{-2\pi m\alpha}{N}}\right]. \tag{2.48}$$

The above explanation deals with how the Depth dependent Greens Function Γ is used to calculate the pressure(for example) over a horizontally stratified medium, but first the Greens Function must be calculated. The Greens function is a solution of the depth separated wave equation 2.26. In the case of propagation in a fluid (such as air) there is only one depth separated wave equation. Two sorts of solution methods for the Greens function in a layered fluid are often used, these are the transmission line (or modified Thompson-Haskell) method used by Lee et al [64] and the global matrix method.

For propagation in a porous elastic solid there are four equations of motion, which can be simplified to give three Helmholtz equations in three displacement potentials. These give rise to three depth separated wave

equations. The Greens function is in most cases a function of all three Hankel transformed displacement potentials. This makes the transmission line method difficult to use in this context. The method of solution of the depth separated wave equations will be explained in chapter 4.

The FFP method has been extensively used for prediction of propagation in both a layered atmosphere over an impedance surface [65], and in a layered ocean environment over an elastic solid ocean bottom [59]. FFP methods are widely regarded as a standard by which other numerical propagation models are tested [66]. The main advantage of the FFP method over the others here described is its accuracy, the disadvantages are firstly the difficulty of using it, because in many situations the production of a correct result is very sensitive to the correct choice of input parameters such as the horizontal wavenumber limits, and secondly the limitations on its application because it is basically a range independent model, although models for a range or azimuthal dependent environment have been produced [67] using similar methods.

Normal Mode model

Taking the depth separated wave equation (equation 2.26) and setting the source term ($\bar{h}$) to zero one obtains an equation [58];

$$\left(\frac{d^2}{dz^2} + \left(k_m^2(z) - k_n^2\right)\right) \Gamma_n(z) = 0 \tag{2.49}$$

the solutions of which are a set of eigenfunctions Γ_n at the k_n values of k. A general solution to equation 2.49 is

$$\Gamma(k, z) = \sum_n a_n(k).\Gamma_n(z) \tag{2.50}$$

where the coefficients $a_n(k)$ are calculated from;

$$a_n(k) = \frac{\rho(z_0)\Gamma_n(z_0)}{2\pi(k^2 - k_m^2)} \tag{2.51}$$

where z_0 is the height of the source.

To obtain the range dependent solution the equivalent to the integration in equation 2.28 must be performed. Again only the Hankel function corresponding to the outgoing wave is normally chosen, and then approximated, so that

$$F(r,z) = \frac{i\rho(z_0)}{(8\pi r)^{1/2}} e^{-i\pi/4} \sum_n \left[\frac{\Gamma(z_0)\Gamma(z)}{k_n^{1/2}} e^{ik_n r} \right] \tag{2.52}$$

This method is demonstrably less accurate than the FFP although it is easier to apply and takes less computation than the FFP. It also is basically a range independent environment model. In underwater acoustics the normal mode model is mostly used for shallow water propagation where there is a limited number of modes at a given frequency, and a definite upper and lower boundary. It is this environment to which it is best suited. There is a simple physical picture of the Normal Mode model: If this method is applied to a water column containing layers of differing wave speeds and densities one can view this as a taut string made up of sections of differing elastic properties and densities. This string will have a set of free vibration modes at different frequencies, which correspond to the set of normal modes at different wavenumber. The excitation of each mode depends on the depth of the source. If it is placed at the node of a mode then that mode will not be excited. The larger the amplitude of the mode at the source depth the more it will be excited. Similarly the importance of a mode in the received signal depends on the position in the water column; a signal due to a particular excited mode will be larger the larger the mode amplitude at the receiver depth. The modes are then allowed to propagate. A similar analogy for a Fast Fourier model would be that of the same string being driven by a source. The free vibration modes would still be excited but at frequencies between the free vibration mode frequencies the string displacement would still have an amplitude. Hence a range of frequencies (corresponding to a range of horizontal wavenumbers) would have to be considered in describing the string vibrations.

Parabolic Equation Model

The P.E was first introduced to the acoustics community by Tappert and Hardin as a full wave alternative to ray tracing [68]. It is used as a long range propagation method (i.e. at ranges of kilometres). Consider the two way wave equation for the velocity potential (Φ) in a cylindrically symmetrical geometry:

$$\frac{\partial^2\Phi}{\partial r^2} + \frac{1}{r}\frac{\partial\Phi}{\partial r} + \frac{\partial^2\Phi}{\partial z^2} + k^2\Phi = 0 \tag{2.53}$$

Change of variables; $u = \Phi / H_0^1(k_0 r)$

leads to;

$$\frac{\partial^2 u}{\partial r^2} + 2ik_0\frac{\partial u}{\partial r} + \frac{\partial^2 u}{\partial z^2} + (k^2 - k_0^2)u = 0 \tag{2.54}$$

Equation 2.54 can be formally solved for $\partial u/\partial r$ using the quadratic equation solution formula. Using this the equation

$$\frac{\partial u}{\partial r} = i\left(\left[\frac{\partial^2}{\partial z^2} + k^2\right]^{1/2} - k_0\right)u \tag{2.55}$$

is obtained. This equation is exact in the far field in a range independent environment, and is regarded as a good approximation in some range dependent environments. Designating the operator:

$$\left[\frac{\partial^2}{\partial z^2} + k^2\right] = Q \tag{2.56}$$

and making a "stair step" range dependence approximation(ie the operator Q is constant over a small range δr), a solution at the range $r_j = j\delta r$ is given by

$$u_j = e^{i\delta r(Q^{\frac{1}{2}} - k_o)}u_{j-1}. \tag{2.57}$$

Numerical solutions for this equation are found using a 'split step' Fourier method, or a finite difference scheme [58].

The ground surface is most often modelled as an impedance surface. Because the solution is marched out there is only propagation in one direction. Therefore no backscattering is allowed, and nearfield effects are not predicted. Because of the one directional nature of the solution method, a range dependent environment can be included.

The solution is started at range $r = 0$ with a Gaussian approximation to a point source and then 'marched out' to the range required. This derivation is for the 'standard' PE which is only valid for near horizontal propagation. Using a slightly different derivation a 'wide angle' PE can be derived [69]. The PE has recently been used in application to outdoor sound propagation [70] and the effects of turbulence have also been included [71].

2.4.3 Rasmussen's method

Rasmussen [72] developed a simplified model for propagation over an impedance boundary under the influence of a linear sound velocity gradient. A point source propagated sound to a semi-infinite vertical line of secondary sources with its base at a point half way between the point source and receiver. The signal at the receiver was the sum of the signals from the vertical line of secondary sources.

The propagation constant for each secondary source was defined as the propagation constant at half the height of the secondary source in the sound velocity gradient. This was proposed as an average propagation constant over the paths from the source to the secondary source being considered, and from the secondary source to the receiver. This approximation will only be accurate when source and receiver are very close to the ground, and the sound velocity gradient is small enough for ray curvature to be small. Rasmussen claims that he includes the effects of ray path curvature by the phase differences between the secondary sources, but in fact these phase differences are only due to the differences in propagation constant between the secondary sources. The paths between source, secondary sources, and receiver, are calculated as straight lines. This method could potentially be extended to include a more complex atmospheric profile, but the approximations made in the derivation severely limit the possible applications.

2.4.4 Choice of numerical model

In the situation of interest the propagation model chosen must be accurate at close ranges(equivalent to low frequencies). This discounts the use of

Normal Mode, and PE models. The FFP allows the inclusion of the nearfield effects which cannot be included in PE. The model should be able to fully account for seismic effects. This is a very difficult problem in Parabolic Equation models, and shear wave effects are particularly awkward to model by this technique [73]. Rasmussen's method suffers from the limitations imposed by the approximations made. The FFP allows for the inclusion of both atmospheric effects, and complicated ground structures. Most small scale soil structures can be readily modelled as horizontally layered and so a range independent model can be chosen. In spite of the numerical problems introduced by use of the FFP this seems the most useful model type of the ones described here.

Chapter 3

Using the Biot-Stoll porous-elastic model for plane wave solutions

3.1 A physical interpretation of the Biot-Stoll model

The Biot-Stoll model predicts the existence of three waves in the porous elastic medium. These consist of two dilatational waves (with propagation constants which are solutions of Equation 3.17) and one rotational, or shear wave (from solution of Equation 3.18). In a material consisting of a dense solid frame with a low density fluid saturating the pores, the first dilatational wave has a velocity very similar to the velocity of a dilatational wave (or geophysical 'P' wave) travelling in the drained frame. The attenuation of the first dilatational wave is, however, higher than that of the 'P' wave in the drained frame. The extra attenuation comes from viscous forces in the pore fluid acting on the pore walls. This viscous coupling leads to some of the energy in this propagating wave being carried in the pore fluid.

The second dilatational wave is of much lower velocity than the first in most cases. Its attenuation also stems from viscous forces acting on the pore walls. Its rigid-frame limit is very similar to the pore wave which travels through the fluid in the pores of a rigid-porous solid in the Rayleigh-Attenborough propagation model. Most of the energy in this wavetype is carried in the pore fluid. However the viscous coupling through the pore

walls leads to some propagation within the solid frame. The attenuation for this second dilatational wave is higher than that of the first in most materials, the real and imaginary parts of the propagation constant being nearly equal in many cases.

The rotational wave has very similar velocity to the rotational (or geophysical 'S') wave carried in the drained frame. Again there is some extra attenuation due to viscous forces, and some of the energy is carried in the pore fluid. The fluid is unable to support rotational waves, but is driven by the solid.

3.2 Single Layer

This layer system has been considered by Sabatier et al [5]. The system simply consists of a single porous elastic layer, with properties defined by the modified Biot-Stoll parameters, overlain by a homogeneous air halfspace, with a semi-infinite nonporous elastic substrate. The system is then subjected to plane wave incident sound from the air. Solution of the resulting boundary conditions enables normal surface impedance and the ratio of acoustic pressure above the ground to particle velocity within the ground to be predicted.

The three propagation constants in the porous layer are derived from a solution to the Biot-Stoll equations for wave propagation [20]

$$\nabla^2(He - C\xi) = \frac{\partial^2}{\partial t^2}(\rho e - \rho_f \xi) \tag{3.1}$$

$$\nabla^2(Ce - M\xi) = \frac{\partial^2}{\partial t^2}(\rho_f e - \rho' \xi) \tag{3.2}$$

$$g_b \nabla^2 \zeta = \frac{\partial^2}{\partial t^2}(\rho \zeta - \rho_f \psi) \tag{3.3}$$

$$\frac{\partial^2}{\partial t^2}(\rho_f \zeta - m\psi) = \frac{\eta}{\kappa}\left(\frac{\partial \psi}{\partial t} F(\lambda)\right) \tag{3.4}$$

where

$$H = [(K_r - K_b)^2/(D - K_b)] + K_b + \tfrac{4}{3}g_b$$
$$C = K_r[(K_r - K_b)/(D - K_b)]$$
$$M = (K_r^2/D) - K_b \tag{3.5}$$
$$D = K_r(1 + \Omega[(K_r/K_f) - 1])$$

,

and

$$\rho' = q^2\rho_f/\Omega + i\omega\frac{\eta}{\kappa}F(\lambda). \tag{3.6}$$

Where.

$$w = \nabla e + \nabla \times \zeta = \Omega(u - U) \tag{3.7}$$

$$u = \nabla\xi + \nabla \times \psi \tag{3.8}$$

u is solid displacement, U is fluid displacement and w is relative fluid displacement. e and ξ are longitudinal displacement potentials. ζ and ψ are transverse displacement potentials. $m = q^2\rho_f/\Omega$ and is a modified fluid density to allow for the fact that fluid movement in the pores is not all in the direction of the potential gradient because the pores are not necessarily straight. Four parameters [12] are used to calculate $F(\lambda)$: flow resistivity σ, porosity Ω, grain shape factor n', and pore shape factor ratio s_p.

$$F(\lambda) = \frac{-(\lambda\sqrt{i})T(\lambda\sqrt{i})}{4[1 - 2T(\lambda\sqrt{i})/(\lambda\sqrt{i})]}, \tag{3.9}$$

where

$$\lambda = \frac{1}{2s_p}\left(\frac{8\Omega^{-n'}\omega\rho_f}{\Omega\sigma}\right)^{\frac{1}{2}}, \tag{3.10}$$

and

$$T(x) = J_1(x)/J_0(x). \tag{3.11}$$

If plane wave solutions are chosen to equations 3.1 to 3.4;

$$e = Ae^{i(lx-\omega t)} \quad \xi = Be^{i(lx-\omega t)} \quad \zeta = Xe^{i(lx-\omega t)} \quad \psi = Ye^{i(lx-\omega t)} \tag{3.12}$$

and substituted into the wave equations then the following frequency equations are derived.

$$\left(Hl^2 - \rho\omega^2\right)A + \left(\rho_f\omega^2 - Cl^2\right)B = 0 \tag{3.13}$$

$$\left(Cl^2 - \rho_f\omega^2\right) A + \left(m\omega^2 - Ml^2 - i.\omega.F(\lambda).(\nu/\kappa)\right) B = 0 \qquad (3.14)$$

$$\left(\rho\omega^2 - g_b l^2\right) X + \rho_f\omega^2 Y = 0 \qquad (3.15)$$

$$\rho_f.\omega^2.X + \left(m\omega^2 - i.\omega.F(\lambda).(\nu/\kappa)\right) Y = 0 \qquad (3.16)$$

As the determinant of the coefficients must be zero the dispersion relations;

$$\begin{vmatrix} (Hl^2 - \rho\omega^2) & (\rho_f\omega^2 - Cl^2) \\ (Cl^2 - \rho_f\omega^2) & (m\omega^2 - Ml^2 - i.\omega.F(\lambda).(\nu/\kappa)) \end{vmatrix} = 0 \qquad (3.17)$$

for compressional waves and

$$\begin{vmatrix} (\rho\omega^2 - g_b l^2) & \rho_f\omega^2 \\ \rho_f\omega^2 & (m\omega^2 - i.\omega.F(\lambda).(\nu/\kappa)) \end{vmatrix} = 0 \qquad (3.18)$$

for transverse waves[25] can be derived, which are then solved to give propagation constants l_i for the three wave types; two compressional and one transverse. Furthermore the ratios m_i of the relative wave amplitude to the matrix wave amplitude for each wavetype can be calculated by solution of the frequency equations 3.13 to 3.16, leading to

$$m_1 = (H.l_1^2 - \rho.\omega^2)/(C.l_1^2 - \rho_f.\omega^2) \qquad (3.19)$$

$$m_2 = (H.l_2^2 - \rho.\omega^2)/(C.l_2^2 - \rho_f.\omega^2) \qquad (3.20)$$

$$m_3 = (\rho.\omega^2 - g_b.l_3^2)/(\rho_f.\omega^2) \qquad (3.21)$$

where the m_i are the ratios of fluid to solid displacements.

Similarly in the elastic substrate the seismic propagation is governed by the two equations

$$H'\nabla^2\alpha = \frac{\partial^2}{\partial t^2}(\rho_g\alpha) \qquad (3.22)$$

$$\mu'\nabla^2\beta = \frac{\partial^2}{\partial t^2}(\rho_g\beta) \qquad (3.23)$$

leading to two wave types with propagation constants l_4(longitudinal) and l_5 (shear). If a plane wave is incident from the air at an incident angle θ, the amplitudes of the three wavetypes in the ground are predicted by solution of boundary condition equations at the air to poro-elastic interface and the

poro-elastic to elastic interface. There are four boundary conditions at the air to layer interface, and five at the layer to half-space interface. These boundary condition equations are in terms of up and down going matrix displacement amplitudes as shown in figure 3.1.

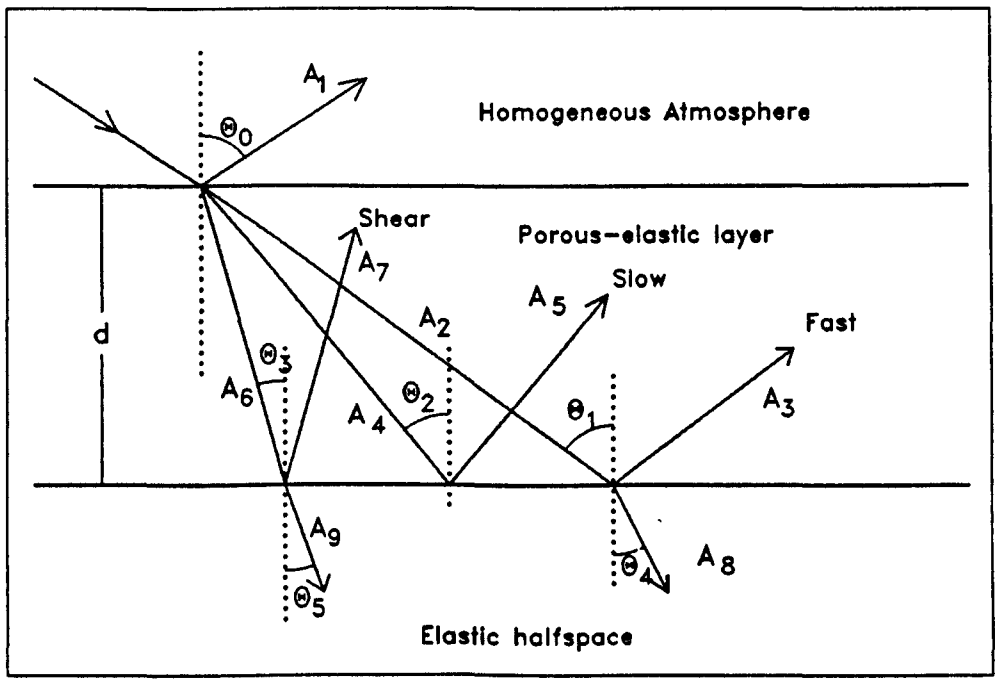

Figure 3.1 Up and downgoing matrix displacements in a single porous elastic layer overlying an elastic halfspace.

This total of nine boundary conditions equations are as follows.

1. Continuity of normal frame displacement at top interface.

$$\cos\theta_0\,[1 - A_1] = (1 - m_1)\cos\theta_1\left[A_2 - A_3 e^{i\cos\theta_1 l_1 d}\right]$$

$$+(1-m_2)\cos\theta_2\left[A_4 - A_5 e^{i\cos\theta_2 l_2 d}\right]$$
$$+(1-m_3)\sin\theta_3\left[A_6 - A_7 e^{i\cos\theta_3 l_3 d}\right] \tag{3.24}$$

2. Continuity of fluid pressure at top interface.

$$k_0 l_0 [1 + A_1] = l_1(C - m_1 M)\left[A_2 + A_3 e^{i\cos\theta_1 l_1 d}\right]$$
$$+l_2(C - m_2 M)\left[A_4 + A_5 e^{i\cos\theta_2 l_2 d}\right] \tag{3.25}$$

3. Continuity of total normal stress at top interface.

$$k_0 l_0 [1 + A_1] = l_1(H - m_1 C - 2g_b \sin^2\theta_1)\left[A_2 + A_3 e^{i\cos\theta_1 l_1 d}\right]$$
$$+l_2(H - m_2 C - 2g_b \sin^2\theta_2)\left[A_4 + A_5 e^{i\cos\theta_2 l_2 d}\right]$$
$$+l_3 2g_b \sin^2\theta_3\left[A_6 + A_7 e^{i\cos\theta_3 l_3 d}\right] \tag{3.26}$$

4. Continuity of tangential stress at top interface.

$$0 = 2l_1\cos\theta_1\sin\theta_1\left[A_2 - A_3 e^{i\cos\theta_1 l_1 d}\right]$$
$$+2l_2\cos\theta_2\sin\theta_2\left[A_4 - A_5 e^{i\cos\theta_2 l_2 d}\right]$$
$$-l_3(\cos^2\theta_3 - \sin^2\theta_3)\left[A_6 + A_7 e^{i\cos\theta_3 l_3 d}\right] \tag{3.27}$$

5. Continuity of normal frame displacement at bottom interface.

$$\cos\theta_1\left[A_2 e^{i\cos\theta_1 l_1 d} - A_3\right] + \cos\theta_2\left[A_4 e^{i\cos\theta_2 l_2 d} - A_5\right]$$
$$+\sin\theta_3\left[A_6 e^{i\cos\theta_3 l_3 d} - A_7\right] = \cos\theta_4 A_8 + \sin\theta_5 A_9 \tag{3.28}$$

6. tangential frame displacement at bottom interface.

$$\sin\theta_1\left[A_2 e^{i\cos\theta_1 l_1 d} + A_3\right] + \sin\theta_2\left[A_4 e^{i\cos\theta_2 l_2 d} + A_5\right]$$
$$-\cos\theta_3\left[A_6 e^{i\cos\theta_3 l_3 d} + A_7\right] = \sin\theta_4 A_8 + \cos\theta_5 A_9 \tag{3.29}$$

7. Continuity of total normal stress at bottom interface.

$$\begin{aligned} l_1(H - m_1C - 2g_b \sin^2\theta_1)\left[A_2 e^{i\cos\theta_1 l_1 d} - A_3\right] \\ +l_2(H - m_2C - 2g_b \sin^2\theta_2)\left[A_4 e^{i\cos\theta_2 l_2 d} - A_5\right] \\ -l_3 2g_b \sin^2\theta_3\left[A_6 e^{i\cos\theta_3 l_3 d} + A_7\right] \\ = (H' - 2\mu')l_4 \cos\theta_4 A_8 + 2\mu' \sin\theta_5 A_9 \end{aligned} \tag{3.30}$$

8. Continuity of tangential stress at bottom interface.

$$\begin{aligned} 2l_1 \cos\theta_1 \sin\theta_1\left[A_2 e^{i\cos\theta_1 l_1 d} - A_3\right] \\ +2l_2 \cos\theta_2 \sin\theta_2\left[A_4 e^{i\cos\theta_2 l_2 d} - A_5\right] \\ -l_3(\cos^2\theta_3 - \sin^2\theta_3)\left[A_6 e^{i\cos\theta_3 l_3 d} + A_7\right] \\ = 2\mu' l_4 \sin\theta_4 \cos\theta_4 A_8 - \mu' A_9 l_5(\cos^2\theta_5 - \sin^2\theta_5) \end{aligned} \tag{3.31}$$

9. Continuity of normal fluid displacement at bottom interface.

$$\begin{aligned} m_1 \cos\theta_1\left[A_2 e^{i\cos\theta_1 l_1 d} - A_3\right] + m_2 \cos\theta_2\left[A_4 e^{i\cos\theta_2 l_2 d} - A_5\right] \\ +m_3 \sin\theta_3\left[A_6 e^{i\cos\theta_3 l_3 d} - A_7\right] = 0 \end{aligned} \tag{3.32}$$

Knowing the propagation constants l_i and the angle of incidence at the top surface the propagation angles in the other media are calculated using

$$l_i \sin\theta_i = l_0 \sin\theta_0 \tag{3.33}$$

These nine equations are then simultaneously solved to give the nine up and down going matrix wave amplitudes A_i . The normal surface impedance can then be calculated from A_1, the reflection coefficient.

Figure 3.2 shows the attenuation (in dB per wavelength) due to viscous forces at the pore walls predicted by the Biot-Stoll model for the soil parameters listed in table 7.1. It can be seen that the attenuation of the slow wave due to viscous forces in the fluid is much greater than that of the fast or shear wave. The attenuation of the pore wave is in most cases only very slightly dependent on the elastic parameters of the solid frame. Most of the attenuation of the fast and shear modes is due to influences other than

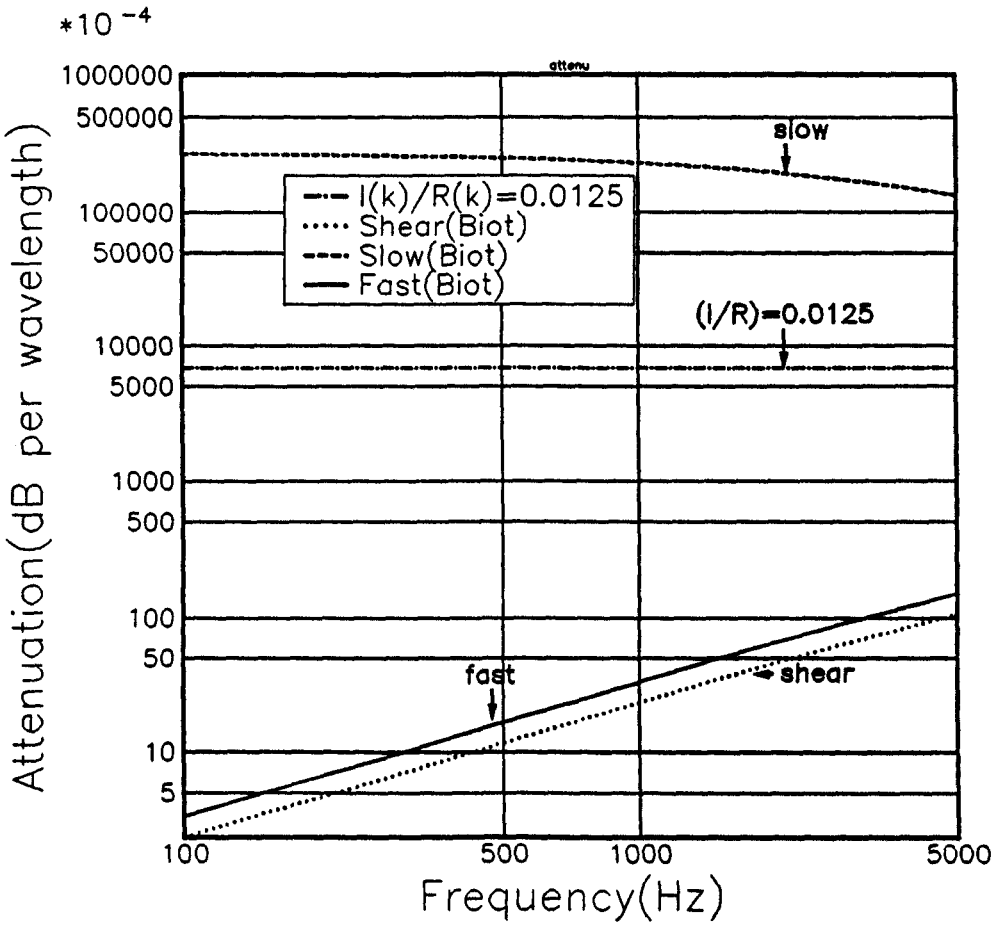

Figure 3.2 Predicted body wave attenuation in a soil from the Biot model, and from a constant ratio of real to imaginary parts of the propagation constant.

the fluid viscosity, such as intergranular friction. Henceforward it will be assumed that the solid frame of the soil behaves as a Voigt solid, and hence the extra attenuation of the fast and shear waves not due to viscous forces at the pore walls can be accounted for by adding a constant small fraction of the real part of the propagation constant to the imaginary part. This is an assumption supported by experiment on many different materials [74]. A value for this fraction of 0.0125 for soil is consistent with results by Prange [75]. For the parameters in table 7.1, figure 3.2 shows that the attenuation of the fast and shear waves due to this value of the fraction is much greater than that predicted by Biot theory alone.

The ratios and phase relationships between the displacements in the fluid and in the solid are given by the m_i for each wavetype.

Biot [14] derived phase relationships between the fluid displacement due to each wave type and the solid frame displacement. All of his calculations were for zero attenuation. He predicted that in the first (fast) dilatational wavetype the fluid and solid moved in phase. He predicted that in the second (slow) dilatational wavetype the fluid and solid were exactly out of phase, and for the rotational wavetype they were in phase. If the m_i in equations 3.19 are calculated for entirely real propagation constants, densities, and elastic parameters, then the phases of the m_i agree with the findings of Biot. However the imaginary parts of the propagation constants and elastic parameters have a marked affect on the predicted phases of the m_is, and Biot's findings on these phase relationships are not applicable when modelling real materials. Figures 3.4 and 3.3 show the phase relationships between the solid and fluid displacements for the three wavetypes for propagation in a dry air saturated sand and an air-saturated snow respectively. Their parameters are given in table 3.2. The predictions are in agreement with those of D Albert [76]. The small differences are probably due to Albert's use of an approximation for the viscosity correction.

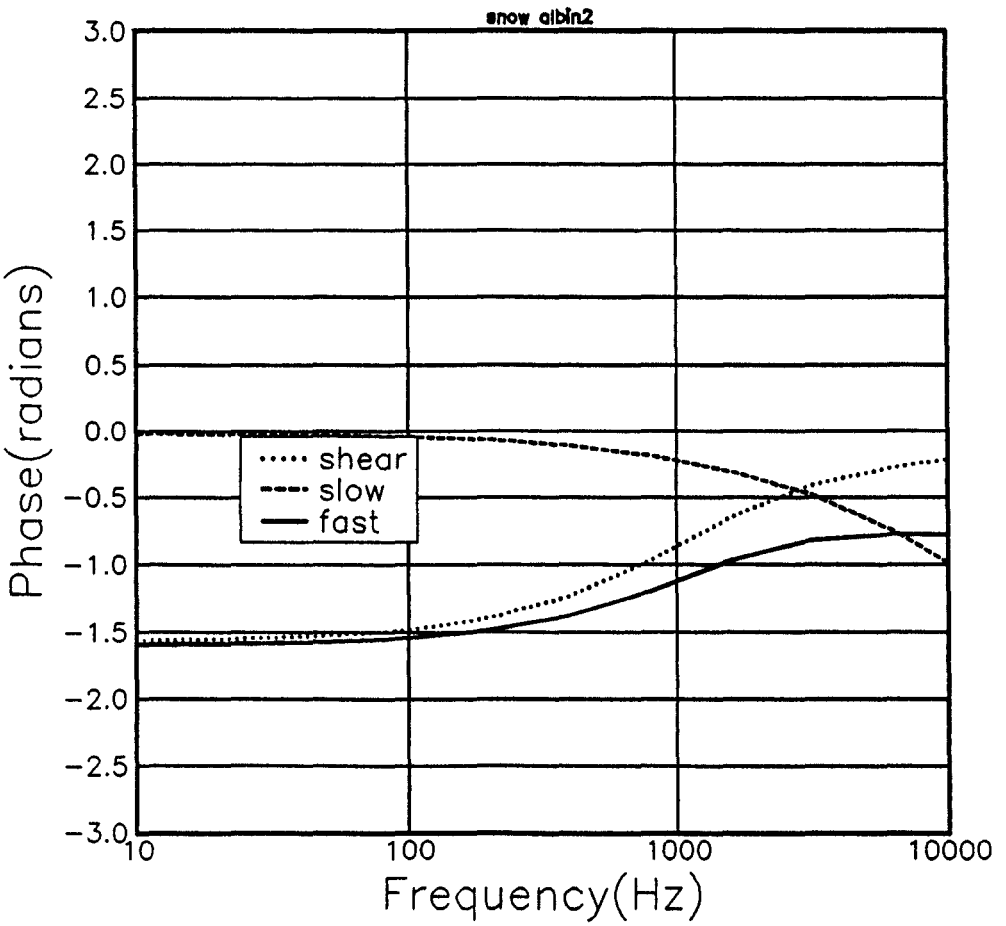

Figure 3.3 Predicted phase relationships between fluid and solid displacement for propagation in a dry snow for the three Biot-Stoll wavetypes.

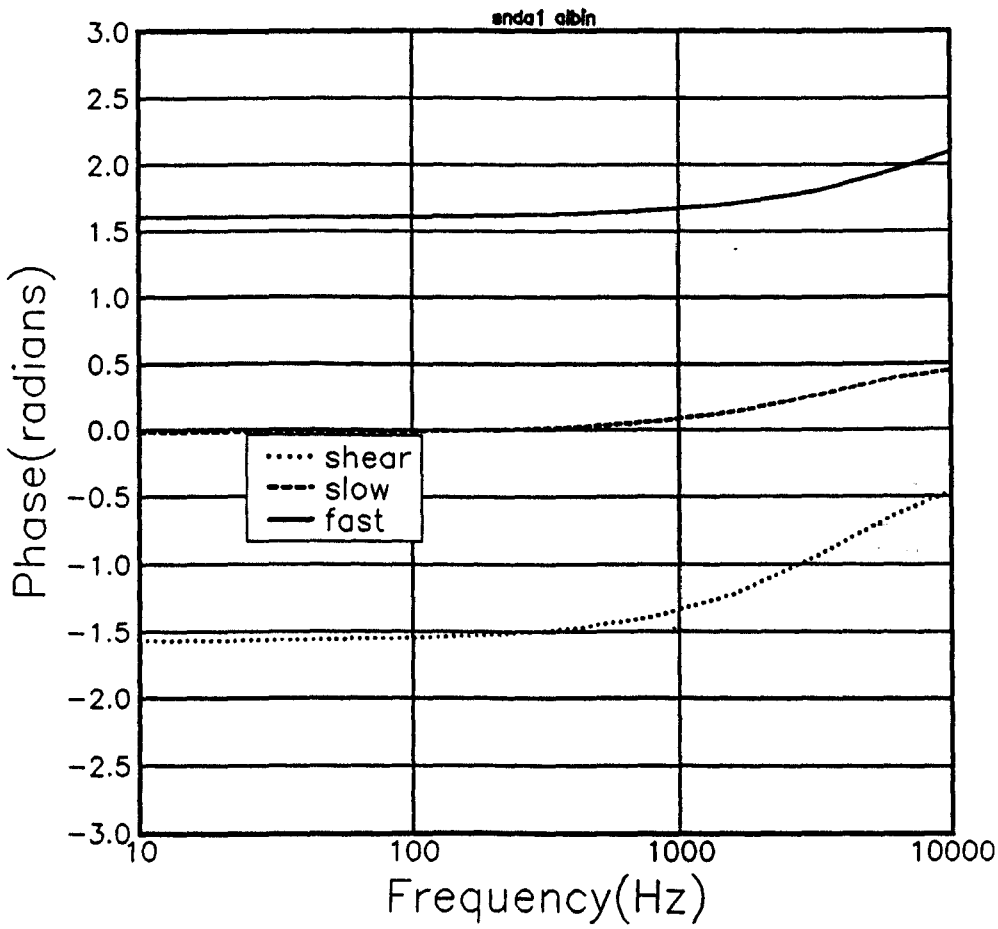

Figure 3.4 Predicted phase relationships between fluid and solid displacement for propagation in a dry sand for the three Biot-Stoll wavetypes.

Table 3.1 Poro-elastic parameters used in prediction of phase of fluid motion.

Material	dry snow	dry soil
Flow resistivity(mks raylsm^{-1})	18100	181000
Porosity	0.783	0.3
Pore shape factor ratio (s_p)	0.5	0.5
Grain shape factor (n')	0.912	0.185
P-velocity (ms^{-1})	300.7	328.5
S-velocity (ms^{-1})	183.3	164.2
bulk density (kgm^{-3})	201	1855
$\Im v/\Re v$	0.01	0.01

3.3 Multiply layered soil

Application of the model described in section 3.2 is severely limited as real soils can rarely be accurately described by a single layer and subsoils rarely have zero air porosity. A better model would allow for any number of porous elastic layers overlying a porous elastic substrate. At a porous-elastic to porous-elastic boundary six independent boundary condition equations are necessary to calculate the wave amplitudes. These boundary conditions are those used for the porous-elastic to elastic boundary in equations 3.28 to 3.32 plus a sixth, the continuity of fluid pressure. As in the single layer model there is an incident plane wave and only quantities such as the normal surface impedance and the ratio of particle velocity in the ground to acoustic pressure above it, can be calculated.

These boundary condition equations assume the open pore condition; that is that the pores at the base of a layer all connect with the pores at the top of the next layer and there are no 'dead end' pores. If one considers that real soils are made up of grains and are not solids containing air filled tubes the open pore condition seems reasonable.

For any porous-elastic layer to porous-elastic layer boundary the boundary condition equations are as follows:

1. Continuity of normal frame velocity .

$$\begin{aligned}
&\cos\theta_{1n}.[A_{1n\downarrow}.e^{q_{1n}} - A_{1n\uparrow}] \quad + \quad \cos\theta_{2n}.[A_{2n\downarrow}e^{q_{2n}} - A_{2n\uparrow}] \\
&+ \quad \sin\theta_{3n}.[A_{3n\downarrow}.e^{q_{3n}} - A_{3n\uparrow}] \quad - \quad \cos\theta_{1(n+1)}.\left[A_{1(n+1)\downarrow} - A_{1(n+1)\uparrow}.e^{q_{1(n+1)}}\right] \\
&- \quad \cos\theta_{2(n+1)}.\left[A_{2(n+1)\downarrow} - A_{2(n+1)\uparrow}.e^{q_{2(n+1)}}\right] \quad - \quad \sin\theta_{3(n+1)}.\left[A_{3(n+1)\downarrow} - A_{3(n+1)\uparrow}.e^{q_{3(n+1)}}\right] \\
&= \quad 0
\end{aligned} \tag{3.34}$$

2. Continuity of tangential frame velocity.

$$\begin{aligned}
&\sin\theta_{1n}.[A_{1n\downarrow}.e^{q_{1n}} + A_{1n\uparrow}] \quad + \quad \sin\theta_{2n}.[A_{2n\downarrow}.e^{q_{2n}} + A_{2n\uparrow}] \\
&- \quad \cos\theta_{3n}.[A_{3n\downarrow}.e^{q_{3n}} + A_{3n\uparrow}] \quad - \quad \sin\theta_{1(n+1)}.\left[A_{1(n+1)\downarrow} + A_{1(n+1)\uparrow}.e^{q_{1((n+1)+1)}}\right] \\
&- \quad \sin\theta_{2(n+1)}.\left[A_{2(n+1)\downarrow} + A_{2(n+1)\uparrow}.e^{q_{2(n+1)}}\right] \quad + \quad \cos\theta_{3(n+1)}.\left[A_{3(n+1)\downarrow} + A_{3(n+1)\uparrow}.e^{q_{3(n+1)}}\right] \\
&= \quad 0
\end{aligned} \tag{3.35}$$

3. Continuity of total normal stress .

$$\begin{aligned}
&l_{1n}.(H - m_{1n}.C - 2g_b.\sin^2\theta_{1n})[A_{1n\downarrow}.e^{q_{1n}} - A_{1n\uparrow}] \\
&+ \quad l_{2n}.(H - m_{2n}.C - 2g_b.\sin^2\theta_{2n})[A_{2n\downarrow}.e^{q_{2n}} - A_{2n\uparrow}] \\
&- \quad l_{3n}.2g_b.\sin^2\theta_{3n}.[A_{3n\downarrow}.e^{q_{3n}} + A_{3n\uparrow}] \\
&- \quad l_{1n}.(H - m_{1n}.C - 2g_b.\sin^2\theta_{1n})[A_{1n\downarrow}.e^{q_{1(n+1)}} - A_{1n\uparrow}] \\
&- \quad l_{2n}.(H - m_{2n}.C - 2g_b.\sin^2\theta_{2n})[A_{2n\downarrow}.e^{q_{2(n+1)}} - A_{2n\uparrow}] \\
&+ \quad l_{3n}.2g_b.\sin^2\theta_{3n}[A_{3n\downarrow}.e^{q_{3(n+1)}} + A_{3n\uparrow}] \quad = \quad 0
\end{aligned} \tag{3.36}$$

4. Continuity of tangential stress .

$$\begin{aligned}
&2l_{1n}.\cos\theta_{1n}.\sin\theta_{1n}.[A_{1n\downarrow}.e^{q_{1n}} - A_{1n\uparrow}] \\
&+ \quad 2l_{2n}.\cos\theta_{2n}.\sin\theta_{2n}.[A_{2n\downarrow}.e^{q_{2n}} - A_{2n\uparrow}] \\
&- \quad l_{3n}.(\cos^2\theta_{3n} - \sin^2\theta_{3n})[A_{3n\downarrow}.e^{q_{3n}} + A_{3n\uparrow}] \\
&- \quad 2l_{1(n+1)}.\cos\theta_{1(n+1)}.\sin\theta_{1(n+1)}.\left[A_{1(n+1)\downarrow} - A_{1(n+1)\uparrow}.e^{q_{1(n+1)}}\right] \\
&- \quad 2l_{2(n+1)}.\cos\theta_{2(n+1)}.\sin\theta_{2(n+1)}.\left[A_{2(n+1)\downarrow} - A_{2(n+1)\uparrow}.e^{q_{2(n+1)}}\right] \\
&+ \quad l_{3(n+1)}.(\cos^2\theta_{3(n+1)} - \sin^2\theta_{3(n+1)})\left[A_{3(n+1)\downarrow} + A_{3(n+1)\uparrow}.e^{q_{3(n+1)}}\right] \quad = \quad 0
\end{aligned} \tag{3.37}$$

5. Continuity of normal fluid velocity .

$$\begin{aligned} & m_{1n}.\cos\theta_{1n}.[A_{1n\downarrow}.e^{q_{1n}} - A_{1n\uparrow}] \quad + \quad m_{2n}.\cos\theta_{2n}.[A_{2n\downarrow}.e^{q_{2n}} - A_{2n\uparrow}] \\ + \quad & m_{3n}.\sin\theta_{3n}.[A_{3n\downarrow}.e^{q_{3n}} - A_{3n\uparrow}] \quad - \quad m_{1(n+1)}.\cos\theta_{1(n+1)}.\left[A_{1(n+1)\downarrow} - A_{1(n+1)\uparrow}.e^{q_{1(n+1)}}\right] \\ & - \quad m_{2(n+1)}.\cos\theta_{2(n+1)}.\left[A_{2(n+1)\downarrow} - A_{2(n+1)\uparrow}.e^{q_{2(n+1)}}\right] \\ & - \quad m_{3(n+1)}.\sin\theta_{3(n+1)}.\left[A_{3(n+1)\downarrow} - A_{3(n+1)\uparrow}.e^{q_{3(n+1)}}\right] \quad = \quad 0 \end{aligned} \tag{3.38}$$

6. Continuity of fluid pressure.

$$\begin{aligned} & m_{1n}.kf_n.l_{1n}.[A_{1n\downarrow}.e^{q_{1n}} + A_{1n\uparrow}] \quad + \quad m_{2n}.kf_n.l_{2n}.[A_{2n\downarrow}.e^{q_{2n}} + A_{2n\uparrow}] \\ & - \quad m_{1(n+1)}.kf_{(n+1)}.l_{1(n+1)}.\left[A_{1(n+1)\downarrow}.e^{q_{1(n+1)}} + A_{1(n+1)\uparrow}\right] \\ & - \quad m_{2(n+1)}.kf_{(n+1)}.l_{2(n+1)}.\left[A_{2(n+1)\downarrow}.e^{q_{2(n+1)}} + A_{2(n+1)\uparrow}\right] \quad = \quad 0 \end{aligned} \tag{3.39}$$

where $q_{jk} = i.\cos\theta_{jk}.l_{jk}.d_k$ where k is the layer number and j is the wavetype (1 to 3).

For each layer there are three upgoing ($A_{jk\uparrow}$) and three downgoing ($A_{jk\downarrow}$) wave amplitudes. There are only the three downgoing waves in the absence of a source in the substrate, hence the $A_{j(n+1)\uparrow}$ terms in the above equations will not appear for the lowest interface. For an airborne source the boundary condition equations at the air-ground interface are those given in equation 3.24 and following.

For any number of ground layers the boundary condition equations are mapped onto a single array and the equations solved simultanaeously for all the wave amplitudes. The solution is made using a NAG library routine F04ADF to solve the complex global matrix [77]. This routine uses Crouts Factorisation to obtain solutions. The mapping of the matrices of interface boundary condition equation terms onto the global matrix is demonstrated in figure 3.5.

This solution method is used by Schmidt [59] in his SAFARI FFP code. However the global matrix is never explicitly formed, the solution being obtained from the arrays representing the boundary condition equations at each interface using a pointer system.

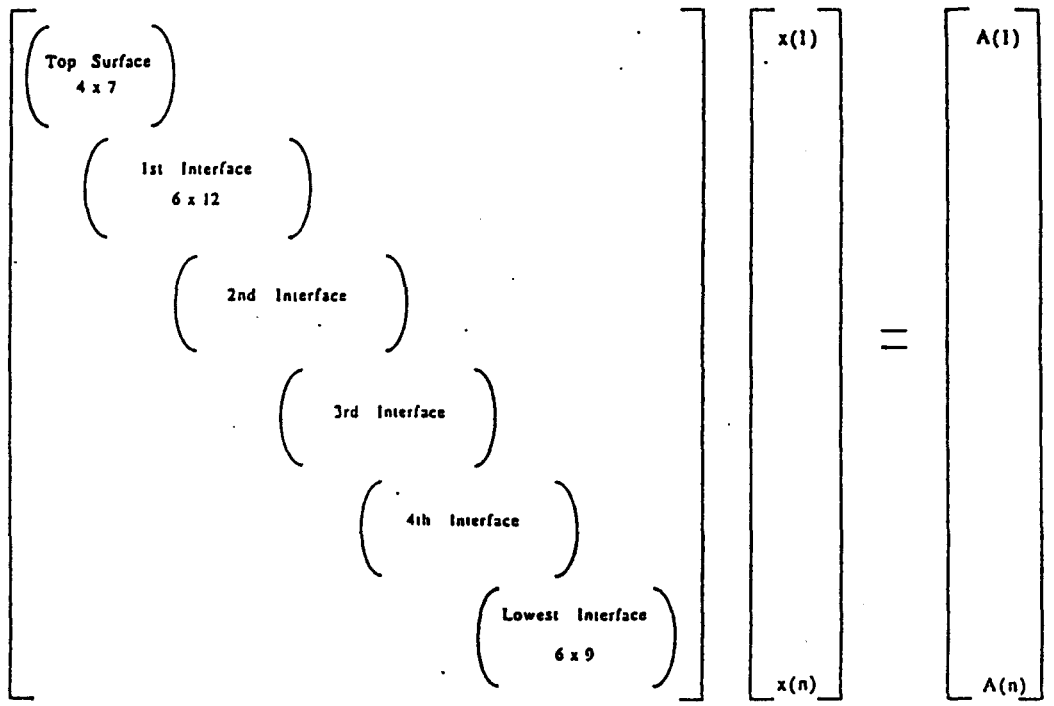

Figure 3.5 Mapping of local boundary condition equations onto global matrix.

Using the wave amplitudes derived from the solution of the boundary condition equations it is possible to calculate acoustic-seismic coupling ratios (the ratio of particle velocity in the ground to acoustic pressure in the air) This quantity can be directly measured using a microphone and geophone. Also the normal acoustic impedance of soils with complicated acoustic and seismic structures can be modelled.

The code used to implement the above calculations is MULTIPORO. It is listed in appendix C.

3.4 The variable porosity model

This section gives one example of the use of the multilayered impedance model described above.

Donato [78] derived an equation for the normal surface impedance of a rigid-porous surface with an exponentially decreasing porosity with depth. Attenborough [79] showed that Donato's results were actually for a porosity exponentially *increasing* with depth. Attenborough rederived the normal surface impedance using the same method as Donato, but for the porosity decreasing with depth. Attenborough's method is shown here. The expression for the normalised propagation constant in the soil is;

$$k_b = (\gamma\Omega)^{1/2}\left[\left(\frac{4}{3} - \frac{\gamma-1}{\gamma}N_{pr}\right)\frac{q^2}{\Omega} + \frac{is_p^2\sigma}{4\rho_0\omega}\right]^{1/2}, \qquad (3.40)$$

This is a low frequency-high flow resistivity approximation of the propagation constant expression derived from Equations ?? and 2.16. Postulating an exponential porosity-depth relation;

$$\Omega(z) = \Omega(0)e^{-\alpha z} \qquad (3.41)$$

and using the Bruggeman relationship between the porosity Ω and the tortuosity q^2 (Equation 2.20), together with the relation;

$$\frac{\sigma\Omega}{q^2} = constant \qquad (3.42)$$

(from reference [80]), leads to

$$\sigma(z) = \sigma(0)e^{(1+n')\alpha z}. \tag{3.43}$$

Putting these depth relations into equation 3.40 and substituting the propagation constant into the wave equation for the soil leads to

$$\frac{d^2\Phi}{dz^2} + \gamma(\frac{\omega}{c_0})^2 \left[a\Omega^{-n'}(0) + \frac{is_p^2\sigma(0)\Omega(0)}{4\rho_0\omega} \right] e^{n'\alpha z}\Phi = 0 \tag{3.44}$$

where $a = \left(\frac{4}{3} - \frac{\gamma-1}{\gamma}N_{pr}\right)$. Making the substitution $x = e^{n'\alpha z/2}$ yields

$$x\frac{d^2\Phi}{dx^2} + \frac{d\Phi}{dx} + \left(\frac{2\beta}{n'\alpha}\right)x\Phi = 0 \tag{3.45}$$

where $\beta = k_b(0)(\omega/c_0)$. This equation has solutions of the form

$$\Phi = AH_0^2(2\beta e^{n'\alpha z/2}/(n'\alpha)) + CH_0^1(2\beta e^{n'\alpha z/2}/(n'\alpha)) \tag{3.46}$$

Attenborough mistakenly set C to zero in order to satisfy the radiation condition

$$z \overset{lim}{\rightarrow} \infty \left(\sqrt{z}\frac{\partial\Phi}{\partial z} + \frac{1}{c_0}\frac{\partial\Phi}{\partial t}\right) = 0. \tag{3.47}$$

Using the relationships $u = \partial\Phi/\partial z$ and $p = -i\omega\rho(z)\Phi$ the following equation was derived for the normal surface impedance.

$$Z_c(0) = iZ_{c0}\frac{H_0^2(2\beta/(n'\alpha))}{H_1^2(2\beta/(n'\alpha))}. \tag{3.48}$$

By making use of the large argument approximations to the Hankel functions

$$\frac{H_0^2(z)}{H_1^2(z)} \approx \left(-i + \frac{1}{2z}\right), \tag{3.49}$$

it became possible to derive a simplified relationship between the characteristic impedance of the material at the surface (Z_{c0}), and the normal surface impedance;

$$Z(0) \approx Z_{c0}(1 + in'\alpha/4\beta). \tag{3.50}$$

By using a high flow resistivity, low frequency approximation, which involves approximation of the characteristic impedance of the porous material at the top surface using a single parameter [79],

$$Z(0) = 0.436(\frac{\sigma_e}{f})^{1/2} + i0.436(\frac{\sigma_e}{f})^{1/2} \tag{3.51}$$

the equation for the normal surface impedance was further simplified to;

$$Z(0) = 0.436(\frac{\sigma_e}{f})^{1/2} + i\left[0.436(\frac{\sigma_e}{f})^{1/2} + 19.48(\frac{\alpha_e}{f})\right] \qquad (3.52)$$

where $\sigma_e = s_p^2\sigma/\Omega$, and $\alpha_e = n'\alpha/\Omega$.

Figure 3.6 compares the predicted normal surface impedance of a soil with an exponential porosity decrease with depth using the two parameter approximation (Equation 3.52) to the MULTIPORO impedance output and the calculated impedance using a multiply layered fluid approximation after Brekhovskikh [55] where the complex fluid effective densities and bulk moduli in each layer are described by a Rayleigh Attenborough model. In both the MULTIPORO and the layered fluid model five layers are used. The input parameters are listed in table 3.4. The predictions of the rigid-frame limit of MULTIPORO and the Brekhovskikh fluid layer model are graphically indistinguishable for these parameters and are represented by a single line in figure 3.6.

Table 3.2 Layer parameters used in the prediction of normal surface impedance for exponential porosity decrease.

Layer depth metres	Flow resistivity mks raylsm^{-1}	Porosity	s_p	n'
0.035	106600	0.4	0.3	1.5
0.070	212000	0.304	0.3	1.5
0.105	421700	0.231	0.3	1.5
0.140	838700	0.175	0.3	1.5
0.175	1688000	0.133	0.3	1.5

The Brekhovskikh and MULTIPORO outputs agree very well and with Attenborough's exponential porosity decrease two parameter approximation in this case. This good agreement is in spite of the fact that the wrong solution to Equation 3.45 was chosen.

Berry [81] showed that to satisfy the radiation condition the Hankel function of the first kind should be chosen as the solution to equation 3.45 instead of the Hankel function of the second kind. This choice then leads to

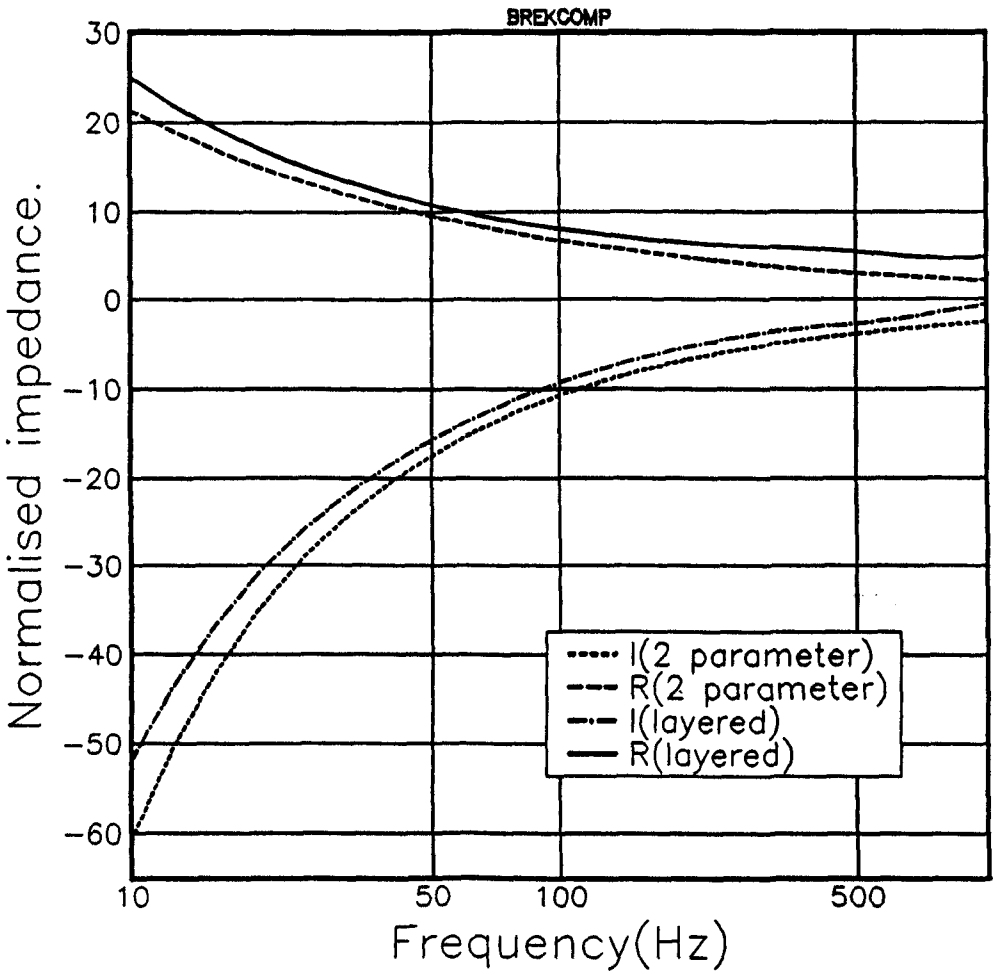

Figure 3.6 Comparison of predicted normal surface impedance using the Brekhovskikh fluid layer model, a two parameter model, and a rigid frame limit of MULTIPORO, for an exponential porosity decrease. α=7.841, σ =106600mks rayls m^{-1}.

the corrected form of equation 3.48;

$$Z_c(0) = -iZ_{c0}\frac{H_0^1(2\beta/n'\alpha)}{H_1^1(2\beta/n'\alpha)}. \tag{3.53}$$

This corrected equation can similarly be simplified to an equation similar to equation 3.51

$$Z(0) = 0.436(\frac{\sigma_e}{f})^{1/2} + i\left[0.436(\frac{\sigma_e}{f})^{1/2} - 19.48(\frac{\alpha_e}{f})\right]. \tag{3.54}$$

However the results of this simplified model fail to agree with predictions of a multilayered model, as it gives an imaginary part of the impedance much smaller than the real part. It can be seen from figure 3.6 that for an exponential porosity decrease the imaginary part of the impedance is larger than the real part at low frequencies.

The exact forms of equations 3.48 and 3.53 give predicted impedances which are shown in figure 3.7 for the same parameters as used in figure 3.6. It can be seen that the exact forms give similar impedances to the approximations, with Attenborough's original version giving a larger imaginary part to the impedance than the real part, and Berry's revised version giving a smaller imaginary part. For the example given here the approximate Attenborough impedance model gives results closer to those of the layered model impedance than the more exact Attenborough equation does, although this is not always the case.

Attenborough's two parameter approximation has been widely used in fitting measured impedances [82,83] and impedances over grassland often show a larger imaginary than real part where the rate of decrease of porosity with depth is large. The effect on normal surface impedance of an exponential porosity decrease will be similar to that of a thin rigidly backed layer. For thin rigidly-backed layers the imaginary part of the impedance exceeds the real part.

Appendix A shows that the two parameter approximation gives reasonable agreement with a multilayered model for a variety of values of α.

In conclusion; The normal surface impedance has been calculated of a ground made up of several layers imitating an exponential porosity decrease.

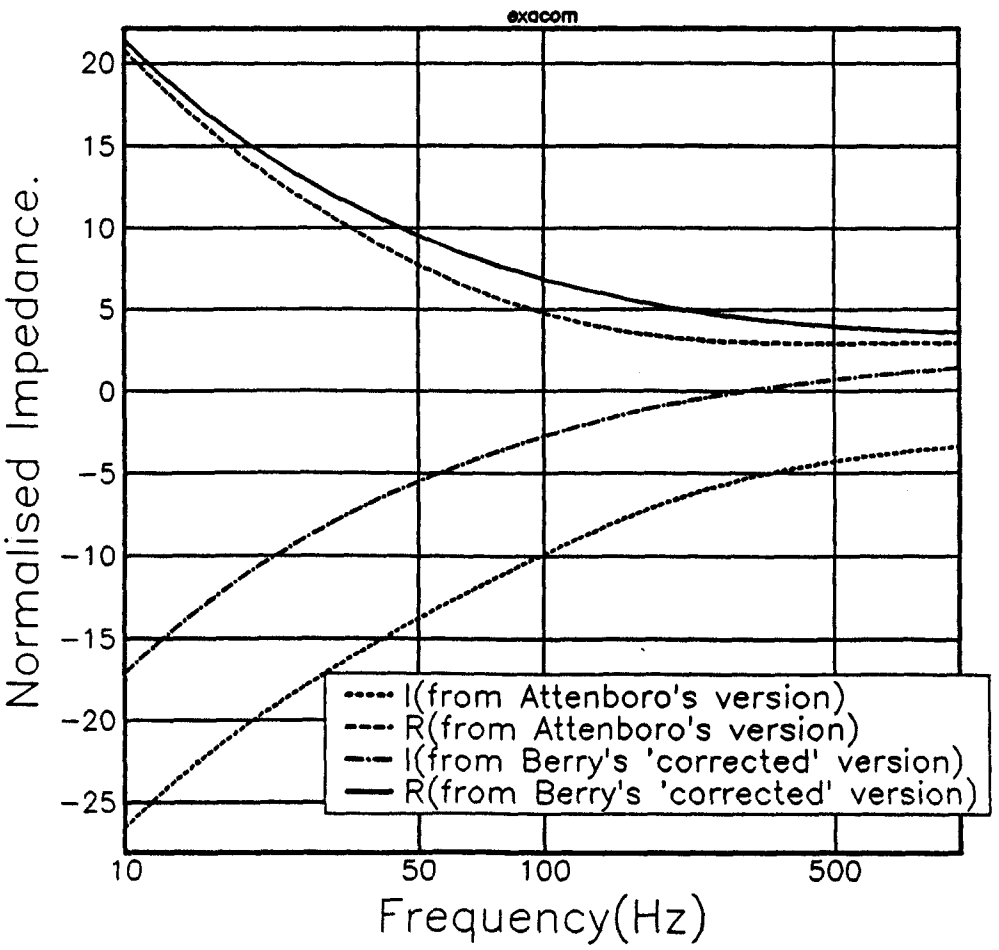

Figure 3.7 Normal surface impedance predicted using equations 3.48 and 3.53 for the parameters used in figure 3.6.

It has been found that the impedance of this ground surface generally agrees in form with a low frequency, high flow resistivity, approximate impedance model for a ground with exponentially decreasing porosity with depth, given by Attenborough. It was shown [81] that the derivation of this impedance model is theoretically incorrect, and a corrected model was derived. This corrected model fails to agree with the layered approximation. The corrected model also fails to agree with measurements over many ground surfaces.

In spite of the fact that Attenborough's two parameter approximation can no longer be based on the variable porosity model, it does show remarkable agreement with the representation of an exponential decrease in porosity by a set of layers using MULTIPORO or the Brekhovskikh fluid layer approximation.

The use of a multiply layered model to derive it gives considerable validity to the two parameter approximation as a ground impedance model for general use in predictions of atmospheric propagation.

Chapter 4

Porous Elastic Propagation Model (FFLAGS)

This propagation model uses the Fast Fourier method described in chapter 2 section 4. The environment is assumed to be range independent and to consist of a fluid (air) upper half-space overlying a set of horizontal fluid (air) layers of differing sound speeds and densities. The lowest of these fluid layers is in contact with a ground made up of a set of horizontal elastic porous layers under which is an elastic porous half-space. The number of layers in either fluid or ground can be set to zero. Height in the fluid (h) is considered positive upward, and depth in the porous elastic solid (d) is considered positive downward.

4.1 Propagation in the fluid(air)

The inhomogeneous Helmholtz equation in the fluid in the presence of a source may be written,

$$\left[\nabla^2 + k^2(r,h)\right]\psi(r,h,\omega) = f(r,h,\omega), \tag{4.1}$$

where ψ is given by

$$\psi_{(r,h)} = \int_{k_h=0}^{\infty} J_\nu(k_h.r).\bar{\psi}_{(k_h,h)}.k_h.dk_h, \tag{4.2}$$

and $f(r,h,\omega)$ is a source term,

$$f(r,h,\omega) = S\frac{\delta(h-h_s)\delta(r)}{2\pi}. \tag{4.3}$$

The source strength S will be set at unity. ψ can be calculated from $\bar{\psi}$ and by performing the integration (Equation 4.2) in the manner described in section 2.4.

The solution to the inhomogeneous Helmholtz equation (Equation 4.1) in a fluid layer containing a source, is the sum of the solution of the inhomogeneous Helmholtz equation in the absence of boundaries, and the solution to the homogeneous Helmholtz equation,

$$\left[\nabla^2 + k^2(r,h)\right]\psi(r,h,\omega) = 0, \tag{4.4}$$

in the presence of the boundaries [59]. The depth dependent Greens function part of the solution to Equation 4.4 in the presence of boundaries at heights h_1 and h_2 $(h_1 < h_2)$ is,

$$\bar{\psi} = \left[R_{\uparrow}.e^{i.(h_1-h).\beta_0} + R_{\downarrow}.e^{i.(h-h_2).\beta_0}\right], \tag{4.5}$$

where,

$$\beta_0 = \left(l_0^2 - k_h^2\right)^{\frac{1}{2}} \tag{4.6}$$

and l_0 is the propagation constant in the medium. Equation 4.5 is the depth dependent Greens function in a layer containing no source. The range dependent part and the integral in Equation 4.2 are identical for the solution to both the homogeneous and inhomogeneous Helmholtz equations and hence the height dependent part of the solution (called the depth dependent Greens function) is the sum of the depth dependent Greens functions of each part of the solution. So $\bar{\psi}$ in the presence of a boundary is the sum of Equation 4.5 and the Greens function in the absence of the boundaries,

$$\bar{\psi} = \left[\frac{1}{\beta_0}e^{i.|h_s-h|.\beta_0} + R_{\uparrow}.e^{i.(h_1-h).\beta_0} + R_{\downarrow}.e^{i.(h-h_2).\beta_0}\right], \tag{4.7}$$

for a layer containing a spherical point source.

The $R_{\updownarrow}$ are calculated by solution of the boundary condition equations at the interfaces (see section 4.3 below).

Schmidt [59] has included in his FFP formulation the effect of a sound velocity gradient within each layer. In the case of a layer not containing a

source the depth dependent part of Ψ is given by

$$\bar{\psi} = \left[R_{\uparrow}.Ai(\zeta).e^{i.(h_1-h).\beta_0} + R_{\downarrow}.Bi(\zeta).e^{i.(h-h_2).\beta_0}\right], \tag{4.8}$$

where Ai and Bi are Airy functions of the first and second kind respectively and $\zeta = (\rho\omega^2 a)^{-2/3}(k_h - \rho\omega^2(az+b))$. The depth dependence of the sound speed is given by $c(z) = \sqrt{1/(\rho(az+b))}$. This gives an approximately linear sound speed gradient. This formulation is not used here.

Wilson [84] attempts to include the effects of turbulence in the atmosphere by stochastic perturbations of the sound speed gradient. This is also not used here.

4.2 Propagation in porous elastic media

From the wave equations for the porous-elastic solid,

$$\nabla^2(H\phi_1 - C\phi_2) = \frac{\partial^2}{\partial t^2}(\rho\phi_1 - \rho_f\phi_2), \tag{4.9}$$

$$\nabla^2(C\phi_1 - M\phi_2) = \frac{\partial^2}{\partial t^2}(\rho_f\phi_1 - \rho'\phi_2), \tag{4.10}$$

$$g_b\nabla^2\chi_1 = \frac{\partial^2}{\partial t^2}(\rho\chi_1 - \rho_f\chi_2), \tag{4.11}$$

$$\frac{\partial^2}{\partial t^2}(\rho_f\chi_1 - m\chi_2) = \frac{\eta}{\kappa}\left(\frac{\partial\chi_2}{\partial t}F(\lambda)\right), \tag{4.12}$$

and assuming a time dependence of $e^{-i\omega t}$ we obtain the frequency dependent equations,

$$\nabla^2(H\phi_1 - C\phi_2) = -\omega^2(\rho\phi_1 - \rho_f\phi_2), \tag{4.13}$$

$$\nabla^2(C\phi_1 - M\phi_2) = -\omega^2(\rho_f\phi_1 - \rho'\phi_2), \tag{4.14}$$

$$g_b\nabla^2\chi_1 = -\omega^2(\rho\chi_1 - \rho_f\chi_2), \tag{4.15}$$

$$\omega^2\left(\rho_f\chi_1 - \rho_c\chi_2\right) = 0, \tag{4.16}$$

where,

$$\rho_c = \left[m - \frac{i\eta}{\kappa\omega}F(\lambda)\right]. \tag{4.17}$$

ϕ_1 and ϕ_2 are scalar displacement potentials, and χ_1 and χ_2 are vector displacement potentials. There are two possible solutions for both ϕ_1 and ϕ_2 in the absence of boundaries (see chapter 2) corresponding to slow and fast waves. The general solution for Φ_1 and Φ_2 is therefore the sum of these solutions, denoted by subscripts slow and fast respectively.

$$\Phi_1 = \phi_{1fast} + \phi_{1slow}, \quad \Phi_2 = \phi_{2fast} + \phi_{2slow}. \tag{4.18}$$

These may be related to the displacements by,

$$u = \nabla\Phi_1 + \nabla \wedge \chi_1, \tag{4.19}$$

$$w = \nabla\Phi_2 + \nabla \wedge \chi_2. \tag{4.20}$$

w is the relative fluid displacement, and u is the solid matrix displacement. From Equations 4.15 and 4.16 it can be seen that χ_1 and χ_2 are simply related and for this case they can be replaced by a scalar displacement potential Φ_3 [44], where,

$$\chi_1 = \hat{\theta}\frac{\partial\Phi_3}{\partial r}, \tag{4.21}$$

and

$$\chi_2 = m_3\chi_1. \tag{4.22}$$

The three scalar displacement potentials are

$$\Phi_1 = \int_0^\infty \bar{\Phi}_1 J_0(k_h.r).k_h.dk_h \tag{4.23}$$

$$\Phi_2 = \int_0^\infty \bar{\Phi}_2 J_0(k_h.r).k_h.dk_h \tag{4.24}$$

$$\Phi_3 = \int_0^\infty \bar{\Phi}_3 J_0(k_h.r).dk_h, \tag{4.25}$$

Φ_1 is the longitudinal displacement potential in the solid, Φ_2 is the longitudinal displacement potential in the fluid, Φ_3 is the transverse displacement potential in the solid, to which the fluid transverse displacement potential is directly proportional.

In a porous-elastic layer, bounded by interfaces at depths d_1 and d_2, in the absence of a source, the $\bar{\Phi}_i$s at a depth z are given by.

$$\bar{\Phi}_1 = A_{1\downarrow}e^{i(z-d_1)\beta_1} + A_{1\uparrow}e^{i(d_2-z)\beta_1} + A_{2\downarrow}e^{i(z-d_1)\beta_2} + A_{2\uparrow}e^{i(d_2-z)\beta_2} \tag{4.26}$$

$$\bar{\Phi}_2 = m_1 \left(A_{1\downarrow} e^{i(z-d_1)\beta_1} + A_{1\uparrow} e^{i(d_2-z)\beta_1} \right) + m_2 \left(A_{2\downarrow} e^{i(z-d_1)\beta_2} + A_{2\uparrow} e^{i(d_2-z)\beta_2} \right) \quad (4.27)$$

$$\bar{\Phi}_3 = A_{3\downarrow} e^{i(z-d_1)\beta_3} + A_{3\uparrow} e^{i(d_2-z)\beta_3} \quad (4.28)$$

The m_i are given in chapter 3 by Equations 3.19

4.3 Boundary conditions

Boundary condition equations in cylindrical polar coordinates $(r, \theta, z)$are needed. However the axisymmetric nature of the problem considered here means that there is no θ dependence.

The boundary condition equations are calculated using the following relations between the parameters used for the boundary conditions and the displacement potentials.

At boundaries between two fluid layers the two boundary conditions are

1. continuity of pressure,

$$p = k_0 \nabla^2 \psi, \quad (4.29)$$

2. continuity of normal particle displacement,

$$u_z = \frac{\partial \psi}{\partial z}. \quad (4.30)$$

At the interface between the fluid and the porous elastic medium there are four boundary conditions,

1. continuity of total normal stress [5],

$$\sigma_{zz} = k_0 \nabla^2 \psi = H \nabla . u - 2 g_b \frac{\partial u_r}{\partial r} - C \nabla . w, \quad (4.31)$$

2. continuity of normal displacement [5],

$$\frac{\partial \psi}{\partial z} = u_z - w_z = \frac{\partial \Phi_1}{\partial z} - \frac{\partial \Phi_2}{\partial z} - (1 - m_3) \frac{1}{r} \frac{\partial}{\partial r} \left(r \frac{\partial \Phi_3}{\partial r} \right), \quad (4.32)$$

3. continuity of fluid pressure [44],

$$p = k_0 \nabla^2 \psi = C \nabla^2 \Phi_2 - M \nabla^2 \Phi_1, \quad (4.33)$$

and

4. continuity of tangential stress,

$$\sigma_{zr} = 0 = g_b \left[\frac{\partial u_r}{\partial z} + \frac{\partial u_z}{\partial r} \right]. \tag{4.34}$$

Six boundary conditions are required at each interface between porous-elastic layers. These boundary conditions are the four above and two others,

5. continuity of normal relative fluid displacement,

$$w_z = \frac{\partial \Phi_2}{\partial z} - m_3 \frac{1}{r} \frac{\partial}{\partial r} \left(r \frac{\partial \Phi_3}{\partial r} \right), \tag{4.35}$$

and

6. continuity of tangential frame displacement,

$$u_r = \frac{\partial \Phi_1}{\partial r} + \frac{\partial^2 \Phi_3}{\partial r \partial z}. \tag{4.36}$$

Taking the above differential equations and inserting the displacement potentials Φ_i leads to the following boundary condition equations.

For the fluid layer interfaces there are two boundary conditions, the first is,

1. continuity of pressure. Taking the differential equation 4.29 and using cylindrical polar coordinates with no azimuthal dependence we arrive at the following differential equation for the fluid pressure,

$$p = k_0 \left[\frac{\partial^2 \psi}{\partial z} + \frac{1}{r} \frac{\partial}{\partial r} \left(r \frac{\partial \psi}{\partial r} \right) \right]. \tag{4.37}$$

Using the recurrence relations for Bessel functions [61] this becomes,

$$p = k0 \int_{k_h=0}^{\infty} \left(\frac{\partial^2 \bar{\psi}}{\partial z^2} - k_h^2 \bar{\psi} \right) J_0(k_h r) k_h dk_h. \tag{4.38}$$

For a layer not containing a source, $\bar{\psi}$ in Equation 4.2 is given by Equation 4.5. Substituting Equation 4.5 into Equation 4.38 gives,

$$p = k0 \int_{k_h=0}^{\infty} l_0^2 . \left[R_{\downarrow} e^{i(h-h_2)\beta_0} + R_{\uparrow} . e^{i(h_1-h)\beta_0} \right] J_0(k_h r) k_h dk_h. \tag{4.39}$$

For both sides of a fluid layer boundary the integral and the Bessel function are identical. Therefore it is only necessary to equate the depth dependent part of the integral(the depth dependent Greens function) at the boundary. If neither the layer above the interface, nor the layer below the interface, contain a source then the equation for continuity of pressure is,

$$k0_m.l_{0m}^2.\left[R_{m\downarrow} + R_{m\uparrow}.e^{g_m}\right] = k0_{(m+1)}.l_{0(m+1)}^2.\left[R_{(m+1)\downarrow}.e^{g_{m+1}} + R_{(m+1)\uparrow}\right], \tag{4.40}$$

where $g_m = i.\beta_{0m}.h_m$.

If a simple spherical source is present in layer m then Equation 4.40 is modified to include the source term,

$$\begin{aligned} & k0_m.l_{0m}^2.\left[R_{m\downarrow} + R_{m\uparrow}.e^{g_m} + \frac{1}{\beta_{0m}}e^{i|h_s-h_m|\beta_{0m}}\right] \\ & = k0_{(m+1)}.l_{0(m+1)}^2.\left[R_{(m+1)\downarrow}.e^{g_{m+1}} + R_{(m+1)\uparrow}\right] \end{aligned}. \tag{4.41}$$

The other boundary condition equation at the fluid layer boundaries is derived similarly. The other boundary condition equations are presented below in the absence of sources. The second boundary condition is,

2. continuity of normal particle displacement,

$$\beta_{0m}.\left[R_{m\downarrow} - R_{m\uparrow}.e^{g_m}\right] = \beta_{0(m+1)}.\left[R_{(m+1)\downarrow}.e^{g_{m+1}} - R_{(m+1)\uparrow}\right]. \tag{4.42}$$

For the porous-elastic layer to fluid interface there are four boundary condition equations. The first of these is,

1. continuity of total normal stress. Beginning with the stress-strain relation of Equation 4.31 and using the differential equations for the solid and relative fluid particle displacements from Equations 4.32, 4.36, and 4.35, leads to the following differential equation for the total normal stress,

$$\begin{aligned} \sigma_{zz} = H & \left[\frac{\partial^2\Phi_1}{\partial z^2} - \frac{\partial}{\partial z}\frac{1}{r}\frac{\partial}{\partial r}\left(r\frac{\partial\Phi_3}{\partial r}\right) + \frac{1}{r}\frac{\partial}{\partial r}\left(r\frac{\partial\Phi_1}{\partial r}\right) + \frac{1}{r}\frac{\partial}{\partial r}\left(r\frac{\partial^2\Phi_3}{\partial r\partial z}\right)\right] \\ & -2g_b\left[\frac{1}{r}\frac{\partial}{\partial r}\left(r\frac{\partial\Phi_1}{\partial r}\right) + \frac{1}{r}\frac{\partial}{\partial r}\left(r\frac{\partial^2\Phi_3}{\partial r\partial z}\right)\right] \\ -C & \left[\frac{\partial^2\Phi_2}{\partial z^2} - m_3\frac{\partial}{\partial z}\frac{1}{r}\frac{\partial}{\partial r}\left(r\frac{\partial\Phi_3}{\partial r}\right) + \frac{1}{r}\frac{\partial}{\partial r}\left(r\frac{\partial\Phi_1}{\partial r}\right) + m_3\frac{1}{r}\frac{\partial}{\partial r}\left(r\frac{\partial^2\Phi_3}{\partial r\partial z}\right)\right] \end{aligned} \tag{4.43}$$

From the independence of the variables r and z, and using the equations for the displacement potentials (Equations 4.23 to 4.28), the total normal stress in the solid is equated to the pressure in the fluid,

$$\begin{aligned}
&(l_{11}^2.(H - m_{11}.C) - 2g_{b1}.k_h^2)\,[A_{11\downarrow}.e^{q_{11}} - A_{11\uparrow}] \\
+\ &(l_{21}^2.(H - m_{21}.C) - 2g_{b1}.k_h^2)\,[A_{21\downarrow}.e^{q_{21}} - A_{21\uparrow}] \\
-\ &2g_{b1}.k_h.\beta_{31}\,[A_{31\downarrow}.e^{q_{31}} + A_{31\uparrow}] \\
&= k0_1.l_{01}^2.\,[R_{1\downarrow} + R_{1\uparrow}.e^{g_1}]
\end{aligned} \quad . \qquad (4.44)$$

The other boundary condition equations are derived in a similar way. The other boundary conditions at the fluid to porous-elastic boundary are,

2. continuity of normal displacement,

$$\begin{aligned}
&(1 - m_{11})\beta_{11}.\,[A_{11\downarrow}.e^{q_{11}} - A_{11\uparrow}] \ + \ (1 - m_{21})\beta_{21}.\,[A_{21\downarrow}e^{q_{21}} - A_{21\uparrow}] \\
+\ &(1 - m_{31})k_h.\,[A_{31\downarrow}.e^{q_{31}} - A_{31\uparrow}] = \beta_{01}.\,[R_{1\downarrow} - R_{1\uparrow}.e^{g_1}]
\end{aligned} \quad , \qquad (4.45)$$

3. continuity of fluid pressure,

$$\begin{aligned}
(C - m_{11}M).l_{11}^2.\,[A_{11\downarrow}.e^{q_{11}} + A_{11\uparrow}] \ + \ &(C - m_{21}M).l_{21}^2.\,[A_{21\downarrow}.e^{q_{21}} + A_{21\uparrow}] \\
= \ &k0_1.l_{01}.\,[R_{1\downarrow} + R_{1\uparrow}.e^{g_1}]
\end{aligned} \quad , \qquad (4.46)$$

and

4. continuity of tangential stress,

$$\begin{aligned}
&2\beta_{11}.k_h.\,[A_{11\downarrow}.e^{q_{11}} - A_{11\uparrow}] \\
+\ &2.\beta_{21}.k_h.\,[A_{21\downarrow}.e^{q_{21}} - A_{21\uparrow}] \\
-\ &.(\beta_{31}^2 - k_h^2)\,[A_{31\downarrow}.e^{q_{31}} + A_{31\uparrow}] = 0
\end{aligned} \quad . \qquad (4.47)$$

For porous-elastic layer interfaces the boundary condition equations are

1. continuity of total normal stress,

$$\begin{aligned}
&(l_{1n}^2.(H - m_{1n}.C) - 2g_{bn}.k_h^2)\,[A_{1n\downarrow}.e^{q_{1n}} - A_{1n\uparrow}] \\
+\ &(l_{2n}^2.(H - m_{2n}.C) - 2g_{bn}.k_h^2)\,[A_{2n\downarrow}.e^{q_{2n}} - A_{2n\uparrow}] \\
-\ &2g_{bn}.k_h^2.\beta_{3n}\,[A_{3n\downarrow}.e^{q_{3n}} + A_{3n\uparrow}] \\
-\ &(l_{1(n+1)}^2.(H - m_{1(n+1)}.C) - 2g_{b(n+1)}.k_h^2)\left[A_{1(n+1)\downarrow}.e^{q_{1(n+1)}} - A_{1(n+1)\uparrow}\right] \\
-\ &(l_{2(n+1)}^2.(H - m_{2(n+1)}.C) - 2g_{b(n+1)}.k_h^2)\left[A_{2(n+1)\downarrow}.e^{q_{2(n+1)}} - A_{2(n+1)\uparrow}\right] \\
+\ &2g_{b(n+1)}.k_h^2.\beta_{3(n+1)}\left[A_{3(n+1)\downarrow}.e^{q_{3(n+1)}} + A_{3(n+1)\uparrow}\right] \;=\; 0
\end{aligned} \tag{4.48}$$

2. continuity of normal displacement,

$$\begin{aligned}
&(1 - m_{1n})\beta_{1n}.[A_{1n\downarrow}.e^{q_{1n}} - A_{1n\uparrow}] \;+\; (1 - m_{2n})\beta_{2n}.[A_{2n\downarrow}e^{q_{2n}} - A_{2n\uparrow}] \\
&+\ (1 - m_{3n})k_h.[A_{3n\downarrow}.e^{q_{3n}} - A_{3n\uparrow}] \\
&-\ (1 - m_{1(n+1)})\beta_{1(n+1)}.\left[A_{1(n+1)\downarrow} - A_{1(n+1)\uparrow}.e^{q_{1(n+1)}}\right] \\
&-\ (1 - m_{2(n+1)})\beta_{2(n+1)}.\left[A_{2(n+1)\downarrow} - A_{2(n+1)\uparrow}.e^{q_{2(n+1)}}\right] \\
&-\ (1 - m_{3(n+1)})k_h.\left[A_{3(n+1)\downarrow} - A_{3(n+1)\uparrow}.e^{q_{3(n+1)}}\right] \\
&=\ 0
\end{aligned} \tag{4.49}$$

3. continuity of fluid pressure,

$$\begin{aligned}
&(C - m_{1n}M).l_{1n}^2.[A_{1n\downarrow}.e^{q_{1n}} + A_{1n\uparrow}] \;+\; (C - m_{2n}M).l_{2n}^2.[A_{2n\downarrow}.e^{q_{2n}} + A_{2n\uparrow}] \\
&-\ (C - m_{1(n+1)}M).l_{1(n+1)}^2.\left[A_{1(n+1)\downarrow}.e^{q_{1(n+1)}} + A_{1(n+1)\uparrow}\right] \\
&-\ (C - m_{2(n+1)}M).l_{2(n+1)}^2.\left[A_{2(n+1)\downarrow}.e^{q_{2(n+1)}} + A_{2(n+1)\uparrow}\right] \;=\; 0
\end{aligned} \tag{4.50}$$

4. continuity of tangential stress,

$$\begin{aligned}
&g_{bn}\{2\beta_{1n}.k_h.[A_{1n\downarrow}.e^{q_{1n}} - A_{1n\uparrow}] \\
&+\ 2.\beta_{2n}.k_h.[A_{2n\downarrow}.e^{q_{2n}} - A_{2n\uparrow}] \\
&-\ .(\beta_{3n}^2 - k_h^2)\,[A_{3n\downarrow}.e^{q_{3n}} + A_{3n\uparrow}]\} + \\
&g_{b(n+1)}\left\{-\ 2.\beta_{1(n+1)}.k_h.\left[A_{1(n+1)\downarrow} - A_{1(n+1)\uparrow}.e^{q_{1(n+1)}}\right]\right. \\
&-\ 2.\beta_{2(n+1)}.k_h.\left[A_{2(n+1)\downarrow} - A_{2(n+1)\uparrow}.e^{q_{2(n+1)}}\right] \\
&+\ .(\beta_{3(n+1)}^2 - k_h^2)\left.\left[A_{3(n+1)\downarrow} + A_{3(n+1)\uparrow}.e^{q_{3(n+1)}}\right]\right\} \;=\; 0
\end{aligned} \tag{4.51}$$

5. continuity of normal fluid displacement,

$$\begin{aligned} & m_{1n}.\beta_{1n}.\left[A_{1n\downarrow}.e^{q_{1n}} - A_{1n\uparrow}\right] \;+\; m_{2n}.\beta_{2n}.\left[A_{2n\downarrow}.e^{q_{2n}} - A_{2n\uparrow}\right] \\ & \quad + \; m_{3n}.k_h.\left[A_{3n\downarrow}.e^{q_{3n}} - A_{3n\uparrow}\right] \;- \\ & \quad m_{1(n+1)}.\beta_{1(n+1)}.\left[A_{1(n+1)\downarrow} - A_{1(n+1)\uparrow}.e^{q_{1(n+1)}}\right] \\ & - \; m_{2(n+1)}.\beta_{2(n+1)}.\left[A_{2(n+1)\downarrow} - A_{2(n+1)\uparrow}.e^{q_{2(n+1)}}\right] \\ & - \; m_{3(n+1)}.k_h.\left[A_{3(n+1)\downarrow} - A_{3(n+1)\uparrow}.e^{q_{3(n+1)}}\right] \;=\; 0 \end{aligned} \qquad (4.52)$$

and

6. continuity of tangential frame displacement,

$$\begin{aligned} & k_h.\left[A_{1n\downarrow}.e^{q_{1n}} + A_{1n\uparrow}\right] \;+\; k_h.\left[A_{2n\downarrow}.e^{q_{2n}} + A_{2n\uparrow}\right] \\ & - \; \beta_{3n}.\left[A_{3n\downarrow}.e^{q_{3n}} + A_{3n\uparrow}\right] \;-\; k_h.\left[A_{1(n+1)\downarrow} + A_{1(n+1)\uparrow}.e^{q_{1((n+1)+1)}}\right] \\ & - \; k_h.\left[A_{2(n+1)\downarrow} + A_{2(n+1)\uparrow}.e^{q_{2(n+1)}}\right] \;+\; \beta_{3(n+1)}.\left[A_{3(n+1)\downarrow} + A_{3(n+1)\uparrow}.e^{q_{3(n+1)}}\right] \\ & \qquad = \; 0 \end{aligned} \qquad (4.53)$$

where $q_{jk} = i.\beta_{jk}.d_k$ (k is the layer number and j is the wavetype (1 to 3)). The boundary condition equations for all of the air and ground layers are mapped onto a single array in the manner shown in figure 4.1. The boundary condition equations for all the interfaces can then be simultaneously solved for all the $A_{jn\updownarrow}$ and $R_{m\updownarrow}$. This is done using Crout's Factorization method implemented using a NAG library routine [77]. The $A_{jn\updownarrow}$ and $R_{m\updownarrow}$ are then used to calculate the relevant depth dependent Greens function for the required output parameter. This process is repeated for the set of N horizontal wavenumbers between ($k_{h(min)}$ and $k_{h(max)}$) to calculate a set of N depth dependent Greens functions. The Hankel transform (equation 2.28) is performed on these Greens functions using the Fast Fourier method detailed in section 2.4. This provides the required output parameter as a function of range.

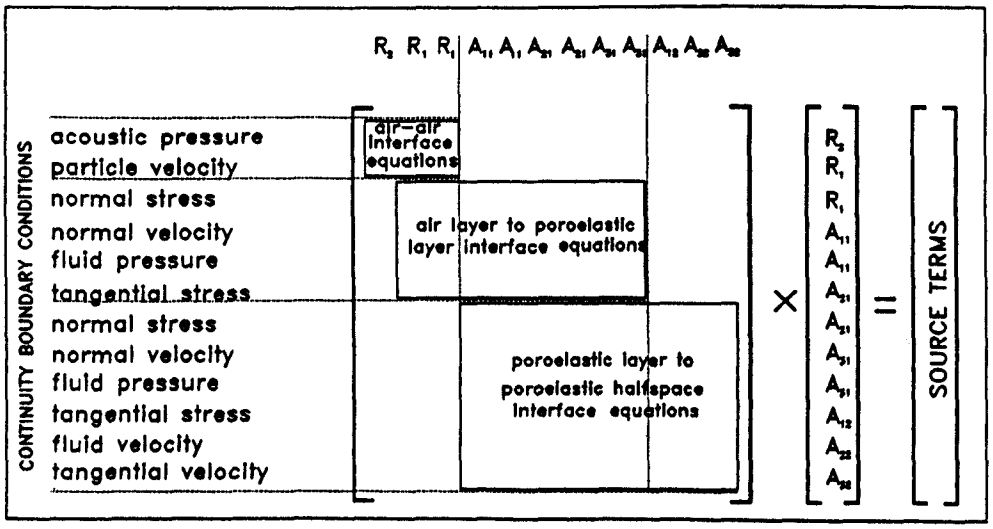

Figure 4.1 Mapping of boundary condition equations onto global matrix, for a single air layer, and a single ground layer, as in figure 4.2.

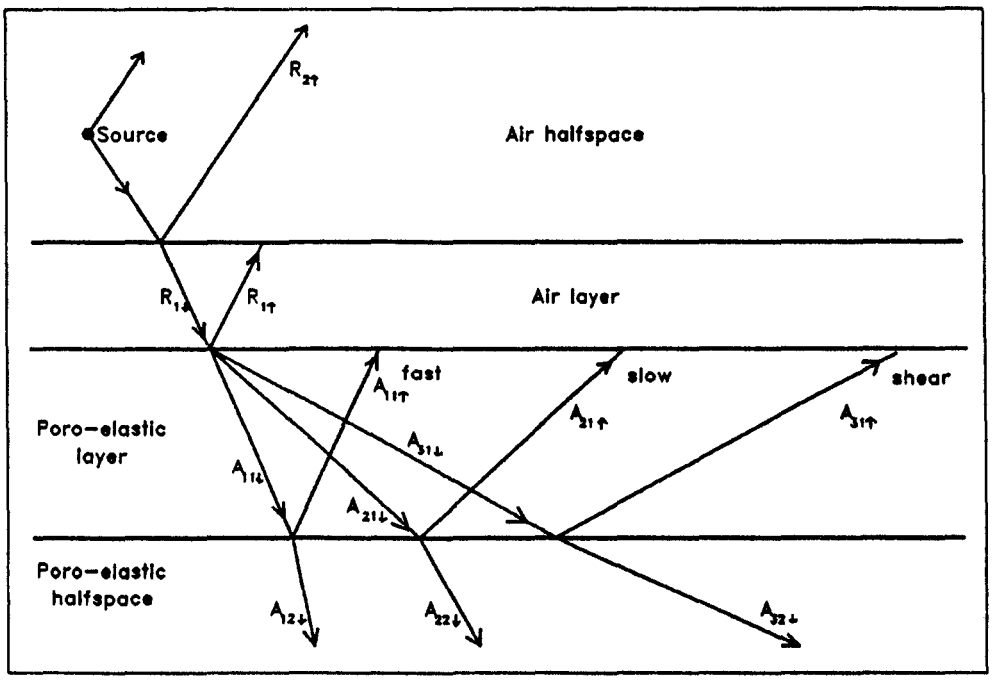

Figure 4.2 An example environment, showing the labelling convention. This is the example for which the boundary conditions are mapped onto the global matrix in figure 4.1.

4.4 Numerical Considerations

For proper computation using this FFP the limits of the numerical integration ($k_{h(max)}$ and $k_{h(min)}$) should be chosen such that all important parts of the integrand lie within them. The number of points of the integration (N) must be chosen so as to represent the integrand accurately. In order to do this the integration range should be initially set very large in order to examine the integrand. The integration range should then be reduced in order to represent the integrand as accurately as possible in the range where it is not small. Figure 4.3 shows the modulus of a typical integrand against k_h for propagation in air over a rigid-backed rigid-porous surface. A reasonable choice of $k_{h(max)}$ is also shown. It must be noted that in using a simple fast Fourier method the distances at which the output occurs are influenced by the choice of the above integration parameters according to the following equations.

$$r_{max} = (N/2)\delta r, \tag{4.54}$$

$$\delta r = \frac{2\pi}{k_{h(max)} - k_{h(min)}}, \tag{4.55}$$

$$r_j = r_{min} + j\delta r \qquad j = 0, 1, 2... \tag{4.56}$$

As in a normal FFT calculation the problem of wrap-around in one domain can occur if undersampling occurs in the other. If a minimum range r_{min} is chosen as greater than 0 then wrap-around occurs of the signal in the range interval 0 to r_{min}into the range $N\delta r$. Because of this effect there is no reason to set r_{min} to anything except zero. In this case the greatest cause of the wrap-around problem is the fact that (unlike most FFP codes) the inward going wave is included. This leads to wrap around from the negative axis. Fortunately this signal is very rapidly attenuated with range, and to avoid the errors due to this signal the maximum range is truncated to $N\delta r/2$ instead of $N\delta r$. Hence the problem of wrap-around from the short range is not encountered. The integration offset α (described in section 2.4) must be carefully chosen. The choice of the value $\alpha = 1.0$ usually gives accurate results. This choice is of the order of ten times that recommended in the CERL FFP [62]. This difference may be because of the interest in this study

in short ranges. Larger values lead to inaccuracies in the approximation to the extra integration path. Smaller values lead to very sharp peaks in the integrand which are difficult to represent accurately with a limited number of points.

In modelling the particle velocity in the ground the integrand at the upper end of the integration range is small enough in all of the cases used in this thesis for a correction for the tail to be unnecessary.

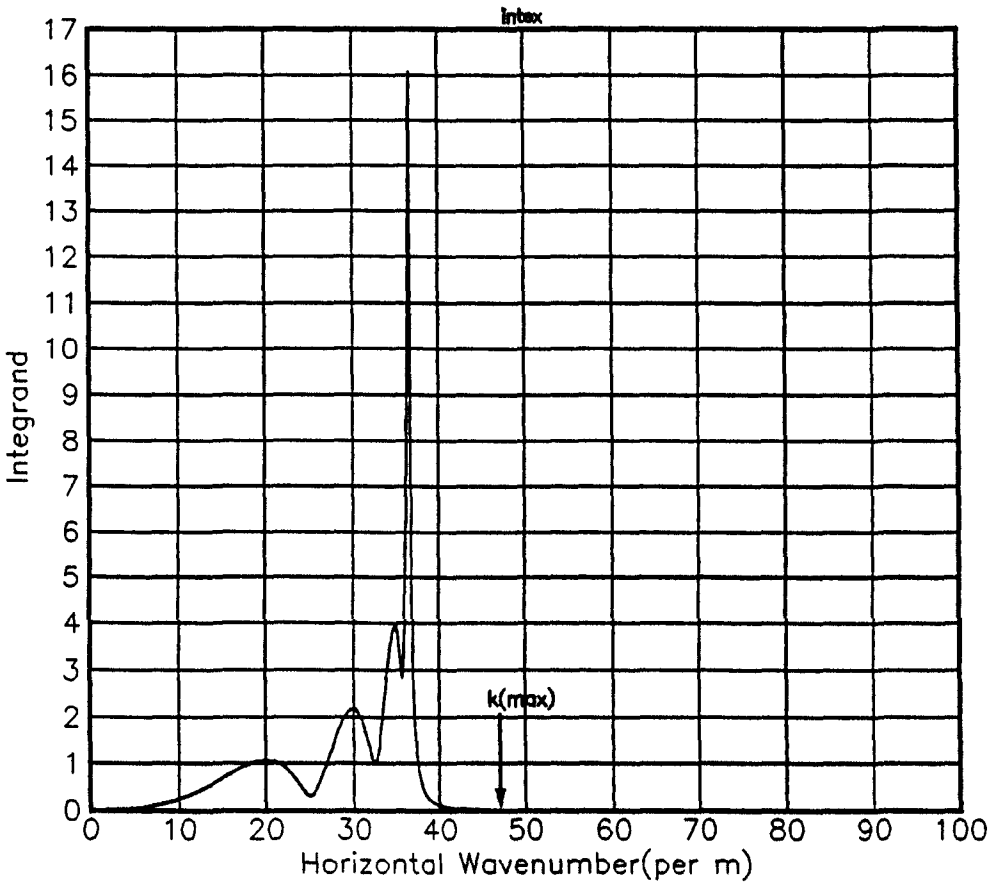

Figure 4.3 Modulus of the integrand for propagation over a non-porous backed rigid porous thin layer at 2kHz.

Many of the predictions shown in this thesis are plotted as a function

of frequency at a single distance from the source. These predictions were achieved by dividing the required frequency range into a number of smaller ranges, usually about an octave in range (for example a frequency range of 50Hz to 500Hz could be divided into three frequency ranges; 50-110Hz,110-240Hz and 240-500Hz). The FFP was performed at the upper and lower frequencies in each of these smaller frequency ranges. The depth dependent Green's function at these frequencies was examined and the integration range and correction parameters were altered to give correct results at these limiting frequencies. The integration was then carried out for all intervening frequencies in each small frequency range using the integration parameters found for the upper and lower frequencies of that frequency range. The result at the relevant distance was picked from the output at each frequency and displayed as a function of frequency at a single distance. For results as a function of frequency a numerical integration method would be more efficient, as only one distance is required. However the overall computational speed would be almost unaffected as the bulk of the computational effort is taken up with calculation of the depth dependent Greens function.

Chapter 5

Comparison of FFLAGS results to Analytic approximations for fields due to a point source above porous media.

The Fast Fourier method described above can be implemented with very high seismic velocities, solid densities, and seismic attenuations for the ground. The model then tends towards being rigid-porous, and can be compared to other models of propagation over rigid-porous surfaces. FFLAGS can then be used to test the validity of analytical models for propagation in an homogeneous halfspace over a rigid porous ground surface. It can be shown [12] that the calculated slow wave or pore wave propagation constant using a Rayleigh-Attenborough rigid porous model, and the rigid frame limit of a modified Biot-Stoll porous-elastic model are almost identical, therefore differences in the predicted sound pressure level between the two models should be due to the propagation model if the seismic wavetypes play no part. To ensure that the seismic effects played no part in the FFLAGS model the seismic velocities, bulk density, and attenuation were all increased until further increase had no discernible effect on the output. It was then assumed that seismic effects would be negligible. The bulk density was set at $20000 kgm^{-3}$, and fast and shear velocities to 5000 and 3000 ms^{-1} respectively. These values are not physically realisable but are set at these values in order to remove any possible effects due to the ground elasticity.

The predictions of FFLAGS were compared to four different propagation

models. For all of these the Rayleigh-Attenborough [12] four parameter description of the propagation constant and characteristic impedance in the porous medium was used.

5.1 Analytic sound propagation models

5.1.1 Attenborough, Hayek and Lawther's 'approximate' extended reaction model

The first model, is the more approximate of the two Attenborough, Hayek and Lawther [44] extended reaction models. The propagation calculation,with misprints corrected, is given by Quartararo for an extended reaction halfspace [85], as an 'approximate' extended reaction model.

$$\Phi_{tot} \approx \frac{e^{ik_1 r_1}}{4\pi r_1} + \frac{e^{ik_1 r_2}}{4\pi r_2}\left[R(\theta_1) + B\{1 - R(\theta_1)\}F(w)\right] \tag{5.1}$$

where R is the plane wave reflection coefficient

$$R = \frac{\cos\theta_1 - M(n^2 - \sin^2\theta_1)^{\frac{1}{2}}}{\cos\theta_1 + M(n^2 - \sin^2\theta_1)^{\frac{1}{2}}} \tag{5.2}$$

$$B = \frac{\left[\cos\theta + \beta(1 - \sin^2\theta/n^2)^{0.5}\right](1 - n^{-2})^{0.5}}{\left[\cos\theta + \beta(1 - n^{-2})^{0.5}/(1 - M^2)^{0.5}\right](1 - \sin^2\theta/n^2)^{0.5}}$$
$$\times \frac{\left[(1 - M^2)^{0.5} + \beta(1 - n^{-2})^{0.5}\cos\theta + \sin\theta(1 - \beta^2)^{0.5}\right]^{0.5}}{(1 - M^2)^{1.5}(2\sin\theta)^{0.5}(1 - \beta^2)^{0.25}} \tag{5.3}$$

and

$$F(w) = 1 + i\pi^{\frac{1}{2}} w e^{-w^2} erfc(-iw) \tag{5.4}$$

and

$$w^2 = ik_1 r_2\left[1 + (\beta_c\cos\theta_1(1 - n^2)^{\frac{1}{2}} - \sin\theta_1(1 - \beta_c^2)^{\frac{1}{2}})/(1 - M^2)^{\frac{1}{2}}\right] \tag{5.5}$$

Where $M = \frac{\rho}{\rho_c}$, n is the complex refractive index and β_c is the normalised characteristic admittance.

5.1.2 Attenborough, Hayek and Lawther's 'exact' extended reaction model.

A more exact formulation for propagation over an extended reaction halfspace is also given by Attenborough, Hayek and Lawther [44]. Misprints are again corrected in Quartararo's thesis [85]. In this the equation 5.1 is replaced by the following

$$\Phi_{tot} \approx \frac{e^{ik_1 r_1}}{4\pi r_1} + R(\theta_1)\frac{e^{ik_1 r_2}}{4\pi r_2} - \frac{k_1 A}{4(1-M^2)}\left[e^{-\frac{x_0^2}{2}} erfc\left(\frac{-ix_0}{\sqrt{2z}}\right) H_0^1(k_1 r_2(1-A^2)^{\frac{1}{2}})(1-A^2)^{\frac{1}{2}} e^{ik_1 r_2}\right] + V' \tag{5.6}$$

$$A = M\left[\frac{n^2-1)}{1-M^2}\right]^{\frac{1}{2}} \tag{5.7}$$

and,

$$x_0^2/2 = ik_1 r_2\left[1 + A\cos\theta_1 - \sin\theta_1(1-A^2)^{\frac{1}{2}}\right], \tag{5.8}$$

where,

$$V' \approx \frac{e^{ik_1 r_2}}{2\pi r_2}\left\{\frac{\cos\theta_0}{\cos\theta_0 + M(n^2-\sin^2\theta_0)} + \frac{A}{\sqrt{2}(1-M^2)}\left(1 + \frac{1+A\cos\theta_0}{(1-A^2)^{\frac{1}{2}}\sin\theta_0}\right)^{\frac{1}{2}} \frac{1}{(A+\cos\theta_0)}\right.$$
$$+ \frac{1}{ik_1 r_2}\left[\frac{F\cos\theta_0}{\cos\theta_0 + M(n^2-\sin^2\theta_0)^{\frac{1}{2}}}\right.$$
$$\left.\left. + \frac{A}{\sqrt{2}(1-M^2)(A+\cos\theta_0)}\left(1 + \frac{1+A\cos\theta_0}{(1-A^2)^{\frac{1}{2}}\sin\theta_0}\right)^{\frac{1}{2}}\left(\frac{1+A\cos\theta_0+(1-A^2)^{\frac{1}{2}}\sin\theta_0}{2(A+\cos\theta_0)^2} + \frac{1}{8\sin\theta_0(1-A^2)^{\frac{1}{2}}}\right)\right]\right\} \tag{5.9}$$

For propagation over a halfspace this model(henceforward referred to as 'exact') was compared to FFLAGS.

5.1.3 Nicholas, Berry and Daigle's approximate extended reaction model for a non-porous backed porous surface layer.

For propagation over a non-porous backed extended reaction porous surface layer Nicholas, Berry and Daigle [50] have modified the reflection coefficient R_{rbl} and the formulation for 'w' from the 'approximate' model of Attenborough, Hayek and Lawther (an error in the equation for 'w' in Nicholas et al's paper has been corrected here).

$$w_{rbl}^2 = (ik_1 r_2/2)[\cos\theta_1 + \rho_1 c_1/Z(l,\theta_1)]^2, \tag{5.10}$$

where $Z(l,\theta_1)$ is the normal surface impedance at an angle of incidence θ_1 over a rigid backed layer of thickness l.

$$Z(l,\theta_1) = \frac{Z}{(1-((k_1/k_2)\cos\theta)^2)^{1/2}} coth(-ik_2 d(1-((k_1/k_2)\cos\theta)^2)^{1/2}), \tag{5.11}$$

and Z is the normalised characteristic impedance. k_2 is the propagation constant of the pore (slow) wave in the porous ground.

$$R_{rbl} = \frac{coth(-ik_2 l(1-n^2\sin^2\theta)^{\frac{1}{2}})\cos\theta - \beta_c\rho_1 c(1-n^2\sin^2\theta)^{\frac{1}{2}}}{coth(-ik_2 l(1-n^2\sin^2\theta)^{\frac{1}{2}})\cos\theta + \beta_c\rho_1 c(1-n^2\sin^2\theta)^{\frac{1}{2}}}. \tag{5.12}$$

These reformulations are then used in equation 5.1.

5.1.4 Attenborough, Hayek and Lawther's local reaction model

For high flow resistivity rigid porous materials the large propagation constant for the slow wave in the material leads to a local reaction approximation. This leads to a simplification of equation 5.1 to,

$$\Phi_{tot} \approx \frac{e^{ik_1 r_1}}{4\pi r_1} + \frac{e^{ik_1 r_2}}{4\pi r_2}[R(\theta_1) + \{1-R(\theta_1)\}F(p_e)], \tag{5.13}$$

where,

$$F(p_e) = 1 + i\pi^{1/2} p_e e^{-p_e^2} erfc(-ip_e), \tag{5.14}$$

and

$$p_e^2 = ik_1 r_2(\beta_c + \cos\theta_0)^2. \tag{5.15}$$

This is identical to the solution due to Rudnick [49], except that the p_e is the approximate value given by Attenborough, Hayek and Lawther [44]. The results due to this formulation are also compared to those of FFLAGS in those cases where the ground is locally reacting.

5.1.5 Thomassons local reaction approximation

Thomasson [86] developed an analytic propagation model over a rigid porous hard backed layer. He assumed that the surface could be approximately

modelled as a locally reacting layer. His expression for the Total field over the surface is as follows

$$\Phi_{tot} \approx \frac{e^{ik_1 r_1}}{4\pi r_1} + \frac{e^{ik_1 r_2}}{4\pi r_2} + \Phi_{ER} \tag{5.16}$$

$$\Phi_{ER} = \Phi_{LR} + \Phi_\epsilon \tag{5.17}$$

Where Φ_ϵ is assumed to be small.

$$\Phi_{LR} = \Phi_1 + \Phi_2 \tag{5.18}$$

$$\Phi_1 = \frac{Ck_0\nu}{2\pi^{1/2}B} e^{ik_0 r_2 \gamma_0} erfc(A) \tag{5.19}$$

$$\begin{aligned} \Phi_2 &= \tfrac{k_0\nu}{\pi^{1/2}B} e^{ik_0 r_2 \gamma_0} \quad (Im(\nu) < 0, Re(\gamma_0) > 1) \\ &= 0 \qquad\qquad\qquad\qquad\qquad\qquad (otherwise) \end{aligned} \tag{5.20}$$

Where

$$\begin{aligned} A &= [ik_0 r_2(\gamma_0 - 1)]^{1/2} && -\tfrac{\pi}{2} \le arg A < \tfrac{\pi}{2} \\ B &= [ik_0 r_2(1 - \gamma_1)]^{1/2} && -\tfrac{\pi}{2} \le arg B < \tfrac{\pi}{2} \\ C &= -1 && (Im(\nu) < 0, Re(\gamma_0) > 1) \\ &= 1 && otherwise \end{aligned} \tag{5.21}$$

where

$$\gamma_0 = -\nu \cos\theta_0 + (1 - \nu^2)^{1/2} \sin\theta_0 \tag{5.22}$$

$$\gamma_1 = -\nu \cos\theta_0 - (1 - \nu^2)^{1/2} \sin\theta_0 \tag{5.23}$$

Where ν is the 'point admittance' of the surface, given by.

$$\nu = n(\rho_0/\rho_1) tan(nk_0 d)/i \tag{5.24}$$

This is the reciprocal of the normal surface impedance of a rigid backed layer given by equation 5.25

$$Z_s = Z coth(ik_1 d) \tag{5.25}$$

where Z is the normalised characteristic impedance of the material of the layer. Attenborough et al [44] showed that Thomasson's calculation was identical to equation 5.13 for a locally reacting rigid backed layer.

5.1.6 Habault and Fillippi's layer potential expansion for a rigidly backed layer

Habault and Fillippi [87] also developed models for propagation over various grounds. These were made using two different methods for each ground type. The first was in terms of layer potentials, and the second in terms of a surface wave representation. Included in this was a series expansion of the layer potential solution,

$$\begin{aligned}\Phi_{tot} \approx & -\frac{e^{ik_1 r_1}}{4\pi r_1} - \frac{e^{ik_1 r_2}}{4\pi r_2}\left\{\frac{Z_h\cos\theta_0 - f}{Z_h\cos\theta_0 + f}\right. \\ & + \frac{i}{2k_1 r_2}\left[\frac{2z_h\cos\theta_0}{(Z_h\cos\theta_0)^2}(2f + f'\cot\theta_0 + f'')\right. \\ & \left.\left. + \frac{4Z_h}{(Z_h\cos\theta_0+f)^3}(f\sin\theta_0 + f'\cos\theta_0)(Z_h\sin\theta_0 - f'')\right] + \ldots\right\},\end{aligned} \tag{5.26}$$

where, Z_h is the normal surface impedance of a rigid backed layer of thickness h,

$$f = K\frac{tan(Kk_2h)}{tan(k_2h)}, \tag{5.27}$$

f' and f'' are the first and second derivatives of f with respect to θ_0 ,

$$K = (1 - k^2\sin^2\theta_0)^{\frac{1}{2}} \tag{5.28}$$

and $k = k_1/k_2$. This series expansion (including only the first two terms) for a rigid backed layer is compared to various results here.

5.2 Numerical comparison of FFP and analytic models.

It was decided to compare FFLAGS and the analytical models for several different conditions. These included various flow resistivities between 300000 mks rayls m^-1 (near local reaction) and 10000 mks rayls m^-1 (extended reaction): a thin(5cm) hard backed layer, rigid surface and an homogeneous halfspace: short range (1 metre) for a range of frequencies between 100Hz and 2000Hz, and two longer ranges (20m and 100m) for a range of frequencies between 100Hz and 5000Hz (800Hz for the longest range). The porosities Ω of the porous media were maintained at 0.3, the grain shape

factor n' at 0.7, and the pore shape factor ratio s_p at 0.5. The flow resistivity was varied independently of the porosity. In section 3.2 it was shown that accepted relationships between flow resistivity and porosity gave flow resistivities much larger than actually measured for soils with low porosity. As there is no porosity-flow resistivity relationship available that corresponds to measurements on soils the flow resistivity has been varied independently of the porosity.

The source and receiver heights were set to 0.3metres and 0.5metres for all the predictions. The first range (one metre) was chosen because similar ranges are used in acoustic ground characterization[88]. Hence it was possible to assess the accuracy of the propagation models used in ground characterisation experiments. The second range (twenty metres) was chosen to test the propagation models at near grazing incidence, as the difference between predicted excess attenuation using plane wave and spherical wave reflection coefficients is greatest at near grazing incidence [89].

5.2.1 Short Range Results

It was found that above a rigid surface the predictions of FFLAGS agreed with the exact result to within 0.05 dB (see Figure 5.1) Most discrepancies in the graphs were due to non-coincidence of the frequencies of the calculation. The comparisons between the aforementioned models for propagation above porous grounds are shown in Figures 5.2 to 5.9. Above the halfspace at a range of one metre both of the Attenborough, Hayek and Lawther extended reaction model predictions agree very well with those of FFLAGS (to within 0.05dB). The local reaction model agrees with the FFP to the same accuracy as the extended reaction models at the high flow resistivity and gradually diverges as the flow resistivity is decreased until at a flow resistivity of 10,000mks rayls the disagreement is up to 0.3 dB(see Figure 5.5). The Habault and Fillippi hard backed layer propagation model was used with a very large layer depth as a comparison. At high flow resistivities the agreement between models was very good, but the disagreement increased as the flow resistivity was decreased until at the lowest flow resistivity the

disagreement between Habault and Fillippi and the other models was up to 0.5dB(see Figures 5.2 to 5.5).

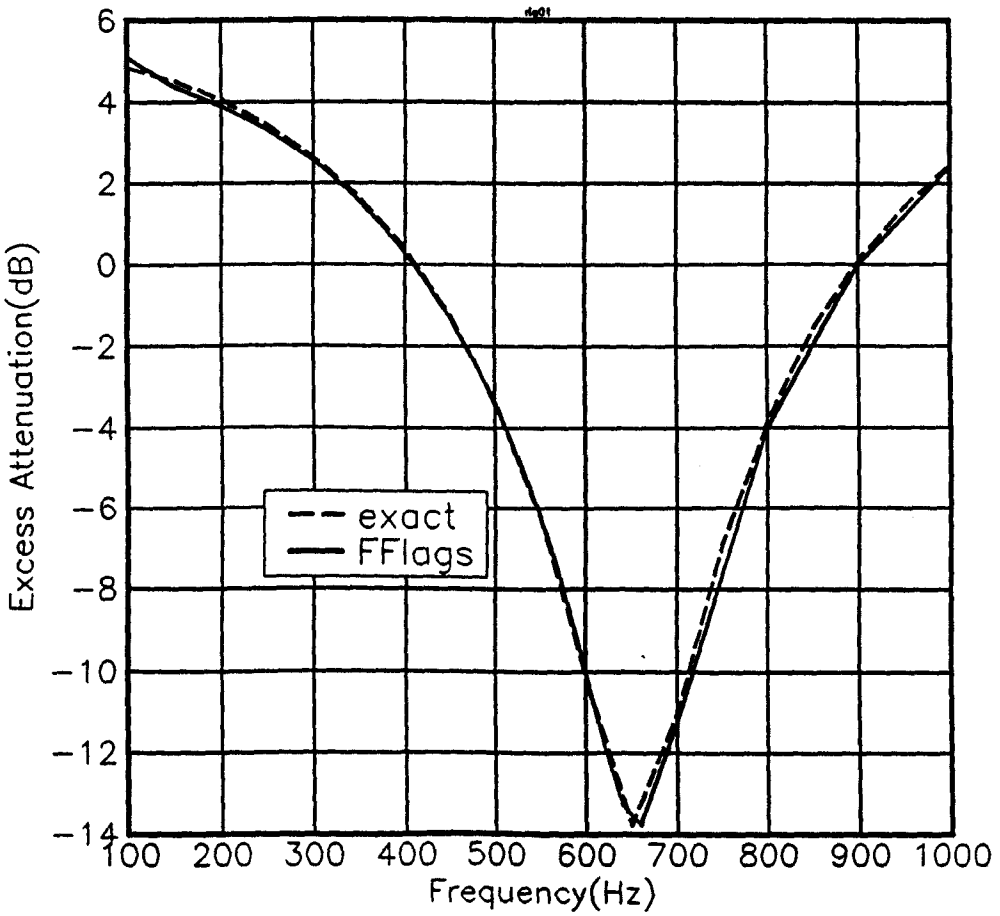

Figure 5.1 Excess attenuation at 1 metre over a rigid surface. FFLAGS, and exact result.

For the rigid backed 5cm layer at a range of one metre predictions of FFLAGS were compared to the Nicholas, Berry and Daigle formulation and the Habault and Fillippi formulation. It was found that for the high flow resistivities all three models agreed extremely well (to within

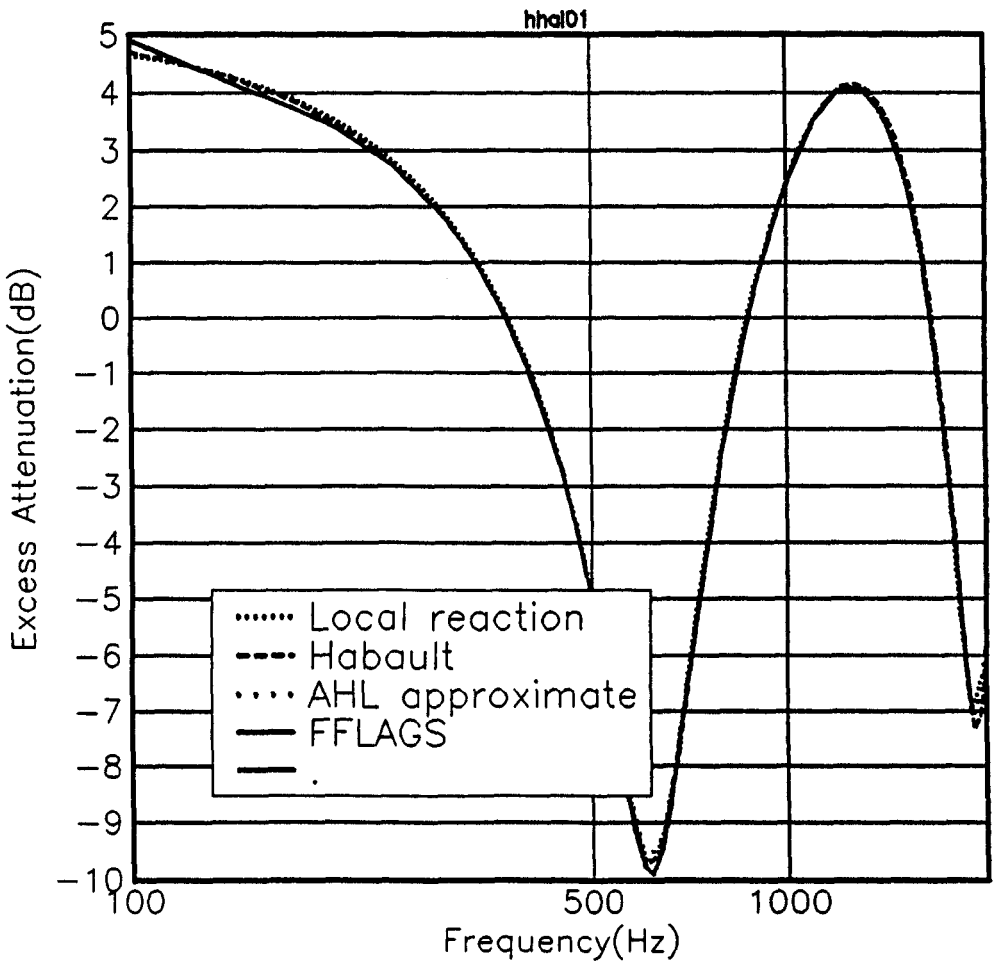

Figure 5.2 Excess attenuation at 1 metre over a near locally reacting half-space, flow resistivity 300000mks units. FFLAGS,Attenborough, Hayek and Lawther exact and approximate model,local reaction, and Habault et al's model.

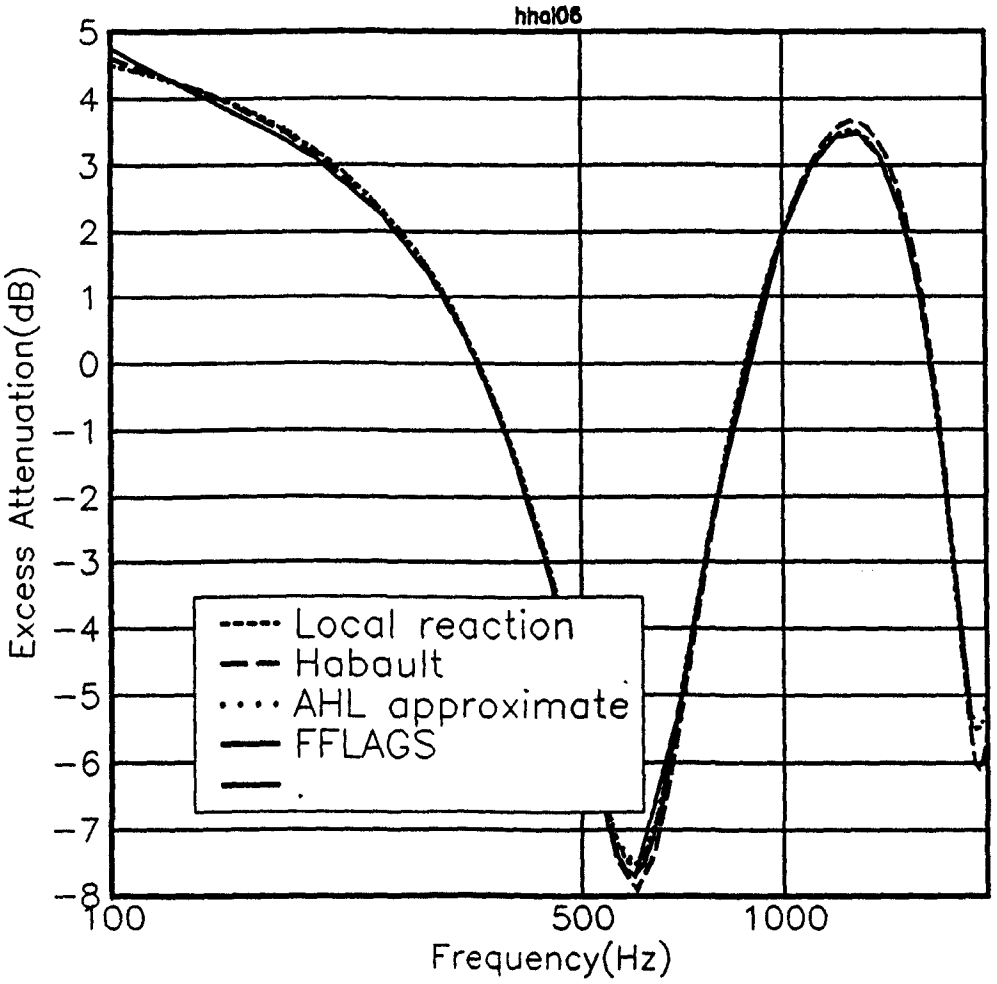

Figure 5.3 Excess attenuation at 1 metre over a porous halfspace. FFLAGS, Habault et al, and Attenborough, Hayek and Lawther approximate models. Flow resistivity 100000mks units.

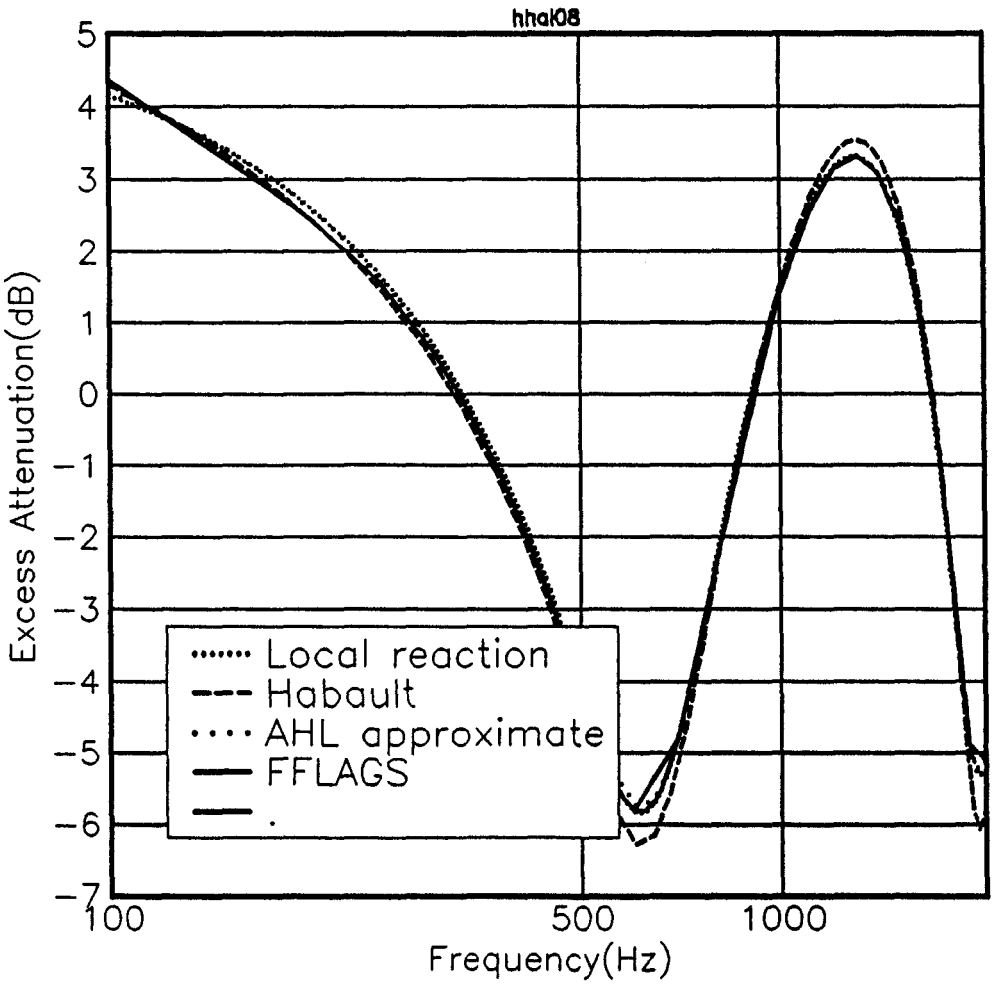

Figure 5.4 Excess attenuation at 1 metre over a porous halfspace. FFLAGS, Habault et al and Attenborough, Hayek and Lawther approximate models. Flow resistivity 30000mks units.

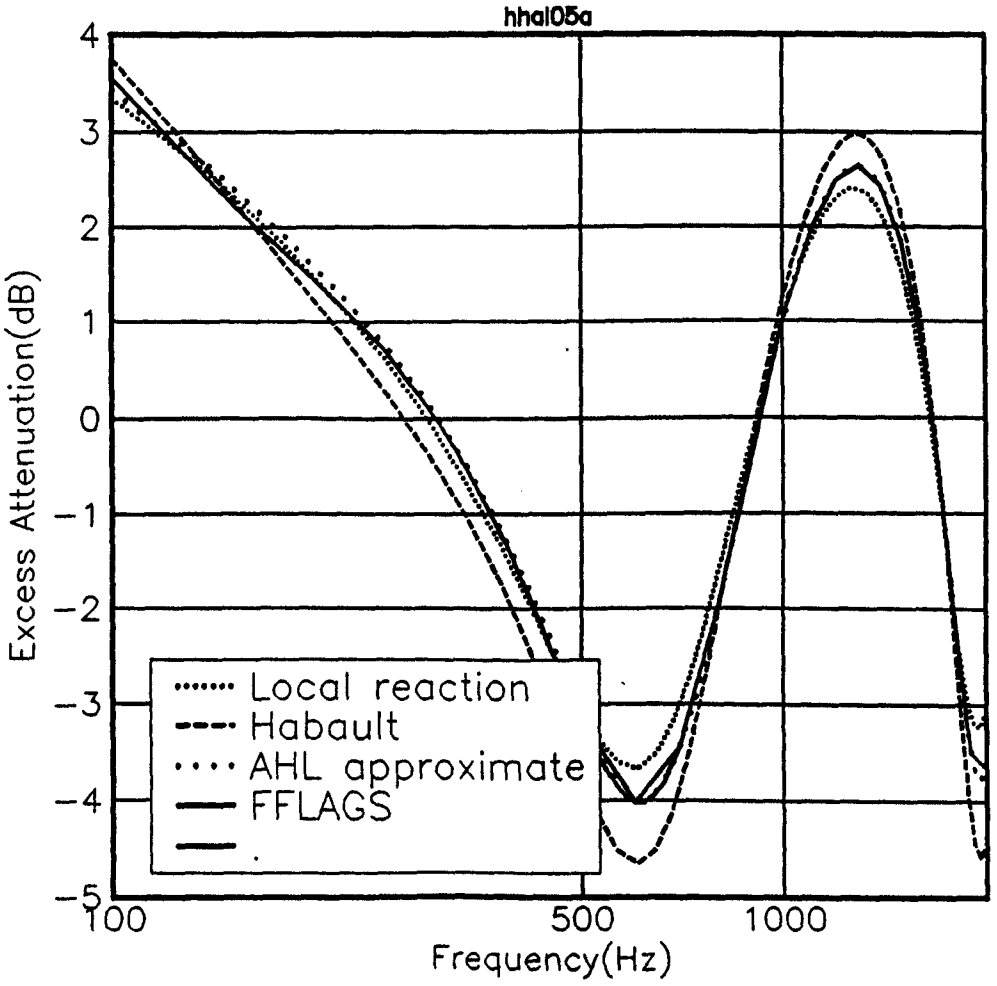

Figure 5.5 Excess attenuation at 1 metre over a porous halfspace. FFLAGS, Habault et al,Local reaction , and Attenborough, Hayek and Lawther approximate model. Flow resistivity 10000mks units.

0.1dB)(figure 5.6). As the flow resistivity was decreased the agreement decreased(Figures 5.7 and 5.8). At a flow resistivity of 10,000mks rayls the disagreement between FFLAGS and the Nicholas, Berry and Daigle formulation had risen to 1.0dB at some frequencies, but the Habault and Fillippi formulation was exhibiting dips at different frequencies and differences of up to 6dB in predicted excess attenuation (Figure 5.9).

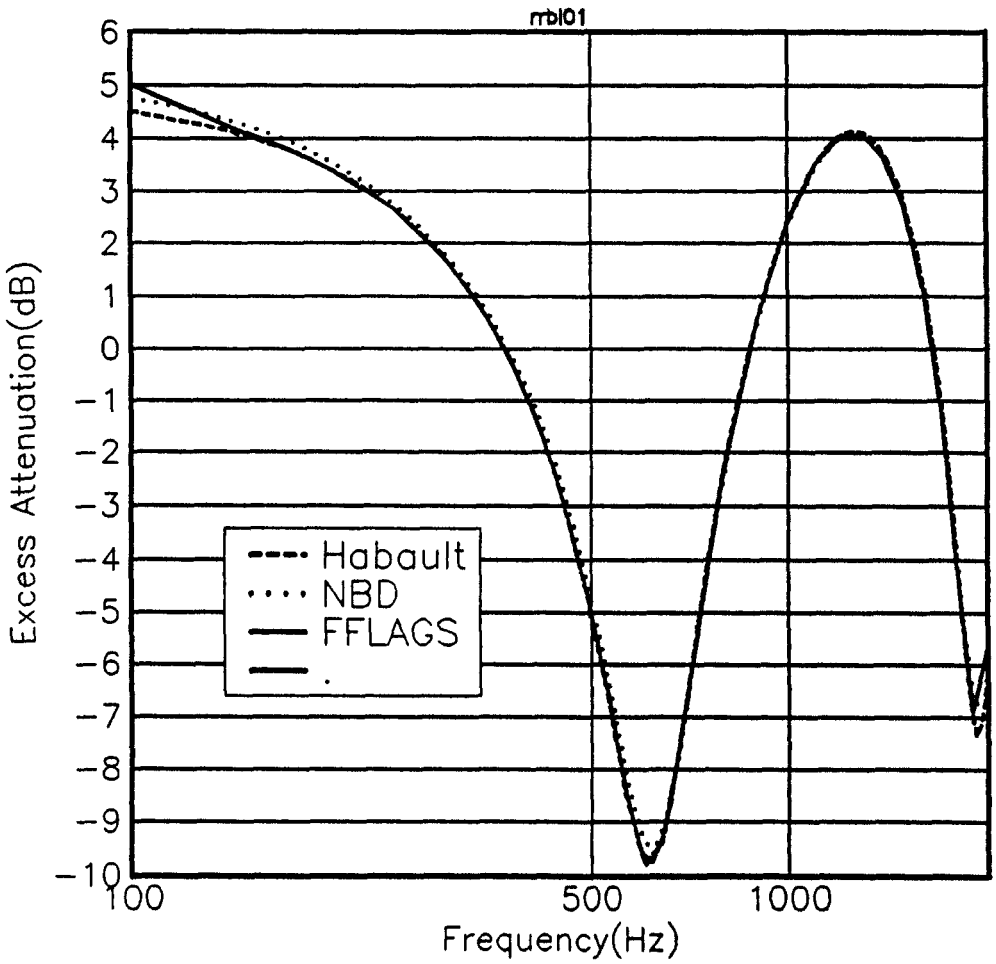

Figure 5.6 Excess attenuation at 1 metre over a rigid backed thin layer. FFLAGS, Habault et al, and Nicholas, Berry and Daigle. Flow resistivity 300000mks units.

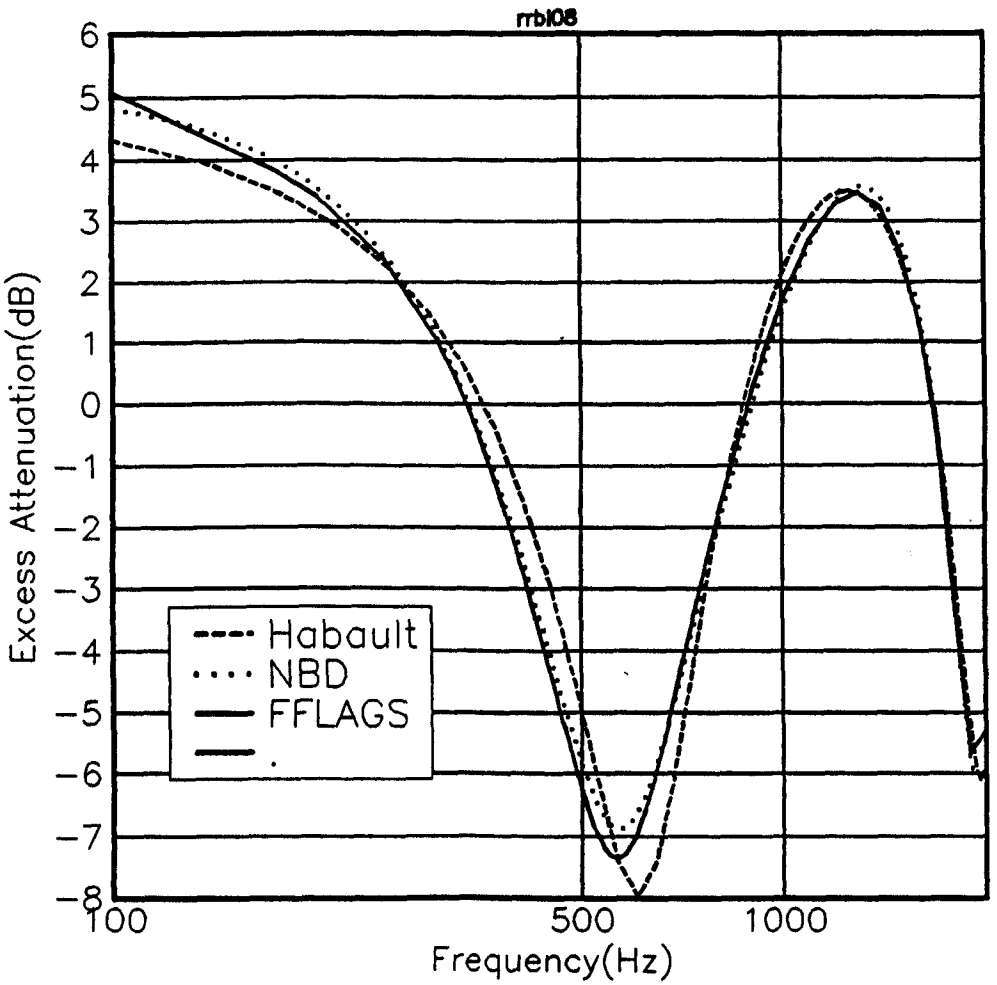

Figure 5.7 Excess attenuation at 1 metre over a rigid backed thin layer. FFLAGS, Habault et al, and Nicholas, Berry and Daigle. Flow resistivity 100000mks units.

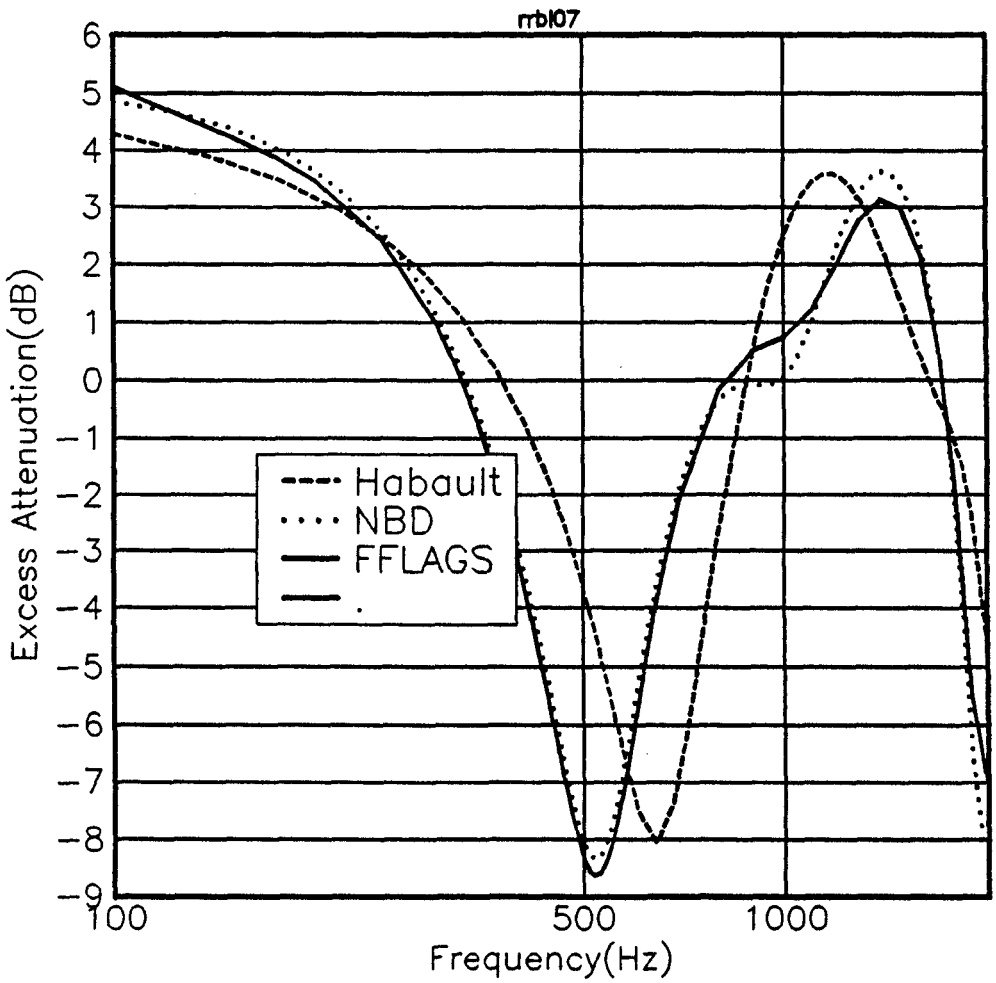

Figure 5.8 Excess attenuation at 1 metre over a rigid backed thin layer. FFLAGS, Habault et al, and Nicholas, Berry and Daigle. Flow resistivity 30000mks units.

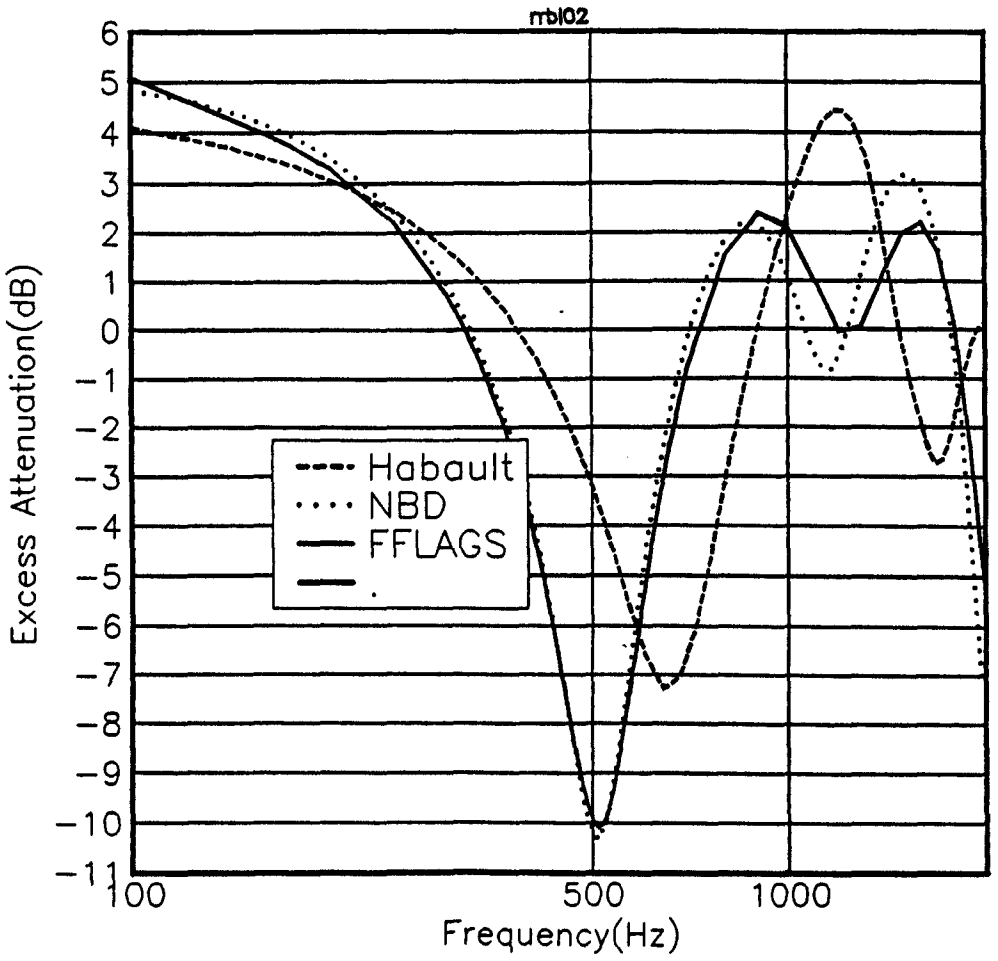

Figure 5.9 Excess attenuation at 1 metre over a rigid backed thin layer. FFLAGS, Habault et al, and Nicholas et al. Flow resistivity 10000mks units.

5.2.2 Long range results

The second range chosen was twenty metres. This range was chosen to examine the performance of the different propagation models at near grazing incidence. Once again source and receiver heights were set at 0.5 and 0.3 metres respectively, and four different ground flow resistivities were used (see Figures 5.10 to 5.13).

For propagation over the halfspace only one dip in the excess attenuation is present in the audible frequency range. The greatest disagreement between the propagation models occurs in this dip. For all of the four flow resistivities chosen the Attenborough, Hayek and Lawther 'exact' propagation model agreed with FFLAGS to within 0.01dB (Better than 0.1 percent). The approximate Attenborough ,Hayek and Lawther result was consistently larger in magnitude then either FFLAGS or the 'exact' result. This difference became greater over the lower flow resistivity materials, being up to 0.3dB over the high flow resistivity material, and up to 0.6dB over the lowest flow resistivity material. The local reaction approximation gave results consistently smaller than FFLAGS or the 'exact' calculation. The maximum discrepancy increased from 0.4dB in the high flow resistivity case, to 1.6dB for the lowest flow resistivity.

The third range chosen was 100 metres. The source and receiver heights were 2.0 metres. The agreement between the results for different models was similar to that for a range of twenty metres (figures 5.14 to 5.17).

The Habault and Fillippi model fails to give physically reasonable predictions with this geometry . The predicted excess attenuations were above 20dB at many frequencies, and the results are not presented here.

For propagation over the rigid-backed layer FFLAGS was compared to the Nicholas, Berry and Daigle predictions and to the local reaction prediction with a normal surface impedance for a rigid backed layer(see Figures 5.18 to 5.21). It was found that for the highest flow resistivity the Nicholas, Berry and Daigle prediction gave results within 0.1dB of the FFLAGS prediction. The local reaction model agreed equally well except at the ground effect dip, where the discrepancy was up to 0.3dB. As the flow

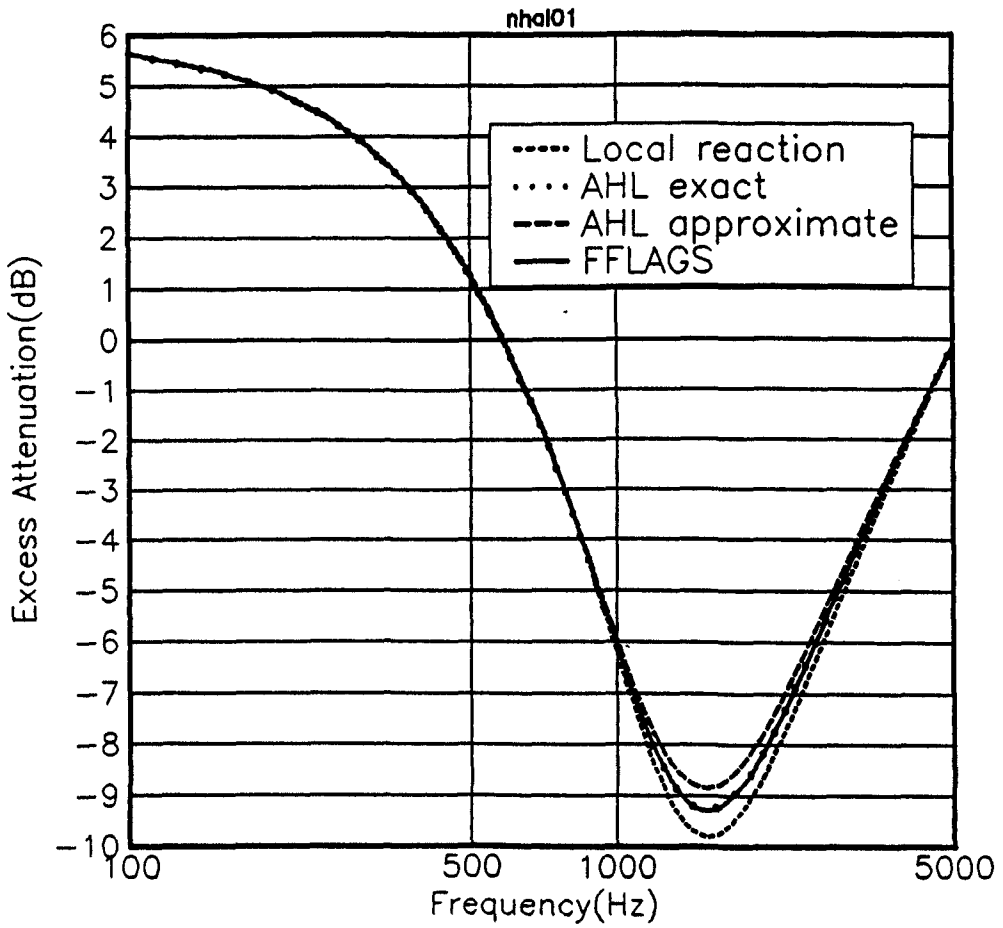

Figure 5.10 Excess attenuation at 20 metres over a porous halfspace. FFLAGS, local reaction , and Attenborough, Hayek and Lawther exact and approximate model. Flow resistivity 300000mks units.

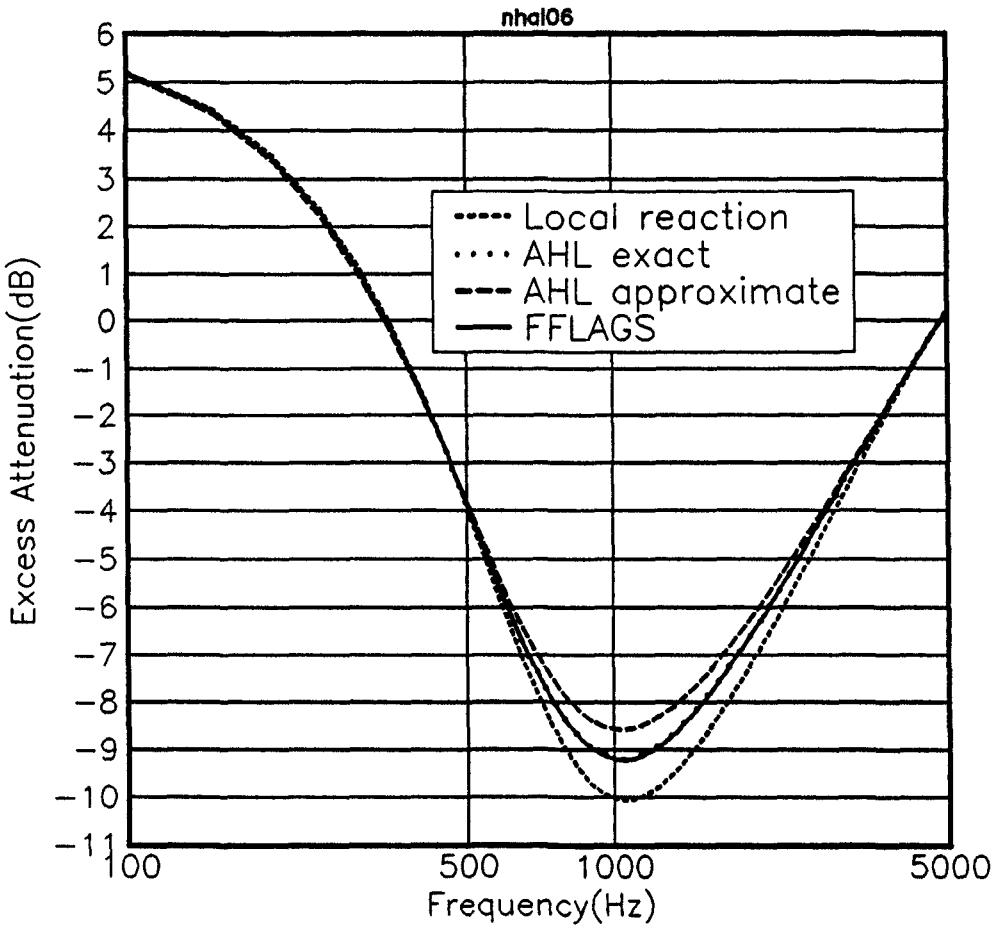

Figure 5.11 Excess attenuation at 20 metres over a porous halfspace. FFLAGS, local reaction , and Attenborough, Hayek and Lawther exact and approximate model. Flow resistivity 100000mks units.

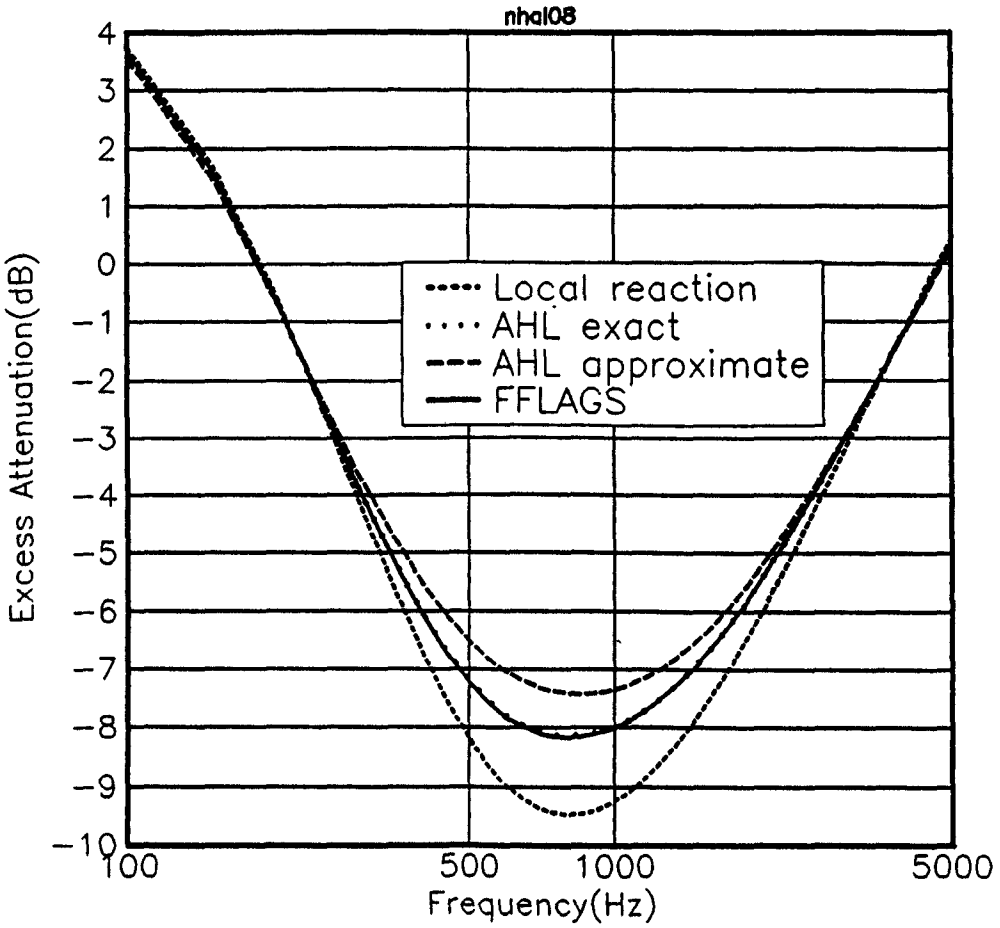

Figure 5.12 Excess attenuation at 20 metres over a porous halfspace. FFLAGS, local reaction , and Attenborough, Hayek and Lawther exact and approximate model. Flow resistivity 30000mks units.

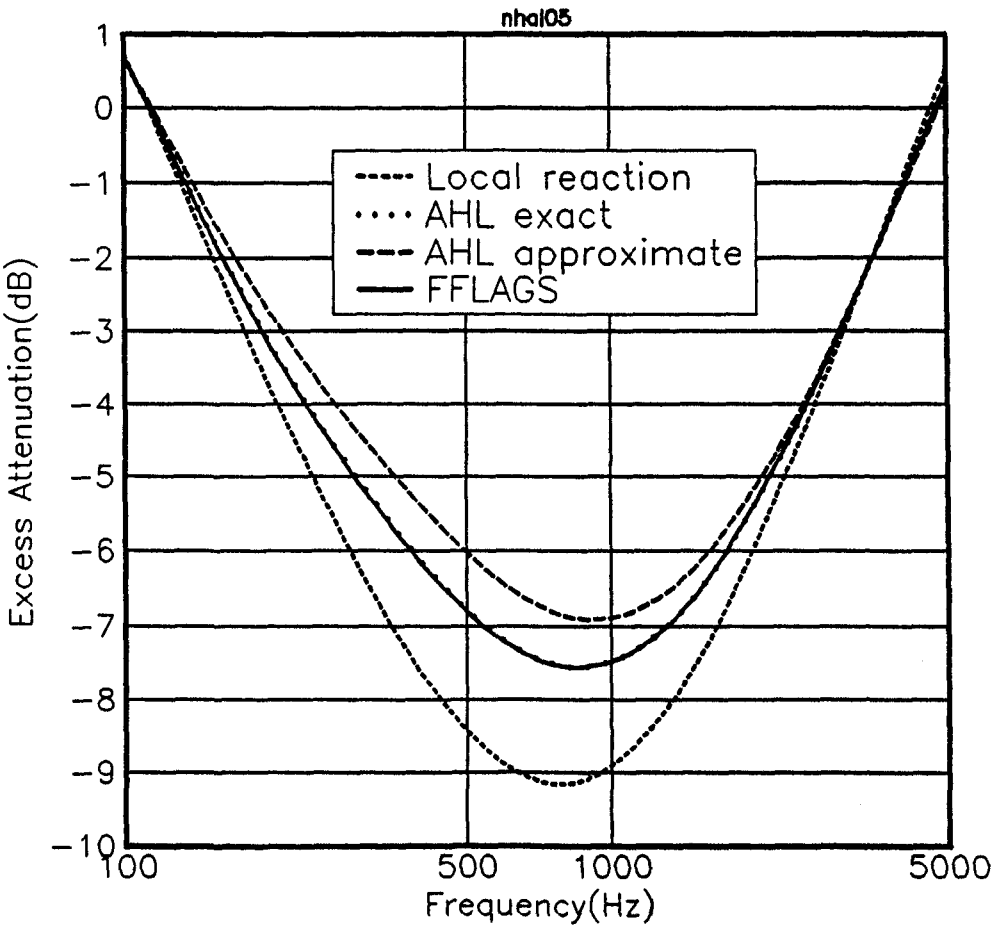

Figure 5.13 Excess attenuation at 20 metres over a porous halfspace. FFLAGS, and Local reaction , and Attenborough, Hayek and Lawther exact and approximate model. Flow resistivity 10000mks units.

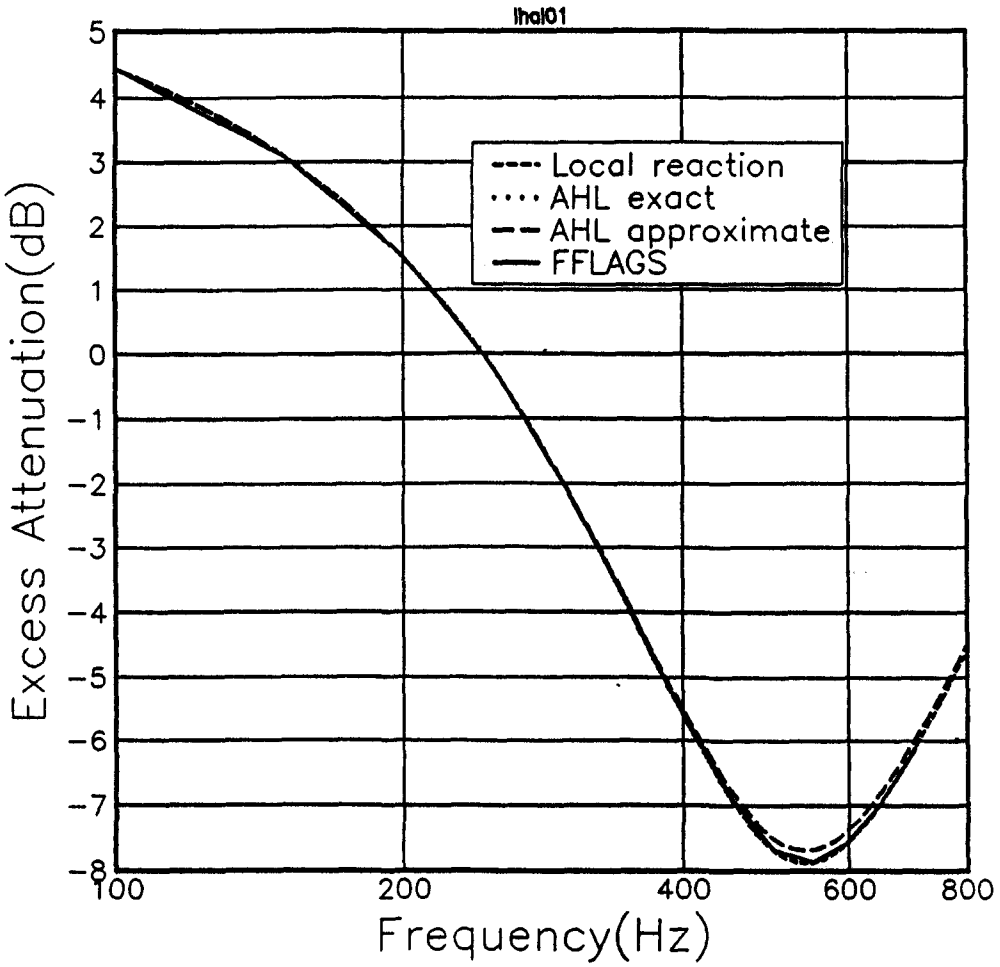

Figure 5.14 Excess attenuation at 100 metres over a porous halfspace. FFLAGS, local reaction , and Attenborough, Hayek and Lawther exact and approximate model. Flow resistivity 300000mks units. Source and receiver height 2.0 metres.

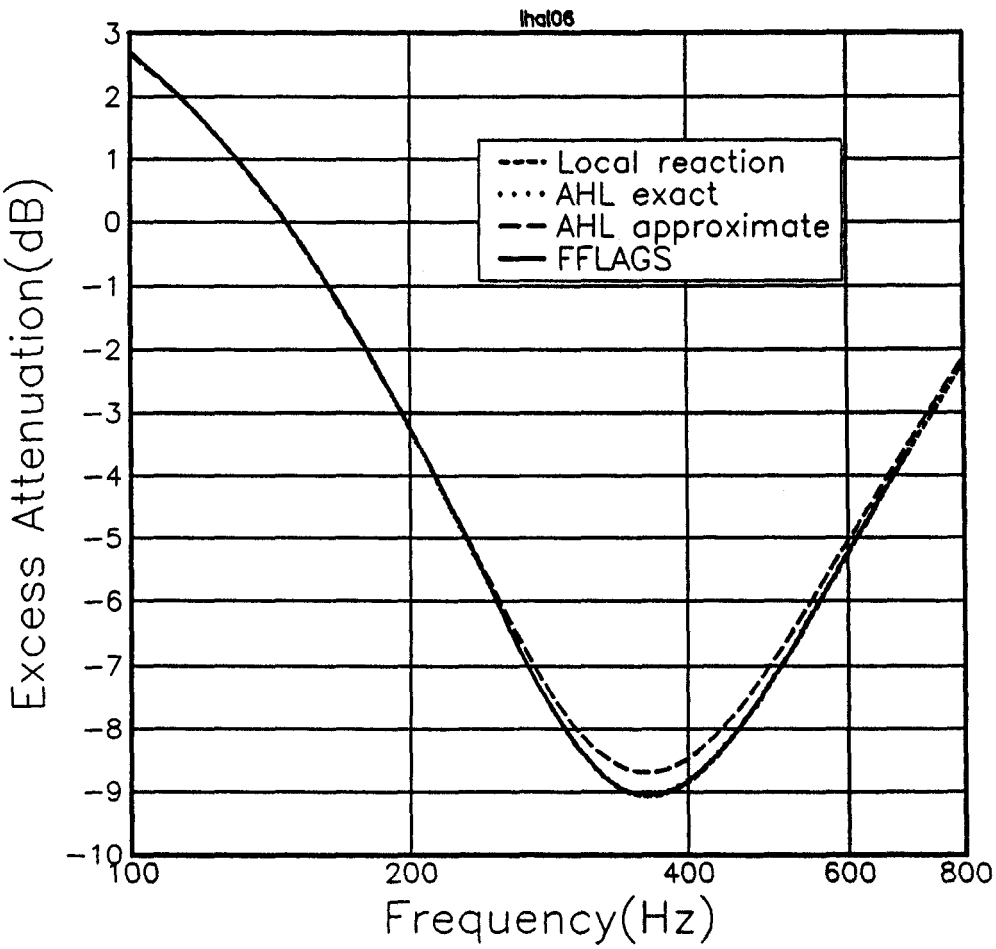

Figure 5.15 Excess attenuation at 100 metres over a porous halfspace. FFLAGS, local reaction , and Attenborough, Hayek and Lawther exact and approximate model. Flow resistivity 100000mks units. Source and receiver height 2.0 metres.

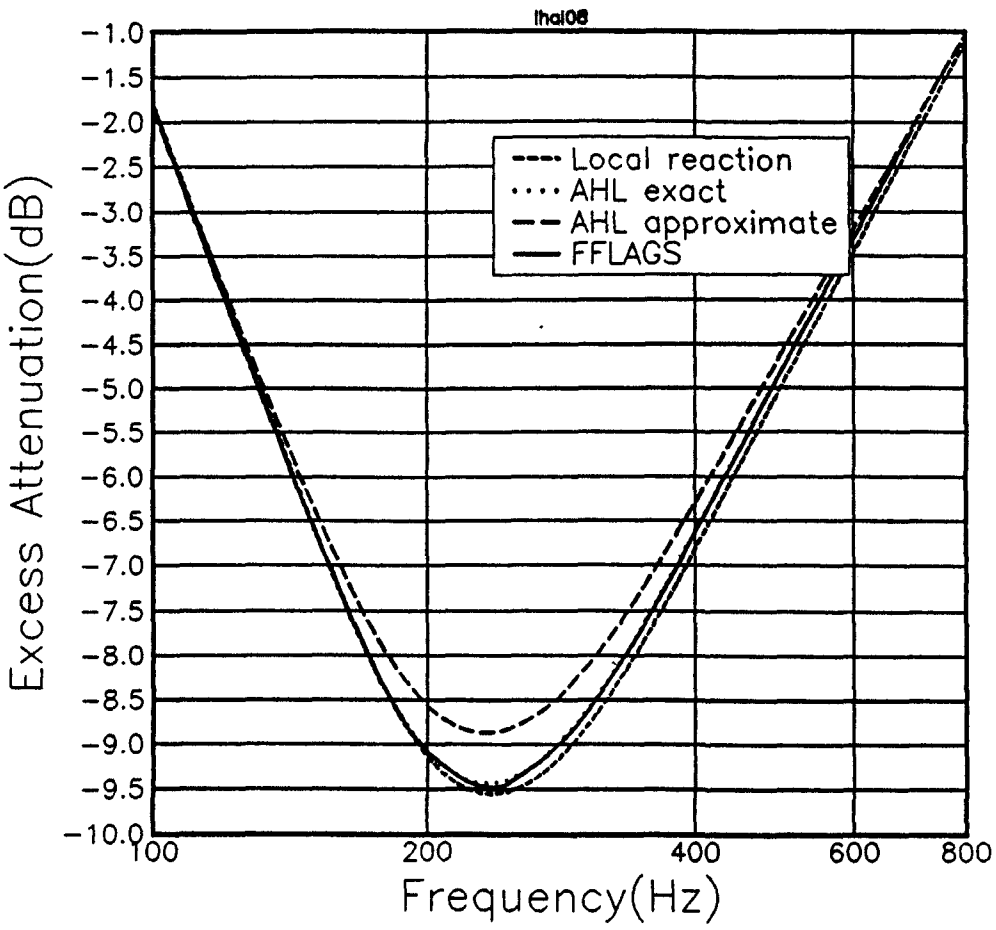

Figure 5.16 Excess attenuation at 100 metres over a porous halfspace. FFLAGS, local reaction , and Attenborough, Hayek and Lawther exact and approximate model. Flow resistivity 30000mks units. Source and receiver height 2.0 metres.

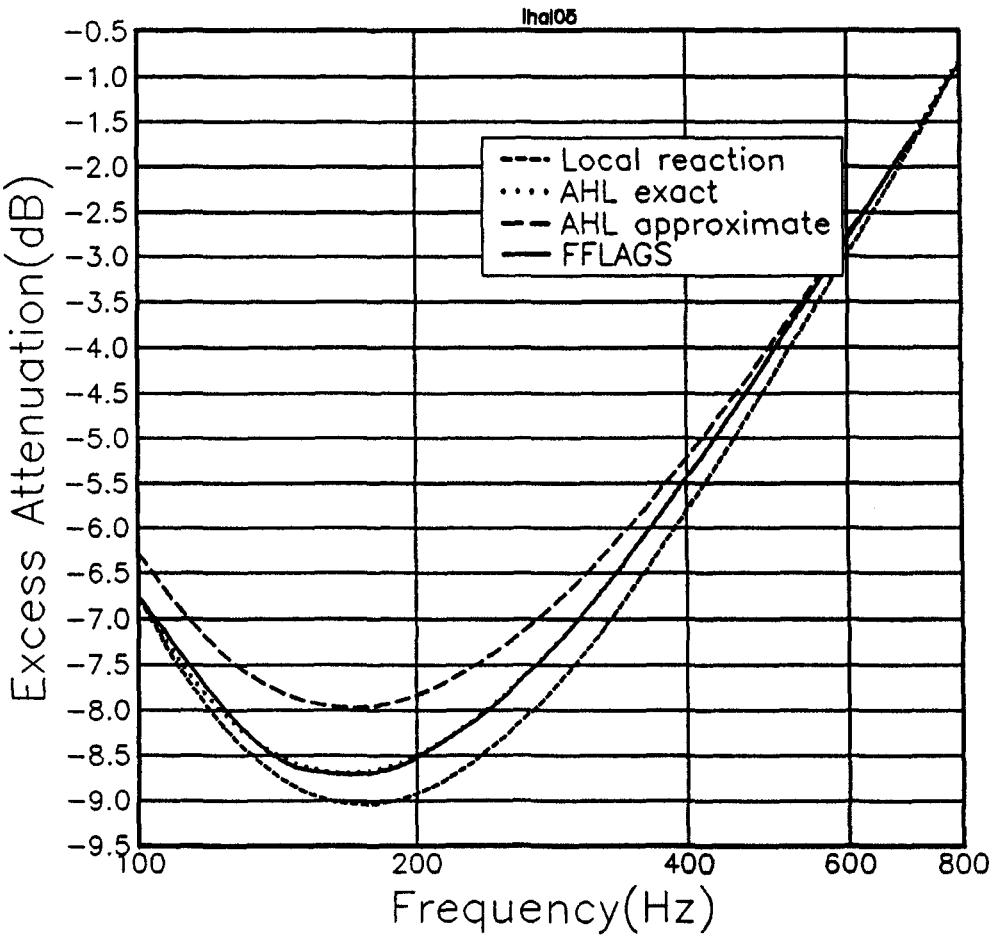

Figure 5.17 Excess attenuation at 100 metres over a porous halfspace. FFLAGS, and Local reaction , and Attenborough, Hayek and Lawther exact and approximate model. Flow resistivity 10000mks units. Source and receiver height 2.0 metres.

resistivity was decreased the discrepancy between the local reaction prediction and FFLAGS increased to over 10dB at some frequencies, although the Nicholas, Berry and Daigle prediction did not deviate by more than 1.0 dB at any frequency.

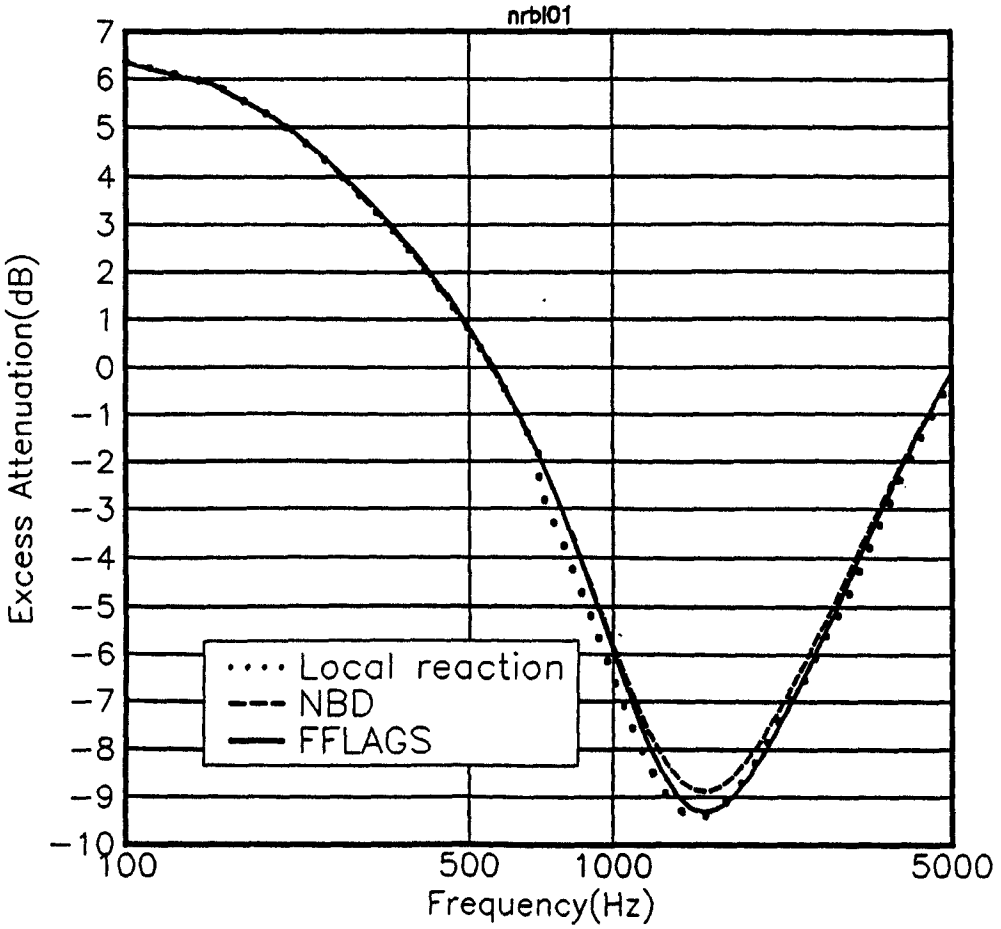

Figure 5.18 Excess attenuation at 20 metres over a rigid backed layer. FFLAGS, local reaction, and Nicholas, Berry and Daigle. Flow resistivity 300000mks units.

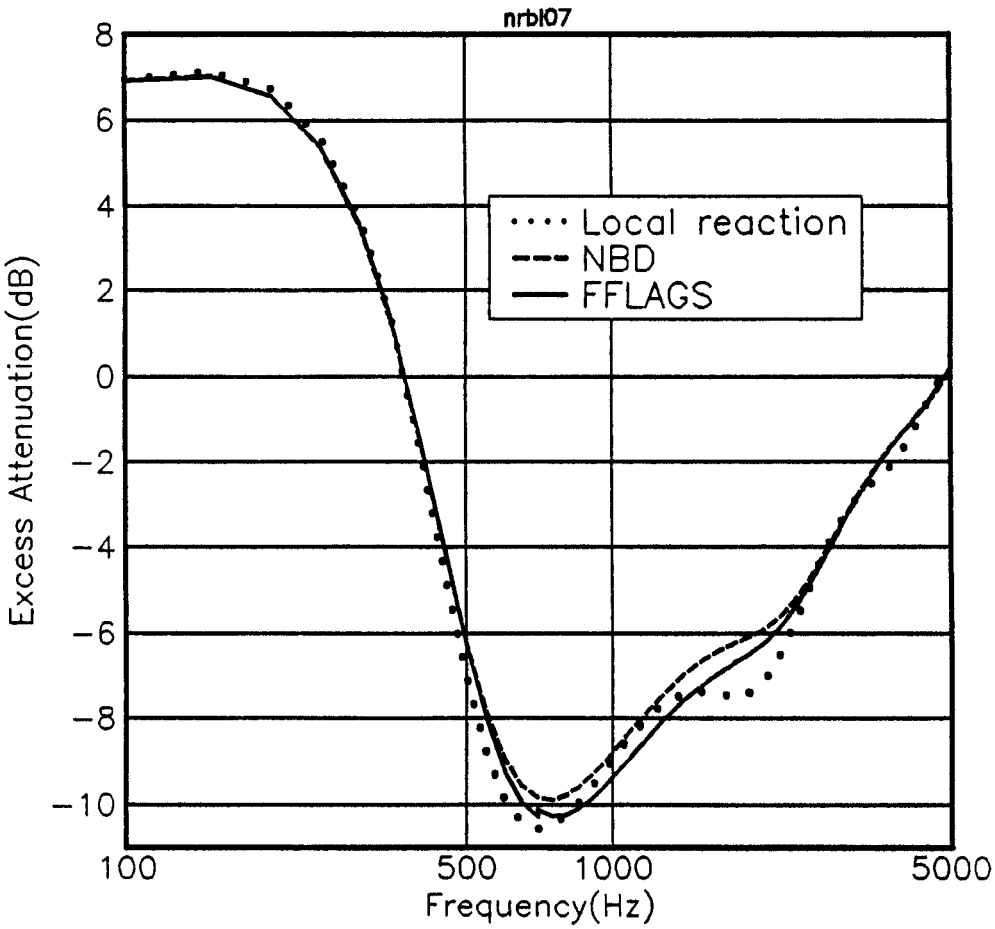

Figure 5.19 Excess attenuation at 20 metres over a rigid backed layer. FFLAGS, local reaction, and Nicholas, Berry and Daigle. Flow resistivity 100000mks units.

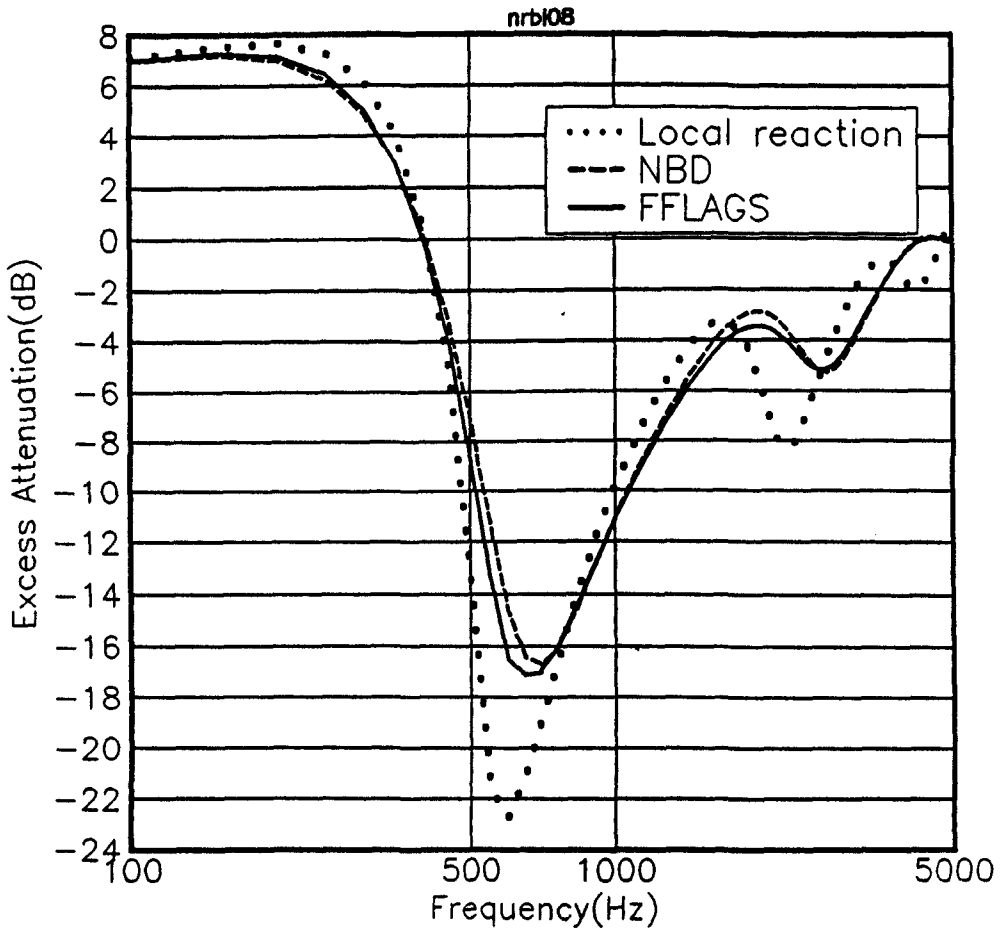

Figure 5.20 Excess attenuation at 20 metres over a rigid backed layer. FFLAGS, local reaction, and Nicholas, Berry and Daigle. Flow resistivity 30000mks units.

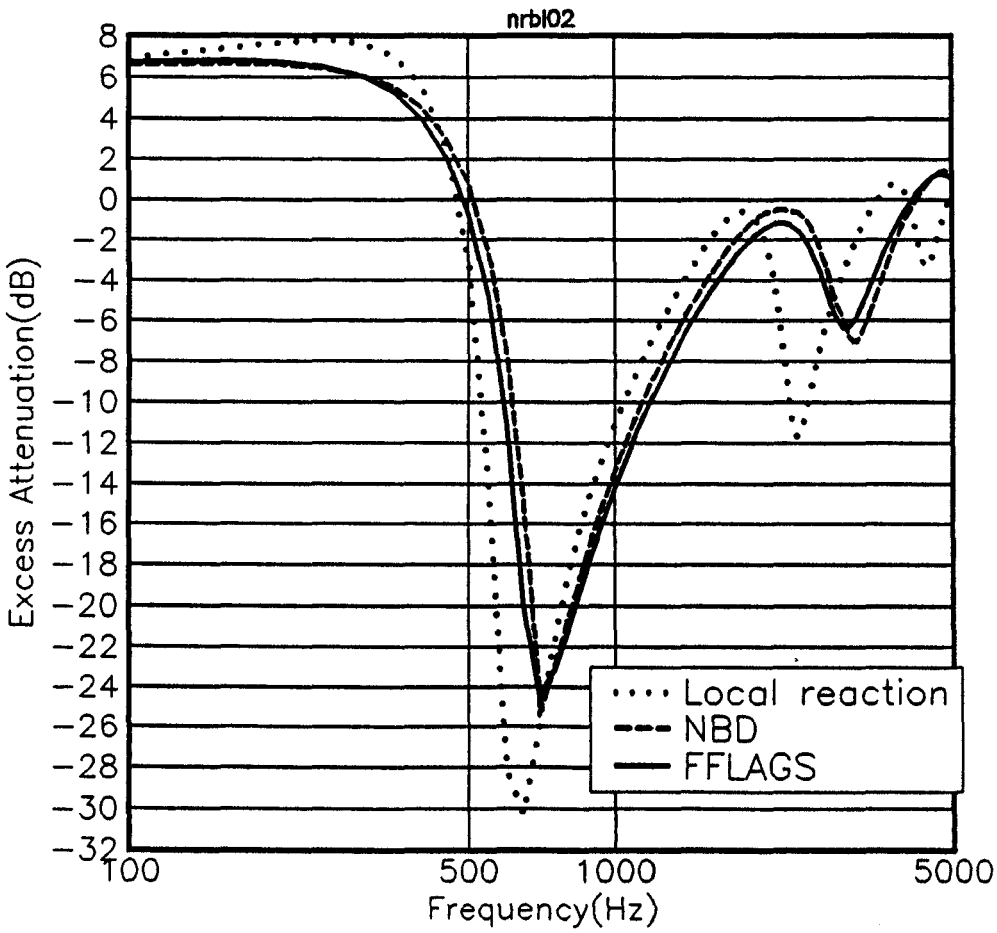

Figure 5.21 Excess attenuation at 20 metres over a rigid backed layer. FFLAGS, local reaction, and Nicholas, Berry and Daigle. Flow resistivity 10000mks units.

5.2.3 Predictions as a function of range

Predicted excess attenuation has been plotted against range for two frequencies. For the halfspace ground these are shown in Figures 5.22 to 5.25. FFLAGS is compared to Attenborough, Hayek and Lawther's exact and approximate extended reaction models. Agreement is generally reasonable (better than 0.5dB) except at short ranges over an extended reaction surface at 2000Hz; here the disagreement with the 'approximate' model is up to 1.5dB (see Figure 5.25). The Attenborough, Hayek and Lawther exact model, is closer to FFLAGS at long ranges (greater than ten metres).

For the thin rigid-backed layer FFLAGS was compared to the Nicholas, Berry and Daigle model only. It was found that the two agreed well (better than 0.3dB) but diverged at long ranges, although the difference would not be possible to deduce from measurements at 100 metres (see Figures 5.26 to 5.29). To further examine the divergence of the two models at long ranges the flow resistivity was further reduced to 1000mks rayls for a porosity of 0.3, and the layer depth increased to 0.5 metres. The divergence of the two results further increased at the low frequency (100Hz) (see Figure 5.30) to 2dB at 100 metres. This flow resistivity was lower than that which might be measured for outdoor ground materials. As a further test of the limits of the Nicholas, Berry and Daigle model snow like parameters were used for the non-porous backed layer. A typical snow would have a porosity of 0.8, a grain shape factor of 0.6, a pore shape factor of 0.5 and a flow resistivity of 5000mks rayls [48] Elastic parameters may be important in snow but for this comparison were ignored. Using a 0.2m thick snow like layer on a rigid backing a comparison was made for three different frequencies; 100Hz, 500Hz, and 2kHz: and ranges from 1.0m to 100.0m (figures 5.31,5.32 and 5.33). For all three frequencies the agreement between the models is better than 1dB, the worst agreement being at the lowest frequency (100Hz).

These comparisons between FFLAGS and various asymptotic approximations demonstrate the very precise agreement of FFLAGS with Attenborough, Hayek and Lawther's 'exact' propagation model. The results also

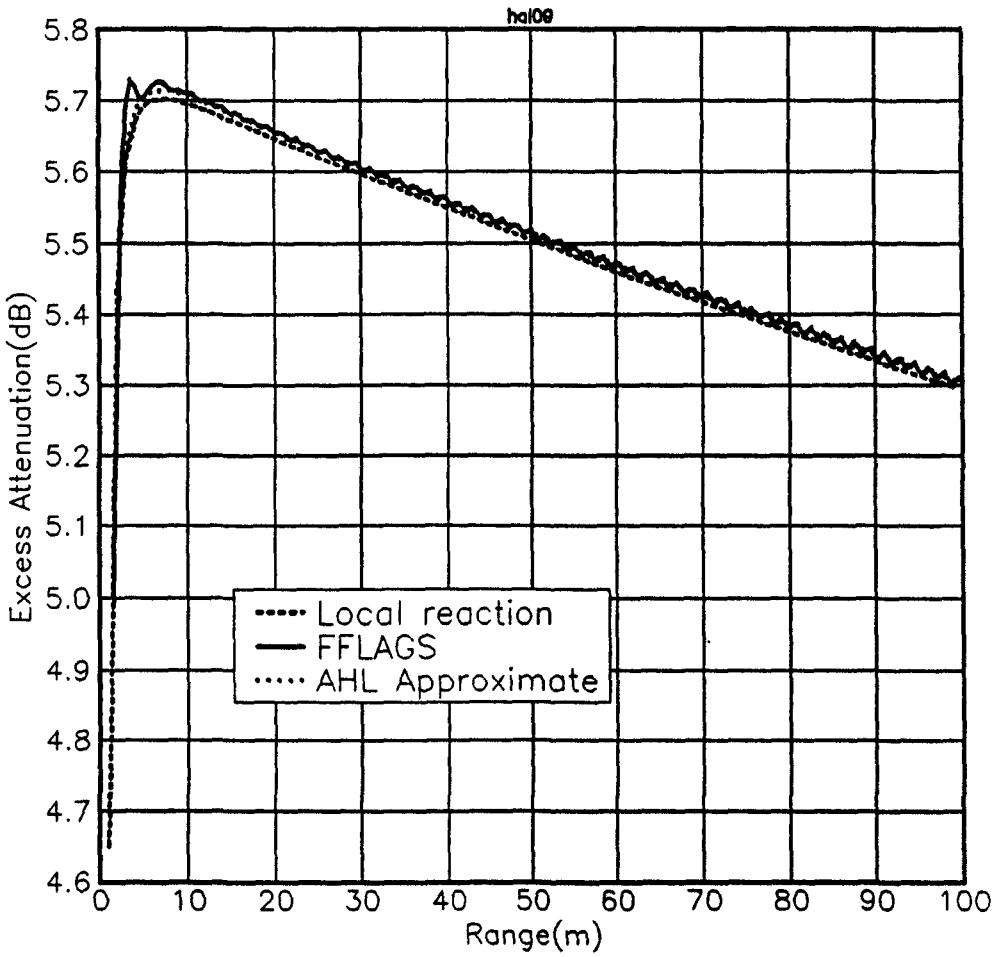

Figure 5.22 Excess attenuation against range at 100Hz over a porous half-space. FFLAGS, local reaction, and Attenborough, Hayek and Lawther approximate model. Flow resistivity 300000mks units.

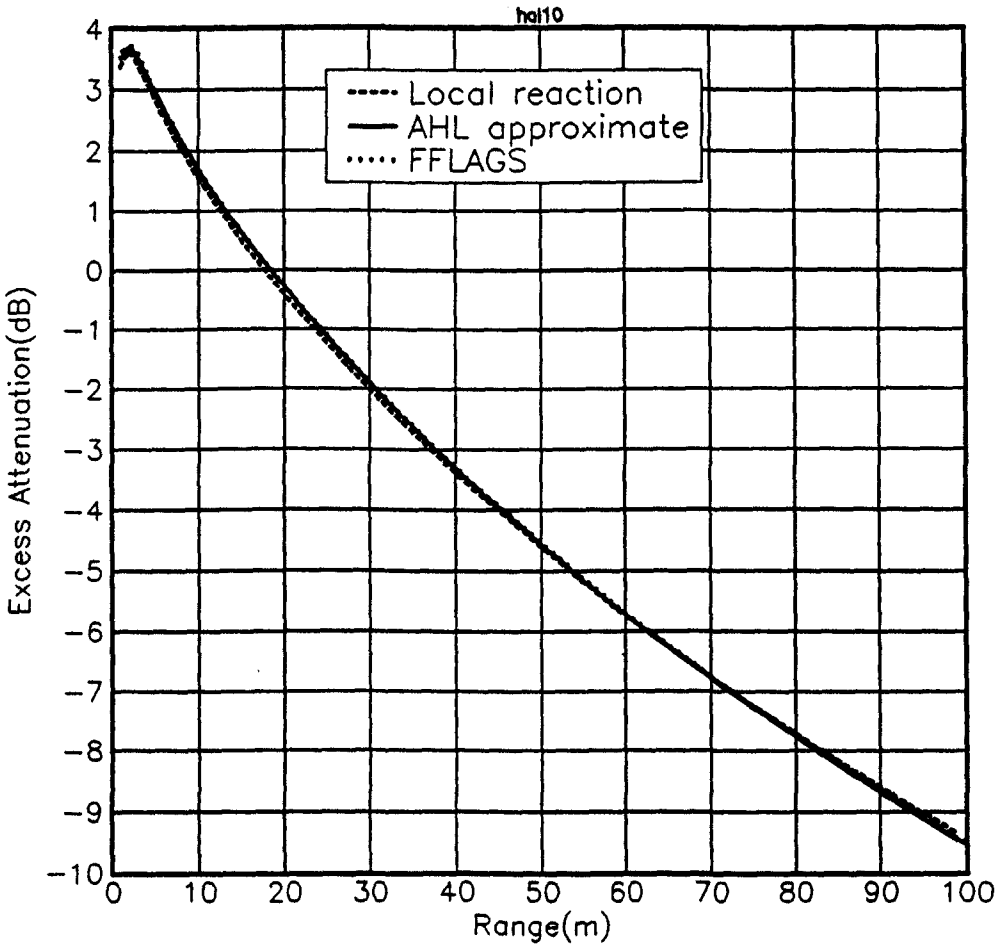

Figure 5.23 Excess attenuation against range at 100Hz over a porous half-space. FFLAGS, local reaction, and Attenborough, Hayek and Lawther approximate model. Flow resistivity 10000mks units.

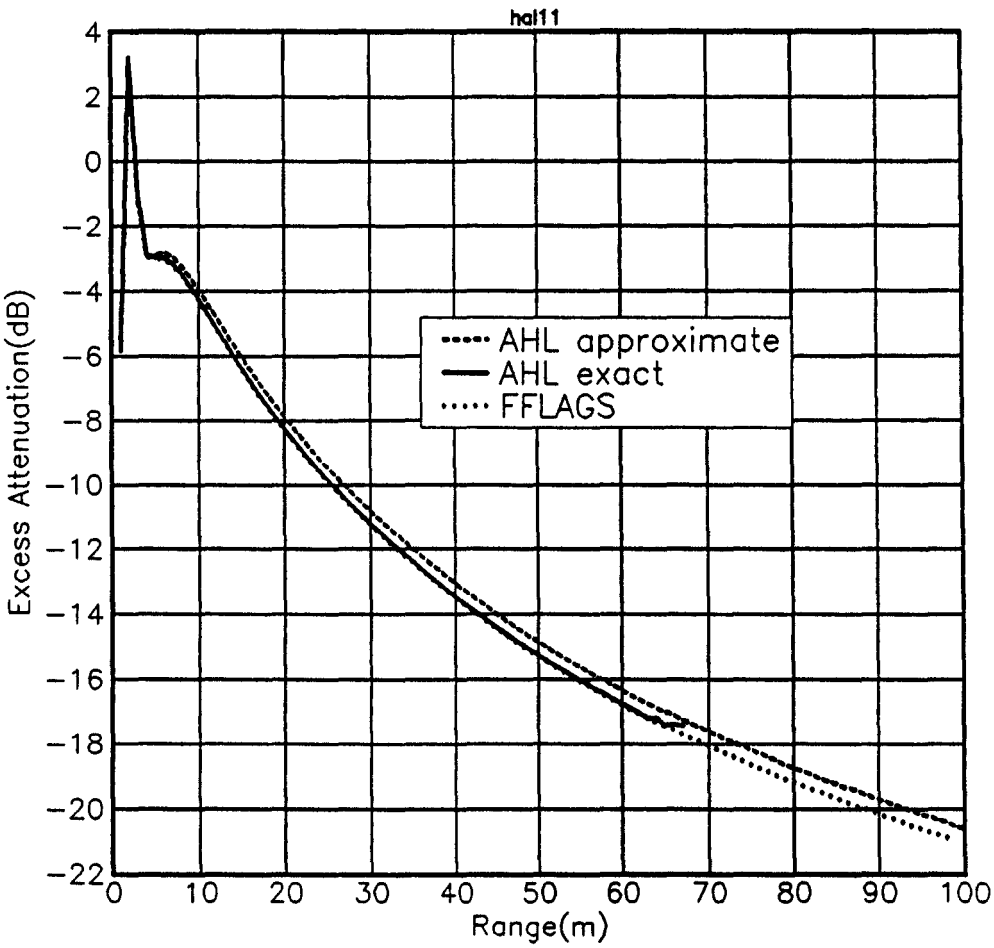

Figure 5.24 Excess attenuation against range at 2000Hz over a porous half-space. FFLAGS, local reaction, and Attenborough, Hayek and Lawther approximate model. Flow resistivity 300000mks units.

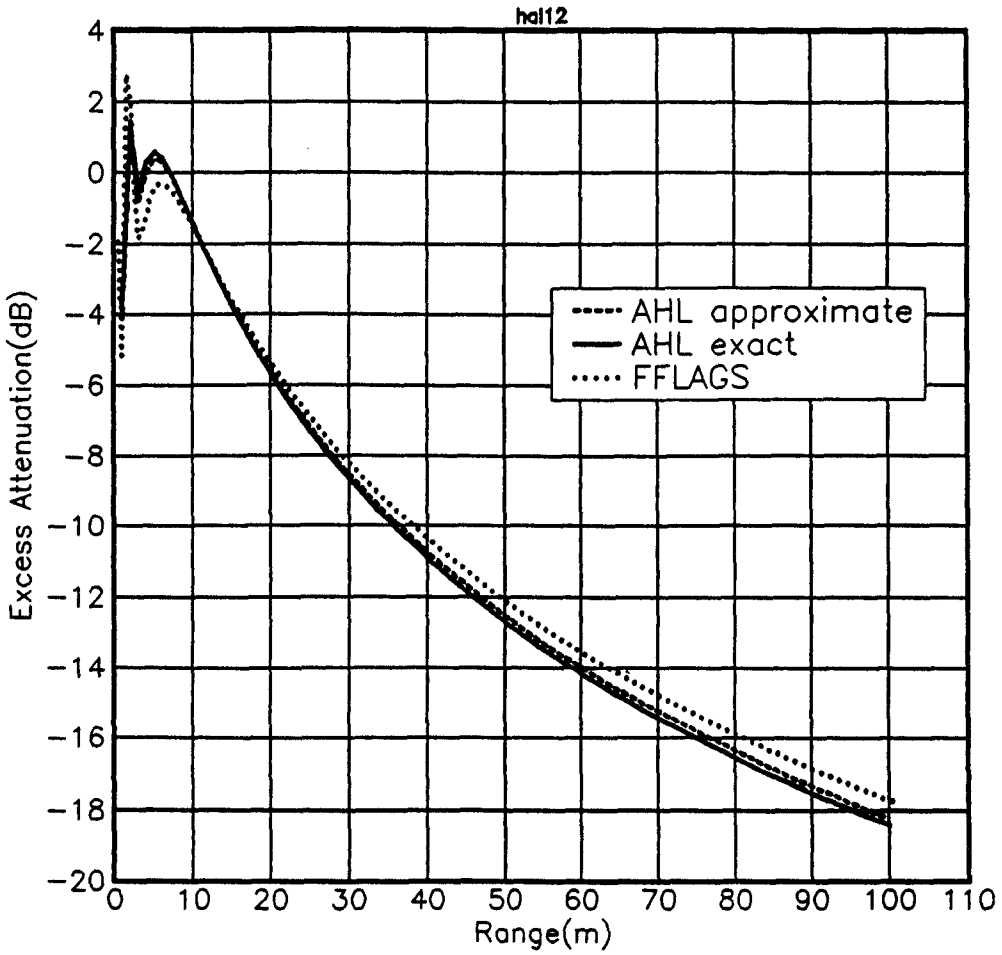

Figure 5.25 Excess attenuation against range at 2000Hz over a porous half-space. FFLAGS, and Attenborough, Hayek and Lawther exact and approximate models. Flow resistivity 10000mks units.

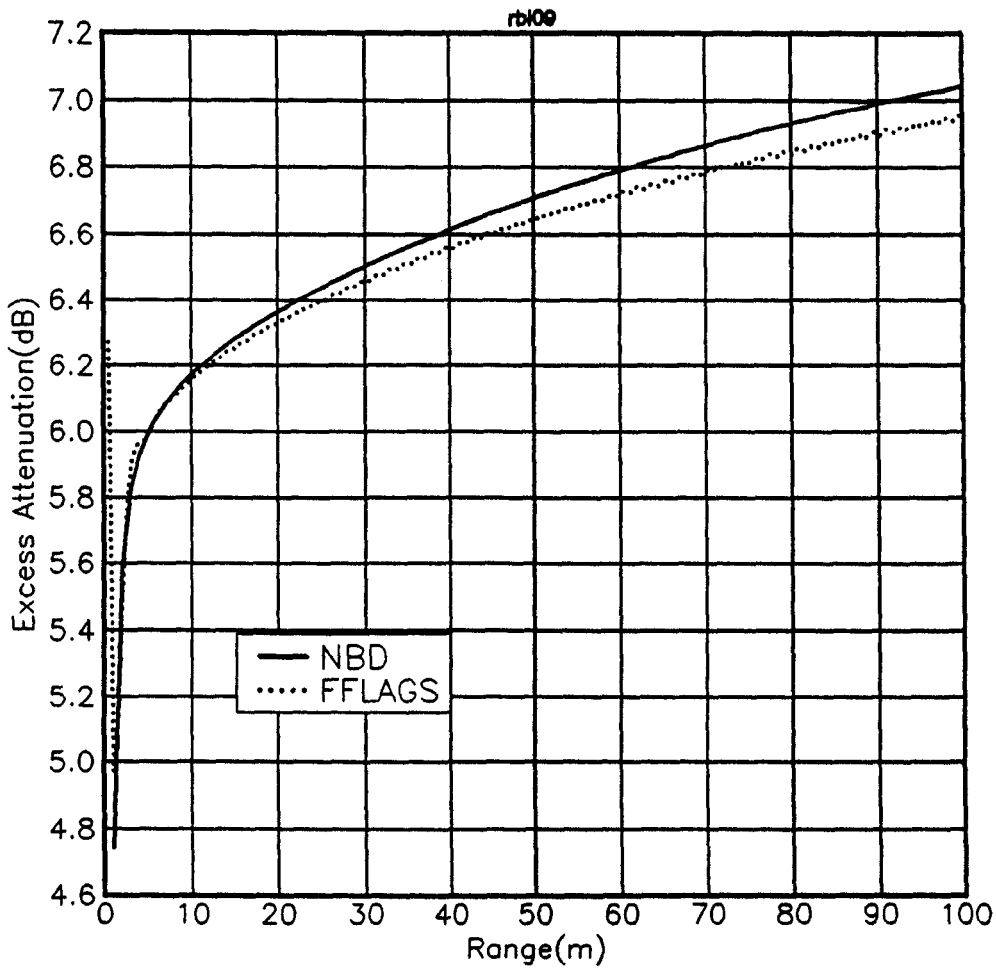

Figure 5.26 Excess attenuation against range at 100Hz over a thin rigid backed porous layer. FFLAGS, and Nicholas et al Flow resistivity 300000mks units.

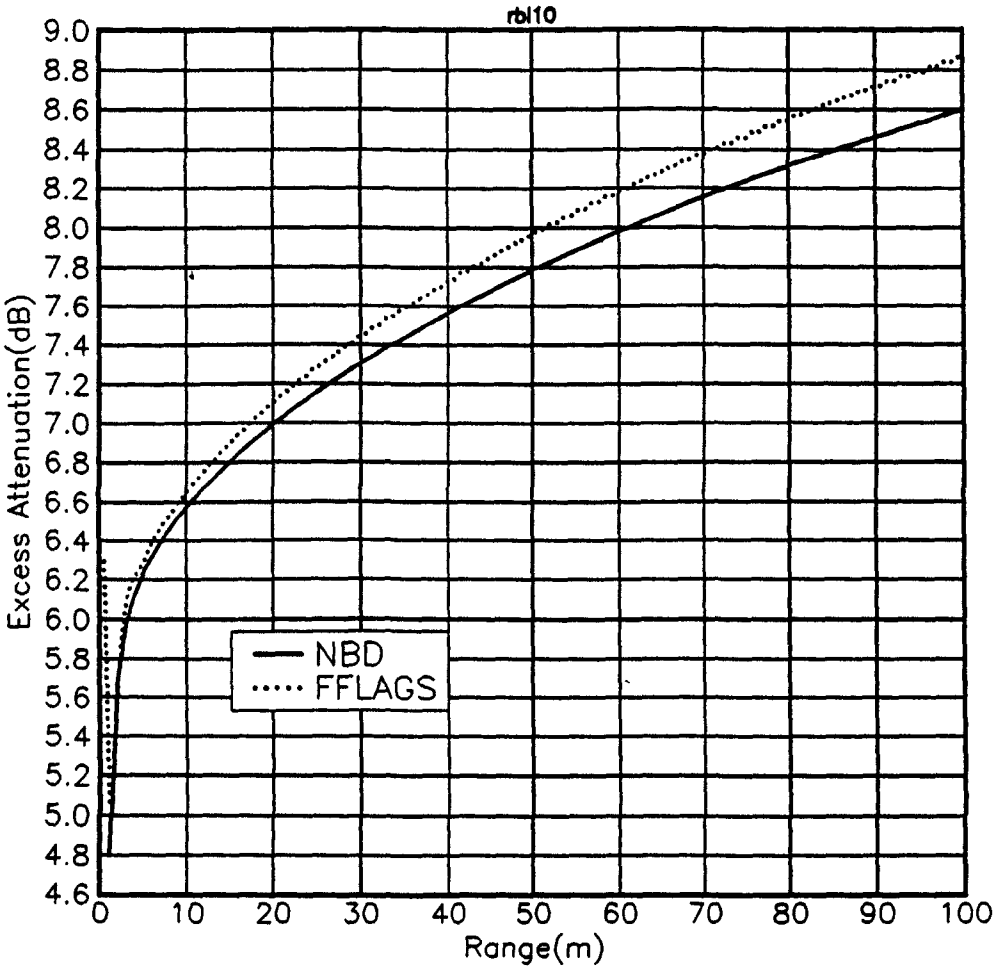

Figure 5.27 Excess attenuation against range at 100Hz over a thin rigid backed porous layer. FFLAGS, and Nicholas et al Flow resistivity 10000mks units.

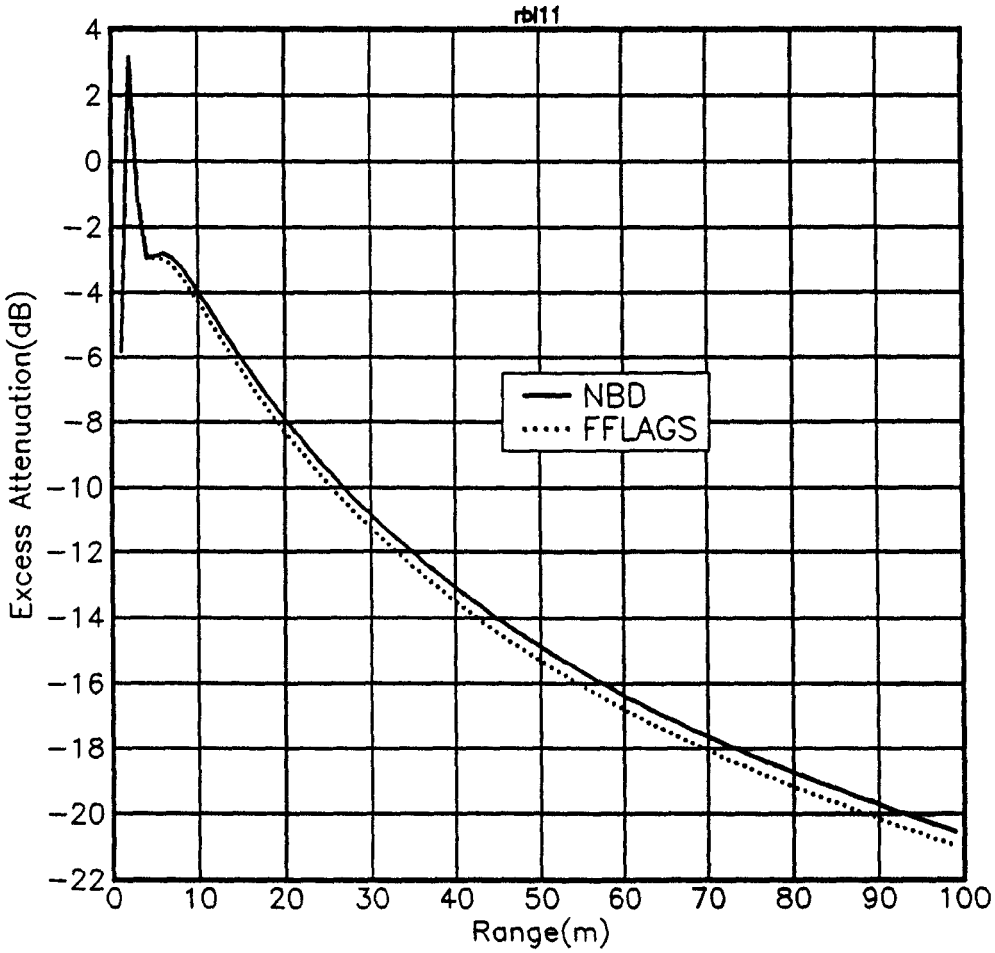

Figure 5.28 Excess attenuation against range at 2000Hz over a thin rigid backed porous layer. FFLAGS, and Nicholas, Berry and Daigle.Flow resistivity 300000mks unit.

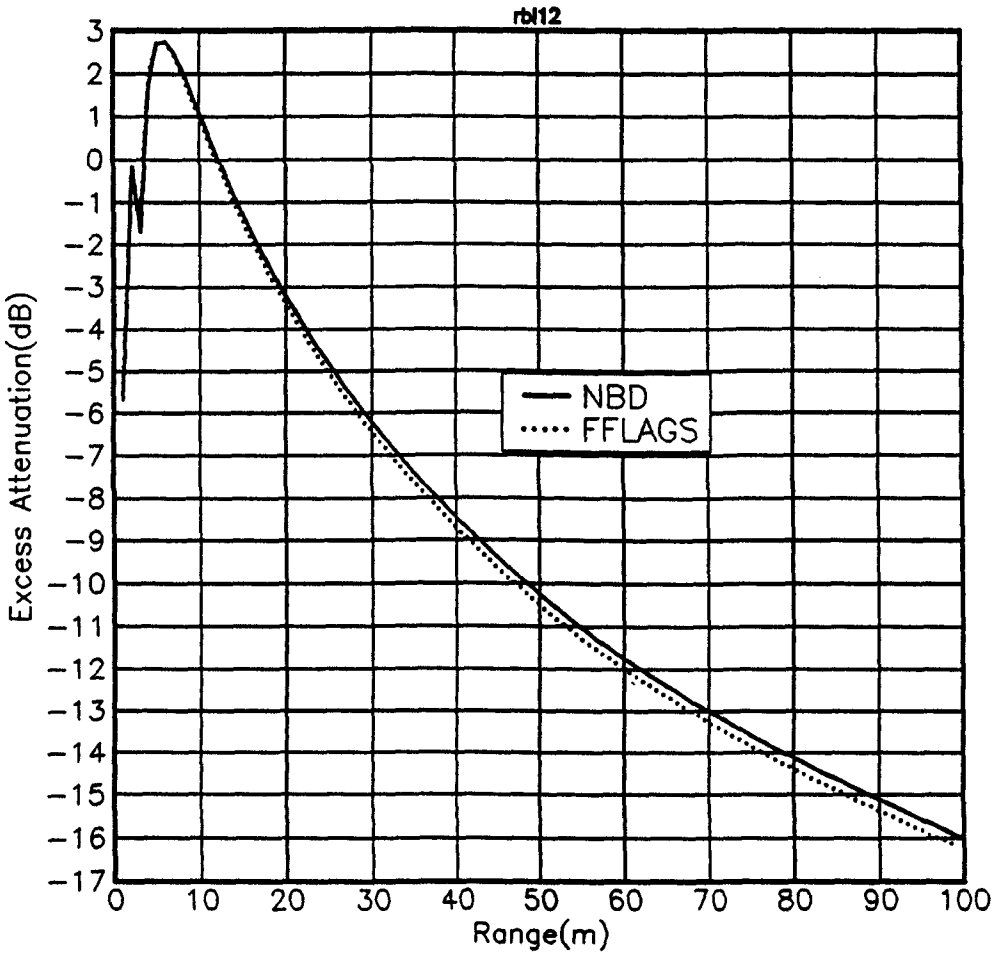

Figure 5.29 Excess attenuation against range at 2000Hz over a thin rigid backed porous layer. FFLAGS, and Nicholas, Berry and Daigle. Flow resistivity 10000mks units.

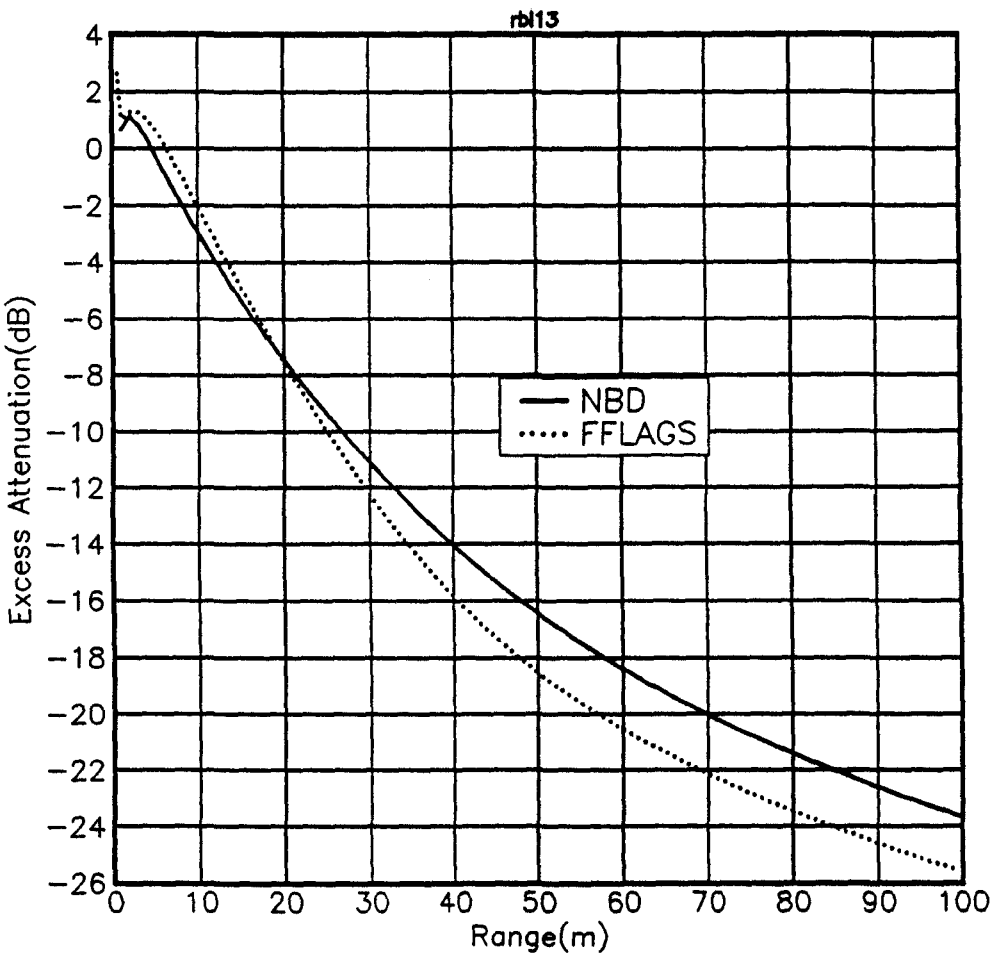

Figure 5.30 Excess attenuation against range at 100Hz over a thin rigid backed porous layer. FFLAGS, and Nicholas, Berry and Daigle. Flow resistivity=1000mks units.

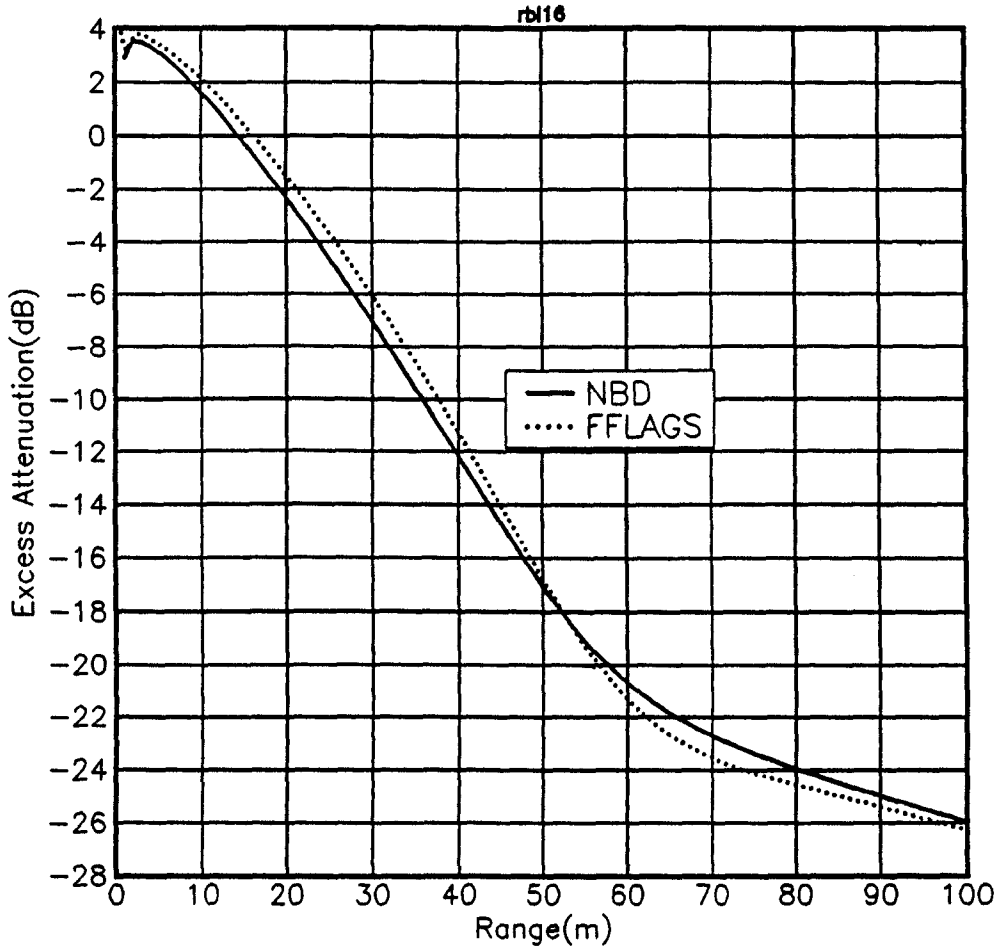

Figure 5.31 Excess attenuation against range at 100Hz over a thin rigid backed porous layer. FFLAGS, and Nicholas, Berry and Daigle. Snow like parameters.

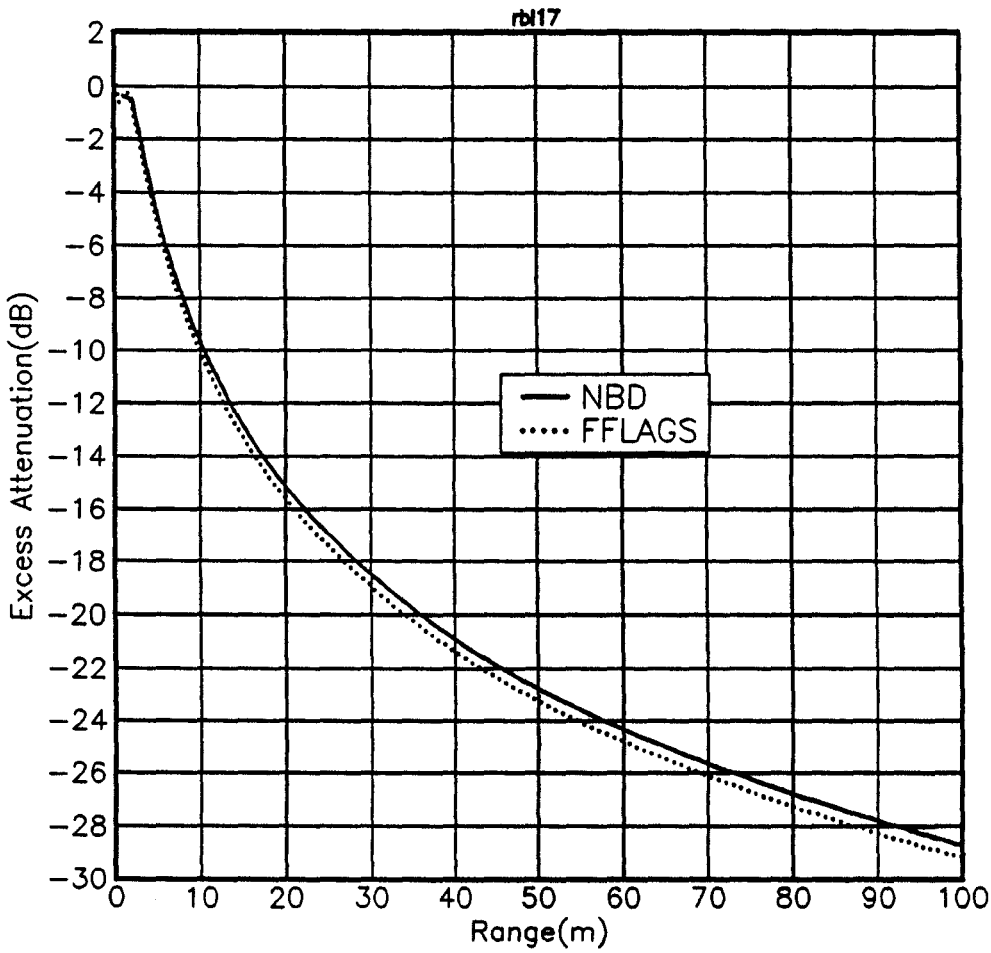

Figure 5.32 Excess attenuation against range at 500Hz over a thin rigid backed porous layer. FFLAGS, and Nicholas, Berry and Daigle. Snow like parameters.

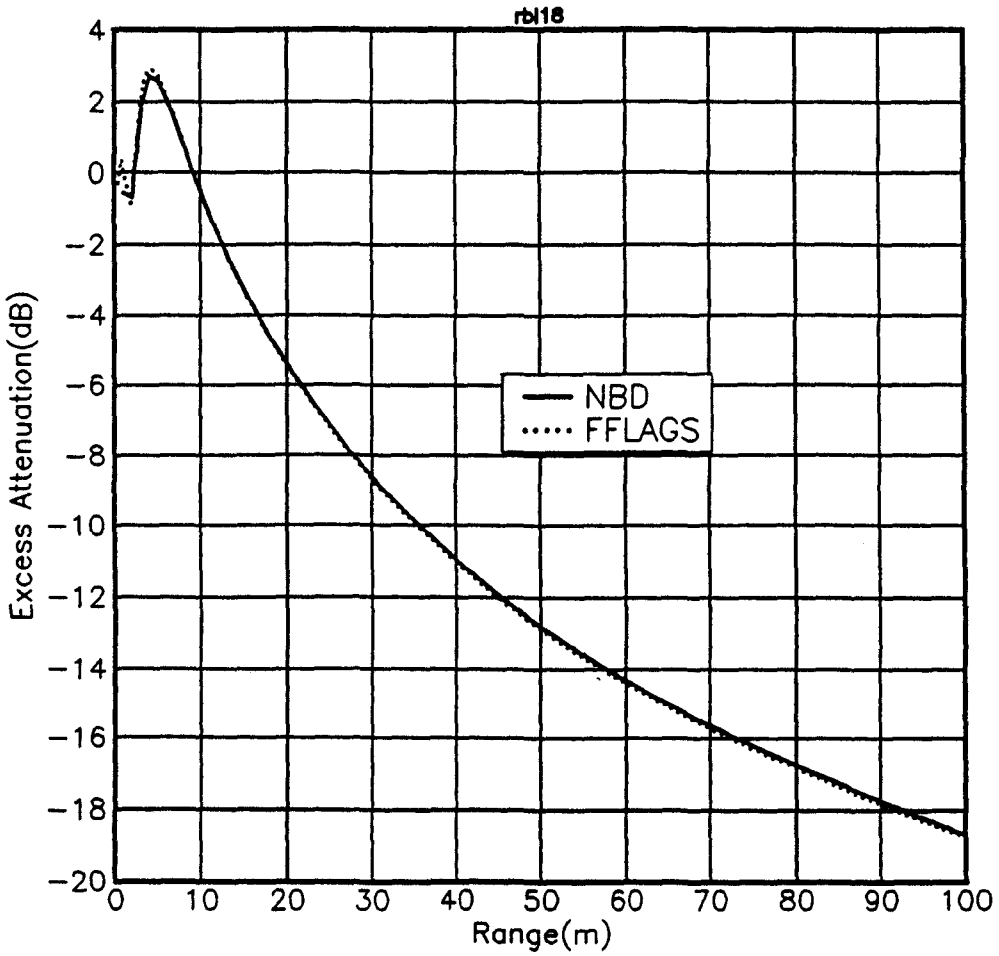

Figure 5.33 Excess attenuation against range at 2000Hz over a thin rigid backed porous layer. FFLAGS, and Nicholas, Berry and Daigle. Snow like parameters.

demonstrate the surprising accuracy of the hard backed layer Nicholas, Berry and Daigle approximation. This asymptotic approximation seems to maintain it's validity over a very wide range of parameters and ranges.

Chapter 6

Solid Particle motion and surface waves.

In vehicle and aircraft detection systems geophones are often used [35]. Therefore it is important to understand the mechanisms by which acoustic signals transfer their energy into ground vibration (acoustic-seismic coupling), and the dependence of this transfer on the porous and elastic properties of the ground. In this chapter FFLAGS is used to examine various aspects of this energy transfer.

6.1 Comparison of FFP predictions of the vertical particle motion at the surface of porous elastic halfspace to the predictions of an asymptotic approximation, and the SAFARI program.

6.1.1 The asymptotic approximation.

Attenborough and Richards [17] have developed an asymptotic approximation for predicting the vertical particle velocity of the surface of an elastic porous material due to a point source in the air. Their solution is the sum of contributions from branch cuts corresponding to each of the three wavetypes in the porous elastic medium and the acoustic wave in the air, and the residue of a surface wave pole. Several approximations are made in the

derivation. These include; The light fluid approximation which is that the pore fluid has no influence on propagation within the rigid frame; and local reaction. For each branch cut the contribution is represented by a Hankel transform. Part of the integrand in the Hankel transform is represented by the first three terms of a Taylor series. This series will only be convergent for the first three terms when the corresponding pole is far from the saddle point. This is so when the range is large. For each branch cut there is a numerical distance which must be large for the predicted vertical particle velocity contribution for that branch cut to be accurate.

6.1.2 Comparison with SAFARI

In order to validate the use of FFLAGS for predicting the motion of a porous elastic halfspace it is first compared to the predictions of an established FFP propagation program for propagation in visco-elastic and fluid media. This program is SAFARI. The elastic analogue of the porous elastic example will be used initially to compare the two programs. Figures 6.1 and 6.2 show the predicted vertical particle velocity as a function of range. The agreement between SAFARI and FFLAGS is extremely good.

6.1.3 Comparison to the asymptotic approximation

The input parameters used for the prediction of vertical particle velocity at the surface of a porous elastic halfspace are in table 6.1. The predicted surface vertical particle velocity as a function of frequency is shown in figure 6.3 for a source height of 1.0 metres at a range of 100 metres. The predictions are for the porous halfspace described in table 6.1, and its non-porous analogue (zero porosity, infinite flow resistivity, but the same bulk density as in the porous case). The difference between the predictions for the porous and non-porous models is similar for both FFLAGS and the asymptotic approximation. However the predicted amplitudes of the vibration do not agree between the two methods, and the frequency dependences also do not agree at the range of 100 metres. This relationship between the predicted vertical particle velocity using porous and non-porous ground models should not be

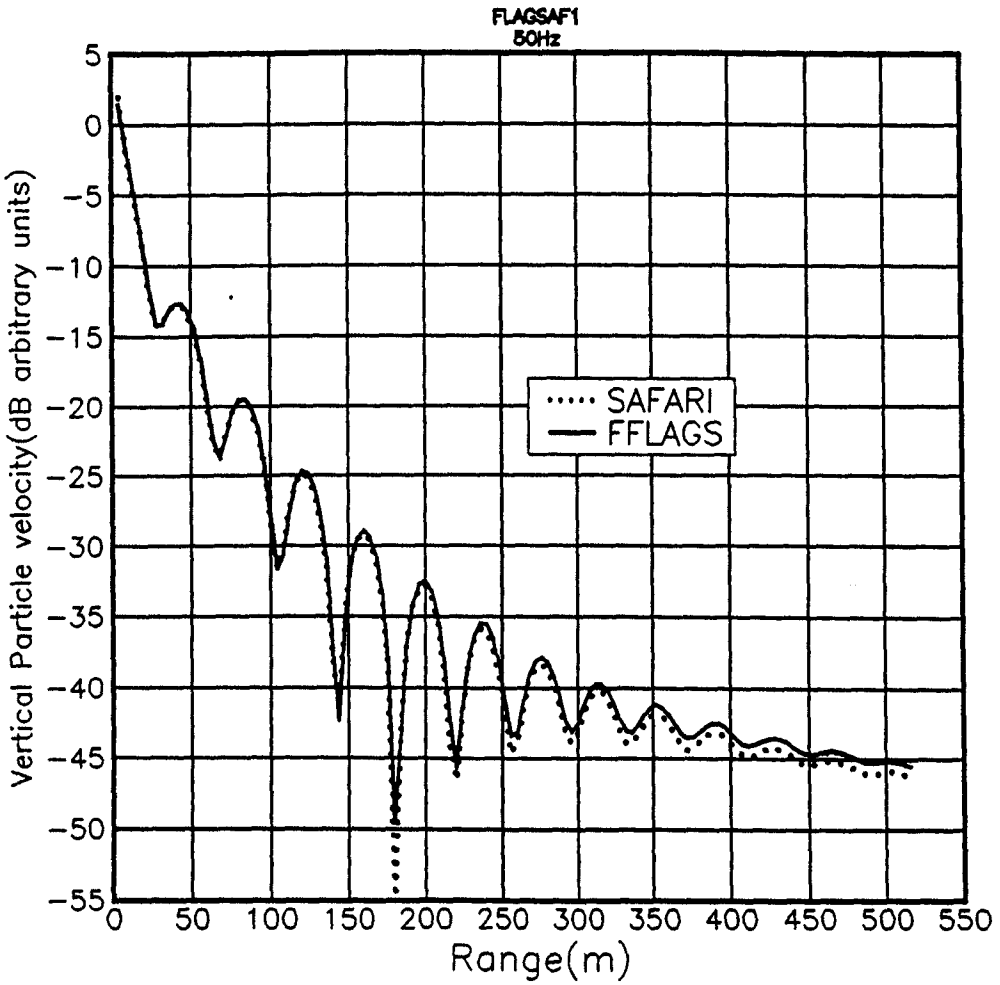

Figure 6.1 Predicted vertical particle velocity at 50Hz at the surface of an elastic halfspace due to a point source at a height of one metre, using SAFARI and FFLAGS.

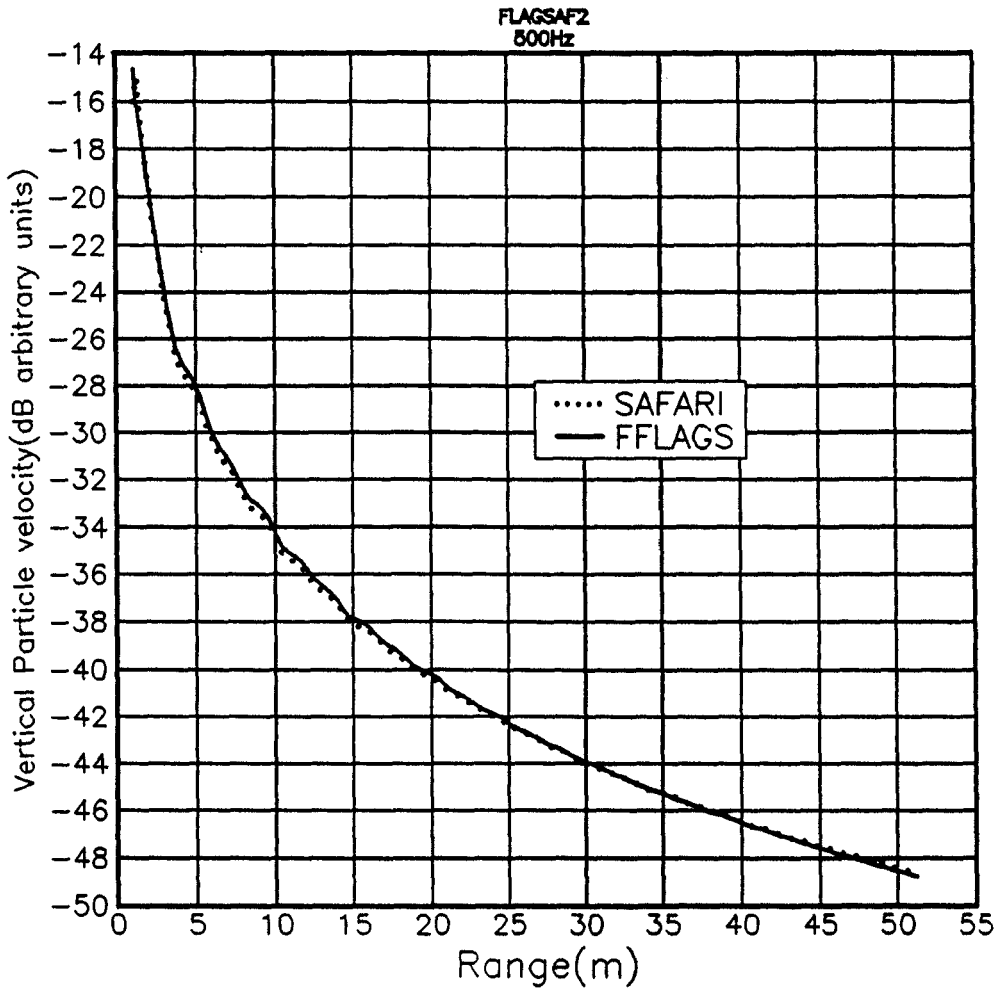

Figure 6.2 Predicted vertical particle velocity at 500Hz at the surface of an elastic halfspace due to a point source at a height of one metre, using SAFARI and FFLAGS.

Table 6.1 Material parameters used in the prediction of vertical particle velocity

Parameter	Unit	Value
Flow resistivity σ	mks raylsm^{-1}	250000
Porosity Ω	-	0.4
Pore shape factor ratio s_p	-	0.375
Grain shape factor n'	-	1.0
Bulk density	kgm^{-3}	1300.0
P-wave velocity v_p	ms^{-1}	500.0
S-wave velocity v_s	ms^{-1}	320.0
$\Im(v)/\Re(v)$	-	0.0125
Grain bulk modulus K_r	Nm^{-2}	$1.2.10^{11}$
Sound velocity c	ms^{-1}	340.0
Air density	kgm^{-3}	1.20

regarded as general. Figure 6.11 shows that the ratio of the predicted particle velocities using porous and non-porous models is extremely dependent on parameters other than porosity.

Figures 6.4 and 6.5 show the predicted surface vertical particle velocity as a function of range for the porous material for a source height of 1.0 metre at frequencies of 50Hz and 500Hz respectively. Figure 6.6 shows the vertical particle velocity for the same environment as in figure 6.4 but the ratio of imaginary to real parts of the propagation constants is zero. The numerical distances in these examples are large enough for the important contributions to be accurate in theory.

6.1.4 Discussion

FFLAGS has been shown to give good agreement with visco-elastic theoretical results in the non-porous limit. However, when compared to the asymptotic approximation it is shown that the predictions of FFLAGS and the asymptotic limit are widely differing. These differences occur both for realistic porous soil parameters and the non-porous limit. The asymptotic approximation is a long range approximation, and it has hitherto been as-

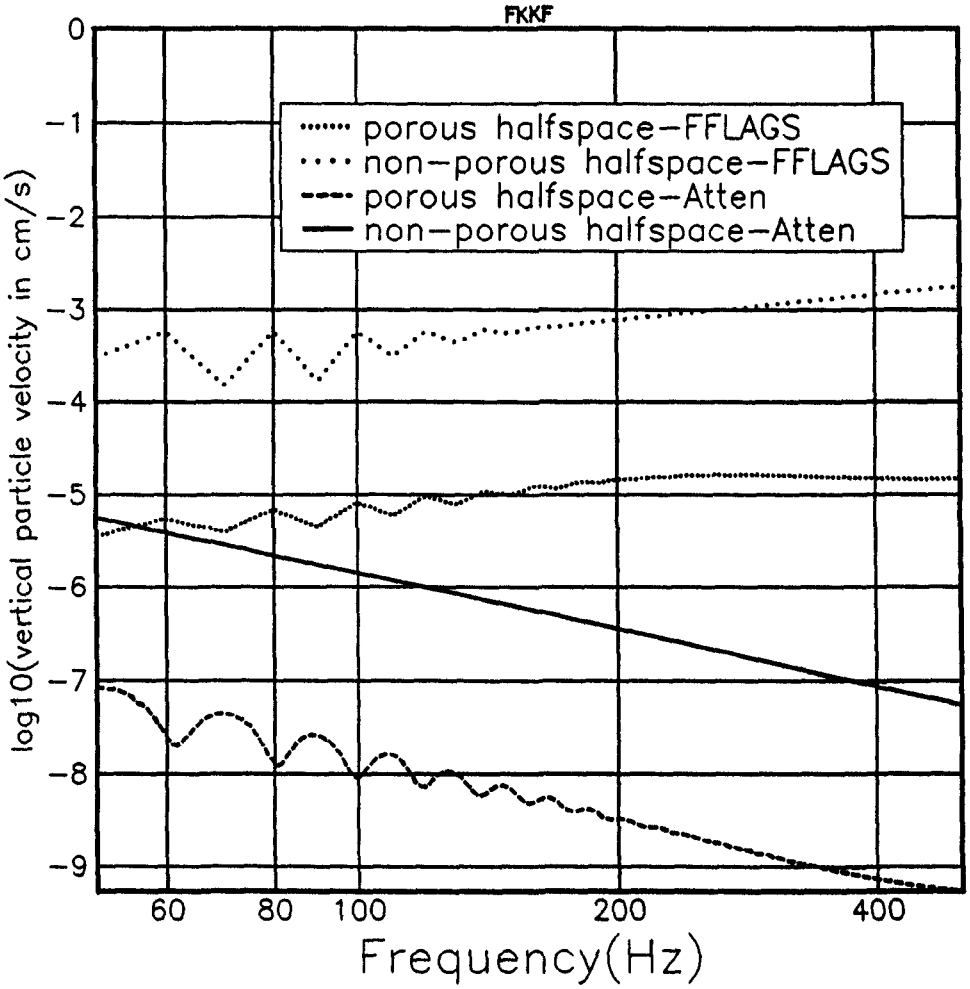

Figure 6.3 Predicted vertical particle velocity on the surface of porous-elastic half space and the equivalent nonporous elastic halfspace. FFLAGS and Attenborough and Richards' asymptotic approx'. Source height 1.0 metre, range 100 metres.

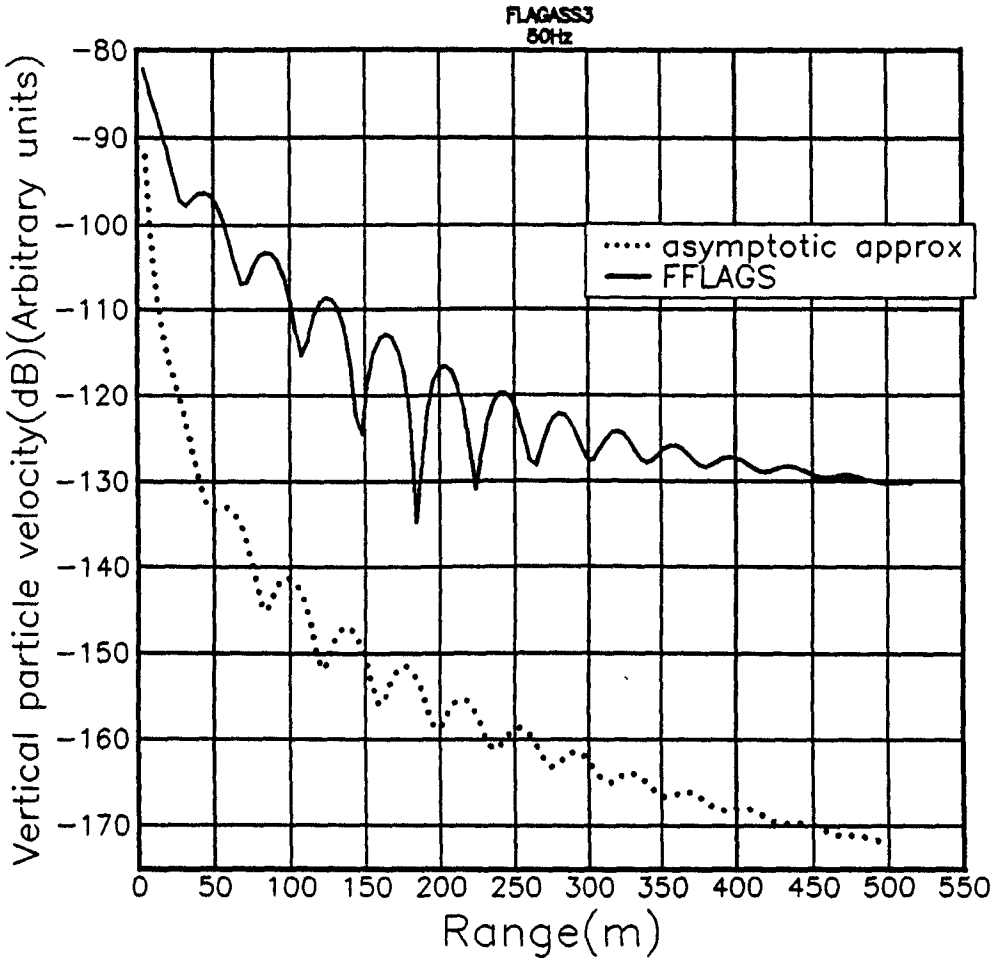

Figure 6.4 Predicted vertical particle velocity on the surface of porous-elastic half space. FFLAGS and Attenborough and Richards' asymptotic approx'. Source height 1.0 metre, frequency 50Hz.

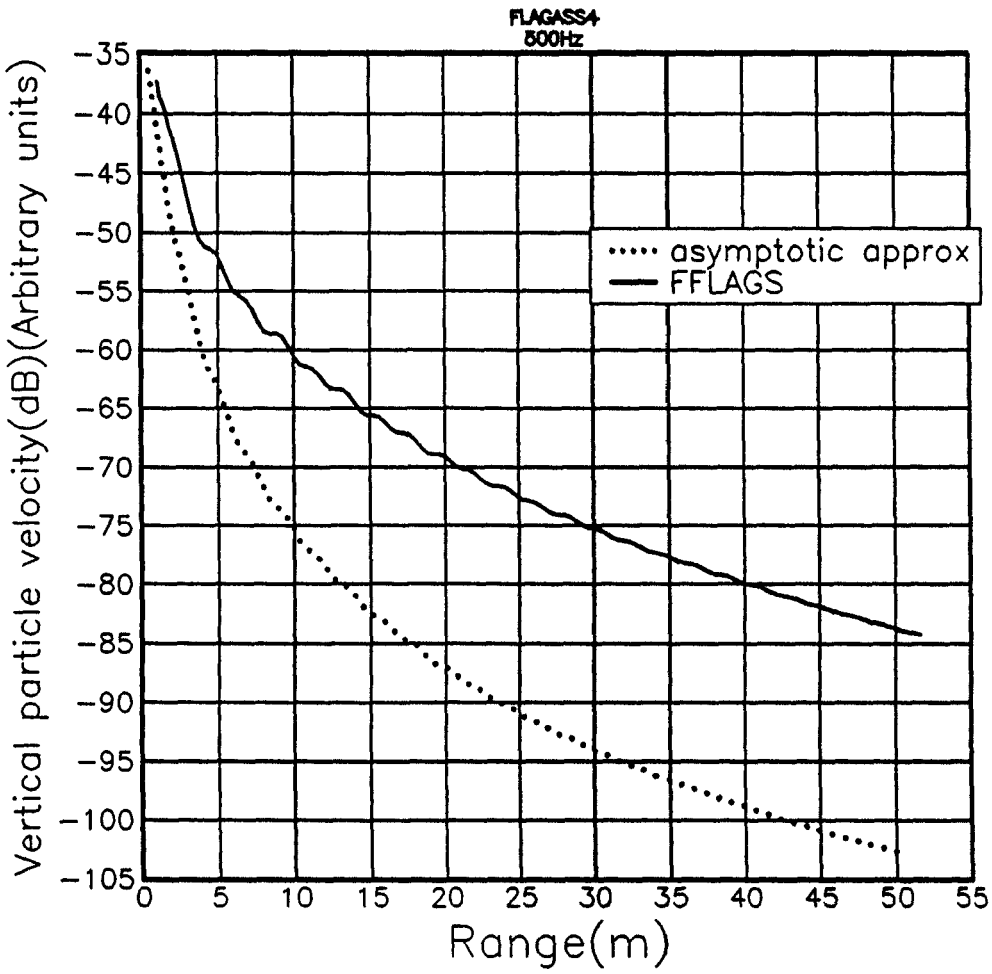

Figure 6.5 Predicted vertical particle velocity on the surface of porous-elastic half space. FFLAGS and Attenborough and Richards' asymptotic approx'. Source height 1.0 metre, frequency 500Hz.

sumed that the minimum valid range is less than the maximum range predicted by the FFP here. It is possible that the minimum valid range is much greater than was assumed.

6.1.5 Examination of the different contributions to the vertical particle velocity.

The contributions from each of the branch cuts and the surface wave pole in the asymptotic result can be calculated separately. Similarly in the FFP method the integrand can be examined to see whether peaks occur in the integrand at the horizontal wavenumber corresponding to the relevant propagation constant. For the vertical particle velocity predictions shown in figure 6.4 the integrand of the FFP is shown in figure 6.7. It can be seen that the predicted vertical particle velocity is mainly the sum of a direct contribution from the air (horizontal wavenumber equal to the air propagation constant $0.935m^{-1}$), and a contribution from a pseudo-Rayleigh wave (propagation constant $1.095m^{-1}$). The interference between these causes the maxima and minima in the predicted particle velocity (figure 6.6). A similar effect can be seen in the asymptotic approximation prediction, but the predicted phase relationship between the direct contribution and the Rayleigh wave contribution is approximately 180^o from that predicted by FFLAGS, leading to maxima and minima in the particle velocity at different ranges to those predicted by FFLAGS. This means that the Rayleigh wave contribution for the asymptotic approximation is added to the other contributions with the wrong phase.

6.2 The influence of porosity on acoustic-seismic coupling coefficient

It has recently been proposed [4] that the influence of ground porosity on the coupling of acoustic energy into ground vibration is negligible, and hence that acoustic-seismic coupling coefficients can be accurately modelled by using a visco-elastic model. By using a low seismic velocity visco-elastic layer

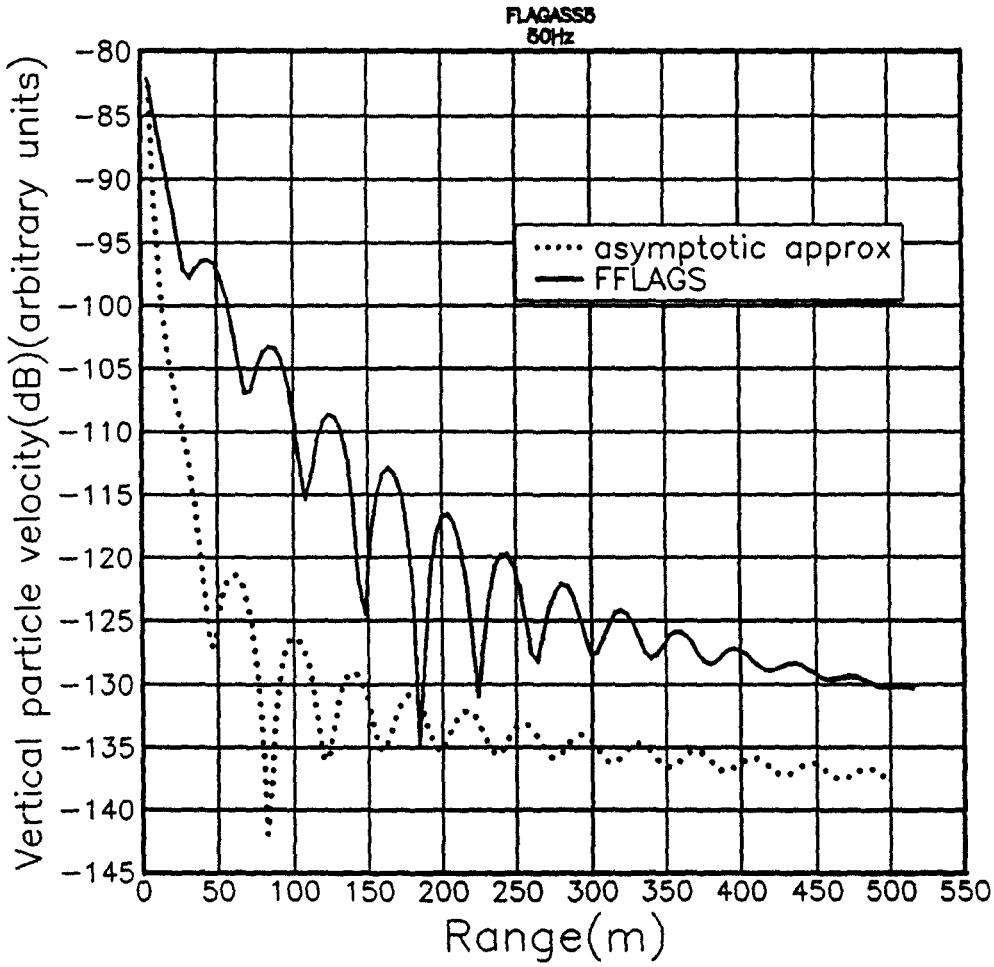

Figure 6.6 Predicted vertical particle velocity on the surface of porous-elastic half space. FFLAGS and Attenborough and Richards' asymptotic approx'. Source height 1.0 metre, frequency 50Hz, parameters as table 6.1 except $\Im v = 0$.

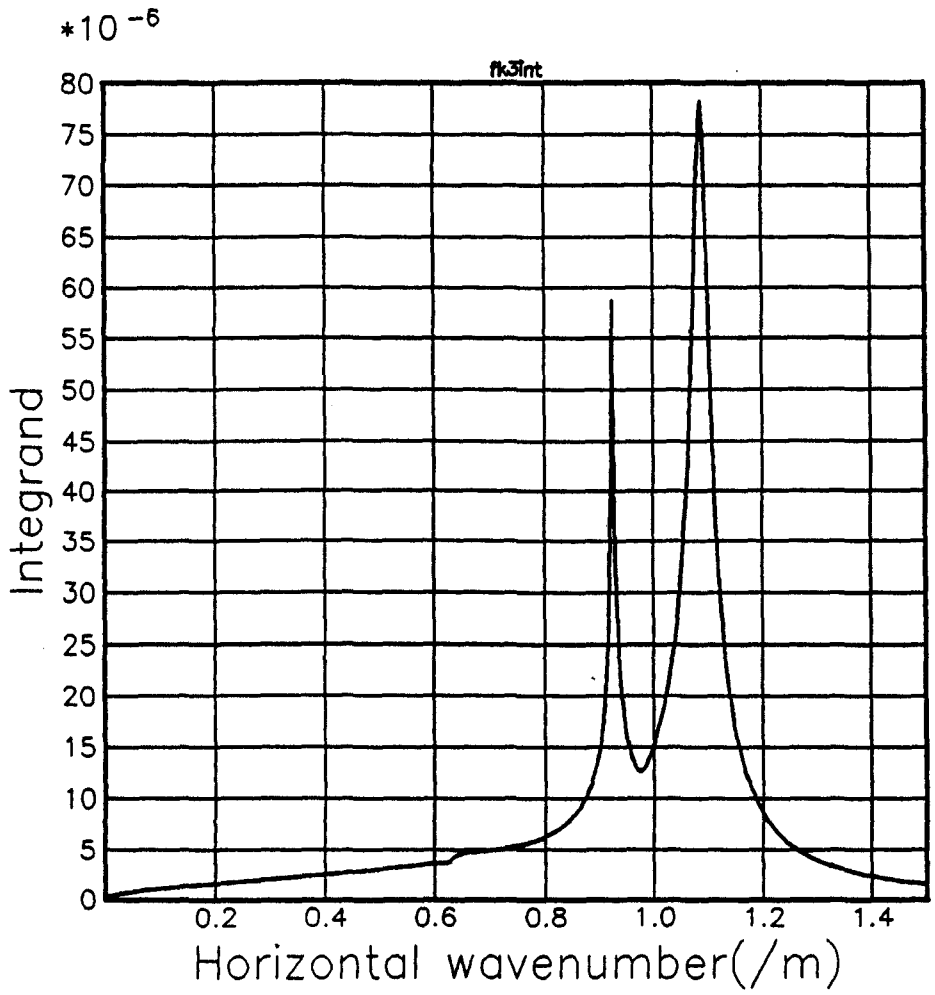

Figure 6.7 FFLAGS depth dependent integrand for vertical particle velocity at the surface of a poro-elastic halfspace at a frequency of 50Hz

at the surface Sabatier [4] found that the predicted vertical particle velocities using a porous-elastic model were nearly identical to those predicted using a visco-elastic model. In this section this supposition will be theoretically investigated by examining the predicted ratios of acoustic pressure at 5cm above the ground surface to particle displacement amplitude at 1cm below the ground surface. Three model ground surfaces will be examined. The first is the thin snow layer examined in section 5.4. The backing is this time modelled as an elastic halfspace, with seismic velocities 500 and $300ms^{-1}$ for P (longitudinal) and S (shear) waves respectively. Figure 6.8 shows the predicted acoustic-seismic coupling coefficient for the snow layer with parameters given in table 7.2 on page 177, and with the same elastic moduli and bulk density, but zero porosity. It is obvious that there is a large theoretical difference.

The second example is for the acoustic-seismic coupling coefficient for a layered porous elastic ground consisting of a two metre thick porous layer overlying an elastic substrate. The parameters are tabulated in table 6.2 Figure 6.9 shows the predicted acoustic-seismic coupling coefficient (ratio of vertical particle velocity to acoustic pressure), for the porous elastic ground with parameters shown in table 6.2, and for the non-porous analogue of it. These demonstrate that the predicted acoustic-seismic coupling coefficient is very dependent on porosity. The third ground is identical to that above but the upper 0.2 metres of the ground are altered so that the seismic velocities are reduced to 160 and $102ms^{-1}$ and the porosity increased to 0.5. The porous and non-porous predictions of vertical particle velocity become very similar (see figure 6.10).

Figure 6.10 shows that it is possible to obtain very similar predicted particle velocities for porous and non-porous ground models by choosing very low seismic velocities for the ground near the surface. This is in general agreement with Sabatier's findings. It is undoubtedly true that near surface seismic velocities are very small. This is because the elastic moduli of the soil near the surface are at least partly due to self loading [20]. Self loading is the phenomenon whereby the restoring force for mechanical wave propagation in

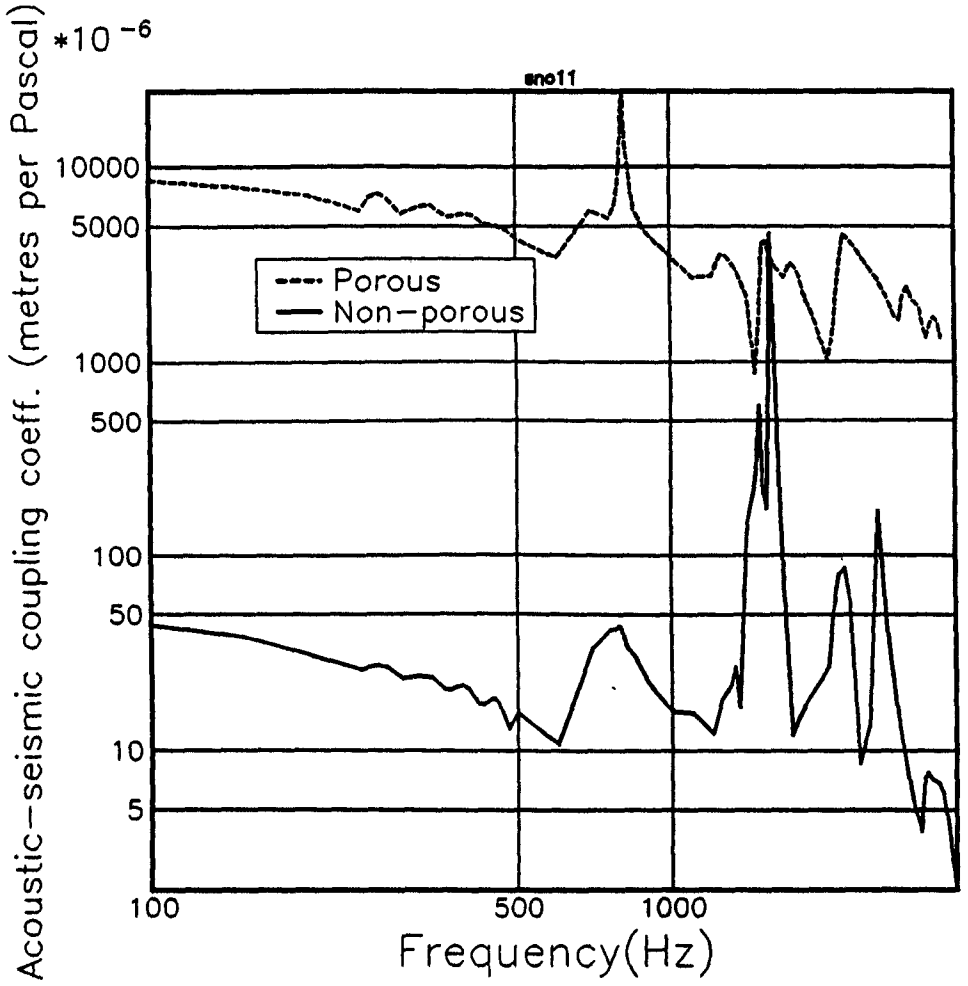

Figure 6.8 Predicted acoustic-seismic coupling coefficient on a thin snow layer. Range 20 metres. Source height 1.0 metre. Receiver heights +0.05m, -0.01m.

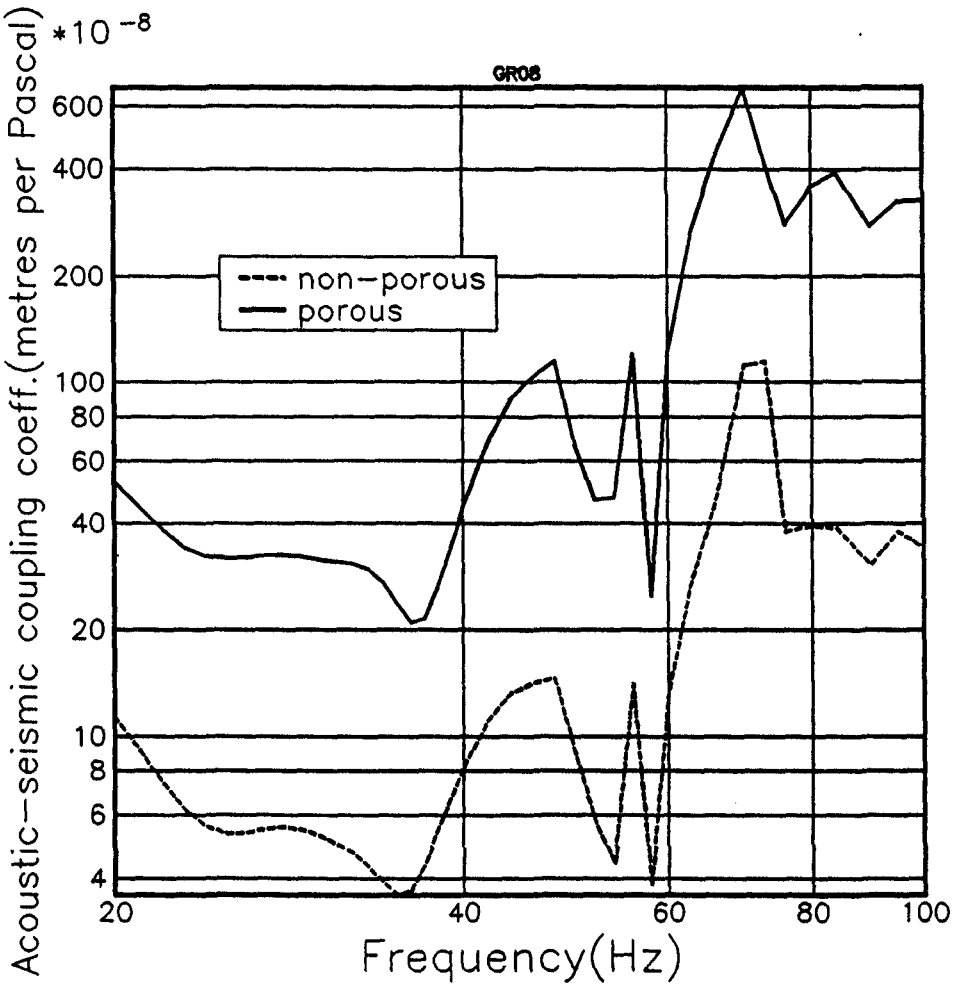

Figure 6.9 Predicted acoustic seismic coupling coefficient for the porous-elastic ground parameters shown in table 6.2 . Source height 1.0 m, receiver heights 0.05 and-0.01 m.

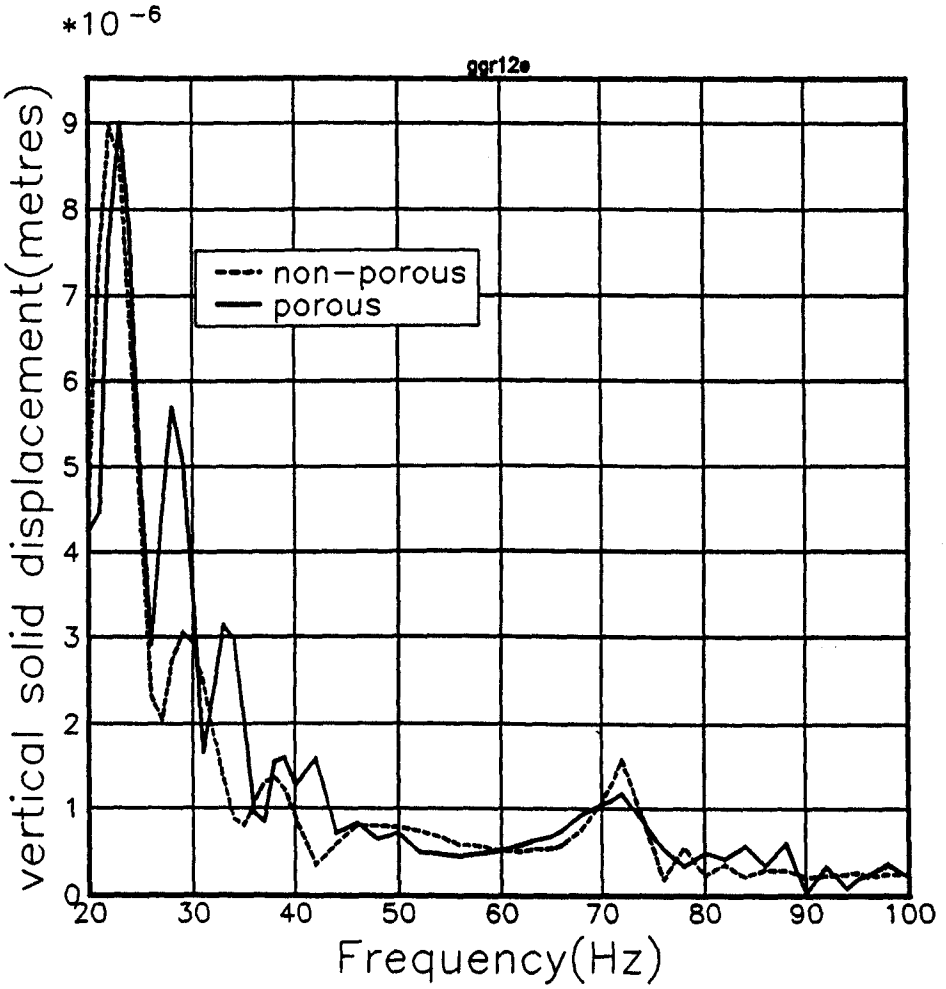

Figure 6.10 Predicted acoustic seismic coupling coefficient for the porous-elastic ground parameters shown in table 6.2 with a surface layer of porosity 0.5,thickness 0.2 metres and seismic velocities of 160 and 102 ms^{-1} for fast and shear waves respectively. Source height 1.0 m, receiver heights 0.05 and -0.01 m.

Table 6.2 Ground parameters used in prediction of acoustic-seismic coupling.

Parameter	Unit	Value
Flow resistivity (σ)	MKS $rayls m^{-1}$	366000
Porosity (Ω)	-	0.27
pore shape factor ratio (s_p)	-	0.5
grain shape factor (n')	-	0.5
upper p velocity	ms^{-1}	270.0
upper s velocity	ms^{-1}	190.0
$\Im(v)/\Re(v) =$	-	0.0
lower p velocity	ms^{-1}	500.0
lower s velocity	ms^{-1}	330.0
solid bulk modulus	Nm^{-2}	$4.6.10^{11}$
upper layer thickness	m	2.0
bulk density ρ_b	kg m^{-3}	1700.

a dry granular material is dependent on the forces between different grains at the grain contacts. These forces are caused by the gravitational forces on the grains above the grain contact. At the grain contacts close to the surface the restoring force will be small because there will be very few grains above the contact. At grain contacts buried deeply the restoring force will be large and hence the elastic modulus of the material will be large

However no evidence has been presented to suggest that the seismic velocities used by Sabatier to show the similarity of porous and non-porous results actually correspond to real near surface seismic velocities. Furthermore the difference between the predictions of porous and non-porous models is very sensitive to the near surface seismic velocities used. This is shown in figure 6.11. This figure shows the ratio of the predicted vertical particle displacements as a function of the near surface layer P wave seismic velocity at 100Hz. The ratio of the p to s wave velocities is kept constant at 0.636. Because the influence of porosity on acoustic-seismic coupling is generally theoretically large (as shown by figures 6.9 and 6.8), a visco-elastic model of the ground could only be used to predict vertical particle velocity if the near surface seismic velocities lay in the narrow band (around v_p=160ms^{-1}

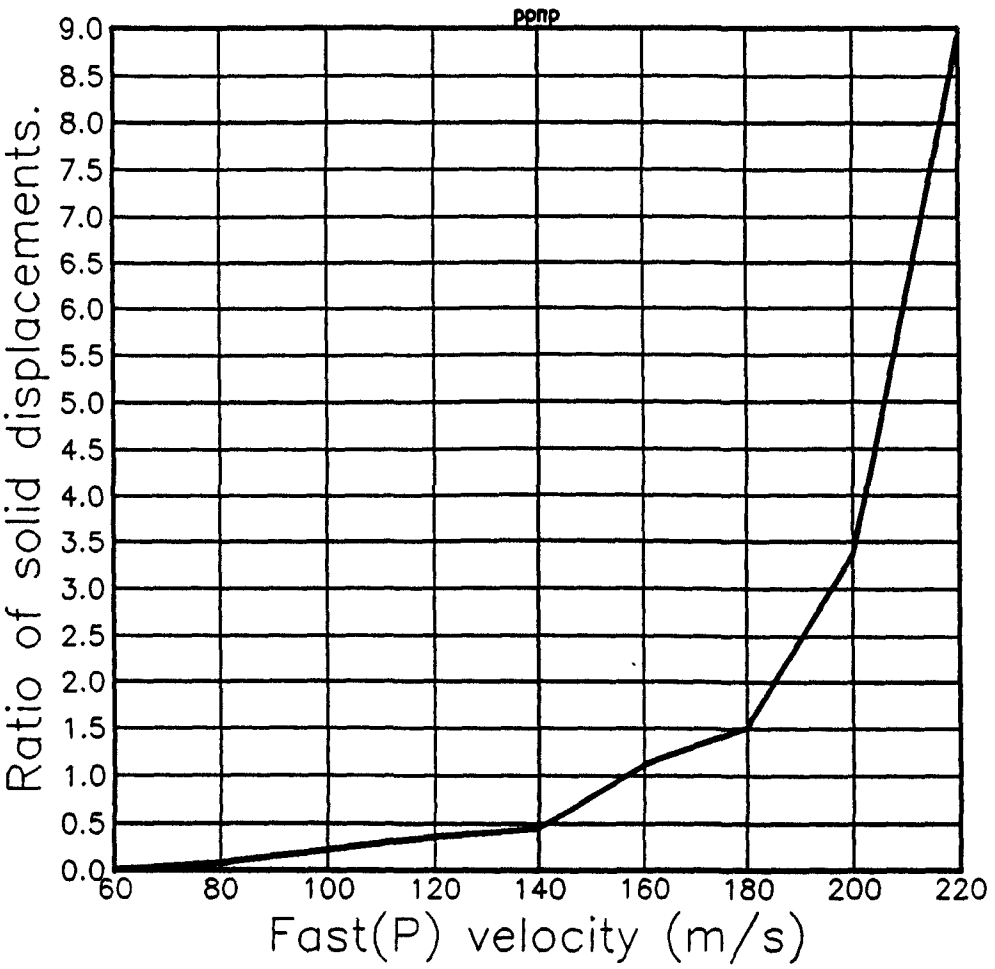

Figure 6.11 The predicted ratio of non-porous model to porous model solid displacements at 100Hz as a function of surface layer seismic velocity.

in figure 6.11) where the influence of porosity was negligible. For characterising grounds for acoustic-seismic coupling it may be possible to calculate notional near surface seismic velocities using a visco-elastic model. However these velocities will not necessarily be related to real seismic velocities which would be measured in the ground.

6.3 Surface waves at the surface of a poro-elastic ground

By examining the depth dependent part of the FFP integrand it is possible to discover which of the postulated surface waves on the surface of a poro-elastic ground will be excited by a point source. Several workers in this field have postulated several different possible sets of surface waves [90],[91] Feng and Johnson [90] used a numerical search for solutions to the Biot dispersion relations. They examined the high frequency behaviour and assumed the lossless case for the porous medium. Attenborough and Chen [1] also used a numerical search to find solutions to the Biot dispersion relations with amplitudes decaying exponentially away from the surface. However their work was more relevant to atmospheric acoustic propagation from the point of view of the material parameters and the frequency range.

For propagation over a porous-elastic halfspace with porous and elastic parameters shown in table 6.3, Attenborough and Chen found the possibility of three surface waves. These were only slightly dispersive and were called the slow surface wave, the pseudo-Rayleigh wave, and the fast surface wave. The slow surface wave was described as a pseudo-Stoneley wave. The phase velocities were approximately $350ms^{-1}$, $800ms^{-1}$, and $1350ms^{-1}$ respectively.

The FFLAGS program was used to calculate the depth dependent Greens function in the solid material as a function of frequency and phase velocity, shown in figure 6.12. The phase velocity was defined as $2\pi fr/k_h$ where k_h is the horizontal wavenumber and fr is the frequency. The source height was 1.0 metres, and the receiver was at the surface of the material. It can be seen

Table 6.3 Material parameters used in the surface wave predictions.

Parameter	Unit	Halfspace	layer	substrate	snow
Flow resistivity σ	mks raylsm^{-1}	300000	36000	30000	5000
Porosity Ω	-	0.4	0.3	0.02	0.8
Pore shape factor ratio s_p	-	0.5	0.36	0.36	0.5
Tortuosity	-	2.5	2.5	2.5	2.25
Bulk density	kgm^{-3}	1000.0	1700.0	2600.0	210.0
frame bulk modulus K_b	Pa	8.10^8	1.10^8	5.10^8	$5.25.10^7$
frame shear modulus μ	Pa	8.10^8	1.10^8	5.10^8	$1.1.10^7$
Grain bulk modulus K_r	Pa	3.10^{10}	3.10^8	3.10^8	$1.1.10^7$

that the point source in the air can excite the pseudo-Rayleigh mode in the porous material. This is shown in figure 6.12 as the peak at around $800ms^{-1}$. A peak at around $341ms^{-1}$ can also be seen in the integrand. In figure 6.13 it can be seen that this peak is only slightly dispersive. This dispersion (a phase velocity shift of $0.5ms^{-1}$ between 100Hz and 500Hz) is less than that predicted by Attenborough and Chen for the slow surface wave. If the porosity is increased to 0.7 then the predicted dispersion of the surface wave is larger. Figure 6.14 shows the depth dependent Green's function for frequencies of 100 and 500Hz. This shows that the Greens function peak is still only slightly dispersive. This indicates that the contribution at approximately $340ms^{-1}$ is not the slow surface wave, but is a direct contribution from the airborne wave. This conclusion is consistent with the predictions of analytical approximations for the field due to a point source above a locally reacting boundary, which suggests that the (slow) surface wave will only be excited near grazing incidence if the imaginary part of the impedance exceeds the real part. According to the modified Biot model this is not possible for a homogeneous halfspace. No peak is seen in figure 6.12 due to the fast surface wave predicted by Attenborough and Chen.

The second surface which Attenborough and Chen examined consisted of a high porosity surface layer of thickness 1 metre overlying a less porous substrate. The parameters are shown in table 6.3. They predicted the existence

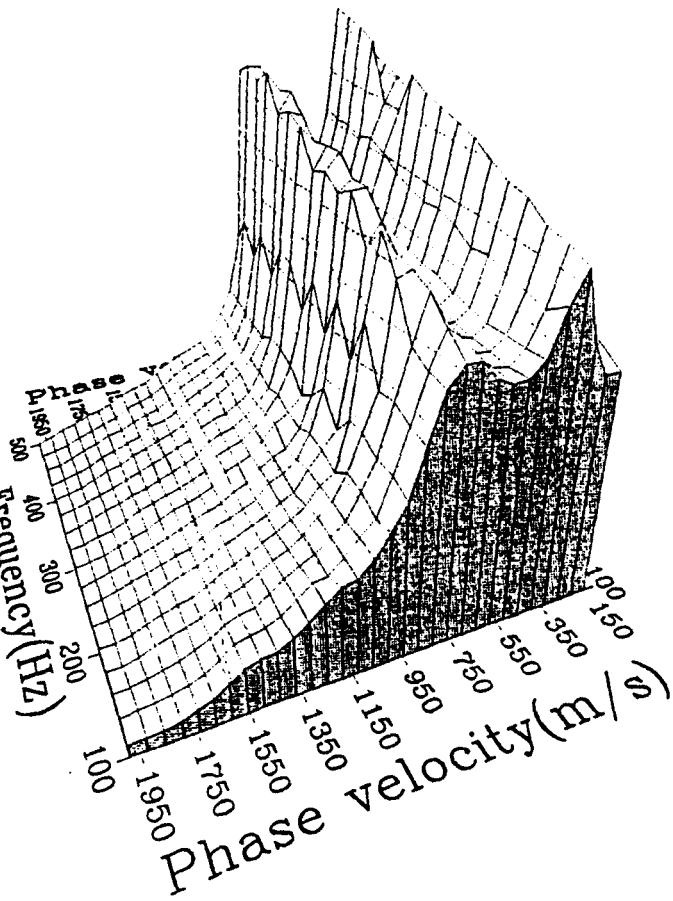

Figure 6.12 Depth dependent Greens function as a function of frequency and phase velocity, for vertical particle velocity at the surface of a porous elastic halfspace with parameters given in table 6.3.

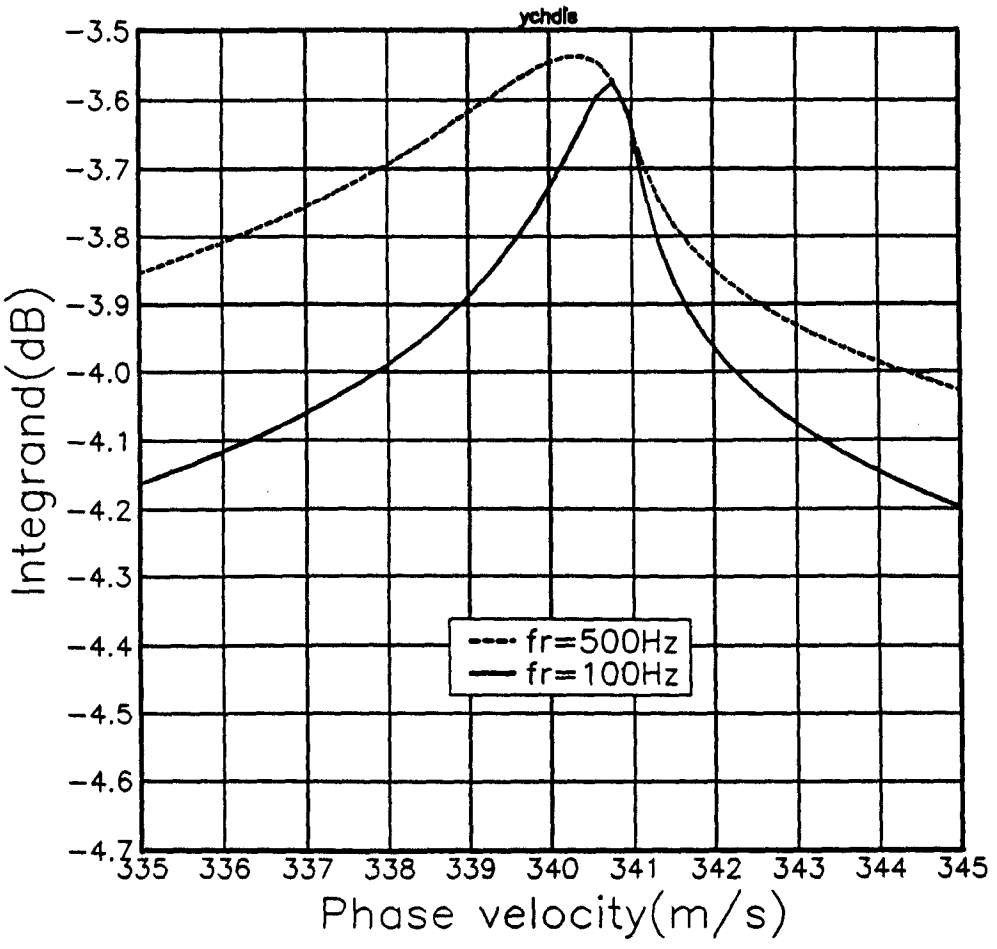

Figure 6.13 Depth dependent Greens function as a function of phase velocity for vertical particle velocity at the surface of a porous elastic halfspace, porosity 0.4, at 100Hz and at 500Hz. Parameters as given in table 6.3.

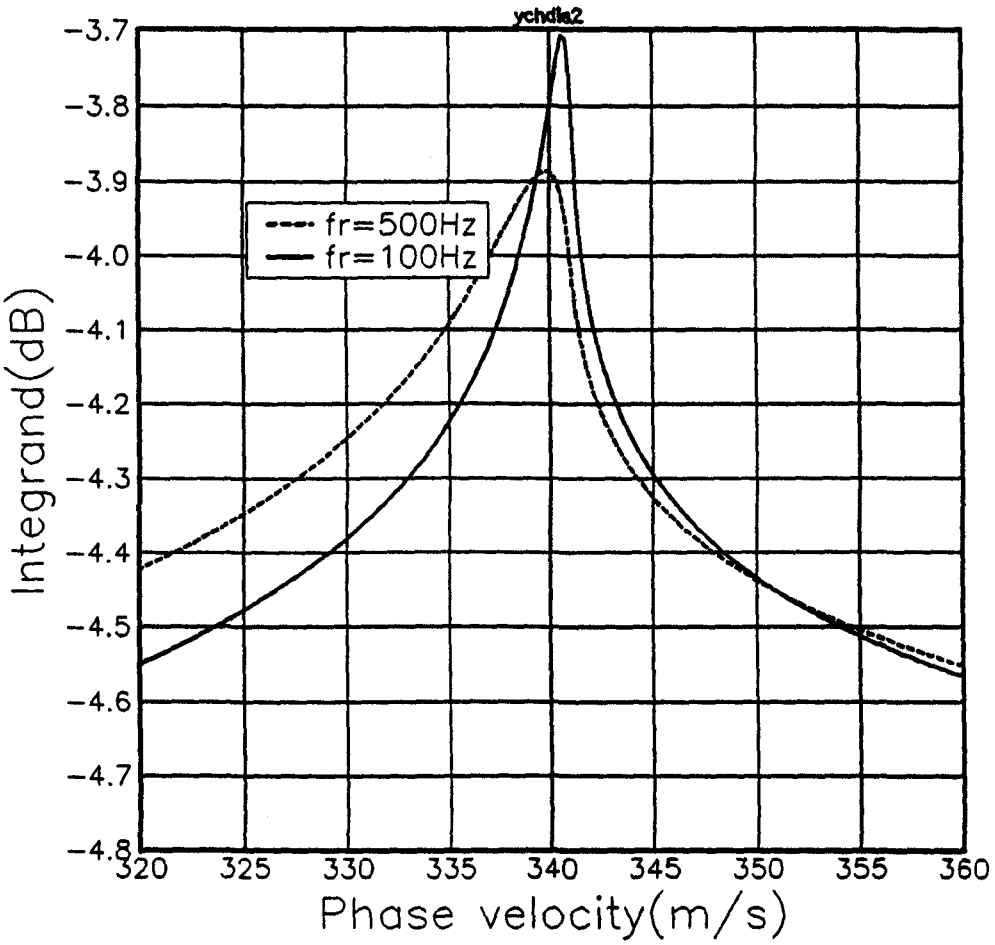

Figure 6.14 Depth dependent Greens function as a function of phase velocity for vertical particle velocity at the surface of a porous elastic halfspace,porosity 0.7, at 100Hz and at 500Hz. Parameters as given in table 6.3.

of three dispersive surface waves. The predicted phase velocities can be seen in figure 6.15. Figure 6.16 shows the depth dependent Green's function for vertical particle velocity at the surface of this system. The Greens function as a function of frequency and phase velocity is much more complex for this system than for the previous one. There appear to be three highly dispersive wavetypes, marked A, B and C in figure 6.16. A is a pseudo-Rayleigh wave. It can be seen that the maximum of the integrand for A is at the phase velocity corresponding to the speed of sound in air. This agrees generally with experimental findings of geophysicists that sources in air excite the Rayleigh wave mode at the frequency where the Rayleigh wave phase velocity equals the speed of sound in air. B and C are other waveguide-like modes in the surface layer [92]. The peak in the Greens function at D is not dispersive. The surface waves predicted by Attenborough and Chen are also dispersive. However they predict phase velocities increasing with increasing frequency(see figure 6.15). Attenborough and Chen claim that one of the surface wave modes predicted can be described as a pseudo-Rayleigh wave. However the dispersive behaviour is dissimilar to a Rayleigh wave [92]. The parameters given by Attenborough and Chen for the layered ground are not physically realisable for real soils. In particular the substrate porosity and bulk density are not consistent with the substrate flow resistivity. If the flow resistivity is increased to be consistent with the porosity, then it should take on a value of $1.10^6 mks\ rayls\ m^{-1}$. Similarly the layer flow resistivity is unusually low and should be increased to $3.10^5 mks\ rayls\ m^{-1}$. With these modified values the depth dependent Green's function will be modified to that given in figure 6.17.

Increasing the flow resistivities in this manner changes the Green's function. A low phase velocity dispersive contribution is seen (A), with phase velocities between $80ms^{-1}$ at 100Hz and $160ms^{-1}$ at 500Hz. There are two relatively non-dispersive contributions at 340 and $400ms^{-1}$(B and C). The region D consists of a dispersive contribution with phase velocities between 400 and $600ms^{-1}$ and ringing which leads to a large set of peaks at many different phase velocities.

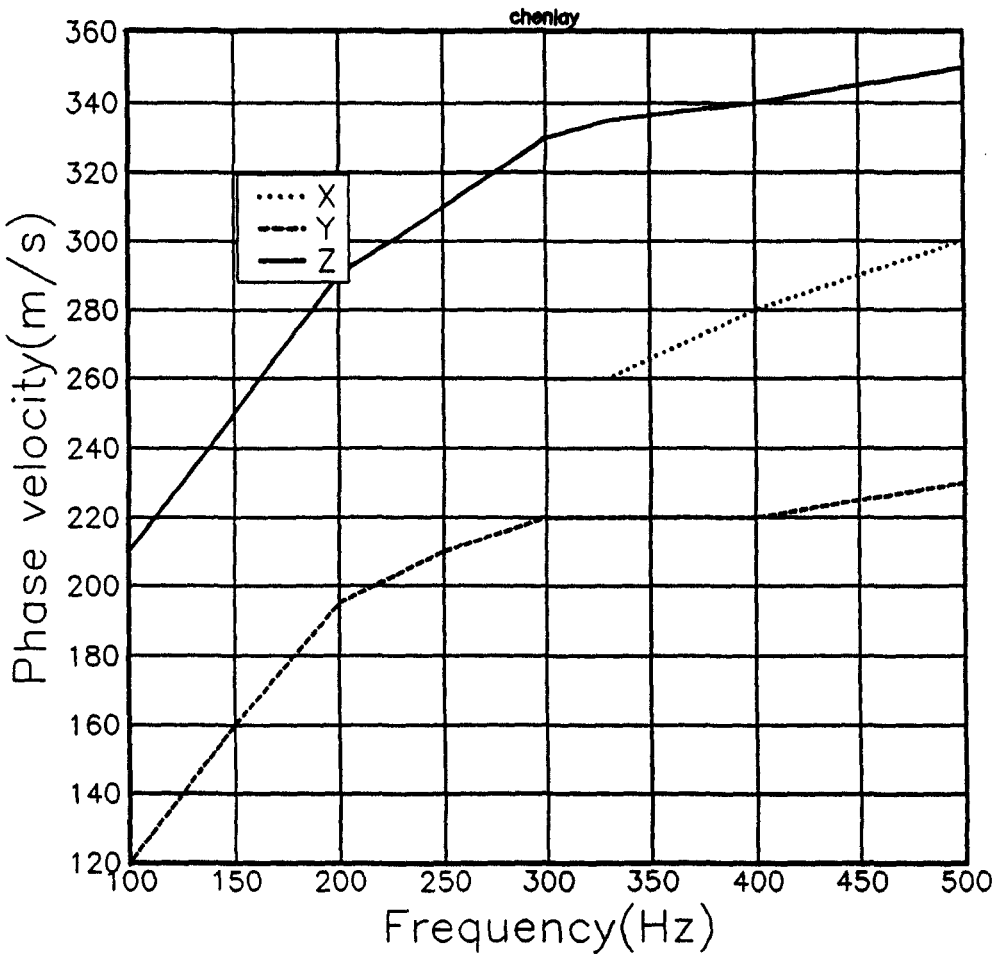

Figure 6.15 Phase velocities of predicted surface wave modes from Attenborough and Chen [1], for a layered porous-elastic soil with parameters as in table 6.3.

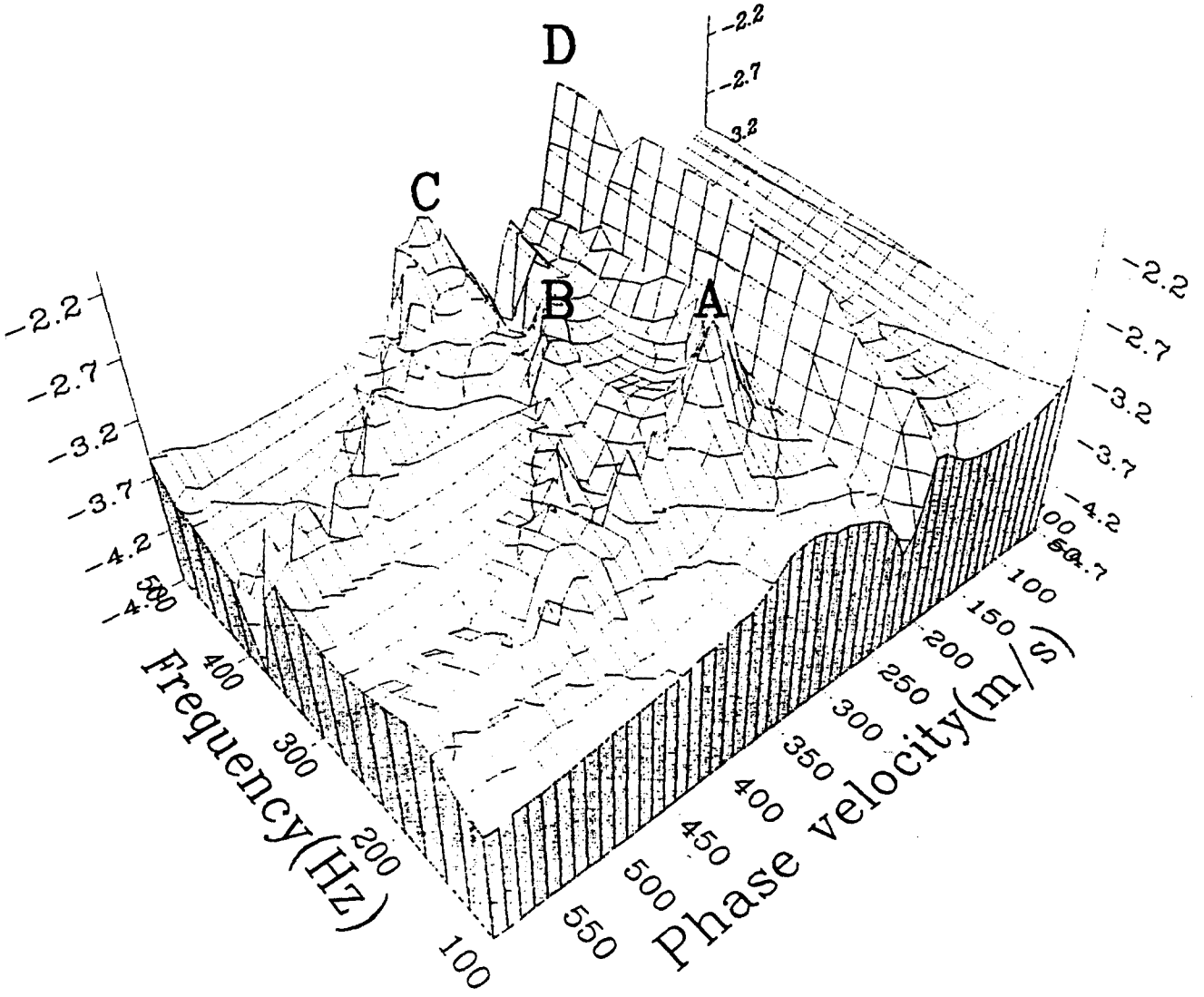

Figure 6.16 log_{10} of the depth dependent Green's function for vertical particle velocity at the surface of a layered porous elastic soil with parameters as in table 6.3.

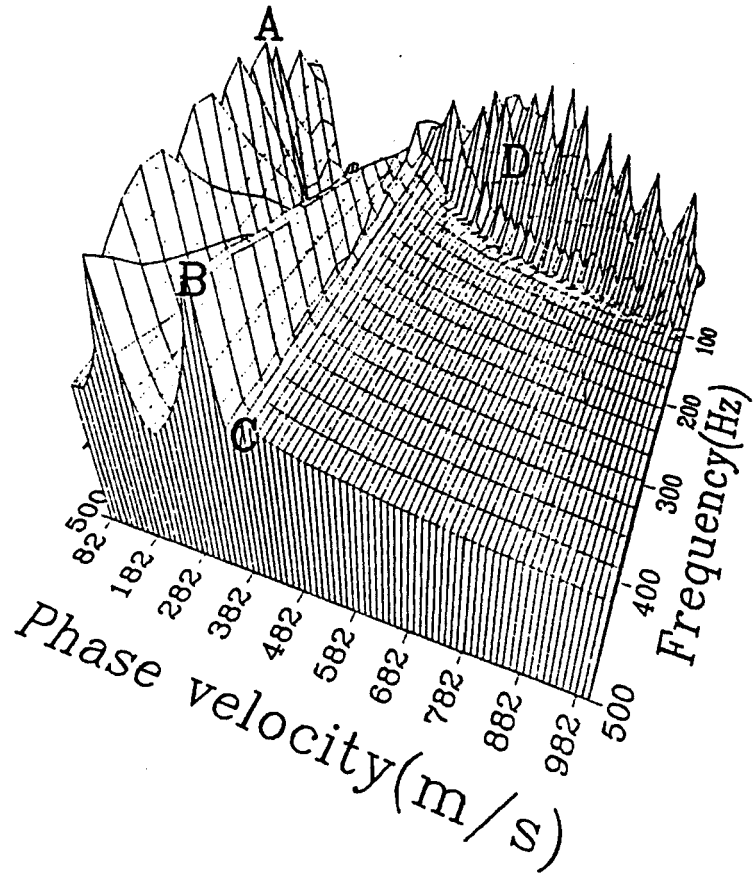

Figure 6.17 log_{10} Depth dependent Greens function as a function of frequency and phase velocity, for vertical particle velocity at the surface of a layered porous elastic ground with parameters given in table 6.3 modified by increasing the flow resistivities as given in the text.

Attenborough and Chen also predict possible surface waves on the surface of a poro-elastic snow-like layer 0.08 metres deep, overlying a porous-elastic substrate. Five of these predicted surface waves are only slightly dispersive with phase velocities of 300,373,570,670,and 800 metres per second. There is also one highly dispersive and attenuated surface wave. Figure 6.18 shows the depth dependent Green's function for vertical particle velocity at the surface of the snow for an acoustic source on the surface of the snow. There are several contributions to the vertical particle velocity in this case. Among these are two contributions (B and C) with phase velocities of 300 and 370 ms^{-1}. These correspond to two of the surface wave modes predicted by Attenborough and Chen. In figure 6.18 there are also two dispersive contributions, one corresponding to phase velocities between 100 and 150 ms^{-1} (A), and the other with phase velocities between 370 and 600 ms^{-1} (D).

6.3.1 Discussion

In the case of the porous halfspace the two lower velocity surface waves predicted by Attenborough and Chen appear to correspond to peaks in the depth dependent Green's function for vertical particle velocity at the surface. The higher velocity surface wave predicted by Attenborough and Chen does not appear to contribute to the predicted particle velocity for a point source in the air. However this does not mean that the higher phase velocity surface wave will not exist, but merely that it is not excited by a point source in the air.

In the case of the layered soil there is little agreement between the peaks in the depth dependent Green's function and the predicted phase velocities of the surface waves. The phase velocities predicted by Attenborough and Chen are dispersive with phase velocities increasing with frequency. If a dispersive air coupled pseudo-Rayleigh wave is to exist (as it has been experimentally been shown to exist [32]) then it's phase velocity will decrease with increasing frequency. This is the behaviour predicted by the Green's function (figure 6.16).For the modified parameters of the layer (figure 6.16)

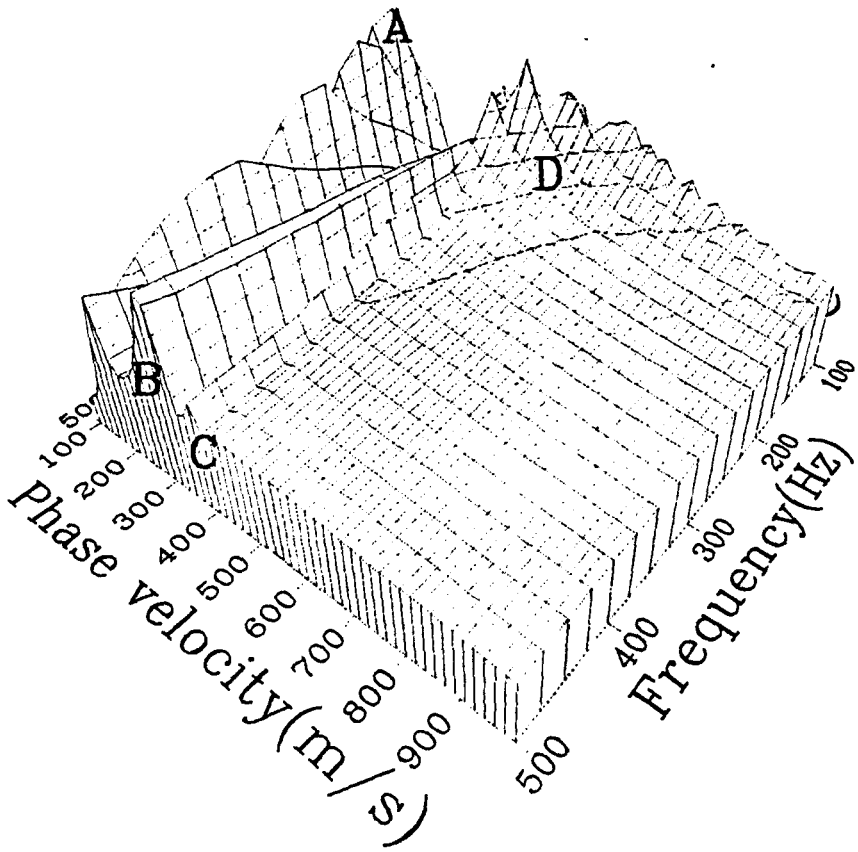

Figure 6.18 Depth dependent Greens function as a function of phase velocity and frequency, for an 8cm snow layer over a porous-elastic substrate.

the Green's function contribution at 340 ms^{-1} is the direct contribution from the airwave. The contribution at $400ms^{-1}$ is at a phase velocity similar to that of the P-wave in the layer.

In the case of the snow layer there is partial agreement between Attenborough and Chen's predicted surface wave phase velocities, and the phase velocities of the contributions to the depth dependent Green's function (figure 6.18). An extra dispersive wave is predicted by the Green's function method, and the two fast surface waves predicted by Attenborough and Chen do not contribute to the Green's function of the vertical particle velocity.

Chapter 7

Modelling the interaction between atmospheric and ground effects on sound propagation

7.1 Comparison with another FFP atmospheric sound propagation model.

In this section predictions of FFLAGS will be compared to those of another FFP atmospheric sound propagation model [62,65,64] known as the CERL FFP. This second FFP models the atmosphere as a set of of horizontal homogeneous fluid layers overlying an impedance surface, or a rigid porous halfspace. The boundary condition equations are solved to obtain the depth dependent Greens functions using a transmission line method. The ground impedance can be chosen from a variety of ground impedance models.

To compare the predictions of the CERL FFP and of FFLAGS, three systems, consisting of a specific ground surface under an atmosphere, have been considered. The ground surface has been modelled as a rigid-porous halfspace using the Rayleigh-Attenborough four parameter model for the CERL FFP and the equivalent rigid frame limit of the modified Biot-Stoll model for FFLAGS. The ground parameters were; flow resistivity 300000 mks rayls m^{-1}, porosity 0.3, grain shape factor 0.7, and pore shape factor ratio 0.5.

The first atmosphere is a homogeneous halfspace. The second atmo-

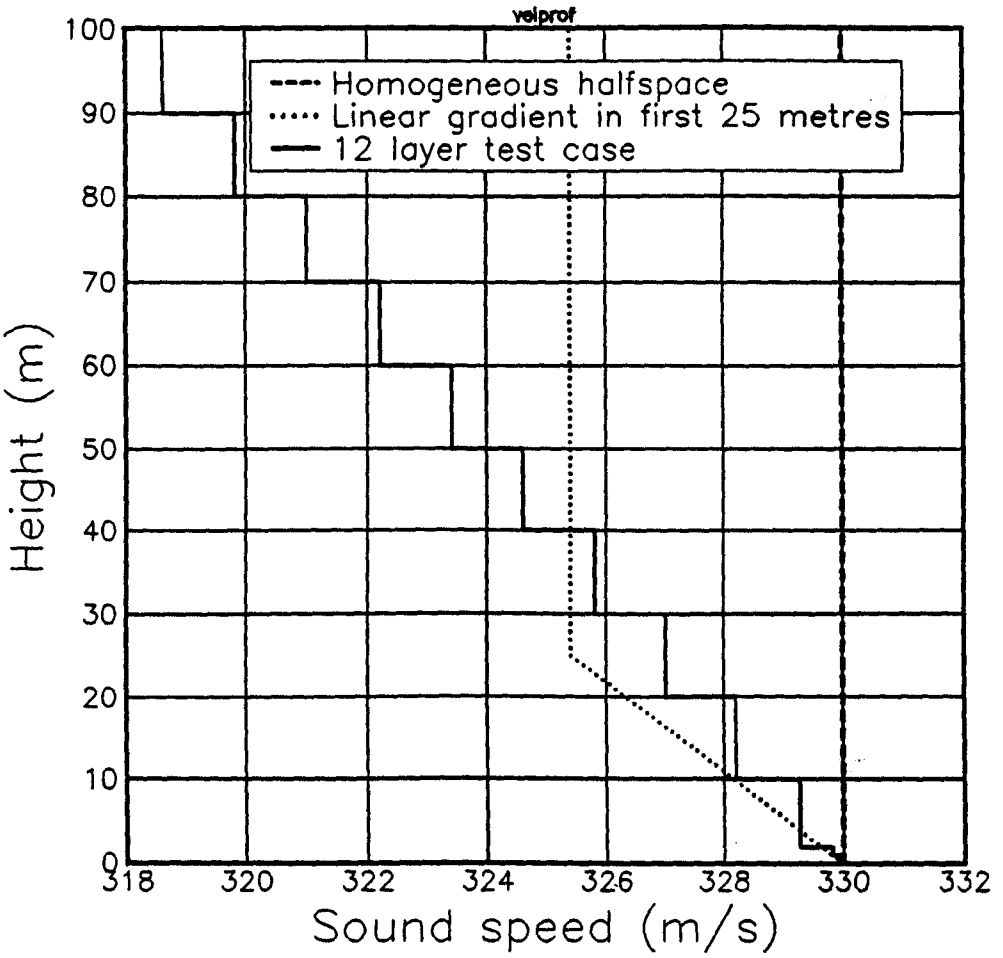

Figure 7.1 Velocity profiles used to compare CERL FFP and FFLAGS.

sphere is a linear upward refracting sound velocity gradient in the lower 25 metres, consisting of fifty homogeneous 0.5 metre layers, capped by a homogeneous halfspace. The third atmosphere is a twelve layer test which is an approximation to a linear gradient. The velocity profiles are shown in Figure 7.1 Both models produce predictions as a function of range at a given frequency. Two frequencies were chosen :100Hz and 1000Hz. The upper frequency has been determined by the desire to include the first interference dip for the chosen geometry.

Frequencies higher than 1kHz were not included because in reality tem-

perature gradients lead to turbulence which effects propagation at higher frequencies. The differences between the two models were expected to be largest when the effect of the ground is largest. This is because the CERL-FFP uses a ground modelled as an impedance surface, but the impedance is allowed to alter with horizontal wavenumber to allow for extended reaction. FFLAGS treats the ground by solving four boundary condition equations which include the the ground elasticity. This comparison therefore also checks whether the rigid frame limit of the FFLAGS ground model is in fact rigid. For this reason the source and receiver were sited close to the ground, at heights of 0.5 and 0.3 metres. These heights are also the source and receiver heights typically used for ground characterisation.

For the system of a halfspace under an homogeneous atmosphere the results are shown in Figures 7.2 to 7.5. The two FFP models produce nearly identical results. For the upward refracting atmosphere the two FFP models again agreed exactly until numerical problems appeared in the CERL FFP (see Figure 7.6).

The third atmosphere consisted of twelve fluid layers with sound velocity decreasing with height in steps of $0.6ms^{-1}$ every ten metres, and two one metre thick layers near to the ground surface. The comparison is shown in figure 7.7.

7.2 The effect of atmospheric sound velocity gradients on the influence of the ground in acoustic propagation

7.2.1 Comparison between predicted excess attenuation using non-porous and porous ground models at low frequency.

A Gudesen [3] used the SAFARI program to model sound propagation in the atmosphere for source and receiver heights of 2.0 metres. He compared the predictions of the CERL-FFP to those of SAFARI for measured atmo-

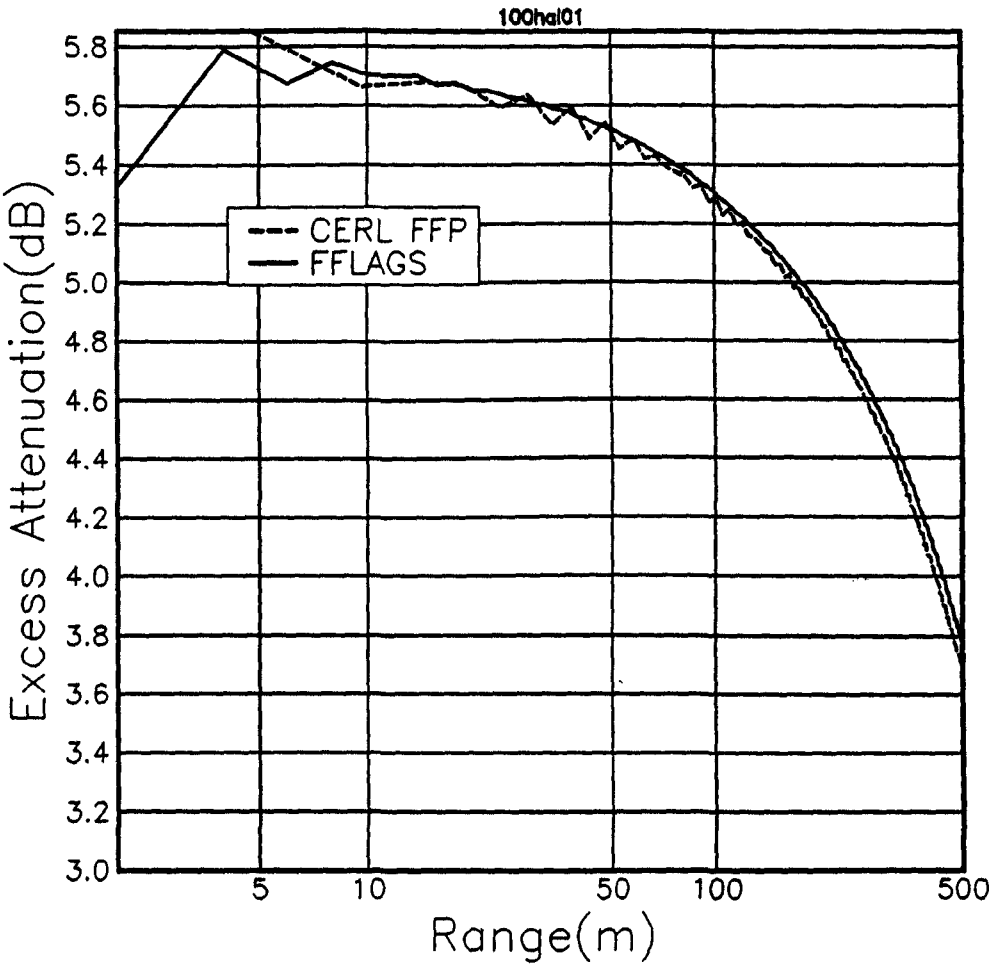

Figure 7.2 Predicted excess attenuation at a frequency of 100Hz as a function of range for a near locally reacting ground surface(σ 300000, Ω 0.3, n' 0.7, s_p 0.5). FFLAGS and CERL FFP.

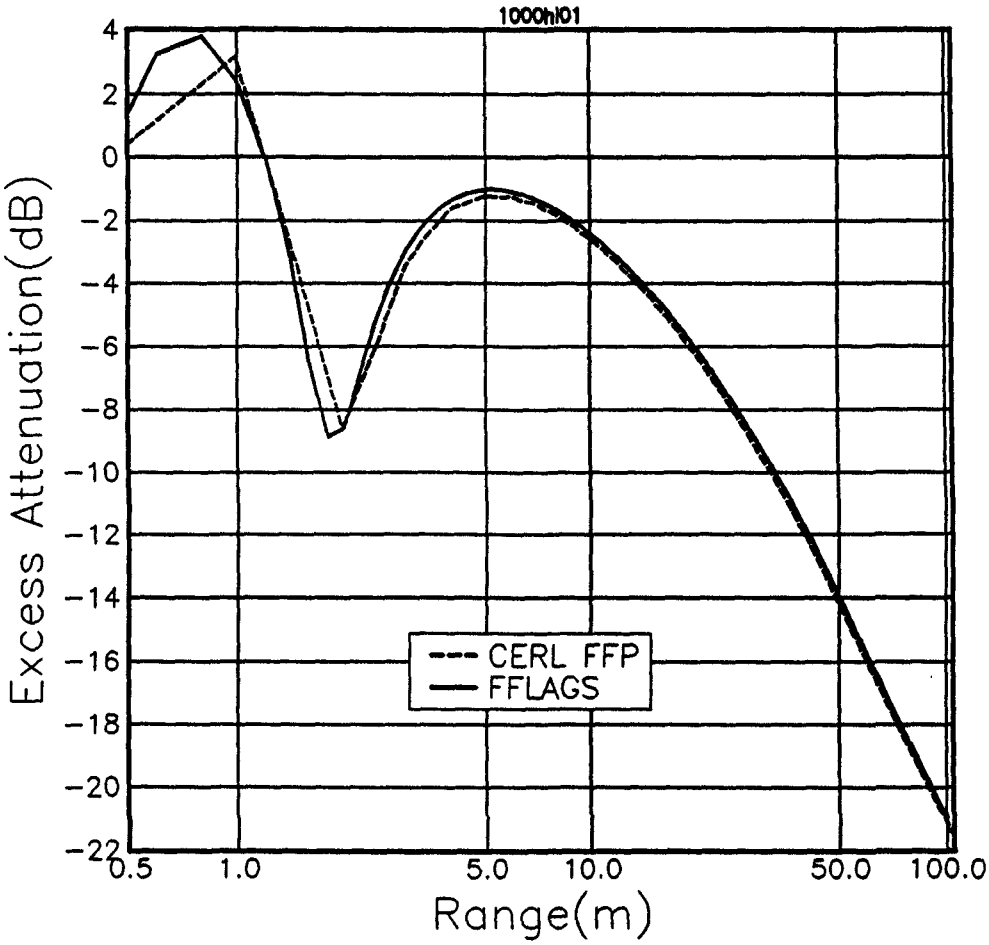

Figure 7.3 Predicted excess attenuation at a frequency of 1000Hz as a function of range for a near locally reacting ground surface(σ 300000, Ω 0.3, n' 0.7, s_p 0.5). FFLAGS and CERL FFP.

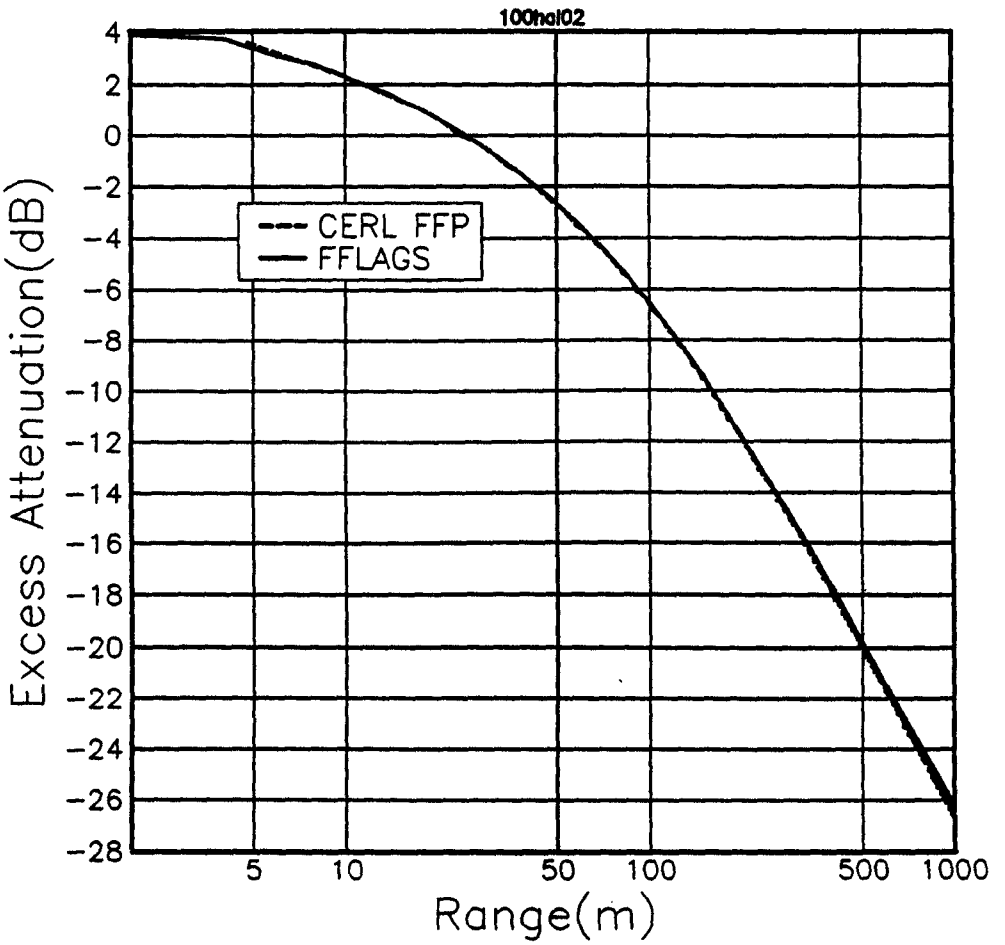

Figure 7.4 Predicted excess attenuation at a frequency of 100Hz as a function of range for an extended reaction ground surface(σ 10000, Ω 0.3, n' 0.7, s_p 0.5). FFLAGS and CERL FFP.

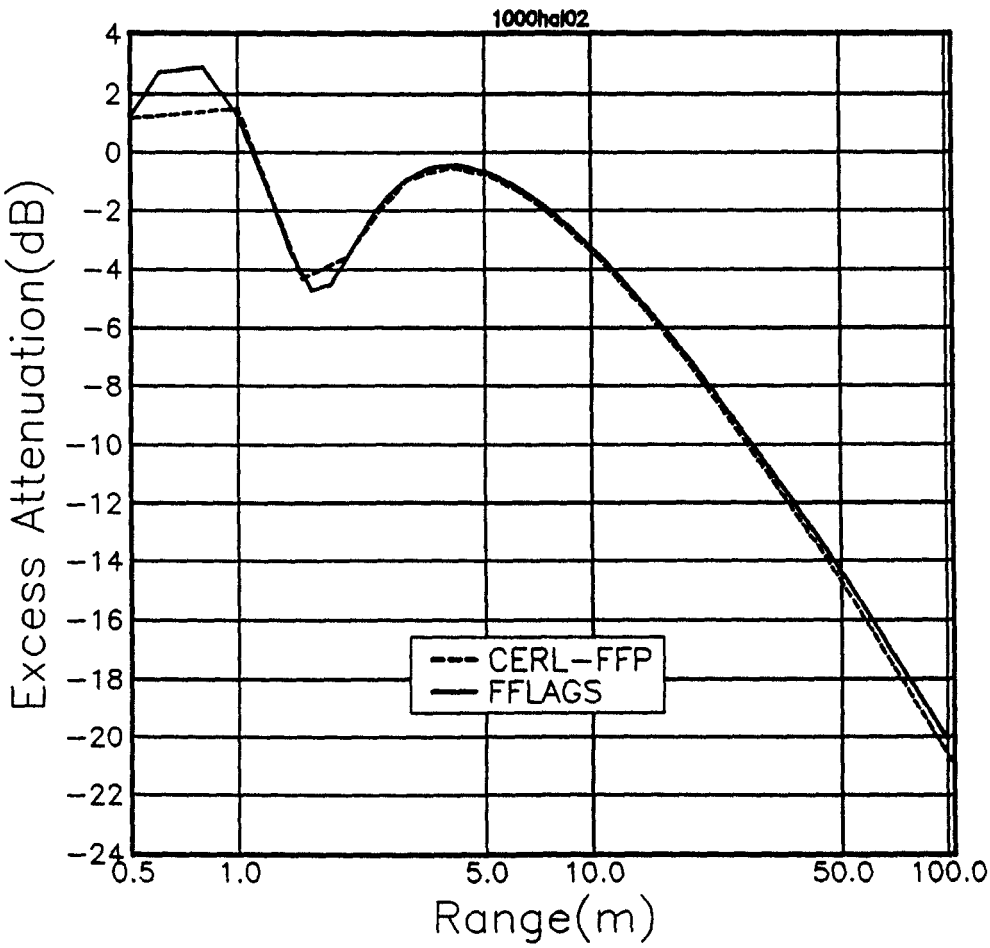

Figure 7.5 Predicted excess attenuation at a frequency of 100Hz as a function of range for an extended reaction ground surface(σ 10000, Ω 0.3, n' 0.7, s_p 0.5). FFLAGS and CERL FFP.

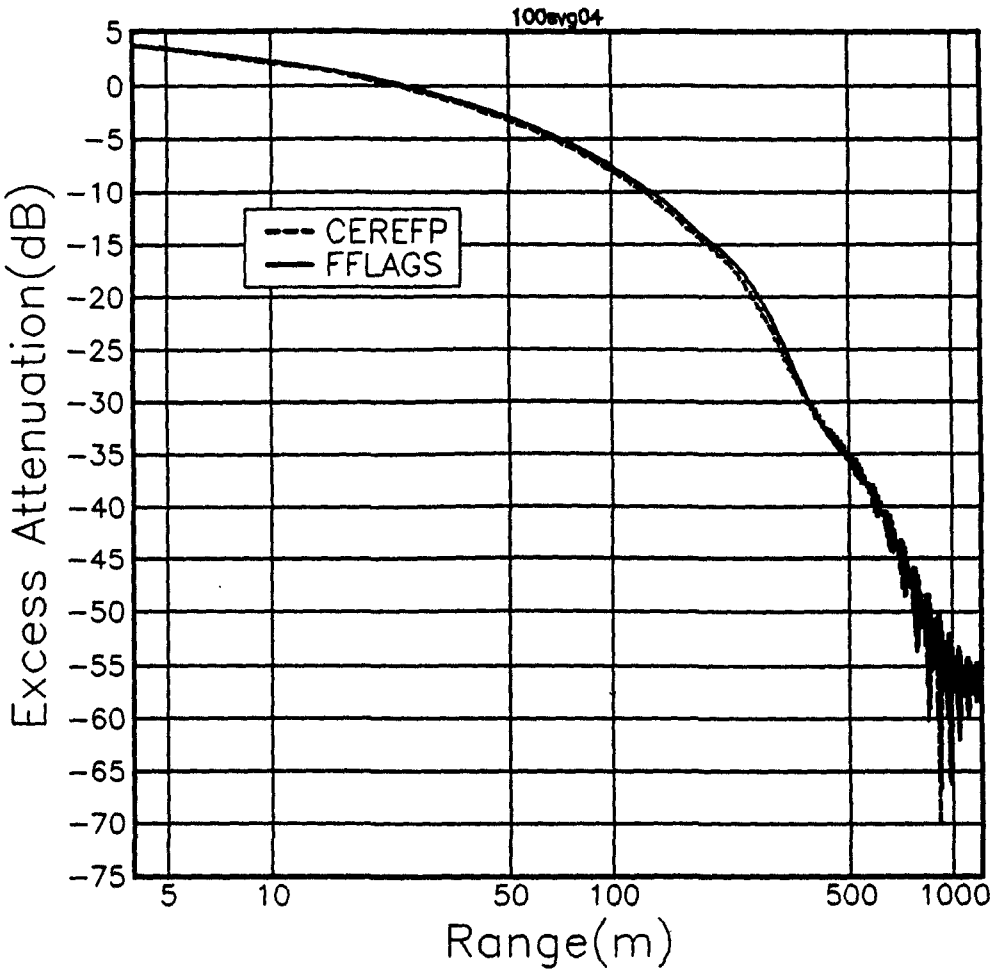

Figure 7.6 Predicted excess attenuation over a near locally reacting surface in and upwardly refracting atmosphere, as a function of range at 100Hz. FFLAGS and CERL-FFP.dc/dz=0.165

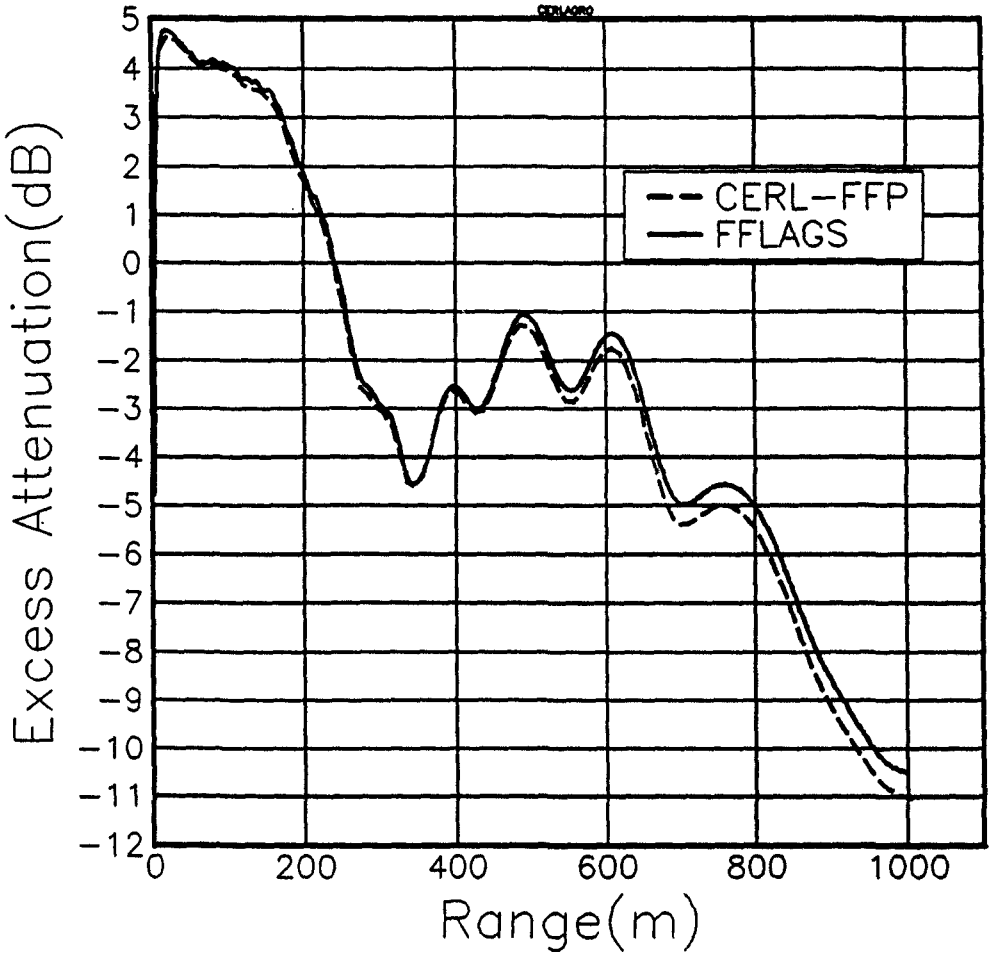

Figure 7.7 Comparison of CERL FFP and FFLAGS for twelve air layer test case over rigid-porous near locally reacting ground surface.

spheric and ground data. He found good agreement between them. The ground data which is used by Gudesen for input to the CERL-FFP is unusual in that the measured flow resistivity of the soil is unusually high. With this flow resistivity the ground surface would appear acoustically as a hard boundary at most frequencies. Also the frequency which is chosen for the comparisons is 20Hz. At this frequency most ground surfaces would act as a hard boundary. Gudesen states that the ground will act as a hard boundary at frequencies up to 200Hz, and hence that SAFARI will be a useful tool up to this frequency. Figure 7.8 shows the predicted excess attenuation using FFLAGS at 100Hz for (i) no pore structure but an elastic frame, (ii) for a rigid pore structure, and (iii) for an elastic frame with a pore structure. In each case the ground parameters used correspond to a measured ground structure [5](the parameters are shown in table 7.1). The atmosphere is an homogeneous halfspace. This shows that if the pore structure is not included then the ground will behave as an acoustically hard surface. The difference between predictions with and without porosity is 4dB at 1km. Figure 7.9 shows that for a frequency of 50Hz the effect of the pore structure is indeed small (i.e. 1dB at 1km). At higher frequencies (e.g. 1kHz) Figure 7.10 shows that the porous ground structure must be included in order to predict sound pressure levels.

Gudesen made the comparison between SAFARI and the CERL FFP in a model atmosphere based on measured meteorological data. That atmosphere included a downwardly refracting sound velocity gradient near to the ground. Using the same ground structure as that assumed in Figure 7.8 and a linear downwardly refracting sound velocity gradient of 0.165 s^{-1}, at 100Hz the effect of the pore structure of the ground is enhanced. The difference between the porous and non-porous ground models then becomes larger (i.e. $\approx$14dB at 1km) (see Figure 7.11). At 50Hz the difference between the predicted excess attenuation using porous and non-porous ground models is also increased by the influence of the same sound velocity gradient (see Figure 7.12). Figures 7.14 and 7.15 show the predicted excess attenuation at 100Hz and 50Hz respectively in an atmosphere consisting of a logarithmic

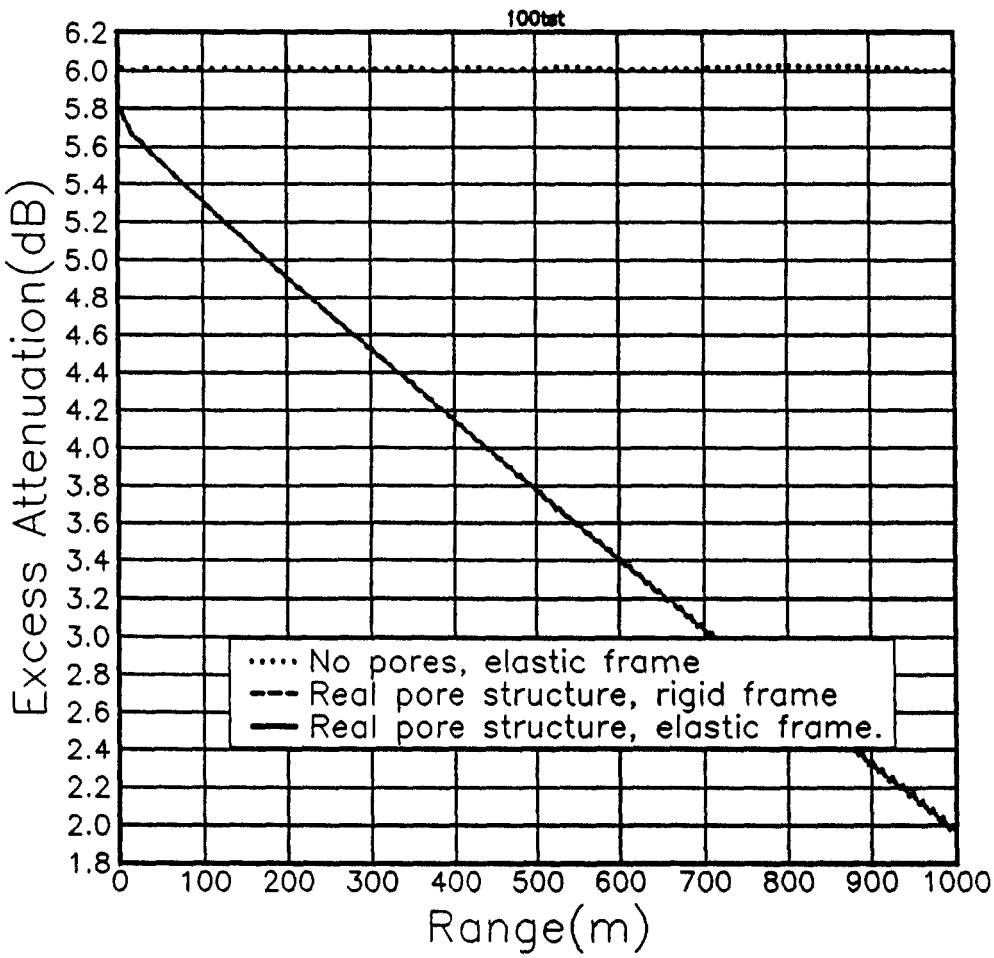

Figure 7.8 Predicted excess attenuation at 100Hz for three different ground models.

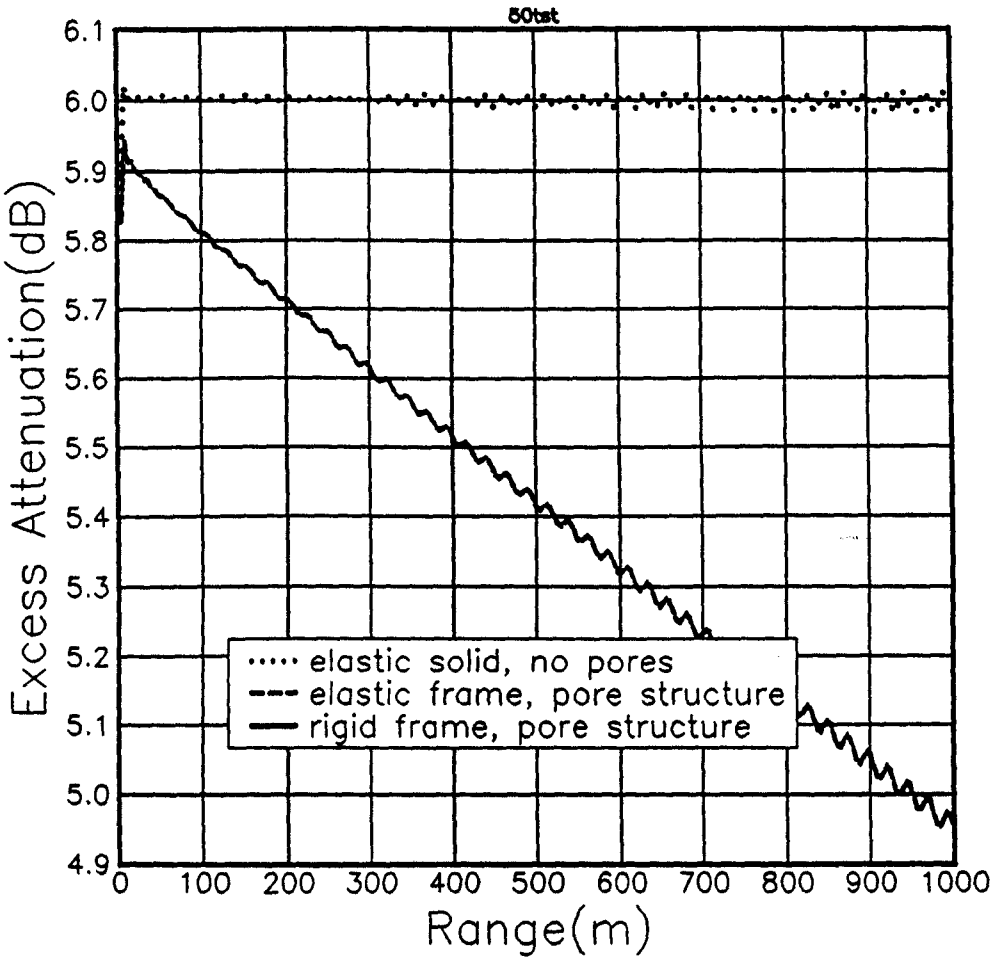

Figure 7.9 Predicted excess attenuation at 50Hz for three different ground models.

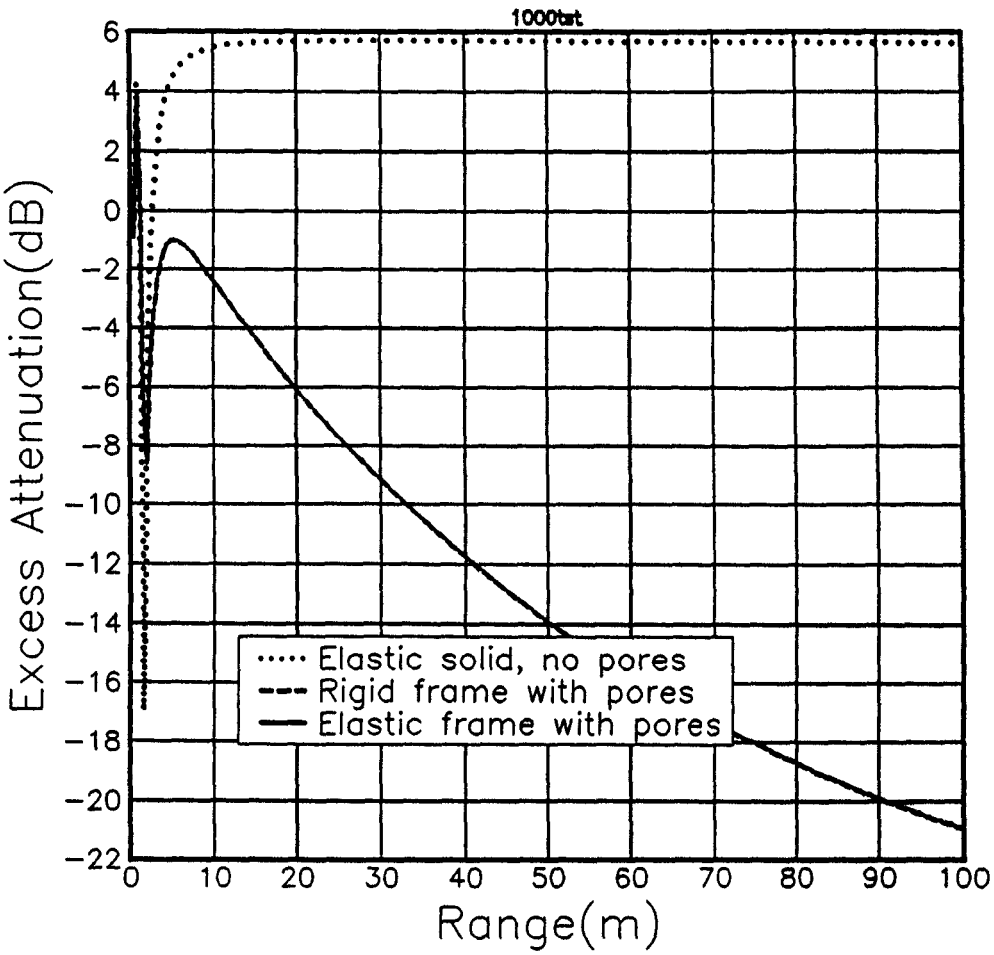

Figure 7.10 Predicted excess attenuation at 1000Hz for three different ground models.

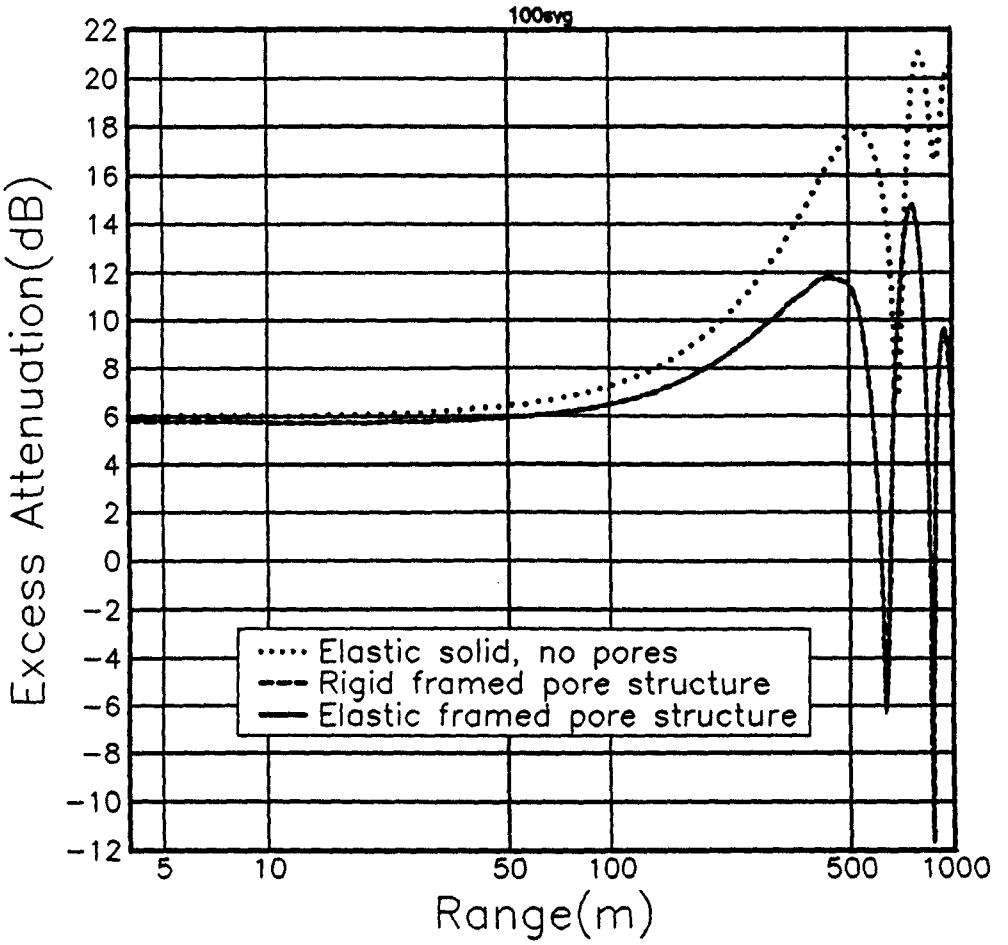

Figure 7.11 Predicted excess attenuation at 100Hz for porous and non porous ground models in the presence of a downwardly refracting linear sound velocity gradient.

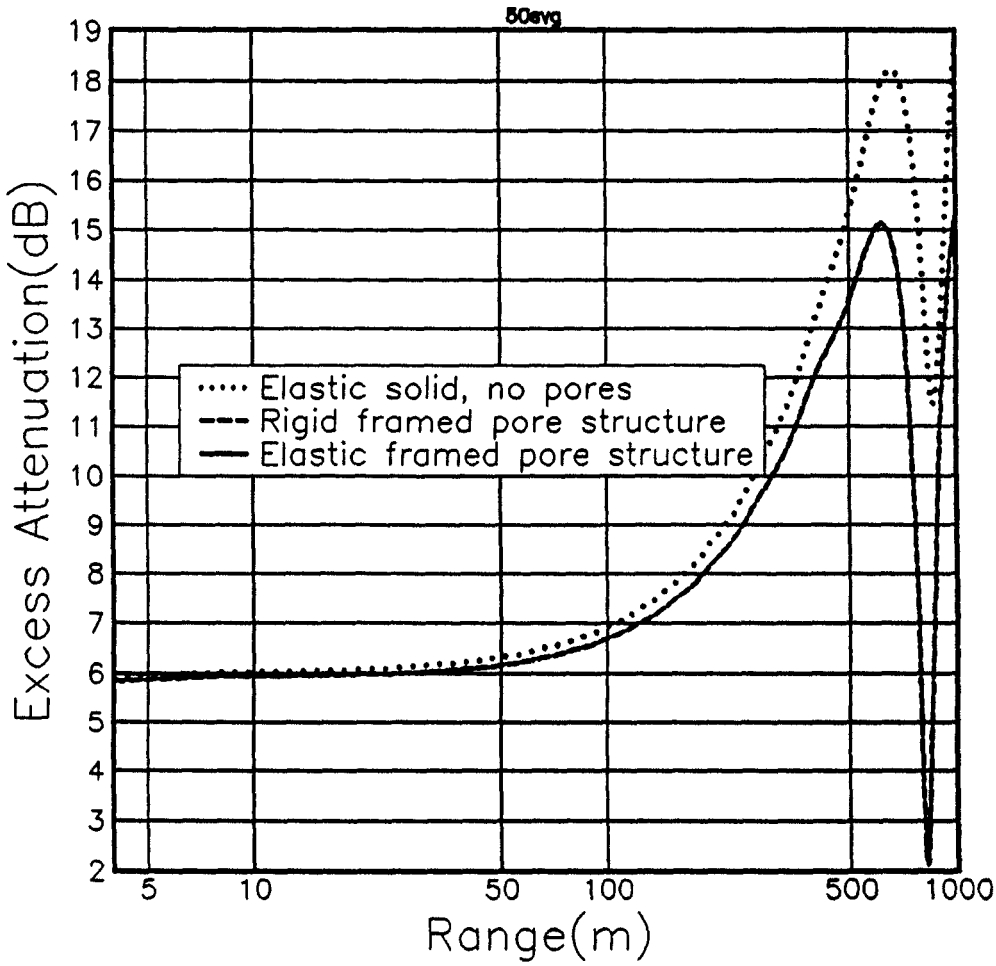

Figure 7.12 Predicted excess attenuation at 50Hz for porous and non porous ground models in the presence of a downwardly refracting linear sound velocity gradient.

Table 7.1 Ground parameters measured at Wezep, Netherlands

Parameter	Unit	Value
Flow resistivity (σ)	MKS $rayls m^{-1}$	366000
Porosity (Ω)	-	0.27
pore shape factor ratio (s_p)	-	0.5
grain shape factor (n')	-	0.5
upper p velocity	ms^{-1}	270.0
upper s velocity	ms^{-1}	190.0
$\Im(v)/\Re(v) =$	-	0.05
lower p velocity	ms^{-1}	500.0
lower s velocity	ms^{-1}	330.0
solid bulk modulus	Nm^{-2}	$4.6.10^{11}$
upper layer thickness	m	2.0
bulk density ρ_b	kg m^{-3}	1700.

sound velocity gradient near the ground, for a ground surface that corresponds to the parameters in table 7.1, and for a non-porous ground surface. The atmosphere is calculated using Monin-Obhulkov similarity theory and its velocity profile is given in Figure 7.13. The profile is intended to represent conditions on a cloudy night with some wind over a grassland. The profile is modelled using 50 0.8 metre thick atmospheric layers. This gives a maximum profile height of 40.0 metres capped by a halfspace. The propagation is downwind. The layer thickness and maximum profile height were repeatedly altered to check the convergence on a stable solution equivalent to that in an infinitely high profile.

In conclusion, this section has shown that the accuracy of predictions of propagation close to the ground made using non-porous ground models at low frequency is dependent on both the ground surface, the frequency and the atmospheric conditions. In downward refracting sound velocity gradients the frequency at which accurate results can be obtained using a non-porous ground model is reduced compared to results in an homogeneous atmosphere. It cannot be assumed that rigid-non-porous ground models will give accurate results at frequencies up to 200Hz.

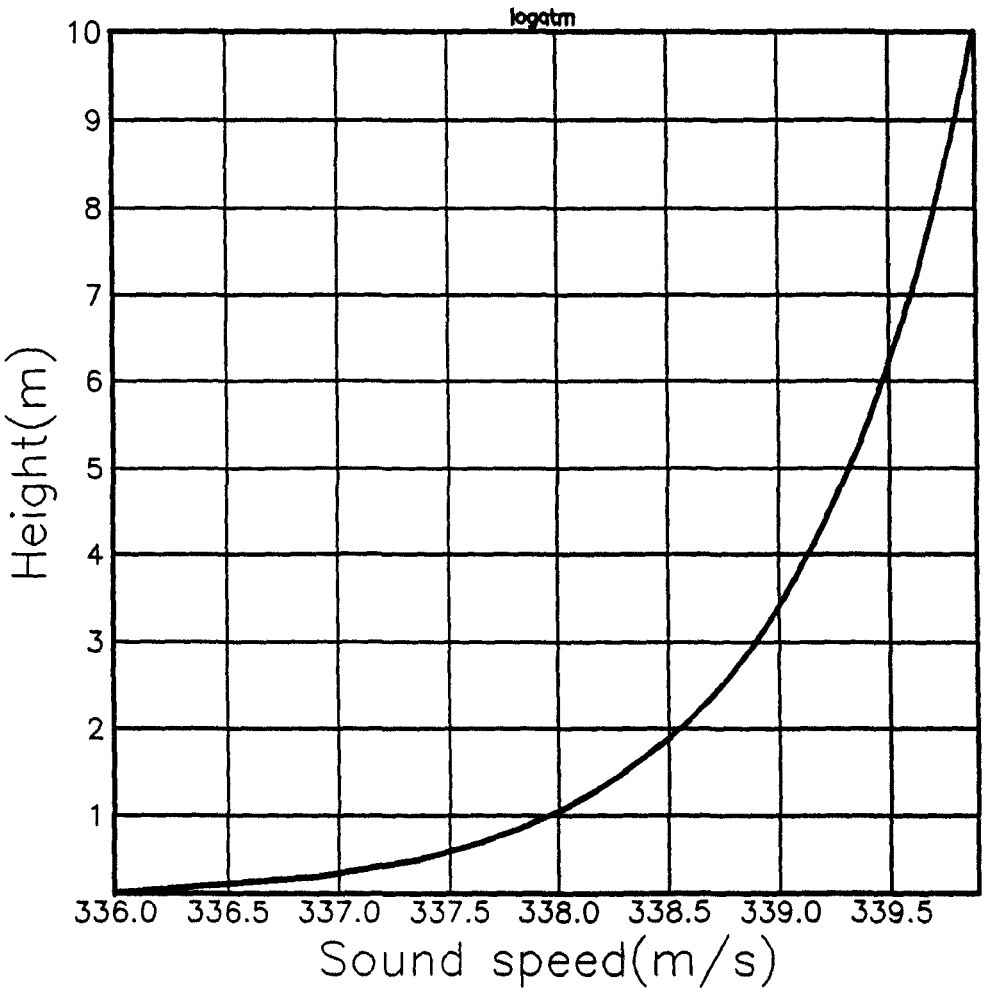

Figure 7.13 Sound velocity profile representing conditions on a cloudy night with some wind. Propagation is downwind.

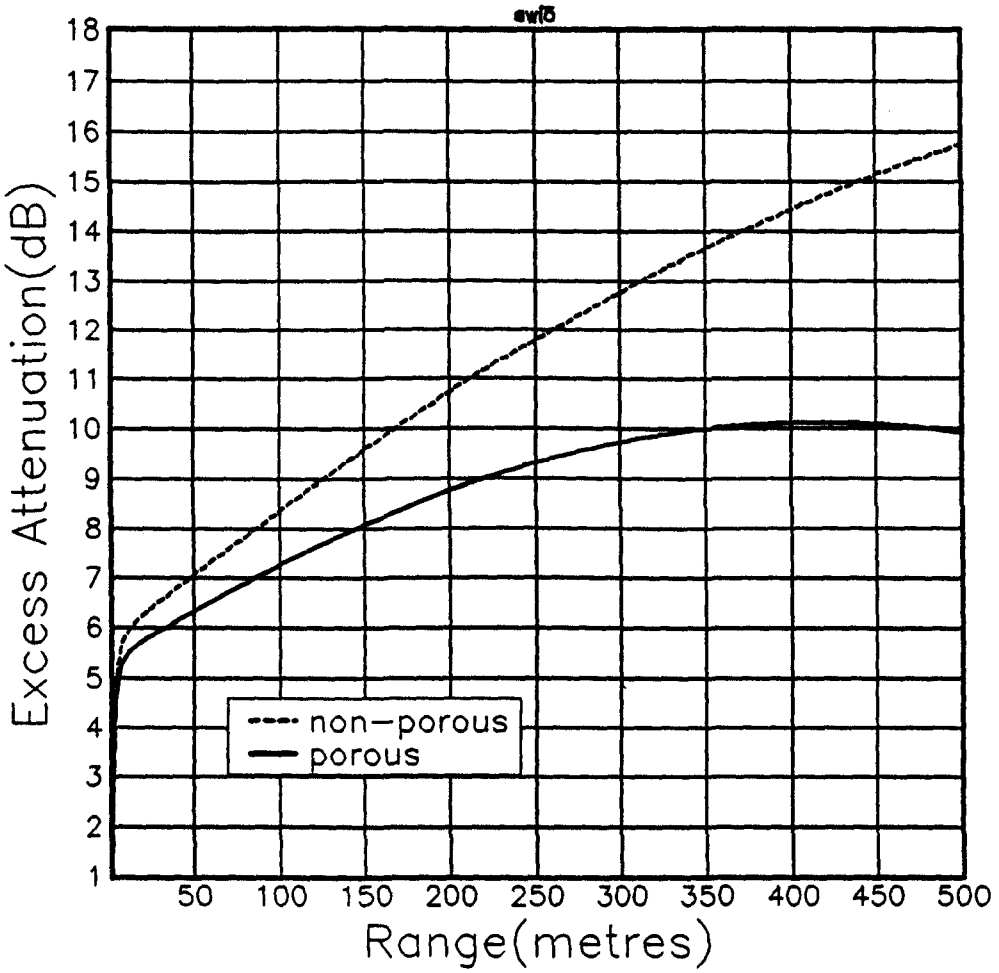

Figure 7.14 Predicted excess attenuation for source and receiver heights of one metre, at a frequency of 100Hz, in the velocity profile given in Figure 7.13, for porous, and non-porous ground models.

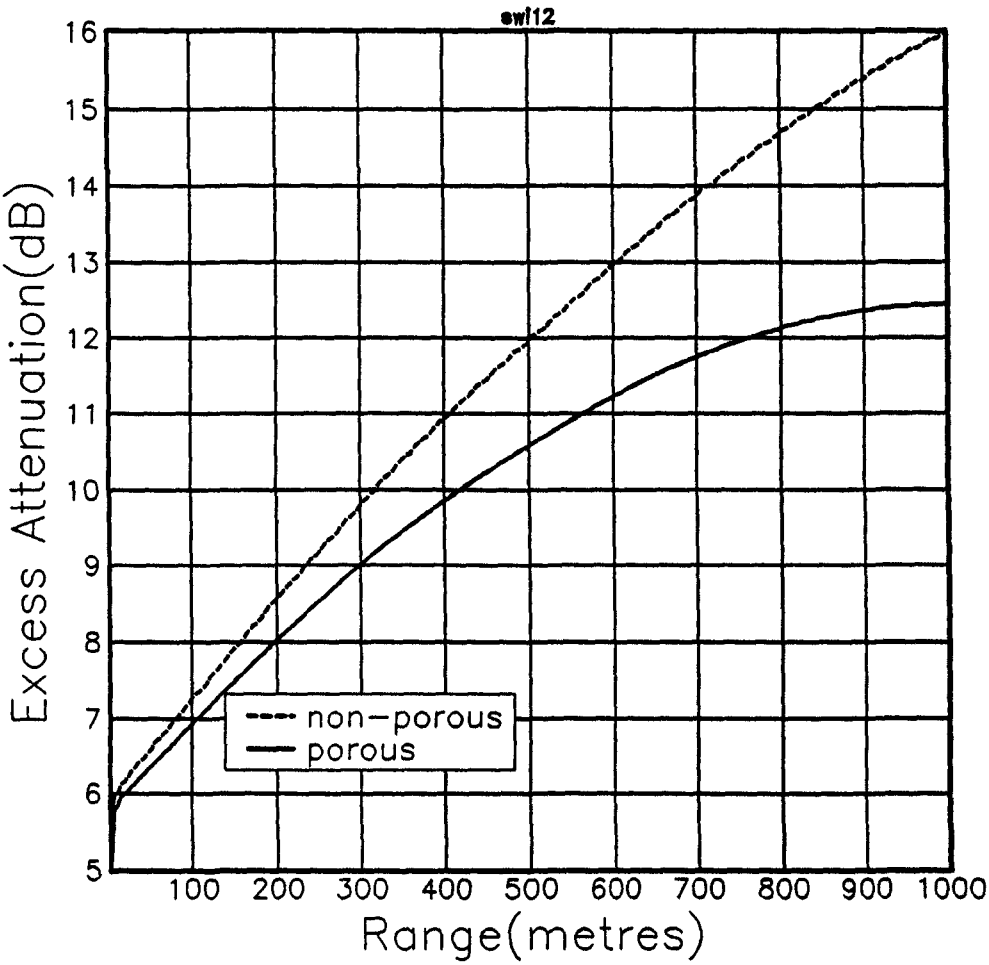

Figure 7.15 Predicted excess attenuation for source and receiver heights of one metre, at a frequency of 50Hz, in the velocity profile given in Figure 7.13, for porous, and non-porous ground models.

7.2.2 The sensitivity of excess attenuation to the flow resistivity of the ground in a linear sound velocity gradient.

It has been shown in the previous section that for propagation in various atmospheric sound velocity gradients the difference between the predictions of excess attenuation from models with and without a porous ground surface was measurable even at low frequencies. In this section the sensitivity of the predicted excess attenuation to different ground flow resistivities will be examined. The ground model chosen was a rigid porous halfspace with porosity 0.3, grain shape factor 0.5, and pore shape factor ratio 0.5. The flow resistivity has been varied between 30000 mks raylsm^{-1} and 1000000 mks raylsm^{-1}. The predictions have been made as a function of range at 200Hz and as a function of frequency (between 100 and 500Hz) at 165 metres range. Five atmospheric conditions have been considered. These are; an upward refracting linear sound velocity gradient of 0.165 s^{-1}, an upward refracting linear sound velocity gradient of 1.65 s^{-1}, a homogeneous atmosphere, a downward refracting linear sound velocity gradient of 0.165s^{-1}, and a downward refracting linear sound velocity gradient of 1.65s^{-1}. The source and receiver heights have been set to one metre. Three of the four sound velocity gradients have been represented by 50 layers of thickness 0.2 metres, giving a cap height to the gradient of 10.0 metres. This layering system has been found to give stable results by varying the cap height and layer thickness in the way described in section 7.2.3. The downward refracting sound velocity gradient of 1.65 s^{-1} did not produce stable results using the above layering system. Stable results have been obtained for a cap height of twenty metres, and layer thickness of 0.4 metres. The layer thicknesses and cap heights are consistent with the suggestions of Franke, Raspet, and Liu [93] that the cap height should be much greater than the creeping wave height, and the layer thickness should be less than the wavelength in an upward refracting gradient. In the downward refracting gradient it has been found that the cap height required is much greater than the highest eigenray height.

Figures 7.16, 7.17, 7.19,7.18 and 7.20 show the predicted excess attenuation as a function of range at 200Hz for homogeneous, two upward refracting, and two downward refracting linear sound velocity gradients respectively. In the two smaller sound velocity gradients the sensitivity of the predicted excess attenuation to the ground flow resistivity is only slightly dependent on the sound velocity gradient. Taking a range of 150 metres, the difference between the predicted excess attenuation at the lowest flow resistivity (30000 mks raylsm^{-1}) and the highest flow resistivity (10^6 mks rayls m^{-1}) is 18.5 dB in the homogeneous atmosphere, 18.0dB in the upward refracting gradient, and 17.8dB in the downward refracting gradient. For the two larger gradients (figures 7.19 and 7.20) the sensitivity of the excess attenuation to the ground flow resistivity is much more dependent on the gradient. Because excess attenuation in the downward refracting atmosphere (figure 7.20) does not change monotonically with range it is difficult to draw general conclusions. However the predicted excess attenuation in the downward refracting case appears to be more sensitive to the ground flow resistivity than in the upward refracting case(Figure 7.19), but giving measurable differences in all cases between the predictions over a ground of flow resistivity 10^5 mks rayls m^{-1} and over a ground flow resistivity of 10^6 mks rayls m^{-1}. This is in agreement with the findings of the previous section. However at a frequency of 50Hz West et al predicted that the sensitivity to the ground flow would be negligible in a strongly upward refracting sound velocity gradient of $1.65s^{-1}$ [94].

Figures 7.21, 7.22,7.24, 7.23 and 7.25 show the predicted excess attenuation as a function of frequency at a range of 165 metres in an homogeneous, two upward refracting upward refracting, and two downward refracting sound velocity gradients. These five figures show that the influence of the ground flow resistivity on the excess attenuation increases as the frequency is increased. They also show that in this frequency range the sensitivity of the excess attenuation to the flow resistivity is not very dependent on the sound velocity gradient for the smaller velocity gradients.

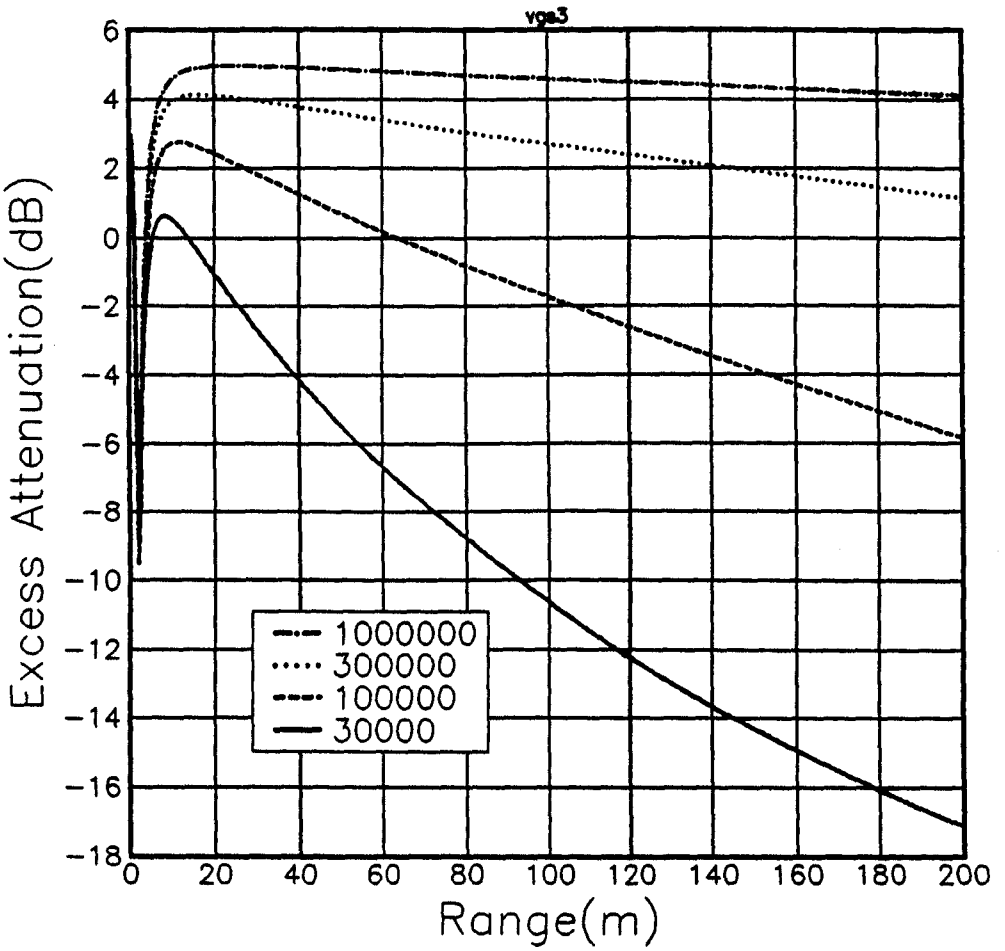

Figure 7.16 Predicted excess attenuation as a function of range at 200Hz in an homogeneous atmosphere for four different ground flow resistivities.

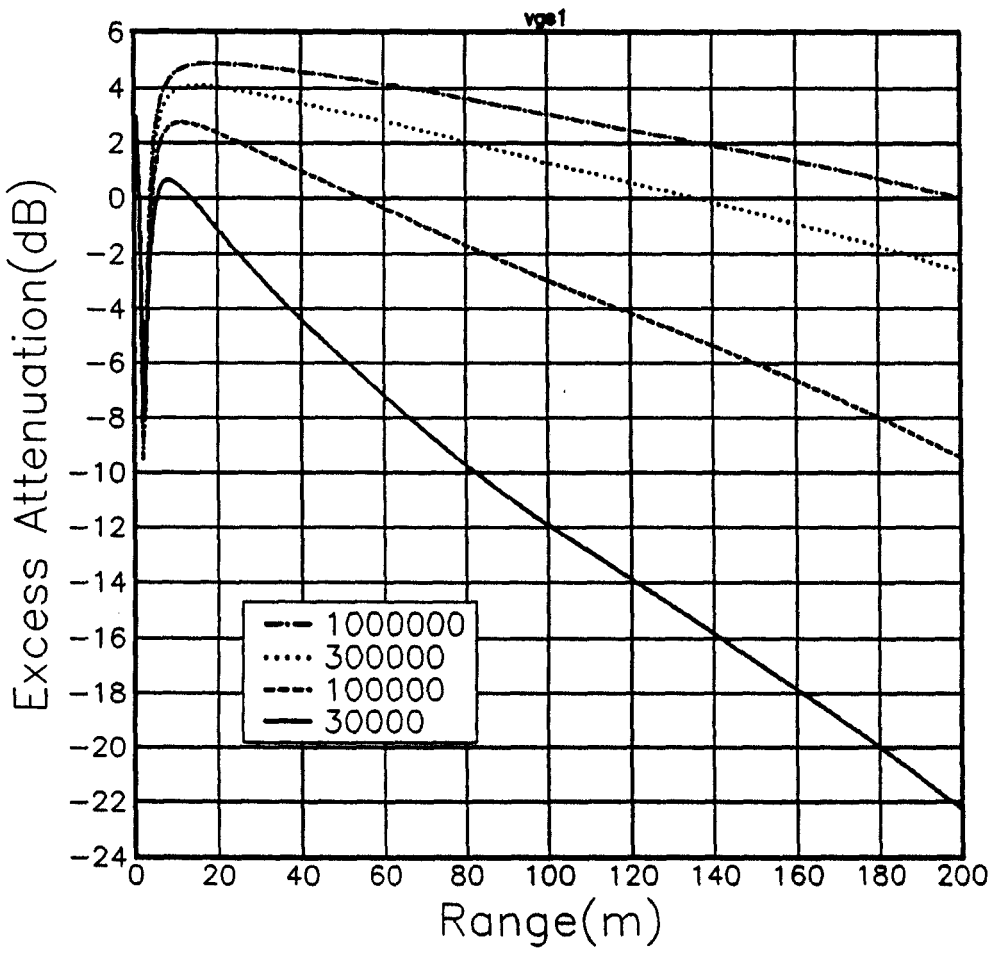

Figure 7.17 Predicted excess attenuation as a function of range at 200Hz in an upward refracting linear sound velocity gradient of $0.165s^{-1}$ for four different ground flow resistivities..

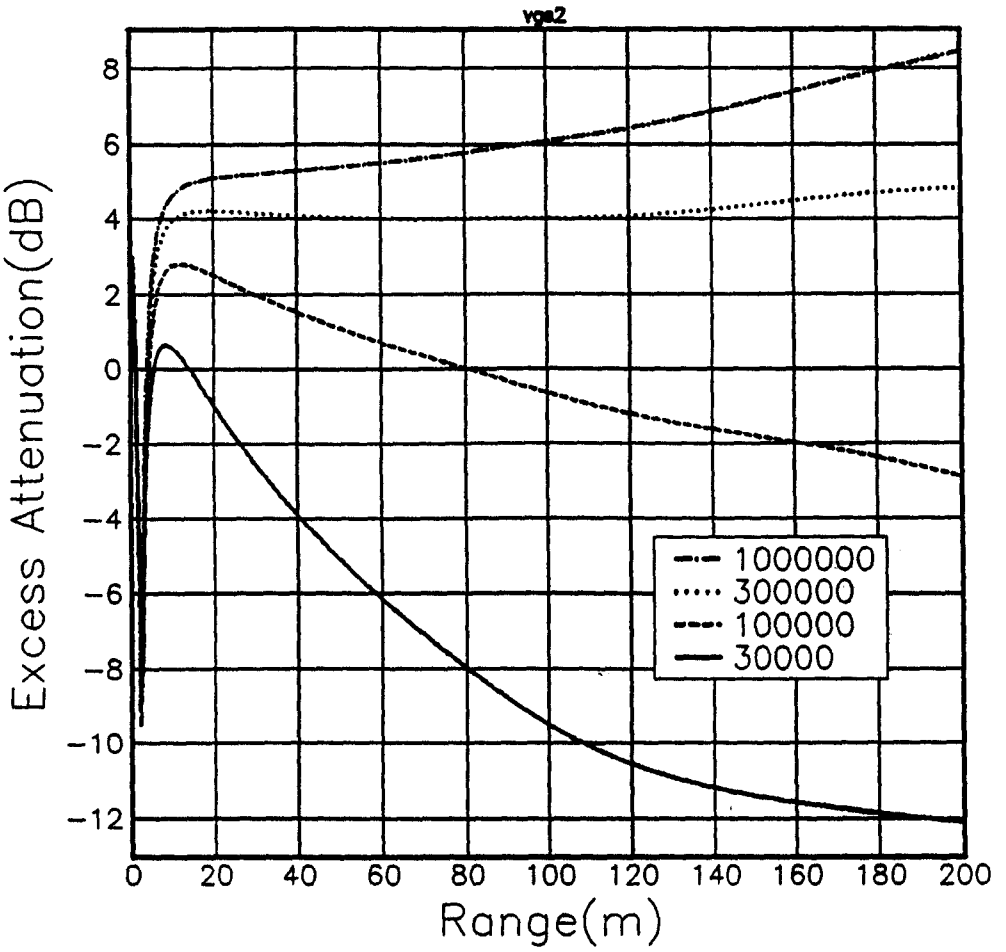

Figure 7.18 Predicted excess attenuation as a function of range at 200Hz in a downward refracting sound velocity gradient of $0.165s^{-1}$ for four different ground flow resistivities..

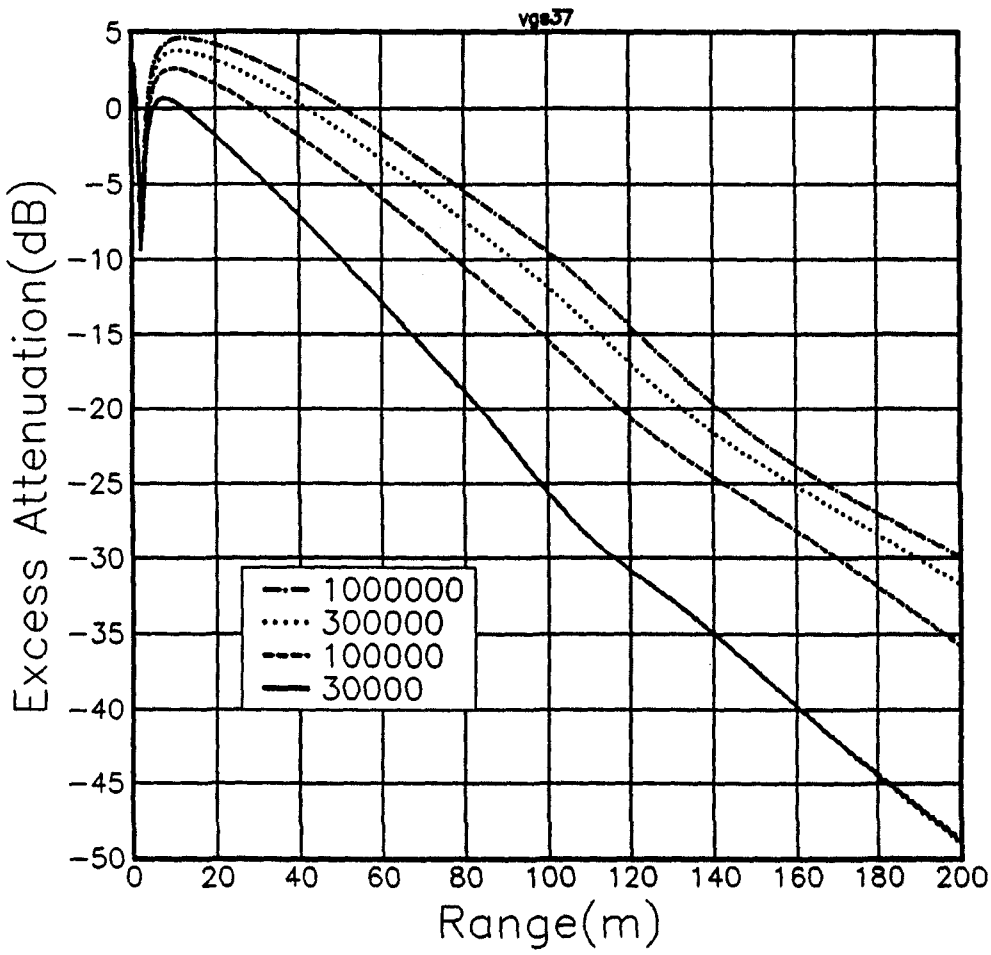

Figure 7.19 Predicted excess attenuation as a function of range at 200Hz in an upward refracting linear sound velocity gradient of $1.65s^{-1}$ for four different ground flow resistivities..

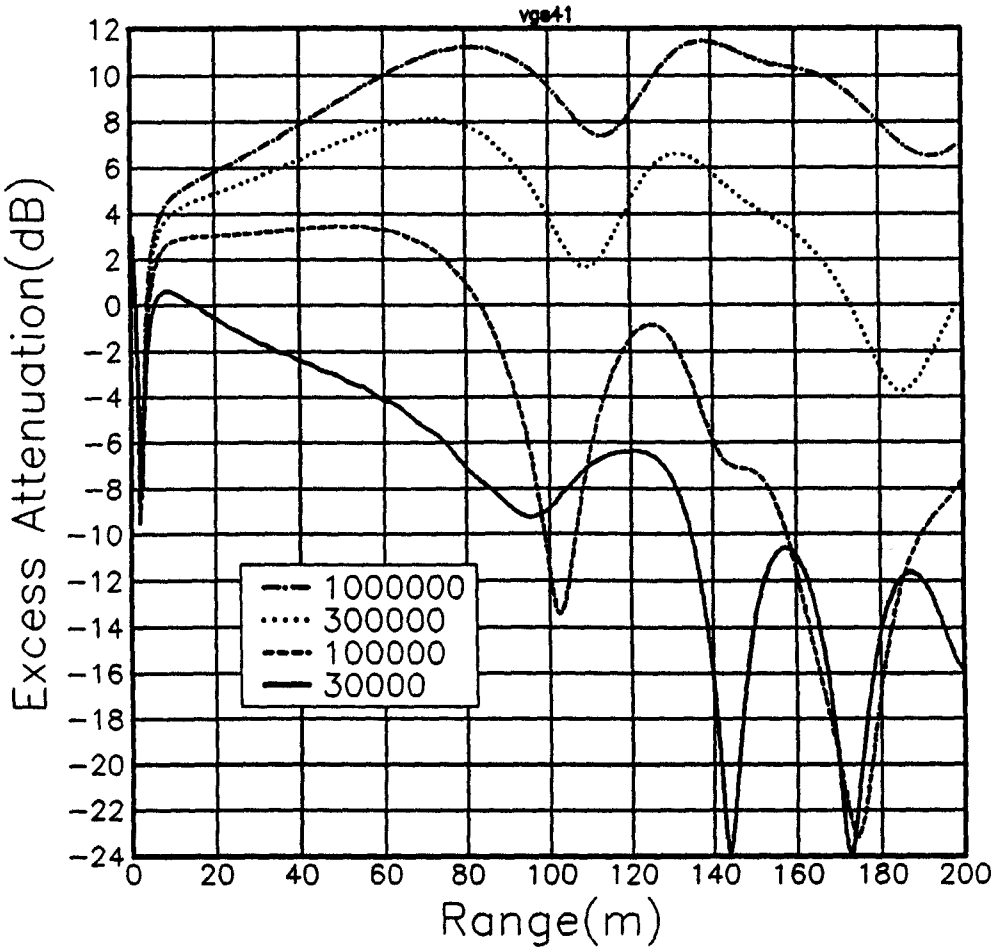

Figure 7.20 Predicted excess attenuation as a function of range at 200Hz in a downward refracting sound velocity gradient of $1.65s^{-1}$ for four different ground flow resistivities..

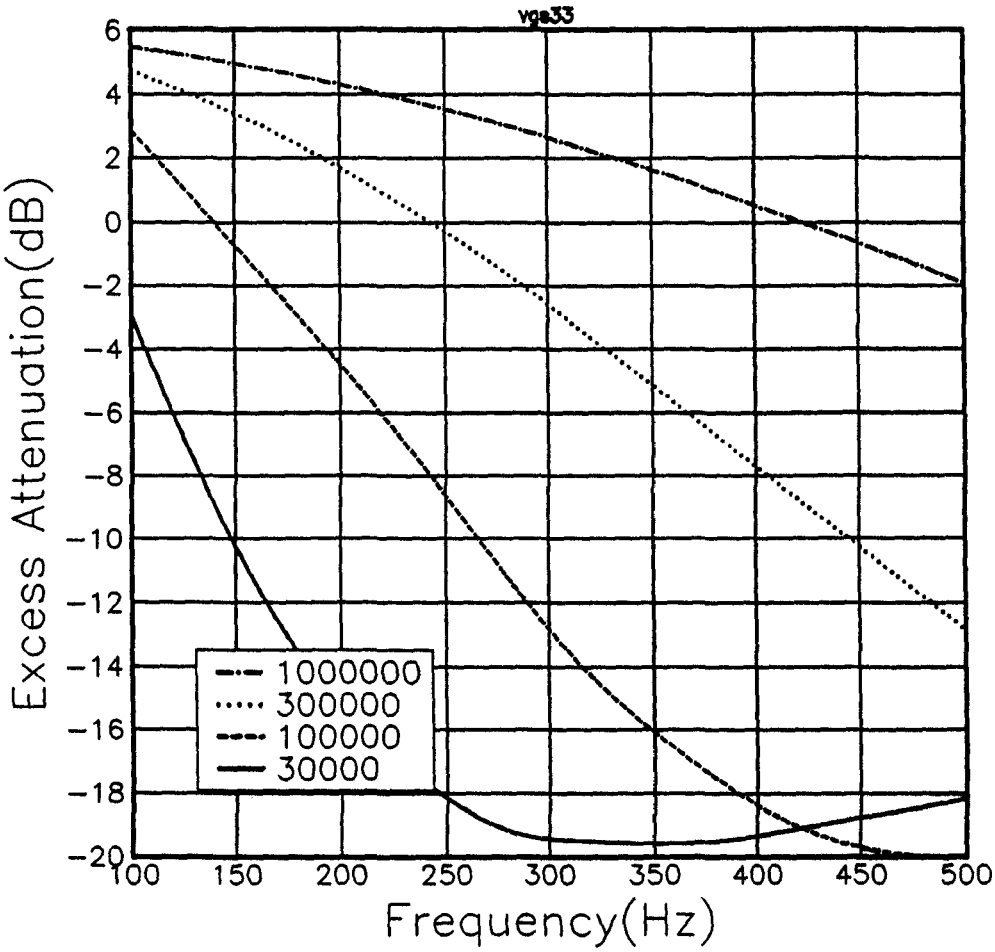

Figure 7.21 Predicted excess attenuation as a function of frequency in an homogeneous atmosphere at a range of 165 metres for four different ground flow resistivities

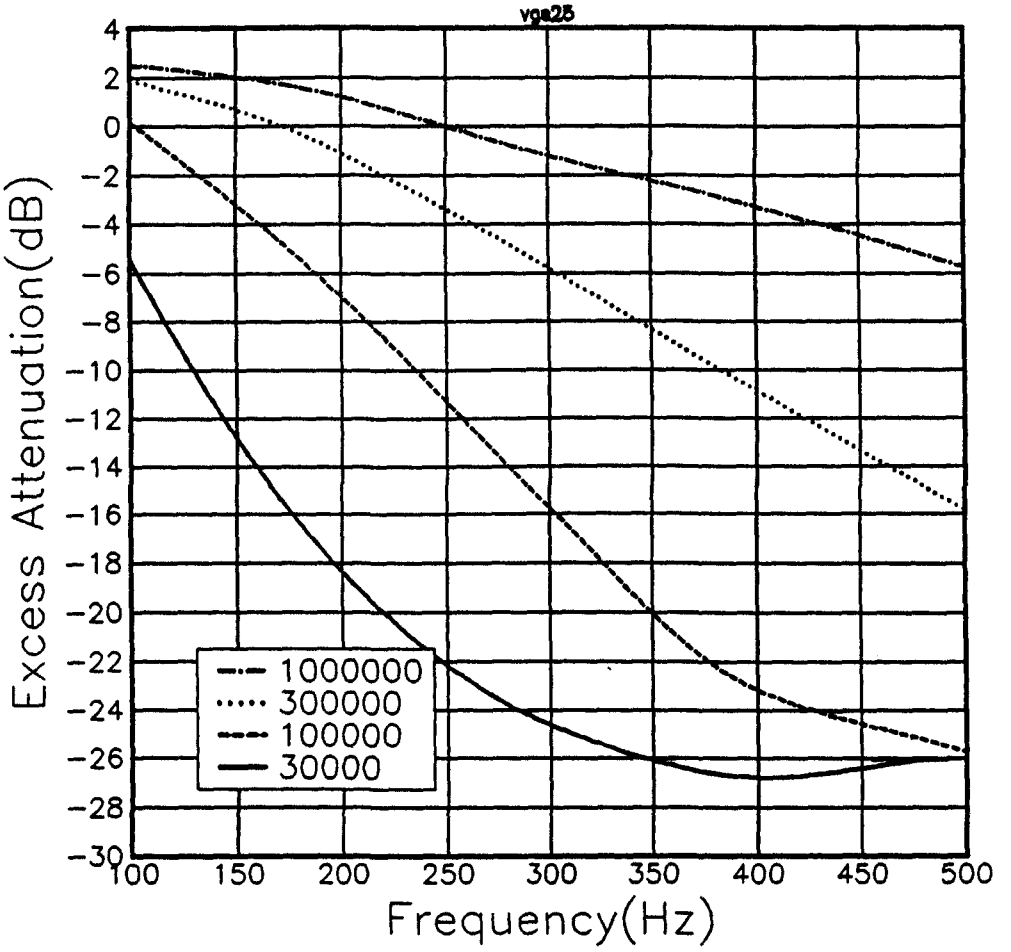

Figure 7.22 Predicted excess attenuation as a function of frequency in a linear upward refracting sound velocity gradient atmosphere with gradient $0.165s^{-1}$ for four different ground flow resistivities

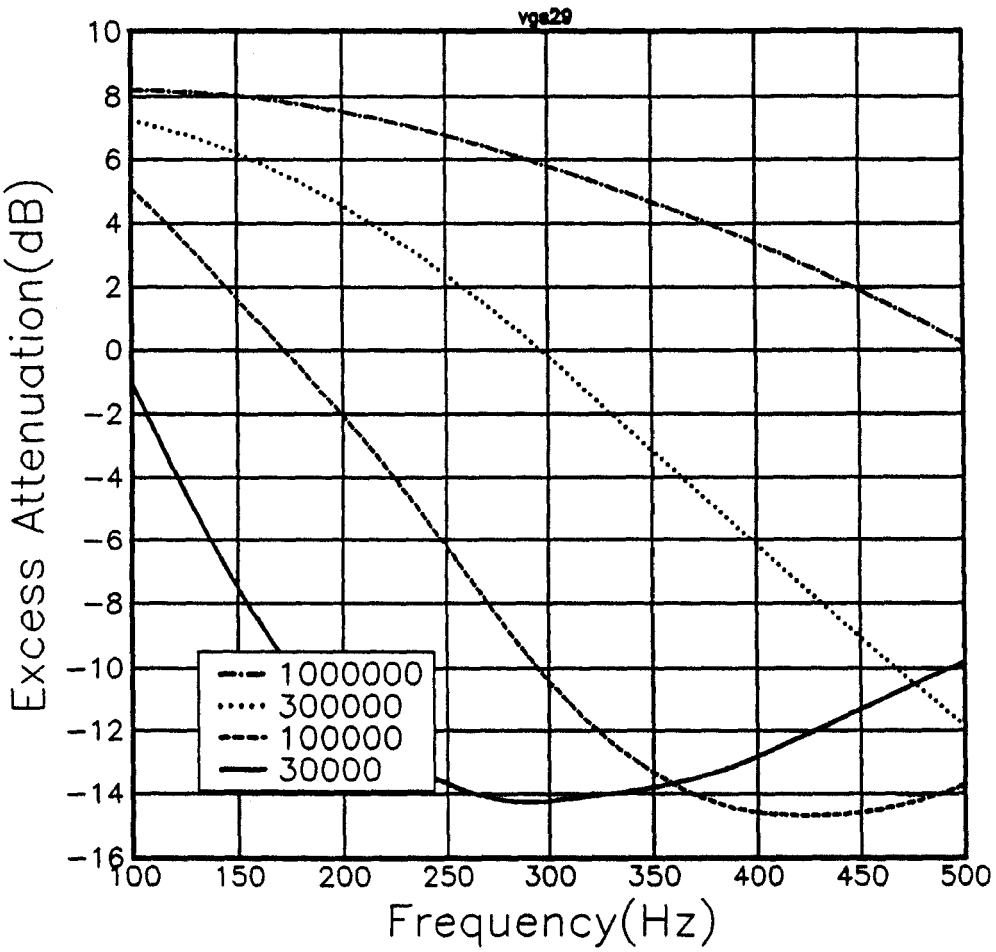

Figure 7.23 Predicted excess attenuation as a function of frequency in a linear downward refracting sound velocity gradient atmosphere with gradient $0.165s^{-1}$ for four different ground flow resistivities.

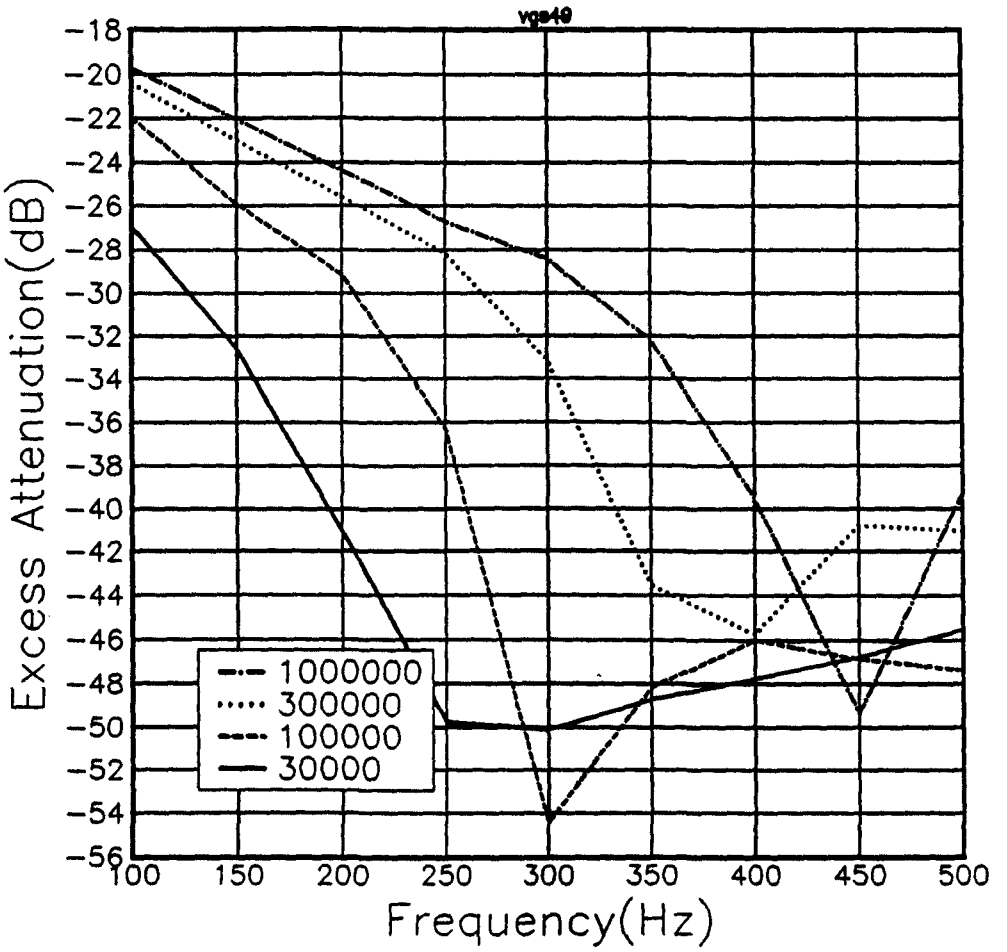

Figure 7.24 Predicted excess attenuation as a function of frequency in a linear upward refracting sound velocity gradient atmosphere with gradient $1.65s^{-1}$ for four different ground flow resistivities.

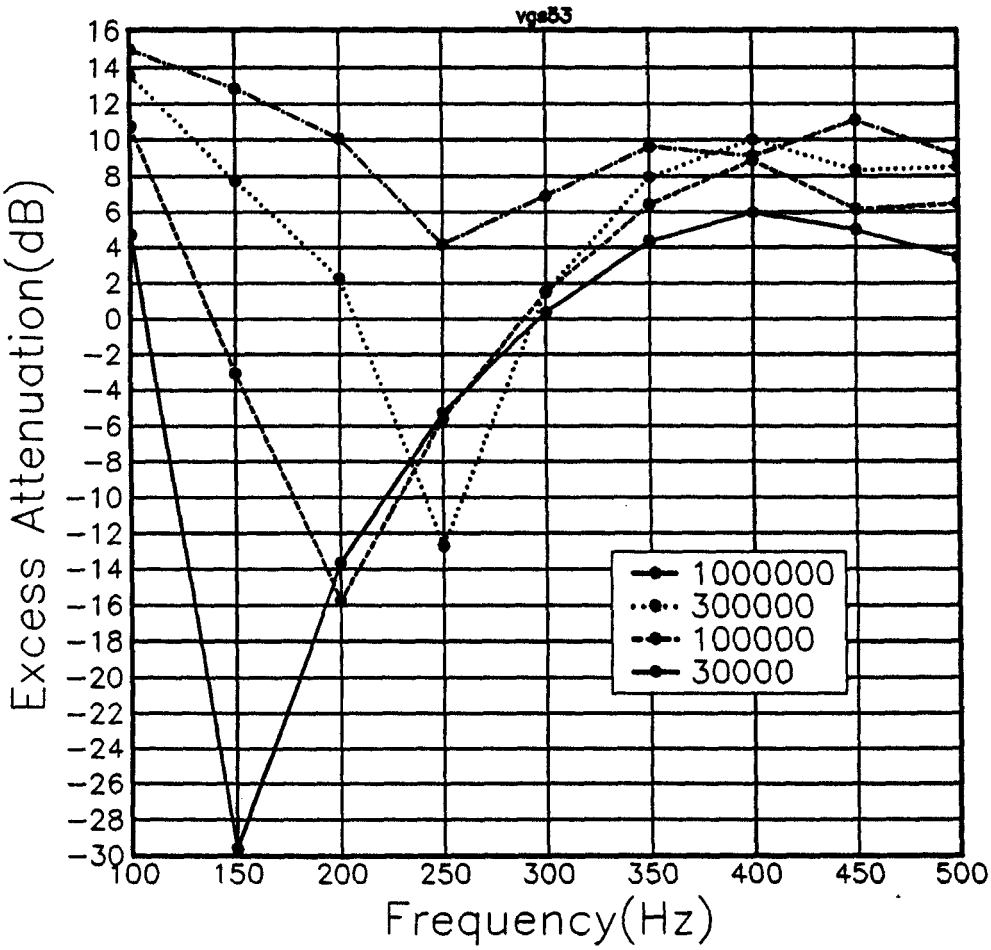

Figure 7.25 Predicted excess attenuation as a function of frequency in a linear downward refracting sound velocity gradient atmosphere with gradient $1.65s^{-1}$ .for four different ground flow resistivities

7.2.3 The effects of a downward refracting sound velocity gradient; comparison of predictions using a ray tracing model and FFLAGS.

Using the downward refracting sound velocity gradient illustrated in Figure 7.13 the excess attenuation at a range of 165 metres has been predicted using a ray tracing model and the FFLAGS FFP. The ray tracing model used (RAYFLUX) was developed by W Huisman [95] and used a spherical wave reflection coefficient for reflections at the surface, with the ground modelled using Attenborough's variable porosity two parameter approximation [79]. The atmosphere is two dimensional. The atmospheric sound velocity profile is divided into horizontal layers containing a linear sound velocity profile. Each ray follows the arc of a circle through each linear gradient layer. By simple geometry the path length through the layer, and the entry and exit points can be calculated for a given ray at a given launch angle from the source. For each ray the energy loss due to attenuation, and the phase can be calculated for the whole path to the receiver. A large set of rays is launched at the source at different angles. The receiver area is one wavelength high. The excess attenuation is calculated by calculation of the number of rays passing through the receiver and their energies and phases in comparison to that in free field. Although a particular ray trace model has been used, some of the conclusions drawn from the particular comparison given here should be relevant to ray tracing models in general.

The source and receiver were at a height of 1.5 metres. Figure 7.26 shows the predicted excess attenuation using the two different methods at frequencies between 100Hz and 1000Hz. The FFP results are for three atmospheres made up of 25 layers capped by a constant velocity halfspace, and for three atmospheres made up of 50 layers capped by a halfspace. The capping height is the height of the top of the highest layer, above which the atmosphere is represented by a constant sound speed halfspace.

The maximum height of the highest Eigenray from the ray tracing is four metres. Hence a capping height above this should represent the sound velocity gradient adequately if the ray approximation can be used in this

case. It can be seen in Figure 7.26 that even for a small layer thickness the predicted excess attenuation will not converge to the solution with a capping height of five metres in spite of the fact that this exceeds the maximum Eigenray height predicted by Ray theory, which is four metres. When the capping height reaches ten metres the solution converges to a stable result, which is shown by repeatedly increasing the capping height until the result of doing this is unchanged. The predicted excess attenuations at frequencies near to the interference dip are the most sensitive to the capping height.

Figure 7.26 also indicates the insensitivity of the result to the layer thickness in the range chosen, demonstrating that an adequately small layer thickness has been chosen (Each line in the figure corresponds to results using at least two different layer thicknesses).

The most obvious conclusion from this figure is that the ray tracing prediction of excess attenuation is extremely different to that of the FFP. It can be seen that the FFP output converges on a result as the capping height and layer thickness become large and and small enough respectively. This suggests that the FFP provides the correct result in this environment. The obvious question, therefore, is why is the ray tracing result wrong? The main reason for the error is probably that the reflections at the ground have been incorrectly treated, giving an incorrect phase relationship between the different reflections, and between the reflections and the unreflected arrival. The low frequencies involved may invalidate the use of the ray approximation in an environment where the major changes in the sound velocity are within a few wavelengths of the reflecting surface, and source and receiver heights are of the order of a few wavelengths. The need for a sound velocity profile which continues up to heights well beyond the highest Eigenray height supports the argument that the ray approximation is invalid in this frequency range for this sound velocity gradient.

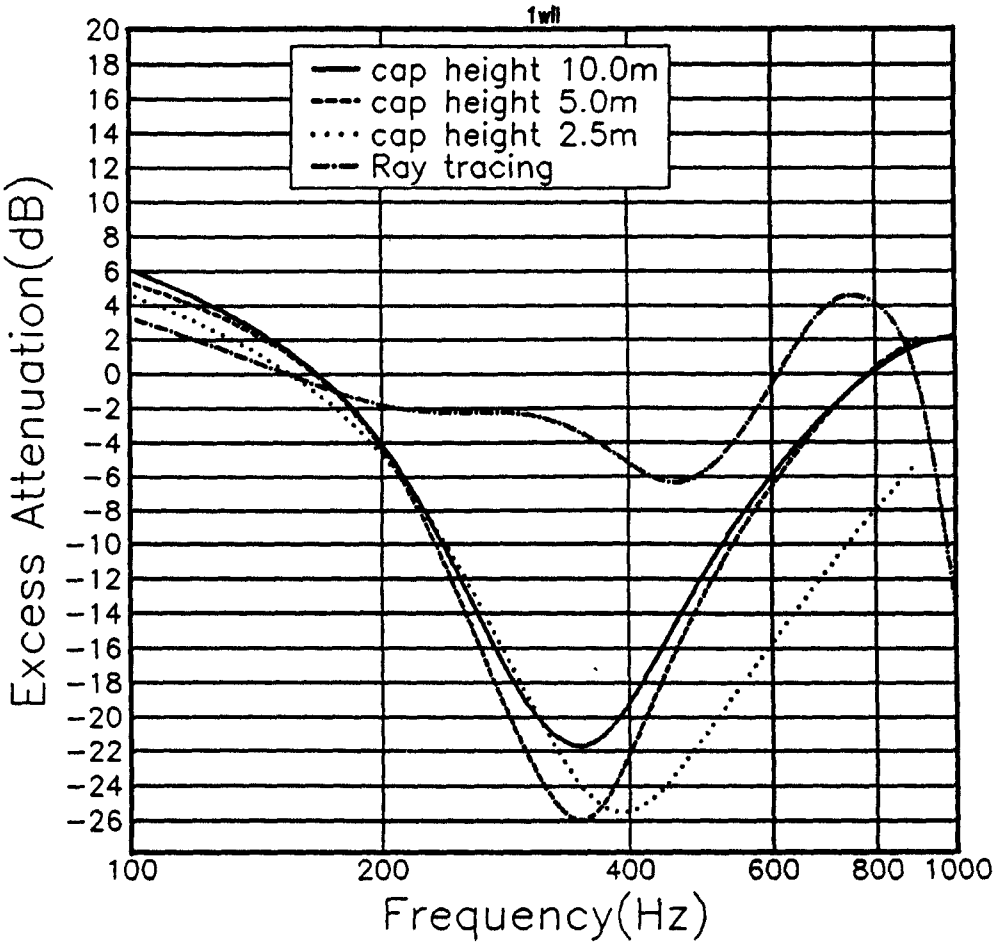

Figure 7.26 Predicted excess attenuation in the sound velocity gradient illustrated in Figure 7.13 for source and receiver heights of 1.5 metres. FFP for various air layer thicknesses, and ray tracing model.

7.3 Effects of ground surface elasticity on sound propagation

The theoretical influence of ground elasticity has been examined for two ground surfaces. These are a soil with measured pore and elastic parameters at Wezep in the Netherlands, and a hypothetical thin snow layer with parameters based on a variety of measurements.

Soil

The soil parameters used here give predicted peaks in the normal surface impedance, due to the ground elasticity, at frequencies between 20 and 100Hz. Therefore this frequency range will be examined here. Figure 7.27 shows the predicted excess attenuation for source and receiver heights of 0.5 metres at a range of 20 metres. The difference between the predicted excess attenuation at this range using rigid and elastic models is negligible.

The effect of ground elasticity on near grazing sound propagation has also been investigated for other realistic model soils. The effect of the ground elasticity on sound propagation over it is predicted to be less than 0.1dB in excess attenuation in all the cases examined.

Thin snow layer

The largest effects of ground elasticity on near grazing sound propagation are likely to be where the bulk density of the ground surface is small. The most common ground cover where this is so is a snow layer. Figure 7.28 shows the predicted excess attenuation over an 8cm thick snow layer overlying a rigid nonporous halfspace, at a range of twenty metres, using a rigid-porous model and an elastic model. Figure 7.28 also shows that the effects due to the elasticity of the snow layer for this geometry are sensitive to the seismic attenuation within the snow. The pore structure and elastic parameters are calculated from Sommerfeld [96], Johnson [97] Ishida [98] and Attenborough and Buser [48] assuming a new snow. These parameters are shown in table 7.2. Two effects of the surface elasticity can be seen. The

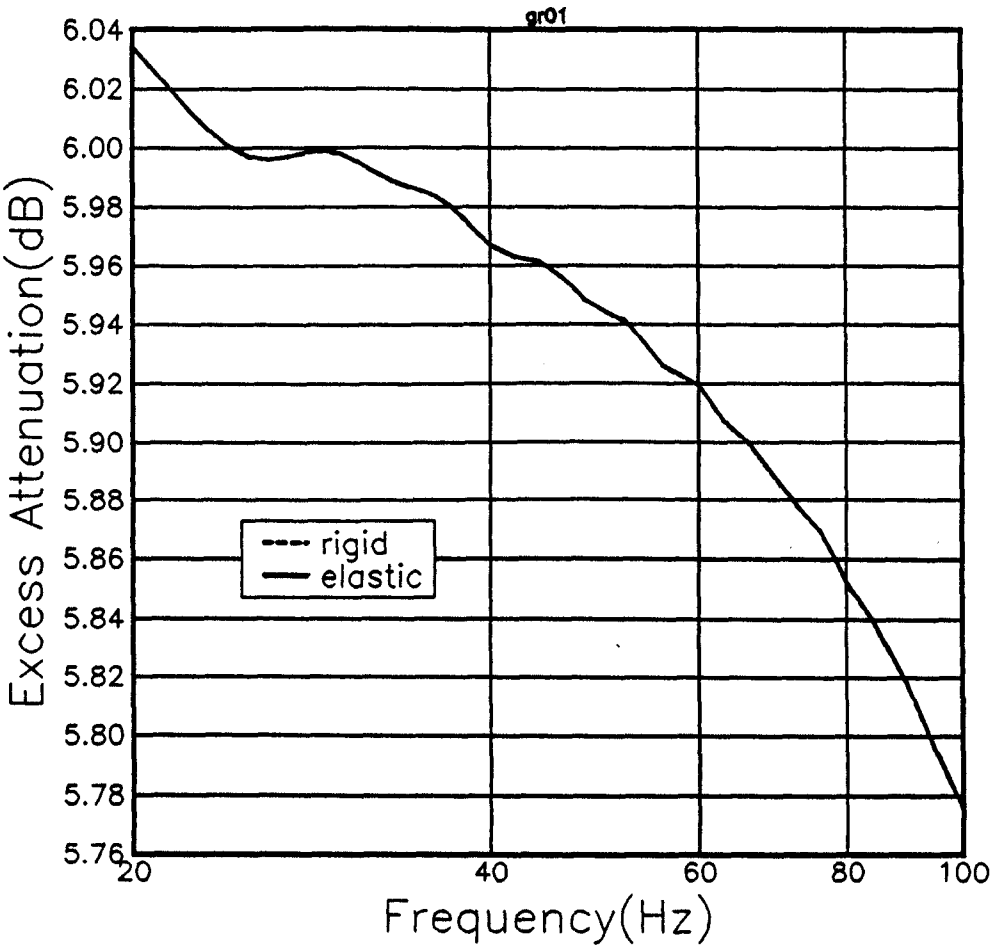

Figure 7.27 Predicted excess attenuation at a range of twenty metres over a layered soil for rigid and elastic models

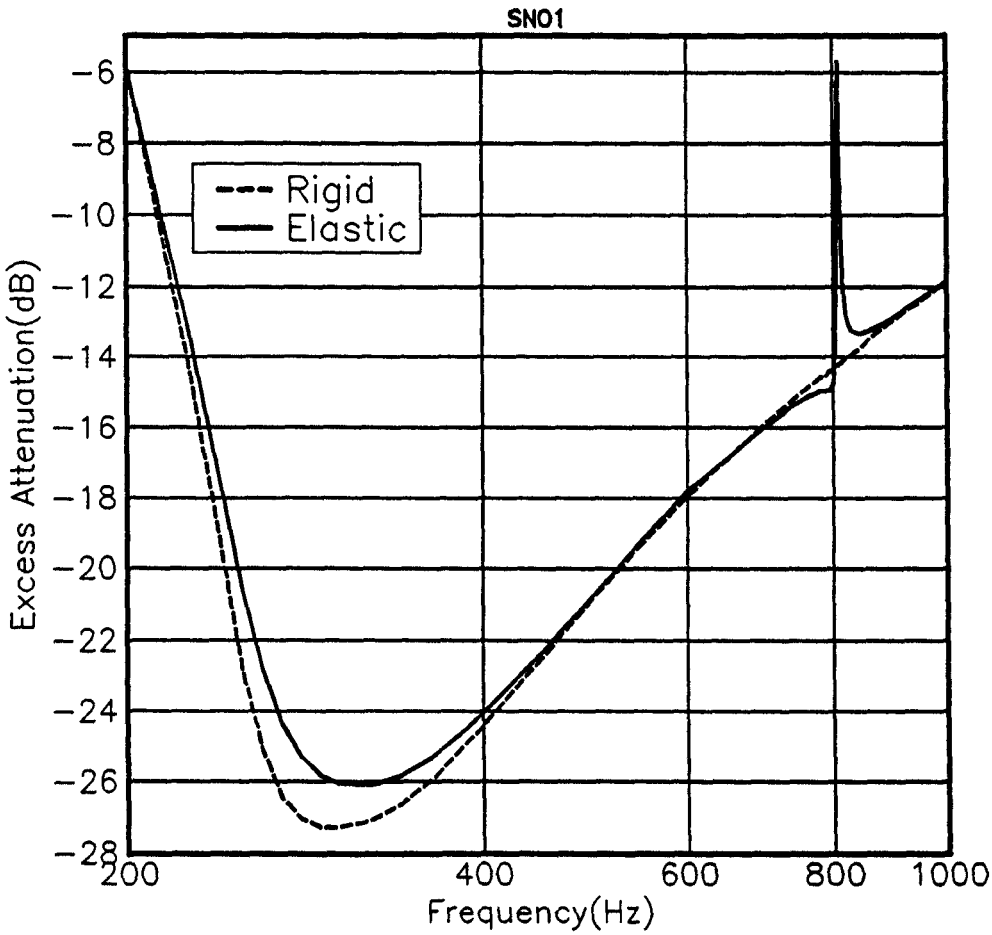

Figure 7.28 Predicted excess attenuation over a new snow layer, thickness 0.08m , as a function of frequency at a range of 20.0 metres. Rigid and elastic models.

Table 7.2 Parameters used to characterise acoustic and elastic parameters of new snow

Parameter	Unit	Value
Flow resistivity (σ)	MKS $rayls m^{-1}$	15900
Porosity (Ω)	-	0.804
pore shape factor ratio (s_p)	-	0.5
grain shape factor (n')	-	0.5
Bulk density	kgm^{-3}	183.4
p velocity(v_p)	$ms6-1$	130.0
s velocity(v_s)	$ms6-1$	90.0
solid bulk modulus	Nm^{-2}	5.10^9
$\Im(v)/\Re(v)$	-	0.05

first is an increased excess attenuation at 300Hz. This corresponds to an increased surface or ground wave. The second effect is a resonant effect at a frequency of about 810Hz. Figure 7.29 shows the predicted excess attenuation over the same snow layer at 300Hz as a function of range. This figure demonstrates that at this frequency the sound pressure level is slightly increased at all ranges. Figure 7.30 shows the predicted excess attenuation over the same thin snow layer at 810Hz. This is near to the maximum of the resonance shown in Figure 7.28.

At longer ranges (figures 7.29 and 7.30) the main effect of elasticity is an increase in signal amplitude due to the reduced attenuation near to the source.

Figure 7.31 shows that the seismic effects on propagation are reduced substantially when the snow thickness is increased to 0.30 metres. However a small peak in the excess attenution is seen at around 216Hz in figure 7.31 and this peak may be due to the same effect as in the thinner snow layer at 810Hz, as $216 = 810 \times 0.08/0.30$. These predicted effects of snow elasticity on sound propagation are very dependent on the additional seismic attenuation, over and above the attenuation predicted by the Biot model. Data on the elastic wave attenuation in snow is very sparse due to the practical difficulties of measurement. For the examples above, the ratio of

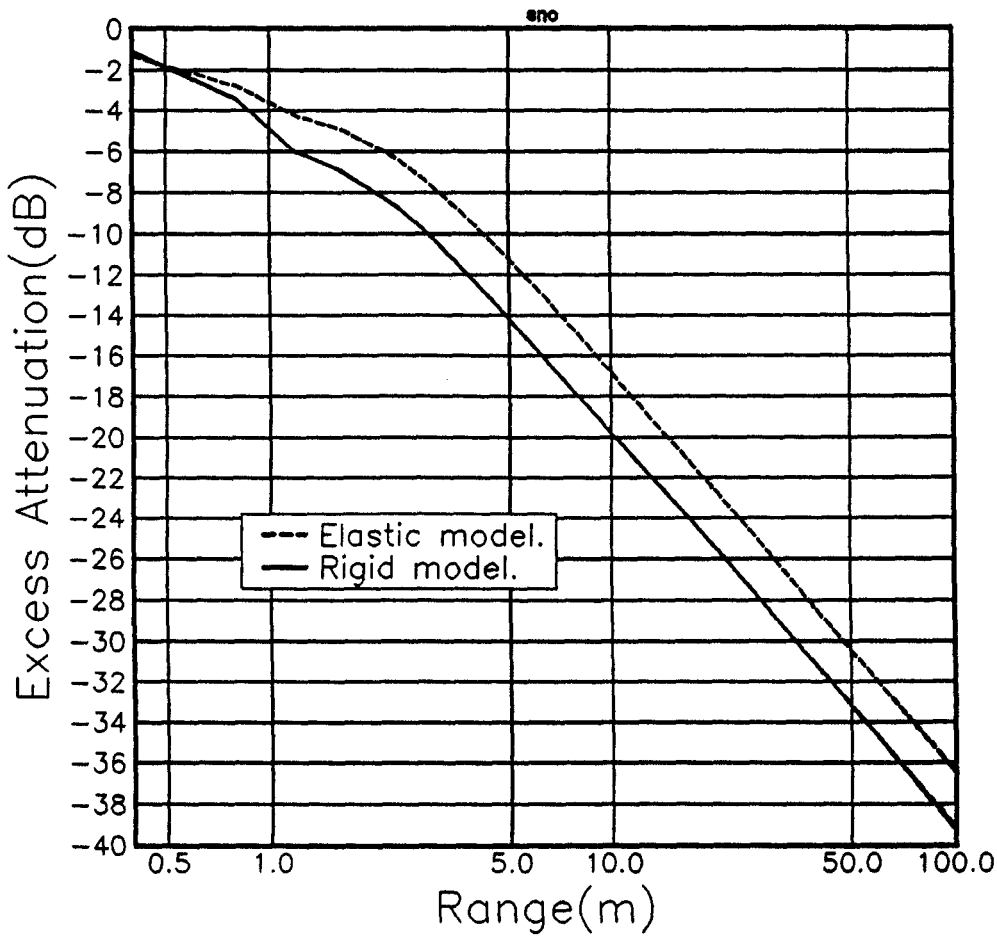

Figure 7.29 Predicted excess attenuation over thin 8cm snow layer at 300Hz as a function of range.

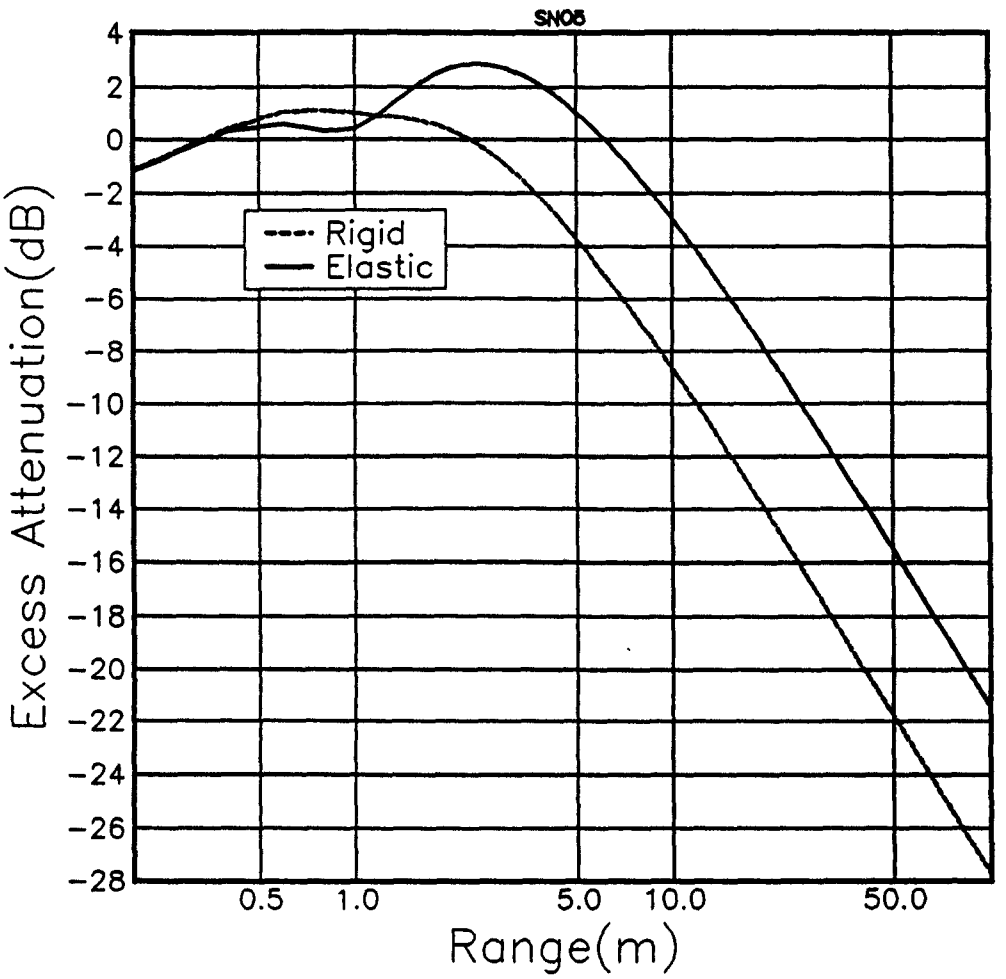

Figure 7.30 Predicted excess attenuation as a function of range at 810Hz

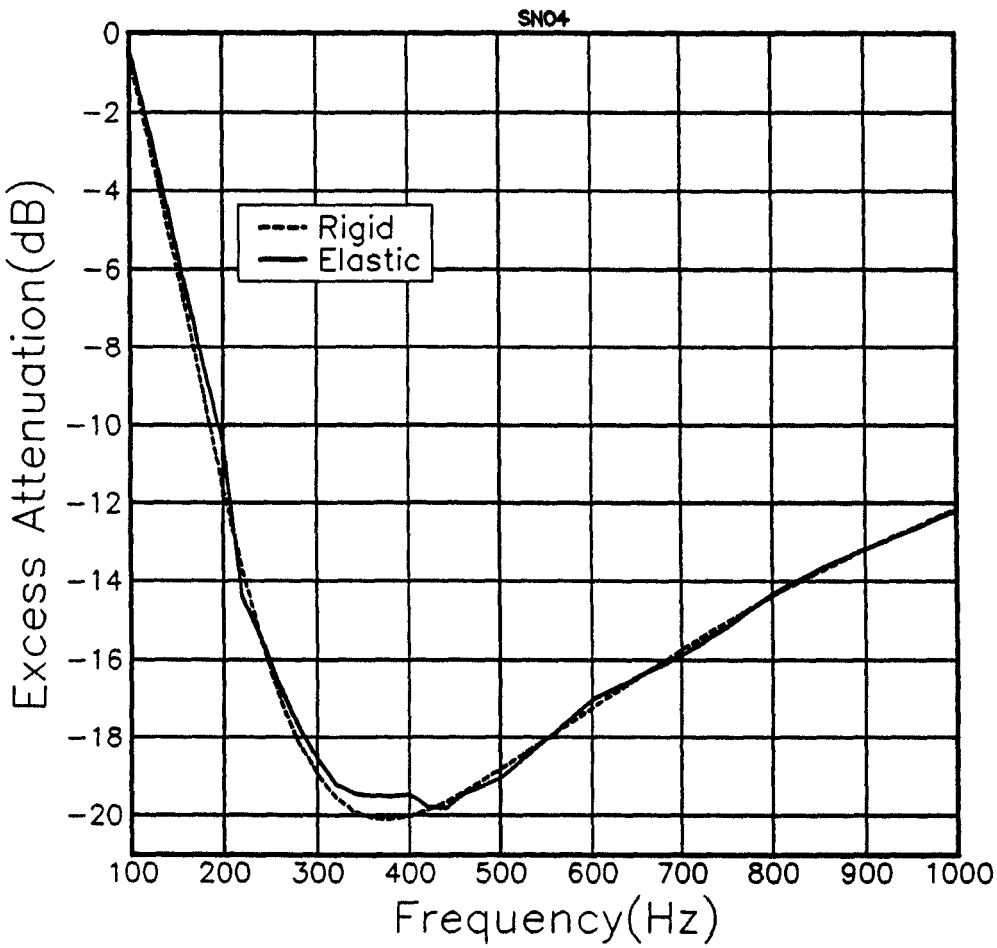

Figure 7.31 Predicted excess attenuation over a new snow layer, thickness 0.30m , as a function of frequency at a range of 20.0 metres. Rigid and elastic models.

imaginary to real parts of the elastic moduli of the pore frame ha s been chosen as 0.1. If this were increased to 0.4 then the predicted effects of frame elasticity on acoustic propagation would disappear.

It has been pointed out [99] that if these elastic effects on propagation really occur then they should be seen in normal surface impedance measurements as quarter wave peaks. The normal sample depth for impedance tube measurements of snow is a few centimetres. The elastic wave phase velocities measured by Yamada et al [96] are too high to give quarter wave resonances at the frequencies normally used in impedance tube measurements of normal surface impedance(100Hz to 5kHz).

Combined effects of elasticity and atmospheric sound velocity gradients

Continuous sound velocity gradients can be modelled by thin homogeneous layers as long as the layer thickness is much less than the wavelength of the sound [93]. In Figure 7.32 the combined effect of the a logarithmic downward refracting sound velocity gradient(roughness length 5.10^{-3} metres, temperature difference between the ground surface and a height of 4.0 metres 7° Centigrade) and an elastic surface are shown. The difference between elastic and rigid models remains approximately the same as for no gradient. This is because the seismic effect on the excess attenuation is mainly a short range phenomenon, whereas the temperature gradient's effects are felt at long range.

7.4 Comparison between creeping wave theory and FFLAGS

7.4.1 Creeping wave theory

Ray-based propagation models fail to predict the sound pressure level in the shadow zone formed during acoustic propagation in an upward refracting sound velocity gradient , where there are no ray landing points. In the

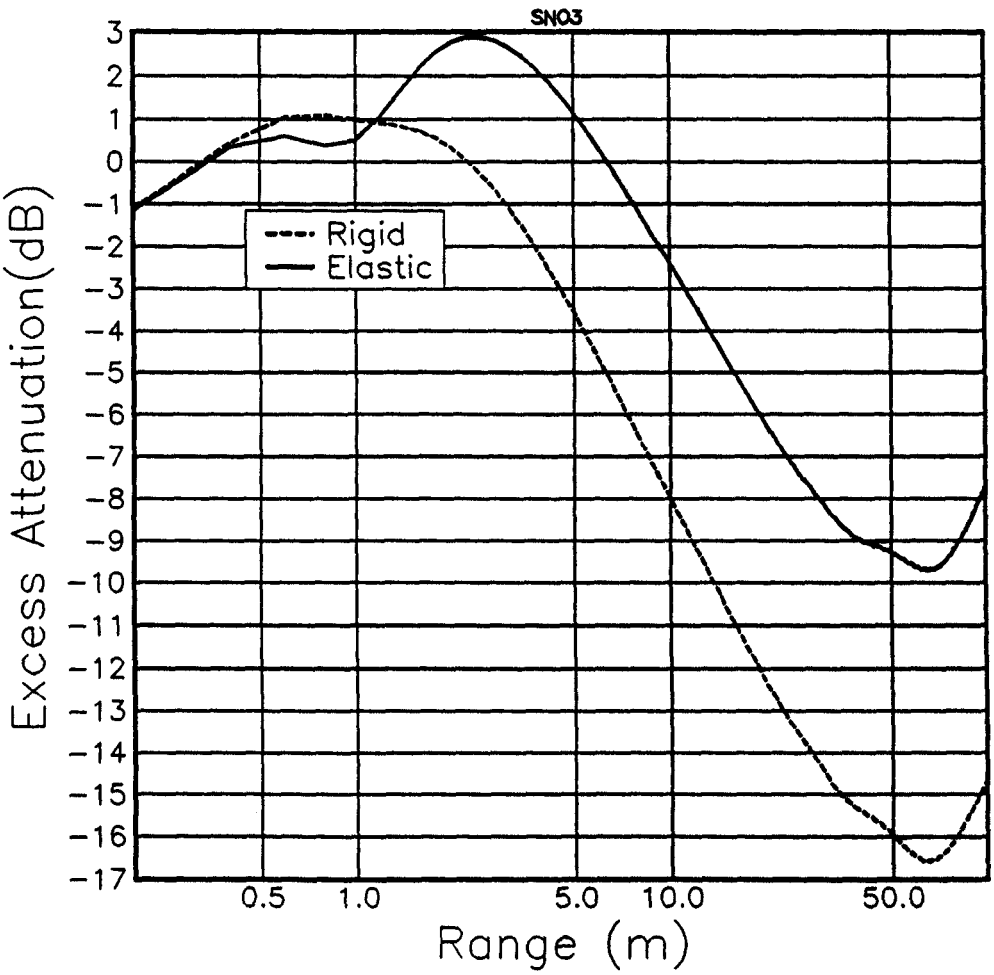

Figure 7.32 Predicted excess attenuation over a thin snow layer in a logarithmic downwardly refracting velocity gradient. Rigid-porous and elastic-porous models.

absence of turbulence and the absence of a surface wave the sound pressure in the shadow zone will be due to a creeping wave. The creeping wave travels with a phase velocity less than the speed of sound. The amplitude decreases as the square root of the range, and exponentially with an attenuation constant proportional to the cube root of the frequency and the (2/3) root of the rate of change of sound speed with height [100]. The creeping wave travels close to the ground in a region of height l given below. The creeping wave sheds energy upwards into the shadow zone as it propagates. It will exist whatever the surface impedance, although it's phase velocity and attenuation depend upon it. Thus the creeping wave is dissimilar to a surface wave, which only exists over certain ground impedances.

In order to be able to predict sound pressure levels in the shadow zone Embleton and Pierce [56] developed a residue solution for predicting sound pressure levels in the shadow region formed by a linear sound velocity gradient.

Berry and Daigle [57] improved this treatment, giving solutions which were valid anywhere by avoiding the approximations made in the development of Pierce's solution.

Berry and Daigle's solution, from which the residue series is derived, can be written

$$p(r,z) = -S \int_{k=-\infty}^{\infty} H_0^1(kr) Z(z,k) k dk. \tag{7.1}$$

where Z is the depth dependent part of the Green's function, and S is the source strength. This equation can be represented by a residue series.

$$p(r,z) = \frac{\pi e^{i\pi/6}}{l} S \sum_n H_0^1(k_n r) Ai(b_n - \frac{h_s}{l} e^{i2\pi/3}) \cdot \frac{Ai(b_n - \frac{h_r}{l} e^{i2\pi/3})}{[Ai'(b_n)]^2 - b_n [Ai(b_n)]^2}. \tag{7.2}$$

h_s and h_r are the source and receiver height respectively. Ai and Ai' are the Airy function and its first derivative with respect to its argument. The b_n are the solutions of the Transcendental equation

$$Ai'(b_n) + q e^{i\pi/3} Ai(b_n) = 0, \tag{7.3}$$

where,

$$q = i k_0 \rho_0 c_0 l / Z_s, \tag{7.4}$$

$$l = [c_0/(g2k_0^2]^{1/3}, \tag{7.5}$$

c_o, k_0 and ρ_0 are the acoustic velocity, propagation constant, and fluid density at the ground surface and g is the sound velocity gradient $|dc/dz|$. West et al [94] solves Equation 7.3 using Newton-Raphson iteration with the zeros (a_n') of Ai' as starting points for the search for all values of q, for the first frequency in a set. Pierce uses the value

$$\begin{aligned} b_n &= a_n' + e^{-i\pi/6}k_0 l/(Z_c a_n') \qquad or \\ b_n &= a_n + e^{-i\pi/6}Z_c/k_0 l \end{aligned} \tag{7.6}$$

as a first estimate in the search for b_n for low and high values of q respectively. Raspet et al [101] show that Pierce's first estimates can only be used when the argument of the surface impedance is less than $\pi/3$. Attenborough [79] showed that for many layered materials the argument can be greater than $\pi/3$. Raspet et al use a method of solution of equation 7.3 which starts from a zero of Ai' and then finds a solution to equation 7.3 with a small q using Newton-Raphson iteration. The value of q is then incremented and the solution found using the previous solution as the starting point for the iteration. This process is repeated up to the desired value of q. This is the method used here.

Raspet et al [101] have examined the relationship between the limit of the residue solution as the velocity gradient goes to zero and the spherical wave solution over an impedance surface. They have found that in this limit the exact solution given by Pierce is identical to the Sommerfeld integral for sound propagation in an homogeneous atmosphere above an impedance surface. In Berry and Daigle's evaluation of Pierce's exact solution for normal surface impedance arguments greater than $\pi/3$, Raspet et al found that there is a residue series term which becomes Donato's surface wave term [43] in the limit as $q(= ik_0\rho c_0/Zs)$ becomes large. This residue series term is the term in Equation 7.2 for which a value of b_n cannot be found using Pierce's method. The behaviour of $e^{i\pi 2/3}b_n$ as the modulus of q is increased from 0 to infinity for four arguments of the surface impedance is shown in Figure 7.33 taken from Raspet et al's paper. These demonstrate why Pierce's

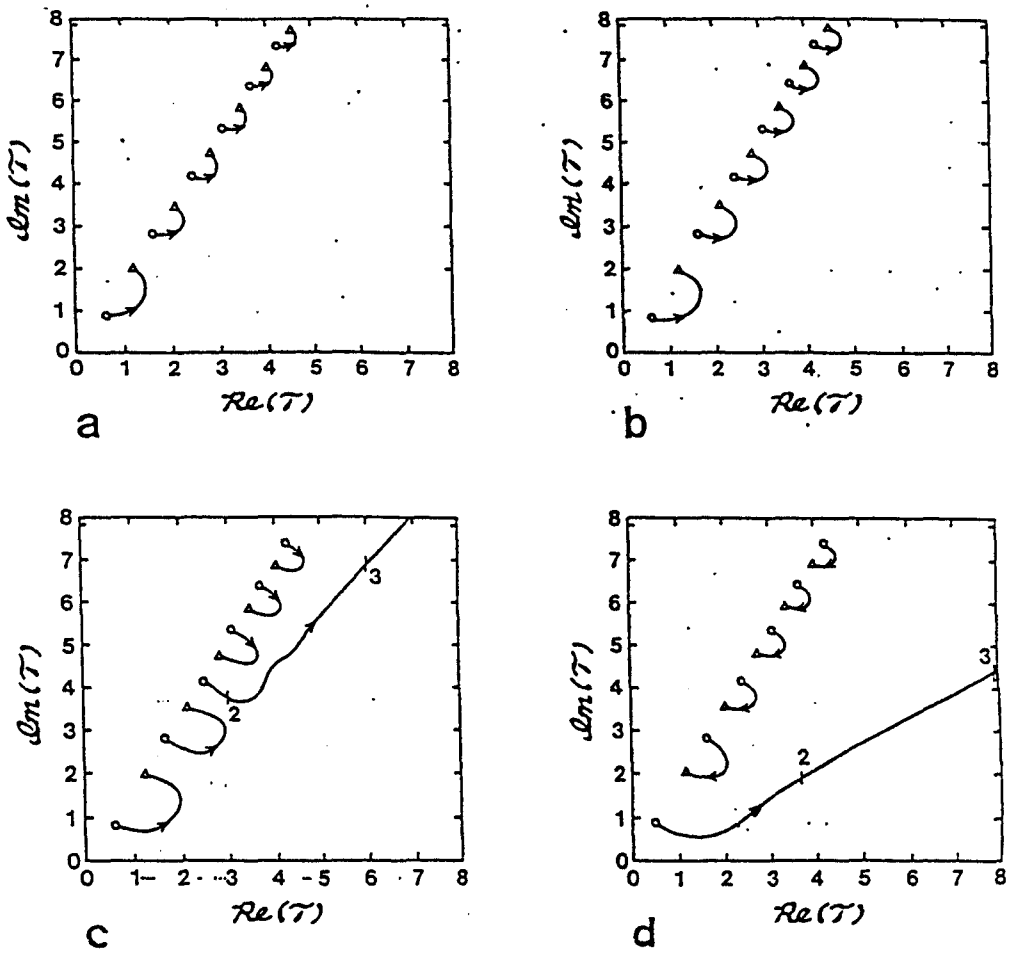

Figure 7.33 Plots of $e^{2i\pi/3}b_n$ for n=1 to 6, as q is increased from zero to infinity, for four arguments of the normal surface impedance; a : 45°, b : 55°, c : 65°, d : 75°. (With thanks to R Raspet). $\triangle$ are the zeros of Ai, $\bigcirc$ are the zeros of Ai'.

method for finding the solutions to equation 7.3 will fail for large values of q. It was found that West et al's method for finding the b_n corresponding to the surface wave also failed for large q when the argument of the impedance was much greater than $\pi/3$. The algorithm failed to converge to the correct root because the starting point was poorly chosen and convergence occured to another root b_{n+1} or b_{n-1}. For large q the sum of terms in Equation 7.2 becomes poorly convergent. Hence it is not possible to calculate the excess attenuation in an homogeneous atmosphere directly using Berry and Daigle's formulation. Also for small q and large l the sum does not converge quickly (for example a small velocity gradient over a very high impedance surface). It has also been found that the residue series is poorly conver-

gent at short ranges. This leads to smaller predicted sound pressure levels at short ranges than would otherwise be the case. This poor convergence explains the discrepancy between the FFP results and the residue series at ranges less than 50 metres (see Figure 7.35).

West et al [94] devised a scheme to accurately approximate real sound speed gradients by linear sound speed gradients, allowing them to use the residue series method in modelling pulse propagation data.

Both Pierce, and Berry and Daigle admitted to over prediction of excess attenuation when compared to real data. Raspet [102] suggested that this was due to the assumption of a linear sound velocity gradient, and hence errors in estimating a representative gradient from meteorological data. There is a further reason for this. Scattering by turbulence into the shadow zone will cause larger sound pressure levels in the shadow zone than predicted from the sound velocity gradient alone [71].

7.4.2 Fast Fourier Model

Franke, Raspet, and Liu [93] showed that predictions of sound pressure levels in shadow zones using an FFP method only agreed with creeping wave theory when the thickness of the constant velocity layers was smaller than the wavelength. They also showed that if a linear upwardly refracting sound velocity gradient is capped by a halfspace, then the difference between the predicted sound pressure levels in the shadow zone for the capped situation, and that where the sound velocity gradient continues upward indefinitely, is small provided that the height of the cap is much greater than the creeping wave height l in Equation 7.5. If the number of fluid layers (n_l) is limited then these two conditions place upper and lower limits on the frequency range in which predictions of an FFP method are valid for a given environment.

7.4.3 Surface wave Comparison

It is interesting to examine the effects of the surface wave discussed by Raspet in the presence of a sound velocity gradient, and to discover whether

the predicted effects are the same using the residue series method as modified by Raspet et al [101], and an FFP method.

The first necessity therefore has been to find parameters for the FFP and the environment in which the errors in the FFP due to the approximations made in the environment were minimised.

Figures 7.34 and 7.35 show the predicted excess attenuation at 50Hz in two different linear sound velocity gradients ($\frac{dc}{dz} = -1.65s^{-1}$ and $\frac{dc}{dz} = -0.165s^{-1}$) modelled by 25 homogeneous layers capped at a height of 25 metres by an homogeneous halfspace. The results are compared to the predictions of the Residue series method for a continuous sound velocity gradient. The source and receiver heights are 0.5 metres and the ground is characterised by the four Rayleigh-Attenborough parameters.

Franke,Raspet, and Liu [93] suggested that l should be much smaller than the capping height for accurate results, hence it would be expected that the FFP would agree with the residue series result most closely in the large sound velocity gradient because at 50Hz the creeping wave layer thickness ,l, is 4.7m in the large gradient, but 10.3m in the small gradient. The greater disagreement for the large velocity gradient suggests that even when the thickness of the homogeneous layers is much smaller than the wavelength the discontinuities at the layer interfaces lead to errors in the predicted sound pressure level if the discontinuities are large enough. At a frequency of 100Hz a similar effect can be seen. Figure 7.36 shows the predicted excess attenuation as a function of range for the steeper sound velocity gradient ($1.65ms^{-1}$ per metre). The FFP again fails to agree with the residue series solution. For the smaller gradient (figure 7.37) the agreement between the two is closer. In Figure 7.34 there is a disturbance in the predicted excess attenuation at range of 600metres. At this point the range exceeds half of the maximum range (R_{max}) and as the signal is so small wrap-around from the negative range (due to the second exponential term in the Hankel function approximation) is interfering with the direct signal at a shorter range than that at which it would normally occur.

The smaller sound velocity gradient has been chosen for further com-

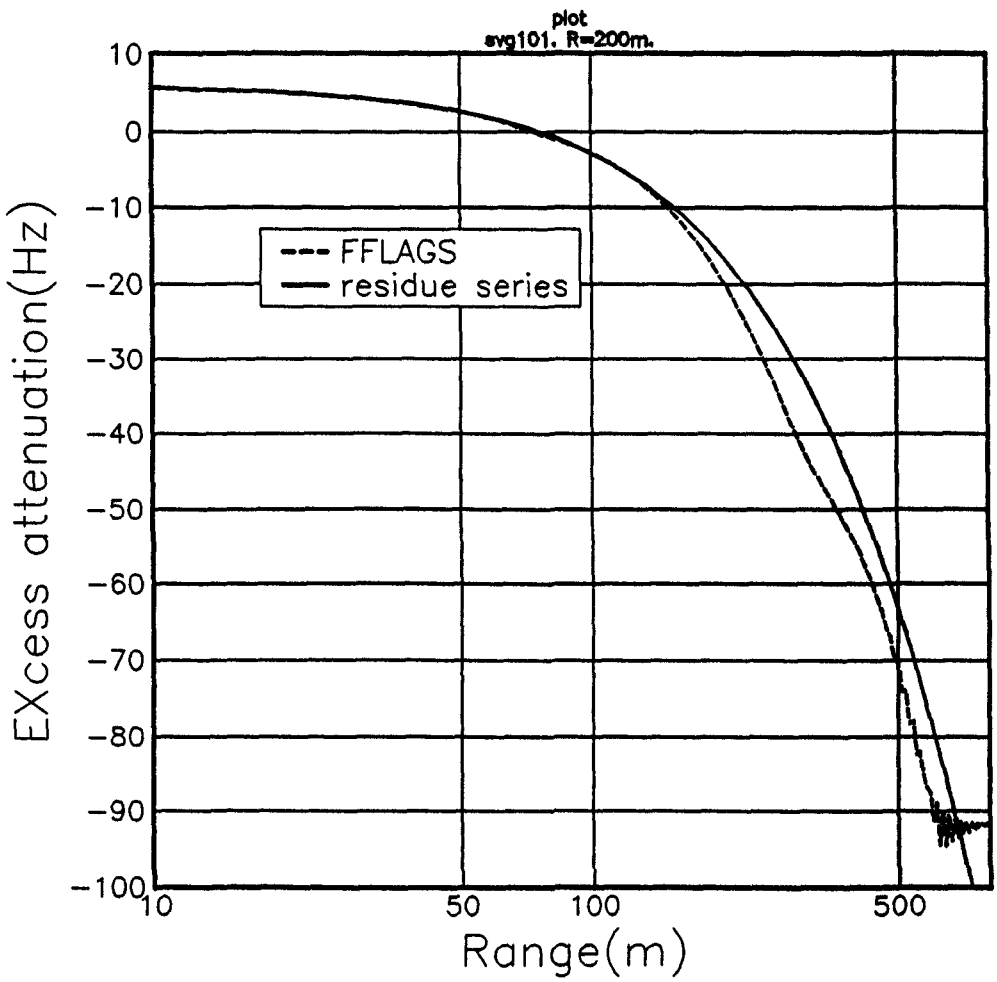

Figure 7.34 Predicted excess attenuation in a linear sound velocity gradient over a porous half-space characterised by $\sigma = 3.10^5$ mks rayls m^1,$\Omega = 0.3$, s_p=0.5, n'=0.7, where $\frac{dc}{dz} = -1.65s^{-1}$ and at 50Hz. Using Berry and Daigle's residue method and an FFP method employing homogeneous fluid layers.

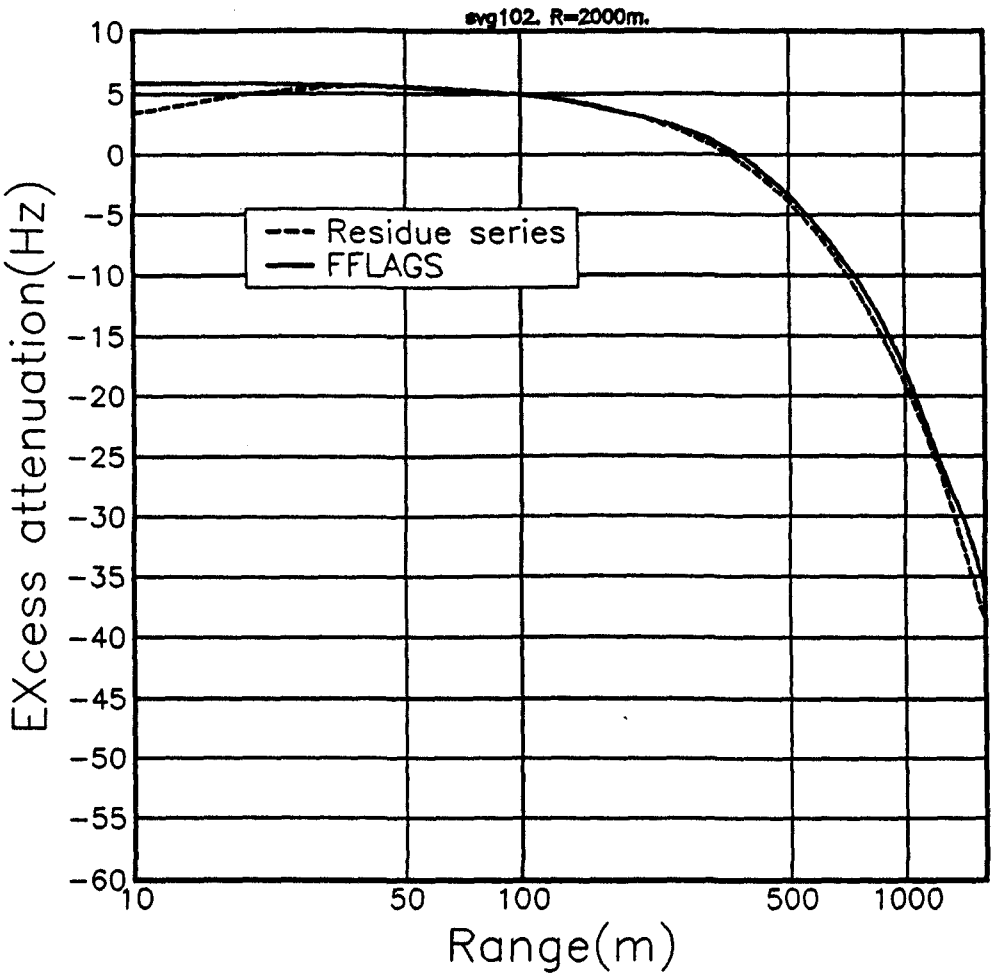

Figure 7.35 Predicted excess attenuation in a linear sound velocity gradient over a porous half-space characterised by $\sigma = 3.10^5$ mks rayls m^1, Ω=0.3 ,s_p=0.5, n'=0.7, where $\frac{dc}{dz} = -0.165s^{-1}$ and at 50Hz. Using Berry and Daigle's residue method and an FFP method employing homogeneous fluid layers.

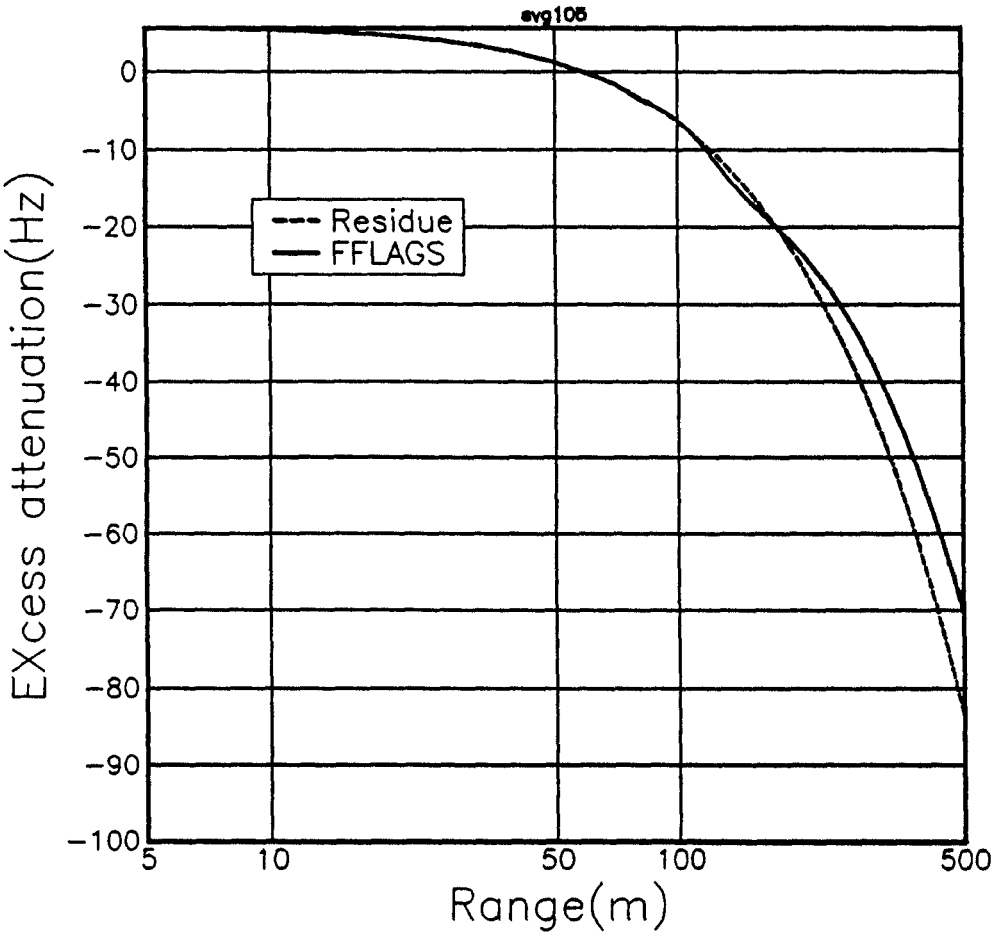

Figure 7.36 Predicted excess attenuation in a linear sound velocity gradient over a porous half-space characterised by $\sigma = 3.10^5 mksraylsm_1, \Omega = 0.3, s_p = 0.5, n' = 0.7$, where $\frac{dc}{dz} = -1.65s^{-1}$ and at 100Hz. Using Berry and Daigle's residue method and an FFP method employing homogeneous fluid layers.

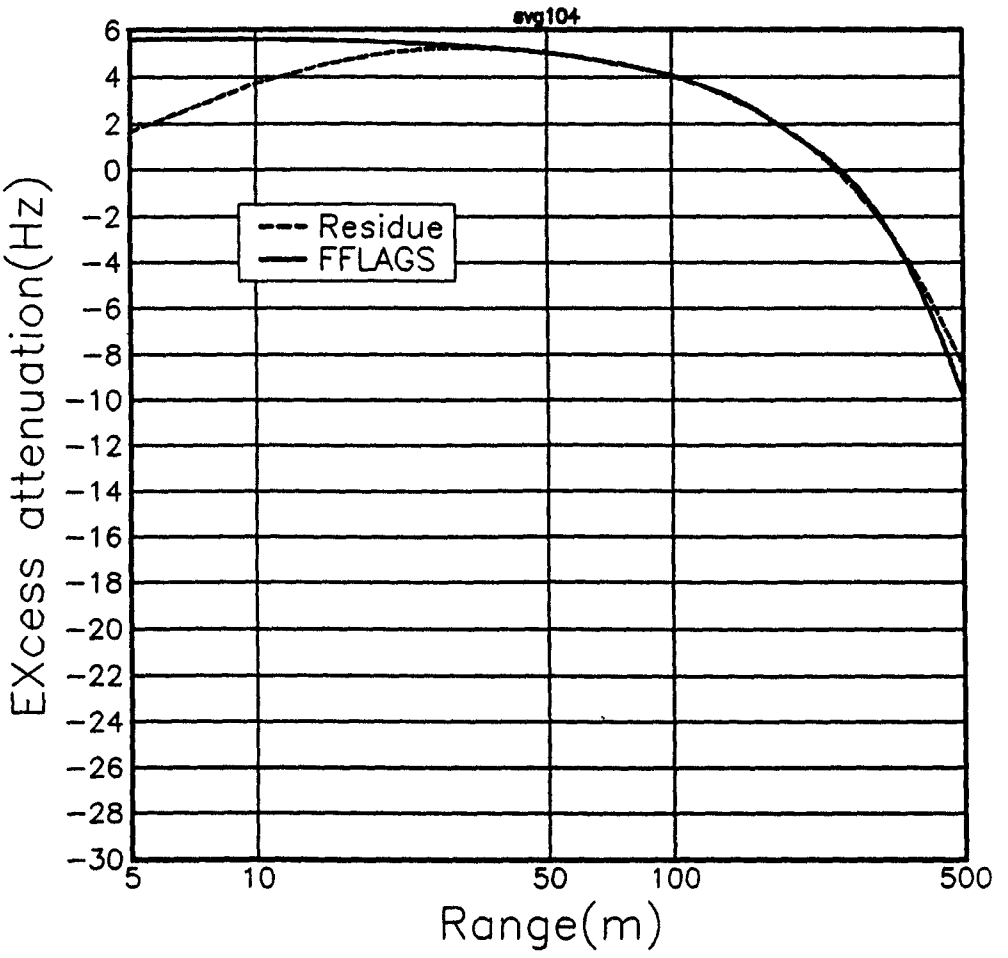

Figure 7.37 Predicted excess attenuation in a linear sound velocity gradient over a porous half-space characterised by $\sigma = 3.10^5 mksrayls m_1, \Omega = 0.3, s_p = 0.5, n' = 0.7$, where $\frac{dc}{dz} = -0.165 s^{-1}$ and at 100Hz. Using Berry and Daigle's residue method and an FFP method employing homogeneous fluid layers.

parisons. Raspet et al[101] have shown that the surface wave results from the ground impedance having an argument greater than $\pi/3$ for the residue series solution. This situation can be found for a thin non-porous backed porous layer. In Donato's solution for propagation over an impedance surface[43], he finds that the surface wave appears when the argument of the normal surface impedance is greater than $\pi/4$. Figures 7.38 to 7.41 show the predicted Excess attenuation over a non-porous backed thin porous layer at 100Hz. Table 7.3 shows the Rayleigh-Attenborough parameters for the ground surface and the normal surface impedance for each of the four surfaces. The local reaction approximation gives very different predicted excess attenuation to the extended reaction model. Because the residue series solution is a solution over an impedance surface it would be expected that it would agree with a local reaction approximation. The argument of the impedance goes from 0.4π in Figure 7.38, to 0.21π in Figure 7.41. Hence the environments are modelled where surface waves exist from both Donato's, and Berry and Daigle's description(figure 7.38), for only Berry and Daigle's(figures 7.39,7.40), and for neither(figure 7.41).

Table 7.3 Rigid-porous parameters and surface impedance for non-porous backed surface used for comparison between FFPs and residue series.

Surface	1	2	3	4	5
Flow res	10^4	10^4	10^4	10^4	10^4
porosity	0.3	0.3	0.3	0.3	0.3
s_p	0.5	0.5	0.5	0.5	0.5
n'	0.5	0.5	0.5	0.5	0.5
layer depth	0.15	0.2	0.25	0.3	0.1
Impedance	2.63+i8.37	2.79+i5.71	3.11+i4.02	3.57+i2.85	2.18+i6.37

These results show that the surface wave predicted by the FFP and by the residue series solution agree closely in amplitude (see Figure 7.38). For propagation over the two surfaces where Donato predicts a surface wave, but the residue series solution does not, the differences between the FFP and residue series predictions is small, and if the surface wave exists in this

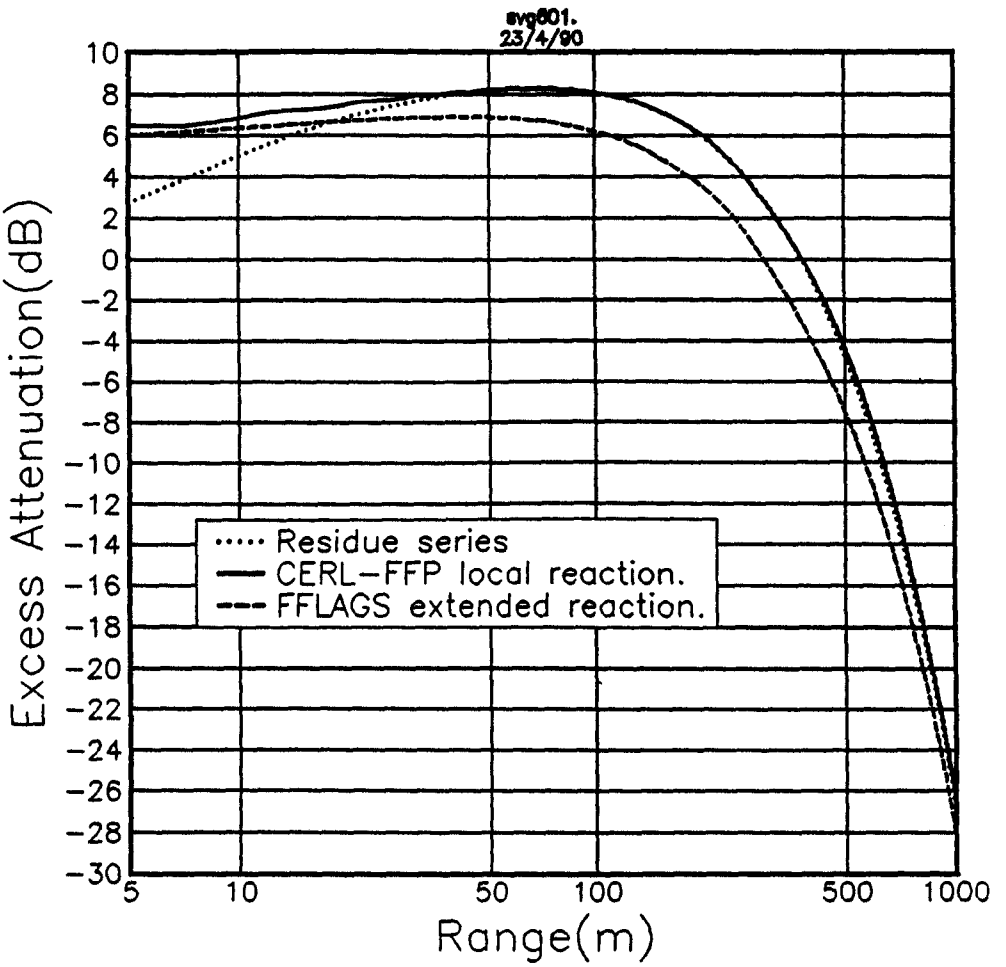

Figure 7.38 Predicted excess attenuation over a non-porous backed porous surface 1., source height=0.5m, receiver height=0.5m, Frequency=100Hz. Residue series and FFPs. Linear sound velocity gradient $\frac{dc}{dz} = -0.165s^{-1}$.

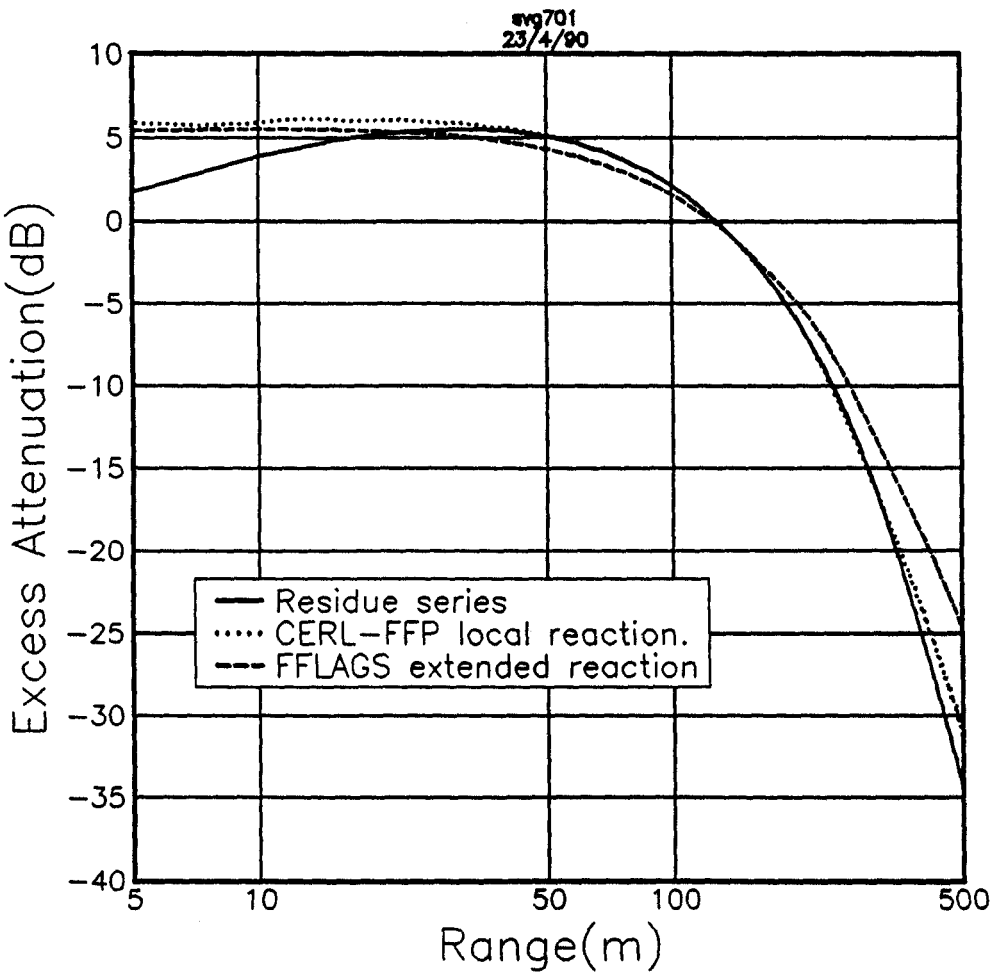

Figure 7.39 Predicted excess attenuation over a non-porous backed porous surface 2., source height=0.5m, receiver height=0.5m, Frequency=100Hz. Residue series and FFPs. $\frac{dc}{dz} = -0.165s^{-1}$.

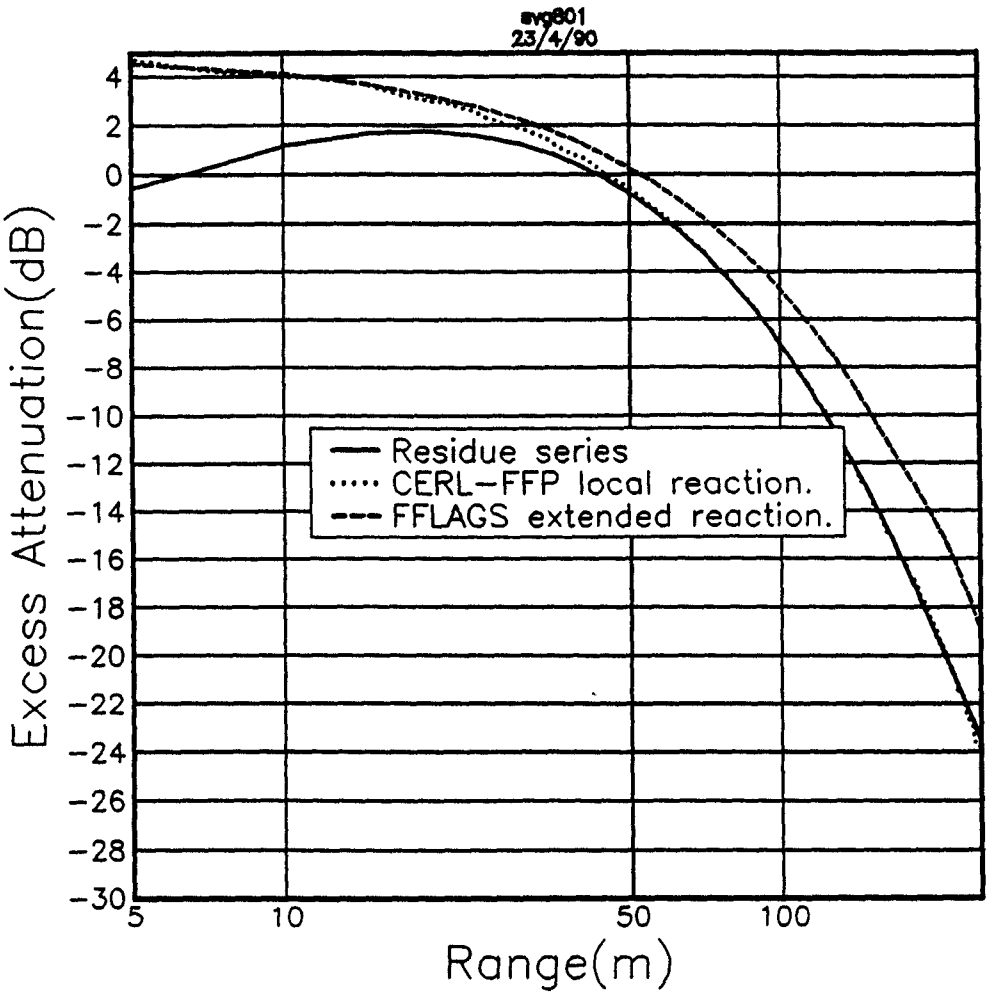

Figure 7.40 Predicted excess attenuation over a non-porous backed porous surface 3., source height=0.5m, receiver height=0.5m, Frequency=100Hz. Residue series and FFPs. $\frac{d\epsilon}{dz} = -0.165s^{-1}$.

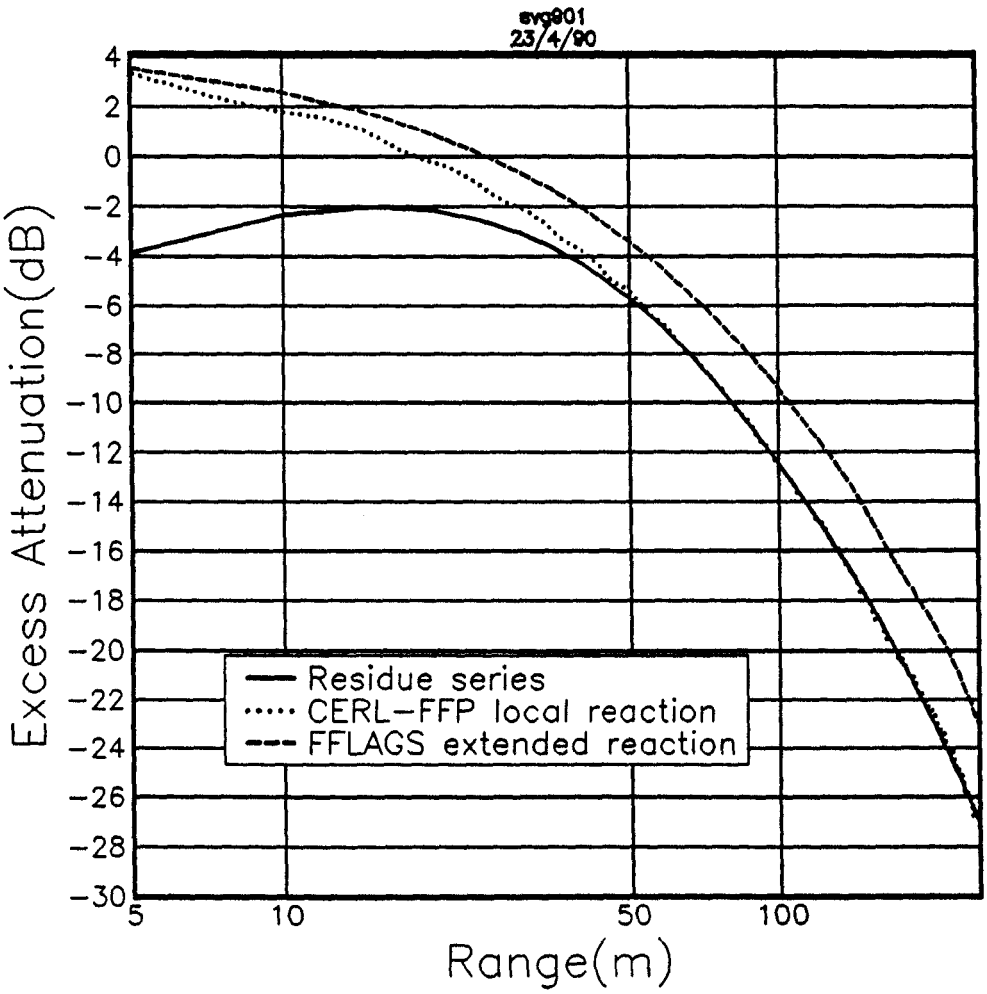

Figure 7.41 Predicted excess attenuation over a non-porous backed porous surface 4., source height=0.5m, receiver height=0.5m, Frequency=100Hz. Residue series and FFPs. $\frac{dc}{dz} = -0.165s^{-1}$.

region its amplitude is too small to make a measurable difference to the predicted results. Other gradients, grounds and frequencies were used to try to find differences in this range, but no significant ones were found. Raspet [103] suggested that no surface wave will be found in this region. Figure 7.42 shows the predicted excess attenuation in the same sound velocity gradient as the above figures, at 200Hz over a ground characterised by flow resistivity $\sigma = 1.10^4$ mks rayls m^{-1}, air porosity $\Omega = 0.3$, pore shape factor ratio s_p=0.5, grain shape factor n'=0.7, layer depth $d = 0.1$. Both the residue series solution and the locally reacting FFP solution show an excess attenuation dip at a range of 250 metres. This dip is probably an interference between the creeping wave and the surface wave. This shows that the predicted surface wave velocity is similar for the FFP and the residue series for this surface. The FFP solution for extended reaction also exhibits a dip, but at 450 metres. This indicates the importance of using an extended reaction model of the ground rather than a locally reacting approximation when the ground has sufficiently low flow resistivity to warrant it.

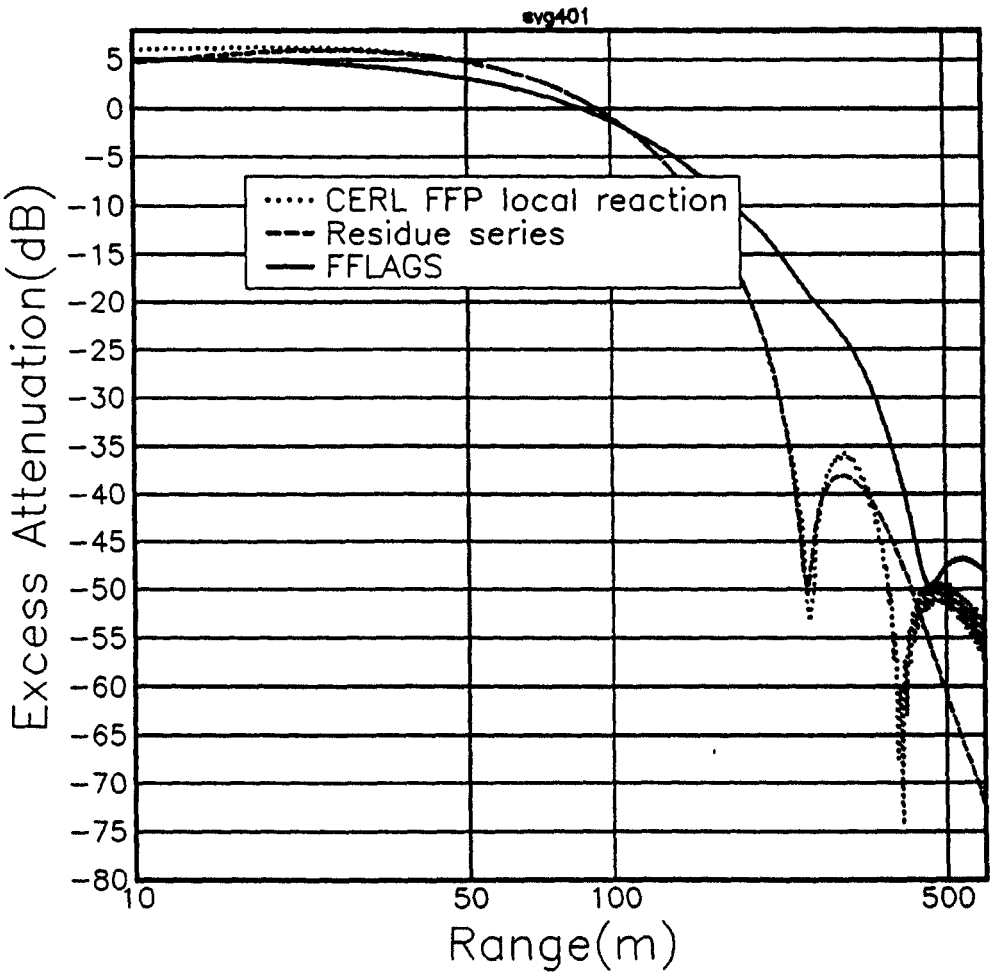

Figure
7.42 Predicted excess attenuation over a non-porous backed porous surface, source height=0.5m,receiver height=0.5m,Frequency=200Hz. Residue series and FFPs. $\frac{dc}{dz} = -0.165s^{-1}$.

Chapter 8

Experimental Comparisons with FFLAGS

8.1 Polyester foam

In order to compare and validate the mathematical model used in the FFLAGS program a physical model of a porous and elastic soil was produced. A material for the model was chosen with well defined and measurable physical parameters. The material chosen was "CAF16" polyester foam. This foam was chosen because of it's very even pore structure, low density, and the fact that the bulk modulus was the same order as that of air. This fact, and the low density of the material made it likely that the elastic properties of the foam would have a measurable effect on acoustic propagation over it. In order to model sound propagation over and into the foam surface it was necessary to deduce (non-acoustically) as many of the required Biot-Stoll parameters as possible.

8.1.1 Elastic parameters

The elastic moduli needed to predict propagation using the Biot-Stoll method are [20]: the dynamic bulk modulus of the solid material were it to have zero porosity(K_r), the dynamic bulk modulus of the solid frame in the absence of pore fluid(K_b), the dynamic shear modulus of the solid frame in the absence of pore fluid(g_b), and the dynamic bulk modulus of the pore fluid (K_f). In

most materials it would be extremely difficult to measure the bulk modulus of the solid material. In foams it can be estimated from the bulk modulus of the original material before foaming. However this would be inaccurate as extra stresses are induced in the material by the foaming process. Allard et al [27] point out that in most sound absorbing materials K_b is much smaller than K_r, as the porosity is very close to unity, and that in the equations for the elastic parameters in the Biot theory the elastic constants simplify when the ratio of the bulk modulus of the solid material K_r to any of the other elastic moduli is much greater than unity. The Biot elastic constants simplified by Allard et al differ from those used here (Equations 3.5), as Allard et al use the results of Biot's first paper on the subject [104], but the equations used here can be similarly simplified to,

$$\begin{aligned} H &\simeq \frac{K_f}{\Omega} + K_b + \frac{4}{3}g_b \\ C &\simeq M \simeq \frac{K_f}{\Omega}, \end{aligned} \tag{8.1}$$

when K_r is much greater than the other elastic moduli. When the ratio of K_r to K_b is twenty, the porosity is 0.97, and the fluid bulk modulus and frame shear modulus are half of K_b, the error in H, C, and$M$ caused by the use of the above estimate (that K_r is very large) rather than equations 3.5, is less than 1%. This implies that large errors in the material bulk modulus K_r, will lead to negligible errors in the Biot elastic constants as long as K_r is large. The dynamic moduli of the porous frame can be measured directly. A resonance method due to T. Pritz was used [105,106] to measure the elastic moduli of the foam .

T.Pritz's method models a sample of material as a rod. Therefore the width of the sample must be much smaller than a wavelength of any propagation mode in the sample.

The long thin sample (dimensions $15mm \times 15mm \times 150mm$)was suspended from the arm of the shaker table, as in figure 8.1. An accelerometer was attached to the shaker table. A second, low mass, accelerometer (Brüel & Kjaer 4375) was attached to a small aluminium mounting plate glued to the lower end of the sample. The top end of the sample was excited by the shaker using a frequency sweep from a frequency well below the estimated

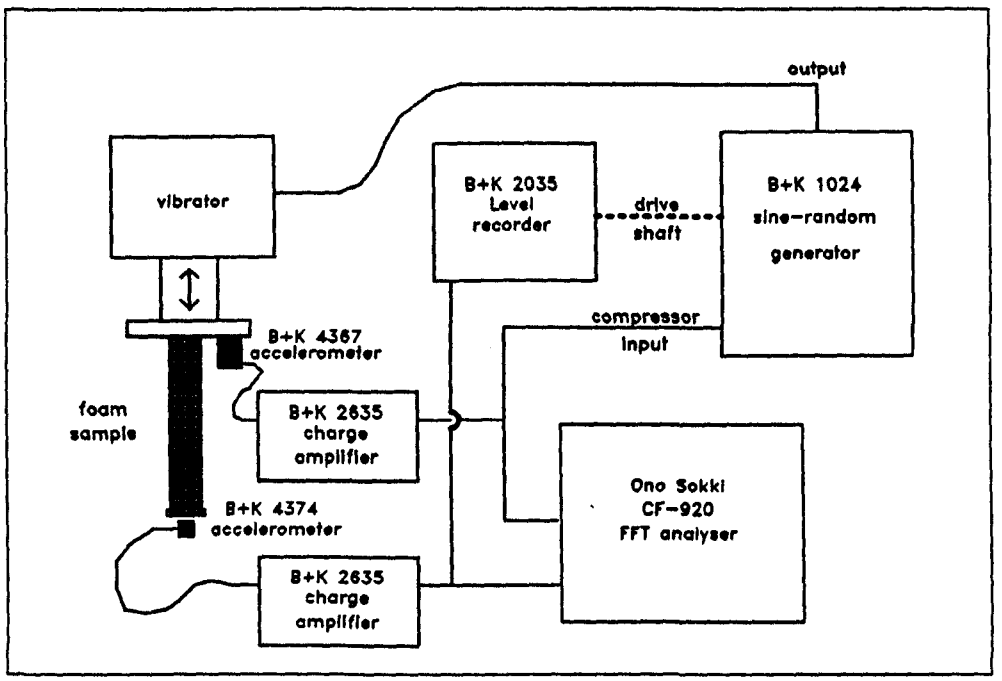

Figure 8.1 Apparatus used to measure the Young's modulus of the polyester foam.

lowest resonant frequency of the sample, to the highest frequency at which resonant frequencies were measurable. For the CAF16 foam samples the lowest frequency was 20Hz, and the highest 1kHz. The frequencies of peaks in the transfer function between the accelerometer on the bottom of the sample and the accelerometer on the table, were noted. Using the equation,

$$E(f_p) = \rho_b 4\pi^2 l^2 \left[\frac{f_p}{(\beta_0 l)_p}\right]^2, \tag{8.2}$$

the Young's modulus $E(f_p)$ was calculated for each resonant frequency f_p. $\beta_0 l$ is the solution to the equation,

$$cot(\beta_0 l) = \frac{M}{m}(\beta_0 l). \tag{8.3}$$

M is the loading mass (the mass of the second accelerometer and the mounting plate at the free end of the sample), and m is the mass of the foam. Where possible the frequencies above and below the resonant frequency, where the transfer function was 3dB down on the peak were measured. This gave the resonance bandwidth (δf) and hence the loss factor,

$$\eta_E(f_p) = \frac{\delta f}{f_p}. \tag{8.4}$$

Using this method the Young's modulus and loss factor were measured at frequencies up to 1kHz.

In some treatments of the elastic properties of foam [27] the Poisson's ratio ν is assumed to be zero. It was decided to make an estimate of Poisson's ratio by using four different foam samples with two different loading masses. It was found that the calculated Young's modulus from all four sample shapes were consistent(see Figure 8.2) which implies that the Poisson's ratio was near to zero.

In order to measure the elastic moduli of the foam in the absence of the fluid it would be necessary to perform them in a vacuum. The effect of the air on the measured Young's modulus was estimated by calculating the predicted fast and shear propagation constants using the Biot-Stoll model, with the Biot elastic constants calculated using the measured Young's Modulus. These were compared to the predicted propagation constants using

visco-elastic theory and the measured Young's modulus. The Biot-Stoll propagation constants include the effects of the viscous fluid in the pores in a continuous porous medium. The visco-elastic propagation constants do not include the effects of the pore fluid. The results are shown in Table 8.1.

Table 8.1 Visco-elastic and Biot Propagation constants for CAF16 polyester foam.

Frequency (Hz)	Visco-elastic longitudinal		Visco-elastic shear		Biot fast		Biot shear	
	real	imaginary	real	imaginary	real	imaginary	real	imaginary
500.00	39.48	3.35	56.71	4.82	37.77	7.28	56.61	4.99
1000.0	78.96	6.71	113.4	9.64	78.07	10.6	112.9	10.1
1500.0	118.4	10.0	170.1	14.4	117.7	14.0	169.1	15.1
2000.0	157.9	13.4	226.8	19.2	157.2	17.5	225.2	20.1
2500.0	197.4	16.7	283.5	24.1	196.7	21.0	281.4	25.0
3000.0	236.8	20.1	340.2	28.9	236.1	24.4	337.5	29.9
4000.0	315.8	26.8	453.6	38.5	314.8	31.4	449.7	39.7
5000.0	394.8	33.5	567.1	48.2	393.5	38.4	561.9	49.4

The table shows that the effect of the air on the real parts of the propagation constants is small.The effect of the air on the imaginary part of the longitudinal propagation constant is to add between 0.1 and 0.01 of the real propagation constant to the value of the imaginary part, depending on the frequency. At most frequencies considered the effect would be negligible.

Because the measured sample was small the effect of the air in the pores will be reduced. It was not possible to calculate the effect and it was assumed that the effect of the air was negligible in the measurement of the elastic constants.

8.1.2 Bulk density and porosity

The bulk density of the material was measured by cutting cuboid specimens, measuring their dimensions, and finding their mass by weighing. The sam-

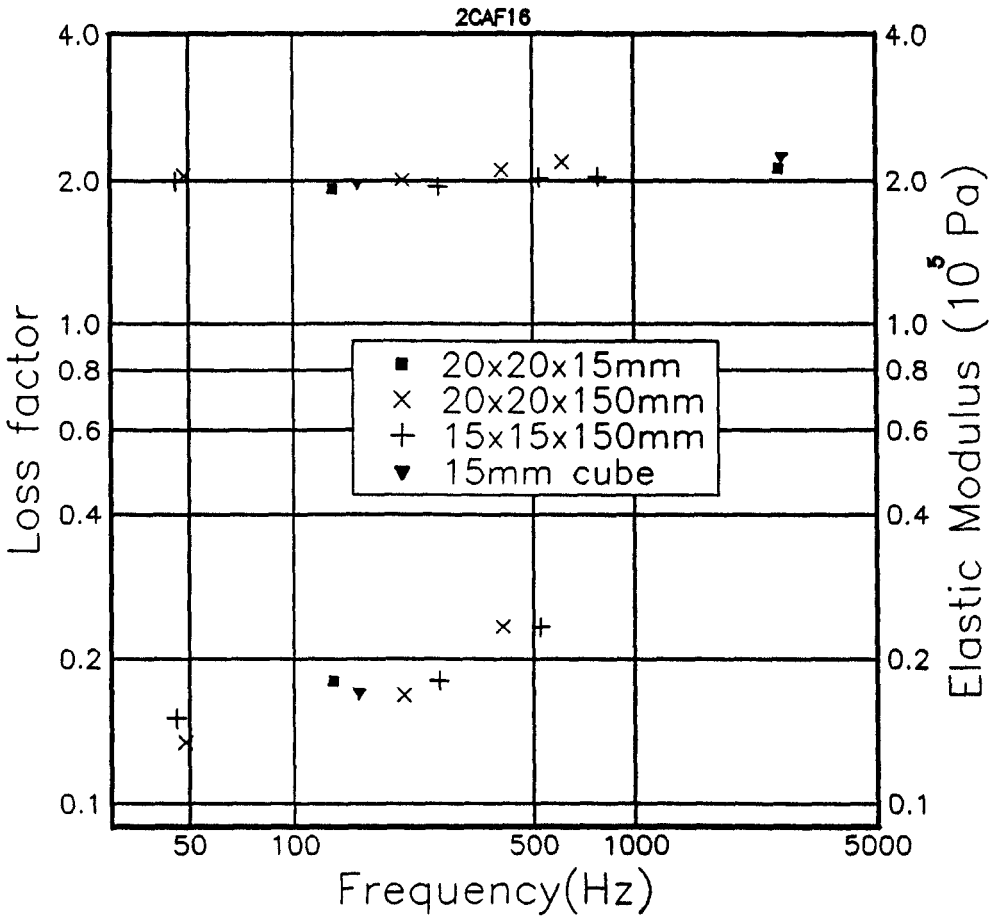

Figure 8.2 Measured Young's modulus of "CAF16" polyester foam. The loss factor is between 0.1 and 0.4, and the Young's modulus is near to 2.10^5Pa.

ples were those used to measure the elastic moduli. The mean bulk density of the material was $(34.0 \pm 1.5).10^{-3} kgm^{-3}$. It would be possible to calculate the porosity by finding the mass of fluid of known density needed to saturate a known volume of the foam. However errors in the calculated porosity would be proportional to errors in the measured volume. By using a measured bulk density, and an estimated solid density the large error in $(1 - \Omega)$ translates into a small error in the porosity (Ω). The porosity was estimated from the bulk density and the known density of solid polyesters. Solid polyesters have a density of between 1.1 and 1.45 kgm^{-3} [107]. This gives a porosity of 0.972 ± 0.005.

8.1.3 Measurement of tortuosity

The tortuosity of the foam sample was measured using an electrical resistance method [108]. The electrical conductivity (ρ_s) of the foam sample soaked in a conductive fluid was measured. The electrical conductivity (ρ_f) of the conductive fluid was also measured. The ratio of these is the formation factor $F = \frac{\rho_f}{\rho_s}$, used in studies of geophysics. The tortuosity (q^2) is simply calculated from,

$$q^2 = \frac{\rho_f}{\rho_s . \Omega}. \tag{8.5}$$

The conductive fluid used was a brine solution. A circular sample of the polyester foam (diameter 97mm) was cut from a sheet of thickness 50mm. The sample was wrapped in insulating waterproof tape around the curved surface leaving only the top and bottom surfaces unsealed. The sample was placed in a snugly fitting cylindrical container containing a porous grid electrode at its base. A second grid electrode was placed on top of the sample. The cylindrical container was placed in a bath of the brine solution and the top of the container attached to a suction pump. The solution was allowed to rise through the foam sample until it came into contact with the top electrode. The electrical conductivity of the saturated foam was measured using an alternating current source and many different currents in order to ascertain that the electrical conductivity was independent of the current in the range used. The measurements were repeated on the sample

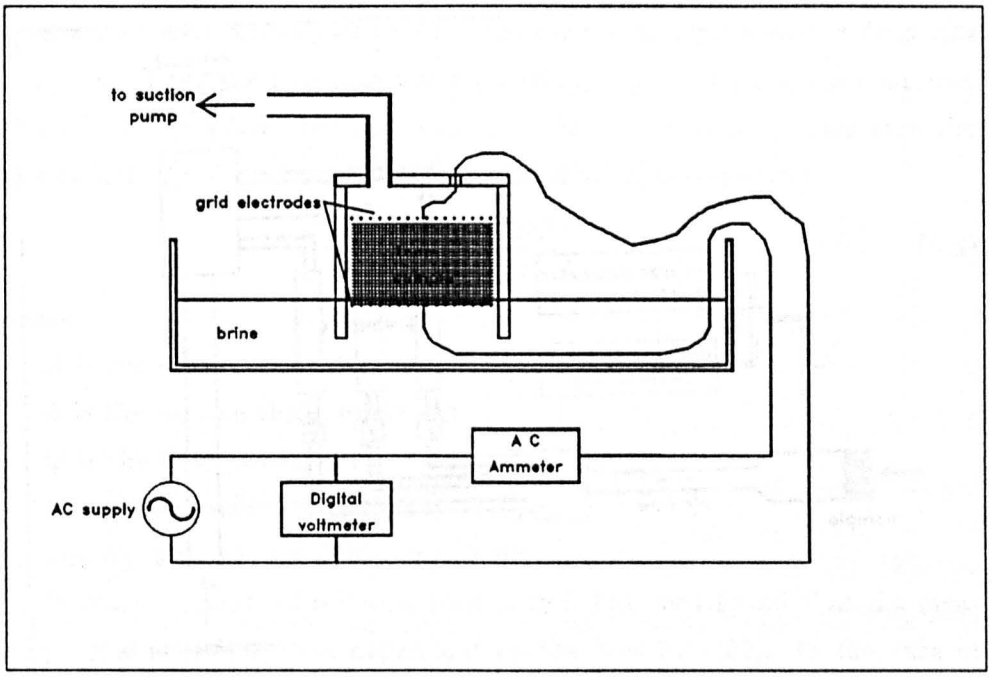

Figure 8.3 Apparatus for measurement of foam tortuosity.

allowing the fluid to fall and then rise again through the foam so as to avoid trapped air pockets affecting the result. The apparatus is shown in figure 8.3

The conductivity of the fluid was measured in a similar fashion. The top electrode in the cylinder was supported and the fluid allowed to rise through the cylinder until it reached the top electrode. The conductivity was measured using the same method. The resulting calculated tortuosity from three samples was 8.0 ± 0.3. This value is reasonable for a highly reticulated foam (a foam where there many membrane walls between the

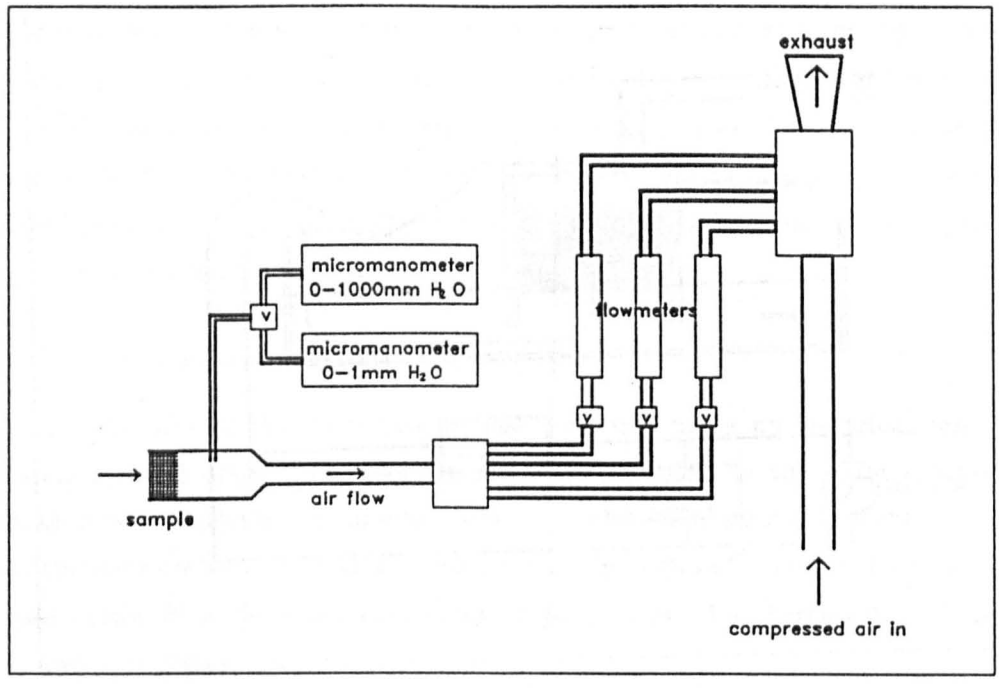

Figure 8.4 Diagram of flow rig.

cells in the foam.)

8.1.4 Measurement of air flow resistivity

The flow resistivity or the foam was measured using a flow rig, following ASTM standard C522-69. The flow rig is shown diagrammatically in Figure 8.4.

A circular sample of the foam, of diameter 97mm , and thickness 50mm, was wrapped in plastic tape on it's curved surface, and inserted into the sample holder. A pressure differential was created on one side of the sam-

ple by the venturi effect, using a compressed air source. Hence air moved through the foam sample to equalise the pressure differential. The flow rate was regulated and measured by a set of three flow meters. The pressure drop across the foam sample was measured by two micromanometers.

Starting with a flow rate of 8.5 litres per minute, the pressure drop was measured. Then the flow rate was reduced in steps to 0.1 litres per minute. At each step the flow rate and pressure drop were noted. At each step the flow resistivity of the sample was calculated using the equation

$$R = \frac{C_1 A \delta P}{QL}, \tag{8.6}$$

where

A is the cross sectional area of the sample in cm^2

L is the sample thickness in cm

Q is the flow rate in $cm^3 s^{-1}$

δP is the pressure drop in mm of H_2O

and C_1 is a conversion factor = 2490.

In measurements of soil flow resistivity it has been found that the measured flow resistivity was dependent on the flow rate [89]. In the case of the foam measurement it was found that the flow resistivity was virtually independent of the flow rate. The flow resistivity of the foam, using three different samples, was found to be 18400±200 mks rayls m^{-1}.

8.1.5 Measurement of acoustic level difference over thin rigid backed foam

Measurements of level difference between two microphones were made over sheets of the polyester foam. The parameters used in the modelling are shown in Table 8.2.

Level Difference

The field due to a point source above a ground surface can be measured using a single microphone. However when comparing experimental results to theoretical results it is necessary to know the source strength. If two

Table 8.2 Parameters used to model the acoustic properties of the polyester foam.

Parameter	unit	Value
Flow resistivity (σ)	mks raylsm^{-1}	18400
porosity (Ω)	-	0.97
Tortuosity (T)	-	8.0
Grain shape factor(n')	-	68.3
Shape factor ratio(s_p)	-	0.5
thickness (d)	metres	0.040
Poisson's ratio (ν)	-	0.0
$\Re$ Young's modulus(Y)	Nm^{-2}	$2.05.10^5$
$\Im(Y)/\Re(Y)$	-	0.17
Bulk density ρ	Kgm^{-3}	34.0

vertically separated microphones are used instead of one then the transfer function (level difference) between the signals from each of them can be predicted without knowledge of the source strength [89]. It is necessary for the source to act as a spherical source.

Method

The experiments were carried out in an anechoic chamber. A concrete paving slab of dimensions 1.2 × 0.9 × 0.05 metres was placed on a large block of foam on the floor of the chamber. A sheet of the polyester foam CAF16 was mounted on the concrete slab using double sided tape. The dimensions of the foam sheet were 1.5 × 1.0 × 0.04 metres, so the sheet overlapped the concrete slab on all edges.

A Tannoy 25 Watt P.D.25 Loudspeaker was used as the source. A brass tube of length 0.3 metres was attached to the loudspeaker. Previous experiments have shown that this can be considered as a point source at ranges greater than 0.4 metres for the frequency range used. The loudspeaker was suspended from the ceiling. Low pass filtered pseudo random noise was used as the signal. The signal was generated by an Ono Sokki FFT Analyser

which incorporates a signal source.

The microphones used were Brüel and Kjaer 1/4 inch type 4135 cartridges on Brüel and Kjaer type 2639 preamplifiers powered by a microphone power supply type 2805. The microphones were supported on retort stands and were vertically separated. The signal from the microphones was fed to the Ono Sokki FFT Analyser where it was displayed and the transfer function between the two microphones (the magnitude of which, in dB, is equal to the level difference) displayed and recorded.

Before any experiments were carried out the level difference over the foam for both rigid porous parameters and porous elastic parameters was predicted using FFLAGS for a fixed lower microphone height of 0.01 metres, various upper microphone and source heights between 0.1 and 0.4 metres, and for various ranges between 0.4 and 0.8 metres (see figures 8.5 to 8.9). The input physical parameters were those measured and deduced in the above experiments. It was found that for certain geometries the predicted level differences using the two models were significantly different. Measurements of level difference between two microphones were then made over the foam using some of those geometries which generated large differences in predicted level difference between the rigid and elastic models.

The size of the rigid-backed surface and the limitations of the anechoic chamber put restrictions on the geometries and frequencies which were used. The maximum possible range was 0.8 metres. The anechoic range of the chamber is from 500Hz to 6kHz. The maximum microphone height was limited by the lateral size of the surface but geometries with a top microphone height of 0.4 metres and above gave level difference predictions which were very similar for both rigid and elastic models (see figure 8.7) at most frequencies, so this limitation had no effect on the experiment. The predictions using FFLAGS are valid only when kr(the product of the horizontal wavenumber and the range) is much greater than unity for all horizontal wavenumber where the depth dependent Greens function is important, and hence the approximation of the Bessel function in equation 2.25 by two exponential functions is valid. At 500Hz and a range of 0.4 metres $kr = 3.7$

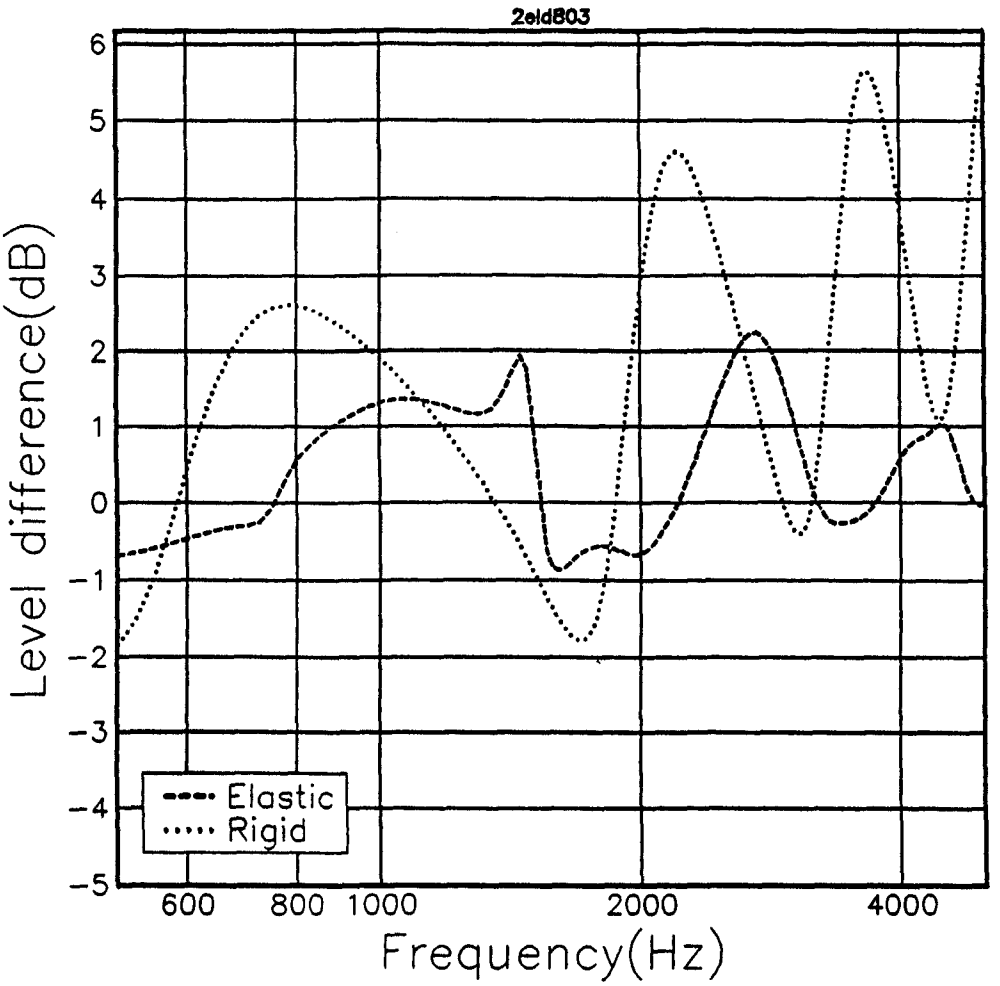

Figure 8.5 Predicted level difference between microphones at heights 0.1 and 0.01 metres at a range of 0.8 metres.

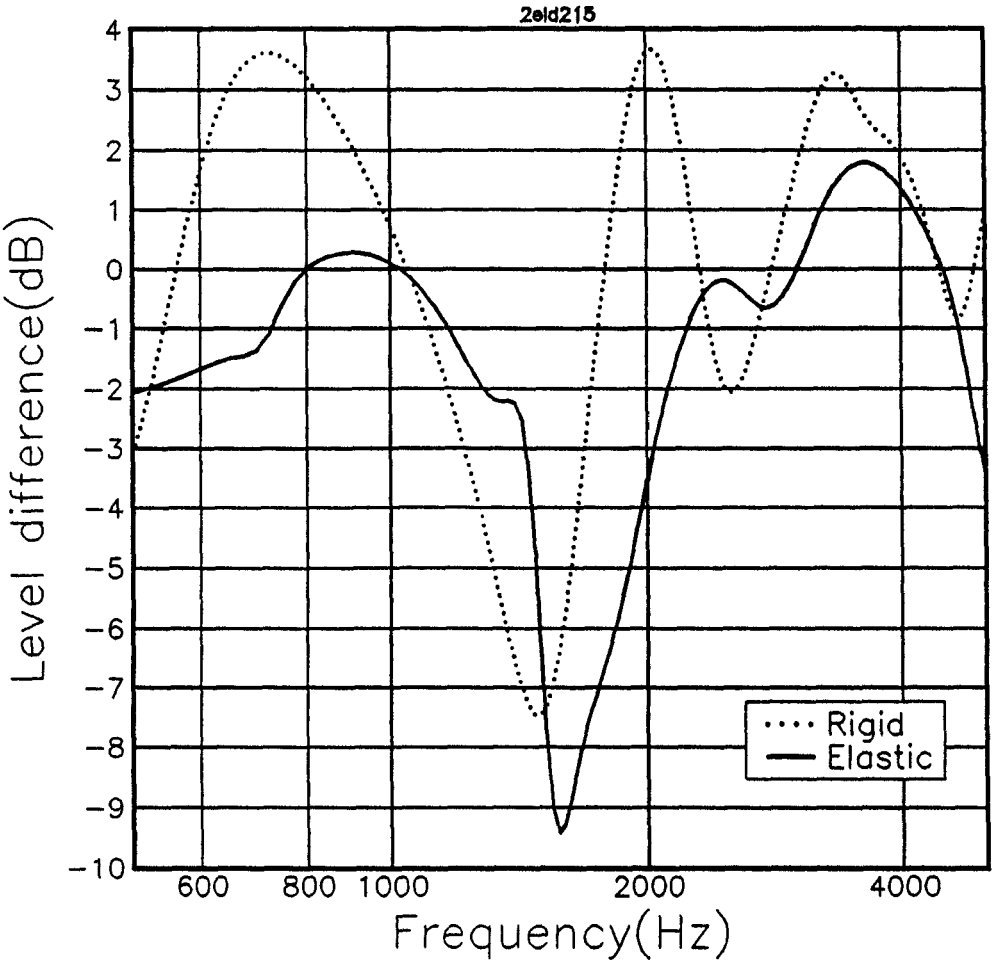

Figure 8.6 Predicted level difference between microphones at heights 0.2 and 0.01 metres at a range of 0.8 metres.

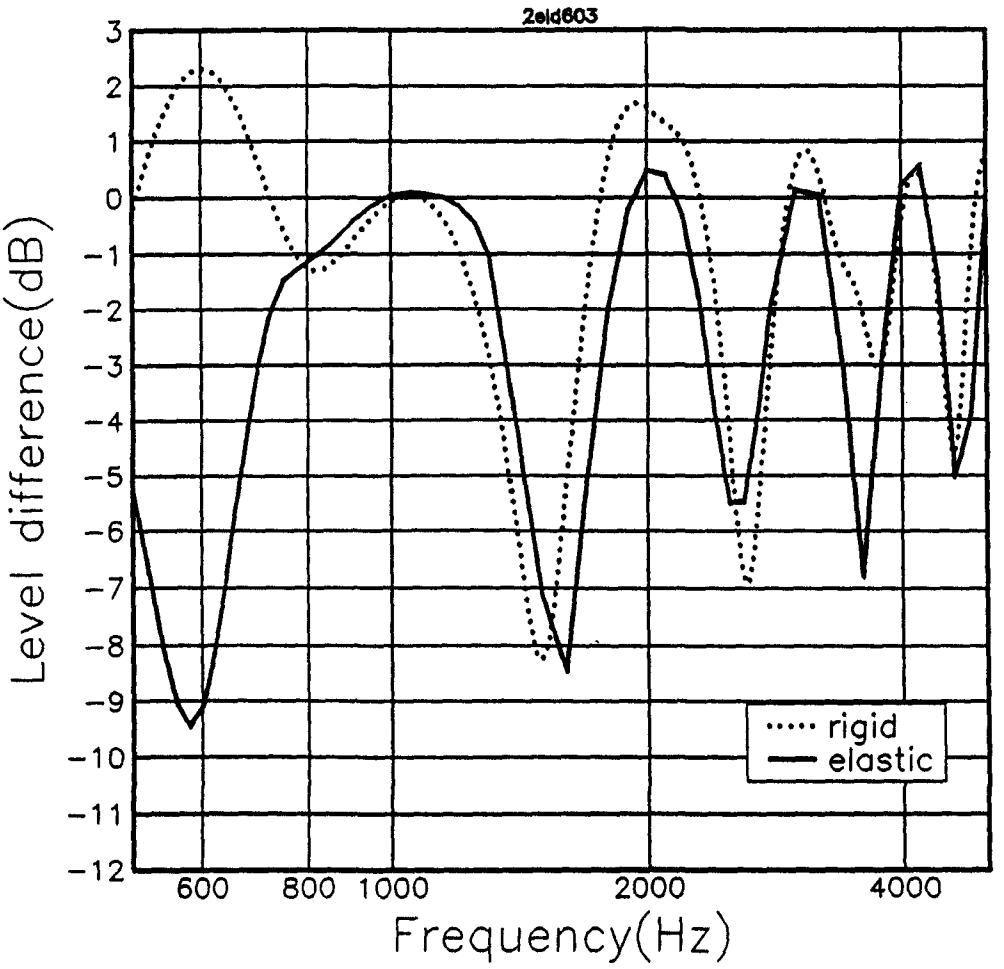

Figure 8.7 Predicted level difference between microphones at heights 0.4 and 0.01 metres at a range of 0.8 metres.

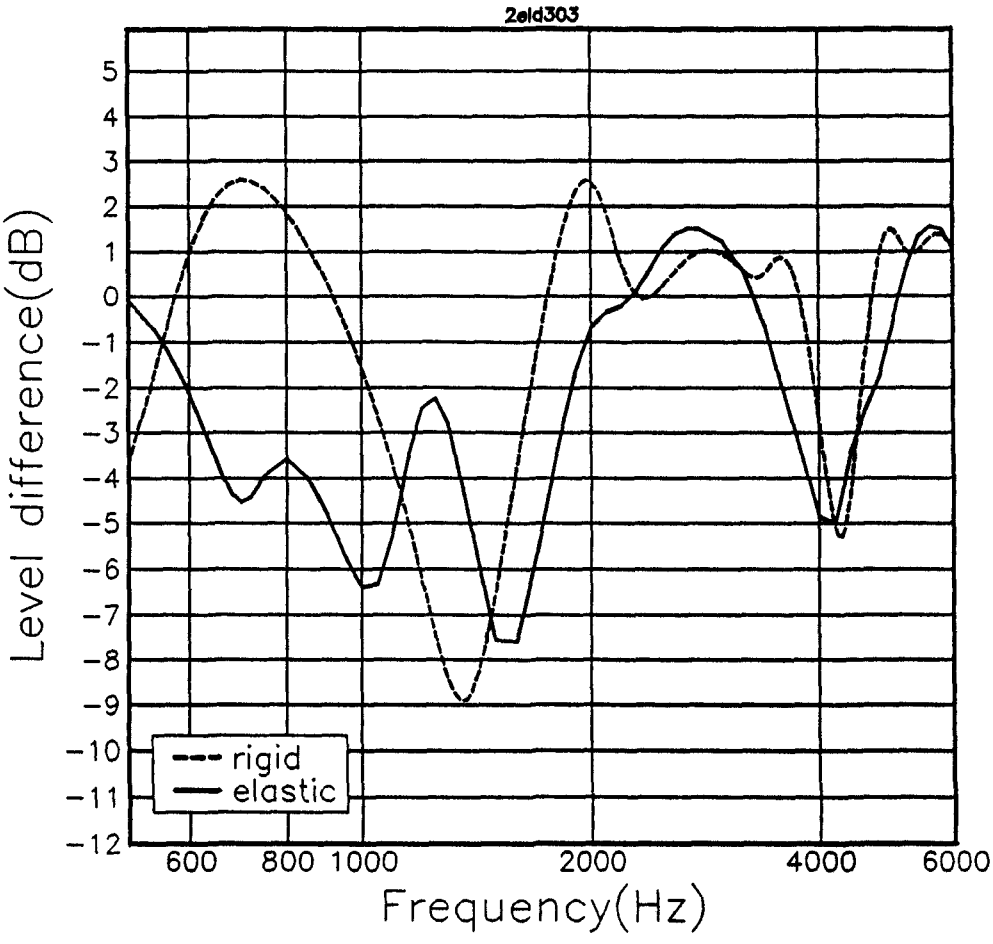

Figure 8.8 Predicted level difference between microphones at heights 0.2 and 0.01 metres at a range of 0.6 metres.

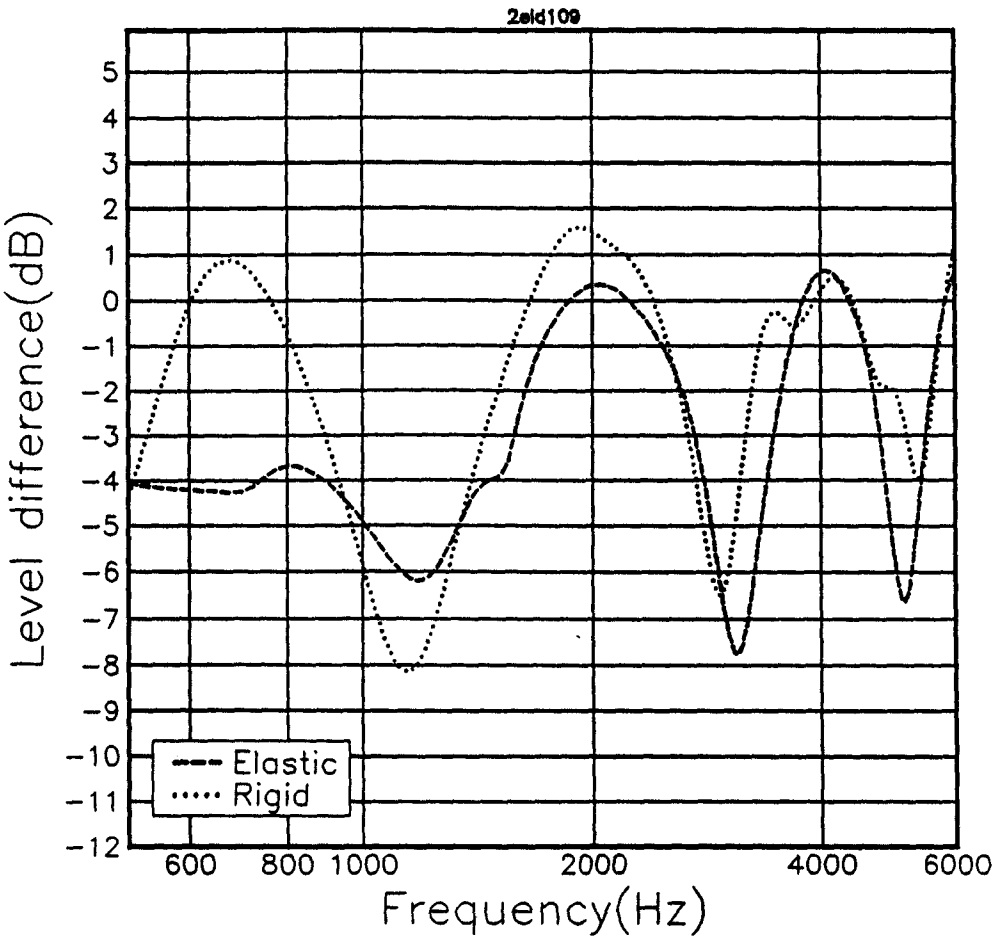

Figure 8.9 Predicted level difference between microphones at heights 0.2 and 0.01 metres at a range of 0.4 metres.

at the peak of depth dependent Greens function. The error in the value of the Bessel function $J_0(3.7)$ due to the use of the exponential approximation made in the FFP is 1.22%. This error will be largest at the lowest frequency used (500Hz).

Results

The data exhibits resonances within the anechoic chamber which are multiples of 80Hz. By applying a three point rolling average it was found possible to remove these. The measured and smoothed data are shown in figures 8.10, 8.11, and 8.12.

Comparisons of the smoothed measured data to that predicted using the two models are shown in figures 8.13, 8.14, and 8.15. The RMS difference between the data (and the smoothed data) and the predicted excess attenuation using the two models was calculated over two different frequency ranges. These differences are tabulated in Table 8.3.

These results show that the porous-elastic model predicts the excess attenuation over the foam surface more accurately (in most cases) than does the rigid-porous model for the same pore parameters. The agreement between the elastic model and the data is better at low frequencies than at high ones, as shown by the smaller rms difference between elastic model prediction and data for the smaller frequency range.

The difference between the data and porous-elastic predictions at high frequency is possibly due to experimental errors in the geometry. The possible errors in any of the distances in the geometry was less than $\pm$10.0mm. In the lower microphone height it was $\pm$2mm. The change in the predicted excess attenuation caused by changing any of the distances by their maximum possible error was negligible. The error in the measured foam thickness was $\pm$1.0mm. This also produces a negligible effect. The chamber may not have been entirely anechoic at the higher frequencies, and this may have lead to errors in the measurements.

Another possible source of the difference between data and model at high frequencies is the increased elastic wave attenuation at high frequencies.

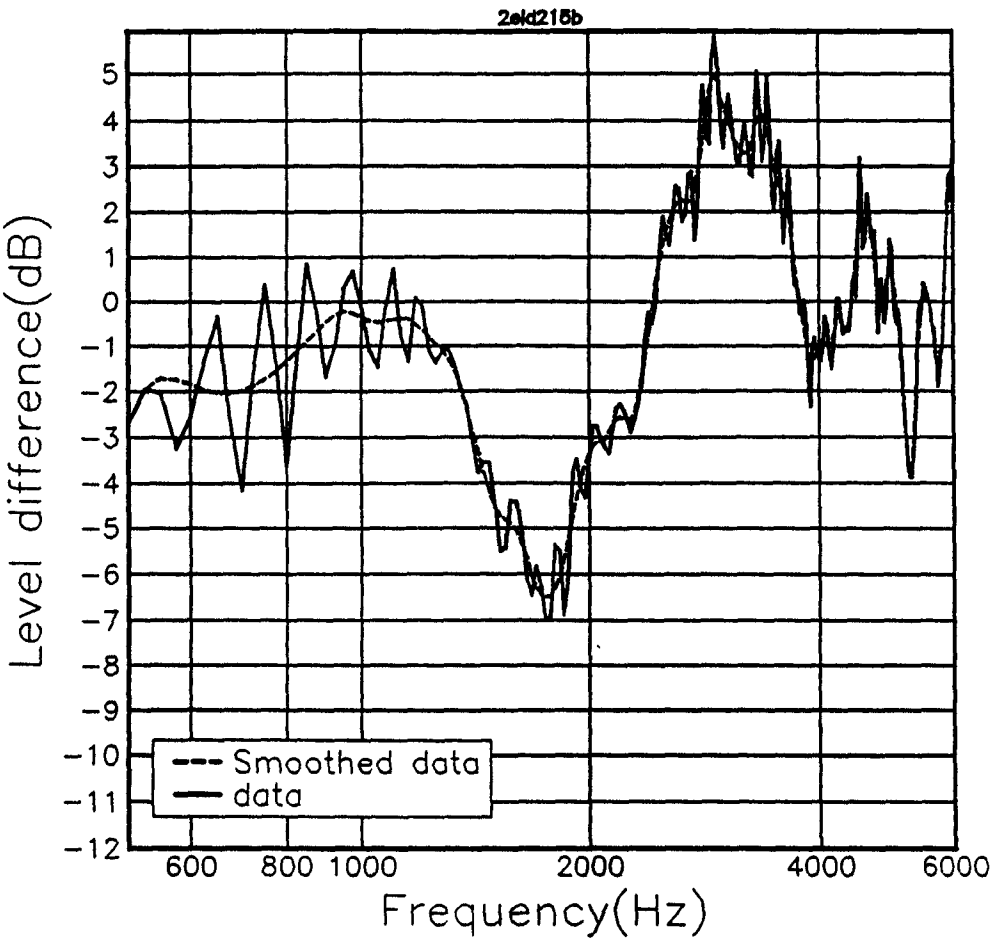

Figure 8.10 Measured and smoothed level difference between microphones at heights 0.2 and 0.01 metres at a range of 0.8 metres, over a 0.04 metre rigidly backed foam layer.

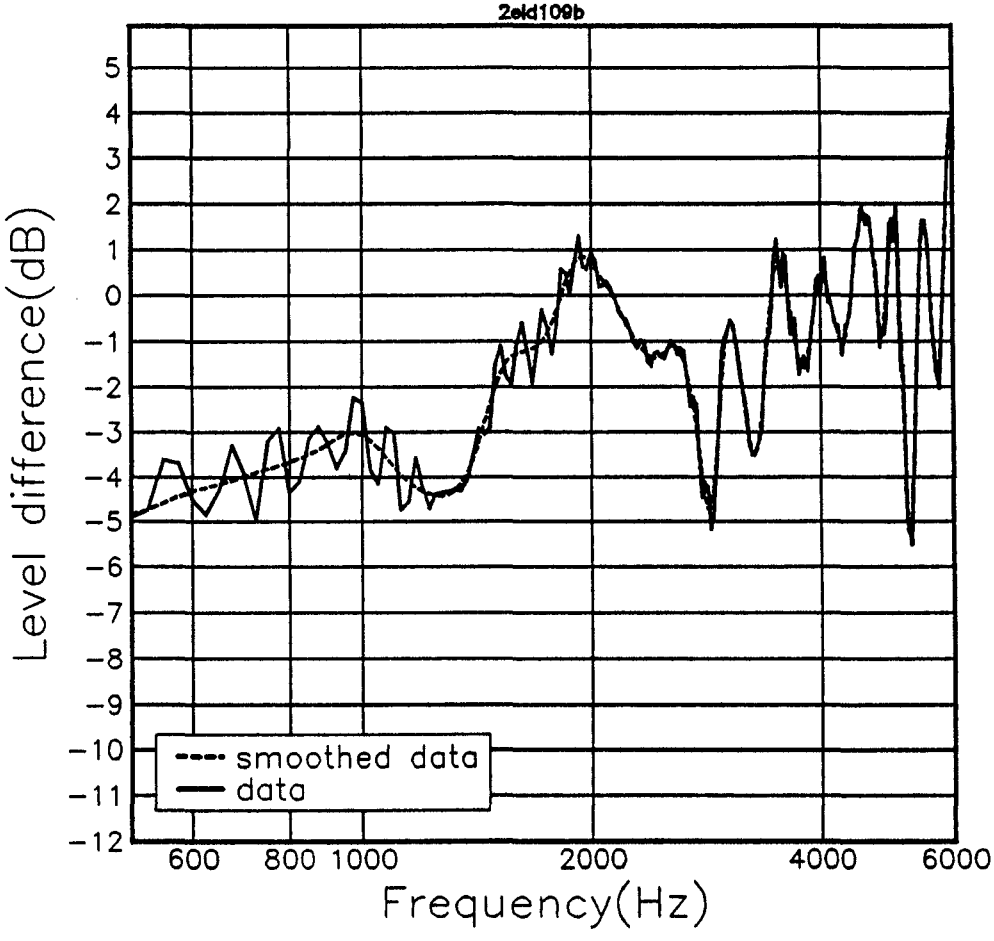

Figure 8.11 Measured and smoothed level difference between microphones at heights 0.2 and 0.01 metres at a range of 0.4 metres, over a 0.04 metre rigidly backed foam layer.

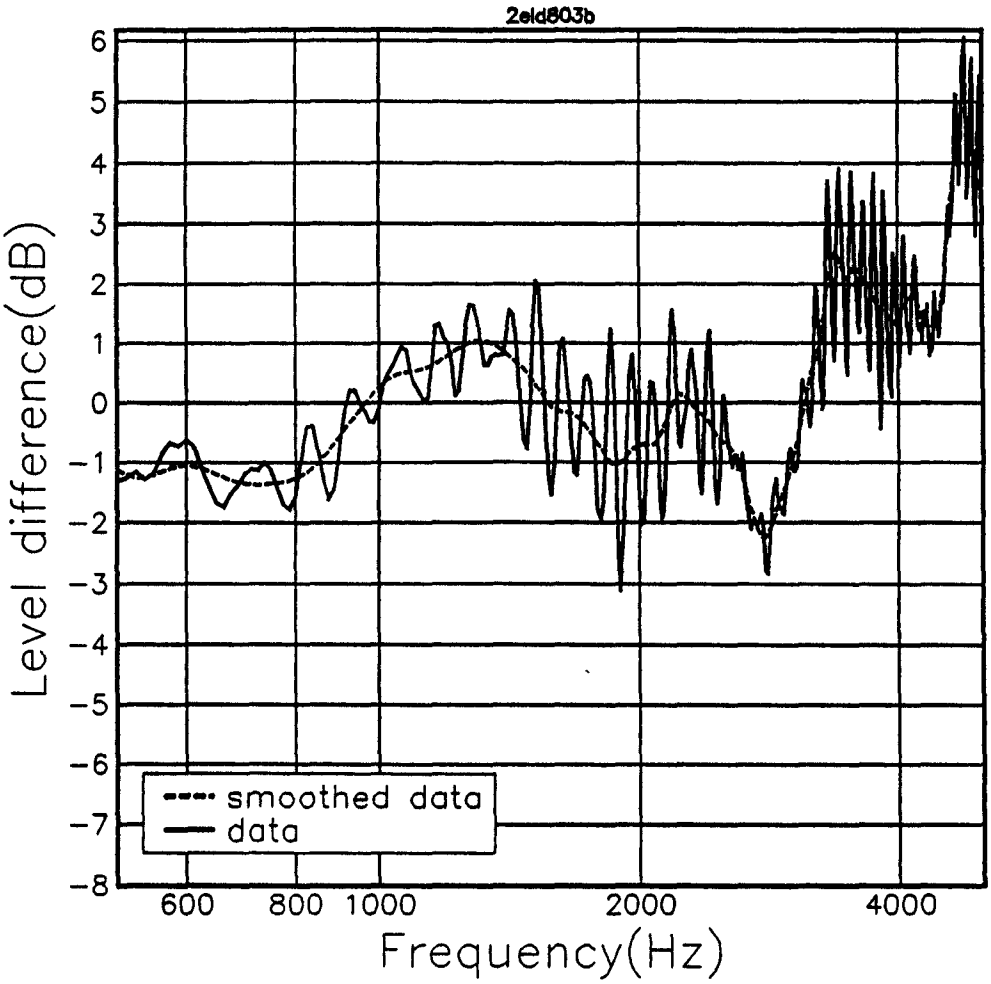

Figure 8.12 Measured and smoothed level difference between microphones at heights 0.1 and 0.01 metres at a range of 0.8 metres, over a 0.04 metre rigidly backed foam layer.

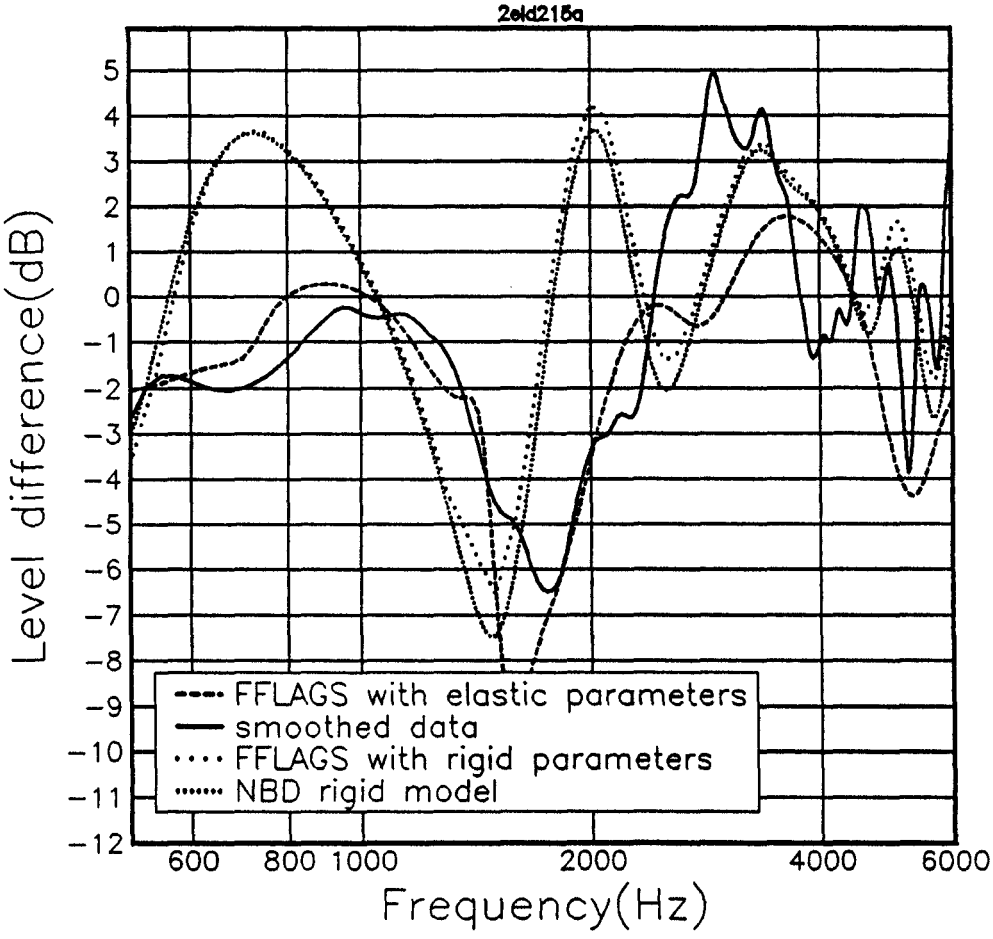

Figure 8.13 Smoothed measured level difference between microphones at heights 0.2 and 0.01 metres at a range of 0.8 metres, over a 0.04 metre rigidly backed foam layer. Compared to the predictions of rigid and elastic models.

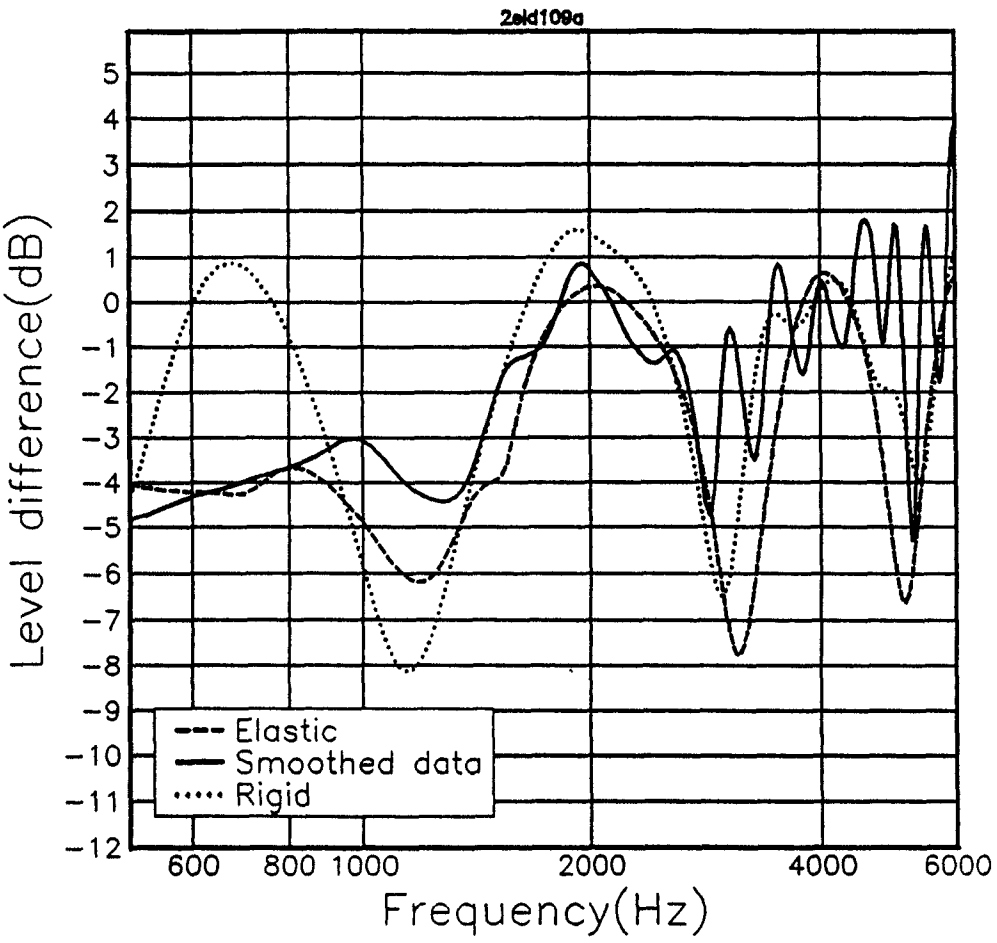

Figure 8.14 Smoothed measured level difference between microphones at heights 0.2 and 0.01 metres at a range of 0.4 metres, over a 0.04 metre rigidly backed foam layer. Compared to the predictions of rigid and elastic models.

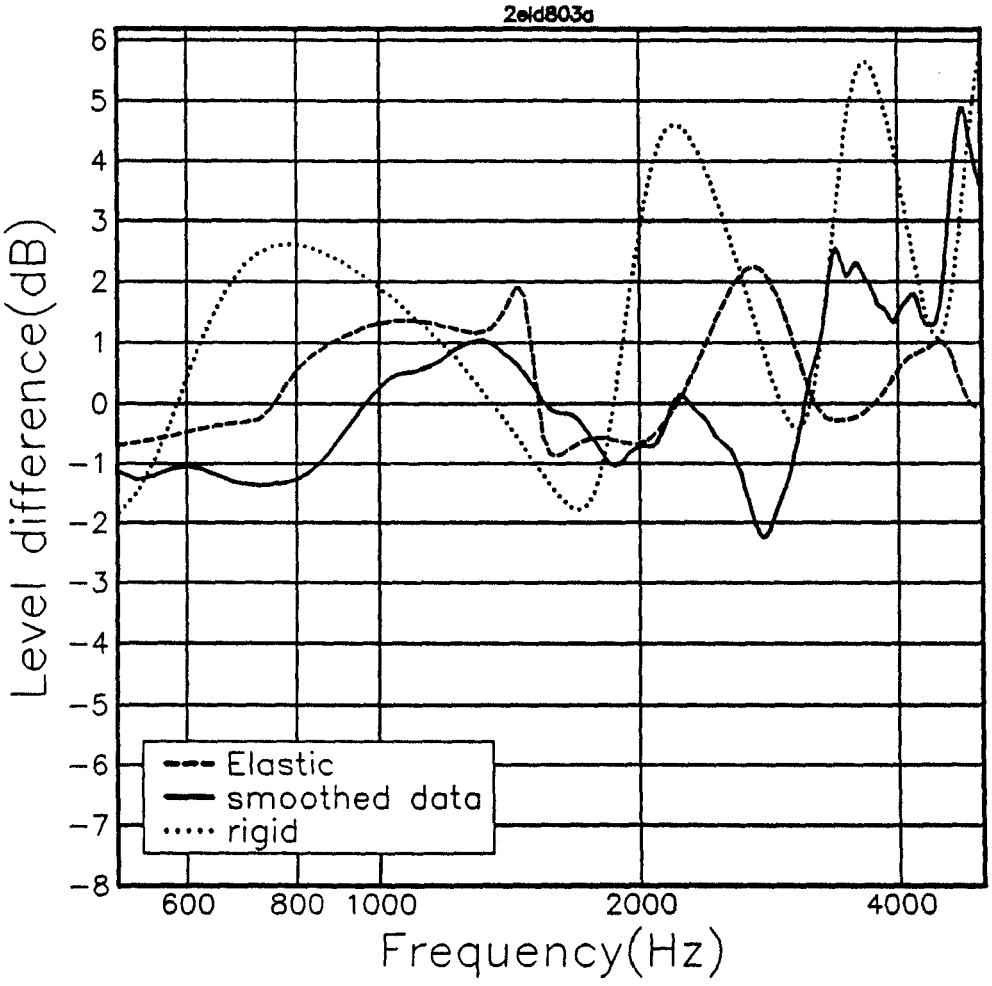

Figure 8.15 Smoothed measured level difference between microphones at heights 0.1 and 0.01 metres at a range of 0.8 metres, over a 0.04 metre rigidly backed foam layer. Compared to the predictions of rigid and elastic models.

Table 8.3 RMS difference between measured and predicted excess attenuation over 0.04 metre rigid-backed foam surface, using rigid-porous and elastic-porous models for three geometries and two frequency ranges. Lower microphone height was 0.01m.

Range (m)	Source and upper receiver height(m)	model	Frequency (Hz)	rms difference (dB)	rms difference smoothed (dB)
0.8	0.2	elastic	500-2000	1.76	1.34
0.8	0.2	rigid	500-2000	4.21	4.14
0.4	0.2	elastic	500-2000	1.95	1.04
0.4	0.2	rigid	500-2000	2.32	2.29
0.8	0.1	elastic	500-2000	0.98	0.87
0.8	0.1	rigid	500-2000	2.79	2.73
0.8	0.2	elastic	500-6000	2.18	2.35
0.8	0.2	rigid	500-6000	3.18	3.11
0.4	0.2	elastic	500-6000	2.58	2.54
0.4	0.2	rigid	500-6000	2.22	2.19
0.8	0.1	elastic	500-6000	2.35	2.30
0.8	0.1	rigid	500-6000	2.41	2.33

Figure 8.2 shows that the imaginary part of the Young's modulus of the material increases with frequency within the measured frequency range. The measurement technique did not allow the Young's modulus to be measured at the higher frequencies used in the level difference experiment.

Because the effects on acoustic propagation of the elasticity of the foam are caused by interference between different propagation paths in the foam, small changes in the propagation constants in the foam may cause large effects in the excess attenuation by moving the frequency of interference maxima and minima. It may be possible to alter the input parameters to improve the fit of the predictions to the data. However this will not be done here for two reasons. Firstly the large number of material input parameters (eleven in all) introduce computational problems, but secondly, and most importantly, the intention here was to compare the two models. If the input parameters were to be altered in order to improve the fit to the data then it might be equally possible (and computationally much easier) to alter the input parameters to the rigid-porous model in order to improve the fit. Therefore altering the parameters to fit the data would invalidate the experiment.

In order to gain some physical understanding of the causes of the differences in excess attenuation brought about by the foam elasticity the possible propagation paths between the point source and a receiver were examined . The possible paths are illustrated in figure 8.16 and are as follows. First there is direct propagation through the air from source to receiver. This path will always form an important part of the received signal. Secondly there is a reflection from the top surface of the porous elastic medium. For the foam material the impedance will be small, and the reflection coefficient from the foam surface will also be small. Thirdly there will be reflections from the rigid non-porous backing. These reflections will be via propagation through the porous-elastic layer. There are three possible body wavetypes in the porous elastic material via which the reflection could take place. These three body waves travel at different velocities, and hence reflections via each of these wavetypes will in general have different phases at the receiver. An-

other propagation path is via an interface wave travelling along the air to porous elastic boundary. This possibility includes an acoustic surface wave travelling above the boundary, and an elastic surface wave travelling within the porous elastic material, and reradiating into the air.

Minima in the excess attenuation spectrum at the receiver should correspond to destructive interference between signals from the source arriving via two different propagation paths. Here we will ignore the possibility of a surface wave, and instead we will examine the reflection paths from the rigid-non-porous backing. In the case of the foam the elastic 'fast' wave and shear wave actually have lower velocities than the mainly pore born 'slow' wave. The largest path length differences (in wavelengths) will therefore be between the direct path and the reflection from the rigid backing via elastic propagation in the foam. If propagation via these paths is important then excess attenuation dips should be seen at frequencies corresponding to phase differences between the paths of π. Figure 8.17 shows the predicted excess attenuation for the two microphones which are used to make the predicted level difference used in figure 8.5. It can be seen that there are dips for the upper microphone at 850 and 1400Hz, and for the lower microphone at 790 and 1400Hz. Table 8.4 shows the path lengths (in wavelengths) for the direct path, and the reflections from the rigid backing, via 'slow', 'fast', and shear propagation in the foam. The phase change on reflection at the rigid-non-porous backing is included.

The table shows that for the lower frequency excess attenuation dip (790Hz and 850Hz for lower and upper microphones respectively) the path length difference between the direct path and the reflection via 'fast' or shear propagation is an odd number of half wavelengths, and hence would lead to destructive interference. On the other hand the higher frequency dips in both cases correspond to a path length difference between the direct path and the backing reflection via the 'slow' wave of an odd number of half wavelengths.

Therefore the differences between the rigid and elastic predictions of the level difference over the foam at low frequencies (less than 1000Hz)

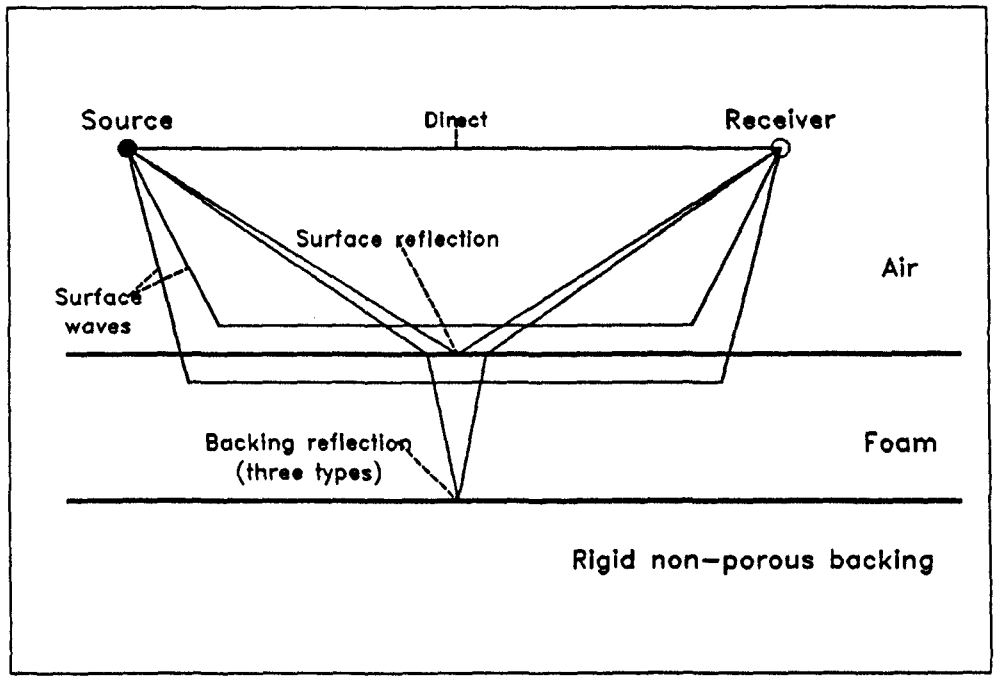

Figure 8.16 Propagation paths between a point source and a receiver over a rigidly backed porous elastic surface.

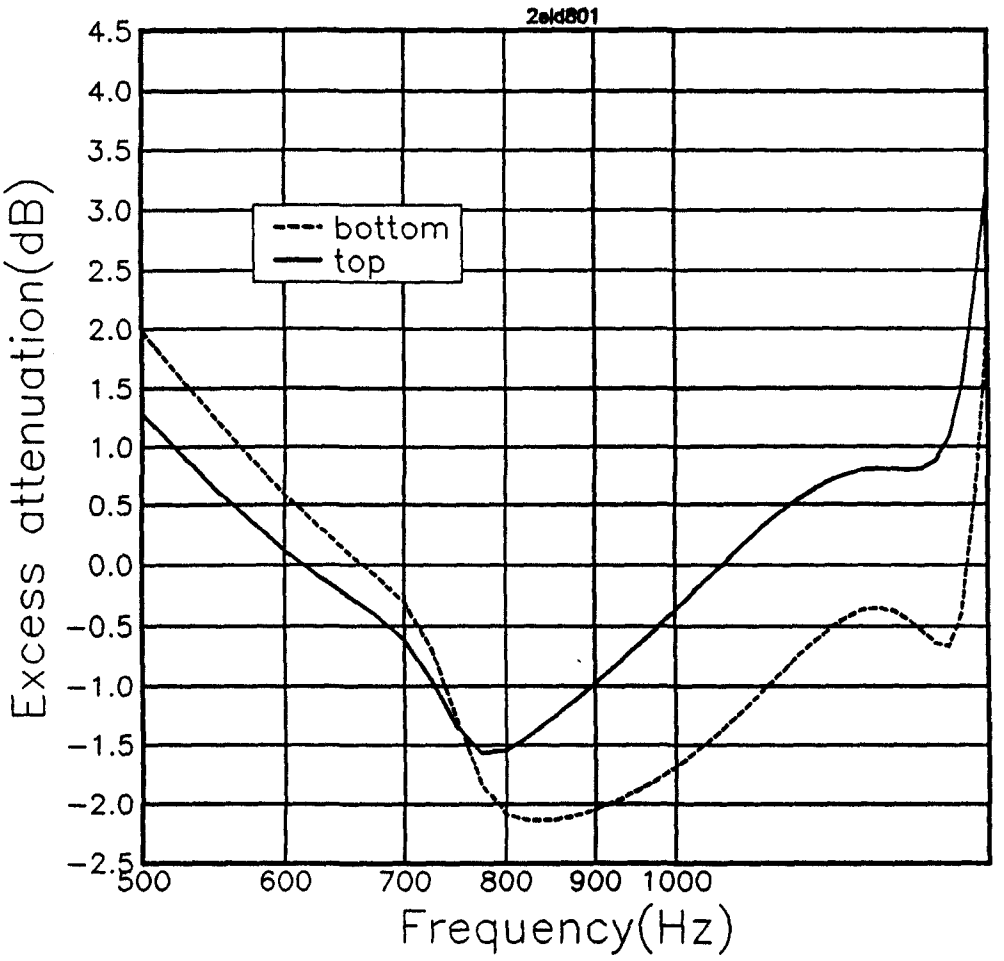

Figure 8.17 Predicted excess attenuation at a range of 0.8metres from a source at height 0.1metres, for receivers at heights 0.01 and 0.1 metres over porous elastic rigidly backed foam layer.

Table 8.4 Path length differences (in wavelengths) between direct path and backing reflected path via slow, fast and shear propagation in the foam layer. Range 0.8 metres. Frequencies are for predicted excess attenuation dips in figure 8.17.

Frequency (Hz)	Receiver height(m)	slow reflection	fast reflection	shear reflection
790.0	0.01	1.03	1.49	1.64
1400.0	0.01	1.43	2.28	2.56
850.0	0.1	1.05	1.48	1.61
1400.0	0.1	1.50	2.32	2.59

can be explained as the effect of interference between the direct signal and reflections at the backing via the elastic wave propagation in the foam.

Because the foam is of such low bulk density and high porosity the predicted 'slow' wave propagation constant is actually influenced by the elastic parameters. This means that the predicted excess attenuation dip caused by interference between the direct path and the 'slow' wave backing reflection is shifted in frequency when the elasticity of the ground is taken into account. This can be seen in figure 8.13 where the dip at 1500Hz is shifted in frequency relative to the rigid-porous model. Figure 8.18 shows the amplitude of the predicted slow-wave propagation constant for the measured foam parameters and the rigid limit.

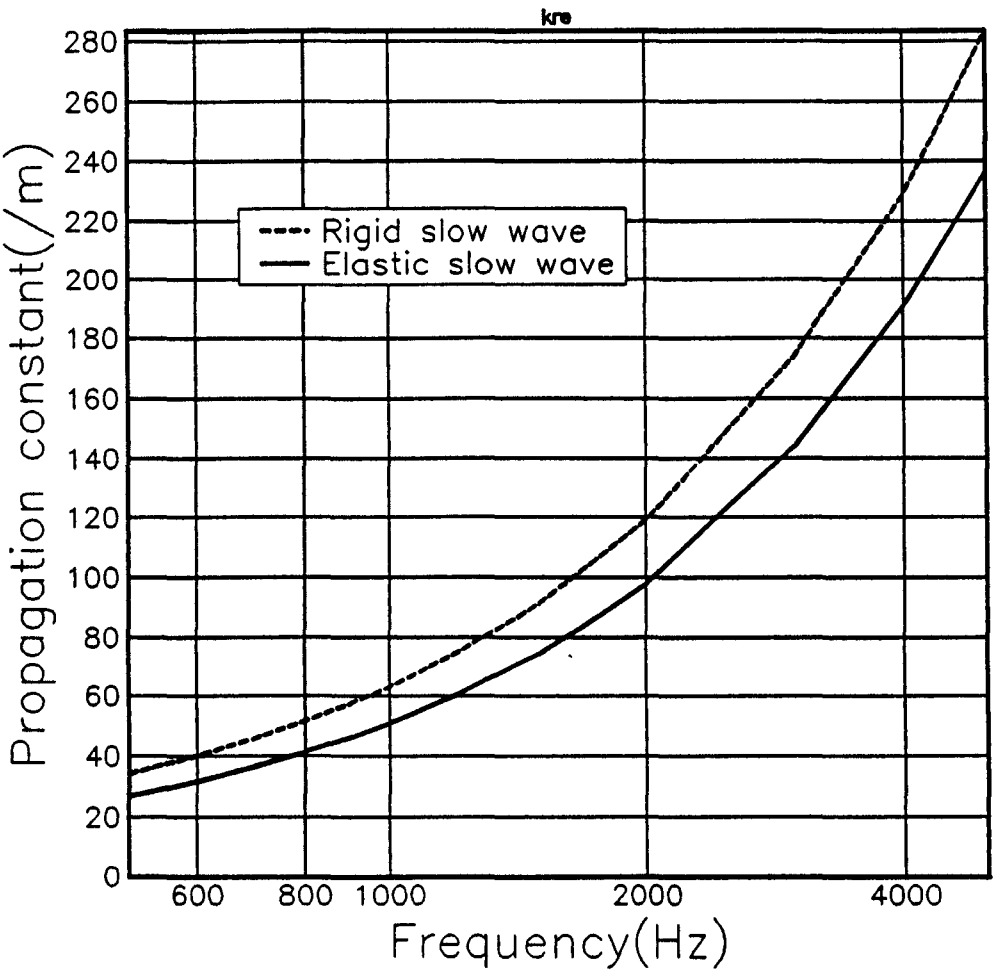

Figure 8.18 Modulus of predicted slow wave propagation constant for elastic and rigid foam parameters.

8.2 Soil bins

8.2.1 Introduction

Using the pulse impedance technique [109] described below Cramond and Don measured the normal surface impedance of a dry soil. The soil was then wetted and the measurement repeated [2]. It was found that the measured impedance exhibited peaks at certain frequencies(see figure 8.19). It was found that the position and amplitude of these changed radically with position of source and receiver; so much so that it proved impossible to obtain similar results by moving equipment back to a position once it had been moved [43]. Various attempts were made to explain this data, but all seem unsatisfactory. It was found that the water had soaked between one and two centimetres into the ground.

One possible explanation for these peaks in impedance is that the wetting of the soil changes the seismic velocity of the soil, reduces the air porosity and increases the bulk density, and hence leads to a discontinuity in both pore wave and seismic velocity at an interface between one and two centimetres deep. Sound incident on the ground will be partially converted into seismic waves, which will travel down to the discontinuity, be reflected at the interface, and travel back to the surface. At the surface at certain frequencies the seismic waves will destructively interfere with vibrations from the air at the same frequency making the surface nearly stationary at these frequencies, hence the reflection coefficient will near unity and the impedance will be very high.

An attempt has been made to reproduce the results of the impedance measurement by modelling the ground as a low seismic velocity, low porosity surface layer overlying a high porosity, high seismic velocity substrate. The program that has been used to do this is MULTIPORO,the development of which has been explained in chapter 3. The original data and the attempt to reproduce it are shown in figure 8.19.

The pore structure parameters of the dry substrate (porosity, grain shape factor, pore shape factor ratio, flow resistivity) were derived from

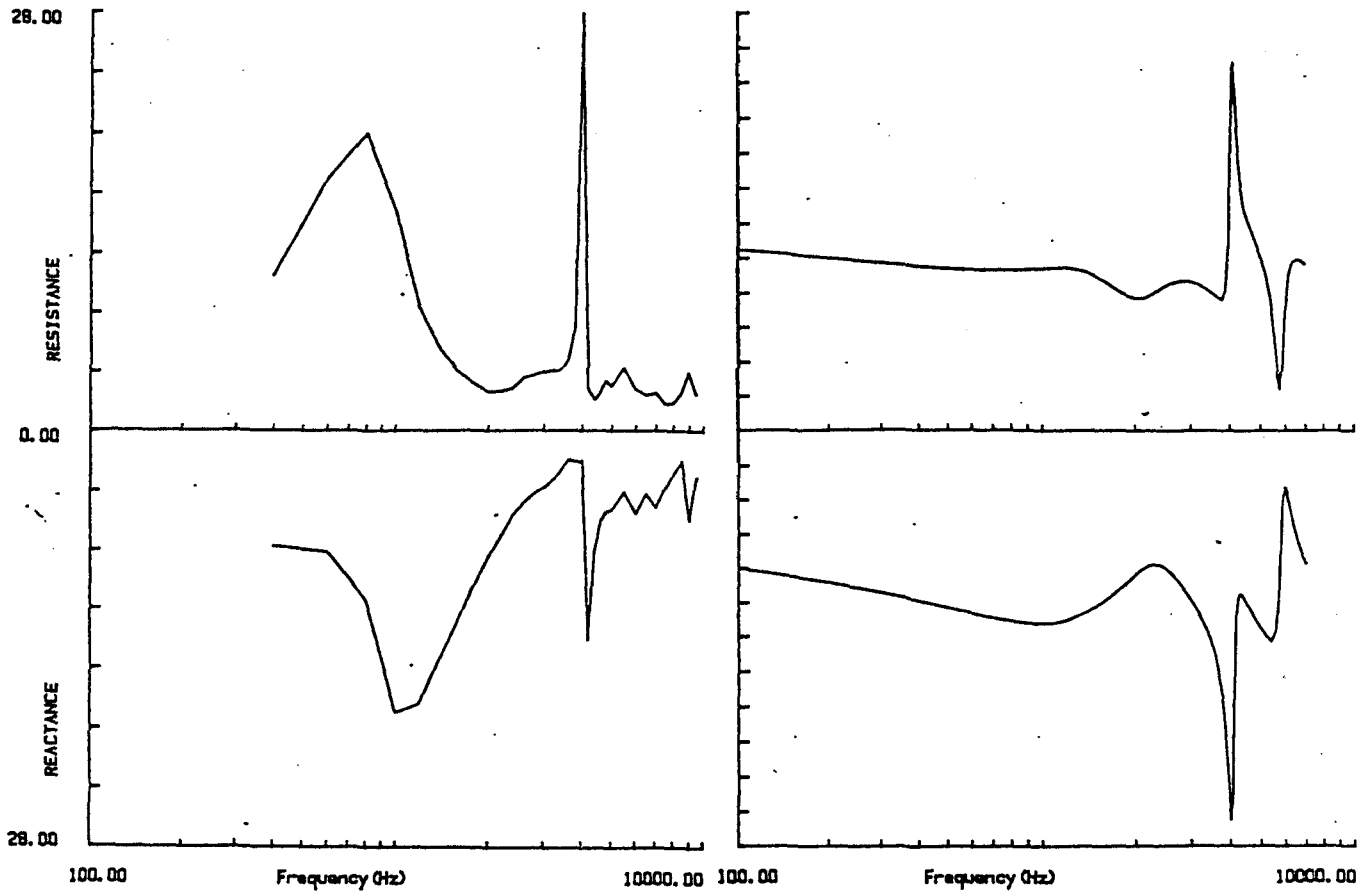

Figure 8.19 (a)Measured normal surface impedance using Crammond and Don's method over a wetted soil, and (b) an attempt to model the impedance.

the measured dry soil impedance by fitting the impedance to the Rayleigh-Attenborough four parameter rigid porous model [79].

No seismic velocities were measured in the Cramond and Don experiments and hence there was no evidence for the change in seismic velocity on wetting. It was decided to create an experiment where as many as possible of the soil parameters , as used in the modified Biot-Stoll model [17], were measured on both the wetted and dry soil, and the effect on the impedance predicted and compared to the measured impedance. In order to achieve this aim a soil bin was prepared at the AFRC Engineering Institute at Silsoe . The soil bin was of dimensions 2 metres by 2 metres by 50 centimetres deep. Dry soil was sieved through a mesh with holes of 6mm diameter to fill the bin to the top. The soil could be described as a clay.

8.2.2 Soil impedance measurement

To measure the normal surface impedance of a soil so that seismic resonant effects could be detected a method which could detect narrow peaks in impedance at high frequency (around 5kHz) was needed. The pulse method due to Cramond and Don [109] was used. The basis of the measurement method is to produce a pulse from a cylindrically symmetric source which is received at a certain range R and a certain angle Φ to the axis of the source, directly, and by a second receiver after travelling the same distance and at the same angle to the source as the direct pulse but via a reflection. If the source is assumed to radiate cylindrically symmetrically then the difference in the received pulses will then be due entirely to the reflection, and a reflection coefficient and hence a normal surface impedance can be directly calculated as a function of frequency by performing a Fourier transform on the pulses and dividing the reflected by the direct at each frequency. In order for these methods to be valid the ground wave must be negligible, and hence a non-grazing geometry is necessary. Another consideration is the size of the effective area of the reflection. This is discussed by Berry and Attenborough [110], who suggest that an area with width approximately half of the source-receiver separation is involved with the reflection.

Technique

The pulse source was a 'gun' firing blank cartridges. A plastic tube sixty centimetres long and three centimetres in diameter was attached to the end of the barrel. The gun was mounted on a tripod with the tube protruding horizontally. The open end of the tube was regarded as the source. This source was assumed to be acoustically cylindrically symmetric. The geometry chosen is illustrated in figure 8.20. The source, direct receiver and reflection receiver were at the corners of a horizontal right-angled triangle of sides 2.60m, 1.77m, 1.90m, and 0.95m above the ground surface.

The accurate setting up of the geometry is vital to this method. The microphones were quarter inch B and K type 4135. The microphones were connected to measuring amplifiers and the output from these recorded as a function of time on an Ono Sokki FFT analyser. A microphone calibrator was used in turn on each microphone and the gain on each measuring amplifier adjusted until the signals were within half a dBV of each other. The two microphones were then placed very close to each other but not touching approximately 2.6 metres from the source along the line of the source tube. The gun was fired about eight times, and each time the pulses received at each microphone recorded using the FFT Analyser in a 4ms time window. These recordings were later used for calibration.

The microphones and source were then moved into the geometry illustrated in figure 8.20. The gun was fired between eight and twenty times and each time the pulses received at the microphones recorded using the FFT Analyser.

Analysis of the pulses was carried out using the programs in appendix C. The programs rename the data files, align the pulses(though not entirely automatically), average the sets of aligned pulses, perform a Fourier transform on the pulses, perform a calibration using the calibration pulses, and produce a normal surface impedance as a function of frequency including a calibration correction calculated from the calibration pulses.

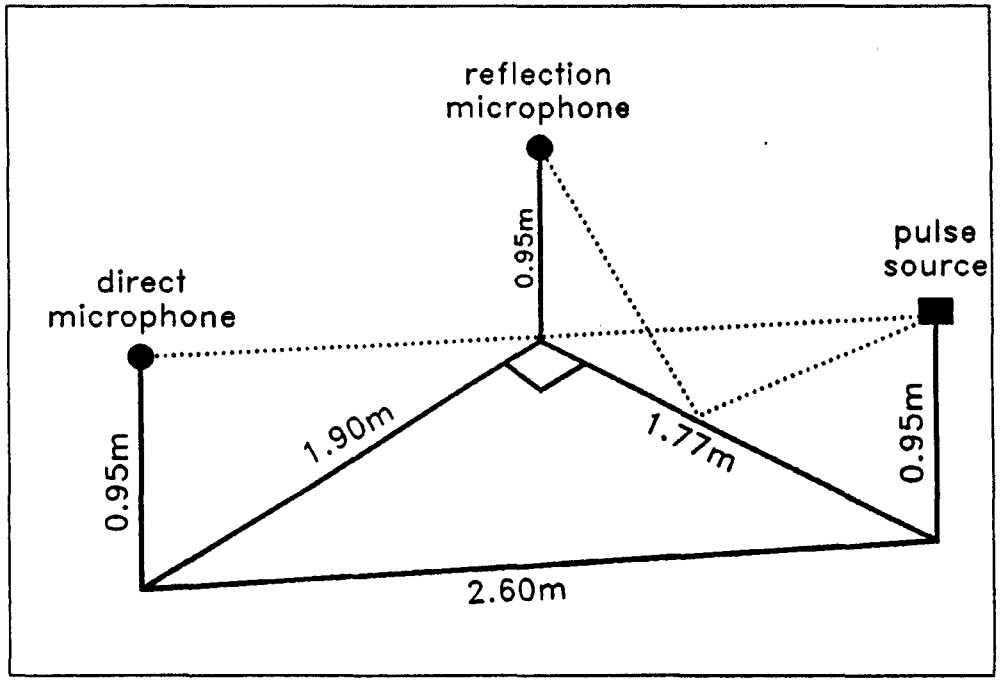

Figure 8.20 The experimental geometry used in the acoustic impedance measurements.

Errors in the method

During the collection of data the avoidance of extra reflections is of great importance. If even a small signal from a reflection is recorded which begins whilst the main pulse is continuing this can lead to spurious peaks in the final impedance calculated.

The geometry must be set up accurately so that the path lengths for direct and reflected paths are identical. As the direct and reflected pulses are recorded simultaneously the error in the geometry can be calculated from the time difference in the arrivals of the direct pulse at one microphone and the reflected pulse at the other.

The other important possible source of error is in the time alignment of the pulses when they are being averaged. An error in the alignment can also lead to spurious peaks in the impedance.

8.2.3 Acoustic-seismic coupling measurements

If the seismic velocities near to the soil surface are known and the pore parameters near to the soil surface are known then the acoustic-seismic coupling can be predicted.

An experiment was performed to measure the acoustic-seismic coupling ratio (the ratio of the sound pressure level in the air to the particle acceleration in the ground). In this experiment an acoustic point source was placed on one side of the soil bin at a height of 7cm. Near to the centre of the soil bin, at a range of one metre from the source, a Brüel and Kjaer accelerometer type 4367 was buried to a depth of one centimetre with its sensitive axis vertical. Above this a Brüel and Kjaer 1/4 inch microphone was placed at a height of 7cm. The experimental geometry is shown in figure 8.21. The microphone was calibrated using a Brüel and Kjaer microphone calibrator type 4230. Low pass filtered white noise was played through the point source and the spectra of the received signals from the microphone and accelerometer were recorded at frequencies up to 10kHz on an Ono Sokki FFT analyser. Measurements of the signals at the microphone and geophone were also made without the noise source turned on. The signal

without noise was subtracted from the signal with noise for microphone and geophone.

8.2.4 Seismic velocity measurements

In order to gather data pertinent to the prediction of impedance and acoustic-seismic coupling over a wetted surface the wet and dry seismic velocities of the material very close(upper 1 or 2 centimetres) to the surface were measured. To achieve this a small scale seismic measurement technique was developed to measure near surface seismic velocities of a soil in situ.

Technique

This technique involved the use of a pulse source and two receivers. Velocities were calculated by measuring the difference in arrival times of a pulse between the two horizontally separated receivers. This is a scaled down version of a standard seismic refraction survey technique [111]. The major differences are in the design of the source to give a reproducable high frequency signal, the use of accelerometers rather than velocimeters, giving greater high frequency sensitivity and hence faster rise times at first breaks, and the horizontal orientation of the accelerometers rather than vertical, giving greater sensitivity to horizontally travelling longitudinal vibration.

The source consisted of a 15cm steel rod mounted vertically on the centre of a circular brass weight of mass 1.0kg. From the top of this rod a horizontal rod was attached from which was suspended a small rubber ball on a cord. To cause a seismic pulse the ball was swung out so that the cord was horizontal, and then released and allowed to strike the side of the weight.

The seismic receivers were Brüel and Kjaer accelerometers type 4367 which have a mass of 13 grams and a minimum measurable signal amplitude of approximately $5mms^{-2}$ in the frequency range 0.1 to 5000Hz. The maximum transverse sensitivity was approximately 1% at 30Hz. Each accelerometer was connected to a charge amplifier, and the output signal

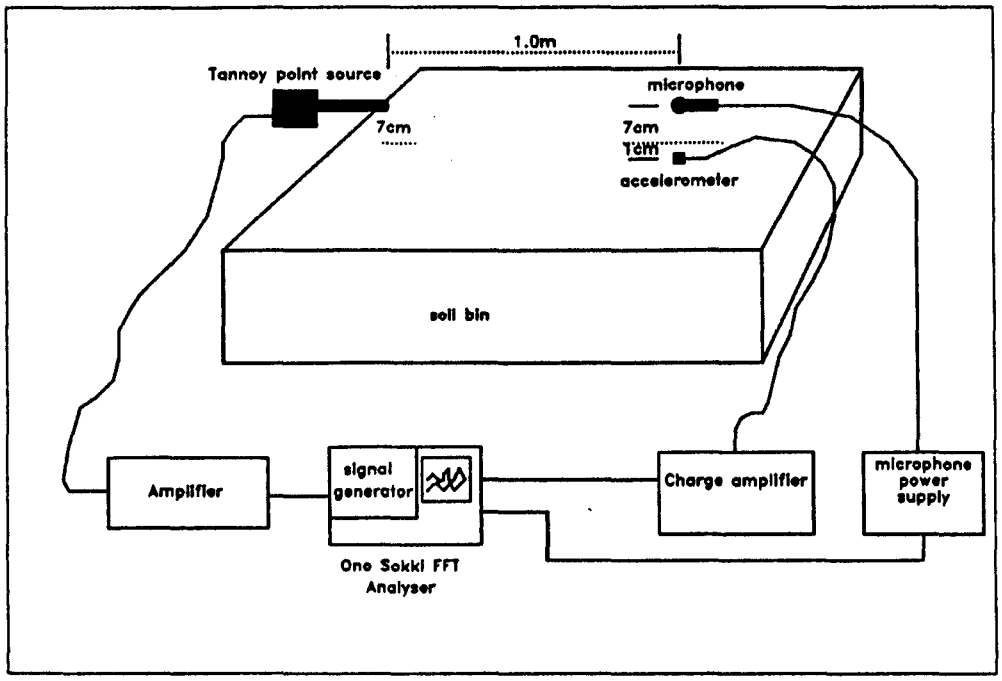

Figure 8.21 The experimental geometry used in the acoustic-seismic coupling experiment.

recorded as a function of time on floppy disc using an Ono Sokki FFT analyser.

Two types of experiment were made, the first to measure longitudinal(fast) velocity, the second to measure transverse velocity.

In the first experiment the first accelerometer was placed next to the source with its sensitive axis pointing horizontally away from the source on the opposite side of the source from the rubber ball. The second accelerometer was placed a distance of 0.7 or 1.0 metres from the first one on a line through the rubber ball, the centre of the brass weight, and the first accelerometer, again with its sensitive axis pointing horizontally away from the source. The rubber ball was lifted and allowed to hit the brass weight, and the signal at each accelerometer was recorded as a function of time. This was done three or four times. The second accelerometer was then moved closer to the source by 5 or 10 centimetres and the experiment repeated. This was done repeatedly until the two accelerometers lay next to each other. The experiment is illustrated in figure 8.22

The second experiment was identical to the first except that the accelerometers were placed with their sensitive axes at right angles to a line through their centres and the centre of the brass weight, and the source was oriented so that the line through the centres of the weight and the rubber ball were at right angles to a line through the centres of the accelerometers.

To calculate the velocity of the seismic waves the time delay between the first arrival of the signal at the first and second accelerometers was plotted against the distance between them. For the first experiment the first arrival should be the longitudinal wave, for the second experiment the first arrival should be a horizontally polarized transverse wave, given that the longitudinal signal should be undetected by the accelerometers in this orientation, and visco-elastic surface waves being slower than the transverse arrival.

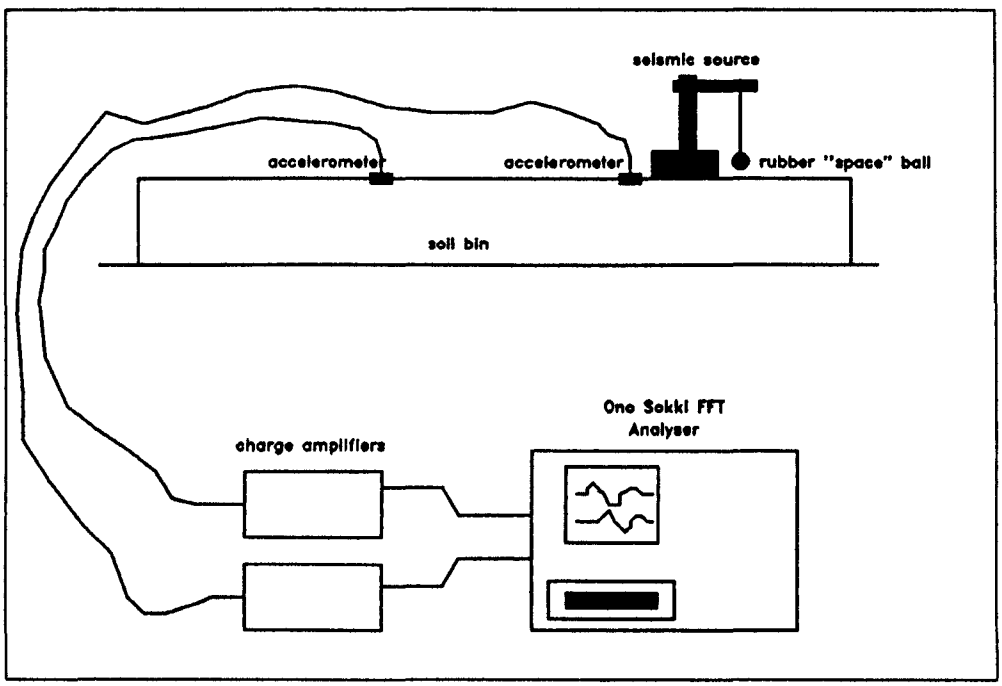

Figure 8.22 The geometry of the seismic velocity measurement method

Sources of error and assumptions

There are several possible sources of error; in the longitudinal velocity experiment errors in distance measurement between the two receivers will lead to a proportional error in the calculated velocity. In the transverse velocity experiment the above source of error is combined with problems of alignment of source and receivers so that they do not detect a longitudinal arrival before the transverse one.

The assumption made in the interpretation of the experimental results as measurements of the near surface seismic velocities is that the soil seismic structure is such that the first arrival at the receivers is via a direct straight line path along (or near to) the surface in the mode of interest. This assumption is supported by the experimental results, as the straight lines in figure 8.23 pass close to the origin.

Because the received pulses consist of arrivals from surface wave modes and deeply reflected and refracted signals it is very difficult to use the signals to examine attenuation or dispersion of the wavetype of interest. It is assumed that as in most geological material the body waves are non dispersive. In measuring the seismic velocities in the dry soil this assumption means that either vibration in deeper, high velocity parts of the soil is not produced, or that the soil near to the surface is seismically homogeneous. The homogeneity was tested by burying the second accelerometer a measured distance vertically beneath the source at various depths and examining the change in apparent seismic velocities with depth.

8.2.5 Measurement of soil porosity, bulk density and flow resistivity

The porosity and bulk density of the soil were calculated by finding the mass of a known volume of the soil. The soil was then dried in an oven to remove the water and reweighed. Knowing the soil mass, and assuming values for the density of the lost water of $1000 \mathrm{kg} m^{-3}$ and density of the dry solid material of $2650 \mathrm{kg} m^{-3}$ the air porosity Ω of the soil could be calculated. The air porosity and bulk density are shown in table 8.5. Flow resistivity

Table 8.5 The measured material parameters of the dry and wetted clay

Parameter	Units	Value
Dry flow resistivity	mks rayls m^{-1}	10100
Dry porosity (measured)	-	0.53
Dry porosity (deduced)	-	0.56
Dry grain shape factor	-	0.5
Dry p-velocity	ms^{-1}	$64. \pm 2.$
Dry s-velocity	ms^{-1}	$46. \pm 2.$
Wet p-velocity	ms^{-1}	$65. \pm 2.$
Wet s-velocity	ms^{-1}	$45. \pm 2.$
layer thickness	m	0.04 ± 0.01

was measured using the flow meter described in section 8.

8.2.6 Dry soil experiments

Several experiments were then carried out on this soil. The first of these was the measurement of seismic velocities on the surface of the soil using the technique described in section 8.2.4. The maximum line length used was 70cm. The line was located along a diagonal of the box. This was so that the reflected and refracted seismic paths via the box walls would have the longest possible path length, and hence would be unlikely to cause the first arrivals. The first arrival times are shown graphically against distance from the source in figure 8.23 and the seismic velocities calculated from these are tabulated in table 8.5. The normal surface impedance of the soil was measured using Cramond and Don's method described in subsection 8.2.2.

The acoustic and seismic signals due to a point source were measured as described in section 8.2.3.

8.2.7 Wet soil measurements

After the dry soil measurements had been completed the soils were wetted by distributing water evenly over the surface using a watering can. The same experiments were then repeated. The aim of the seismic measurements was

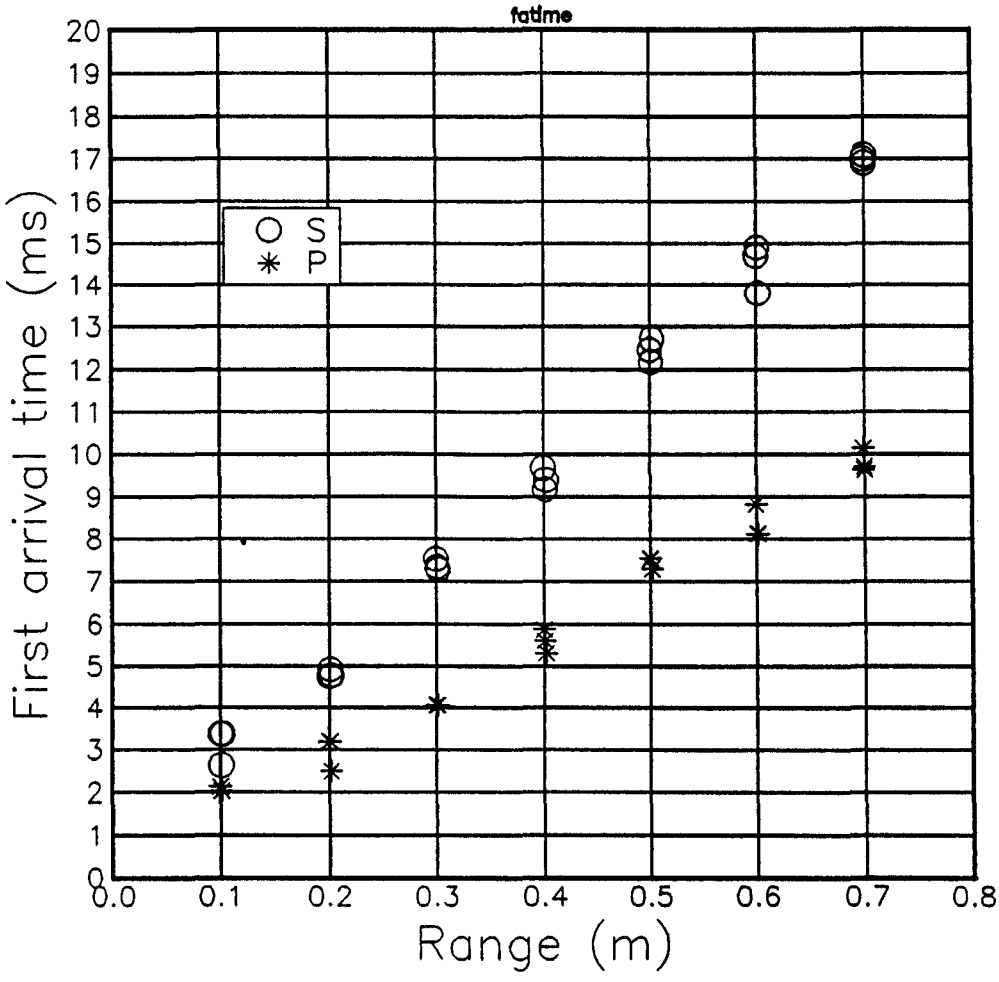

Figure 8.23 First arrival times against range for seismic velocity measurements

to measure the seismic velocities in the wetted surface layer. It was found that when the wetted layer was thin the measured seismic velocities were identical to the dry velocities. Therefore the soil was wetted to a greater depth by the addition of more water and alllowing it to soak in. It was found that when the wetted layer thickness reached 0.2m the measured seismic velocities were still within the error bounds of the dry soil velocities.

8.2.8 Analysis of results

Impedance

The impedance measurements over the dry soil gave results which were consistent with the directly measured pore parameters of the soil. The measured impedance is shown in figure 8.24. Pore parameters were deduced from the measured dry impedance by finding a best fit to the measured impedance using a three parameter model [89] and assuming a value for the pore shape factor ratio (s_p) of 0.375. These deduced parameters are shown in table 8.5.

The impedance measurements over the wetted soil gave the large peaks in the impedance which were expected. However for a given set of pulses the impedance derived from any subset were different to each other, having large peaks in the impedance at different frequencies for different subsets. This occurred for several sets of pulses measured in different atmospheric conditions on different days. It was concluded that for the wetted soil the reflection coefficient was very close to unity for a wide frequency range. If a very small amount of noise was introduced to the received reflected pulse then the apparent reflection coefficient was increased to above unity. This would explain the failure to produce consistent results using this method. The method was badly conditioned for calculating impedance for materials with a reflection coefficient very close to unity. Examples of the calculated normal surface impedance over the wet soil are shown in figure 8.25

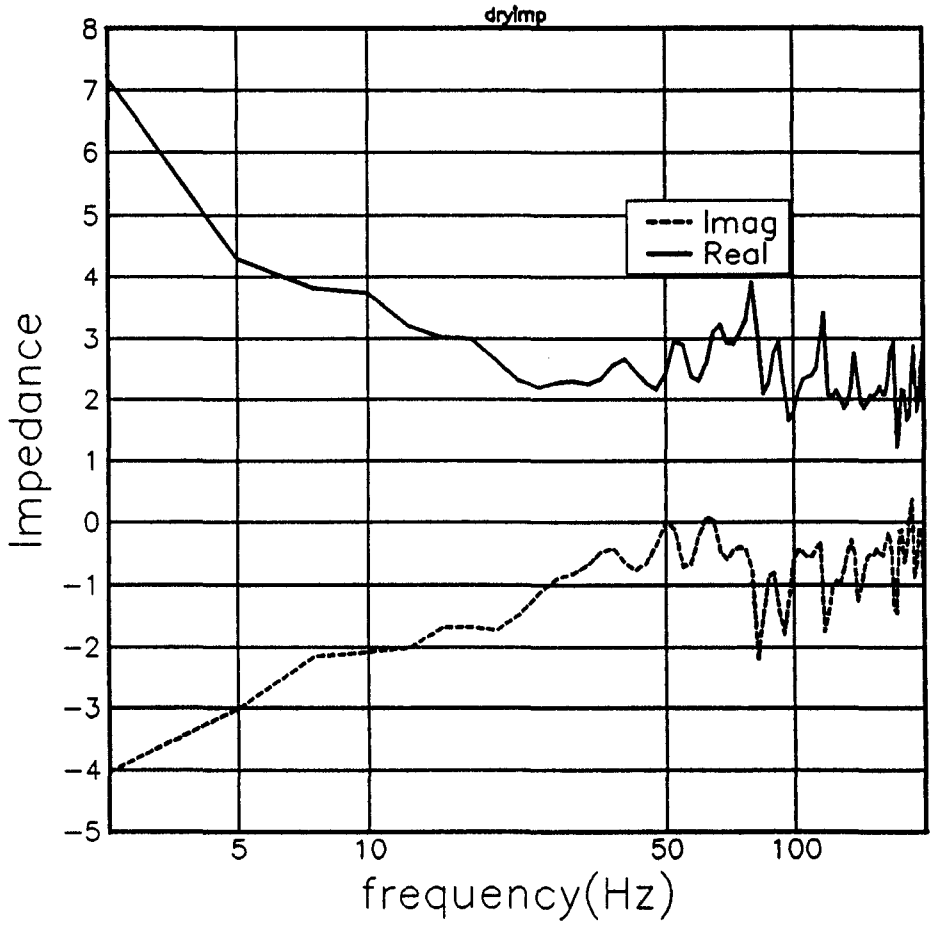

Figure 8.24 Normal surface impedance of the dry soil measured using Cramond and Don's method.

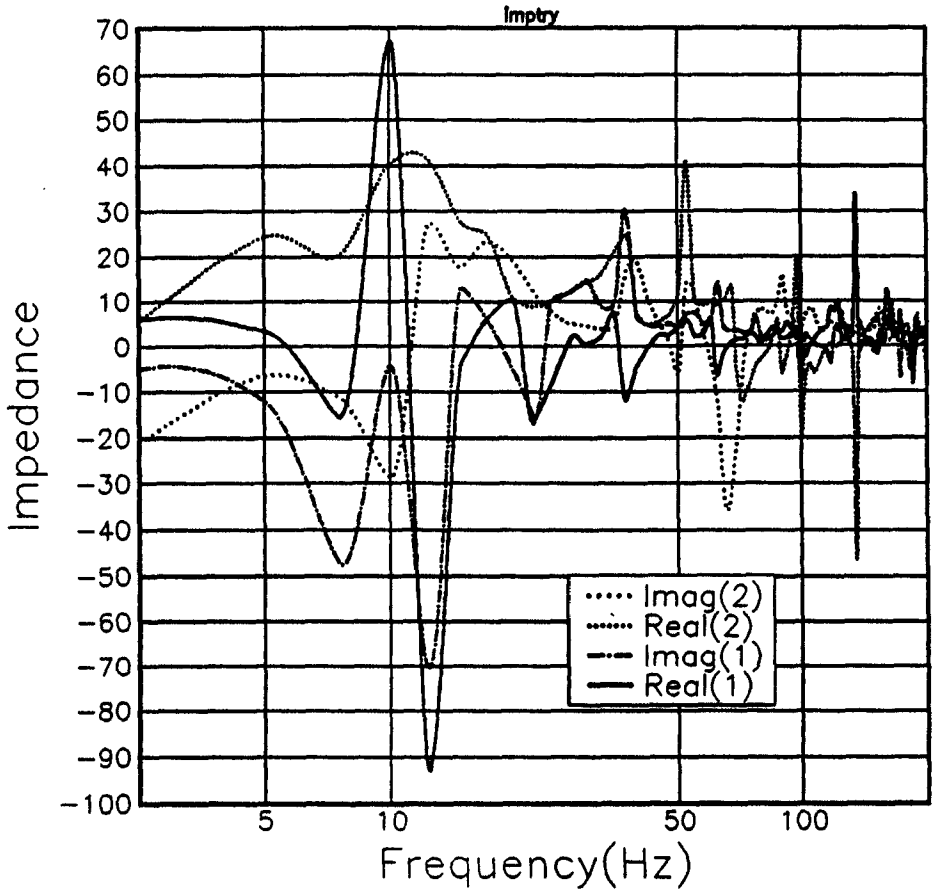

Figure 8.25 Examples of the calculated normal surface impedance over the wetted soil using different subsets of a set of pulses.

Acoustic-seismic coupling

The ratio of the vertical particle acceleration at 1cm depth in the soil to the sound pressure level at a height of 7cm above the soil was calculated from the results for both the dry and wetted soil. The soil bin had a depth of 50cm, and other dimensions of 2 metres by 2 metres. Therefore at low frequencies the box would exhibit box resonances. If the imaginary part of the elastic wave propagation constant is 0.05 of the real part and the maximum elastic wave velocity is $70ms^{-1}$ in the dry soil then the maximum amplitude of a signal travelling down from the top surface reflecting from the bottom of the box and returning to the top surface (assuming a perfectly reflecting base) is 7.10^{-3} of the incident amplitude at 1kHz. This indicates that at 1kHz the box resonances will be sufficiently damped so as to be insignificant. Therefore the analysis of the acoustic-seismic coupling was confined to a frequency range above 1kHz.

At frequencies above 1kHz the load imposed by the dense accelerometer on the less dense soil may lead to errors in the measurement of the seismic signal. To overcome this the predictions made were predictions of the ratio of the acoustic-seismic coupling ratio in the dry soil to the acoustic-seismic coupling ratio in the wetted soil. It was this ratio that was compared to the data. The use of this ratio is valid provided that the sensitivity of the accelerometer to the acceleration of the soil is the same in both the wet and the dry case.

The measured ratio of the acoustic-seismic coupling ratios for the wet and dry soil is shown in figure 8.26. Also shown is the best fit ratio using the parameters in table 8.5 and 8.6 It can be seen that the wetting of the soil has the effect of increasing the acoustic-seismic coupling in the frequency range from 1200Hz to 3200Hz and from 3600Hz upwards.

The ratio of the acoustic-seismic coupling coefficients in the wet and dry soil was modelled using FFLAGS. The measured and deduced parameters shown in table 8.5 were varied only within their error bounds, and the unknown parameters were varied to obtain the best fit with the data.

The parameters found by fitting the predicted ratio to the measurements

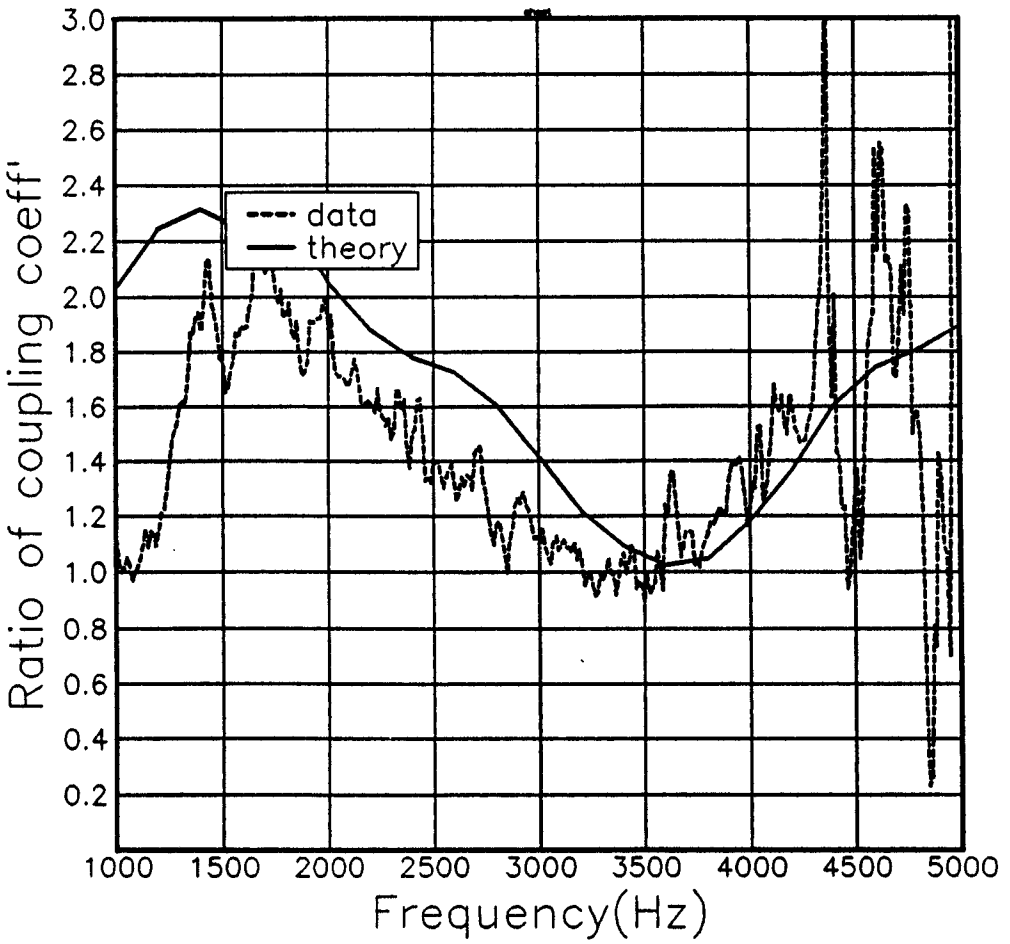

Figure 8.26 The measured and fitted ratio of the acoustic-seismic coupling coefficient in the wet soil, to the acoustic-seismic coupling coefficient in the dry soil.

Table 8.6 The material parameters of the dry and wetted clay found by fitting the ratio of acoustic-seismic coupling ratios.

Parameter	Units	Value
wet flow resistivity	mks raylsm^{-1}	1.10^5
grain shape factor	-	0.5
wet porosity	-	0.2
bulk density	kgm^{-3}	1625
wet layer thickness	m	0.05

are shown in table 8.6.

8.2.9 Discussion

The failure of the impedance measurement technique to give consistent results is due to the existence of other reflecting surfaces. For measurements of normal surface impedance where the reflection coefficient is near to unity the technique is extremely sensitive to reflections from surfaces other than the ground. In this case the soil bin adds reflecting surfaces such as the hard edges of the box. Other impedance techniques also suffer from sensitivity to reflections [108]. The original experiments carried out by Cramond and Don [109] had the advantage of using a very large flat surface. This reduced the errors due to reflections.

The measured seismic velocities of the dry and wettted soil yielded the surprising result that the near surface seismic velocities were changed by less than the uncertainty in the velocity measurements upon wetting. However the change in bulk density will still provide a seismic discontinuity at the base of the wetted layer. The measurement of the ratios of acoustic-seismic coupling coefficients shows that the wetting does have a significant effect upon the acoustic to seismic coupling. The prediction of the ratio of coupling coefficients was made using FFLAGS and fitting to the data by adjusting the grain shape factor, the wetted flow resistivity, the wetted layer thickness (within its error bounds) and the wetted porosity. The predicted flow resistivity is increased and the porosity decreased by the wetting, as

expected.

Chapter 9

Two applications of FFLAGS.

9.1 The influence of acoustic-seismic coupling on vehicle induced vibration of the ground.

The ground particle motion induced by a heavy vehicle can be modelled as the sum of two contributions. These are the direct excitation of the soil from the contact of the vehicle with the ground, and the vibration due to coupling of airborne engine and exhaust noise into the seismic motion of the ground.

9.1.1 Predictions of the vertical particle velocity due to direct coupling through vehicle ground contact.

The vibration produced by vehicle ground contact can be modelled as that due to a vertical point source (or the sum of a set of such sources).

To predict vertical particle velocity as a function of range a visco-elastic FFP program (SAFARI) was used. This predicts particle velocity in fluid and visco-elastic media. The elastic attenuation in the visco-elastic ground is input in decibels per wavelength on the assumption that the ground can be modelled as a Voigt solid. The elastic wave attenuation due to the air in the pores in the ground has been shown to be a very small contribution to the total attenuation of elastic waves in the ground (section 1.2), and it will be ignored here. This visco-elastic FFP program uses only one exponential

function instead of two in equation 2.31. This will reduce the accuracy of the program at very short ranges.

In order to check that the visco-elastic program predicts vertical particle velocity at the ground surface at the ranges of interest correctly, the program was run for two simple cases. The first of these was horizontal particle motion at short range from a point source in an infinite visco-elastic space (figure 9.1). The attenuation even at very short range (a few wavelengths) was the 6dB per doubling of distance expected.

The second example, more relevant to this study, is the prediction of vertical particle velocity as a function of range along the surface of an elastic halfspace as a result of excitation from a vertical point source also on the surface. The soil seismic velocities are shown in table 9.1(a). These velocities are those measured at a site in Fort Hood in the USA [112]. At more than a few wavelengths from the source the signal is dominated by the Rayleigh wave, which can be seen in figure 9.2 to decay at 3dB per doubling of distance, the expected rate for a lossless medium. At short ranges there is interference between Rayleigh and body-wave signals, which soon die out, as the body wave signals decay at a faster rate (6dB per doubling of distance) due to spherical rather than cylindrical spreading.

9.1.2 Predicted effects of layering.

If we consider excitation at 50Hz and use the elastic parameters for a competent soil layer over a substrate from table 9.1(b) and vary the layer thickness between 1.0 and 8.0 metres, it is seen (figure 9.3) that the attenuation is greatest in the thin layers , because the higher attenuation of the substrate dominates, whereas when the layer thickness is 8.0 metres the predicted vertical particle velocity is identical to that for a halfspace. For the thin surface layers, moreover, there are dips in the predicted transmission loss where destructive interference occurs between the Rayleigh wave contribution and the other transmission modes within the layer.

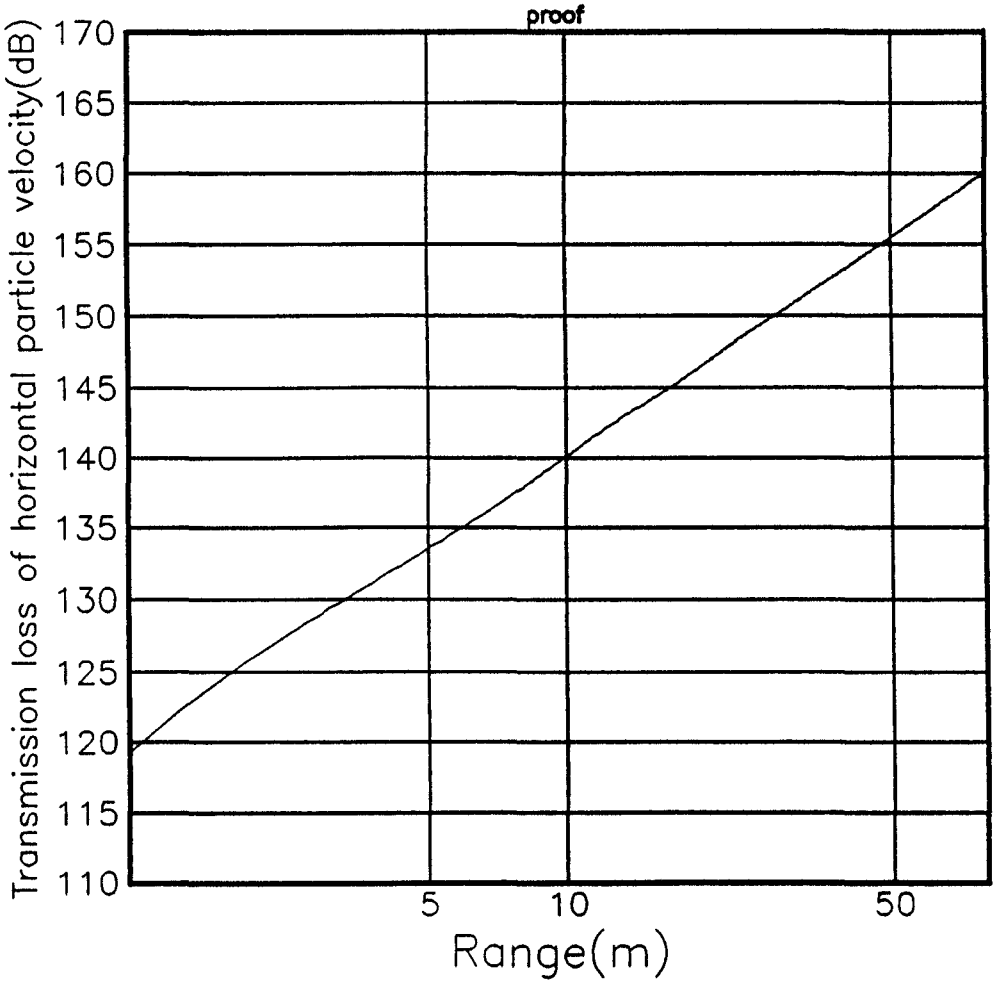

Figure 9.1 Predicted horizontal particle velocity as a function of range from a point source

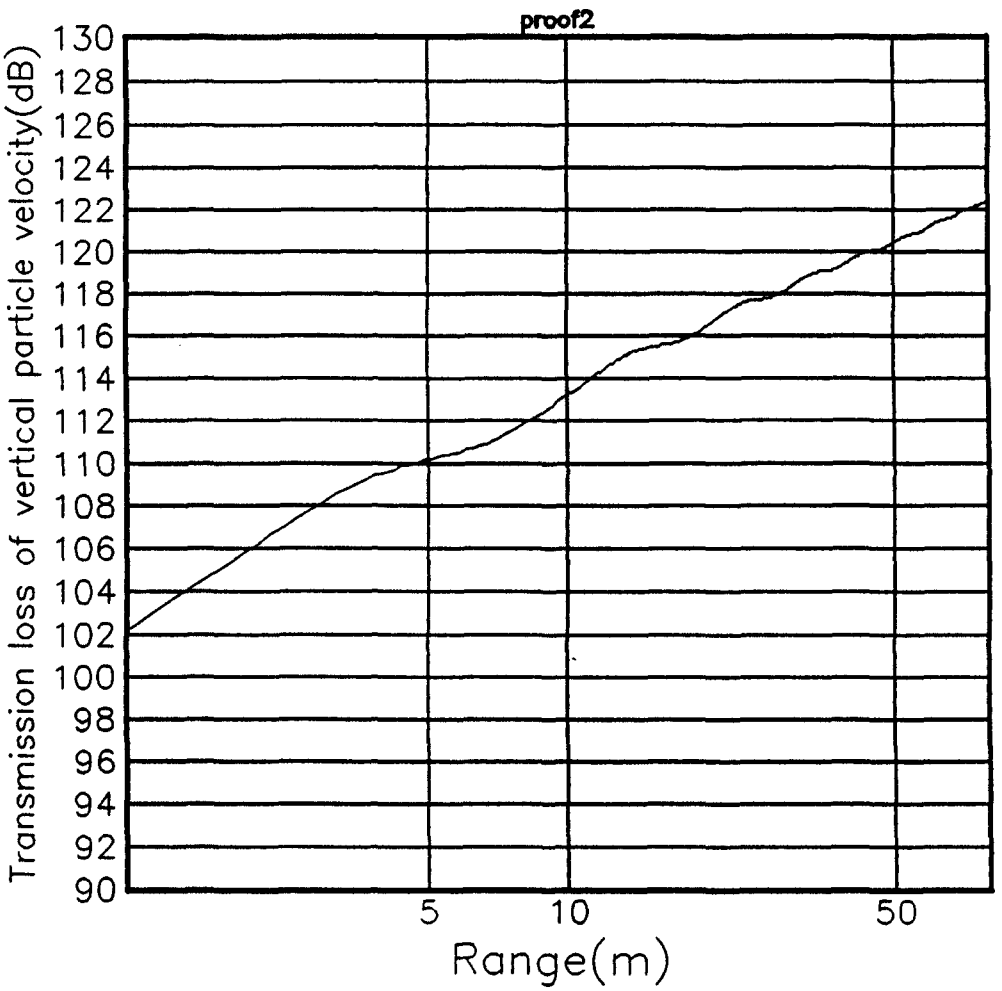

Figure 9.2 Predicted vertical particle velocity as a function of range from a point vertical source at the surface of a poro-elastic halfspace.

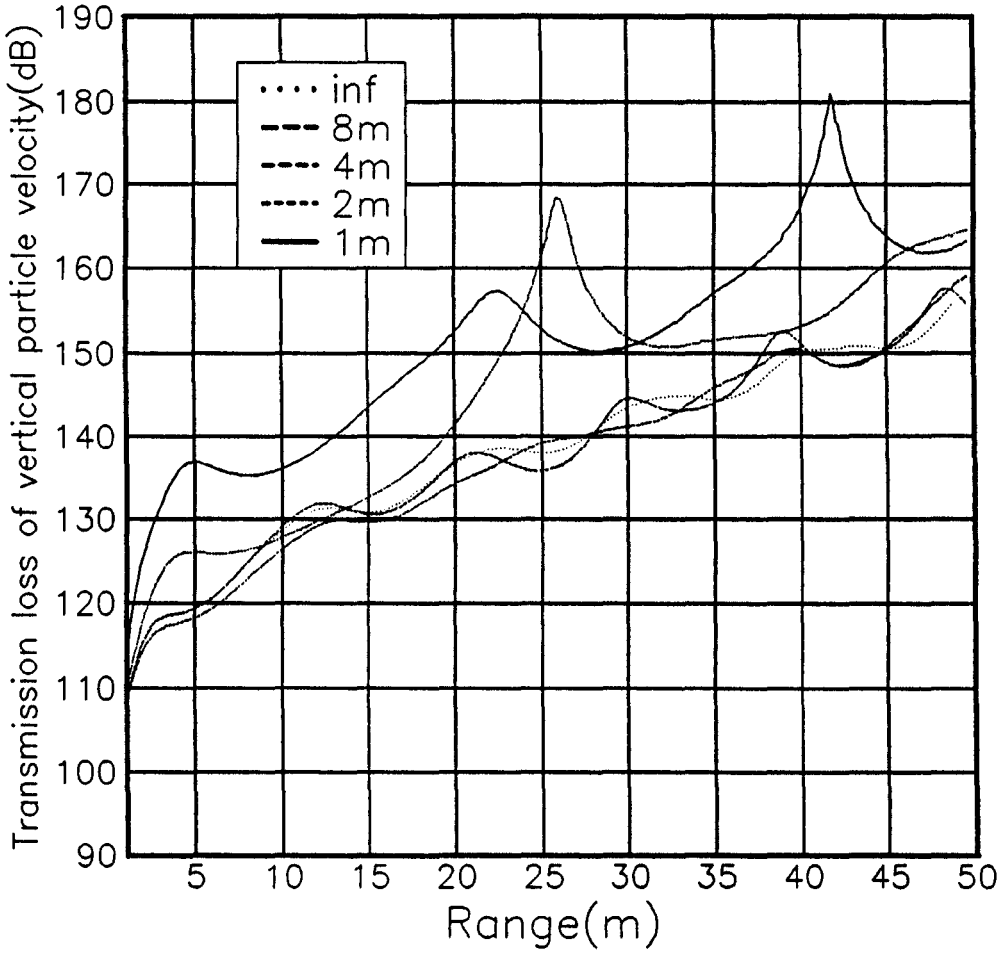

Figure 9.3 Predicted vertical particle velocity as a function of range at 50Hz for different upper layer depths

Table 9.1 Ground elastic parameters used in the prediction of vertical particle velocity due to a heavy vehicle.

Description of ground	P-wave velocity ms^{-1}	S-wave velocity ms^{-1}	P-wave attenuation dB/λ	S-wave attenuation dB/λ	bulk density kgm^{-3}
(a) lossless elastic halfspace	537.6	268.8	0	0	1700
(b) high attenuation layer	537.6	268.8	1.092	2.729	1700
high attenuation substrate	1075.3	537.6	2.184	5.46	1700

9.1.3 Effects of acoustic-seismic coupling

FFLAGS may be used to examine the effect of acoustic-seismic coupling. The ground is modelled as a porous elastic layer overlying an elastic half-space, with elastic parameters as in table 9.1(b) and porous parameters of flow resistivity (σ) = 50000 mks rayls m^{-1}, porosity (Ω) = 0.4, shape factor ratio (s_p) = 0.36, and grain shape factor (n') = 0.5. The layer depth is 2.0 metres. Figure 9.4 shows the predicted vertical particle velocity at the surface due to a vertical point source at the surface and an acoustic point source at a height of 1.0 metres. The acoustic source is supposed to have a sound pressure level of 90dB at 1.0 metre from the source. The acoustic source is intended to represent a typical acoustic output of a heavy vehicle at 50Hz. The vertical particle displacement due to the ground contact is again modelled using SAFARI. The phase relationship between the acoustic output and the seismic output at the ground contact will not be constant, as they are from different sources. The acoustic signal is mostly from engine and exhaust noise, whereas the seismic signal is mostly from track plate impacts with the ground. Hence the vertical particle velocity at the ground surface is modelled as the incoherent addition of the ground contact signal and the seismically coupled acoustic signal.

At short range this simulation predicts that the signal induced by direct ground contact dominates, but as the range is increased the seismic signal is attenuated and the acoustic source dominates. This effect is very dependent on the seismic attenuation, because if the attenuation is decreased the seismic signal will dominate out to much larger ranges. Figure 9.5 shows a similar effect at 100Hz.

9.2 The importance of near surface sound velocity gradients at short range.

Vehicle acoustic output is limited by European regulations and is tested using the EEC 81/334 test method. The geometry used in vehicle tests is a microphone at a height of 1.2 metres and at a range of 7.5 metres from the vehicle over a highly reflective surface.

Some vehicle manufacturers send their vehicles to be tested in Southern Italy in preference to testing in Northern Europe. It has been suggested that this preference is due to the beneficial effects of an air temperature gradient near to the hot ground surface, leading to upward refraction in the atmosphere and reduction of the received signal at 7.5metres. Quite small intersite differences of the order of 0.5dB can be significant in determining whether vehicles pass the test. The wind speed might also have a marked effect on the received signal. However it is possible to change the orientation of tests to minimise the effect of the wind.

In order to model the effects of meteorology on sound propagation, FFLAGS was used with the atmosphere modelled as a set of fluid layers (with range independent properties) over an asphalt surface.

Geometry

In the case of a car the engine height is approximately 0.5 metres. This was considered as a point source at the range of interest. For a moving vehicle the tyres should be considered as a noise source. The tyres of a car have a thickness of approximately 0.09metres. The noise from the tyre

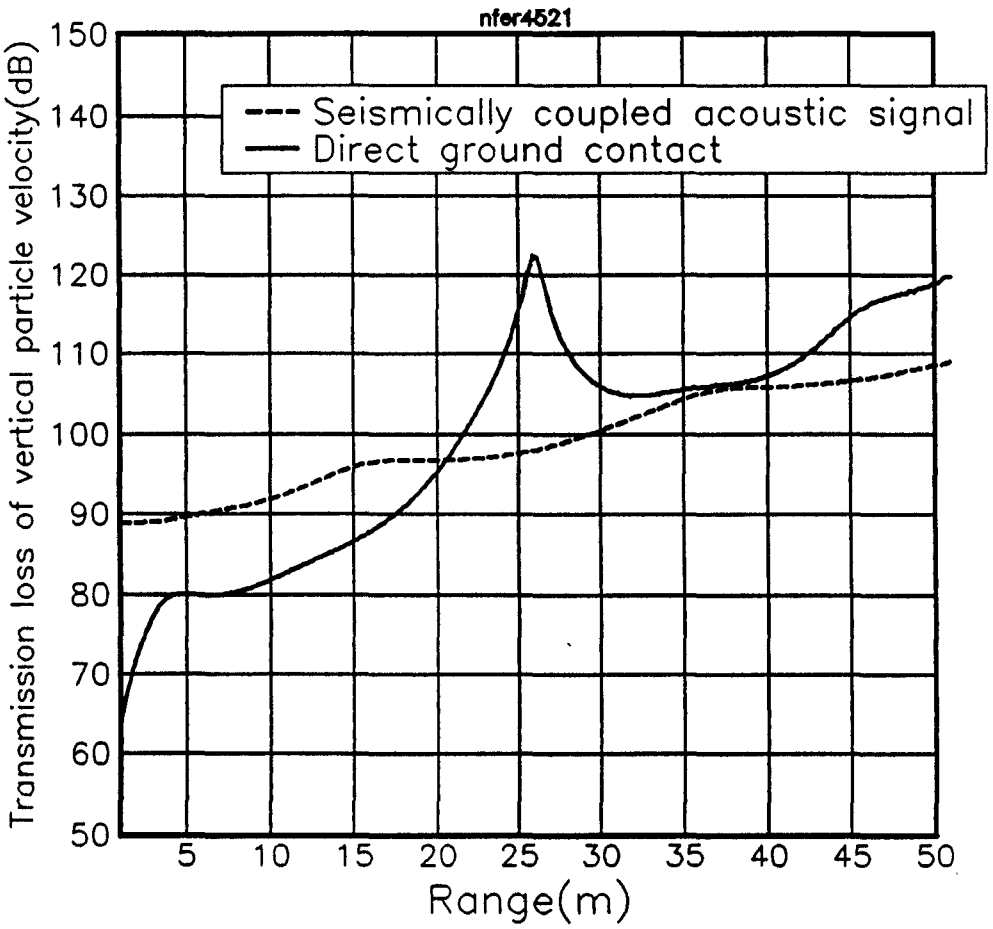

Figure 9.4 The predicted influence of acoustic-seismic coupling on transmission loss of vertical particle velocity vs range at 50Hz along the surface of a layered porous-elastic soil.

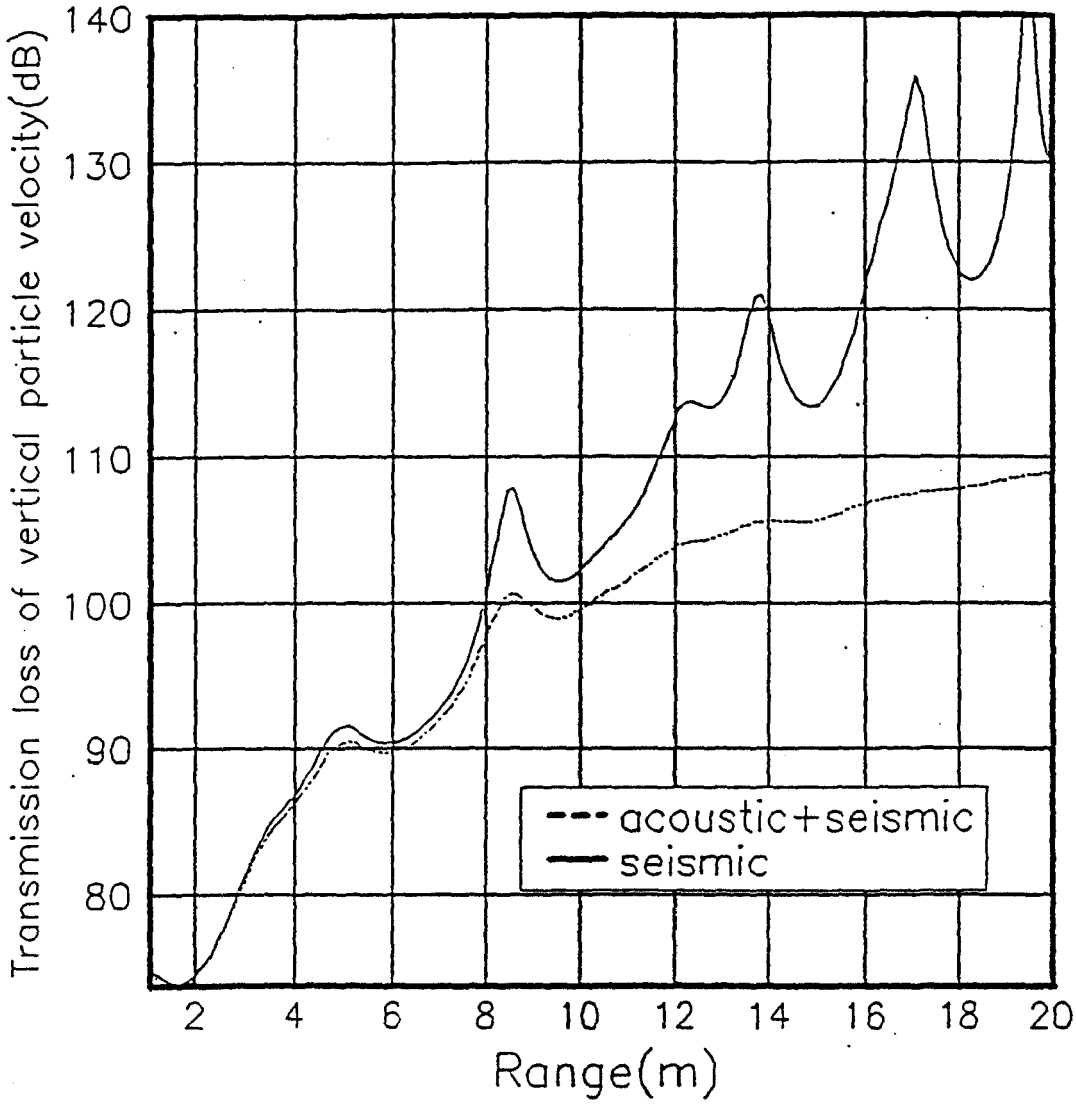

Figure 9.5 The predicted influence of acoustic-seismic coupling on transmission loss of vertical particle velocity vs range at 100Hz along the surface of a layered porous-elastic soil.

consists of two sources. The first is the sound from the ground contact of the tyre and is centred at the rear of the ground contact patch. The second is the vibration of the tyre wall. The combination of these tyre noise sources has been modelled as a point source at a height of 0.045metres [113]. The geometry of the simulation is shown in figure 9.6

9.2.1 Considerations in modelling the sound propagation.

Wind speed

The effect of the wind on sound propagation can not be modelled accurately using this FFP model. If propagation is modelled in a moving fluid from a stationary source then the medium becomes effectively anisotropic. Sound speeds in the vertical and horizontal directions become different. At long ranges where propagation is nearly horizontal this will be insignificant, but at the short ranges considered here, with different source and receiver heights, the effect may be significant. This question is examined by Pierce [100]. Sound speeds in the outward and backward directions will also be different. At very short ranges and low frequencies the second exponential term in the Bessel Function approximation (Equation 2.30) will make a non-negligible contribution (see figure 2.1). The second exponential term corresponds to propagation towards the source. Because the outward and backward sound speeds are different in all but cross wind conditions, a different depth dependent Green's function for each of the two exponential functions would be required. Finally the wind introduces an azimuthal dependence to the environment. The FFP approach is not easily adjustable to include an azimuthal dependence. Ingard and Singhal [114] showed experimentally that for flow in a duct the ratio of the downstream to upstream received sound pressures from a stationary source placed halfway between them, lay between $(1-M)/(1+M)$ and $[(1-M)/(1+M)]^2$, where M is the Mach number of the flow. For a Mach number of 0.05 this gives a ratio of between 0.82 and 0.90. When the effects of meteorology on sound pressure levels at short range are of the order of one dB, this effect is large enough to invalidate predictions of the effect of the wind on the received sound pressure

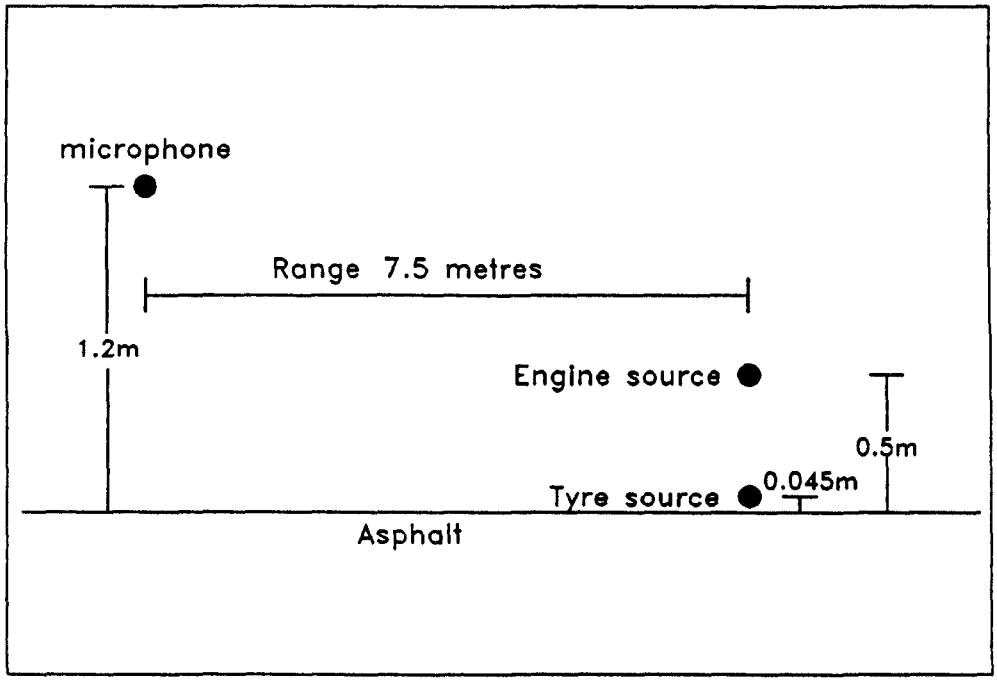

Figure 9.6 The geometry assumed in predicting the excess attenuation for propagation from a car

levels based on an azimuthally invariant environmental model.

Temperature

The temperature gradient near to the ground can be modelled using the Monin-Obhukhov Similarity theory described in appendix B. The wind speed gradient and temperature gradient are related by the similarity theory. As described above the use of the FFLAGS model is inappropriate for wind velocity gradients at short range. Howeverit is possible to orient short range tests so that propagation is crosswind.

For propagation over asphalt the roughness length z_h is very small, having a value of between 10^{-3} and $10^{-4}m$. These values are supported by the temperature measurements made above asphalt surfaces reported by Daigle et al [115].

In this study the effects of large positive and negative differences between ground and air temperature (at 1.2 metres) were studied. In order for the large temperature differences between the ground surface and a height of 1.2 metres to exist the Obhukhov length must be large positive or negative. In these conditions the correction factors Φ become small, and hence the temperature gradient is reduced to a logarithmic one.

The speed of sound c can be calculated from the air temperature T (in Kelvin) using

$$c \propto \sqrt{T}. \tag{9.1}$$

Differences between ground temperature on road surfaces and air temperature at a height of 1.2 metres, $(T_{gro} - T_{mic})$ have been found to vary between +13 degrees Celsius and -7 degrees Celsius over an asphalt surface [113]. These variations were in the presence of a wind speed of $5ms^{-1}$ at a height of 1.2 metres

Calculations of excess attenuation were done, using an air temperature at the microphone(T_{mic}) of twenty degrees Celsius and a temperature at the ground(T_{gro}) of $T_{mic} + 14$,$T_{mic} + 7$, $T_{mic} + 1$,$T_{mic} - 1$ and $T_{mic} - 7$ degrees Celsius.

Fluid Layering

There are two obvious ways that a non-linear sound velocity gradient could be represented using discrete homogeneous layers; either the layers have a constant difference in sound velocity to their neighbours and the layer thicknesses vary, or the layer thickness is kept constant and the differences in sound velocity between neighbouring layers is varied.

There are several considerations in choosing between these two methods. The first is the accurate representation of the sound velocity gradient. Near to the ground the velocity gradient will be highest and hence to represent it accurately the layer thickness should be smaller near the ground than at greater heights where the velocity gradient is small.

The second consideration is the related problem of avoidance of trapped modes within layers which are only approximations to a continuous velocity gradient. These modes can be avoided by making the layer thicknesses small and by making the velocity changes across interfaces small. The layer thicknesses can be most easily controlled if they are all identical but velocity changes across interfaces are most easily controlled by the use of identical velocity changes at each interface. In using variable layer thicknesses with constant velocity variations across interfaces it has been found that for large temperature gradients where the ground was warmer than the air at 1.2metres, and the source height was 4.5 centimetres, large oscillations with frequency in the predicted excess attenuation occurred at frequencies above 1kHz. Use of constant layer thicknesses did not give rise to these oscillations. At frequencies outside these oscillatory regions and for temperature gradients where these did not occur, the agreement between the two layering methods was good. It is suggested that the oscillations are due to spurious trapped modes in the layers near ground surface.

The number of constant velocity layers required to obtain a result that is close to the result from a hypothetical continuous velocity gradient model can be deduced from the convergence of predicted excess attenuation to a stable result as the number of layers is increased. Figures 9.7 and 9.8 show the predicted excess attenuation for different numbers of fluid layers for the

largest temperature gradient. This shows that when the number of layers is twelve and source height is 0.5 metres the rate of change of the predicted excess attenuation with number of layers becomes very small for frequencies below 2kHz. The high frequency result is very layer depth dependent above 2kHz. As mentioned in section 7.4.2 Franke, Raspet, and Liu [93] suggest that their FFP predictions of sound levels in shadow zones agree with residue series results only when the thickness of the constant velocity layers is smaller than the wavelength. This leads to an upper frequency limit to the validity of the predictions. If Franke, Raspet, and Lui's [93] suggested maximum layer thickness of one wavelength is used, and it is assumed that when the layer thickness is one quarter of a wavelength then the result is exact, then the errors due to using twelve one wavelength thick (0.1 metre) layers are approximately 0.2dB at 3kHz for the source height of 0.5 metres, and approximately 0.15dB at 3kHz for the source height of 0.045 metres. At a frequency of 5kHz the difference in predicted excess attenuation between the use of twelve 0.1 metre thick layers and fifty 0.024 metre thick layers is approximately 0.2dB for the 0.5 metre source height, and 0.4dB for the lower source height. These results suggest that Franke et al's suggested layer thickness limit is inadequate for this study. For frequencies above 2kHz a layer thickness of 0.024 metres was used. However even for such small layer thicknesses the result had not converged to a stable result at a frequency of 5kHz. Limited computation facilities did not allow further investigations of the sensitivity to layer thickness. However the error due to the non-convergence of the result could be estimated as less than 0.1dB at 5kHz. The layer thickness at 5kHz was less than half a wavelength.

Above a frequency of a few kHz errors are introduced into the prediction due to turbulence. These errors are not accounted for in this model.

If the layer thickness was allowed to vary with height then the maximum layer thickness would be greater than for constant layer thickness and the frequency at which the maximum layer thickness was one wavelength would be decreased for a given number of layers.

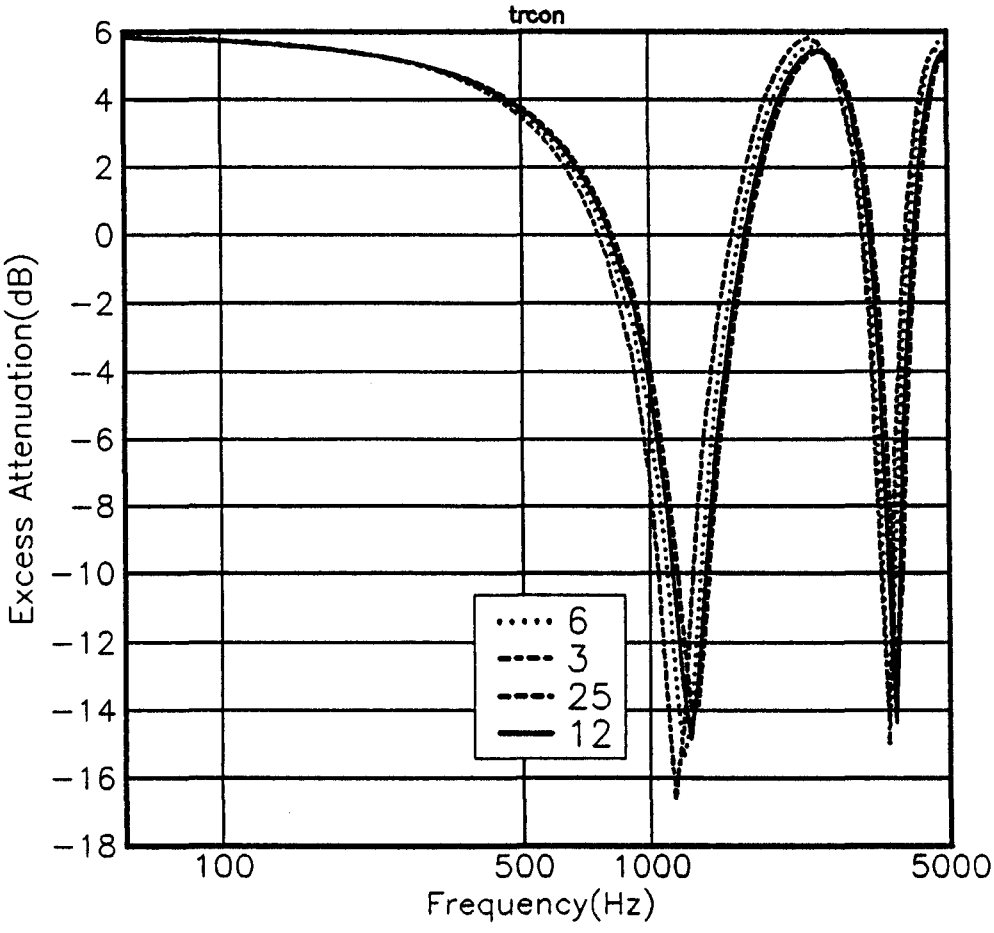

Figure 9.7 Predicted excess attenuation at range of 7.5 metres, for source height 0.5 metres, and receiver height 1.2 metres in a temperature gradient as a function of the number of layers in the atmospheric model.

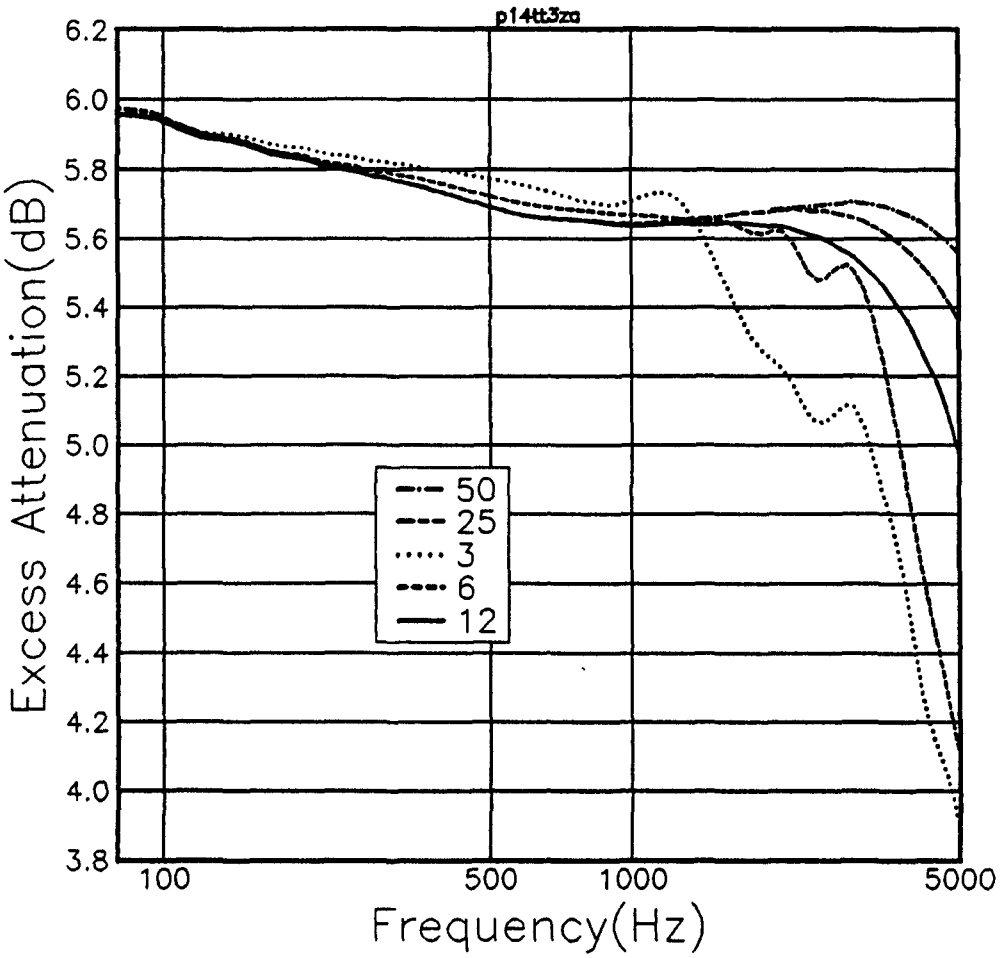

Figure 9.8 Predicted excess attenuation at range of 7.5 metres, for source height 0.045 metres, and receiver height 1.2 metres, in temperature gradient as a function of the number of layers in the atmospheric model.

Road surface description.

Most road surfaces are non-porous and of high bulk density. However a flat, rigid, non-porous surface will not have an infinite normal surface impedance. This is because the surface cannot follow the rapid temperature fluctuations involved in the acoustic wave, and the existence of the viscous boundary layer at the surface. This effect will give values of effective flow resistivity of approximately 10^9 mks rayls/m. Measurements of the acoustic impedance of non-porous road surfaces have derived values for the effective flow resistivity, from fitting to the Delaney-Bazley one parameter model [116], of 3.10^7 mks rayls/m [115]. Equivalent values of the Rayleigh Attenborough pore parameters are flow resistivity $\sigma = 3.10^6$, porosity $\Omega = 0.03$, pore shape factor ratio $s_p = 0.5$, grain shape factor n'=0.7. These values do not give identical normal surface impedance to the Delaney-Bazley model, but the impedances are of the same order throughout the frequency range studied here.

Temperature Gradient Results

The first geometry considered here models a car engine as a point source at a height of 0.5metres, with a receiver at a height of 1.2metres, and a range of 7.5metres. The two temperature gradients both produce similar effects on the excess attenuation spectrum. These effects are a frequency shifted first dip and an alteration in the depth of the dip (see Figures 9.9 and 9.10). As the roughness length (z_h) is decreased the effect of the temperature gradient is decreased. When the ground temperature is higher than the air temperature the interference dips are shifted down in frequency and become deeper. When the ground temperature is less than the air temperature the reverse occurs, and the interference dips are shifted up in temperature and become less deep.

The effect on the predicted 1/3 octave excess attenuation (Figures 9.11 and 9.12) is similar except that the averaging effect of the wide (1/3 octave) frequency bands hides the alteration in the interference dips' depths. The actual effect of the modelled temperature gradient on the received sound

pressure level (and hence the 'A' weighted sound pressure level) will be dependent on the source spectrum. If the source spectrum contained peaks near to the interference dips of the excess attenuation spectra then the temperature gradients modelled here might have a large effect.

For the tyre source model the effects of both of the model gradients were similar (see figures 9.13 and 9.14). With the ground warmer than the air, at low frequencies the sound pressure level was lowered, but at higher frequencies (above 700Hz) the sound pressure was increased. The reverse occurred where the ground was colder than the air. These effects gave differences between the predictions for temperature gradients and no temperature gradient of less than 1.0dB at frequencies up to 3kHz.

The one third octave sound pressure level spectrum was measured using the geometry shown figure 9.6. The vehicle was a Vauxhall Astra 1.6. Two sets of measurements were made. In the first measurement the car was stationary with the engine running at a speed of 1500 revolutions per minute. In the second measurement the car was coasting at a speed of 70 kilometres per hour with the engine turned off. It was assumed that in the first measurement the noise was entirely due to the engine noise, and in the second measurement that the noise was entirely due to tyre noise. It was further assumed that weather conditions were neutral and hence there was no sound velocity gradient near to the ground.

Figures 9.17 and 9.18 show the predicted effect of a temperature gradient on the one third octave sound pressure level spectra for roughness lengths of 10^{-3} and 10^{-4} metres respectively, for the stationary car with the engine running. The source height is assumed to be 0.5 metres Figures 9.19 and 9.20 show the predicted effect of the gradients for the coasting car with the engine turned off.The source height is assumed to be 0.045 metres.

The differences between the predicted sound pressure levels for the engine source are due to the shifting of the predicted interference dips for the interference between the direct and reflected paths. In reality a car is a distributed source and hence the interference dips will not be as deep as those predicted from a point source. Therefore the effect of the tempera-

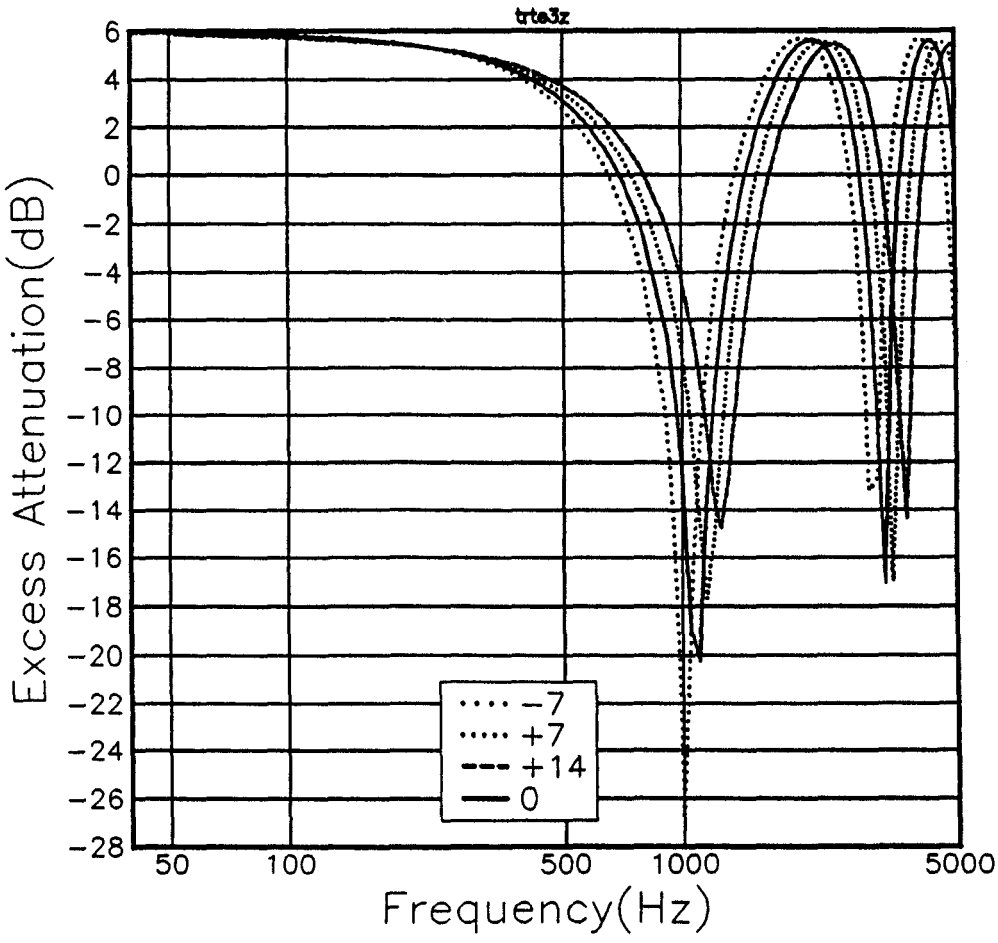

Figure 9.9 Predicted excess attenuation over an asphalt surface at range 7.5metres, receiver height 1.2 metres, source height 0.5 metres. Temperature differences($T_{ground} - T_{microphone}$) + 14° to −7°. Temperature gradient modelled using equation B.3 with roughness length 10^{-3}.

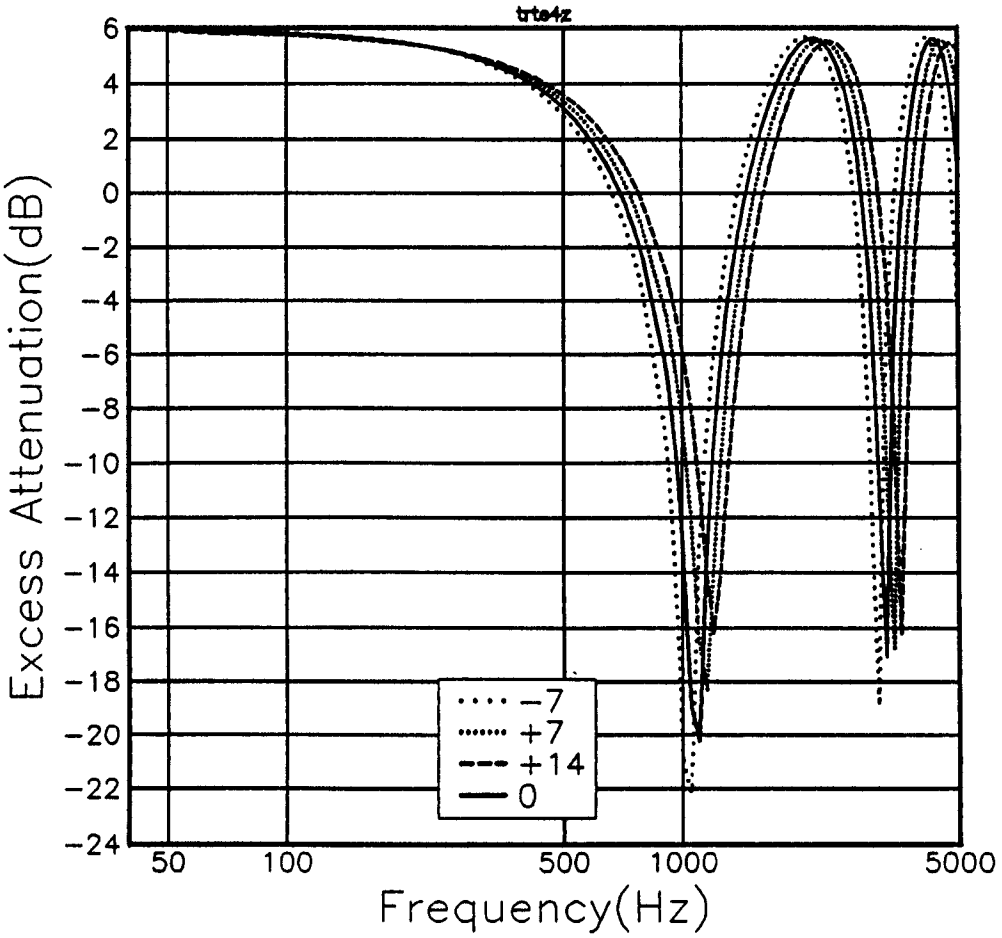

Figure 9.10 Predicted excess attenuation over an asphalt surface at range 7.5metres, receiver height 1.2 metres, source height 0.5 metres. Temperature differences($T_{ground} - T_{microphone}$) + 14° to −7°. Temperature gradient modelled using equation B.3 with roughness length 10^{-4}.

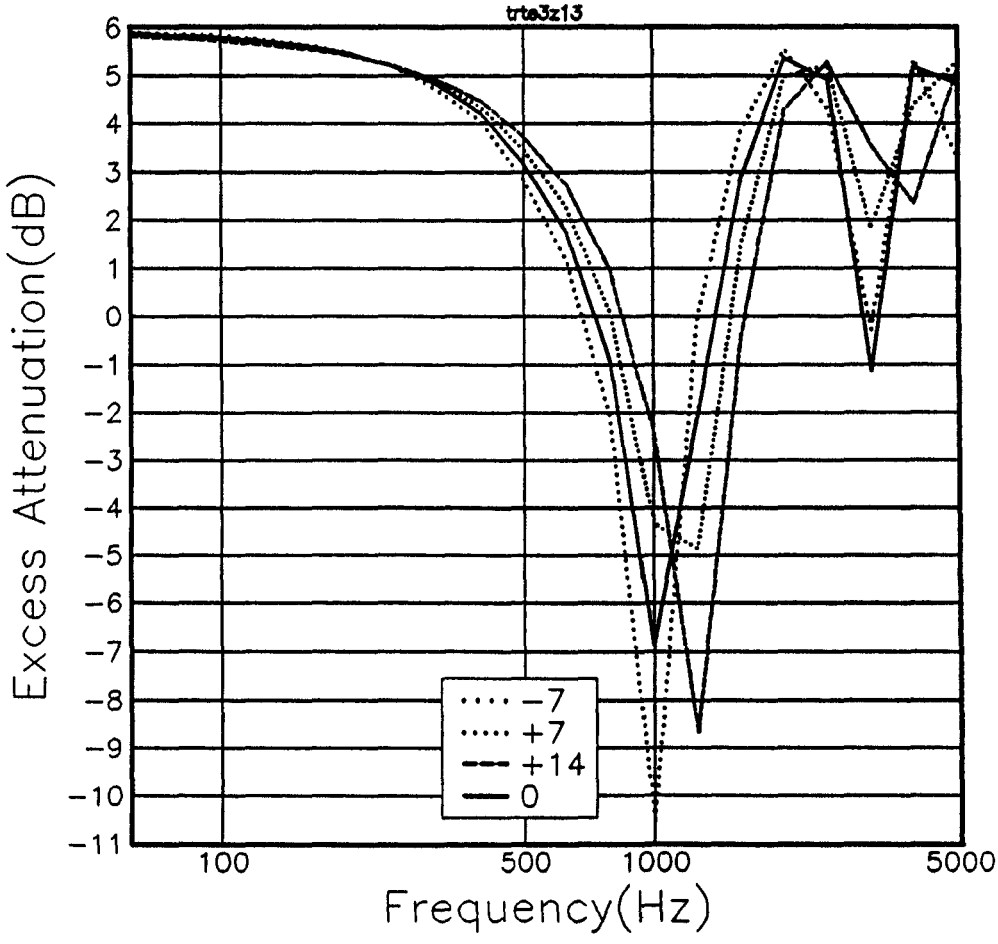

Figure 9.11 Predicted 1/3 octave excess attenuation over an asphalt surface at range 7.5metres, receiver height 1.2 metres, source height 0.5 metres. Temperature differences($T_{ground} - T_{microphone}$) + 14° to −7°. Temperature gradient modelled using equation B.3 with roughness length 10^{-3}.

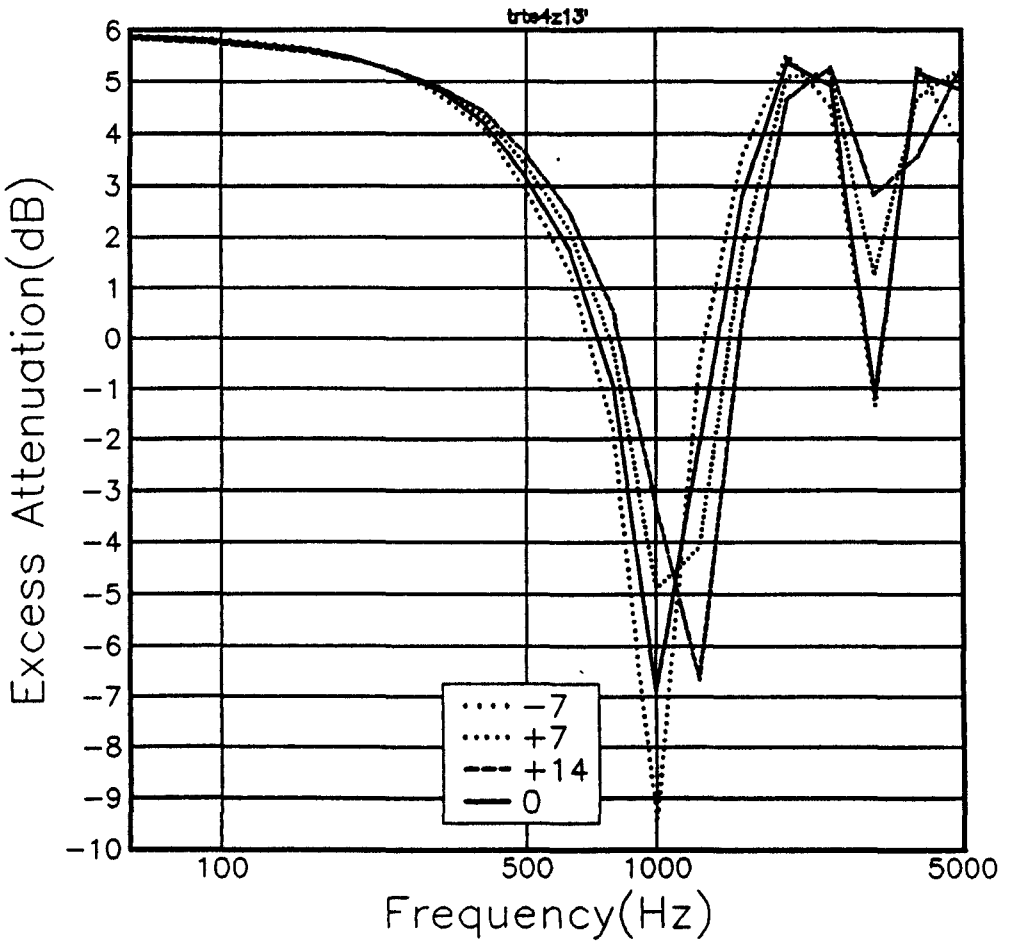

Figure 9.12 Predicted 1/3 octave excess attenuation over an asphalt surface at range 7.5metres, receiver height 1.2 metres, source height 0.5 metres. Temperature differences($T_{ground} - T_{microphone}$) + 14° to −7°. Temperature gradient modelled using equation B.3 with roughness length 10^{-4}.

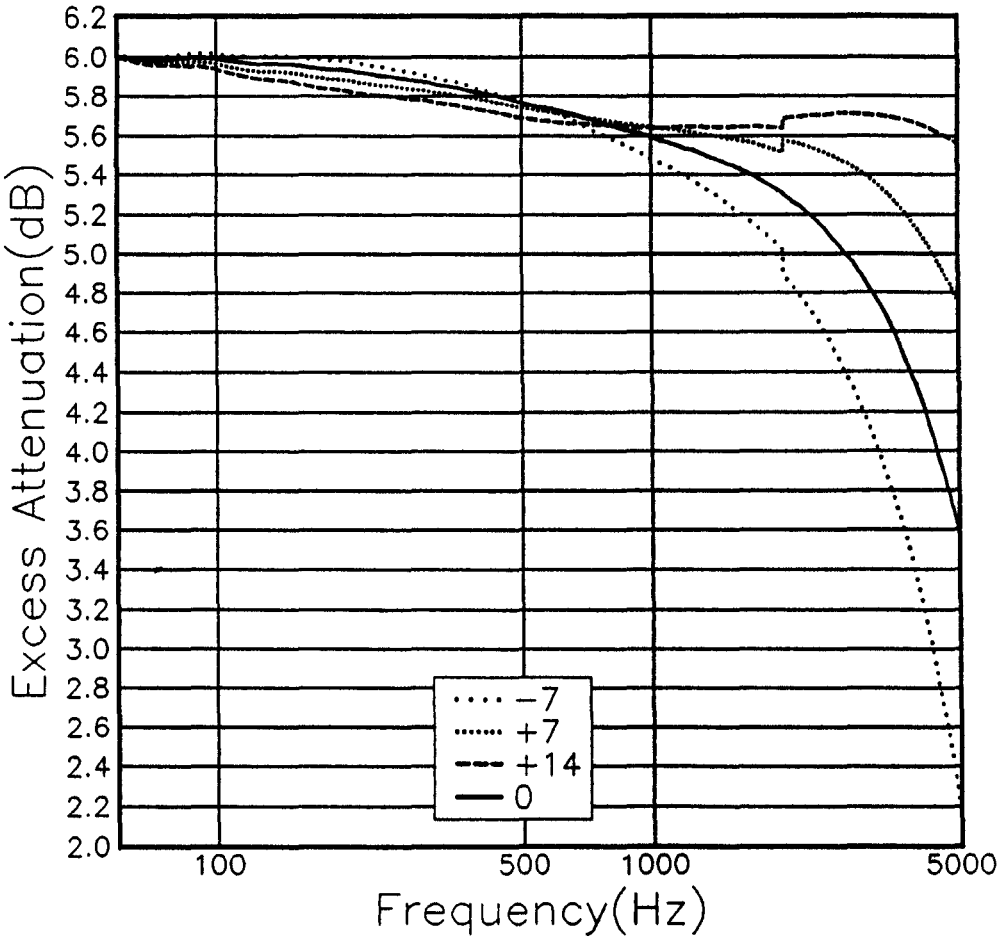

Figure 9.13 Predicted excess attenuation over an asphalt surface at range 7.5metres, receiver height 1.2 metres, source height 0.045 metres. Temperature differences($T_{ground} - T_{microphone}$) + 14° to −7°. Temperature gradient modelled using equation B.3 with roughness length 10^{-3}.

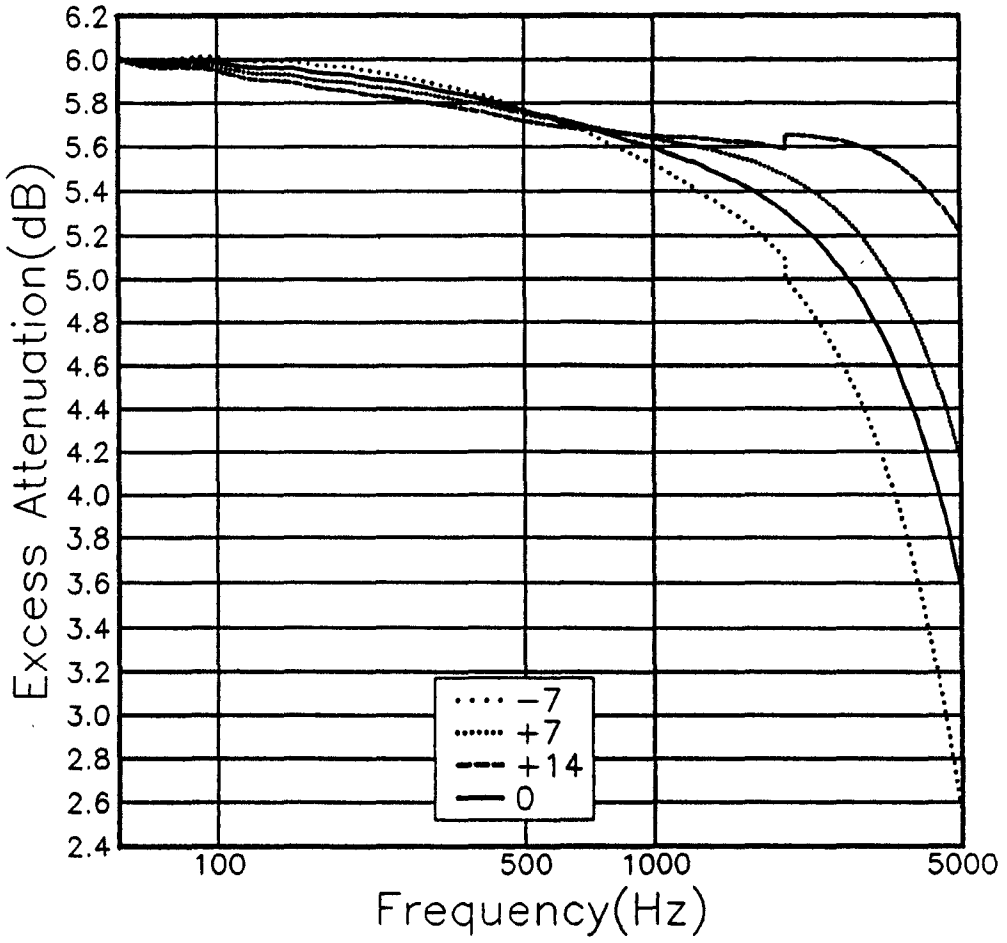

Figure 9.14 Predicted excess attenuation over an asphalt surface at range 7.5metres, receiver height 1.2 metres, source height 0.045 metres. Temperature differences($T_{ground} - T_{microphone}$) + 14° to −7°. Temperature gradient modelled using equation B.3 with roughness length 10^{-4}.

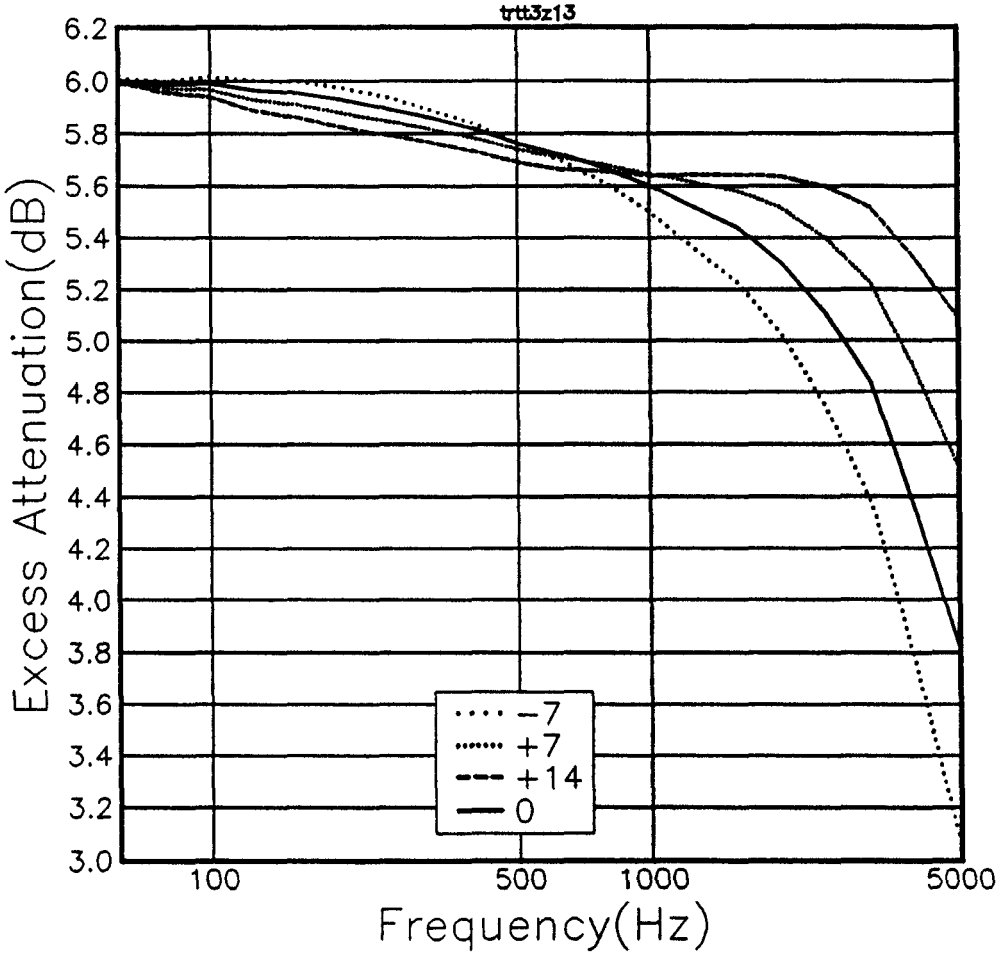

Figure 9.15 Predicted 1/3 octave excess attenuation over an asphalt surface at range 7.5metres, receiver height 1.2 metres, source height 0.045 metres. Temperature differences($T_{ground} - T_{microphone}$) + 14° to −7°. Temperature gradient modelled using equation B.3 with roughness length 10^{-3}.

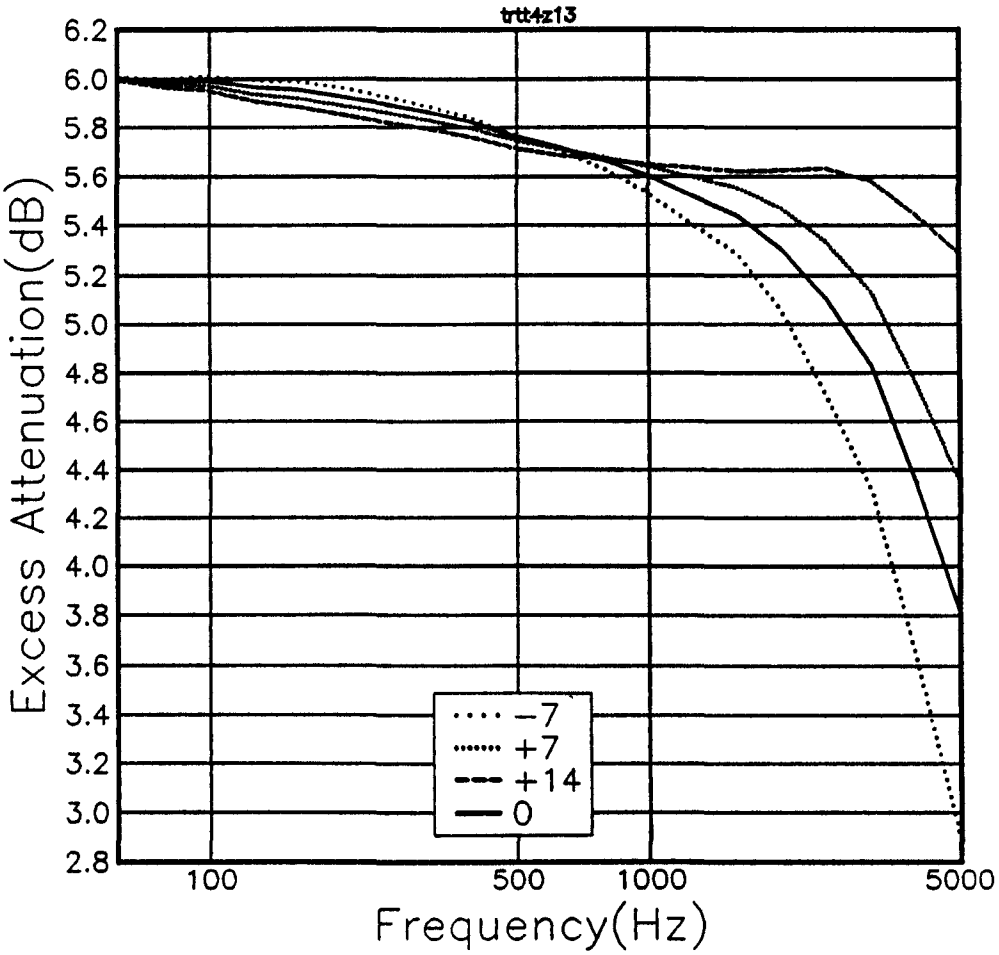

Figure 9.16 Predicted 1/3 octave excess attenuation over an asphalt surface at range 7.5metres, receiver height 1.2 metres, source height 0.045 metres. Temperature differences($T_{ground} - T_{microphone}$) + 14° to −7°. Temperature gradient modelled using equation B.3 with roughness length 10^{-4}.

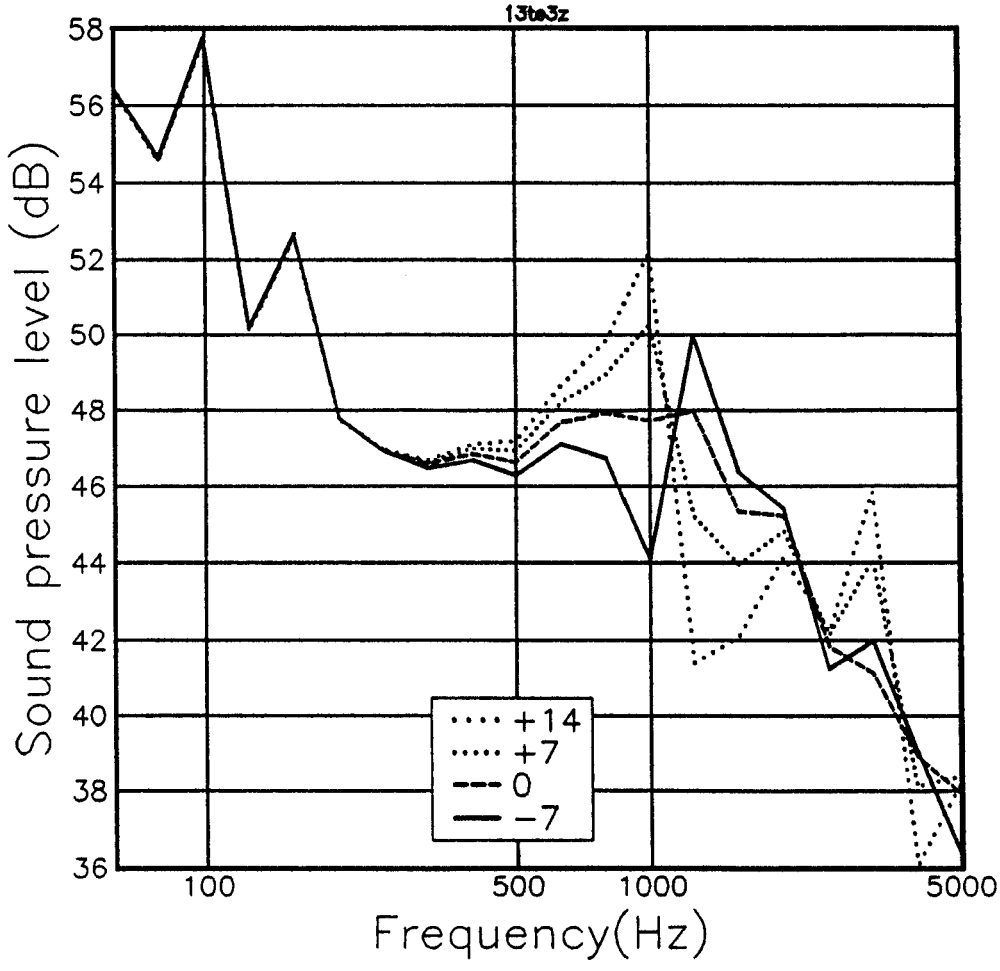

Figure 9.17 The predicted effect of temperature differences between the ground and the air ($T_{gro} - T_{air}$) of -7, +7 and +14 Celsius, on the 1/3 octave sound pressure level spectrum of a stationary car with the engine running, for a roughness length of 10^{-3} metres.

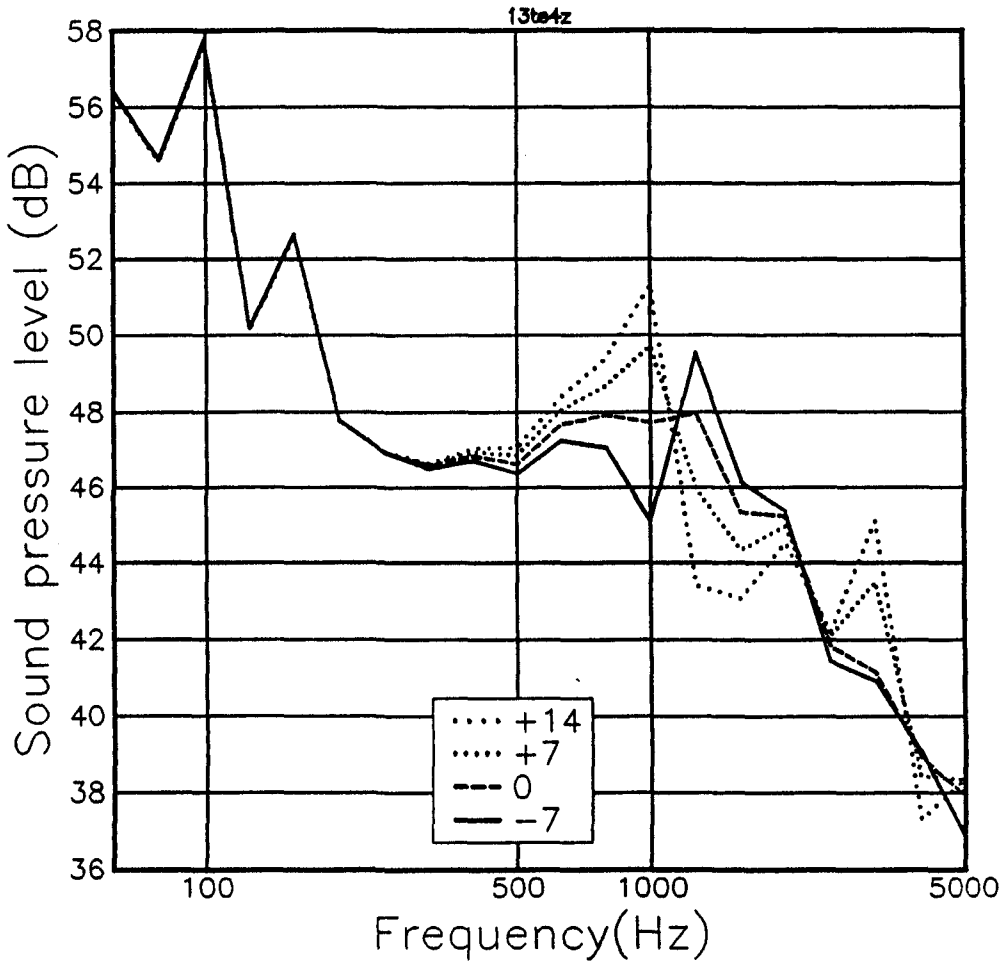

Figure 9.18 The predicted effect of temperature differences between the ground and the air ($T_{gro} - T_{air}$) of -7, +7 and +14 Celsius, on the 1/3 octave sound pressure level spectrum of a stationary car with the engine running, for a roughness length of 10^{-4} metres.

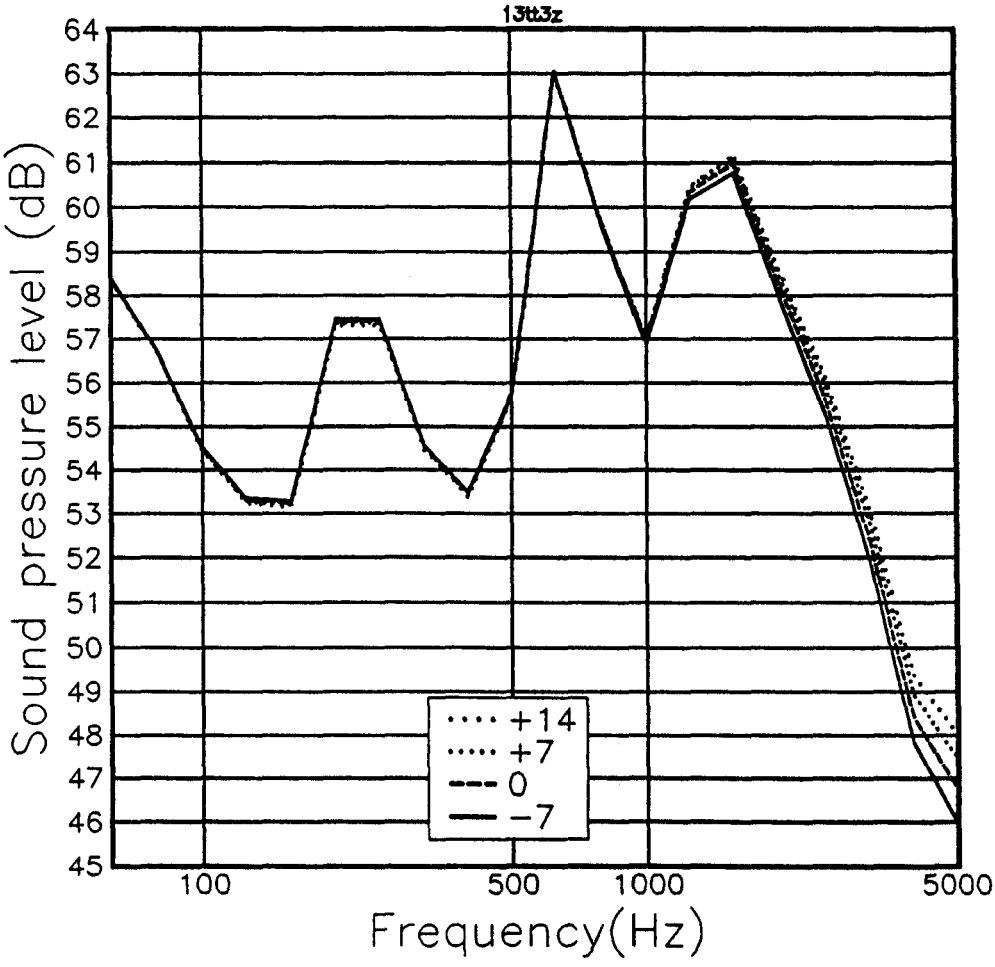

Figure 9.19 The predicted effect of temperature differences between the ground and the air ($T_{gro} - T_{air}$) of -7, +7 and +14 Celsius, on the 1/3 octave sound pressure level spectrum of a coasting car with the engine off, for a roughness length of 10^{-3} metres.

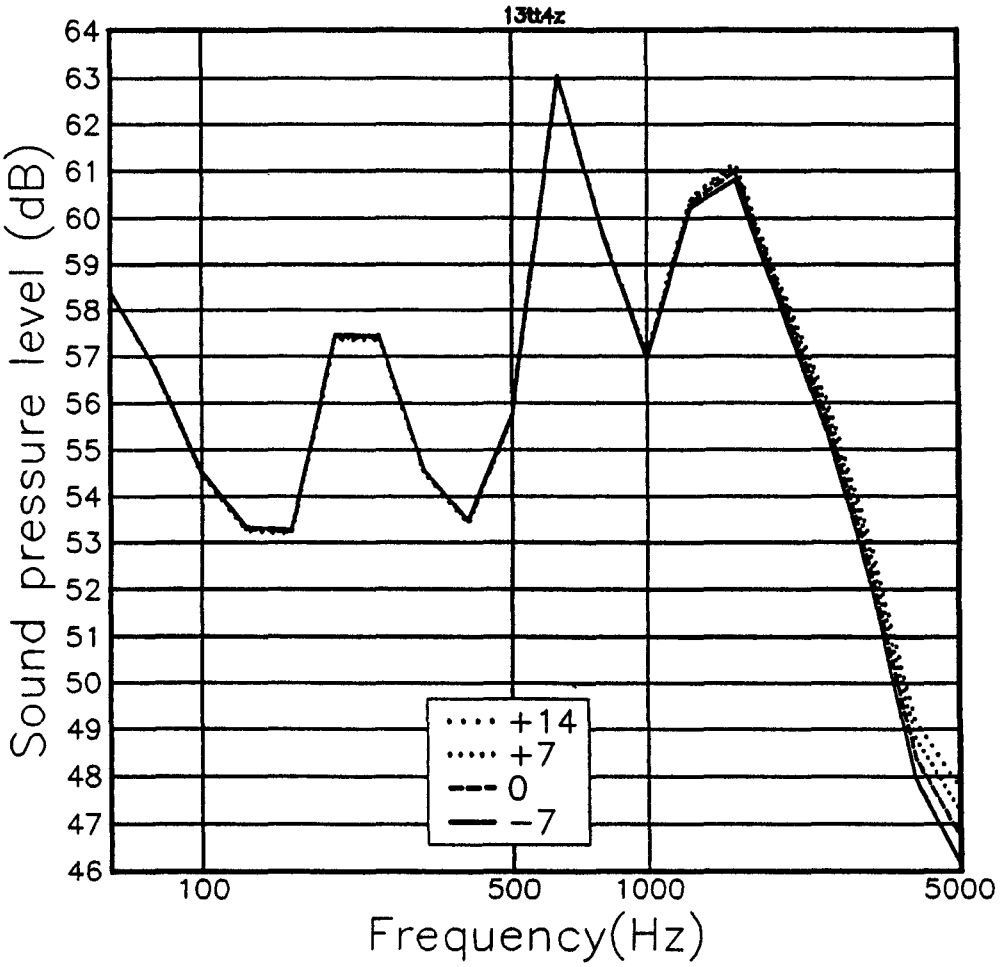

Figure 9.20 The predicted effect of temperature differences between the ground and the air ($T_{gro} - T_{air}$) of -7, +7 and +14 Celsius, on the 1/3 octave sound pressure level spectrum of a coasting car with the engine off, for a roughness length of 10^{-4} metres.

Table 9.2 Predicted db(A) levels for various temperature gradients at a range of 7.5 metres from a car for tyre and engine noise sources.

Source height m	Temperature difference $T_{gro} - T_{air}$	roughness length m	A-weighted averaged spl dB
0.5	0	-	42.391
0.5	-7	10^{-3}	42.254
0.5	+7	10^{-3}	42.623
0.5	+14	10^{-3}	42.714
0.5	-7	10^{-4}	42.251
0.5	+7	10^{-4}	42.581
0.5	+14	10^{-4}	42.685
0.045	0	-	53.541
0.045	-7	10^{-3}	53.319
0.045	+7	10^{-3}	53.702
0.045	+14	10^{-3}	53.780
0.045	-7	10^{-4}	53.378
0.045	+7	10^{-4}	53.639
0.045	+14	10^{-4}	53.754

ture gradient on the one third octave spectra is unlikely to be as large as is predicted here.

The differences between predicted sound pressure levels for the tyre source for different temperatures are mainly due to refraction at frequencies above 1kHz. It was shown in figure 9.8 that the number of layers used at frequencies above 2kHz had not caused convergence of the result. This lack of convergence means that the effect of the temperature gradient on the result is underpredicted at frequencies above approximately 3.5kHz. This error is estimated to be of the order of 0.1dB at 5kHz for a temperature difference $(T_{gro} - T_{air})$ of $+14^0$ Celsius. This error will lead to negligible errors in the predicted dB(A) level for the car spectrum.

Table 9.2 shows the predicted dB(A) level derived from figures 9.17 to 9.20 above. This table shows that the predicted effects of the temperature gradients on the dB(A) level are generally less than 0.4dB in the frequency range examined.

The conclusion from this study is that at frequencies where near surface

temperature gradients can be modelled acoustically as homogeneous horizontal layers the effect of temperature gradients on received sound pressure levels at short range (7.5 metres) from a source at a height of 0.5 metres is to shift the frequencies of interference dips, and cause small other changes in excess attenuation. But the overall effect on 'A' weighted sound pressure levels will be negligible unless the source spectrum contains peaks which are near to the interference dips.

For a source at a height of 0.045 metres at a range of 7.5 metres the effect of the temperature gradients is negligible at frequencies below 1kHz. Above this frequency diffraction effects change the predicted excess attenuation. However the effect of these gradients on the dB(A) level will be negligible in the frequency range considered here because of the low source level at frequencies above 2kHz.

In order to continue this study it would be necessary to obtain detailed acoustic and meteorological data, including wind speeds and temperatures at several different heights, over the different test sites which are suspected of giving different results. Differences of a similar order to those predicted here could result from differences in the ground surface, and from temperature effects on engine efficiency and tyre/road noise generation.

Chapter 10

Conclusions

10.1 Rigid porous ground models

10.1.1 The variable porosity model

It has been shown, by comparison to multiply layered impedance models, that the two parameter approximate impedance model is in good agreement with the impedance predicted using a multiply layered ground model where the porosity decreases exponentially with depth, for a wide range of rates of porosity decrease, surface flow resistivity and porosity at frequencies up to 1kHz.

10.1.2 Analytic sound propagation models

The FFLAGS propagation model has been compared to several different non-numerical propagation models. This has allowed the range of validity of approximate analytic ground models (such as that of Nicholas, Berry and Daigle[50]) to be examined. It has been found that Nicholas, Berry and Daigle's analytic approximation for propagation over a thin, rigidly backed, externally reacting layer maintains good agreement with FFLAGS over a much larger range of ground parameters than those for which it was originally intended. Also the 'exact' and 'approximate' models for propagation over an externally reacting surface, by Attenborough, Hayek, and Lawther[44] have been shown to give good agreement with FFLAGS at

ranges of 1 and 20 metres. Another analytic model, by Habault and Fillippi [87], has been shown to give very poor predictions at a range of 20 metres.

10.1.3 Low frequency sound propagation over porous grounds.

Predictions of sound pressure levels as a function of range assuming non-porous, and porous ground surfaces within realistic atmospheres, have been compared. It has been possible to show that the porous nature of the ground can have substantial effects on received sound pressure levels even at frequencies of 50Hz and 100Hz. The magnitude of the effect of the ground on sound propagation has been predicted to be affected by the atmospheric conditions at these low frequencies, with the largest effects occurring in conditions of downward refraction.

For higher frequencies (100Hz to 500Hz) the sensitivity of the predicted excess attenuation to the flow resistivity of the ground has been examined for an homogeneous atmosphere and for upward and downward refracting linear sound velocity gradients. It has been shown that for source and receiver one metre from the ground the sensitivity of the predicted excess attenuation to the ground flow resistivity is dependent on the sound velocity gradient. However in all cases examined the sensitivity to ground flow resistivity was large enough to give measurable differences for different ground parameters.

For conditions of propagation in a linear upwardly refracting sound velocity gradient it has been confirmed that results from a residue series solution, and an FFP using homogeneous air layers, generally agree as long as the layer thicknesses and the capping height of the profile are optimised. It has been shown that the simple rules suggested by Franke et al for calculating the necessary layer thicknesses and capping height [93] are not universally applicable.

Comparison of a residue series solution (including a surface wave term) to FFP predictions has shown that the surface wave contribution predicted by the residue series is consistent with FFP predictions. It has also been demonstrated that for long range prediction over an externally reacting layer the local reaction approximation is inadequate, giving predicted sound pres-

sure levels that are less than those predicted using an externally reacting ground model.

It has been shown that a ray tracing model prediction for propagation in a downward refracting logarithmic sound velocity gradient is in poor agreement with an FFP prediction in a frequency range between 100Hz and 1kHz. This poor agreement could be said to be due to a mistake in the ray tracing model program used. However, in the process of finding the minimum profile height for the convergence of the FFP prediction to a stable solution it was found that this minimum height exceeded the height of the highest Eigenray by at least one metre. In such a profile it has been shown that sound propagation above the highest Eigenray height influences predicted sound pressure level. This shows that Ray tracing in general, and not only this ray tracing model, is an inadequate method for predicting propagation in such an environment.

10.2 Effects of ground elasticity on sound propagation

By using elastic moduli and pore parameters measured in soils as inputs to the FFLAGS model the effects of the ground elasticity on sound propagation were examined. While previous predictions of seismic resonances in the normal surface impedance are substantiated, the predicted effects of the ground elasticity on long range sound propagation were negligible.

However, by using realistic elastic moduli and pore parameters for snow it has been predicted that the elasticity of a thin (8 cm) rigidly backed snow layer will have a measurable effect provided that the elastic wave attenuation in snow is small. Data on elastic wave attenuation in snow is very sparse and these predictions must be regarded as tentative until data on elastic wave attenuation is available. For thicker snow layers the predicted effects of elasticity were diminished. It was found that for propagation over the thin snow layer in the presence of a downward refracting sound velocity gradient the difference between the rigid and elastic model predictions was

unaffected by the sound velocity gradient.

Propagation from a point source over a thin rigidly backed polyester foam layer has been measured. It was found that by using the FFLAGS propagation model including independently measured elastic parameters of the foam, better agreement was found with the measurements than if only the measured pore parameters were used (without including elasticity). It was shown that the predicted excess attenuation, including the foam elasticity, included an interference dip corresponding to a reflection from the rigid backing via an elastic wave in the foam. This interference dip explained the difference in the predictions for the rigid and elastic models. This experiment was intended as a physical model for propagation over a snow layer. However the results should be of some relevance to the acoustics of foam lined ducts and enclosures, and other situations in building acoustics where propagation takes place close to flexible porous materials.

10.3 Coupling of airborne sound into the ground motion.

Predictions were made of the vertical particle velocity at the surface of an elastic halfspace (with elastic parameters similar to those of a soil), due to a point source in the air. Three models were used to make the predictions. These models were; FFLAGS, SAFARI(a visco-elastic FFP), and an asymptotic approximation. It was found that all three predict that a pseudo-Rayleigh wave makes a large contribution at low frequency. The predictions of amplitude decay with distance were in precise agreement for FFLAGS and SAFARI. This shows that the Biot-Stoll model reduces to a visco-elastic model, numerically as well as theoretically, for zero porosity. The asymptotic approximation was in poor agreement with either of the numerical models. Both FFLAGS and the asymptotic approximation predict that ,if realistic ground pore parameters were assumed, the predicted vertical particle velocity was reduced by approximately two orders of magnitude relative to the prediction for a visco-elastic, non-porous halfspace.

It should be emphasised that this result is not generally applicable; Figure 6.11 shows that predicted vertical particle displacement at the surface of a layered porous-elastic soil can be greater than, or less than, its non-porous equivalent.

It has been shown by Sabatier et al [4] that if certain small seismic velocities are assumed for the near surface ground then predictions of vertical particle velocity using porous and non-porous ground models will give nearly identical results. It is shown here that this agreement occurs over a very limited velocity range, and hence that the near surface seismic velocities calculated from acoustic-seismic coupling measurements, ignoring porosity, will not necessarily correspond to the actual near surface seismic velocities.

10.3.1 Experimental examination of the effect of wetting on the transfer of acoustic energy into ground vibration.

Experiments were performed in a soil bin whereby as many as possible of the elastic and pore parameters of a soil were measured. The acoustic-seismic coupling coefficient of the dry soil, and of the soil after wetting, was measured. It proved possible to fit the ratio of the measured coupling coefficients by using the measured parameters and fitting others.

10.3.2 Surface waves on porous elastic media.

Predictions of the surface waves on the surface of porous elastic soil by Attenborough and Chen [1] have been assessed by calculating the depth dependent Greens function in FFLAGS. There is partial agreement with these predictions in some cases. However the fast surface waves predicted by Attenborough and Chen are not predicted to be excited by an acoustic point source. Expected pseudo-Rayleigh waves and waveguide like modes in layered media are predicted to be excited. An additional low phase velocity mode which is not predicted by Attenborough and Chen is predicted to exist in some conditions.

10.4 The effects of near surface temperature gradients at short range

At short range, for a highly reflective ground surface, the effect of near surface temperature gradients on predicted excess attenuation has been examined. It has been found that for a point source at a height 0.5 metres and a receiver at a range of 7.5 metres and a height of 1.2 metresthe result of temperature gradients, is to shift the frequencies of the interference dips in the received excess attenuation spectrum, and alter the depth of the interference dips. For an upward refracting gradient the dips were moved up in frequency and the depth of the dips lessened. For a downward refracting sound velocity gradient the interference dips were moved down in frequency and their depths increased. The magnitude of these effects was very dependent on the roughness length of the gradient for a given temperature difference between the ground surface and a height of 1.2 metres.

For a receiver at the ground surface the effects of the near surface temperature gradients at the frequency range studied were very small at frequencies below 2kHz. Above this frequency refraction effects lead to differences of up to 2dB in the predicted excess attenuation. However the sound pressure level spectrum of a car in this test exhibits a reduced level above 2kHz and hence the influence of near surface temperature gradients on predicted dB(A) level is predicted to be less than 0.4 dB.

10.5 Possible directions for future work

It has been shown both here and elsewhere that the coupling of acoustic energy into the ground is very sensitive to both the near surface seismic structure and the near surface porous structure [4]. The pore structure has been examined using both acoustical and non-acoustical methods and the models used to describe the porous structure appear to be quite successful. On the other hand the seismic structure has up to now been measured almost exclusively by using traditional seismic survey techniques which allow only

large scale features to be modelled. It has been shown here that it is possible to use very small scale seismic survey techniques to measure the seismic velocities in the upper few centimetres of the soil. These techniques should be employed in order to test the ground models being used for acoustic-seismic coupling prediction.

The FFP program developed here could be usefully developed to give predictions of pulse response in both particle velocity in the ground and acoustic pressure in the atmosphere. Wilson's method [84] for the inclusion of the effects of turbulence could be included. A more sophisticated model of the acoustic behaviour of porous solids has recently been developed [117] which allows two different pore fluids to be present. It is possible that the inclusion of this theory will allow propagation in porous elastic partially water filled solids to be described accurately.

Bibliography

[1] K Attenborough and Yu Chen. Surface waves at the interface between air and air-filled poro-elastic ground. *J. Acoust. Soc. Am.*, 87(3):1010–1016, March 1990.

[2] A.J. Cramond and C.G. Don. Impulse propagation over grassland in the presence of temperature and wind gradients. *J.Acoust.Soc.Am.*, 78(3):1029–1037, Sept. 1985.

[3] Alwin Gudesen. Applying the safari model to sound propagation. *J.Acoust.Soc.Am*, 87(5):1968–1974, May 1990.

[4] J.M.Sabatier. In W.Willshire, editor, *Proceedings of the 4th International Symposium on long range sound propagation*, NASA, Langley, VA, May 1990.

[5] J.M. Sabatier, H.E. Bass, L.M. Bolen, K. Attenborough, and V.V.S.S. Sastry. The interaction of airborne sound with the porous ground: the theoretical formulation. *J.Acoust.Soc.Am.*, 79(5):1345–1352, May 1986.

[6] K.B. Rasmussen. Outdoor sound propagation under the influence of wind and temperature gradients.

[7] P.M.Morse and K.U.Ingard. *Theoretical Acoustics.* Princeton University Press, reprint edition, 1986.

[8] C.Zwikker and C.W.Kosten. *Sound Absorbing Materials.* Elsevier, 1949.

[9] M.E. Delany and E.N. Bazley. Acoustical properties of fibrous absorbent materials. *Applied Acoustics*, 3:309–322, 1970.

[10] C.I. Chessel. Propagation of noise along a finite impedance boundary. *J.Acoust.Soc.Am.*, 62:825–834, 1977.

[11] H.M.Hess, K.Attenborough, and N.W.Heap. Acoustical characterisation of soils by short range propagation measurements. *J.Acoust.Soc.Am.*, 1990. Accepted for publication.

[12] K. Attenborough. On the acoustic slow wave in air filled granular media. *J.Acoust.Soc.Am.*, 81(1):93–102, Jan. 1987.

[13] R.P. Janse. Sound absorption at the soil surface. *Centre for Agricultural Publishing and Documentation*, 89–123, 1969.

[14] M.A. Biot. Thermoelasticity and irreversible thermodynamics. *J.Applied Physics*, 27(3), March 1956.

[15] P.C.Carman. *Flow of Gases through Porous Media.* Academic Press, 1956.

[16] W. Brutsaert. The propagation of elastic waves in unconsolidated, granular mediums. *J. Geophysical Research*, 69(2):243–257, 1964.

[17] K.Attenborough and T.L.Richards. Solid particle motion induced by a point source above a poroelastic halfspace. *J.Acoust.Soc.Am.*, 86(3):1085–1091, 1989.

[18] M.A. Biot. Mechanics of deformation and acoustic propagation in porous media. *J.Applied Physics*, 33(4):1482–1498, 1962.

[19] M.A. Biot. Generalized theory of acoustic propagation in porous dissapative media. *J.Acoust.Soc.Am*, 34(9):1254–1264, 1962.

[20] R.D.Stoll. Theoretical aspects of sound transmission in sediments. *Journal of the Acoustical Society of America*, 68(5):1341–1350, November 1980.

[21] T.J.Plona. Observation of a second bulk compressional wave in a porus medium at ultrasonic frequencies. *Appl.Phys.Lett.*, 36:259, 1980.

[22] J.G.Berryman. Confirmation of Biot's theory. *Appl. Phys. Lett.*, 37(4):382–384, 1980.

[23] J.G.Berryman. Long wavelength propagation in composite elastic media, 1. spherical inclusions. *J.Acous.Soc.Am.*, 68(6):1809–1819, 1980.

[24] J.G.Berryman. Long wavelength propagation in composite elastic media 2.ellipsoidal inclusions. *J.Acous.Soc.Am.*, 68(6):1820–1831, 1980.

[25] P.R.Ogushwitz. Applicability of the biot theory. *J.Acoust.Soc.Am.*, 77(2):429–464, 1985.

[26] K. Attenborough and H.M. Hess. Acoustical surveying of porous soils. In *14th International Symposium on Acoustical Imaging*, 1985.

[27] J.F. Allard, A. Akine, and C. Depollier. Acoustical properties of partially reticulated foams with high and medium flow resistance. *J. Acoust. Soc. Am.*, 79(6):1734–1740, June 1986.

[28] G.S. Rosin. Oscillations induced in porous materials with an elastic matrix by sound waves at normal incidence. *Soviet Physics-Acoustics*, 19(1).

[29] J.G. Berryman and S.C. Blair. Kozeny-carman relations and image processing methods for estimating darcy's constant. *J. Appl. Phys.*, 62(6), Sept 1987.

[30] S.H. Burns. The absorption of sound by pine trees. *J. Acoust. Soc. Am.*, 65(3):658–661, March 1979.

[31] M P Cleary. Elastic and dynamic regimes of fluid impregated solids with diverse microstructures. *Int. J. Solid Struct.*, 14:795–891, 1978.

[32] F. Press and M. Ewing. Ground roll coupling to atmospheric compressional waves. *Geophysics*, XVI(1-4):416–430, 1951.

[33] H.M.Mooney and R.A.Kaasa. Airwaves in engineering seismology. *Geophysical Prospecting*, 10:84–91, 1962.

[34] McCarty and Dalius. Frequency shift in air coupled surface waves originated by a rocket launcher. *Journal of Geophysical Research*, 76:7027–7034, 1971.

[35] F.A.Crowley and H.A.Ossing. *On the applicationof air coupled seismic waves.* Technical Report AFRCL690312, USAF Cambridge Research Lab, 1969.

[36] Flohr M.D. and Cress D.H. *Acoustic-seismic coupling: Properties and applications to seismic sensors.* WES technical report EL-79-1, WES, Waterways experimental station, Vicksburg, MS, 1979.

[37] Peck L. Acoustic seismic coupling under winter conditions. Presentation at 114th meeting of Acoust. Soc. Am., November 1987.

[38] H.E. Bass and L.N. Bolen. Coupling of airborne sound into the earth: frequency dependency. *J.Acoust.Soc.Am.*, 67(5), May 1980.

[39] A. Espanosa and W. Sierra, P.and Mickey. Seismic waves generated by sonic booms: a geoacoustical problem. *J.Acoust.Soc.Am.*, 44(4):1074–1081, 1971.

[40] Bass H.E. and Bolen L.N. *Coupling of airborne sound into the earth.* PARGUM report 84-01, University of Mississippi, Physical acoustics research group, The University of Mississippi, University, MS 38677, August 1984.

[41] S-I. Thomasson. Diffraction by a screen above an impedance boundary. Nov 1977.

[42] C.F. Chien and W.W. Soroka. A note on the calculation of sound propagation along an impedance surface. *J. Sound and Vib.*, 69(2):340–343, 1980.

[43] C.G. Don and A.J. Cramond. Impulse propagation in a neutral atmosphere. *J.Acoust Soc.Am.*, 81(5):1341–1349, May 1987.

[44] K.Attenborough, S.I.Hayek, and J.M.Lawther. Propagation of sound above a porous half-space. *J.Acoust.Soc.Am.*, 68(5):1493–1501, November 1980.

[45] D. Habault. Sound propagation over ground: analytical approximations and experimental results. *J. Sound and Vib.*, 79(4):551–560, 1981.

[46] M.A. Nobile and S.I. Hayek. Acoustic propagation over an impedance plane. *J.Acoust.Soc.Am.*, 78(4), Oct. 1985.

[47] F.P.Mechel. Analysis of spherical wave propagation over absorbing ground. In *Proceedings of the institute of acoustics*, pages 231–255, 1989.

[48] K.Attenborough and O.Buser. On the application of rigid-porous models to impedance data for snow. *J.Sound and Vib.*, 124(2):315–327, 1988.

[49] I Rudnick. The propagation of an acoustic wave along a boundary. *J.Acoust.Soc.Am.*, 19:348–356, 1947.

[50] J.Nicholas, J.L.Berry, and G.A.Daigle. Propagation of sound above a finite layer of snow. *J.Acoust.Soc.Am*, 77(1):67–73, January 1985.

[51] L.M. Brekhovskikh. Surface waves in acoustics. In *Review: 4th All Union Acoustics Conf.*, June 1958.

[52] D.I.Paul. Acoustical radiation from a point source in the presence of two media. *J.Acoust.Soc.Am.*, 29:1102–1109, 1957.

[53] D.I.Paul. Wave propagation in acoustics using the saddle point method. *J.Math.Phys.*, 38:1–15, 1959.

[54] T.L.Richards and K.Attenborough. Accurate fft-based hankel transforms for prediction of outdoor sound propagation. *J. Sound and Vib.*, 109(1):157–167, 1986.

[55] L.M.Brekhovskikh. *Waves in Layered Media. Applied Maths and Mechanics*, Academic Press, 1960. Translated by David Lieberman.

[56] T.F.W. Embleton and J.E. Piercy. Effective flow resistivity of ground surfaces determined by acoustical measurements. *J.Acoust.Soc.Am.*, 74:1239–1244, 1983.

[57] A Berry and G A Daigle. Controlled experiments of the diffraction of sound by a curved surface. *J.Acoust.Soc.Am.*, 83(6):2047–58, 1988.

[58] W. Kuperman, M. Werby, and K. Gilbert. Mathematical foundations of propagation models in underwater acoustics. In *AIAA 8th Aeroacoustics Conf.*, April 1983.

[59] H. Schmidt and F.B. Jensen. A full wave solution for propagation in multilayered viscoelastic media with application to gaussian beam reflections at fluid-solid interfaces. *J.Acoust.Soc.Am.*, 77(3):813–825, 1985.

[60] A.Papoulis. *Systems and transforms with application to optics.* R.E.Kreiger Pub Co, reprint edition, 1981.

[61] M.Abramowitz and I.A.Stegun. *Handbook of Mathematical Functions.* Dover NY USA, 1970.

[62] S.J.Franke and G.W.Swenson(Jr). A brief tutorial on the fast field program (ffp) as applied to sound propagation in the air. *Applied Acoustics*, 27(3):203–216, September 1989. Univ of Illinois at Urbana-Champaign.

[63] M.West, R.A.Sack, and F.Walden. The fast field program. a second tutorial; application to long range sound propagation in the atmosphere. *Applied Acoustics*, 1990. Not yet published.

[64] S.W.Lee, N.Bong, W.F.Richards, and R.Raspet. Impedance formulation for the fast field program for acoustic wave propagation in the atmosphere. *J.Acoust.Soc.Am.*, 79:628–634, 1986.

[65] R.Raspet, S.W.Lee, E.Keuster, D.C.Chang, W.F.Richards, R Gilbert, and N. Bong. A fast field program for sound propagation in a layered atmosphere over an impedance ground. *J.Acoust.Soc.Am*, 77:345–352, 1985.

[66] A.M.Chrestman. *Validity of the ray approximation applied to sound propagation in the atmosphere.* Master's thesis, University of Mississippi, Physical Acoustics Research Lab,University of Mississippi, University,Mississippi 38677, January 1990.

[67] H. Schmidt. A fast field model for three dimensional wave propagation in stratified environments based on the global matrix method. *J.Acoust.Soc.Am.*, 78(6):2105–2114, Dec 1985.

[68] F.D.Tappert and R.H.Hardin. In *A Synopsis of the AESD workshop on acoustic modelling by non-ray-tracing techniques*, 1973.

[69] J.F.Claerbout. *Fundamentals of Geophysical Data Processing.* Mcgraw-Hill, 1976.

[70] M.J.White and K.E.Gilbert. Application of the parabolic equation to outdoor propagation of sound. *Applied Acoustics*, 27(3):227–238, 1989.

[71] KE Gilbert, R Raspet, and X Di. Calculation of turbulence effects in an upward refracting atmosphere. *J. Acoust. Soc. Am.*, 87(6):2428–2437, June 1990.

[72] K.B.Rasmussen. Outdoor sound propagation under the influence of wind and temperature gradients. *J. Sound and Vib.*, 1989.

[73] K.Gilbert. Personal communication.

[74] WM Ewing, WS Jardetsky, and F Press. *Elastic waves in layered media.* McGraw-Hill, 1957.

[75] B Prange. Parameters affecting damping properties. *Proc.DMSR 77 Karlsruhe*, 1:61, 1977.

[76] D Albert. Personal communication, 1990.

[77] Numerical Algorithm Group. *Fortran Library Manual, Mark 13*, chapter F04. Volume 5, 1988.

[78] R.J. Donato. Impedance models for grass covered ground. *J.Acoust.Soc.Am.*, 61(6), June 1977.

[79] K. Attenborough. Acoustical impedance models for outdoor ground surfaces. *J.Sound and Vib.*, 99(4):521–544, 1985.

[80] K. Attenborough. Acoustical characteristics of rigid fibrous absorbent and granular materials. *J.Acoust.Soc.Am.*, 73:785–799, 1983.

[81] A.Berry and J.Nicholas. Modeles d'impedance pour les sols non homogenes. May 1986. Personal communication.

[82] D C Waddington. *Acoustical Impedance Measurement using a two microphone transfer function technique.* PhD thesis, University of Salford, 1990.

[83] D. Habault and C. Corsain. Identification of acoustical properties of a ground surface. *J. Sound and Vib.*, 1985.

[84] K Wilson and D Thompson. Comparison of ffp predictions with measurements of a low frequency signsl propagated in the atmosphere. In W.Willshire, editor, *Proceedings of the 4th International Symposium on Long Range Sound Propagation*, NASA, Langley, VA, 1990.

[85] L.R.Quartararo. *A Theoretical Investigation of Sound Propagation above a Half-space of Extended Reaction.* Master's thesis, Pennsylvania State University, 1983.

[86] S-I. Thomasson. Sound propagation above a layer with large refraction index. *J.Acoust.Soc.Am.*, 61:659–674, 1977.

[87] D. Habault and P. Filippi. Ground effect analysis: surface wave and layer potential approximation. *J. Sound and Vib.*, 79(4):529–550, 1981.

[88] H.M. Hess, K. Attenborough, and N. Heap. The deduction of soil properties from acoustic measurements. In *Sound Propagation in Forrested Areas and Shelterbelts*, March 1986.

[89] HM Hess. *Acoustical Determination of Physical Properties of porous grounds*. PhD thesis, Open University, Walton Hall, 1988.

[90] S Feng and DL Johnson. High frequency acoustic properties of a fluid-porous solid interface. *J.Acoust.Soc.Am.*, 74(3):906–924, Sept 1983.

[91] M Tajuddin. Rayleigh waves in a poro-elastic halfspace. *J.Acoust.Soc.Am.*, 75(3):682–684, March 1984.

[92] I Tolstoy. *Wave Propagation. International series in the Earth and Planetary Sciences*, McGraw-Hill, 1973.

[93] S.J.Franke, R.Raspet, and C.H.Liu. Numerical predictions of atmospheric sound pressure levels in shadow zones. *J.Acoust.Soc.Am.*, 83(2):816–820, 1988.

[94] M.West, F.Walden, and R.A.Sack. The acoustic shadow produced by wind speed and temperature gradients near the ground. *Applied Acoustics*, 27(3):239–260, 1989.

[95] W.Huisman. Users guide to rayflux ray tracing program. 1987. report published by Oldenburg University.

[96] R A Sommerfeld. A review of snow acoustics. *Reviews of Geophysics and Space Physics*, 20(1):62–66, February 1982.

[97] J.B. Johnson. On the application of biot's theory to acoustic wave propagation in snow. *Cold regions Science and Technology*, 6:49–60, 1982.

[98] T. Ishida. Acoustic properties of snow. *Contributions from the Intensity of Low Temperature Science Series A.*, 20:23–63, 1965.

[99] G.Daigle. Personal communication. 1990.

[100] A.D.Pierce. *Acoustics: an Introduction to its Physical Principles and Applications.* McGraw-Hill, New York, 1981.

[101] R Raspet, Gordon E Baird, and Wenliang Wu. The relationship between upward refraction above a complex plane and the spherical wave evaluation for a homogeneous atmosphere. *submitted to J.Acoust.Soc.Am*, 1989.

[102] R Raspet. Residue series solution of impulse noise propagation into a shadow zone. *J.Acoust.Soc.Am.*, 83(5):1964–7, 1988.

[103] R.Raspet. Personal communication. 1990.

[104] M.A. Biot. Theory of propagation of elastic waves in a fluid saturated porous solid. *J.Acoust.Soc.Am.*, 168–191, 1956.

[105] T Pritz. Frequency dependence of frame dynamic characteristics of mineral and glass wool materials. *Journal of Sound and Vibration*, 106(1):161–169, 1986.

[106] T Pritz. Transfer function method for investigating the complex modulus of acoustic materials: rod like specimen. *Journal of Sound and Vibration*, 81(3):359–376, 1982.

[107] C.T.Lynch, editor. *Handbook of Material Science.* Volume 3, CRC Press, 1989.

[108] C Howorth. *Sound propagation over rigid porous layered media.* PhD thesis, Open University, Walton Hall, Milton Keynes, September 1990.

[109] A.J. Crammond and C.G. Don. Effects of moisture content on soil impedance. *J.Acoust.Soc.Am.*, 82(1):293–301, July 1987.

[110] D.L.Berry and K.Attenborough. Area of ground influencing sound propagation from a point source. In *Proceedings of the third International Symposium on Long Range Sound Propagation and Coupling into the Ground*, pages 143–151, The University of Mississippi, Physical Acoustics Research Grp, March 1988.

[111] W.M.Telford, L.P.Telford, R.E.Sheriff, and D.A.Keys. *Applied Geophysics*. Cambridge University Press, 1976.

[112] BL Carnes and JR Lundein. *Analysis of short to medium range seismic attenuation tests using a multi-lasyered visco-elastic seismic propagation model.* Technical Report EL 84 9, USAE WES, 1984.

[113] Dr Paul Nelson. Personal communication.

[114] U Ingard and VK Singhal. Upstream and downstream sound readiation into a moving fluid. *J.Acoust.Soc.Am*, 84(5):1343–1346, 1973.

[115] GA Daigle, JE Piercy, and TFW Embleton. Propagation of noise over short distances above asphalt-refractive and impedance effects. *J.Acoust.Soc.Am.*, 73, 1983.

[116] M.E. Delany and E.N. Bazley. Monopole radiation in the presence of an absorbing plane. *J. Sound and Vib.*, 13(3):269–279, ????

[117] J.E.Santos, J.Douglas, J.Corbero, and O.M.Lovera. A model for wave propagation in a porous medium saturated by a two phase fluid. *J. Acoust. Soc. Am.*, 87(4):1439–1448, 1990.

[118] B de Jong. *The influence of wind and temperature gradients on outdoor sound propagation.* Delft University Press, 1983.

[119] *VAX Fortran user manual.* Digital Equipment Corporation, Maynard, Mass, USA, 5.0 edition, 1989.

[120] *VAX DCL concepts manual.* Digital Equipment Corporation, Maynard,Mass, USA, 5.0 edition, 1988.

Appendix A

The two parameter approximation

In this appendix the predicted impedance using Attenborough's two parameter model will be compared to impedance predicted using Brekhovskikh's multiple fluid layer model [51] where the propagation constants in the layers are derived using Attenborough's four parameter rigid-porous ground model. It has been shown that Brekhovskikh's fluid layer model agrees precisely with the rigid frame limit of a multilayered poro-elastic impedance model (MULTIPORO). In the following graphs the layer thicknesses for the multilayered case have been decreased and the number of layers increased until further changes produced negligible changes in the output.

It was shown in chapter 2 that the two parameter approximation is a low frequency, high flow resistivity approximation. Therefore the comparisons between the two parameter approximation and the multilayered model are in a frequency range from 10Hz to 1000Hz. In the first section comparisons are presented for a single surface flow resistivity and porosity, for four different exponential porosity decreases. In the second section the effect of changing the grain shape factor (n') has been examined by comparing the results of using four different grain shape factors for two different gradients. In the third section the effect of changing the surface flow resisitivity has been examined.

A.1 The effect of changing the exponential porosity decrease α.

The surface pore parameters in this section are set as follows; flow resisitivity σ 100000 mks rayls m^{-1}; porosity Ω 0.4 ; grain shape factor n' 1.0 ; pore shape factor ratio s_p 0.5 . It can be seen from figures A.1,A.2, A.3 and A.4 that for this set of parameter values the two parameter and layer model impedance predictions gradually diverge as the value of α increases. The upper limit to α that one could use ground characterisation obviously depends on the accuracy required.

A.2 The influence of grain shape factor.

Figures A.5, A.3, A.6 and A.7 show the influence of the grain shape factor on the agreement between the two parameter model and the layer model for a value of α of 10.0. It can be seen from this that as the grain shape factor is increased from 0.5 to 2.0 the agreement between the two impedance models is dramatically improved. Figures A.8, A.2, A.9 and A.10 ($\alpha = 3.33$) also show poor agreement between the two model outputs for a grain shape factor of 0.5, but for values above that the predicted impedances using the two models agree very well.

A.3 The influence of flow resistivity.

Figures A.11, A.3 and A.12 show the predicted influence of surface flow resistivity on the agreement between the predictions of impedance using the layer and two parameter methods.

It can be seen from these figures that the two parameter model is indeed a high flow resistivity model. The difference between the resistances predicted by the two impedance models is much increased by reducing the assumed flow resistance.

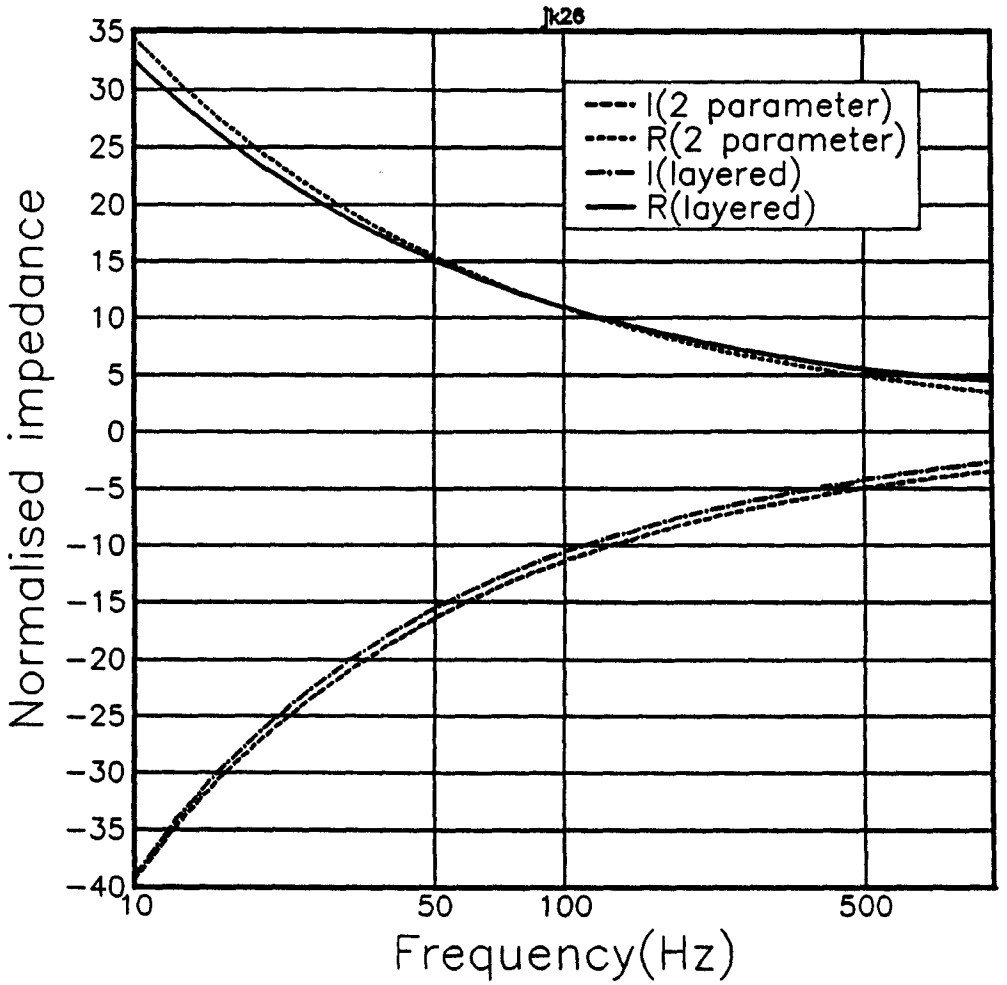

Figure A.1 Predicted impedance for exponential porosity decrease ; α = 1.0 using Brekhovskikh and two parameter models. Surface pore parameters σ =100000mks rayls m^{-1} , Ω = 0.4, n'=1.0 ,s_p=0.5.

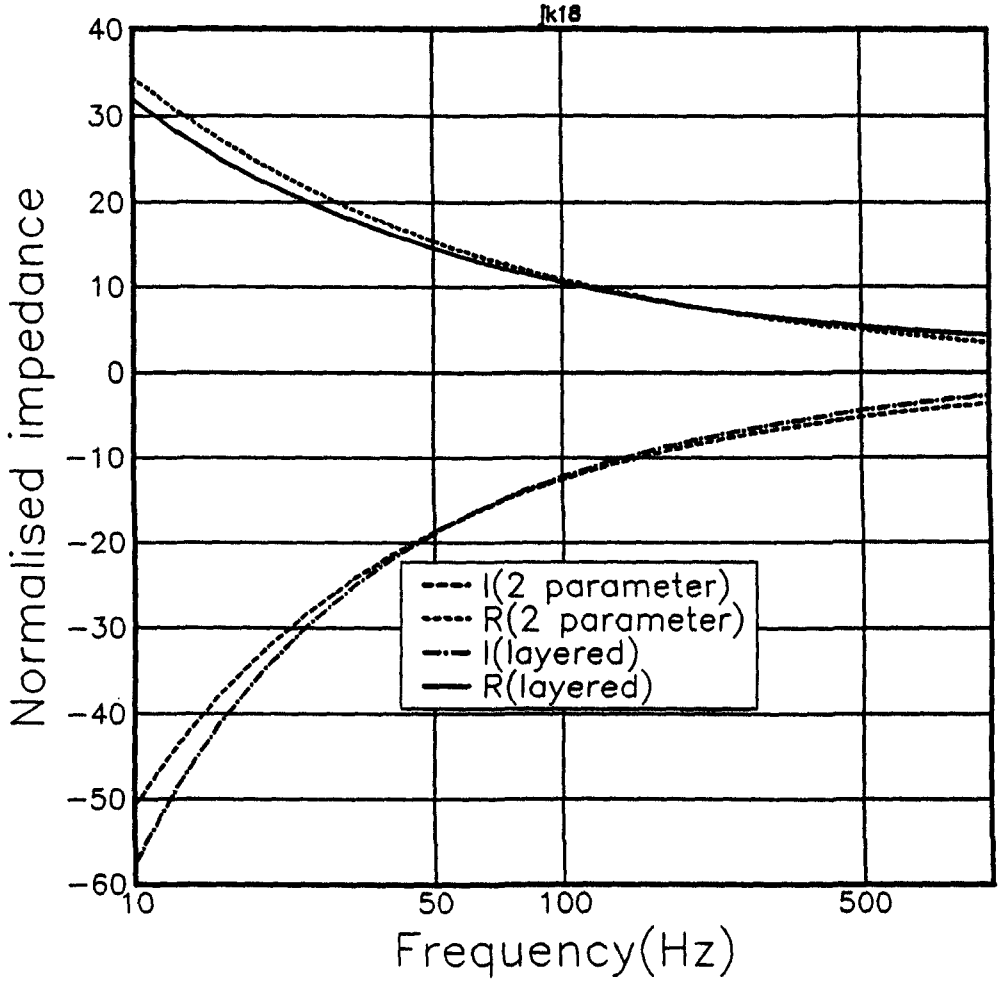

Figure A.2 Predicted impedance for exponential porosity decrease ; α = 3.33 using Brekhovskikh and two parameter models. Surface pore parameters σ =100000mks rayls m^{-1} , Ω = 0.4, n'=1.0 ,s_p=0.5.

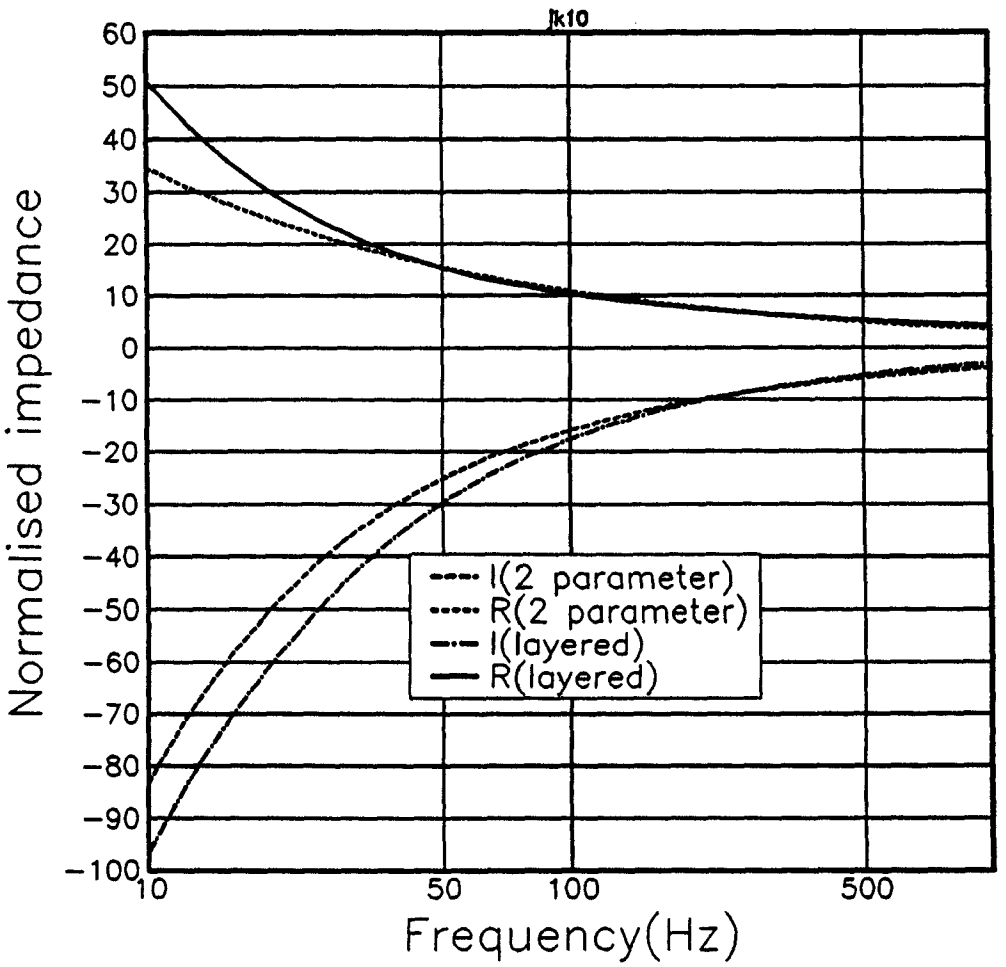

Figure A.3 Predicted impedance for exponential porosity decrease ; α = 10.0 using Brekhovskikh and two parameter models. Surface pore parameters σ =100000mks rayls m^{-1} , Ω = 0.4, n'=1.0 ,s_p=0.5.

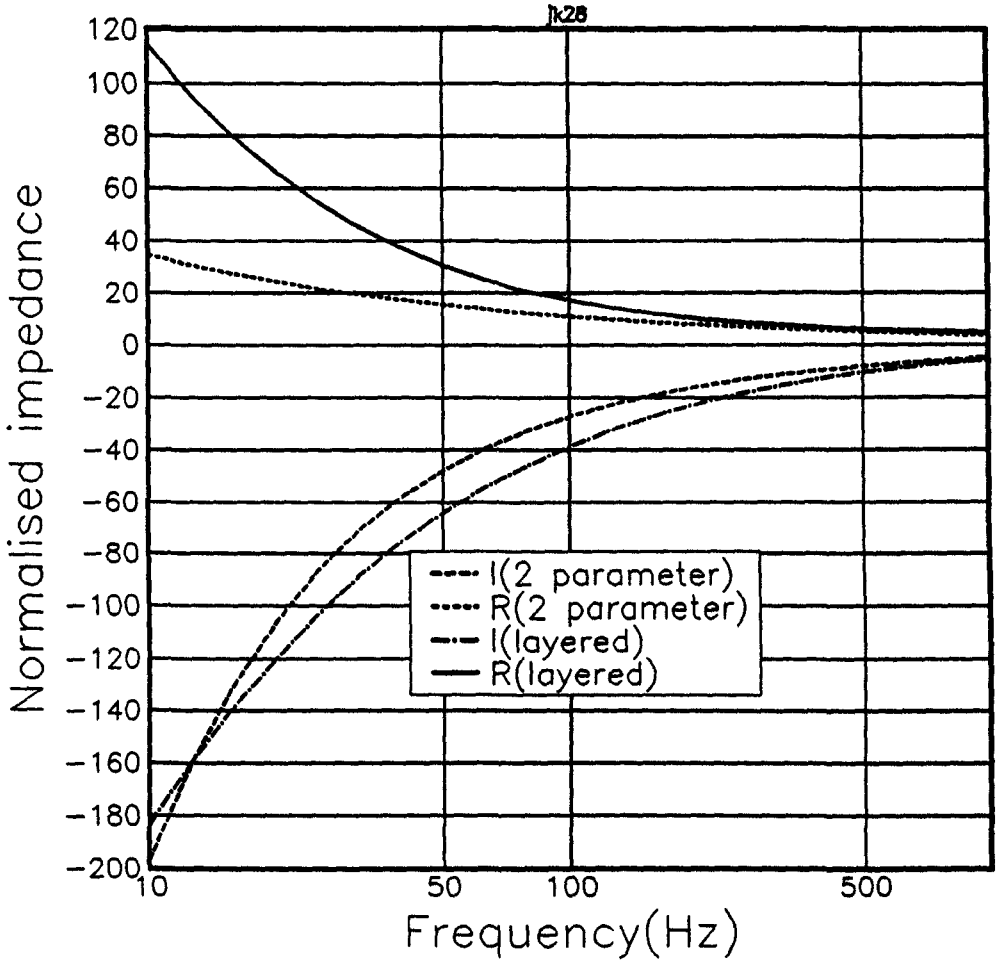

Figure A.4 Predicted impedance for exponential porosity decrease ; α = 33.3 using Brekhovskikh and two parameter models. Surface pore parameters σ =100000mks rayls m^{-1} , Ω = 0.4, n'=1.0 ,s_p=0.5.

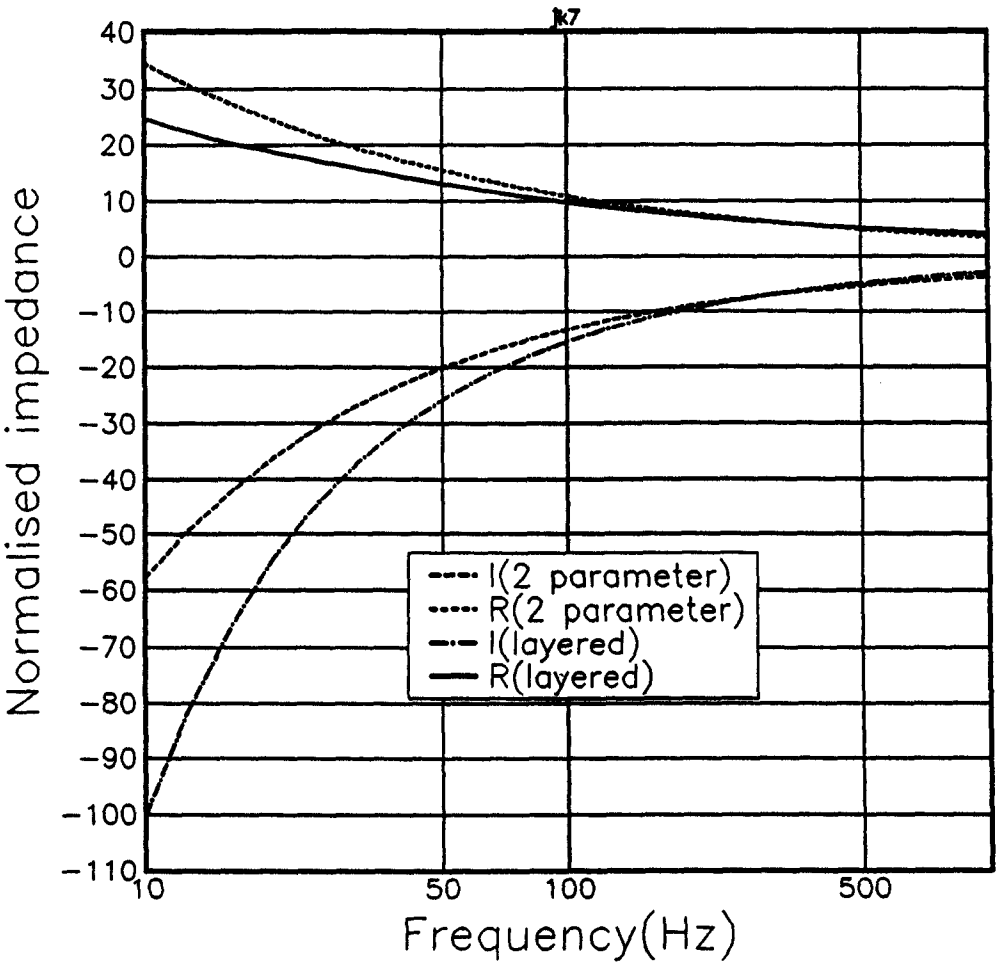

Figure A.5 Predicted impedance for grain shape factor;n'=0.5, exponential porosity decrease ; α = 10.0 using Brekhovskikh and two parameter models. Surface pore parameters σ =100000mks rayls m^{-1} , Ω = 0.4, s_p=0.5.

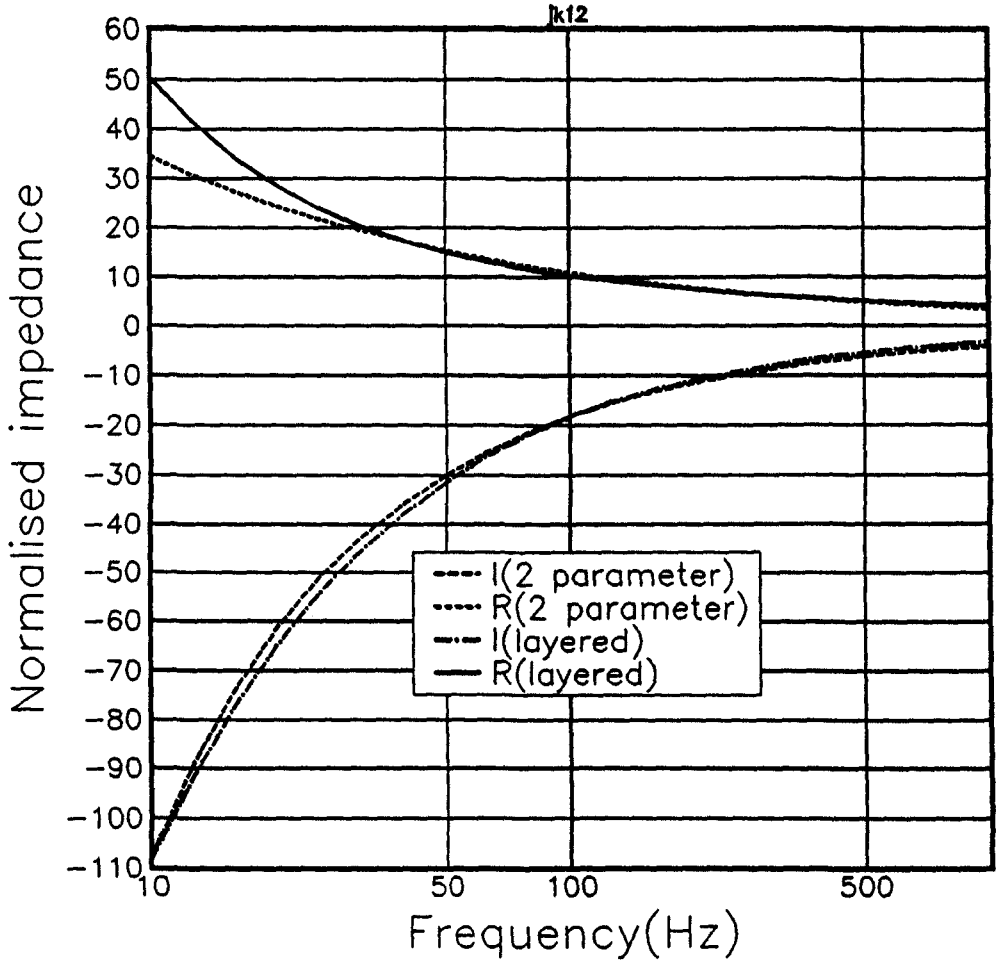

Figure A.6 Predicted impedance for grain shape factor;n'=1.5, exponential porosity decrease ; α = 10.0 using Brekhovskikh and two parameter models. Surface pore parameters σ =100000mks rayls m^{-1} , Ω = 0.4, s_p=0.5.

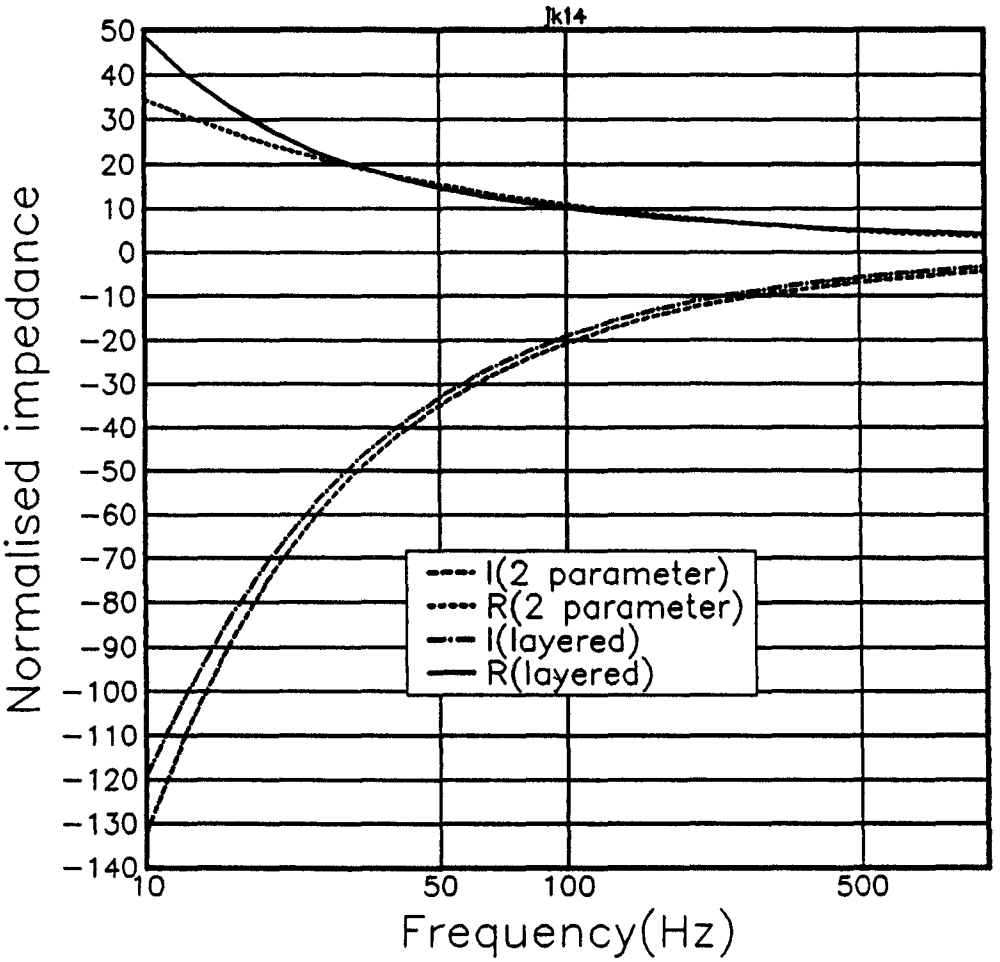

Figure A.7 Predicted impedance for grain shape factor;n'=2.0, exponential porosity decrease ; α = 10.0 using Brekhovskikh and two parameter models. Surface pore parameters σ =100000mks rayls m^{-1} , Ω = 0.4, s_p=0.5.

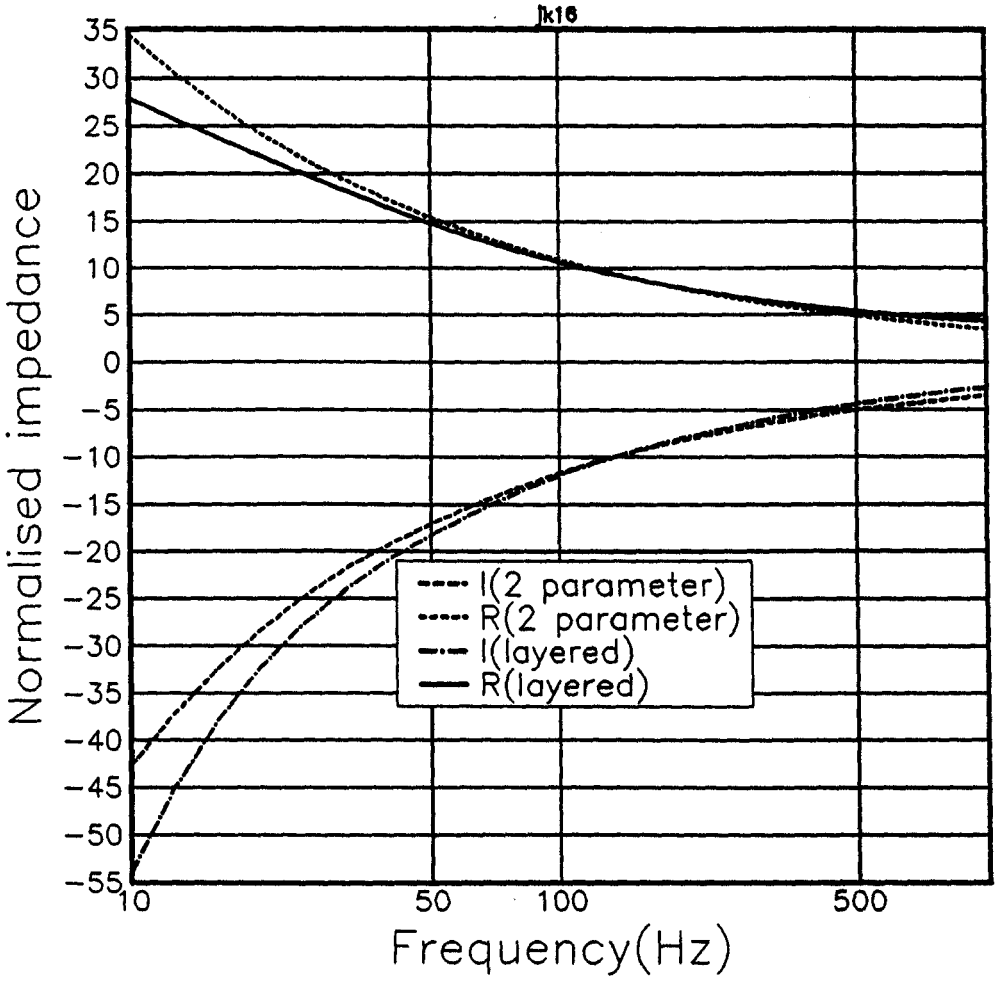

Figure A.8 Predicted impedance for grain shape factor;n'=0.5, exponential porosity decrease ; $\alpha = 3.33$ using Brekhovskikh and two parameter models. Surface pore parameters σ =100000mks rayls m^{-1} , $\Omega = 0.4$, s_p=0.5.

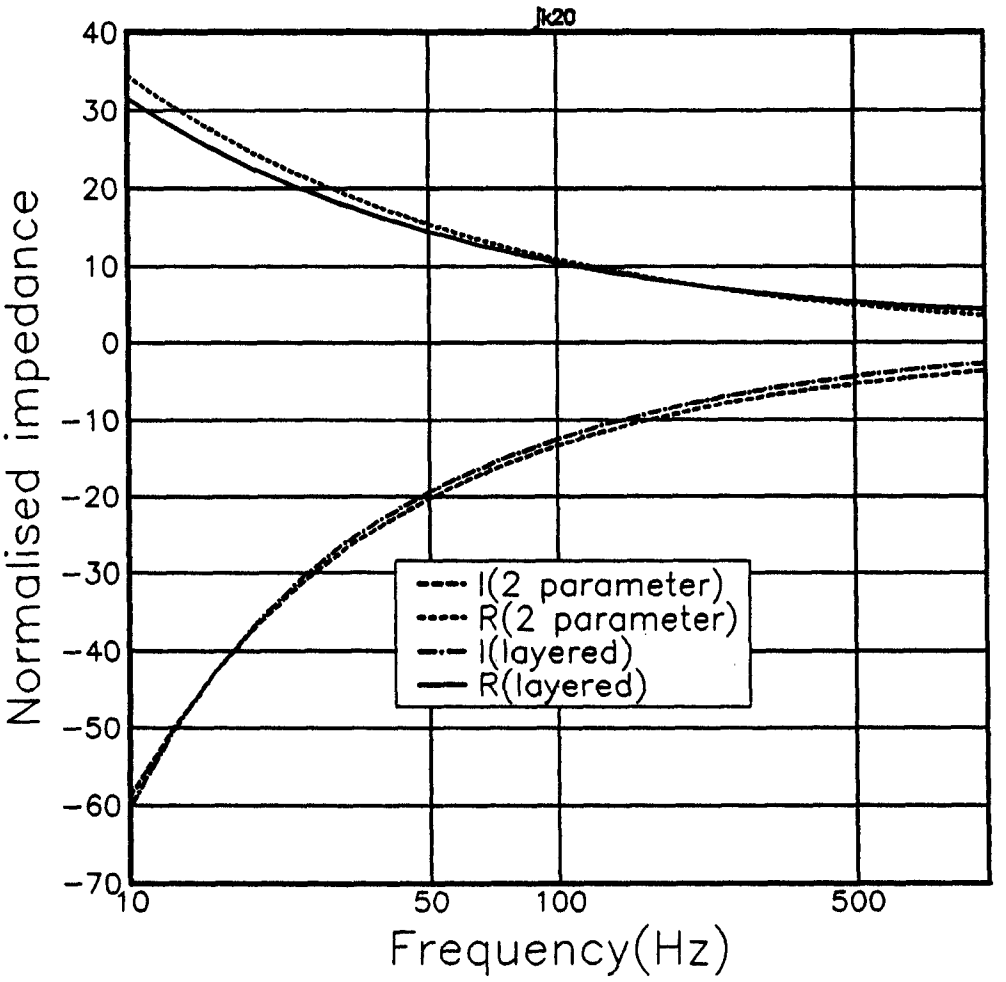

Figure A.9 Predicted impedance for grain shape factor;n'=1.5, exponential porosity decrease ; α = 3.33 using Brekhovskikh and two parameter models. Surface pore parameters σ =100000mks rayls m^{-1} , Ω = 0.4, s_p=0.5.

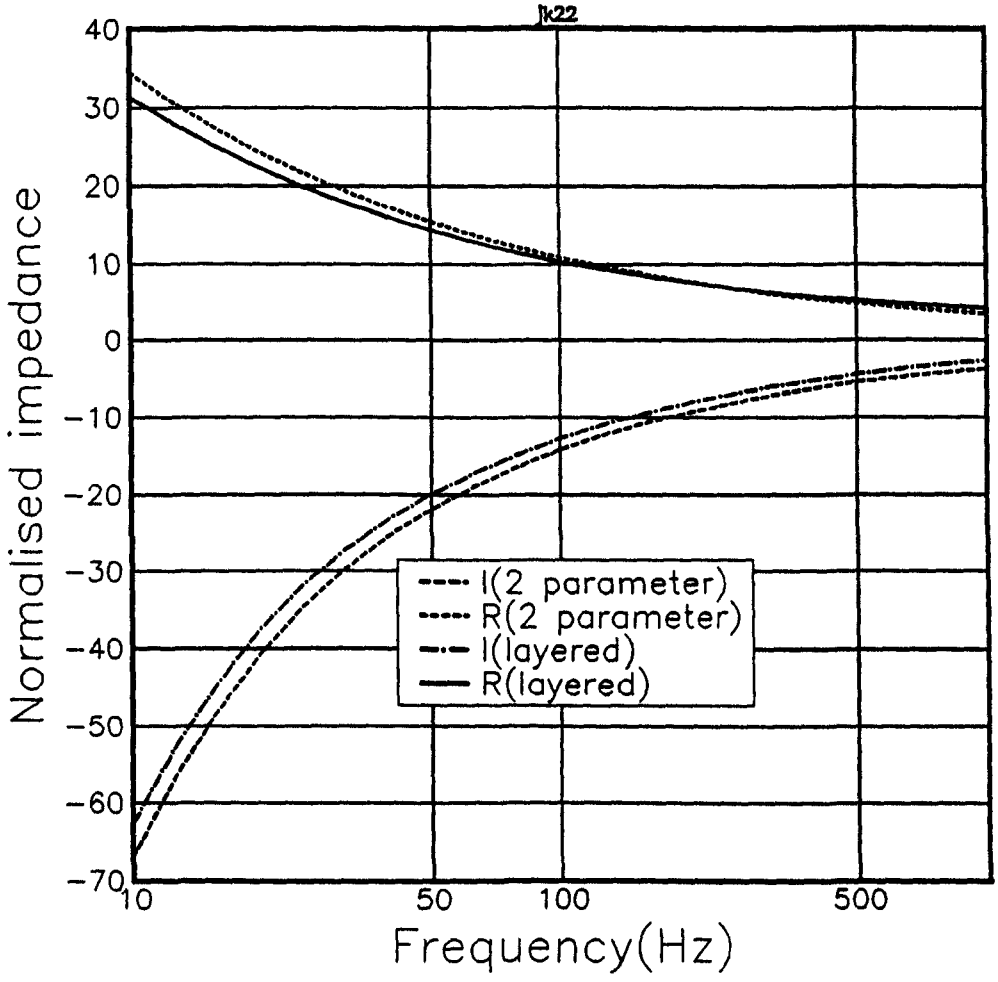

Figure A.10 Predicted impedance for grain shape factor;n'=2.0, exponential porosity decrease ; α = 3.33 using Brekhovskikh and two parameter models. Surface pore parameters σ =100000mks rayls m^{-1} , Ω = 0.4, s_p=0.5.

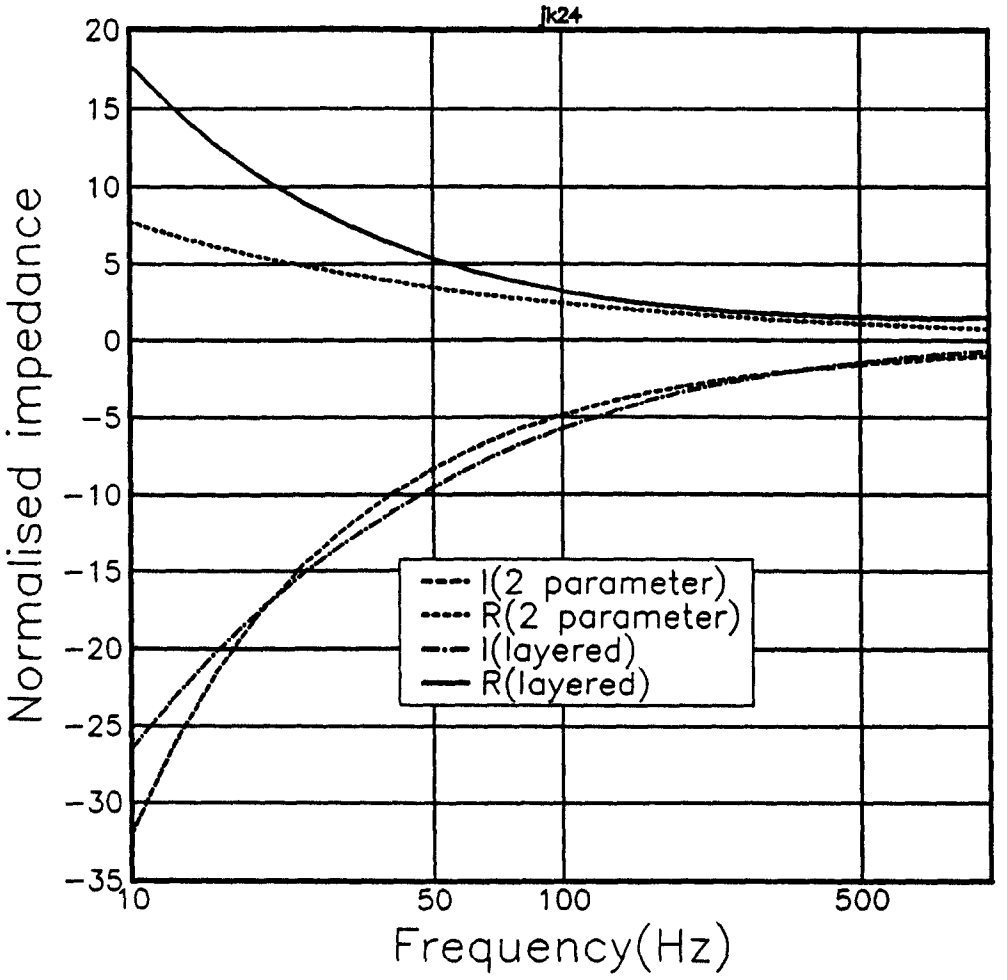

Figure A.11 Predicted impedance for flow resistivity 10000mks rayls m^{-1}, exponential porosity decrease ; α = 10.0, using Brekhovskikh and two parameter models. Surface pore parameters σ =100000mks rayls m^{-1}, n'=1.0, Ω=0.4, s_p=0.5.

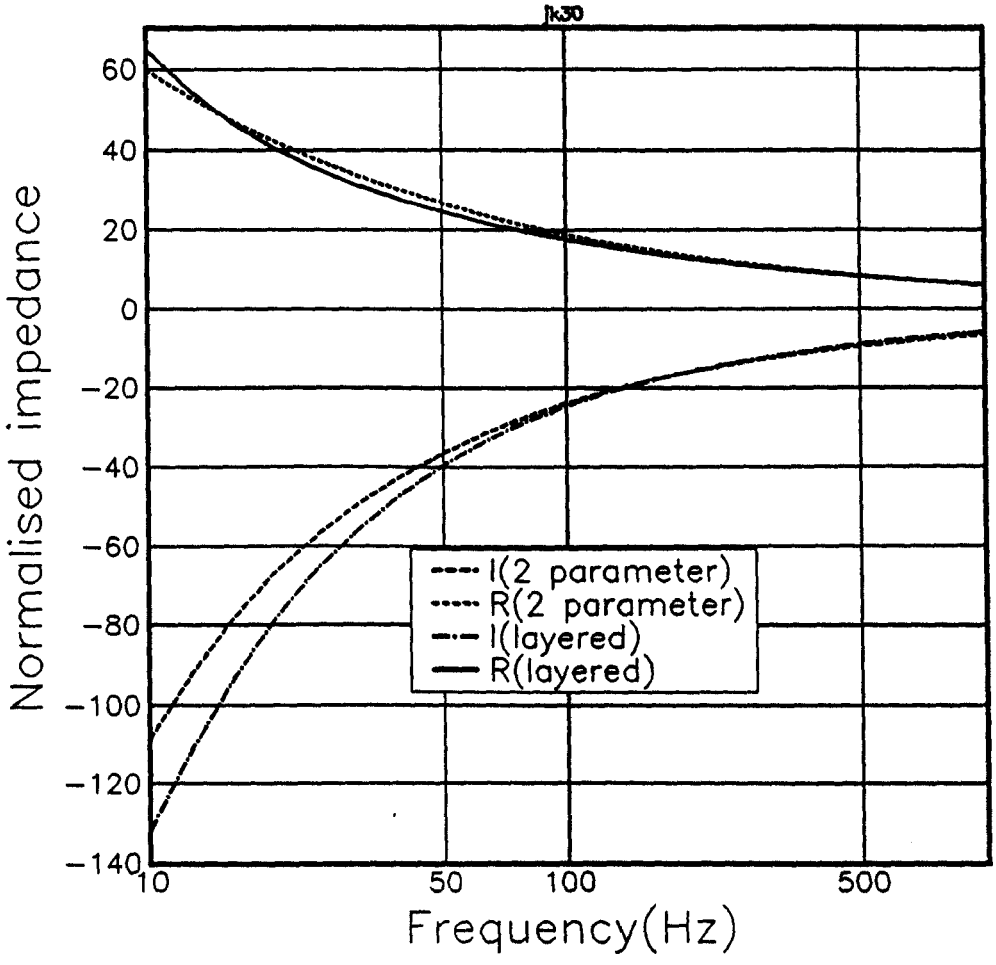

Figure A.12 Predicted impedance for flow resistivity 300000mks rayls m^{-1}, and exponential porosity decrease $\alpha = 10.0$ using Brekhovskikh and two parameter models. Surface pore parameters σ =100000mks rayls m^{-1}, n'=1.0 $\Omega = 0.4$, s_p=0.5.

Appendix B

Representation of Meteorology in the FFP propagation model.

B.1 Meteorological influences on sound propagation.

The influence of meteorological conditions on sound propagation can be broken down into four major factors. These factors are humidity, temperature gradient, wind speed, and turbulence.

Humidity influences attenuation and its influence can be accounted for addition of an imaginary part to the air propagation constant.

Temperature gradients can be represented by horizontal layers of different sound velocities as long as the ground is flat. The layer thickness of these homogeneous layers must be small enough to act as a continuous gradient. The sound speed c is related to the absolute temperature T by

$$c\alpha\sqrt{T}. \tag{B.1}$$

Wind speed gradients can similarly be represented by homogeneous layers. However this is a greater approximation for wind speed than it is for temperature. This is because wind speed is a vector quantity and so sound speeds in the horizontal and vertical directions will be different, and there will also be azimuthal variation. Therefore any number of homogeneous layers cannot represent the gradient accurately. The difference between vertical and horizontal propagation constants is unlikely to have much affect at

long horizontal ranges where the direction of propagation is predominantly horizontal, but at short ranges the effects may be much more pronounced. Some ray tracing models do include the effect of the wind as a vector quantity, however there is no satisfactory way of estimating the errors due to the homogeneous layer approximation at short range and at low frequencies.

Turbulence will have a great affect on propagation, and especially at long ranges and high frequencies. The effects of turbulence can be estimated in measurements from the amplitude of the fluctuations in the acoustic signal (although obviously this can be due to rapidly changing wind speeds and temperature gradients). De Jong has estimated that turbulence can cause fluctuations in measured sound pressure levels of up to 5dB in stable weather conditions and 15dB in unstable conditions for point to point propagation near to the ground surface [118]. Wilson [84] has attempted to include the effects of turbulence by stochastic perturbation of the sound velocity gradient. In the usual FFP model the effects of turbulence are not included.

In examinations of the influence of the ground on sound propagation in chapter 7 several atmospheric sound velocity profiles are used. Many of these sound velocity gradients are linear. Linear gradients are widely used to approximate real sound velocity gradients because residue series solutions exist [94]. A second type of profile that was used was a Monin-Obhukhov profile. This was derived using the Monin-Obhukhov similarity theory which is described below. This theory is only valid in the constant flux layer, which has a thickness of between 30 metres (on a clear night) and a few hundred metres (on a bright day). Monin-Obhukhov similarity theory was also used in the derivation of the temperature profiles used in chapter 9.

In the FFLAGS propagation model the atmosphere is represented by a set of horizontally stratified homogeneous fluid layers. The fluid layers are an approximation which is only valid where the effect on propagation of turbulence is very slight and the layer thicknesses are small enough for the discontinuities in the sound velocity not to affect propagation.

B.2 Monin-Obhukov Similarity theory

Monin-Obhukov Similarity theory is used to model temperature and wind-speed profiles. The atmosphere is defined by a stability parameter; the Monin-Obhukhov length L.

$$L \approx \frac{T_r u_*^2}{kgT_*} \tag{B.2}$$

where T_r is a representative temperature close to the ground, u_* is a friction velocity, k is the von Karman constant, g is the acceleration due to gravity, and T_* is a scaling temperature.

The Temperature T and horizontal wind speed u can be calculated as a function of height z within the constant flux layer from the equations

$$T(z) = T_0 + \frac{T_*}{k}\left[ln\left(\frac{z+z_h}{z_h}\right) + \Psi_h\left(\frac{z}{L}\right)\right] + \Gamma(z) \tag{B.3}$$

and

$$u(z) = \frac{u_*}{k}\left[ln\left(\frac{z+z_m}{z_m}\right) + \Psi_m\left(\frac{z}{L}\right)\right]. \tag{B.4}$$

The form of the profile correction functions depends on the Monin-Obukhov length L. z_h and z_m are heat and momentum roughness lengths.

In unstable conditions ($L < 0$) ;

$$\Psi_m(\frac{z}{L}) = -2ln\left(\frac{1+x}{2}\right) - ln\left(\frac{1+x^2}{2}\right) + 2arctan(x) - \pi/2 \tag{B.5}$$

where $x = [1 - 16z/L]^{1/4}$.

$$\Psi_h(\frac{z}{L}) = -ln\left(\frac{(1+(1-16z/L)^{1/2})}{2}\right). \tag{B.6}$$

This corresponds to conditions where the temperature gradient is negative (i.e the temperature decreases with height) and usually corresponds to sunny conditions with some wind.

In stable conditions ($L > 0$);

$$\Psi_m = \frac{5z}{L} \tag{B.7}$$

and

$$\Psi_h = \frac{5z}{L}. \tag{B.8}$$

This corresponds to the temperature increasing with height and usually corresponds to cloudy conditions with little wind.

In neutral conditions ($L = \infty$);

$$\Psi_h = \Psi_m = 0. \tag{B.9}$$

This corresponds to a very small temperature gradient where there is very little heat transport vertically through the atmosphere.

There is some disagreement in the form of these equations between different authors. The equations given here are taken from Huisman et al [95].

Appendix C

Programs

The following programs are all written in VAX Fortran. This conforms to FORTRAN 77 except for some extra implicit functions [119] and extra data types that can be used as arguments to some implicit functions. In most cases the following programs avoid the use of these extra features. The inputs and outputs to some of these programs are controlled by command programs written in DCL [120]. Hence open and close statements are not always included in the Fortran code.

C.1 Poroelay

Calculates normal surface impedance and acoustic-seismic coupling coefficient for a single porous elastic layer overlying an elastic halfspace. This includes a subroutine (SOAIRJ) which is also used in Multiporo and FFLAGS. Subroutines which calculate Bessel functions (CBJ and CMPBJ) are not included here.

```
c      Poroelay- A program for calculating seismic transfer fn  and
c      normal surface impedance.
c      Link with soair,vtrnf,bessel,sys$naglib/library.
c      Version copied April 87 includes corrections and modifications
c      to allow use at high frequencies.
c
       implicit real * 8 (a-h,o-z)
       dimension wk(9),pmag1(2000),vmag1(2000),fr1(2000),zreall(2000)
         dimension zimagg(2000)
       complex *16   hh1,cc1,mm1,znot,vp1,vs1,kbbar,gb
         complex *16 pres,vel,vs2,vmag,vp2
        complex vmg,vmag1
       complex *16 temp3,temp4,temp5
       complex *16 q3,q4,q5,c4,c5
       complex *16  j,l1,l2,l3,l1s,l2s,l3s,c1,c2,c3,s1,s2,s3,q1,q2
       complex *16  exp1,exp2,exp3,exp4,exp5,exp11,exp12
       complex *16  exp13,exp14,exp15
       complex *16  v1,v2,v3,z1,z2,m1,m2,m3
       real *8  omega,kr
         complex *16 kf
       real *8  gb2,lam2
       complex *16    a(9,9),b(9)
       real *8  l0,l4,l5,l0s,l4s,l5s,l0s0
       common /blk3/ shfr,rhof,gb,kbbar,kr,rhos,omega,rho
       common /blk5/ v0,c0,s0,c1,l0,l1,c2,l2,s3,l3,c3
       common /blk4/ phi
         common /blk7/ hh1,cc1,mm1,kf
        common /blk8/ vmag1
       j=(0.d0,1.d0)
        open(8,file='datafile2',status='new')
        open(9,file='vmag1',status='new')
        open(10,file='phas',status='new')
       twopi=4.d0*dasin(1.d0)
c
c
c     dep is layer thickness
c
c     d is propagation depth
c
         write(6,17)
 17      format(1x,'input layer depth,propagation depth')
         read *,dep,d
         write(6,18)
 18      format(1x,'input flow res')
         read*,phi
         phi=phi/1000.d0
```

```
c         phi = 366.d0
c
c*********************************************************
c      fr is frequency
c      thet0 is incident angle
       write(6,9919)
 9919  format(1x,'input frequency interval')
       read*,f0
c
       write(6,9920)
 9920  format(1x,'input max frequency')
       read*,frequmax
       npts =2*frequmax/f0
c       f0 = 1.0
        fr = f0
c       npts = 1024
        sfr = npts*f0/2
13       write(6,14)
14       format(1x,'input thet0')
15       read *,thet0
c
       thet0=twopi*thet0/360.d0
c       fr = 10.d0
c
c     d is propagation depth below surface.
c     d1 is propagation depth above surface/
c
c*********************************************************
c      wave numbers:     0  incident wave in air at thet0.
c                        1  fast wave in porous medium
c                        2  slow wave in porous medium
c                        3  shear wave in porous medium
c                        4  shear wave  in 3rd medium
c                        5  fast wave in 3rd medium
c
c
c      ****************************************************
c      v0 to v5 are the wave velocities in mks units
c
c      v0= sound speed in air
c      v1= biot fast wave velocity
c      v2= biot slow wave velocity
c      v3= shear wave velocity in layer
c      v4= shear wave velocity in lower midium
c      v5= compressional wave velocity in lower medium
c
```

```
        write(6,19)
19      format(1x,'input the ratio Vi/Vr ')
        read *,ratio
c
        write(6,221)
221     format(1x,'input vel number')
        read *,inumber
        write(6,9923)
 9923   format(1x,'input  velocities vp1 vs1 vp2 vs2')
        read*,vp1,vs1,vp2,vs2
        vp1 = (vp1 + (j*vp1*ratio))
         vs1 = (vs1 + (j*vs1*ratio))
c
         rhos = 2.65d0
c
c
c       densities of materials for the system:
c
c       density of air, rhof (cgs units)
c
        rhof=1.204d-03
c
c       density of clay, rhos and meas val. = 2.65 gcm**-3
c
c
c       density of porous layer, rho
c
c
        write(6,9921)
9921   format(1x,'input porosity')
        read*,omega
c            omega = 0.269d0
c
        write(6,9922)
 9922   format(1x,'input shape factor ratio 0.5 to 1.0')
        read*,shfr
c       shfr = 0.725d0
c
c       rho=rhos+omega*(rhof-rhos)
c         rho = (1.d0 - omega) * rhos + omega * rhof
          rho= 1.7d0
c
c
c*************************************************************
c
c       gb and gb2 are the shear moduli for the layer and clay
```

```
c
        gb = vs1*vs1*rho
c
c
        gb2=vs2*vs2*rhos
        kbbar = vp1*vp1*rho - 2.d0/3.d0*gb
c
        kr = vp2*vp2*rhos - 2.d0/3.d0*gb2
c       kr = 3.6e11
c
c
c      ******************************************************
c      equations to calculate h,c,m for the porous medium
c      are taken from  steve addisons seminar.
c      h is hh1,c is cc1, m is mm1
c
c
c      for the layer:  bulk mod for the grains is same as clay, kr
c                      bulk mod for the frame is input, kbbar
c                      bulk mod of fluid =atm. pres. 1.01e6 kf
c
c
c      temp=kr*(1.d0+omega*(kr/kf-1.d0))
c
c      hh1=(kr-kbbar)**2.d0/(temp-kbbar)+kbbar+gb*4.d0/3.d0
c     hh1=hh1+j*hh1/2.d0
c      cc1=kr*(kr-kbbar)/(temp-kbbar)
c     cc1=cc1+j*cc1/2.d0
c      mm1=kr**2.d0/(temp-kbbar)
c     mm1=mm1+j*mm1/2.d0
c
c     write(6,30)hh1,cc1,mm1
30     format(1x,'h=',2e13.6,2x,'c=',2e13.6,2x,'m=',2e13.6)

c*************************************************************
c
        i = 1
        vmag1(1) = (0.d0,0.d0)
16      continue
        i = i + 1
c         do 1111 i=1,ifr,inc
c       write(6,*)l1,l2,l3
11       call soair(fr,l2,l1,l3)
c
c
c       write(6,*)l1,l2,l3
```

```
c        write(6,30)hh1,cc1,mm1
c
       v1=twopi*fr/l1
       v2=twopi*fr/l2
         v3=twopi*fr/l3
         td = 2.d0*dep/v1
c50     format(5x,'biot wave constants',/
c    2  ,10x,'slow wave con. = ',e13.6,',',e13.6,
c    2  /,10x,'fast wave con = ',e13.6,',',e13.6
c    2  ,/,10x,'shear wave con. = ',e13.6,',',e13.6)
c
c
c
c
c        write(6,50)v1,v2,v3,fr
 50     format(5x,'biot wave speeds',/
     2   ,10x,'slow wave  = ',e13.6,',',e13.6,
     2   /,10x,'fast wave  = ',e13.6,',',e13.6
     2   ,/,10x,'shear wave  = ',e13.6,',',e13.6,
     2   /,10x,'time delay(ms) = ',e13.6)
       v0=3.43d4
c
c
c
c        write(6,30)hh1,cc1,mm1
c
c      write(6,65)kbbar,kr,gb,kf
65     format(1x,'kbbar=',2e13.2,2x,'kr=',e13.2,2x,'gb=',2e13.2,2x,///
     2  ,2x,'kf=',2e13.2,///)
c
c
c*****************************************************************
c
c      m1 and m2 are the ratios of the  relative wave to the
c      matrix wave(fast, slow)
c
c      equations for m1 and m2 taken from geertsma and smit
c      geophysics v.26 apr 1961
c      aspects og elastic wave prog. in fld. sat. porous solids.
c
c*****************************************************************
c
       z1= hh1*l1*l1/(rho*twopi*twopi*fr*fr)
c
       z2= hh1*l2*l2/(rho*twopi*twopi*fr*fr)
c
```

```
      m1= (hh1*(z1-1.d0))/(z1*cc1-rhof*hh1/rho)
c
      m2= (hh1*(z2-1.d0))/(z2*cc1-rhof*hh1/rho)
c
        m3 = (rho*twopi*fr*twopi*fr - gb*l3*l3)/rhof*twopi*fr*twopi*fr
        m3 = 1.d0/m3
c       write(6,40)m1,m2,m3
c       write(6,*)kr,kbbar,gb
c40      format(1x,'m1=',e13.6,e13.6,/,'m2=',e13.6,e13.6,/
c   2   ,1x,'m3 = ',e13.6,e13.6)
c
c*************************************************************
c
c lame's constants for the lower medium are lam2,gb2
c
 888      lam2 = vp2*vp2*rhos
c
c
c
c
c*****************************************************************

c       l0  -  l5  are the wave numbers
c
c
      l0=twopi*fr/v0
      l4=twopi*fr/vs2
      l5=twopi*fr/vp2
c
c
      l0s=l0*l0
      l1s=l1*l1
      l2s=l2*l2
      l3s=l3*l3
      l4s=l4*l4
      l5s=l5*l5
c     ***************************************************
c
c     s0,s1,c0,c1, etc ate the sines and cosines of the
c     incident, reflected and refracted angles.
c
c     ***************************************************
      s0=dsin(thet0)
      c0=dcos(thet0)
      ssq=s0*s0
      c1=cdsqrt(1.d0-l0s*ssq/l1s)
```

```
      c2=cdsqrt(1.d0-l0s*ssq/l2s)
      temp3=1.d0-l0s*ssq/l3s
      temp4=1.d0-l0s*ssq/l4s
      temp5=1.d0-l0s*ssq/l5s
      c3=cdsqrt(temp3)
      c4=cdsqrt(temp4)
      c5=cdsqrt(temp5)
      l0s0=l0*s0
      s1=l0s0/l1
      s2=l0s0/l2
      s3=l0s0/l3
      s4=l0s0/l4
      s5=l0s0/l5
c
c     ******************************************************
c
c     q1 - q5 is the wave number * cos(angle) * layer thickness
c
c     dep is the depth of layer
c
      q1=l1*c1*dep
      q2=l2*c2*dep
      q3=l3*c3*dep
      q4=l4*c4*dep
      q5=l5*c5*dep
c     write(6,*)q1,q2,q3,q4,q5
c
c     ******************************************************
c
c     expi or expii are the exponentials in the b. c. equations
c
c
      exp11 =cdexp(-j*q1)
      exp1=cdexp(j*q1)
      exp12=cdexp(-j*q2)
      exp2=cdexp(j*q2)
      exp3=cdexp(j*q3)
      exp13=cdexp(-j*q3)
      exp4=cdexp(j*q4)
      exp14=cdexp(-j*q4)
      exp5=cdexp(j*q5)
      exp15=cdexp(-j*q5)
c
c
c     the a sub ii's are the coef. in the b. c. equations.
c
```

```
c
c
c
c         calculate normal ccomponents of matrix velocity for each wave
c           at depth d.
c
c        writing matrix and relative  velocities.
c
c

c     call trans1(b,m1,m2,fr,d,maggo,magpb,phsgo,phspb)
c
       a(1,1)=(1.d0-m1)*c1
       a(1,2)=-a(1,1)
       a(1,3)=(1.d0-m2)*c2
       a(1,4)=-a(1,3)*exp2
       a(1,5)=(1.d0-m3)*s3
       a(1,6)=-(1.d0-m3)*s3*exp3
       a(1,7)=(0.d0,0.d0)
       a(1,8)=(0.d0,0.d0)
       a(1,9)=c0
       a(2,1)=2.d0*l1*s1*c1
       a(2,2)=-a(2,1)
       a(2,3)=2.d0*l2*c2*s2
       a(2,4)=-a(2,3)*exp2
       a(2,5)=-(l3*c3*c3-l3*s3*s3)
       a(2,6)=-a(2,5)*exp3
       a(2,7)=(0.d0,0.d0)
       a(2,8)=(0.d0,0.d0)
       a(2,9)=(0.d0,0.d0)
       a(3,1)=l1*(hh1-m1*cc1-2.d0*gb*s1*s1)
       a(3,2)=a(3,1)
       a(3,3)=l2*(hh1-m2*cc1-2.d0*gb*s2*s2)
       a(3,4)=a(3,3)*exp2
       a(3,5)=2.d0*gb*l3*s3*c3
       a(3,6)=a(3,5)*exp3
       a(3,7)=(0.d0,0.d0)
       a(3,8)=(0.d0,0.d0)
         a(3,9)=-kf*l0
       a(4,1)=l1*(cc1-m1*mm1)
       a(4,2)= a(4,1)
       a(4,3)=l2*(cc1-m2*mm1)
       a(4,4)=a(4,3)*exp2
       a(4,5)=(0.d0,0.d0)
       a(4,6)=(0.d0,0.d0)
       a(4,7)=(0.d0,0.d0)
```

```
a(4,8)=(0.d0,0.d0)
  a(4,9)=-kf*l0
a(5,1)=c1*exp1
a(5,2)=-c1*exp11
a(5,3)=c2*exp2
a(5,4)=-c2
a(5,5)=s3*exp3
a(5,6)=-s3
a(5,7)=-c5
a(5,8)=-s4
a(5,9)=(0.d0,0.d0)
a(6,1)=s1*exp1
a(6,2)=s1*exp11
a(6,3)=s2*exp2
a(6,4)=s2
a(6,5)=-c3*exp3
a(6,6)=-c3
a(6,7)=-s5
a(6,8)=c4
a(6,9)=(0.d0,0.d0)
a(7,1)=a(3,1)*exp1
a(7,2)=a(3,2)*exp11
a(7,3)=a(3,3)*exp2
a(7,4)=a(3,4)
a(7,5)=2.d0*gb*l3*s3*c3*exp3
a(7,6)=2.d0*gb*l3*s3*c3
a(7,7)=-l5*(lam2-2.d0*gb2*c5*c5)
a(7,8)=2.d0*gb2*l4*s4*c4
a(7,9)=(0.d0,0.d0)
a(8,1)=2.d0*gb*l1*s1*c1*exp1
a(8,2)=-2.d0*gb*l1*s1*c1*exp11
a(8,3)=2.d0*gb*l2*s2*c2*exp2
a(8,4)=-2.d0*gb*l2*s2*c2
a(8,5)=-gb*l3*(c3*c3-s3*s3)*exp3
a(8,6)=gb*l3*(c3*c3-s3*s3)
a(8,7)=-2.d0*gb2*l5*c5*s5
a(8,8)=gb2*l4*(c4*c4-s4*s4)
a(8,9)=(0.d0,0.d0)
a(9,1)=m1*c1*exp1
a(9,2)=-m1*c1*exp11
a(9,3)=m2*c2*exp2
a(9,4)=-m2*c2
a(9,9)=(0.d0,0.d0)

a(9,7)=(0.d0,0.d0)
a(9,8)=(0.d0,0.d0)
```

```
      a(9,5)=m3*s3*exp3
c
c
c
c     ***********************************************
c
c
9996      continue
      b(1)=c0
      b(2)=(0.d0,0.d0)
        b(3)=kf*l0
        b(4)=kf*l0
      b(5)=(0.d0,0.d0)
      b(6)=(0.d0,0.d0)
      b(7)=(0.d0,0.d0)
      b(8)=(0.d0,0.d0)
      b(9)=(0.d0,0.d0)
c     write(6,*)(b(i),i=1,9)
c
c
c     ***********************************************
c
c     subroutine leqt1c
c
c     solves simultaneous algrebraic equationc
c
c
      ia=9
      ib=9
      n=9
      ijob=0
      mn=1
      ic=0
C      call leqt1c(a,n,ia,b,mn,ib,ijob,wk,ier)
      call f04adf(a,ia,b,ib,n,mn,b,ib,wk,ijob)
c      write(6,2996)
      b(4) = b(4)*exp2
      b(6) = b(6)*exp3
      b(7) = b(7)*exp15
      b(8) = b(8)*exp14

c 2996  format(1x,'leq2c has finished running')

c
c     ***********************************************
c
```

```
c
c204c   write(6,205)
c205c   format(5x,'frequency',5x'incident angle')
c       write(6,210)fr,ltheti
c210c   format(6x,i4,15x,i2,//)
c       write(6,300)
300     format(9x,'fast wave (down)',20x,' fast wave (up)')
c       write(6,305)b(1),b(2)
305     format(1x,e14.8,1x,',',1x,e14.8,5x,e14.8,1x,',',1x,e14.8,//)
cc       write(6,310)
310     format(9x,'slow wave (down)',21x,'slow wave (up)')
c       write(6,305)b(3),b(4)
c       write(6,320)
320     format(9x,'shear wave (down)',20x,'shear wave (up)')
c       write(6,305)b(5),b(6)
c       write(6,330)
330     format(9x,'trans. comp. wave',20x,'trans. shear wave')
c       write(6,305)b(7),b(8)
c       write(6,340)
340     format(9x,'refl wave')
c       write(6,305)b(9)
c       write(6,*)(b(im),im=1,9)
c          drefl(i) = dsqrt(dreal(b(9))**2.d0 + dimag(b(9))**2.d0)
c          refl(i) = b(9)
c
c*************************************************************************
c         if(d.gt.dep) go to 1090
c
c        calculation of surface impedance
c
c
          pres = -j*kf*l0*(1.d0 + b(9))
c
          vel = c0*(1.d0 - b(9))*(-j*twopi*fr)

          znot = pres/vel
c
          zreal = dreal(znot)/(rhof*v0)
          zimag = dimag(znot)/(rhof*v0)
c
          zreall(i)=zreal
          zimagg(i)=zimag
346      format(1x,e13.6)
256      format(1x,'zreal = ',e12.4,10x,'zimag = ',e12.4,10x,e12.4)
c
         phspb = inumber
```

```
      call vtrnf(b,m1,m2,fr,d,dep,vmag,amag,phsgo,phspb)
c
        vmag1(i) = vmag
         pmag1(i) = amag
        write(9,*)vmag1(i)
        write(10,77)phsgo
257      format(1x,'magnitude = ',e12.4,10x,'freq = ',e12.4)
c
         fr1(i) = fr
         fr=fr+ f0
        vmg = vmag
        aval = cabs(vmg)
        write(8,77)log10(fr),aval
        if(fr .le. sfr) go to 16
1111     continue
 77      format(2(1x,e13.6))
9997          stop
         end
```

```
c      subroutine soairj
c
c      to calculate Biot propagation constants and elastic parameters.
c       outputs              zslow1,zfast1,zshe,hbar,cbar,mbar
c
c
c subroutines used
c
c             cbesj
c             cbj
c
       subroutine soairj(fr,zslow1,zfast1,zshe,shfr,rhof,gb,kbbar,
     1   kr,rhos,omega,rho,nprime,hbar,cbar,mbar,kf,phi0)
c
       implicit real*8(a-h,o-z)
c
      real*8mu,k,nprime,shfr
      complex*16j,rootj,capb,capc,sdisc,arg,z1,z2,disc
      complex*16xarg1,xj0,xj1,t1,comp,kf,zshe
      complex*16d,hbar,cbar,mbar,capa,kr
      complex*16m
      complex*16bj0,bj1,t,f,bbya,bbya2
      complex*16kbbar,gb,hbar1,cbar1,mbar1
      complex*16zfast1,zslow1
      complex*16xarg
c
c       ------------------------------------------------------------
c
       icomp = 0
c
       mu = .1495d-04
c
c      omeqa = 0.600d0
c
d      nprime = .5
c
c      shfr = 0.325d0
c
       eta = .181d-04
c
       k = (eta/phi0)
c
c
c      ------------------------------------------------------------
c
      pi = 4.d0*datan(1.d0)
```

```
c       omega=porosity(no units).
c       kr=bulk modulus of grains (Newtons/m**2)
c
c       mu=kinematic viscosity (m**2/sec)
c       eta=dynamic fluid viscosity (Newton-sec/m**2)
c       rhos=density of solid (kg/m**3)
c       rhof=density of fluid(kg/m**3)
c
c       rho = (1.d0-omega)*rhos + omega*rhof
c
c       ---------------------------------------------------------
c
c       compute prandtl number.
        cp = 1006.d0
        cofvis = 1.81d-05
        thecon = 0.0257d0
        prn = cofvis*cp/thecon
        sprn = dsqrt(prn)
c
c       k=permeability of the porous frame (m**2)
c
c
c
        qsq = (omega)**(-nprime)
c                                       .
c       ---------------------------------------------------------
c
        gama = 1.4d0
        stwo = dsqrt(2.d0)
        j = (0.d0,1.d0)
        rootj = cdsqrt(j)
c       rootj  = cmplx( real (rootj),-aimag(rootj))
        om = 2.d0*pi*fr
        om2 = om*om
        om4 = om2*om2
c
c       ---------------------------------------------------------
c
c       compute complex compressibility.
        xlam1 = 8.d0*qsq*om*rhof/phi0
        xlam1 = dsqrt(xlam1)/(shfr*2.d0)
        xlam1 = xlam1/dsqrt(omega)
        xarg1 = rootj*sprn*xlam1
        axarg1 = cdabs(xarg1)
        if(.not.(axarg1.le.7.0))goto 23000
           call cbesj(xarg1,0,xj0)
```

```
         call cbesj(xarg1,1,xj1)
23000 continue
      if(.not.(axarg1.gt.7.0))goto 23002
         call cbj(xarg1,0,xj0)
         call cbj(xarg1,1,xj1)
23002 continue
      t1 = xj1/xj0
      comp = (1.d0+2.d0*(gama-1.d0)*t1/xarg1)/(gama*1.01325d05)
      kf = 1.d0/comp
      if(.not.(icomp.eq.1))goto 23004
         comp = 9.86923d-06
         kf = 1.d0/comp
c
c      ------------------------------------------------------
c
23004 continue
      d = kr*(1.d0+omega*(kr/kf-1.d0))
      hbar = (kr-kbbar)*(kr-kbbar)/(d-kbbar)+kbbar+(4.d0/3.d0)*gb
      cbar = kr*(kr-kbbar)/(d-kbbar)
      mbar = kr*kr/(d-kbbar)
      m = qsq*(rhof/omega)
      capa = -hbar*mbar+cbar*cbar
c
c      viscosity correction
c
      xarg = dsqrt(8.d0*qsq*om*rhof/phi0)/(shfr*2.d0)
      xx = xarg/dsqrt(omega)
      arg = rootj*xx
      if(.not.(cdabs(arg).le.7.0))goto 23006
         call cbesj(arg,0,bj0)
         call cbesj(arg,1,bj1)
23006 continue
      if(.not.(cdabs(arg).gt.7.0))goto 23008
         call cbj(arg,0,bj0)
         call cbj(arg,1,bj1)
23008 continue
      t = bj1/bj0
c      write(6,*)' t = ',t
      f = (-0.25d0)*(arg*t/(1.d0-2.d0*t/arg))*(shfr*2.d0)**2.d0
      freal = dreal(f)
      fimag = dimag(f)
      capb = om2*(m*hbar-2.d0*cbar*rhof+rho*mbar)+j*om*f*eta*hbar/k
      capc = om4*(rhof*rhof-m*rho)-om2*(rho*j*om*f*eta/k)
      bbya = -capb/(2.d0*capa)
      bbya2 = bbya*bbya
      disc = bbya2-capc/capa
```

```
      sdisc = cdsqrt(disc)
      z1 = bbya+sdisc
      z2 = bbya-sdisc
      z1 = cdsqrt(z1)
      z2 = cdsqrt(z2)
c
if (dimag(z1).lt.0d0) z1=dconjg(z1)
if (dimag(z2).lt.0d0) z2=dconjg(z2)

      zslow1 = z1
      zfast1 = z2
c
c write(6,*)'z1=',z1,'z2=',z2
c
c     propagation constants for shear waves
c
      zshe = rho*om2/gb
      zshe = zshe-rhof*rhof*om4/(gb*(j*om*eta*f/k+m*om2))
      zshe = cdsqrt(zshe)
if (dimag(zshe).lt.0d0) zshe=dconjg(zshe)
c write(6,*)'zshe=',zshe
      return
      end
```

C.2 Multiporo

Calculates normal surface impedance and acoustic-seismic coupling coefficient for a number of porous elastic layers overlying a porous elastic halfspace.

```
c          ***************************************************
c Program MULTIPORO for calculating the ratio between the normal
c soil particle velocity at some given depth to the sound pressure
c received at a vertically separated above ground microphone,for a
c multilayered ground surface,and plane incident waves.
c LINK with SID,VTRNF,BESSELSD,MAP,SYS$NAGLINK/OPT
c
      implicit real*8(a-h,o-z)
      dimension rho(8),shfr(8),nprime(8),omega(8),phi(8),dep(8),wk(40)
      complex*16  a(4,7),a1(6,9),a2(6,6,12),b(40),c(40),a3(40,40)
      complex*16 hh1(8),cc1(8),mm1(8),znot,vp(8),vs(8),kbbar(8),gb(8)
      complex*16 vmag,pres,vel
      complex*16 temp3,temp4,temp5
      complex*16 q3(8),c3(8),c1(8),c2(8),s1(8),s2(8),s3(8),q1(8),q2(8)
      complex*16 j,l1(8),l2(8),l3(8),l1s(8),l2s(8),l3s(8),kr(8)
      complex*16 exp1(8),exp2(8),exp3(8)
      complex*16 v1(8),v2(8),v3(8),z1(8),z2(8),m1(8),m2(8),m3(8)
      real*8omega,fr,nprime
      complex*16 kf
      real*8l0,l0s0,l0s
      common/blk3/shfr,rhof,gb,kbbar,kr,rhos,omega,rho,nprime
      common/blk5/v0,c0,s0,c1,l0,l1,c2,l2,s3,l3,c3
      common/blk4/phi
      common/blk7/hh1,cc1,mm1,kf
c      open(8,file = 'datafile2',status = 'new')
c      open(10,file = 'phas',status = 'new')
c      open(11,file = 'impseis',status = 'new')
c      open(12,file = 'propseis',status='new')
      j = (0.d0,1.d0)
      twopi = 4.d0*dasin(1.d0)
c
c
c     dep is layer thickness
c
c     d is propagation depth
c
        ichi = 5
c       write(6,100)
c       write(6,110)
c       read(5,*)int
c       if(int.eq.1)goto 4
        int=2
        ichi = 2
c       open(unit=2,name='acoseis.dat',type='old')
4       if(int.eq.1)write(6,20)
      read(ichi,*),d
```

```
c
        if(int.eq.1)write(6,25)
        read(ichi,*),numlay
      if(int.eq.1)write(6,30)
      read(ichi,*),thet0
c
      thet0 = twopi*thet0/360.d0
c       fr = 10.d0
c
c
c     d is propagation depth below surface.
c
c**********************************************************************
c      wave numbers:     0  incident wave in air at thet0.
c                        1  fast wave in porous medium
c                        2  slow wave in porous medium
c                        3  shear wave in porous medium        '
c
c
c      ******************************************************
c      v0 to v5 are the wave velocities in mks units
c
c      v0= sound speed in air
c      v1= biot fast wave velocity
c      v2= biot slow wave velocity
c      v3= shear wave velocity in layer
c
      if(int.eq.1)write(6,40)
      read(ichi,*),pratio
        read(ichi,*),sratio
c       pratio is the ratio of the imaginary part to the real part of
c       the p-wave speed in the layer.
c       sratio is the ratio of the imaginary part to the real part of
c       the s-wave speed in the layer.
c       inumber = 7 for seismic transfer function
c
      if(int.eq.1)write(6,50)
      read(ichi,*),inumber
      rhos = 2.65d3
c      modification for sensitivity study
      read(ichi,*),rhof
      read(ichi,*),v0
c      rhof = 1.204d0
c         v0 = 3.43d2
c
        do 1121 in=1,numlay+1
```

```
      if(int.eq.1)write(6,55),in
      if(int.eq.1)write(6,60)
      read(ichi,*),phi(in)
      read(ichi,*),omega(in)
      read(ichi,*),vp(in)
      read(ichi,*),vs(in)
      read(ichi,*),rho(in)
      read(ichi,*),dep(in)
      read(ichi,*),kr(in)
c         vp1 = (270.d0)
      vp(in)= (vp(in)+(j*vp(in)*pratio))
c         vs1 = (190.d0)
      vs(in)= (vs(in)+(j*vs(in)*sratio))
c
c       write(6,*)vp(in),vs(in)
c
c       shfr is shape factor ratio Sp
        if(int.eq.1)write(6,75)
        read(ichi,*),shfr(in),nprime(in)
c
c**********************************************************************
c
c      gb is  the shear modulus for the layer
c
      gb(in) = vs(in)*vs(in)*rho(in)
c
      kbbar(in) = vp(in)*vp(in)*rho(in)-4.d0/3.d0*gb(in)
c
1121    continue
c
c**********************************************************************
      i = 0
c     repeat
23000    continue
        DO 9911 J1=1,40
            DO 9912 I1=1,40
9912    A3(I1,J1)=(0.D0,0.D0)
9911    CONTINUE
         if(int.eq.1)write(6,90)
         read(ichi,*),fr
d       type*,'fr = ',fr
         if(fr.eq.0)goto 23002
c
        ome = twopi*fr
         l0 = twopi*fr/v0
         l0s = l0*l0
```

```
         s0 = dsin(thet0)
         c0 = dcos(thet0)
         ssq = s0*s0
         l0s0 = l0*s0
        data a3/1600*0.d0/
c
        do 1122 in=1,numlay+1

       call soairj(fr,l2(in),l1(in),l3(in),shfr(in),rhof,gb(in),
     1 kbbar(in),kr(in),rhos,omega(in),rho(in),nprime(in),hh1(in),
     2 cc1(in),mm1(in),kf,phi(in))
c
c
c       l1(in)=cdabs(l1(in))
c       l2(in)=cdabs(l2(in))
c       l3(in)=cdabs(l3(in))
         v1(in) = twopi*fr/l1(in)
         v2(in) = twopi*fr/l2(in)
         v3(in) = twopi*fr/l3(in)
         td = 2.d0*dep(in)/v1(in)
c
        print*,v1(in),v2(in),v3(in)
c
c*************************************************************************
c
c      m1(in) and m2(in) are the ratios of the  relative wave to the
c      matrix wave(fast, slow)
c
c*************************************************************************
c
         z1(in) = hh1(in)*l1(in)*l1(in)/(rho(in)*twopi*twopi*fr*fr)
c
         z2(in) = hh1(in)*l2(in)*l2(in)/(rho(in)*twopi*twopi*fr*fr)
c
      m1(in) = (hh1(in)*(z1(in)-1.d0))/(z1(in)*cc1(in)
     *-rhof*hh1(in)/rho(in))
c
      m2(in) = (hh1(in)*(z2(in)-1.d0))/(z2(in)*cc1(in)
     *-rhof*hh1(in)/rho(in))
c
        m3(in) = (rho(in)*ome*ome-(gb(in)*l3(in)*l3(in)))/(rhof*ome*ome)
c
c
c*************************************************************
c
c       l0  -  l3   are the wave numbers
```

```
c
c
        l1s(in) = l1(in)*l1(in)
        l2s(in) = l2(in)*l2(in)
        l3s(in) = l3(in)*l3(in)
c       ***************************************************
c
c       s0,s1,c0,c1, etc ate the sines and cosines of the
c       incident, reflected and refracted angles.
c
c       ***********************************************************
        c1(in) = cdsqrt(1.d0-l0s*ssq/l1s(in))
        c2(in) = cdsqrt(1.d0-l0s*ssq/l2s(in))
        c3(in) = cdsqrt(1.d0-l0s*ssq/l3s(in))
        s1(in) = l0s0/l1(in)
        s2(in) = l0s0/l2(in)
        s3(in) = l0s0/l3(in)
c
c       ***************************************************
c
c       q1 - q5 is the wave number * cos(angle) * layer thickness
c
c       dep is the thickness of layer
c
        q1(in) = l1(in)*c1(in)*dep(in)
        q2(in) = l2(in)*c2(in)*dep(in)
        q3(in) = l3(in)*c3(in)*dep(in)
c
c       *********************************************************
c
c       expi or expii are the exponentials in the b. c. equations
c
c
        exp1(in) = cdexp(j*q1(in))
        exp2(in) = cdexp(j*q2(in))
        exp3(in) = cdexp(j*q3(in))
1122    continue
c
c       the a sub ii's are the coef. in the b. c. equations.
c
        a(1,1) = c0
        a(1,2) = (1.d0-m1(1))*c1(1)
        a(1,3) = -a(1,2)*exp1(1)
        a(1,4) = (1.d0-m2(1))*c2(1)
        a(1,5) = -a(1,4)*exp2(1)
        a(1,6) = (1.d0-m3(1))*s3(1)
```

```
      a(1,7) = -(1.d0-m3(1))*s3(1)*exp3(1)
c
      a(2,1) = (0.d0,0.d0)
      a(2,2) = 2.d0*l1(1)*s1(1)*c1(1)
      a(2,3) = a(2,2)*exp1(1)
      a(2,4) = 2.d0*l2(1)*c2(1)*s2(1)
      a(2,5) = a(2,4)*exp2(1)
      a(2,6) = -(l3(1)*c3(1)*c3(1)-l3(1)*s3(1)*s3(1))
      a(2,7) = a(2,6)*exp3(1)
c
      a(3,1) = -kf*l0
      a(3,2) = l1(1)*(hh1(1)-m1(1)*cc1(1)-2.d0*gb(1)*s1(1)*s1(1))
      a(3,3) = -a(3,2)*exp1(1)
      a(3,4) = l2(1)*(hh1(1)-m2(1)*cc1(1)-2.d0*gb(1)*s2(1)*s2(1))
      a(3,5) = -a(3,4)*exp2(1)
      a(3,6) = 2.d0*gb(1)*l3(1)*s3(1)*c3(1)
      a(3,7) = -a(3,6)*exp3(1)
c
      a(4,1) = -kf*l0
      a(4,2) = l1(1)*(cc1(1)-m1(1)*mm1(1))
      a(4,3) = a(4,2)*exp1(1)
      a(4,4) = l2(1)*(cc1(1)-m2(1)*mm1(1))
      a(4,5) = a(4,4)*exp2(1)
      a(4,6) = (0.d0,0.d0)
      a(4,7) = (0.d0,0.d0)

      n=numlay
      A1(1,1) = c1(n)*exp1(n)
      A1(1,2) = -c1(n)
      A1(1,3) = c2(n)*exp2(n)
      A1(1,4) = -c2(n)
      A1(1,5) = s3(n)*exp3(n)
      A1(1,6) = -s3(n)
      A1(1,7) = -c1(n+1)
      A1(1,8) = -c2(n+1)
      A1(1,9) = -s3(n+1)
c
      A1(2,1) = s1(n)*exp1(n)
      A1(2,2) = s1(n)
      A1(2,3) = s2(n)*exp2(n)
      A1(2,4) = s2(n)
      A1(2,5) = -c3(n)*exp3(n)
      A1(2,6) = -c3(n)
      A1(2,7) = -s1(n+1)
      A1(2,8) = -s2(n+1)
      A1(2,9) = c3(n+1)
```

```
c
      A1(3,1) = l1(n)*(hh1(n)-m1(n)*cc1(n)-2.d0*gb(n)*s1(n)*s1(n))
     1    *exp1(n)
      A1(3,2) = A1(3,1)/exp1(n)
      A1(3,3) = l2(n)*(hh1(n)-m2(n)*cc1(n)-2.d0*gb(n)*s2(n)*s2(n))
     1    *exp2(n)
      A1(3,4) = A1(3,3)/exp2(n)
      A1(3,5) = 2.d0*gb(n)*l3(n)*s3(n)*c3(n)*exp3(n)
      A1(3,6) = 2.d0*gb(n)*l3(n)*s3(n)*c3(n)
      A1(3,7) = -l1(n+1)*(hh1(n+1)-m1(n+1)*cc1(n+1)-2.d0*gb(n+1)
     1  *s1(n+1)*s1(n+1))
      A1(3,8) = -l2(n+1)*(hh1(n+1)-m2(n+1)*cc1(n+1)-2.d0*gb(n+1)
     1  *s2(n+1)*s2(n+1))
      A1(3,9) = -2.d0*gb(n+1)*l3(n+1)*s3(n+1)*c3(n+1)
c
      A1(4,1) = 2.d0*gb(n)*l1(n)*s1(n)*c1(n)*exp1(n)
      A1(4,2) = -2.d0*gb(n)*l1(n)*s1(n)*c1(n)
      A1(4,3) = 2.d0*gb(n)*l2(n)*s2(n)*c2(n)*exp2(n)
      A1(4,4) = -2.d0*gb(n)*l2(n)*s2(n)*c2(n)
      A1(4,5) = -gb(n)*l3(n)*(c3(n)*c3(n)-s3(n)*s3(n))*exp3(n)
      A1(4,6) = gb(n)*l3(n)*(c3(n)*c3(n)-s3(n)*s3(n))
      A1(4,7) = -2.d0*gb(n+1)*l1(n+1)*c1(n+1)*s1(n+1)
      A1(4,8) = -2.d0*gb(n+1)*l2(n+1)*c2(n+1)*s2(n+1)
      A1(4,9) = gb(n+1)*l3(n+1)*(c3(n+1)*c3(n+1)-s3(n+1)*s3(n+1))
c
      A1(5,1) = m1(n)*c1(n)*exp1(n)
      A1(5,2) = -m1(n)*c1(n)
      A1(5,3) = m2(n)*c2(n)*exp2(n)
      A1(5,4) = -m2(n)*c2(n)
      A1(5,5) = m3(n)*s3(n)*exp3(n)
      A1(5,6) = -m3(n)*s3(n)
      A1(5,7) = -m1(n+1)*c1(n+1)
      A1(5,8) = -m2(n+1)*c2(n+1)
      A1(5,9) = -m3(n+1)*s3(n+1)
c
      A1(6,1) = l1(n)*(cc1(n)-m1(n)*mm1(n))*exp1(n)
      A1(6,2) = l1(n)*(cc1(n)-m1(n)*mm1(n))
      A1(6,3) = l2(n)*(cc1(n)-m2(n)*mm1(n))*exp2(n)
      A1(6,4) = l2(n)*(cc1(n)-m2(n)*mm1(n))
      A1(6,5) =(0.d0,0.d0)
      A1(6,6) = (0.d0,0.d0)
      A1(6,7) =-l1(n+1)*(cc1(n+1)-m1(n+1)*mm1(n+1))
      A1(6,8) =-l2(n+1)*(cc1(n+1)-m2(n+1)*mm1(n+1))
      A1(6,9) = (0.d0,0.d0)

c
```

```
c
      if (numlay.eq.1) goto 2212
c
      do 2211 n=1,numlay-1
       a2(n,1,1) = c1(n)*exp1(n)
       a2(n,1,2) = -c1(n)
       a2(n,1,3) = c2(n)*exp2(n)
       a2(n,1,4) = -c2(n)
       a2(n,1,5) = s3(n)*exp3(n)
       a2(n,1,6) = -s3(n)
       a2(n,1,7) = -c1(n+1)
       a2(n,1,8) = c1(n+1)*exp1(n+1)
       a2(n,1,9) = -c2(n+1)
       a2(n,1,10) = c2(n+1)*exp2(n+1)
       a2(n,1,11) = -s3(n+1)
       a2(n,1,12) = s3(n+1)*exp3(n+1)
c
       a2(n,2,1) = s1(n)*exp1(n)
       a2(n,2,2) = s1(n)
       a2(n,2,3) = s2(n)*exp2(n)
       a2(n,2,4) = s2(n)
       a2(n,2,5) = -c3(n)*exp3(n)
       a2(n,2,6) = -c3(n)
       a2(n,2,7) = -s1(n+1)
       a2(n,2,8) = -s1(n+1)*exp1(n+1)
       a2(n,2,9) = -s2(n+1)
       a2(n,2,10) = -s2(n+1)*exp2(n+1)
       a2(n,2,11) = c3(n+1)
       a2(n,2,12) = c3(n+1)*exp3(n+1)
       a2(n,3,1) = l1(n)*(hh1(n)-m1(n)*cc1(n)-2.d0*gb(n)*s1(n)
     1   *s1(n))*exp1(n)
       a2(n,3,2) = A2(n,3,1)/exp1(n)
       a2(n,3,3) = l2(n)*(hh1(n)-m2(n)*cc1(n)-2.d0*gb(n)*s2(n)
     1   *s2(n))*exp2(n)
       a2(n,3,4) = A2(n,3,3)/exp2(n)
       a2(n,3,5) = 2.d0*gb(n)*l3(n)*s3(n)*c3(n)*exp3(n)
       a2(n,3,6) = 2.d0*gb(n)*l3(n)*s3(n)*c3(n)
       a2(n,3,7) = -l1(n+1)*(hh1(n+1)-m1(n+1)*cc1(n+1)-2.d0*gb(n+1)
     1  *s1(n+1)*s1(n+1))
       a2(n,3,8) = -l1(n+1)*(hh1(n+1)-m1(n+1)*cc1(n+1)-2.d0*gb(n+1)
     1  *s1(n+1)*s1(n+1))*exp1(n+1)
       a2(n,3,9) = -l2(n+1)*(hh1(n+1)-m2(n+1)*cc1(n+1)-2.d0*gb(n+1)
     1  *s2(n+1)*s2(n+1))
       a2(n,3,10) = a2(n,3,9)*exp2(n+1)
       a2(n,3,11) = -2.d0*gb(n+1)*l3(n+1)*s3(n+1)*c3(n+1)
       a2(n,3,12) = -2.d0*gb(n+1)*l3(n+1)*s3(n+1)*c3(n+1)*exp3(n+1)
```

```
c
        a2(n,4,1) = 2.d0*gb(n)*l1(n)*s1(n)*c1(n)*exp1(n)
        a2(n,4,2) = -2.d0*gb(n)*l1(n)*s1(n)*c1(n)
        a2(n,4,3) = 2.d0*gb(n)*l2(n)*s2(n)*c2(n)*exp2(n)
        a2(n,4,4) = -2.d0*gb(n)*l2(n)*s2(n)*c2(n)
        a2(n,4,5) = -gb(n)*l3(n)*(c3(n)*c3(n)-s3(n)*s3(n))*exp3(n)
        a2(n,4,6) = gb(n)*l3(n)*(c3(n)*c3(n)-s3(n)*s3(n))
        a2(n,4,7) = -2.d0*gb(n+1)*l1(n+1)*c1(n+1)*s1(n+1)
        a2(n,4,8) = 2.d0*gb(n+1)*l1(n+1)*c1(n+1)*s1(n+1)*exp1(n+1)
        a2(n,4,9) = -2.d0*gb(n+1)*l2(n+1)*s2(n+1)*c2(n+1)
        a2(n,4,10) = 2.d0*gb(n+1)*l2(n+1)*s2(n+1)*c2(n+1)*exp2(n+1)
        a2(n,4,11) = gb(n+1)*l3(n+1)*(c3(n+1)*c3(n+1)-s3(n+1)*s3(n+1))
        a2(n,4,12) = -gb(n+1)*l3(n+1)*(c3(n+1)*c3(n+1)-s3(n+1)*s3(n+1))
     1   *exp3(n+1)
c
        a2(n,5,1) = m1(n)*c1(n)*exp1(n)
        a2(n,5,2) = -m1(n)*c1(n)
        a2(n,5,3) = m2(n)*c2(n)*exp2(n)
        a2(n,5,4) = -m2(n)*c2(n)
        a2(n,5,5) = m3(n)*s3(n)*exp3(n)
        a2(n,5,6) = -m3(n)*s3(n)
        a2(n,5,7) = -m1(n+1)*c1(n+1)
        a2(n,5,8) = m1(n+1)*c1(n+1)*exp1(n+1)
        a2(n,5,9) = -m2(n+1)*c2(n+1)
        a2(n,5,10) = m2(n+1)*c2(n+1)*exp2(n+1)
        a2(n,5,11) = -m3(n+1)*s3(n+1)
        a2(n,5,12) = m3(n+1)*s3(n+1)*exp3(n+1)
c
        a2(n,6,1) = l1(n)*(cc1(n)-m1(n)*mm1(n))*exp1(n)
        a2(n,6,2) = l1(n)*(cc1(n)-m1(n)*mm1(n))
        a2(n,6,3) = l2(n)*(cc1(n)-m2(n)*mm1(n))*exp2(n)
        a2(n,6,4) = l2(n)*(cc1(n)-m2(n)*mm1(n))
        a2(n,6,5) =(0.d0,0.d0)
        a2(n,6,6) = (0.d0,0.d0)
        a2(n,6,7) =-l1(n+1)*(cc1(n+1)-m1(n+1)*mm1(n+1))
        a2(n,6,8) =-l1(n+1)*(cc1(n+1)-m1(n+1)*mm1(n+1))*exp1(n+1)
        a2(n,6,9) =-l2(n+1)*(cc1(n+1)-m2(n+1)*mm1(n+1))
        a2(n,6,10) =-l2(n+1)*(cc1(n+1)-m2(n+1)*mm1(n+1))*exp2(n+1)
        a2(n,6,11) = (0.d0,0.d0)
        a2(n,6,12) = (0.d0,0.d0)

2211    continue
2212    continue
c
        b(1) = c0
        b(2) = (0.d0,0.d0)
```

```
         b(3) = kf*l0
         b(4) = kf*l0
        do 2213 jib=5,40
           b(jib)=(0.d0,0.d0)
2213    continue
        irray = 4+6*numlay
c
        call map(numlay,irray,a,a1,a2,b,c,a3,wk)
c**********************************************************************
c
c       calculation of surface impedance
c
c
         pres = -j*kf*l0*(1.d0+c(1))
c
         vel = c0*(1.d0-c(1))*(-j*twopi*fr)
c
         znot = pres/vel
c
         zreal = dreal(znot)/(rhof*v0)
         zimag = dimag(znot)/(rhof*v0)
c
c
         phspb = inumber
c
         aval = cdabs(vmag)
         write(8,80)fr,cdabs(c(1))
c        write(8,80)fr,aval
         write(11,85) fr,zreal,zimag
c       do 1212 il=1,16
c       write (10,*)'c(',il,') ',c(il)
1212    continue

         if(int.eq.1)write(6,10)
         ndec = 0
         if(int.eq.1)read(5,*)ndec
        type*,'fr = ',fr
23001    if(.not.(ndec.ne.0))goto 23000
23002   stop
10     format(1x,'input 1 to stop, 0 for new frequency')
20     format(1x,'input propagation depth')
25     format(1x,'input number of layers')
30     format(1x,'input thet0')
40     format(1x,'input the ratio vi/vr for p and s ')
50     format(1x,'input vel number')
55     format(1x,'next data is for layer ',i3)
```

```
60    format(1x,'input:phi omega rvp1 rvs1 rho lay_dep grain_blk_mod')
75    format(1x,'input shfr(sp),nprime(gsf)')
80    format(1x,e13.6,3x,e13 .6)
85    format(1x,e13.6,3x,e13.6,3x,e13.6)
90    format(1x,'input frequency')
100   format(1x,'interactive or from acoseis.dat?')
110   format(1x,'interactive = 1')
      end
```

C.3 FFLAGS

Calculates excess attenuation and vertical particle velocity as a function of range or frequency in an environment consisting of a horizontally stratified fluid overlying a horizontally stratified porous elastic ground.

```
c Program FFLAGS for calculating the sound pressure
c received at an above ground microphone, or vert ptcle vel in the ground.
c For a 15 layered air over a 5 layered porous elastic surface,and a point
c source in the air.
c Using T.Richards' method incuding corrections for avoidance
c of poles on real axis and truncation of Fourier series.
c JSV Vol 109(1) 1986 pp157-67
c
      implicit real*8(a-h,o-z)
      dimension rha(15),h(15),wkspce(62)
dimension rho(8),dep(8),omega(8),phi(8),shfr(8)
real*8    nprime(8)
complex*16  a(4,8),a1(6,9),a2(6,6,12)
        complex*16 hh1(8),cc1(8),mm1(8),gb(8),kr(8),kbbar(8)
complex*16 c1(8),c2(8),c3(8),s1(8),s2(8),s3(8)
complex*16 v1(8),v2(8),v3(8),l1(8),l2(8),l3(8)
complex*16 l1s(8),l2s(8),l3s(8)
complex*16 exp1(8),exp2(8),exp3(8)
        complex*16 m1(8),m2(8),m3(8)
      complex*16 ftot(2048),rtot(2048),F1,FINOR
      complex*16 b(62),c(62),ai(14,2,4),a3(62,62)
      complex*16 j,hor,exp0(15)
      complex*16 c0(15),s0(15),q0(15)
      complex*16 l0(15),k0(15),v0(15)
complex*16 vp,vs
      real*8 fr
      complex*16 kf
c      open(10,file = 'out1',status = 'new')
      j = (0.d0,1.d0)
      twopi = 4.d0*dasin(1.d0)
      pi=twopi/2
ichi=2
c icho is used to choose the kind of output wanted
read(ichi,*)icho
c icho=1     Excess attenuation at a single range for many freqs.
c icho=2     Excess attenuation at whole range set for single freq.
c icho=3     Excess attenuation at whole range set and integrand at
c     all horiz wavenumbers (in .int) for single frequency.
c     ------------------------------------------------------------
c This reads air params from ground upwards
read(ichi,*) ial
c NB:ial includes upper halfspace
c        --
do 1120 in=1,ial
      read(ichi,*) rha(in),v,h(in)
v0(in)= cmplx(v,0d0)
```

```
1120 continue
c
c read ground params from surface downwards.
read(ichi,*) numlay
c NB: numlay excludes lower halfspace
c                  --
do 1121 in=1,numlay+1
      read(ichi,*) phi(in),omega(in),shfr(in),nprime(in)
      read(ichi,*) vp,vs,rho(in),dep(in),kr(in),pratio
      sratio=pratio
      vp = (vp-(j*vp*pratio))
      vs= (vs-(j*vs*sratio))
c material bulk modulus
      kr(in)= (kr(in)-(2*j*kr(in)*pratio))
c       gb is  the shear modulus for the layer
      gb(in) = vs*vs*rho(in)
c kbbar is the bulk modulus
      kbbar(in) = vp*vp*rho(in)-4.d0/3.d0*gb(in)
1121 continue
c
c       Wave number integration limits; lowest k, number of steps,highest k
read(ichi,*) horlo,ihor,horup
dhor = (horup-horlo)/ihor
c
c Source height
read(ichi,*) hs
c receiver height
read(ichi,*) hr
c range
read(ichi,*) rang
c Minimum range
read(ichi,*) ralo
c Params for Richards' corrections alph and delt
read(ichi,*) alph,delt
c      ------------------------------------------------------------
c Find source layer and dist to up and low interfaces
call scefnd(isl,sun,sdn,hs,h,ial)
c Find receiver layer, and dists to top and bot of layer from receiver
if (hr.gt.0d0) then
call recfnd(irl,run,rdn,hr,h,ial)
else
call grecfnd(irl,run,rdn,hr,dep,numlay)
end if
c      ------------------------------------------------------------
c Frequency loop start.
c     repeat
```

```
23000    continue
         read(ichi,*) fr
d type*,'fr = ',fr
 if(fr.eq.0)goto 23002
c      ------------------------------------------------------------
c Calc l0 and flag errors in integration limits
         call wave(l0,k0,v0,rha,ial,twopi,fr,dhor,horup)
c SOAIRJ to calc Biot propagation constants
do 212 in=1,numlay+1
       call soairj(fr,l2(in),l1(in),l3(in),shfr(in),rha(1),gb(in),
     1 kbbar(in),kr(in),rhos,omega(in),rho(in),nprime(in),hh1(in),
     2 cc1(in),mm1(in),kf,phi(in))
if(cdabs(l1(in)).gt.(horup/1.2))print*,'l1(',in,')too big'
if(cdabs(l2(in)).gt.(horup/1.2))print*,'l2(',in,')too big'
if(cdabs(l3(in)).gt.(horup/1.2))print*,'l3(',in,')too big'
212 continue
c Calc mi for ground layers.
 call sub1(v1,v2,v3,l1,l2,l3,m1,m2,m3,hh1,gb,rho
     * ,rha(1),l1s,l2s,l3s,twopi,fr,numlay)
c      ------------------------------------------------------------
c do loop for horizontal wavenumber increment
hor = horlo-dhor*j*alph
do 9913 i1=1,ihor
DO 9911 J2=1,62
    DO 9912 I2=1,62
9912 A3(I2,J2)=(0.D0,0.D0)
9911    continue
c Calc cos,sin and expon function for all air layers.
call costh(c0,s0,q0,l0,exp0,hor,ial,h,j)
c Calc cos sin and exp fns for all ground layers.
call sub2(hor,l0(1),s1,s2,s3,c1,c2,c3,l1,l2,l3,dep,
     *    exp1,exp2,exp3,l1s,l2s,l3s,j,numlay)
c      ------------------------------------------------------------
c Calculate boundary condition equations at ground interfaces
call grbce(k0(1),l0(1),c0(1),l1,l2,l3,exp1,exp2,exp3,exp0(1)
     *   ,numlay ,m1,m2,m3,hh1,cc1,mm1,gb,c1,c2,c3,s1,s2,s3,a,a1,a2)
c Calculate bces at air interfaces.
call grairtrm(ai,ab,c0,l0,exp0,k0,ial)
c      ------------------------------------------------------------
c  Source terms.
c
c       Calc source terms on l.h.s. of bces
call grsce(b,isl,ial,sun,sdn,c0(isl),l0(isl),k0(isl),j)
irray = 2*ial+2+numlay*6
c      ------------------------------------------------------------
c       Map local b.c.e.s onto global matrix and solve.
```

```
call ngrmap(numlay,irray,ial,ai,a,a1,a2,b,c,a3,wkspce)
c print*,'c(1)=',c(1)
c      ------------------------------------------------------------
c Calc Greens function.
c Receiver in air:
if (hr.gt.0d0) then
call ingra(c,c0(irl),l0(irl),hs,hr,j,hor,ial,irl
     *  ,isl,ftot(i1),run,rdn)
else
c Receiver in ground:
call gingra(c,c1(irl),c2(irl),s3(irl),l1(irl),l2(irl),
     *  l3(irl),hr,j,hor,ial,irl,numlay,ftot(i1),run,rdn)
end if
if (icho.eq.3) write(8,80) dreal(hor),cdabs(ftot(i1))
hor = horlo + dhor*(i1-j*alph)
9913     continue
c End of wavenumber loop
c Modify Greens Fn according to T.Richards
f1=ftot(1)
do 8801 i1=1,ihor
8801     call intmod(ftot(i1),f1,i1,ihor,delt,alph,j)
fihor=ftot(ihor)
m=10
do 8802 i1=1,ihor
    sta=(0d0,0d0)
    call star(m,ihor,sta,i1,alph,j)
8802     call intmod2(ftot(i1),ihor,i1,fihor,sta,j,alph)
c Perform FFT
sing=1d0
call fork(ihor,ftot,sing)
ra= ralo
if (ftot(1).eq.(0d0,0d0)) ftot(1)=ftot(2)
c Further modifications acording to T Richards
call ramult2(dhor,ihor,pi,j,alph,ftot,rtot,i4)
if (icho.eq.1) then
  i2=1+iidnnt(rang*dhor*ihor/(2*pi))
  if (i2.gt.(ihor/2)) then
     write(6,*) 'range out of bounds'
     goto 23002
  end if
  if (hr.gt.0d0) then
c      Write Excess Attenuation
     ra= (I2-1)*2*pi/(ihor*dhor)
     ra= sqrt(ra**2+(hs-hr)**2) ! added 12/10/89
     rt=20*dlog10(cdabs(rtot(i2)*ra/(dexp(-dimag(l0(irl))))))
     ra= (I2-1)*2*pi/(ihor*dhor)
```

```
c            write(10,80)fr,rt
             write(10,80)fr,cdabs(rtot(i2))

  else if (hr.le.0d0) then
    ra= (I2-1)*2*pi/(ihor*dhor)
    rt=dlog10(fr*cdabs(rtot(i2)))
c     write(10,80)fr,rt
    write(10,80)fr,cdabs(rtot(i2))
  end if
       else if (icho.ne.1) then
  if (hr.gt.0d0) then
  do 9915 i2=2,ihor
     ra= (I2-1)*2*pi/(ihor*dhor)
     ra= sqrt(ra**2+(hs-hr)**2) ! added 12/10/89
     rt=20*dlog10(cdabs(rtot(i2)*ra/(dexp(-dimag(l0(irl))))))
           ra= (I2-1)*2*pi/(ihor*dhor)
c      write(10,80)ra,rt
     write(10,80)ra,cdabs(rtot(i2))
9915     continue
  else if (hr.le.0d0) then
    do 9916 i2=2,ihor
     ra= sqrt(ra**2+(hs-hr)**2) ! added 12/10/89
    rt=dlog10(fr*cdabs(rtot(i2)))
     ra= (I2-1)*2*pi/(ihor*dhor)
    write (10,80)ra,cdabs(rtot(i2))
c     write (10,80)ra,rt
9916     continue
  end if
end if
     write(6,*)'actual range=',ra
9914 continue
 ndec = 0
         if(int.eq.1)read(5,*)ndec
type*,'fr = ',fr
23001    if(.not.(ndec.ne.0))goto 23000
23002   stop
c      ---------------------------------------------------------
c
80    format(1x,e13.6,3x,e13.6)
81    format(4(2x,e11.5))
82    format(1x,e13.6)
85    format(1x,e13.6,3x,e13.6,3x,e13.6)
110   format(1x,'interactive = 1')
      end

*********************************************************************
```

```
SUBROUTINE ingra(c,c0,l0,hs,hr,j,hor,ial,irl
     *  ,isl,ftot,run,rdn)
c To calculate depth dependent part of integrand for source and
c receiver in air.
c (9/5/88 Steve Tooms)For T.Richards method.
c
implicit real*8 (a-h,o-z)
complex*16 l0,c(62),ftot,j,c0,hor
c
ftot=c(2*ial-2*(irl-1)-1)*cdexp(j*c0*l0*rdn)
if (irl.ne.ial) then
ftot=ftot+c(2*ial-2*(irl-1)-2)*cdexp(j*c0*l0*run)
end if
if (irl.eq.isl) then
ht=(dabs(hs-hr))
ftot=ftot+cdexp(j*ht*l0*c0)/(c0*l0)
end if
ftot = ftot*hor
RETURN
END

*************************************************************


SUBROUTINE gingra(c,c1,c2,s3,l1,l2,l3,hr,j,hor,ial,irl
     *  ,igl,ftot,run,rdn)
c To calculate depth dependent part of integrand for vert ptcle displ
c receiver in ground.
c (23/2/90 Steve Tooms)For T.Richards method.
c
implicit real*8 (a-h,o-z)
complex*16 l1,l2,l3,c1,c2,c3,c(62),ftot,j,hor
c
ij=2*ial+6*irl
if (irl.le.igl) then
ftot= c1*c(ij-6)*cdexp(j*c1*l1*rdn)
ftot=ftot-c1*c(ij-5)*cdexp(j*c1*l1*run)
ftot=ftot+c2*c(ij-4)*cdexp(j*c2*l2*rdn)
ftot=ftot-c2*c(ij-3)*cdexp(j*c2*l2*run)
ftot=ftot+s3*c(ij-2)*cdexp(j*c3*l3*rdn)
ftot=ftot-s3*c(ij-1)*cdexp(j*c3*l3*run)
else
ftot= c1*c(ij-6)*cdexp(j*c1*l1*rdn)
ftot=ftot+c2*c(ij-5)*cdexp(j*c2*l2*rdn)
ftot=ftot+s3*c(ij-4)*cdexp(j*c3*l3*rdn)
```

```
end if
ftot = ftot*hor
RETURN
END

*****************************************************************


  SUBROUTINE intmod(ftot,ftini,i1,ihor,delt,alph,j)
c Modification to integrand from T.Richards' method
c
implicit real*8 (a-h,o-z)
complex*16 ftot,ftini,j
complex*16 fadd
c
fadd=j*ihor*ftini*(1-cdexp(delt*(j*alph-(i1-1))/ihor))
     1  /(alph*delt)
ftot=ftot-fadd
return
end

*****************************************************************


SUBROUTINE star(m,ihor,sta,i1,alph,j)
c Calculation of parameter "s*" in T.Richards' method
implicit real*8(a-h,o-z)
complex*16 z,zm,sta,j
c
z=(dfloat(i1)-1d0-(j*alph))/ihor
em=dfloat(m)
zm=z+em
sta=(0d0,0d0)
do 10 jay=1,m
sta=sta+1/cdsqrt(dfloat(jay)+z)
10  continue
sta=sta+2*(dsqrt(em)-cdsqrt(zm))
sta=sta-0.5d0*(1/cdsqrt(zm))*(1+(1/(zm*12))-(1/(192*zm**3)))
return
end

*****************************************************************


SUBROUTINE intmod2(ftot,ihor,i1,ftfin,sta,j,alph)
c calculation of integrand modification from T.Richards' method
```

```
c
implicit real*8 (a-h,o-z)
complex*16 ftot,ftfin,sta,j
c
ftot=ftot/cdsqrt(dfloat(i1)-1d0-j*alph)
ftot=ftot+ftfin/(dsqrt(dfloat(ihor)))*sta
return
end

*************************************************************


SUBROUTINE ramult2(dhor,ihor,pi,j,alph,ftot,rtot,i4)
c Final calculation of range dependent function for T.Richards' method
c
implicit real*8(a-h,o-z)
complex*16 ftot(1024),rtot(1024),j,pha
c
pha=(1d0,0d0)
if (i4.eq.2) pha=cdexp(j*pi/2)
do 10 m=1,(ihor-1)
        rm=ihor*dhor/(2*pi*dsqrt(dfloat(m)))
rtot(m+1)=ftot(m+1)*cdexp(-j*pi*0.25d0)/pha
     1  *dexp(2*pi*m*alph/ihor)
rtot(m+1)=rtot(m+1)-ftot(ihor-m+1)*cdexp(j*pi*0.25d0)
     1  *dexp(-2*pi*m*alph/ihor)*pha
10 rtot(m+1)=rtot(m+1)*rm
return
end

*************************************************************



        SUBROUTINE FORK(LX,CX,SIGNI)
C
C  FFT AS GIVEN BY J.F.CLAERBOUT, "FUNDAMENTALS OF GEOPHYSICAL
C  DATA PROCESSING" page 12.
C
C CX(LX) : THE DEPTH DEPENDENT PART OF THE INTEGRAND
C LX     : A WHOLE POWER OF TWO
C
C
IMPLICIT REAL*8(a-h,o-z)
COMPLEX*16 CX(LX),CARG,CW,CTEMP
CCC        COMPLEX CX(512),CARG,CW,CTEMP
```

```
D TYPE *, 'FORK: LX=', LX, '  SIGNI=', SIGNI
pi= 2*dasin(1d0)
        J=1
        SC=dSQRT(1d0/LX)
        DO 30 I=1,LX
        IF(I.GT.J)GO TO 10
        CTEMP=CX(J)*SC
        CX(J)=CX(I)*SC
        CX(I)=CTEMP
   10       M=LX/2
   20       IF(J.LE.M)GO TO 30
        J=J-M
        M=M/2
        IF(M.GE.1)GO TO 20
   30       J=J+M
        L=1
   40       ISTEP=2*L
        DO 50 M=1,L
        CARG=(0d0,1d0)*(pi*SIGNI*(M-1))/L
        CW=CdEXP(CARG)
        DO 50 I=M,LX,ISTEP
        CTEMP=CW*CX(I+L)
        CX(I+L)=CX(I)-CTEMP
   50       CX(I)=CX(I)+CTEMP
        L=ISTEP
        IF(L.LT.LX)GO TO 40
        RETURN
        END

*****************************************************************


SUBROUTINE costh(c0,s0,q0,l0,exp0,hor,ial,h,j)
c  To calculate cos,sin,exponential fn.
        implicit real*8(a-h,o-z)
        complex*16 c0(15),s0(15),q0(15)
complex*16 l0(15),j,exp0(15),hor
dimension h(15)
do 1123 in=1,ial
         s0(in) = hor/l0(in)
         c0(in) = cdsqrt(1.d0-s0(in)*s0(in))
         q0(in) = l0(in)*c0(in)*h(in)
         exp0(in) = cdexp(j*q0(in))
1123 continue
return
end
```

```
*************************************************************

SUBROUTINE wave(l0,k0,v0,rha,ial,twopi,fr,dhor,horup)
c to calc prop const and bulk modulus
implicit real*8 (a-h,o-z)
dimension rha(15)
        complex*16 l0(15),k0(15),v0(15)
real*8 twopi,fr
do 1122 in=1,ial
         l0(in) = twopi*fr/v0(in)
         k0(in) = v0(in)**2*rha(in)
c
if (dhor.gt.dreal(l0(in)/20)) then
write(6,*) 'wavenumber interval is large for l0',in
        else if (dreal(l0(in)).gt.0.8*horup) then
write(6,*)'upper wavenumber bound too small l0',in
end if
1122    continue
return
end

*************************************************************

SUBROUTINE scefnd(isl,sun,sdn,hs,h,ial)
c to find layer with source in and distance to top and bottom.
implicit real*8 (a-h,o-z)
dimension h(15)
ha=0d0
do 10 isl=1,ial-1
  ha=ha+h(isl)
  if(ha.gt.hs) goto 20
10 continue
sdn=hs-ha
isl=ial
return
20 sun=ha-hs
sdn=h(isl)-sun
return
end

*************************************************************
```

```
SUBROUTINE recfnd(irl,run,rdn,hr,h,ial)
c to find layer with receiver in and distance to top and bottom.
implicit real*8 (a-h,o-z)
dimension h(15)
ha=0d0
do 10 irl=1,ial-1
  ha=ha+h(irl)
  if(ha.gt.hr) goto 20
10 continue
rdn=hr-ha
irl=ial
return
20 run=ha-hr
rdn=h(irl)-run
return
end

*****************************************************************


SUBROUTINE grecfnd(irl,run,rdn,hr,dep,igl)
c to find layer with receiver in and distance to top and bottom.
implicit real*8 (a-h,o-z)
dimension dep(8)
ha=0d0
hr=-hr
do 10 irl=1,igl
  ha=ha+dep(irl)
  if(ha.gt.hr) goto 20
10 continue
rdn=hr-ha
irl=igl+1
return
20 run=ha-hr
rdn=dep(irl)-run
hr=-hr
return
end

*****************************************************************


subroutine ngrmap(numlay,irray,ial,ai,a,a1,a2,b,c,a3,wkspce)
c to write a,a1,a2(ground bces) and ai(air bces) to a3(global)
c  and solve a3 using source terms from b. Answers in c.
complex*16 a(4,8),a1(6,9),a2(6,6,12),b(62),c(62)
```

```
complex*16 ai(14,2,4)
complex*16 a3(62,62)
real*8 wkspce(62)
c      ------------------------------------------------------------
c air-ground interface.
do 2 j=1,8
  do 4 i=1,4
    i3=2*ial-2+i
    j3=2*ial-3+j
            if (j3.ge.1.and.j3.le.irray) a3(i3,j3)=a(i,j)
4   continue
2 continue
if (numlay.gt.1) then
c      ------------------------------------------------------------
c ground layer-ground layer interfaces.
do 6 k=1,numlay-1
    do 8  j=1,12
do 10 i=1,6
    i3=2*(ial-1)+4+(k-1)*6+i
    j3=2*(ial-1)+1+(k-1)*6+j
10              a3(i3,j3)=a2(k,i,j)
8     continue
6  continue
end if
c      ------------------------------------------------------------
c Ground layer-lower halfspace interfaces.
if (numlay.gt.0) then
7 do 12 j=1,9
    do 14 i=1,6
i3=4+6*(numlay-1)+i+2*(ial-1)
j3=1+6*(numlay-1)+j+2*(ial-1)
14 a3(i3,j3)=a1(i,j)
12 continue
end if
if (ial.gt.1) then
c      ------------------------------------------------------------
c air-air interfaces.
c a3(1,2)=ab(2)
  do 16 k=1,ial-1
    do 18 i=1,2
      do 20 j=1,4
        i3= 2*ial+1-2*k-i
j3= 2*ial+2-2*k-j
if (j3.ge.1) a3(i3,j3) = ai(k,i,j)
20           continue
18     continue
```

```
16        continue
end if
c      ------------------------------------------------------------
c NAG library simultaneous equation solution.
ia=62
ib=ia
n=irray
m=1
ifail=1
ic=ib
call f04adf(a3,ia,b,ib,n,m,c,ic,wkspce,ifail)
if (ifail.ne.0)  print*,'f04adf failed ifail=',ifail
return
end

*************************************************************


SUBROUTINE grsce(b,isl,ial,sun,sdn,c0,l0,k0,j)
c To write source terms in 'b' for layered ground, layered air
c and source in air
implicit real*8 (a-h,o-z)
complex*16 b(62),c0,l0,k0,j
do 10 jib=1,62
    b(jib)=(0.d0,0.d0)
10 continue
        if (isl.eq.1) then
          b(2*(ial-1)+1) = cdexp(j*c0*l0*sdn)/l0
  b(2*(ial-1)+3) = k0*cdexp(j*l0*c0*sdn)/c0
  b(2*(ial-1)+4) = k0*cdexp(j*c0*l0*sdn)/c0
  if (ial.gt.1) then
    b(2*(ial-1))=  +cdexp(j*c0*l0*sun)/l0
           b(2*(ial-1)-1)= +k0*cdexp(j*l0*c0*sun)/c0
  end if
else
  ii= 2*(ial-1)-2*(isl-1)
  b(ii+2)= cdexp(j*c0*l0*sdn)/l0
         b(ii+1)= -k0*cdexp(j*l0*c0*sdn)/c0
    if (ii.gt.0) then
    b(ii)= +cdexp(j*c0*l0*sun)/l0
           b(ii-1)= k0*cdexp(j*l0*c0*sun)/c0
  end if
end if
return
end
```

```
*************************************************************


SUBROUTINE grairtrm(ai,ab,c0,l0,exp0,k0,ial)
c calcs layered air bces in abscence of source
c over layered ground.
implicit real*8 (a-h,o-z)
      complex*16 ai(14,2,4),ab(2)
      complex*16 c0(15),k0(15),l0(15),exp0(15)
c npd at rigid boundary
c ab(1)= -c0(1)
c ab(2)= -ab(1)*exp0(1)
do 10 k=1,ial-1
c npd
    ai(k,1,2)= +c0(k)
    ai(k,1,1)= -ai(k,1,2)*exp0(k)
    ai(k,1,3)= +c0(k+1)
    ai(k,1,4)= -ai(k,1,3)*exp0(k+1)
c pressure
    ai(k,2,2)= -k0(k)*l0(k)
    ai(k,2,1)= ai(k,2,2)*exp0(k)
    ai(k,2,3)= +k0(k+1)*l0(k+1)
    ai(k,2,4)= ai(k,2,3)*exp0(k+1)
10 continue
return
end

*************************************************************


Subroutine grbce(k0,l0,c0,l1,l2,l3,exp1,exp2,exp3,exp0
     *  ,numlay,m1,m2,m3,hh1,cc1,mm1,gb,c1,c2,c3,s1,s2,s3,a,a1,a2)
c To calculate boundary condition equations at ground interfaces
      implicit real*8(a-h,o-z)
      complex*16  a(4,8),a1(6,9),a2(6,6,12)
      complex*16 hh1(8),cc1(8),mm1(8),gb(8)
      complex*16 l0,c0,k0,exp0
      complex*16 c3(8),c1(8),c2(8),s1(8),s2(8),s3(8)
      complex*16 l1(8),l2(8),l3(8)
      complex*16 exp1(8),exp2(8),exp3(8)
      complex*16 m1(8),m2(8),m3(8)
c
c       Ground-Air Interface
c Pressure
 a(4,1) = -k0*l0*exp0
 a(4,2) = -k0*l0
```

```
          a(4,3) = l1(1)*(cc1(1)-m1(1)*mm1(1))
          a(4,4) = a(4,3)*exp1(1)
          a(4,5) = l2(1)*(cc1(1)-m2(1)*mm1(1))
          a(4,6) = a(4,5)*exp2(1)
          a(4,7) = (0.d0,0.d0)
          a(4,8) = (0.d0,0.d0)
c Normal Particle Velocity
 a(1,1) = -c0*exp0
 a(1,2) = c0
          a(1,3) = (1.d0-m1(1))*c1(1)
          a(1,4) = -a(1,3)*exp1(1)
          a(1,5) = (1.d0-m2(1))*c2(1)
          a(1,6) = -a(1,5)*exp2(1)
          a(1,7) = (1.d0-m3(1))*s3(1) ! sign changed 13/10/89
          a(1,8) = -(1.d0-m3(1))*s3(1)*exp3(1)
c Tangential Stress
 a(2,1) = (0d0,0d0)
          a(2,2) = (0.d0,0.d0)
          a(2,3) = 2.d0*l1(1)*s1(1)*c1(1)
          a(2,4) = a(2,3)*exp1(1)
          a(2,5) = 2.d0*l2(1)*c2(1)*s2(1)
          a(2,6) = a(2,5)*exp2(1)
          a(2,7) = -(l3(1)*c3(1)*c3(1)-l3(1)*s3(1)*s3(1))
          a(2,8) = a(2,7)*exp3(1)
c Normal Stress
 a(3,1) = a(4,1)
 a(3,2) = a(4,2)
          a(3,3) = l1(1)*(hh1(1)-m1(1)*cc1(1)-2.d0*gb(1)*s1(1)*s1(1))
          a(3,4) = -a(3,3)*exp1(1)
          a(3,5) = l2(1)*(hh1(1)-m2(1)*cc1(1)-2.d0*gb(1)*s2(1)*s2(1))
          a(3,6) = -a(3,5)*exp2(1)
          a(3,7) = 2.d0*gb(1)*l3(1)*s3(1)*c3(1)
          a(3,8) = -a(3,7)*exp3(1)
c      ------------------------------------------------------------
c Layer-Lower Half Space Interface
 n=numlay
c npv
          A1(1,1) = c1(n)*exp1(n)
          A1(1,2) = -c1(n)
          A1(1,3) = c2(n)*exp2(n)
          A1(1,4) = -c2(n)
          A1(1,5) = s3(n)*exp3(n)
          A1(1,6) = -s3(n)
          A1(1,7) = -c1(n+1)
 A1(1,8) = -c2(n+1)
          A1(1,9) = -s3(n+1)
```

```
c tpv
          A1(2,1) = s1(n)*exp1(n)
          A1(2,2) = s1(n)
          A1(2,3) = s2(n)*exp2(n)
          A1(2,4) = s2(n)
          A1(2,5) = -c3(n)*exp3(n)
          A1(2,6) = -c3(n)
          A1(2,7) = -s1(n+1)
 A1(2,8) = -s2(n+1)
          A1(2,9) = c3(n+1)
c ns
          A1(3,2) = l1(n)*(hh1(n)-m1(n)*cc1(n)-2.d0*gb(n)*s1(n)*s1(n))
          A1(3,1) = -A1(3,2)*exp1(n)
          A1(3,4) = l2(n)*(hh1(n)-m2(n)*cc1(n)-2.d0*gb(n)*s2(n)*s2(n))
          A1(3,3) = -A1(3,4)*exp2(n)
          A1(3,5) = -2.d0*gb(n)*l3(n)*s3(n)*c3(n)*exp3(n)
          A1(3,6) = 2.d0*gb(n)*l3(n)*s3(n)*c3(n)
          A1(3,7) = l1(n+1)*(hh1(n+1)-m1(n+1)*cc1(n+1)-2.d0*gb(n+1)
     1 *s1(n+1)*s1(n+1))
 A1(3,8) = l2(n+1)*(hh1(n+1)-m2(n+1)*cc1(n+1)-2.d0*gb(n+1)
     1 *s2(n+1)*s2(n+1))
          A1(3,9) = 2.d0*gb(n+1)*l3(n+1)*s3(n+1)*c3(n+1)
c ts
          A1(4,1) = 2.d0*gb(n)*l1(n)*s1(n)*c1(n)*exp1(n)
          A1(4,2) = 2.d0*gb(n)*l1(n)*s1(n)*c1(n)
          A1(4,3) = 2.d0*gb(n)*l2(n)*s2(n)*c2(n)*exp2(n)
          A1(4,4) = 2.d0*gb(n)*l2(n)*s2(n)*c2(n)
          A1(4,5) = -gb(n)*l3(n)*(c3(n)*c3(n)-s3(n)*s3(n))*exp3(n)
          A1(4,6) = -gb(n)*l3(n)*(c3(n)*c3(n)-s3(n)*s3(n))
          A1(4,7) = -2.d0*gb(n+1)*l1(n+1)*c1(n+1)*s1(n+1)
 A1(4,8) = -2.d0*gb(n+1)*l2(n+1)*c2(n+1)*s2(n+1)
          A1(4,9) = gb(n+1)*l3(n+1)*(c3(n+1)*c3(n+1)-s3(n+1)*s3(n+1))
c nfpv
          A1(5,1) = m1(n)*c1(n)*exp1(n)
          A1(5,2) = -m1(n)*c1(n)
          A1(5,3) = m2(n)*c2(n)*exp2(n)
          A1(5,4) = -m2(n)*c2(n)
          A1(5,5) = m3(n)*s3(n)*exp3(n)
          A1(5,6) = -m3(n)*s3(n)
          A1(5,7) = -m1(n+1)*c1(n+1)
 A1(5,8) = -m2(n+1)*c2(n+1)
          A1(5,9) = -m3(n+1)*s3(n+1)
c fp
 A1(6,1) = l1(n)*(cc1(n)-m1(n)*mm1(n))*exp1(n)
 A1(6,2) = l1(n)*(cc1(n)-m1(n)*mm1(n))
 A1(6,3) = l2(n)*(cc1(n)-m2(n)*mm1(n))*exp2(n)
```

```
 A1(6,4) = l2(n)*(cc1(n)-m2(n)*mm1(n))
 A1(6,5) =(0.d0,0.d0)
 A1(6,6) = (0.d0,0.d0)
 A1(6,7) =-l1(n+1)*(cc1(n+1)-m1(n+1)*mm1(n+1))
 A1(6,8) =-l2(n+1)*(cc1(n+1)-m2(n+1)*mm1(n+1))
 A1(6,9) = (0.d0,0.d0)
c
if (numlay.eq.1) goto 2212
c
c      ------------------------------------------------------------
c Layer-Layer Interfaces
c
do 2211 n=1,numlay-1
c npv
          a2(n,1,1) = c1(n)*exp1(n)
          a2(n,1,2) = -c1(n)
          a2(n,1,3) = c2(n)*exp2(n)
          a2(n,1,4) = -c2(n)
          a2(n,1,5) = s3(n)*exp3(n)
          a2(n,1,6) = -s3(n)
          a2(n,1,7) = -c1(n+1)
 a2(n,1,8) = c1(n+1)*exp1(n+1)
 a2(n,1,9) = -c2(n+1)
 a2(n,1,10) = c2(n+1)*exp2(n+1)
          a2(n,1,11) = -s3(n+1)
 a2(n,1,12) = s3(n+1)*exp3(n+1)
c tpv
          a2(n,2,1) = s1(n)*exp1(n)
          a2(n,2,2) = s1(n)
          a2(n,2,3) = s2(n)*exp2(n)
          a2(n,2,4) = s2(n)
          a2(n,2,5) = -c3(n)*exp3(n)
          a2(n,2,6) = -c3(n)
          a2(n,2,7) = -s1(n+1)
 a2(n,2,8) = -s1(n+1)*exp1(n+1)
 a2(n,2,9) = -s2(n+1)
 a2(n,2,10) = -s2(n+1)*exp2(n+1)
          a2(n,2,11) = c3(n+1)
 a2(n,2,12) = c3(n+1)*exp3(n+1)
c ns
          a2(n,3,2) = -l1(n)*(hh1(n)-m1(n)*cc1(n)-2.d0*gb(n)*s1(n)
     1      *s1(n))
          a2(n,3,1) = -A2(n,3,2)*exp1(n)
          a2(n,3,4) = -l2(n)*(hh1(n)-m2(n)*cc1(n)-2.d0*gb(n)*s2(n)
     1      *s2(n))
          a2(n,3,3) = -A2(n,3,4)*exp2(n)
```

```
          a2(n,3,5) = 2.d0*gb(n)*l3(n)*s3(n)*c3(n)*exp3(n)
          a2(n,3,6) = -2.d0*gb(n)*l3(n)*s3(n)*c3(n)
          a2(n,3,7) = -l1(n+1)*(hh1(n+1)-m1(n+1)*cc1(n+1)-2.d0*gb(n+1)
     1     *s1(n+1)*s1(n+1))
 a2(n,3,8) = l1(n+1)*(hh1(n+1)-m1(n+1)*cc1(n+1)-2.d0*gb(n+1)
     1    *s1(n+1)*s1(n+1))*exp1(n+1)
 a2(n,3,9) = -l2(n+1)*(hh1(n+1)-m2(n+1)*cc1(n+1)-2.d0*gb(n+1)
     1    *s2(n+1)*s2(n+1))
 a2(n,3,10) = -a2(n,3,9)*exp2(n+1)
          a2(n,3,11) = -2.d0*gb(n+1)*l3(n+1)*s3(n+1)*c3(n+1)
 a2(n,3,12) = 2.d0*gb(n+1)*l3(n+1)*s3(n+1)*c3(n+1)*exp3(n+1)
c ts
          a2(n,4,1) = 2.d0*gb(n)*l1(n)*s1(n)*c1(n)*exp1(n)
          a2(n,4,2) = 2.d0*gb(n)*l1(n)*s1(n)*c1(n)
          a2(n,4,3) = 2.d0*gb(n)*l2(n)*s2(n)*c2(n)*exp2(n)
          a2(n,4,4) = 2.d0*gb(n)*l2(n)*s2(n)*c2(n)
          a2(n,4,5) = -gb(n)*l3(n)*(c3(n)*c3(n)-s3(n)*s3(n))*exp3(n)
          a2(n,4,6) = -gb(n)*l3(n)*(c3(n)*c3(n)-s3(n)*s3(n))
          a2(n,4,7) = -2.d0*gb(n+1)*l1(n+1)*c1(n+1)*s1(n+1)
 a2(n,4,8) = -2.d0*gb(n+1)*l1(n+1)*c1(n+1)*s1(n+1)*exp1(n+1)
   a2(n,4,9) = -2.d0*gb(n+1)*l2(n+1)*s2(n+1)*c2(n+1)
   a2(n,4,10) =-2.d0*gb(n+1)*l2(n+1)*s2(n+1)*c2(n+1)*exp2(n+1)
          a2(n,4,11) = gb(n+1)*l3(n+1)*(c3(n+1)*c3(n+1)-s3(n+1)*s3(n+1))
 a2(n,4,12) = gb(n+1)*l3(n+1)*(c3(n+1)*c3(n+1)-s3(n+1)*s3(n+1))
     1    *exp3(n+1)
c nfpv
          a2(n,5,1) = m1(n)*c1(n)*exp1(n)
          a2(n,5,2) = -m1(n)*c1(n)
          a2(n,5,3) = m2(n)*c2(n)*exp2(n)
          a2(n,5,4) = -m2(n)*c2(n)
          a2(n,5,5) = m3(n)*s3(n)*exp3(n)
          a2(n,5,6) = -m3(n)*s3(n)
          a2(n,5,7) = -m1(n+1)*c1(n+1)
 a2(n,5,8) = m1(n+1)*c1(n+1)*exp1(n+1)
   a2(n,5,9) = -m2(n+1)*c2(n+1)
 a2(n,5,10) = m2(n+1)*c2(n+1)*exp2(n+1)
          a2(n,5,11) = -m3(n+1)*s3(n+1)
 a2(n,5,12) = m3(n+1)*s3(n+1)*exp3(n+1)
c fp
 a2(n,6,1) = l1(n)*(cc1(n)-m1(n)*mm1(n))*exp1(n)
 a2(n,6,2) = l1(n)*(cc1(n)-m1(n)*mm1(n))
 a2(n,6,3) = l2(n)*(cc1(n)-m2(n)*mm1(n))*exp2(n)
 a2(n,6,4) = l2(n)*(cc1(n)-m2(n)*mm1(n))
 a2(n,6,5) =(0.d0,0.d0)
 a2(n,6,6) = (0.d0,0.d0)
 a2(n,6,7) =-l1(n+1)*(cc1(n+1)-m1(n+1)*mm1(n+1))
```

```
 a2(n,6,8) =-l1(n+1)*(cc1(n+1)-m1(n+1)*mm1(n+1))*exp1(n+1)
 a2(n,6,9) =-l2(n+1)*(cc1(n+1)-m2(n+1)*mm1(n+1))
 a2(n,6,10) =-l2(n+1)*(cc1(n+1)-m2(n+1)*mm1(n+1))*exp2(n+1)
 a2(n,6,11) = (0.d0,0.d0)
 a2(n,6,12) = (0.d0,0.d0)
2211    continue
2212 continue
return
end

*************************************************************

SUBROUTINE sub1(v1,v2,v3,l1,l2,l3,m1,m2,m3,hh1,gb,rho
     * ,rhof,l1s,l2s,l3s,twopi,fr,numlay)
      implicit real*8(a-h,o-z)
      dimension rho(8)
      complex*16 hh1(8),cc1(8),gb(8)
      complex*16 l1(8),l2(8),l3(8),l1s(8),l2s(8),l3s(8)
      complex*16 v1(8),v2(8),v3(8),z1(8),z2(8),m1(8),m2(8),m3(8)
      real*8 omega,fr
c
do 10 in=1,numlay+1
         v1(in) = twopi*fr/l1(in)
         v2(in) = twopi*fr/l2(in)
         v3(in) = twopi*fr/l3(in)
c         td = 2.d0*dep(in)/v1(in)
c
c      ------------------------------------------------------------
c
c      m1(in) and m2(in) are the ratios of the  relative wave to the
c      matrix wave(fast, slow)
c      equations for m1(in) and m2(in) taken from geertsma and smit
c      geophysics v.26 apr 1961
c      aspects og elastic wave prog. in fld. sat. porous solids.
c
c      ------------------------------------------------------------
c
        z1(in) = hh1(in)*l1(in)*l1(in)/(rho(in)*twopi*twopi*fr*fr)
c
        z2(in) = hh1(in)*l2(in)*l2(in)/(rho(in)*twopi*twopi*fr*fr)
c
      m1(in) = (hh1(in)*(z1(in)-1.d0))/(z1(in)*cc1(in)
     *-rhof*hh1(in)/rho(in))
c
      m2(in) = (hh1(in)*(z2(in)-1.d0))/(z2(in)*cc1(in)
     *-rhof*hh1(in)/rho(in))
```

```
c
        m3(in) = (rho(in)*twopi*fr*twopi*fr-
     *(gb(in)*l3(in)*l3(in)))/(rhof*twopi*fr*twopi*fr)
c
c      ------------------------------------------------------------
c
c       l0  -  l3   are the wave numbers
c
         l1s(in) = l1(in)*l1(in)
         l2s(in) = l2(in)*l2(in)
         l3s(in) = l3(in)*l3(in)
10 continue
return
end

*****************************************************************

SUBROUTINE sub2(hor,l0,s1,s2,s3,c1,c2,c3,l1,l2,l3,dep,
     *    exp1,exp2,exp3,l1s,l2s,l3s,j,numlay)

      implicit real*8(a-h,o-z)
      dimension dep(8)
      complex*16 c0,s0,ssq,hor
      complex*16 c1(8),c2(8),c3(8),s1(8),s2(8),s3(8),q1(8),q2(8),q3(8)
      complex*16 j,l1(8),l2(8),l3(8),l1s(8),l2s(8),l3s(8)
      complex*16 exp1(8),exp2(8),exp3(8)
      complex*16 l0,l0s0,l0s
c      revised definitions for s0 and c0 in terms of wavenumber
         s0 = (hor/l0)
         ssq = s0*s0
         c0 =(cdsqrt(1-ssq))
         l0s0 = l0*s0
 l0s=l0*l0
c
c      ------------------------------------------------------------
do 1123 in=1,numlay+1
c
c      s0,s1,c0,c1, etc are the sines and cosines of the
c      incident, reflected and refracted angles.
c
         c1(in) = cdsqrt(1.d0-l0s*ssq/l1s(in))
         c2(in) = cdsqrt(1.d0-l0s*ssq/l2s(in))
         c3(in) = cdsqrt( 1.d0-l0s*ssq/l3s(in))
         s1(in) = l0s0/l1(in)
         s2(in) = l0s0/l2(in)
         s3(in) = l0s0/l3(in)
```

```
c
c      ------------------------------------------------------------
c
c      q1 - q3is the wave number * cos(angle) * layer thickness
c      dep is the thickness of layer
c
         q1(in) = l1(in)*c1(in)*dep(in)
         q2(in) = l2(in)*c2(in)*dep(in)
         q3(in) = l3(in)*c3(in)*dep(in)
c
c      ------------------------------------------------------------
c
c      expi or expii are the exponentials in the b. c. equations
c
         exp1(in) = cdexp(j*q1(in))
         exp2(in) = cdexp(j*q2(in))
         exp3(in) = cdexp(j*q3(in))
1123 continue
return
end

*****************************************************************
```

C.4 Resid

Calculates excess attenuation in an upward refracting sound velocity gradient over an impedance plane using a residue series.

```
C
C PROGRAM DESCRIPTION:
C
C        Program RESID to calculate sound pressure level in propagation through
C        a linear sound velocity gradient  over an impedance surface, after
C       Berry and Daigles modifications to Pierces method, with Raspet's
C       method for finding the roots of the transendental equations.
C
C AUTHORS:
C
C        S Tooms
C
C CREATION DATE:        17-April-1990
C
C
C            C H A N G E   L O G
C
C        Date     | Name  | Description
C ---------------+-------+-----------------------------------------------------
C [change_entry]
C
        implicit real*8 (a-h,o-z)
        complex*16 z,zres(11),q,b(11),i,k(11),expon
        complex*16 cdens,propc,ccc,y
        real*8 k0
        ichi=2
        i=(0d0,1d0)
        pi=2*dasin(1d0)
        expon=cdexp(i*pi/3d0)
        read(ichi,*) hs,hr,dr,rmax
        read(ichi,*) g,c0,rho0,fr
        read(ichi,*) sig,ome,enp,sp,d
c       Calculate normal surface impedance
        call pcall(fr,0,q2,enp,sp,sig,ome,ae,y,ccc,propc)
        call cdall(fr,0,q2,enp,sp,sig,ome,cdens)
        call zlrigpor(fr,propc,cdens,d,z)
c       End of impedance calculation
c       Calculate other functions
        call kay0(fr,c0,pi,k0)
        call arr(c0,g,rr)
        call ell(rr,k0,el)
        call que(k0,c0,rho,el,z,i,q)
c       calculate roots of transendental equation.
        call ben(q,expon,b)
        call wy(hr,el,y1)
        call wy(hs,el,y0)
```

```
        call zedres(el,b,y1,y0,expon,zres)
        call kiy(k0,b,el,expon,k)
        call pres(el,expon,k,i,dr,rmax,pi,zres,p,hs,hr)
        stop
        end

*************************************************************************

chx     Subroutine CDALL(f, aq, q2, enpr, sfr, sigma, poros, cdens)
chx     Calculates a single value of complex density (cdens) using the
chx     Rayliegh-Attenborough model given the frequency(f),
chx     the tortuosity q2 (only if aq=1), grain shape factor (n prime - enpr),
chx     pore shape factor ratio (sfr), flow resistivity (sigma) and
chx     porosity (poros).

        Subroutine CDALL(f, aq, q2, enpr, sfr, sigma, poros, cdens)
        implicit real*8 (a-h,o-z)
        real*8 mu,nuf,enpr,lambdap
        complex*16 i,yp,tp,j0,j1,cdens
c       complex*16 dyp,dj0,dj1
c
c calculate q2 if it has not been input directly (ie. aq.ne.1)
c       and set up constants.
c
        if(aq.eq.1)goto 10
        q2 = poros**-enpr
10      q=dsqrt(q2)
        pi=3.141592653
        i=dcmplx(0.0,1.0)
        cf=330.0
        gamma=1.4
C       prandtl=0.76
        PRANDTL=0.708506
        mu=171d-7
        rhof=1.204
        nuf=mu/rhof
        ae=8*mu*(q**2)/(poros*sigma)
        ae=ae**0.5
        omega=2*pi*f
        lambdap=(ae/(2.*sfr))*((omega/nuf)**0.5)
        yp=lambdap*(i**0.5)
c
calls Bessel function routine CMPBJ
c
        n1=0
        call cmpbj(yp,n1,j0)
```

```
      n1=1
      call cmpbj(yp,n1,j1)
      tp=j1/j0
c
      cdens=q**2*rhof/((1-(2/yp)*tp)*poros)
c
      return
      end

*************************************************************************

chx   Subroutine PCALL(f, aq, q2, enpr, sfr, sigma, poros, ae, y, ccc, propc)
chx   Calculates a single value of complex propagation constant (propc)using
chx   the Rayliegh-Attenborough model, given the frequency(f),
chx   the tortuosity q2 (only if aq=1), grain shape factor (n prime - enpr),
chx   pore shape factor ratio (sfr), flow resistivity (sigma) and
chx   porosity (poros).
c     The functions ae, y and ccc are also returned by this subroutine in
c     case they are required.

      Subroutine PCALL(f, aq, q2, enpr, sfr, sigma, poros, ae, y, ccc, propc)
      implicit real*8 (a-h,o-z)
      real*8 mu,nuf,enpr,lambdap
      complex*16 i,y,t,yp,tp,zkkb,j0,j1,ccc,propc
      if(aq.eq.1.0)goto 10
      q2 = poros**-enpr
10    q=dsqrt(q2)

      pi=3.141592653
      i=dcmplx(0.0,1.0)
      cf=330d0
      gamma=1.4
c     prandtl=0.76
      prandtl=0.708506
      dsqrtenp=dsqrt(prandtl)
      mu=181d-7
      rhof=1.2
      nuf=mu/rhof
      ae=8*mu*(q**2)/(poros*sigma)
      ae=ae**0.5

      omega=2*pi*f
      lambdap=(ae/(2.*sfr))*((omega/nuf)**0.5)
      y=dsqrtenp*lambdap*(i**0.5)
c
```

```
calls Bessel function routine CMPBJ
c
c
        n1=0
        call cmpbj(y,n1,j0)
        n1=1
        call cmpbj(y,n1,j1)
        t=j1/j0
c
        ccc=1+2*((gamma-1)/y)*t
        yp=lambdap*(i**0.5)

        n1=0
        call cmpbj(yp,n1,j0)
        n1=1
        call cmpbj(yp,n1,j1)
        tp=j1/j0
        zkkb=ccc/(1-(2/yp)*tp)
        zkkb=zkkb*(q*omega/cf)**2
        propc=zkkb**0.5
        return
        end

*************************************************************************

chx     Subroutine ZLRIGPOR( f, propc, cdens, d, zr)
chx     Calculates a single value of the surface impedance of a rigid-backed
chx     layer(zr), given the frequency (fr), propagation constant(propc)
chx     and complex*16density(cdens) of the top layer and the layer depth.

        Subroutine ZLRIGPOR( f, propc, cdens, d, zr)
        implicit real*8 (a-h,o-z)
        complex*16 i,cdens,propc,zc,ikd,ikd1,zr,ccoth
        pi=3.141592653
        i=dcmplx(0.0,1.0)
        rhof=1.204
        omega=2*pi*f
        cf=330d0
        zc=(cdens*omega)/(propc*rhof*cf)
        ikd=-1*i*propc*d
        ikd1=ccoth(ikd)
        zr=ikd1*zc
        return
        end

*************************************************************************
```

```
      Subroutine kay0(fr,c0,pi,k0)
c     Calculates air propagation constant.
      real*8 k0,pi,c0,fr
      k0=2*pi*fr/c0
      return
      end

*************************************************************************

      Subroutine arr(c0,g,rr)
c     Calculates radius of curvature in linear svg.
      real*8 c0,g,rr
      rr=c0/g
      return
      end

*************************************************************************

      Subroutine ell(rr,k0,el)
      real*8 rr,k0,el
      el=rr/(2*k0*k0)
      el=el**(1d0/3d0)
      return
      end

*************************************************************************

      subroutine que(k0,c0,rho,el,z,i,q)
      complex*16 q,i,z
      real*8 k0,rho,el,c0
      q=i*k0*el/z
      return
      end

*************************************************************************

      Subroutine ben(q,expon,b)
      implicit real*8 (a-h,o-z)
      complex*16 q,b(11),expon,x,y,f,df,dai,dbi,ai
      complex*16 dq,qx,bi,ddai,az(11)
c     az are zeros of Airy fn on -ve real axis
      data az/(-1.0188d0,0.0d0),(-3.24794d0,0.0d0),
     *  (-4.82055d0,0.0d0),(-6.1633d0,0.0d0),(-7.372d0,0.0d0),
     *  (-8.488d0,0.0d0),(-9.535d0,0.0d0),(-10.527d0,0.0d0),
     *  (-11.475d0,0.0d0),(-12.384d0,0.0d0),(-13.25d0,0.0d0)/
```

```
      dq=q/200d0
      do 10 ij=1,11
      x=az(ij)
c     print*,'1',x
      do 40 ijk=1,200
      qx=ijk*dq
          do 20 ji=1,100
c     Calulates Airy function
          call clairy(x,ai,bi,dai,dbi,itest)
          ddai=x*ai
          f=dai+qx*expon*ai
          df=ddai+qx*expon*dai
          x=x-f/df
          if (cdabs(f/df).lt.(cdabs(x*1d-5)))then
              if (ijk.eq.1) then
c                 print*,'2',x
                  goto 30
                 else if (ijk.eq.200) then
                  b(ij)=x
c                 print*,'3',x
                  goto 50
              else
                  goto 30
              end if
          end if
      if (ijk.eq.200) then
c                 print*,'4',x
                  b(ij)=x
      end if
20    continue
30    continue
40    continue
50    continue
10    continue
      return
      end

*************************************************************************

      subroutine wy(h,el,y)
      real*8 h,el,y
      y=h/el
      return
      end

*************************************************************************
```

```
      subroutine zedres(el,b,y,y0,expon,zres)
c     Calulates residue at each zero.
      implicit real*8 (a-h,o-z)
      real*8 el,y,y0
      complex*16 b(11),expon,zres(11),ai1,ai2,dais,ais
      complex*16 dum1,dum2,dum3
      do 10 ij=1,11
      itest=0
      call clairy(b(ij),ais,dum1,dais,dum2,itest)
      call clairy((b(ij)-y*expon**2),ai1,dum1,dum2,dum3,itest)
      call clairy((b(ij)-y0*expon**2),ai2,dum1,dum2,dum3,itest)
      ais=ais**2
      dais=dais**2
      zres(ij)=el*ai1*ai2/(expon**2*(dais-b(ij)*ais))
10    continue
      return
      end

*************************************************************************

      subroutine kiy(k0,b,el,expon,k)
      implicit real*8 (a-h,o-z)
      complex*16 k(11),b(11),expon
      real*8 k0
      do 10 ij=1,11
      k(ij)=1+b(ij)/((k0*el*expon)**2)
      k(ij)=k0*cdsqrt(k(ij))
10    continue
      return
      end

*************************************************************************

      Subroutine pres(el,expon,k,i,dr,rmax,pi,zres,p,hs,hr)
c     Calculates sound pressure level
      implicit real*8 (a-h,o-z)
      complex*16 expon,i,k(11),p,pp,px,zres(11)
      p=cdexp(-i*pi/12)*pi/(el**2)
      ir=nint(rmax/dr)
      do 10 ji=1,ir
      r=dr*ji
      pp=(0d0,0d0)
      do 20 ij=1,11
      px=cdsqrt(2/(pi*k(ij)*r))*cdexp(i*k(ij)*r)*zres(ij)
c     if (cdabs(px).lt.(1d-2*cdabs(pp))) print*,'CONV',ij
```

```
        pp=pp+px
20      continue
        pp=pp*p
        pp=20*dlog10((r**2+(hs-hr)**2)**(5d-1)*cdabs(pp))
        write (10,*) r,dreal(pp)
10      continue
        return
        end

*************************************************************************


        complex*16 function ccoth(z)
chx     complex*16 function ccoth(z)
chx     calculates coth of a complex number if the real part of z is
chx     large then ccoth(z) is equal to 1 + i0
        implicit real*8 (a-h,o-z)
        complex*16 z,i
        i=dcmplx(0.0,1.0)
        if (dreal(z) .gt. 44.3) then
                ccoth=(1d0,0d0)
                return
        else
                rz2=2.*dreal(z)
                az2=2.*dimag(z)
                c1=dcosh(rz2)-dcos(az2)
                ccoth=(dsinh(rz2)-i*dsin(az2))/c1
        end if
        return
        end
```

C.5 Nich

Calculates excess attenuation in an homogeneous fluid halfspace overlying a non-porous backed externally reacting rigid porous layer. Uses the formulation due to Nicholas, Berry and Daigle

```
C
C PROGRAM DESCRIPTION:
C
C        NICH
C        This program impliments the model for propagation
C        over an extended reaction rigid backed layer
c       according to Nicholas, Berry and Daigle
C
C AUTHORS:
C
C        Steve Tooms
C
C CREATION DATE:        30/1/90
C
C
C            C H A N G E   L O G
C
C       Date     | Name  | Description
C---------------+-------+-----------------------------------------------------
C 6-April-1990     |  S Tooms  | change output so no range output
C ---------------+-------+-----------------------------------------------------
        COMPLEX ptot,p1,ak1,ak2,rho2,j,zr,y,ccc
        j=(0.0,1.0)
        pi=4*atan(1.0)
        RHO1=1.204
c       Read Input
        read(2,*) sigma
        read(2,*)omeg
        read(2,*)enp
        read(2,*)sp
        read(2,*)dep
        read(2,*)hs
        read(2,*)hr
        read(2,*)ranbot
        read(2,*)rantop
        read(2,*)iran
        if(iran.ne.1) dran=(rantop-ranbot)/(iran-1)
        read(2,*)freqbot
        read(2,*)freqtop
        read(2,*)ifreq
        if (ifreq.ne.1) dfreq=(freqtop-freqbot)/(ifreq-1)
c       if(iran.eq.1) goto 3
        do 20 i=1,iran
3       ran=ranbot+(i-1)*dran
c       if (ifreq.eq.1) goto 5
        do 30 k=1,ifreq
```

```
5       freq=freqbot+(k-1)*dfreq
c       Calc prop consts
        call PCALL(freq,enp,sp,sigma,omeg,ae,y,ccc,ak2)
c       Calc complex density
        call cdall(freq,enp,sp,sigma,omeg,rho2)
c
        CALL ZLRIGPOR(freq,ak2,rho2,dep,hr,hs,ran,zr)
c       Final calculation of ptot
        CALL EXTEND(freq,ZR,hr,hs,ran,P1,PTOT)
        out=20*log10(cabs(ptot/p1))
        write(10,*)  freq,ran,out
30      continue
20      continue
        stop
        END

*************************************************************************

        SUBROUTINE EXTEND(FREQ,z,HR,HS,SEP,P1,PTOT)
        complex j,ck,cg,cr1,cr2,cpi,rp,beta,p1,p2,p3,ptot,reflind
        complex pe,pe2,wiz,f,c1,c2,c4,cssqth,ktheta,kthetam,A
        complex numa,dena,bnum1,bnum2,bden1,bden2,zkkb1,b,wsquared
        COMPLEX Z
        real k0,ssqth
        BETA=CMPLX(1.0,0.0)/z
        PI=3.141592653
        K0=(2.0*PI*FREQ)/343.
        h=hs+hr
        r1=sqrt((hs-hr)**2+sep*sep)
        r2=sqrt(h*h+sep*sep)
        cth=h/r2
        J  =CMPLX(0.0,1.0)
        c1=(1.0,0.0)
        c2=(2.0,0.0)
        c4=(4.0,0.0)
        cg=cmplx(cth,0.0)
        ck=cmplx(k0,0.0)
        cr1=cmplx(r1,0.0)
        cr2=cmplx(r2,0.0)
        cpi=cmplx(pi,0.0)
        rp=(Z*CTH-1.)/(Z*CTH+1.)
        p1=cexp(j*ck*cr1)/(c4*cpi*ck*cr1)
        p2=rp*cexp(j*ck*cr2)/(c4*cpi*ck*cr2)
c       WSQUARED=0.5*cEXP(J*CR2*K0)*((CTH+(1/Z))**2.)
        WSQUARED=0.5*(J*CR2*K0)*((CTH+(1/Z))**2.)
c
```

```
c       If the real part of the arguement pe2 is negative, the
c       subroutine w returns a large value of wiz which tends to cause
c       an overflow in the following calculations or a sharp discontinuity in
c       the attenuation result. Therefore steps are taken
c       to avoid this occuring. A negative imaginary part of wsquared gives
c       a negative real part of pe2, a negative imaginary part of wsquared is
c       therefore set to 0.
c
c       This is evidently an approximation but does seem to give 'sensible'
c       results.
c
c       wtestr=real(wsquared)
c       wtesti=aimag(wsquared)
c       if(wtesti.lt.0.0)wtesti=0.0
c       wsquared=cmplx(wtestr,wtesti)
        pe2     =  -j*csqrt(wsquared)
c
        call aw(pe2,wiz)
c
        f       =  c1+j*csqrt(cpi)*csqrt(wsquared)*wiz
        p3=(c1-rp)*f*cexp(j*ck*cr2)/(c4*cpi*ck*cr2)
        ptot=p1+p2+p3
        return
        end

*************************************************************************

chx     Calculation of the error function term of the propagation model
chx     s calculated according to the method of Chien and Soroka(1975),(1980)
chx     (JSV 43(1) p9-20 and JSV 69 p340-343).

        subroutine aw(z,wiz)
        logical lx,ly
        complex*8 z,wiz,cefw,s,t1,t2,t3
        data cons/1.128379167095/
        x=-aimag(z)
        y=real(z)
c
        x1=y
        y1=-x
c
c       determine quadrant for z
c
10      lx=x.ge.0.0
        ly=y.ge.0.0
        if(lx.and.ly)iq=1
```

```
      if(.not.lx.and.ly)iq=2
      if(.not.lx.and..not.ly)iq=3
      if(lx.and..not.ly)iq=4
c
c     convert to 1st quadrant
c
      x=abs(x)
      y=abs(y)
      s=cmplx(x,y)
      xs=x
      ys=y
c
100   if(y.ge.4.29.or.x.ge.5.33)goto 110
      s=(1.0-y/4.29)*sqrt((1.0-(x*x)/28.41))
      h=1.6*s
      h2=2.0*h
      ncap=6.5+23.0*s
      alamda=h2**ncap
      nu=9.5+21.0*s
      goto 120
110   t1=4.613135e-1/(s*s-1.901635e-1)
      t2=9.999216e-2/(s*s-1.7844927)
      t3=2.883894e-3/(s*s-5.5253437)
      wiz=s*(t1+t2+t3)
      v=real(wiz)
      u=-aimag(wiz)
      goto 180
120   r1=0.0
      r2=0.0
      s1=0.0
      s2=0.0
      n=nu
130   if(n.lt.0)goto 150
      p1=n+1
      t1=y+h+p1*r1
      t2=x-p1*r2
      c=0.5/(t1*t1+t2*t2)
      r1=c*t1
      r2=c*t2
      if(h.eq.0.0.or.n.gt.ncap)goto 140
      t1=alamda+s1
      s1=r1*t1-r2*s2
      s2=r2*t1+r1*s2
      alamda=alamda/h2
140   n=n-1
      goto 130
```

```
150     if(alamda.eq.0.0)goto 160
        u=cons*s1
        v=cons*s2
        goto 180
160     u=cons*r1
        v=cons*r2
180     cefw=cmplx(u,v)
c
c       test for underflow and overflow
c
        test=-xs*xs+ys*ys
        if(test.lt.-85.0)test=-85.0
        if(test.gt.87.)test=87.0
c test for quadrant
        goto(230,220,210,210),iq
210     cefw=2.0*cexp(cmplx(test,-2.*xs*ys))-cefw
        if(iq.eq.3)goto 230
        if(iq.eq.4)goto 220
c       for 2nd and 4th quads conjugate cefw
c
220     cefw=conjg(cefw)
c
c
230     wiz=cefw
        return
        end

*****************************************************************************

chx     Subroutine ZLRIGPOR( f, propc, cdens, d, h, hs, sep, zr)
chx     Calculates a single value of the surface impedance of a rigid-backed
chx     layer(zr), given the frequency (fr), propagation constant(propc)
chx     and complex density(cdens) of the top layer and the layer depth.

        Subroutine ZLRIGPOR( f, propc, cdens, d,
     1  h, hs, sep, zr)
        complex i,cdens,propc,zc,ikd,ikd1,zr,ccoth
        complex zr1,DK,CFCOST,ZR2
        pi=3.141592653
        i=cmplx(0.0,1.0)
        rhof=1.2
        FCOST=(SEP)/(SQRT(SEP**2.+(HS+H)**2.))
        CFCOST=CMPLX(FCOST,0.)
        omega=2*pi*f
        cf=343.
        DK=OMEGA/CF
```

```
        zc=(cdens*omega)/(propc*rhof*cf)
        zr1=CSQRT(1.-(((DK**2.)/(PROPC**2.))*(CFCOST**2.)))
        ZR=((ZC/ZR1)*CCOTH(-1*I*D*PROPC*ZR1))
        return
        end

*************************************************************************


        complex function ccoth(z)
chx     complex function ccoth(z)
chx     calculates coth of a complex number if the real part of z is
chx     large then ccoth(z) is equal to 1 + i0
        complex z,i
        i=cmplx(0.0,1.0)
        if (real(z) .gt. 44.3) then
                ccoth=(1.0,0.0)
                return
        else
                rz2=2.*real(z)
                az2=2.*aimag(z)
                c1=cosh(rz2)-cos(az2)
                ccoth=(sinh(rz2)-i*sin(az2))/c1
        end if
        return
        end
```

C.6 Quar

Calculates excess attenuation in an homogeneous fluid halfspace overlying an externally reacting rigid-porous halfspace. Uses Attenborough, Hayek, and Lawther's exact formulation[44]

```
C
C PROGRAM DESCRIPTION:
C
C        QUAR
C        This program impliments the 'exact' model for propagation
C        over an extended reaction half space according to
C        Attenborough, Hayek, and Lawther.
C
C AUTHORS:
C
C        Steve Tooms
C
C CREATION DATE:        5/10/88
C
C
C            C H A N G E   L O G
C
C       Date     | Name  | Description
C---------------+-------+-----------------------------------------------------
C 11-jan-1990     |  s tooms  | change to double precision
C ----------------+-------+-----------------------------------------------------
C 15_jan-1990     |  s tooms  | rename common blocks to avoid clash with bessels
C ----------------+-------+-----------------------------------------------------
C 15_jan-1990     |  s tooms  | change sign of a final term
C -----------------+-------+-----------------------------------------------------
C 16-jan-1990     |  s_tooms  | remove inputs for soairj
C ----------------+-------+-----------------------------------------------------
C [change_entry]
        implicit  real*8 (a-h,o-z)
        COMPLEX*16 phi,em,ay,ref,x0,ak1,ak2,rho2,arg,hank,j
c       complex*16 hbar,cbar,mbar,gb,kbbar,zfast,zshe
        complex*16 complem,kf,vee
        COMMON /blk2/hs,hr,ran,theta,r1,r2
        COMMON/blk3/ay,em,ak1,ak2,j
        j=(0.0,1.0)
        pi=4*atan(1.0)
        RHO1=1.204
c       Read Input
        read(2,*) sigma
        read(2,*)omeg
        read(2,*)enp
        read(2,*)sp
c       Enables use of soair to find prop consts
c       read(2,*)vp
c       read(2,*)vs
c       read(2,*)ratp
```

```
c       read(2,*)rats
c       read(2,*)aks
c       read(2,*)rhob
        read(2,*)hs
        read(2,*)hr
        read(2,*)ranbot
        read(2,*)rantop
        read(2,*)iran
        if(iran.ne.1) dran=(rantop-ranbot)/(iran-1)
        read(2,*)freqbot
        read(2,*)freqtop
        read(2,*)ifreq
        if (ifreq.ne.1) dfreq=(freqtop-freqbot)/(ifreq-1)
c       if(iran.eq.1) goto 3
        do 20 i=1,iran
3       ran=ranbot+(i-1)*dran
c       if (ifreq.eq.1) goto 5
        do 30 k=1,ifreq
5       freq=freqbot+(k-1)*dfreq
c
c       gb=vs*vs*rhob
c       kbbar=vp*vp*rhob-4/3*gb
        r1=dsqrt((hs-hr)*(hs-hr)+ran*ran)
        r2=dsqrt((hs+hr)*(hs+hr)+ran*ran)
c                                                   common blks used
c       Calculate propagation constants
c       call soair(freq,ak2,zfast,zshe)
        call prop(freq,ak1)
        aq=0.0
        call PCALL(freq,aq,q2,enp,sp,sigma,omeg,ak2)
c       Calc complex density
        call cdall(freq,aq,q2,enp,sp,sigma,omeg,rho2)
c
c       Another bit
        call ayandem(rho1,rho2)
c       Calculate angle of specular reflection              2
        call thet1(theta)
c       Calculate refn coefficient                          3
        call refn(ref,theta)
c       print*,ref
c       another bit                                         2,3
        call ex0(x0)
c       error function calculation using subroutine 'w'
        call w(x0,complem)
c       Argument for Hankel Function                        2,3
        call argu(arg)
```

```
c       Hankel function
        call h01(arg,hank)
c       Adds second correction term                              3
        call vdash(vee,co,si)
c       Final calculation of phi
        phi=ak1*ay/(4*(1-em**2))
        phi=phi*complem
        phi=phi*hank*cdexp(-j*arg)*cdexp(j*ak1*r2)
        phi=-phi
        phi=phi+cdexp(j*ak1*r1)/(4*pi*r1)
        phi=phi+ref*cdexp(j*ak1*r2)/(4*pi*r2)
        phi=phi+vee
        out=20*dlog10(cdabs(phi))
        out=out-20*dlog10(cdabs(cdexp(j*ak1*r1)/(4*pi*r1)))
        write(10,*) freq,ran,out
30      continue
20      continue
        stop
        END
```

```
      Subroutine prop(freq,ak1)
c     Calcs prop const for air at 20 deg C
      real*8 freq
      complex*16 ak1
      ak1=8*datan(1d0)*freq/343d0
      return
      end

*****************************************************************

      subroutine ayandem(rho1,rho2)
c     Calcs ay and em
      real*8 rho1
      complex*16 ay,em,ak1,ak2,j,rho2
      common/blk3/ay,em,ak1,ak2,j
      em=rho1/rho2
      ay=em*cdsqrt(((ak2/ak1)**2-1)/(1-em*em))
      return
      end

*****************************************************************

      subroutine thet1(theta)
c     calcs specular reflection angle
      real*8 hs,hr,ran,theta
      common/blk2/hs,hr,ran
      theta=datan(ran/(hs+hr))
      return
      end

*****************************************************************

      subroutine refn(ref,theta)
c     calcs reflection coeff
      real*8  theta
      complex*16 ref,a1,ay,em,ak1,ak2,j
      common/blk3/ay,em,ak1,ak2,j
      a1=em*cdsqrt((ak2/ak1)**2-(dsin(theta))**2)
      ref=(dcos(theta)-a1)/(dcos(theta)+a1)
      return
      end

*****************************************************************

      Subroutine vdash(vee,co,si)
```

```
c       Calcs vee correction function
        implicit real*8 (a-h,o-z)
        complex*16 vee,a1,ay,em,ak1,ak2,j,bit,ac,aa,am,apc,f
        common/blk2/hs,hr,ran,theta,r1,r2
        common/blk3/ay,em,ak1,ak2,j
        co=dcos(theta)
        si=dsin(theta)
        call eff(f,si,co)
        ac=1d0+ay*co
        aa=cdsqrt(1d0-ay*ay)*si
        am=dsqrt(2d0)*(1d0-em*em)
        apc=ay+co
        bit=cdsqrt(1d0+(ac/aa))*ay/(am*apc)
        vee=co+em*cdsqrt((ak2/ak1)**2-si*si)
        vee=f*co/vee
        vee=vee+bit*(1/(8*aa)+(ac+aa)/(2*apc*apc))
        vee=vee/(j*ak1*r2)+bit
        vee=vee*cdexp(j*ak1*r2)/(2*3.1415926*r2)
        return
        end

*****************************************************************

        subroutine eff(f,si,co)
c       calculates f in vdash
        implicit real*8 (a-h,o-z)
        complex*16 ay,em,ak1,ak2,j,f,a,en
        common/blk3/ay,em,ak1,ak2,j
        en=cdsqrt((ak2/ak1)**2-si*si)
        a=((si*(en+em*co))/(en*(em*en+co)))**2
        f=em*(co*co*2-si*si*3)/(2*en)
        f=f+co+em*co*co*si*si/(2*en**3)
        f=1-f*co/(si*si)
        f=-1-f*si*si/(co*(co+em*en))+a
        return
        end

*****************************************************************

        subroutine ex0(x0)
        implicit real*8 (a-h,o-z)
        complex*16 x0,ak1,ay,em,ak2,j
        common/blk3/ay,em,ak1,ak2,j
        common/blk2/hs,hr,ran,theta,r1,r2
        x0=cdsqrt(1-ay*ay)*dsin(theta)
        x0=-x0+ay*dcos(theta)+1
```

```
        x0=-j*cdsqrt(x0*j*ak1*r2)
c       x0=cdsqrt(x0*j*ak1*r2)
        return
        end

*****************************************************************

        subroutine argu(arg)
        implicit real*8 (a-h,o-z)
        complex*16 arg,ay,em,ak1,ak2,j
        common/blk3/ay,em,ak1,ak2,j
        common/blk2/hs,hr,ran,theta,r1,r2
        arg=ak1*ran*cdsqrt(1-ay*ay)
        return
        end

*****************************************************************

chx     Calculation of the error function term of the propagation model
chx     s calculated according to the method of Chien and Soroka(1975),(1980)
chx     (JSV 43(1) p9-20 and JSV 69 p340-343).

        subroutine w(z,wiz)
        implicit real*8 (a-h,o-z)
        complex*16 z,wiz,cefw,s,t1,t2,t3
        logical lx,ly
        data cons/1.128379167095e0/
        x=-dimag(z)
        y=dreal(z)
c
        x1=y
        y1=-x
c
c       determine quadrant for z
c
10      lx=x.ge.0.0d0
        ly=y.ge.0.0d0
        if(lx.and.ly)iq=1
        if(.not.lx.and.ly)iq=2
        if(.not.lx.and..not.ly)iq=3
        if(lx.and..not.ly)iq=4
c
c       convert to 1st quadrant
c
        x=dabs(x)
        y=dabs(y)
```

```
      s=dcmplx(x,y)
      xs=x
      ys=y
c
100   if(y.ge.4.29d0.or.x.ge.5.33d0)goto 110
      s=(1.0d0-y/4.29d0)*dsqrt((1.0d0-(x*x)/28.41d0))
      h=1.6d0*s
      h2=2.0d0*h
      ncap=6.5+23.0*s
      alamda=h2**ncap
      nu=9.5+21.0*s
      goto 120
110   t1=4.613135d-1/(s*s-1.901635d-1)
      t2=9.999216d-2/(s*s-1.7844927d0)
      t3=2.883894d-3/(s*s-5.5253437d0)
      wiz=s*(t1+t2+t3)
      v=dreal(wiz)
      u=-dimag(wiz)
      goto 180
120   r1=0.0d0
      r2=0.0d0
      s1=0.0d0
      s2=0.0d0
      n=nu
130   if(n.lt.0)goto 150
      p1=n+1
      t1=y+h+p1*r1
      t2=x-p1*r2
      c=0.5d0/(t1*t1+t2*t2)
      r1=c*t1
      r2=c*t2
      if(h.eq.0.0d0.or.n.gt.ncap)goto 140
      t1=alamda+s1
      s1=r1*t1-r2*s2
      s2=r2*t1+r1*s2
      alamda=alamda/h2
140   n=n-1
      goto 130
150   if(alamda.eq.0.0d0)goto 160
      u=cons*s1
      v=cons*s2
      goto 180
160   u=cons*r1
      v=cons*r2
180   cefw=dcmplx(u,v)
c
```

```
c       test for underflow and overflow
c
        test=-xs*xs+ys*ys
        if(test.lt.-85.0d0)test=-85.0d0
        if(test.gt.87.0d0)test=87.0d0
c test for quadrant
        goto(230,220,210,210),iq
210     cefw=2.0d0*cdexp(dcmplx(test,-2.0d0*xs*ys))-cefw
        if(iq.eq.3)goto 230
        if(iq.eq.4)goto 220
c       for 2nd and 4th quads conjugate cefw
c
220     cefw=dconjg(cefw)
c
c
230     wiz=cefw
        return
        end
```

C.7 Hab

Calculates excess attenuation in an homogeneous fluid halfspace overlying a non-porous backed externally reacting rigid porous layer. Uses the layer potential formulation of Habault and Fillippi [87].

```
C
C PROGRAM DESCRIPTION:
C
C        HAB
C        This program impliments the model for propagation  over an
C        extended reaction layer over a rigid surface  according to the
C       series expansion of the  layer potential representation
C       by Habault+Filippi. Densities and propagation constants according
C       to Attenborough
C
C AUTHORS:
C
C        Steve Tooms
C
C CREATION DATE:        24/1/90
C
C
C            C H A N G E   L O G
C
C       Date     | Name  | Description
C---------------+-------+-------------------------------------------------------
C
        implicit  real*8 (a-h,o-z)
        COMPLEX*16 phi,ak1,ak2,rho2,arg,hank,j,nu
        complex*16 phi1,phi2,litk,bigk,ef,efd,efdd
        COMMON /blk2/hs,hr,ran,theta,r1,r2
        j=(0.0,1.0)
        pi=4*atan(1.0)
        RHO1=1.204
c       Read Input
        read(2,*) sigma
        read(2,*)omeg
        read(2,*)enp
        read(2,*)sp
        read(2,*)d
        read(2,*)hs
        read(2,*)hr
        read(2,*)ranbot
        read(2,*)rantop
        read(2,*)iran
        if(iran.ne.1) dran=(rantop-ranbot)/(iran-1)
        read(2,*)freqbot
        read(2,*)freqtop
        read(2,*)ifreq
        if (ifreq.ne.1) dfreq=(freqtop-freqbot)/(ifreq-1)
c       if(iran.eq.1) goto 3
```

```
      do 20 i=1,iran
3     ran=ranbot+(i-1)*dran
c     if (ifreq.eq.1) goto 5
      do 30 k=1,ifreq
5     freq=freqbot+(k-1)*dfreq
      r1=dsqrt((hs-hr)*(hs-hr)+ran*ran)
      r2=dsqrt((hs+hr)*(hs+hr)+ran*ran)
c                                                  common blks used
c     Calculate propagation constants
      call prop(freq,ak1)
      aq=0.0
      call PCALL(freq,aq,q2,enp,sp,sigma,omeg,ak2)
c     Calc complex density
      call cdall(freq,aq,q2,enp,sp,sigma,omeg,rho2)
c     Calculate angle of specular reflection              2
      call thet1(theta)
c     Find "point admittance"
      call nyoo(ak1,ak2,rho1,rho2,d,nu)
c     Find K and k
      call kay(theta,ak1,ak2,litk,bigk)
c     Find f,f',f''
      call eff(litk,bigk,ak2,d,theta,ef,efd,efdd)
c
      call ter1(theta,ef,nu,phi1)
      call ter2(theta,ef,efd,efdd,ak1,r2,nu,phi2)
      phi=(phi1+phi2)*cdexp(j*ak1*r2)/(4*pi*r2)
c     print*,'phi1+phi2=',phi
      phi=phi+cdexp(j*ak1*r1)/(4*pi*r1)
c     print*,'phi=',phi
      out=20*dlog10(cdabs(phi))
      out=out-20*dlog10(cdabs(cdexp(j*ak1*r1)/(4*pi*r1)))
      write(10,*) freq,ran,out
30    continue
20    continue
      stop
      END
```

```
      Subroutine kay(theta,ak1,ak2,litk,bigk)
c     To calc K and k
      complex*16 ak1,ak2,litk,bigk
      real*8 theta
      litk=ak1/ak2
      bigk=cdsqrt(1-litk*dsin(theta))
      return
      end

*********************************************************************

      Subroutine eff(litk,bigk,ak2,d,theta,ef,efd,efdd)
c     to calc f,f',f''
      implicit real*8 (a-h,o-z)
      complex*16 litk,bigk,ak2,ef,efd,efdd,tanb,tan2
      complex*16 tanbin,tan2in,ctbn2,defdd
      tanbin=bigk*ak2*d
      tan2in=ak2*d
      call comtan(tanbin,tanb)
      call comtan(tan2in,tan2)
      if (cdabs(tanbin).gt.50d0) then
         ctbn2=(1d35,5d34)
      else
         ctbn2=(cdcos(tanbin))**2
      end if
      tt=2*theta
      ef=bigk*tanb/tan2
      efd=(tanb+tanbin/(ctbn2))
      efdd=efd
      efd=-efd*(litk*litk*dsin(tt)/(2*bigk*tan2))
      efdd=efdd*(dcos(tt)+litk*litk*(dsin(tt))**2/(4*bigk*bigk))
      defdd=litk*litk*ak2*d*((dsin(tt))**2)/(2*ctbn2)
      defdd=defdd*(1/bigk+ak2*d*tanb)
      efdd=efdd-defdd
      efdd=-(litk*litk/(bigk*tan2))*efdd
      return
      end

*********************************************************************

      Subroutine ter1(theta,ef,nyoo,phi1)
      real*8 theta
      complex*16 ef,nyoo,phi1
      phi1=nyoo*dcos(theta)
      phi1=(phi1-ef)/(phi1+ef)
      return
```

```
      end

*********************************************************************

      Subroutine ter2(theta,ef,efd,efdd,ak1,r2,nyoo,phi2)
      complex*16 ef,efd,efdd,ak1,nyoo,phi2,dphi2,i
      real*8 theta,r2
      i=(0d0,1d0)
      phi2=(2*ef+(efd/dtan(theta))+efdd)
      phi2=phi2*2*nyoo*dcos(theta)/((nyoo*dcos(theta)+f)**2)
      dphi2=ef*dsin(theta)+efd*dcos(theta)
      dphi2=dphi2*(nyoo*dsin(theta)-efd)*4*nyoo
      dphi2=dphi2/((nyoo*dcos(theta)+f)**3)
      phi2=i*(phi2+dphi2)/(2*ak1*r2)
      return
      end

*********************************************************************

      Subroutine nyoo(ak1,ak2,rho1,rho2,d,nu)
      real*8 rho1,d
      complex*16 ak1,ak2,rho2,nu,i,zed,coth
      i=(0d0,1d0)
      zed=ak1*rho2/(ak2*rho1)
      i=ak2*d
c     i=i*ak2*d
      call ccoth(i,coth)
      nu=zed*coth
c     nu=1/nu
      return
      end

*********************************************************************

      Subroutine prop(freq,ak1)
c     Calcs prop const for air at 20 deg C
      real*8 freq
      complex*16 ak1
      ak1=8*datan(1d0)*freq/343d0
      return
      end

*********************************************************************


      subroutine thet1(theta)
```

```
c       calcs specular reflection angle
        real*8 hs,hr,ran,theta
        common/blk2/hs,hr,ran
        theta=datan(ran/(hs+hr))
        return
        end

*****************************************************************


chx function to calculate tangent of complex argument
c
        Subroutine comtan(z,ctan)
        complex*16 z,ctan
        if (cdabs(z).ge.50d0) then
            ctan=(1d34,1d34)
        else
            ctan=cdsin(z)/cdcos(z)
        end if
        return
        end
```

C.8 Pulse impedance programs

These three programs; sum, imp, and pulse, are used to calculate normal surface impedance from direct and reflected pulses,using Crammond and Don's method [109].

```
c   Program SUM
c             shifts and sums pulse files
c
c  Input number of files to be added. Produces a single
c  file of length 512 points, with pulse at 50 and beginning
c  and end set to zero.
c
c  A second file of only 499 points is also produced for use
c  with unigraph if desired.
c
c  There is an option for including a "prepulse" in the sum file.
c
DIMENSION A(2000),T(2000),B(1000)
CHARACTER CAT$*10,DOG$*15,Z1$*15,Z2$*15,Z3$*15,Z4$*15
CHARACTER DAG$*15,CA$*5

nn=1
print*, 'input number of files to be processed'
read(5,71) nm
print*,' do you want any prepulse ? type 1 for yes, 3 for no'
read(5,71) nll
c initially zero sum file
do 88 i=1,512
t(i)=0.
88  continue
c adjustment and summation loop
do 101 ll=1,nm
print*, 'input file name (no "a.dat") '
read(5,70) ca$
if(nn.gt.1) goto 99
dog$=ca$//'s'//'.dat'
dag$=ca$//'p'//'.dat'
open(2,file=dog$,status='unknown')
open(3,file=dag$,status='unknown')
99  continue
nn=nn+1
cat$=ca$//'a.dat'
open(1,file=cat$,status='unknown')
do 5 i=1,499
read (1,*)zz,a(i)
5 continue
c adjust pulse so starts at 50th data word
print*,' start of pulse is ?  (dont forget decimal point)'
read(5,72) p1
```

```
if(nll.gt.1) then
p2=p1
else
print*,' zero input up to ?'
read(5,72) p2
endif
do 80 i=1,512
b(i)=0.
80 continue
d=p1-p2
do 82 i=1,400+d
b(i+49-d)=a(i+p2-1)
82 continue
c makes tail of pulse come to zero smoothly
do 83 i=1,162
b(i+350)=b(I+350)*(1.-(I/112.))**2
83 continue
c sums pulses
do 85 i=1,512
t(i)=t(i)+b(i)
85 continue
c
101 continue
c puts an average pulse into file
do 60 i=1,512
zz=real(i)
write(2,*) zz,t(i)/nm
60 continue
do 61 i=1,499
write(3,*) t(i)/nm
61 continue
write(6,75) dog$,dag$
c
70 format(a)
71 format(i200)
72 format(f12.2)
73 format(i4,f12.5)
74 format(e15.10)
75 format(' data stored in ',a,' for calc., in ',a,' for viewing')
76 format(' pulse end = ',$)
78 format(2e12.4)
79 format(f12.2,i6,2f12.2)
end
c
```

```
c    Program IMP
c    to   calculate impedance from two pulse waveforms
c
c  assumes pulses already conditioned -using "sum" program
c
c  may require a calibration file giving the ratio, in freq.domain,
c   of reflected/direct mikes receiving identical pulses.
c
c  The rp file may be used as a cal file if two "directs" are
c                       used as the input.
c
c
character dir$*8,ref$*8,rp$*17,imp$*17,cal$*23
complex*16 at(1024),bt(1024),cx(1024),rp(512),z(512),calib(512)
dimension a(1024),b(1024)
REAL*8 signi
c
c  geometry of measuring system
print*,' input source receiver distance'
read(5,74)d
print*,' input source height (assumed same as rec. height)'
read(5,74)hs
hr=hs
hyp=sqrt(d*d+(hr+hs)*(hr+hs))
s=(hr+hs)/hyp
c
c  input direct (a) and reflected (b) pulses
c
print*,' input direct file name (no ".dat")'
read(5,70) dir$
print*,' input reflected file name (no ".dat")'
read(5,70) ref$
print*,' if want to have cal. file input 1, else input 3'
read(5,73) mm
if (mm.gt.1) goto 32
print*,' input mic. calibration file name (n0 ".dat")'
read(5,70) cal$
cal$=cal$//'.dat'
32 imp$=dir$//'imp.dat'
rp$=dir$//'rp.dat'
dir$=dir$//'.dat'
ref$=ref$//'.dat'
open(1,file=dir$,status='unknown')
open(2,file=ref$,status='unknown')
open(3,file=imp$,status='unknown')
open(4,file=rp$,status='unknown')
```

```
open(8,file=cal$,status='unknown')
c
nb=1024
lx=1024
do 10 i=1,512
read(1,*) zz,a(i)
read(2,*) zx,b(i)
if (mm.gt.1) then
calib(i)=(1.,0.)
else
if (i.lt.100) then
read(8,*) calib(i)
else
calib(i)=(1.,0.)
endif
endif
10      continue
c
c   perform fourier transform on waveforms
c
signi=1d0
do 20 i=1,512
cx(i)=dcmplx(a(i),0.)
cx(i+512)=(0.,0.)
20      continue
call fork(lx,cx,signi)
do 30 i=1,512
at(i)=cx(i)
cx(i)=dcmplx(b(i),0.)
cx(i+512)=(0.0,0.0)
30      continue
call fork(lx,cx,signi)
c
c  calculate impedance values
do 40 i=2,100
c write(6,*)i,cx(i)
rp(i)=cx(i)/(at(i)*calib(i))
z(i)=dconjg(1./(s*(1-rp(i))/(1+rp(i))))
f=250.*(i-1)
write(3,78) f, z(i)
write(4,79) rp(i)
40      continue
write(6,76) imp$,rp$
do 42 i=2,5
write(6,75) rp(i),z(i)
42 continue
```

```
c
70 format(a)
73 format(i5)
74 format(f12.4)
75 format(4f10.2)
76 format( 'imp data stored in ',a,' while rp (IE. cal) in ',a)
78 format(f7.1,2f8.3)
79 format(2f8.3)
end
c
c

        subroutine fork(lx,cx,signi)
c
c  fft as given by j.f.claerbout, "fundamentals of geophysical
c  data processing" PAGE 12.
c
c cx(lx) : the variable being processed
c lx     : a whole power of two
c
c
implicit real*8(A-H,O-Z)
complex*16 cx(lx),carg,cw,ctemp
ccc        complex cx(512),carg,cw,ctemp
d type *, 'fork: lx=', lx, '  signi=', signi
PI= 2*DASIN(1D0)
c write(6,*)lx,cx(1)
        j=1
        sc=Dsqrt(1D0/lx)
        do 30 i=1,lx
        if(i.gt.j)go to 10
        ctemp=cx(j)*sc
        cx(j)=cx(i)*sc
        cx(i)=ctemp
   10       m=lx/2
   20       if(j.le.m)go to 30
        j=j-m
        m=m/2
        if(m.ge.1)go to 20
   30       j=j+m
        l=1
   40       istep=2*l
        do 50 m=1,l
        carg=(0D0,1D0)*(PI*signi*(m-1))/l
        cw=cDexp(carg)
        do 50 i=m,lx,istep
```

```
      ctemp=cw*cx(i+1)
      cx(i+1)=cx(i)-ctemp
50          cx(i)=cx(i)+ctemp
      l=istep
      if(l.lt.lx)go to 40
      return
      end
```

```
c     Program PULSE
c             modifies pulse files
c
c  Input number of files to be processed. A time file is
c  created and a set of pulse only files are created from
c  combined time/pulse files.
c
c
c
dimension a(2000),t(2000)
character cat$*10,dog$*15,z1$*15,z2$*15,z3$*15,z4$*15
character tim$*15,ca$*2,fred$*2,bin$*6,fre$*3

print*, 'input number of files to be processed'
read(5,71) nm
print*, 'input first two letters of reqd. output file'
read(5,70)ca$
print*, 'input starting integer of reqd. output file'
read(5,71)nan
print*, 'input starting part of input file'
read(5,70)bin$
do 101 ll=1,nm
print*, 'input file number (no start or ".dat") '
read(5,71) nib
write(fre$,98)nib
cat$=bin$//fre$
write(fred$,81)nan+ll-1
dog$=ca$//fred$//'a'//'.dat'
cat$=cat$//'.dat'
open(1,file=cat$,status='unknown')
open(2,file=dog$,status='unknown')
read(1,72)z1$,z2$,z3$,z4$

do 5 i=1,512
read (1,74)t(i),a(i)
a(i)=a(i)*1000.
5 continue
do 80 i=2,500
w=(a(i)-a(15))*(a(i)-a(15))
if (w.gt.250000.) goto 85
80 continue
85 continue
do 82 j=1,20
write(6,79) a(i+j-29),i+j-10,a(i+j-10),a(i+j+11)
```

```
82 continue
print*,'start of pulse is ?'
write(6,75) cat$,dog$
c
do 60 i=1,499
zz=real(i)
write(2,*) zz,a(i)
60 continue
101 continue
c
70 format(a)
71 format(i20)
72 format(2a,/,2a)
74 format(2e15.10)
75 format(' this file is ',a,' stored as file ',a)
76 format(i3,f12.5)
78 format(2e12.4)
79 format(f12.2,i6,2f12.2)
81 format(i2)
98 format(i3)
end
c
```